2-P
MIX

jpl

JET PROPULSION LABORATORY

CALIFORNIA INSTITUTE OF TECHNOLOGY

PASADENA, CALIFORNIA

FACILITY FORM 602

N70-23470
(ACCESSION NUMBER)

588
(PAGES)

CR# 109338
(NASA CR OR TMX OR AD NUMBER)

(THRU)

/

(CODE)

31
(CATEGORY)

SOLAR ELECTRIC PROPULSION
ASTEROID BELT MISSION STUDY
FINAL REPORT

VOLUME II
TECHNICAL REPORT

SD 70-21-2

CONTRACT 952566

January 1970

This work was performed for the Jet Propulsion Laboratory, California
Institute of Technology, as sponsored by the National Aeronautics and
Space Administration under Contract NAS7-100.

Prepared by

SPACE DIVISION
NORTH AMERICAN ROCKWELL CORPORATION
DOWNEY, CALIFORNIA

Prepared by:

E. H. Richardson, Project Engineer

Approved by:

L. E. Schwaiger, Study Manager
Unmanned Space Systems

Space Division
North American Rockwell

PRECEDING PAGE BLANK NOT FILMED.

- iii -

FOREWORD

This Technical Report is Volume II of the final documentation of the Solar Electric Propulsion Asteroid Belt Mission Study. The complete final documentation consists of three volumes:

Volume I   General Summary Report, SD 70-21-1   *14824*

Volume II   Technical Report, SD 70-21-2

Volume III Program Development Plan,   *14853*
            SD 70-21-3

The study was conducted by the Space Division of North American Rockwell Corporation. The Research Laboratory of Hughes Aircraft Company participated as subcontractor in the areas of electric propulsion system and low-thrust trajectory analysis. The study was performed for the Jet Propulsion Laboratory, California Institute of Technology, under JPL Contract Number 952566.

ACKNOWLEDGEMENTS

ABSTRACT

This three volume report presents the final study results of an asteroid belt mission using a solar electric propulsion spacecraft. The asteroid belt, located between the orbits of Mars and Jupiter, is of major scientific interest; its potential hazards to spacecraft are of major concern.

The solar electric propulsion system described in this study is based on roll-up type solar cell arrays, mercury electron bombardment ion thrusters, and associated power conditioning and control units.

Mission and system analyses are presented that show the rationale for selecting a 3.5-AU aphelion trajectory, a 7.8-kilowatt electric propulsion system with specific impulse of 3500 seconds, and an Atlas/Centaur to launch the electric propulsion spacecraft. Results of spacecraft design studies show the configuration trade-offs and subsystem design analysis leading to a 1600-pound recommended electric propulsion spacecraft concept capable of accommodating more than 750 feet^2 of particle-penetration detectors. The program development plan describes an orderly plan of activities for the development and delivery of one or two flight qualified spacecraft and the associated cost estimate of $74.5 million for two spacecraft to be launched in 1975.

Space Division
North American Rockwell

CONTENTS

ILLUSTRATIONS

Figure   Page

TABLES

1. INTRODUCTION

This Technical Report is the second of three volumes documenting the results of a solar electric propulsion asteroid belt mission study. Mission and systems analyses were performed providing the background, system philosophy, mission trajectory selection, and rationale for the selected system design. A detailed spacecraft design analysis is presented with discussions of performance limitations and flexibility to perform alternate missions: solar probe, out-of-the-ecliptic, and asteroid intercept.

Before this study, few attempts have been made to assess in detail the applicability of using solar electric propulsion for the prime thrust source. This study attempted to identify those problems associated with the integration of electric propulsion with required science and spacecraft systems to accomplish an asteroid belt probe mission.

A spacecraft conceptual design was synthesized identifying in detail subsystem designs, interface (and interference) problems and recommended design solutions. Spacecraft design mechanization was evaluated for a variety of solar power levels and two launch vehicles, Atlas/Centaur and Titan IIIC.

The two major study objectives were: to provide valuable scientific and engineering data about the environment and potential hazards of the asteroid belt region, and to demonstrate for the first time the applicability and readiness of solar electric ion propulsion as a prime propulsion source for an unmanned interplanetary exploration spacecraft. In keeping with the major mission objectives, the study program adopted the following as its major goals:

1. The establishment of a meaningful and effective Asteroid Belt Survey mission concept

2. The development of a minimum cost solar electric propulsion spacecraft design and subsystems selection and design compatible with the selected mission concept

3. The formulation of a viable program development plan to enable the implementation of the SEP asteroid belt mission program, and

4. The generation of the program cost elements for the budgetary and planning considerations necessary to undertake such a program

One of the major milestones planned in the progression of the study was the establishment of the baseline system parameters; solar array power level, ion engine system specific impulse, and launch vehicle selection. These parameters were of primary importance in their ability to progress with the spacecraft and electric propulsion system design activities. Based on trajectory analyses and science payload requirements studies performed during the initial phase of the study, an input power level of 7.8 kilowatts to the propulsion system at 1.0 AU was selected. A total spacecraft power of 10.0 kilowatts before any degradation resulted in the recommended configuration. The ion thruster specific impulse was established at 3500 seconds and the Atlas/Centaur launch vehicle was selected. The detailed spacecraft design, electric propulsion system design, and spacecraft subsystem analyses and definition activities were implemented for these baseline parameters. The major contents of this report are the products of these activities. Section 2.0, Mission Analyses, and Section 3.0, Systems Analysis and Design Concept Selection, provide the background, system philosophy, trajectory parameters, and rationale for the subsequent system design and analyses effort contained in the design, science payload, and subsystem sections.

2. MISSION ANALYSIS

In this section the selected Asteroid Belt Mission is defined. The mission objectives and requirements, trajectory and performance analysis, guidance analysis, and selected mission timeline and sequence of events are presented. Selection of the mission trajectory is influenced by the science measurement requirements, knowledge of the natural environment, and launch vehicle performance.

The mission objectives are reduced to scientific and engineering knowledge requirements. These knowledge requirements lead to the more specific requirements imposed on the mission trajectory. Knowledge (or lack of) on the space environment is a key factor in influencing the selection of the trajectory profile; aphelion, and thrust program.

The optimum mission concept (from viewpoint of science) is rarely achieved in practice as launch vehicle and spacecraft propulsion limits mission performance. A parametric performance analysis was conducted to identify the influence of trajectory parameters on spacecraft payload using both Atlas/Centaur and Titan III C launch vehicles. Influence of selected aphelion, heliocentric distance at SEP thrust cutoff, thrust time, and SEP parameters (I_{sp}, power level, thrust orientation) on the net payload mass is determined.

A guidance analysis was conducted to determine the guidance require- ments for the "area" target asteroid belt mission. Effects of initial trajectory conditions (heliocentric injection errors) and in-flight random acceleration (thrust control errors) are defined. Guidance correction and associated penalty are determined using two basic concepts for trajectory position error control. Velocity requirements using impulse ΔV corrections at specified mission times and an adaptive guidance approach in which trajectory errors are controlled through thrust augmentation of the SEP system.

A mission timeline and sequence of events is presented for the selected mission concept. These data were used as the basis for generating the subsystem performance requirements: operating times, power profile, and maneuvers.

MISSION REQUIREMENTS

Mission Objectives

The solar electric propulsion asteroid belt mission to be launched in 1975 represents the first mission opportunity fully devoted to obtaining data on the space environment beyond the orbit of Mars through the asteroid belt. In 1972 and 1973, Pioneers F and G, respectively, will be launched with the primary intent of investigating the environments of Jupiter. Only a small portion of the payload is applied to the determination of the asteroid belt region space environment (cometary and asteroidal). Although data obtained from Pioneers F and G will further the understanding of the asteroid belt region, little statistical significance can be realized. The primary objective of the solar electric propulsion asteroid belt is to obtain meaningful scientific and engineering data on the space environment in the egion of the asteroid belt.

The Space Science Board of the National Academy of Sciences has defined the scientific problem areas facing the planetary exploration program to be; to improve our understanding of the origin and evolution of life, of the universe, and of the solar system; and to improve our understanding of dynamic processes which affect terrestrial environments. In a series of reports culminating in Reference 2-1, the Space Science Board has related these broad scientific problems to more precisely defined knowledge requirements appropriate to exploration of the outer planets and of interplanetary space at great distances from the sun. The knowledge requirements appropriate to missions in the asteroid belt are to determine the origin of asteroids and comets, and to investigate interactions between the solar wind and magnetic field, galactic plasmas and fields, and energetic charged particles of solar and galactic origin.

Meteoroid Measurement Objectives

The main competing theories as to the origin of most asteroids are the accretion and disruption theories. The accretion theory holds that the asteroids were formed in nearly the present physical state and size distribution by mutual adhesion of relatively small particles or by the condensation of gaseous materials from very small planetesimals, without formation at any time of a major planetary body in either the gaseous solid phase. The disruption theory, on the other hand, holds that a body approaching the dimensions of one of the inner planets was formed by condensation from the primordial solar nebula, and was then broken into fragments by the gravitational attraction of a heavy object passing through the solar system, by gravitational instability resulting from Jupiter, or by collision.

Similarly, there are two principal competing theories as to the origin of comets. One theory holds that the sun is surrounded to distances as

great as one light year by a swarm of photo-comets, and that the random
motion of the latter or gravitational pertubations due to the outer planets
occasionally cause a proto-comet to leave the swarm, enter the solar
system and appear in the form which we call a comet. Another theory
(Reference 2-2) holds that the cometary material exists in interstellar space
in the form of plasma clouds originally emitted from stars, including plasma
clouds originating in solar flares and prominences. The galactic wind
forces these plasma clouds into the vicinity of the sun where gravitational
attraction of the outer planets is capable of capturing them into highly
eccentric solar orbits.

Convincing answers to the above questions must await close inspection,
and possibly in situ chemical analysis, of asteroidal and cometary bodies.
Nevertheless, measurements of the number versus mass distribution of
asteroidal and cometary meteoroids as a function of solar distance will
contribute greatly to the ultimate answers. Correlation of mass and bright-
ness data (giving inferred size) will enable estimates of the particle density
to be made. Thus it may be possible to determine the nature of particle
composition: metallic, chondritic, or hydrogenous. Knowledge of particle
composition is of major value to the determination of the origin of asteroids
and comets.

The meteoroid environment is of engineering importance because of
the hazard which it represents to spacecraft, especially those passing into
or through the asteroid belt. Even very small meteoroids, those with
masses of 10^{-9} grams or less, can erode exposed spacecraft surfaces.
This effect may be particularly important in the case of solar cell covers,
thermal protective coatings, and exposed optical surfaces such as star
tracker lenses. Meteoroids at masses of 10^{-6} grams and up can penetrate
typical thin spacecraft structures such as fuel tanks. Finally, the
occasional large particles at masses of several milligrams and above, may
cause catastrophic damage to the spacecraft in a single collision.
Catastrophic collisions, although quite unlikely on the basis of any rea-
sonable present model of meteoroid spacial density versus size distribution,
are impossible to predict with any accuracy on a statistical basis. The
aspect of the meteoroid environment of greatest engineering importance is,
therefore, the number flux of particles at masses of the order of 10^{-6} to
10^{-9}. Better definition of this environment will allow a more precise
definition of the requirements for protective shielding to reduce the
probability of penetration to an acceptable level.

Particle and Field Measurement Objectives

As distance from the sun increases, the solar wind density and plasma temperature decrease. The normal solar magnetic field also becomes weaker and assumes a direction increasingly tangential to the sun. With increasing solar distance, high energy proton radiation associated with solar flares becomes weaker in both flux and in integral flux over a given solar flare event. The correlation of charged particle radiation with specific solar events also becomes more and more difficult because of the twisting of the magnetic lines of force about the sun and the spread in proton propagation times from the chromosphere to large solar distances (Reference 2-3 and 2-4). Galactic charged particles of lower and lower energies can be detected as the solar distance increases because of the progressive weakening of the solar magnetic fields. The energy density of the solar magnetic field and the solar wind plasma eventually becomes comparable to the energy density of galactic fields and plasmas. Thus it is expected that a region exists where the heliosphere (the region dominated by solar particles and fields) merges into the interstellar medium. This transition region is expected to occur at solar distances at 10 AU or more.

Interplanetary charged particle and field environments have been established with considerable precision at 1 AU from numerous Explorer and Pioneer spacecraft missions. They have also been determined in reasonable detail at solar distances from 0.7 to 1.5 AU as a result of the Mariner experiments. Particle and field instrumentation on the Pioneer F and G missions planned for 1972 and 1973, respectively, will extend the results out to 5 AU. Including particle and field measurements on the solar electric propulsion asteroid belt mission would seem at first merely to duplicate the Pioneer F and G experiments, which is not true. The Pioneer F and G spacecraft will be launched during a declining period of solar activity, when a small but appreciable background of solar energetic charged particles may be expected at distances from 2 to 3.5 AU. On the other hand, the solar electric spacecraft will be in the early state of its outbound trajectory at the minimum of solar activity between sunspot number cycles 20 to 21 (see Figure 2-1). This time period is optimum for the penetration of low energy galactic charged particles in the solar system to a given heliocentric distance. As seen from Figure 2.1 this condition will be investigated simultaneously at 2 to 3 AU by the solar electric spacecraft and at 5 AU by Pioneer G.

The solar electric spacecraft will still be operating in the 1977 to 1979 time period, during the rising portion of solar activity cycle 21, affording numerous opportunities to observe the directionality of solar flare protons at distances from 2 to 3 AU from the sun. Because the solar electric spacecraft returns to the inner solar system from its aphelion at

JUPITER

1974-5

PIONEER .

1973-4

3.5 AU

1977

SEP

2 AU

1975

1972-3

1979

EARTH

SUN
QUIET 1974 - 76
ACTIVE 1978 - 81
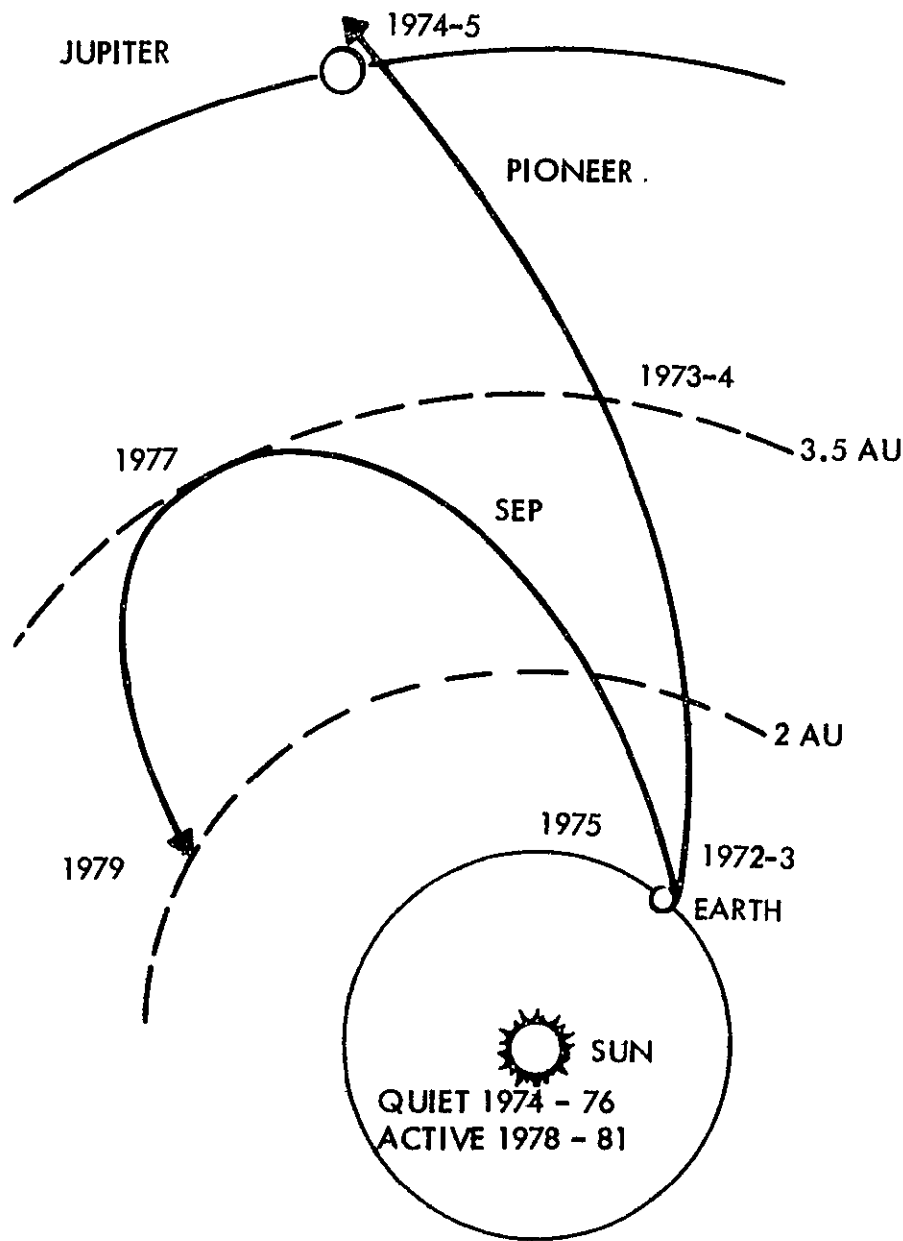
PIONEER F&G

JUPITER DATA
ENVIRONMENTS TO 5 AU
LOW ENERGY GALACTIC
 PROTONS AT SOLAR
 MINIMUM, 3.5 - 5 AU
≈220 DAYS AT 2 - 3.5 AU

SEP ASTEROID BELT

EMPHASIS ON METEOROIDS
 (1000 DAYS AT 2 - 3.5 AU)
LOW ENERGY GALACTIC
 PROTONS AT SOLAR MINIMUM,
 2 - 3 AU
SOLAR PARTICLES & FIELDS
 AT SOLAR MAXIMUM, 2 - 3 AU

Figure 2-1. Solar Electric Propulsion Versus Pioneer F and G Missions

3.5 AU, the solar wind flux versus solar distance and the propagation velocity of local concentrations of solar plasma can be measured at two different levels of solar activity. The same remark applies to measurements of the strength and direction of the solar magnetic field. In addition, some inference of the direction and strength of the galactic magnetic field may be drawn from observing anisotropies in the flux of medium energy galactic protons. All of these observations will be reinforced by similar experiments on interplanetary monitoring probe (IMP) type spacecraft in heliocentric orbits near 1 AU.

From an engineering standpoint, the radiation environmental aspects of greatest importance are: energetic protons and other charged particles capable of damaging sensitive components such as semiconductors and thinly shielded solar cells; and the combined effects of solar wind protons and ultraviolet on the degradation of the optical and thermal properties of spacecraft surface materials including thermal coatings. Since these environments are less severe at 2 to 3.5 AU than at 1 AU, the engineering measurement requirements in the particle and fields area are not of paramount importance (Reference 2-5).

Summary of Mission Objectives

The asteroid belt mission measurement objectives include two categories, scientific and engineering. The scientific measurements data will be used to: develop further the theories on the origin and evolution of the asteroidal and cometary particles; and obtain a better understanding of the radiation environment in space. Engineering measurements data will be used to define the space hazard to spacecraft: surface erosion, penetration, catastrophic collision by particles, component damage from energetic proton flux and damage to thermal coating (long lifetime) from solar wind and ultraviolet radiation.

Measurements necessary to support these mission objectives include the following:

Meteoroid Environment

Spacecraft Hazard   spatial distribution

mass distribution

velocity distribution

penetration rates

physical properties (inferred)

Science   spatial distribution

                            mass distribution

                            velocity distribution

                            physical properties

Particle and Field Environment

Science and
   Spacecraft Hazard   solar magnetic field intensity

                            solar flare radiation

                            high energv charged particle flux

Mission Environment Models

Since the primary intent of the mission is to provide data on the space
environment (meteoroidal radiation), the selection of trajectory and science
sensors is dictated by the anticipated environment. The sensor size,
sensitivity, orientation, location in the spacecraft and the spacecraft design
are critically dependent upon the environment models used. Selection of
the trajectory aphelion is based on obtaining maximum information.
Clearly it may be realized that mission success is dependent upon the
spacecraft encountering the environment that it was designed and intended
to investigate.

Meteoroid Environment Model

The meteoroid environment model used for this study is from
Reference 2-6. Both asteroidal and cometary particle models are defined.
The asteroidal model is defined as:

$$\log_{10} S_a = -15.79 - 0.84 \log_{10} m + f(R)$$

where S_a is the number of asteroids of mass(m) in grams and larger at a
distance R (in AU) from the sun per cubic meter. f(R) is a function based
on distribution of equal size particles versus distance from the Sun.

2-7

Values of the particle distribution function f(R) for use in the equation are given in Figure 2-2.

The cometary model is defined by:

$$\log_{10} S_c = -18.264 - 1.207 \log_{10} m - 1.5 \log_{10} R$$

$$(10^{-6} \leq m \leq 10^{2})$$

and,

$$\log_{10} S_c = -18.273 - 1.584 \log_{10} m - 0.063$$

$$(\log_{10} m)^{2} - 1.5 \log_{10} R$$

$$(10^{-12} \leq m \leq 10^{-6})$$

where S_c is the number of cometary meteoroids of mass (m) in grams and larger at a distance R (in AU) from the sun per cubic meter.

Solar Radiation Model (Power Expression)

The solar energy available as a function of distance from the sun, as used for this study, is given by

$$P = \frac{P_o \Sigma a_i R^{\frac{i}{2}}}{R^2 \Sigma a_i} \qquad i = 0, 1, 2, 3, 4$$

$$a_0 = -38.6773$$

$$a_1 = 363.8135$$

$$a_2 = -381.5077$$

$$a_3 = 104.7369$$

$$a_4 = 0$$

where

P is power at R

P_o is power at earth distance, 0.10085 kilowatts per square meter

R is solar distance in AU
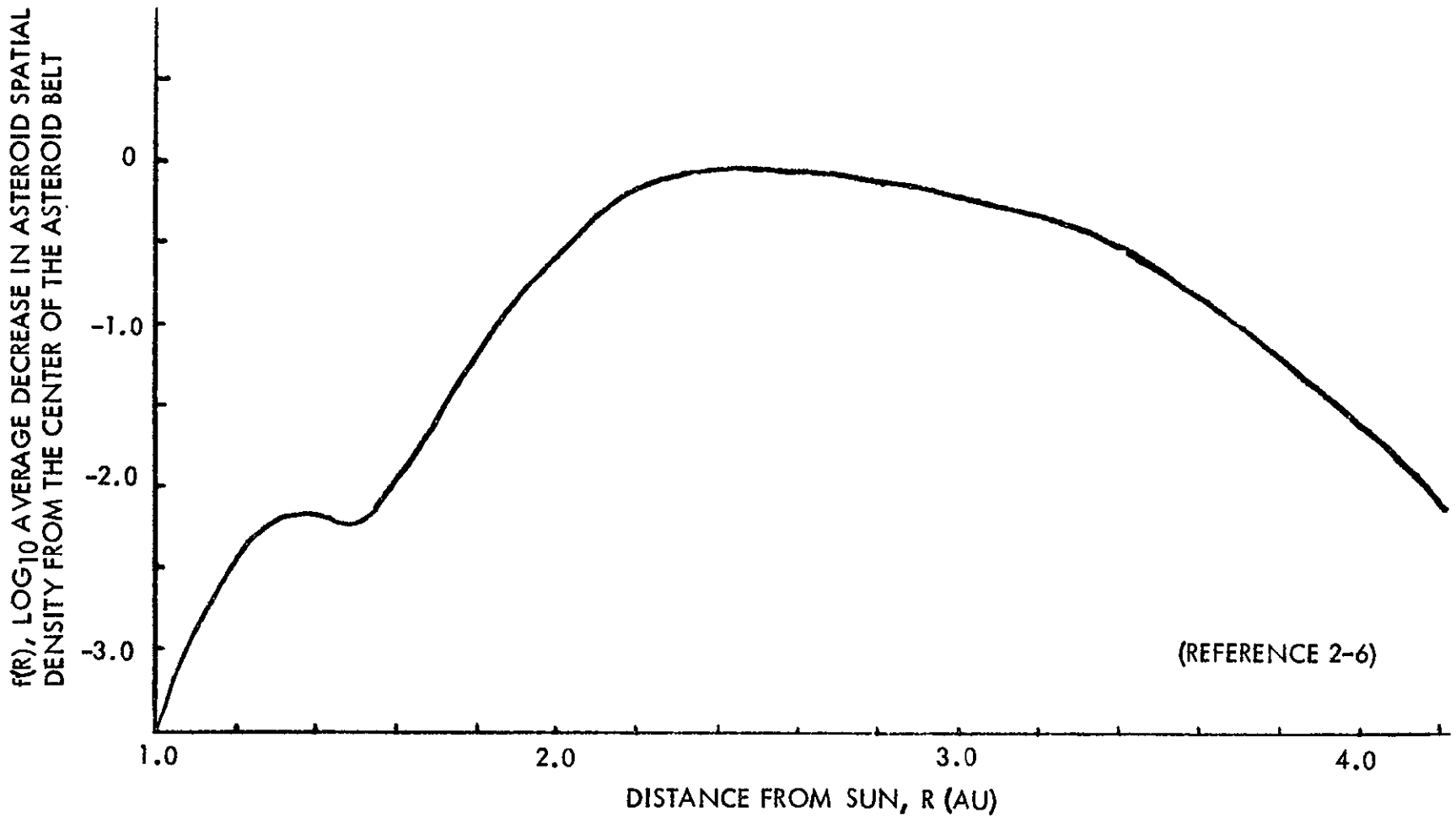
Figure 2-2. Asteroid Radial Distribution

A 15 percent degradation factor for radiation damage to solar cells is to be included as specified in JPL study contract work statement. Micro-meteoroid damage is determined in Section 12 and Appendix A for which P/P_o must be corrected.

Mission Trajectory Requirements

From the mission engineering and science viewpoint the requirement exists to select an optimum trajectory which will provide a maximum encounter of meteoroids. The number of asteroids encountered is depedent . upon the length of stay in the region of interest and the average encounter rate.

The length of stay in a particular region of space is determined by the ephemeris of the orbit, aphelion, perihelion and ellipticity. Assuming that the electrical propulsion system has completed thrusting, then the orbit during coast is Keplerian.

Based on the meteoroid environment model, Figure 2-2, it may be seen that the anticipated asteroid flux density increases rapidly from 2.0 AU to a peak around 2.5 and then trails off more gradually until at 3.6 AU, the flux is approximately equal to that at 2.0 AU.

Four SEP trajectories with aphelions ranging from 3.0 to 4.5 AU were investigated to determine the influence of trajectory aphelion on total asteroid encounter during passage through the asteroid belt. A constant area of exposure, surface area normal to the angle of incidence (asteroid impact direction), was assumed. The asteroids were assumed in circular orbit with a velocity

$$V_a = \sqrt{\frac{\mu}{R}}$$

where

μ is the solar gravitational constant

R is solar distance from the Sun

Figure 2-3 shows the results of this analysis. The encounter dependency is normalized so that it does not become dependent upon the absolute value of the environment model used. From Figure 2-3 it is clear that a trajectory aphelion of 3.5 AU is the best choice, but the curve in Figure 2-3 has a fairly flat peak. At aphelion of 3.45 and 3.55 AU, the loss of data from the maximum at 3.5 AU is 2 percent or less. Hence it is it is concluded that although 3.5 AU aphelion is most desirable, no stringent requirements exist for the precise aphelion selection.
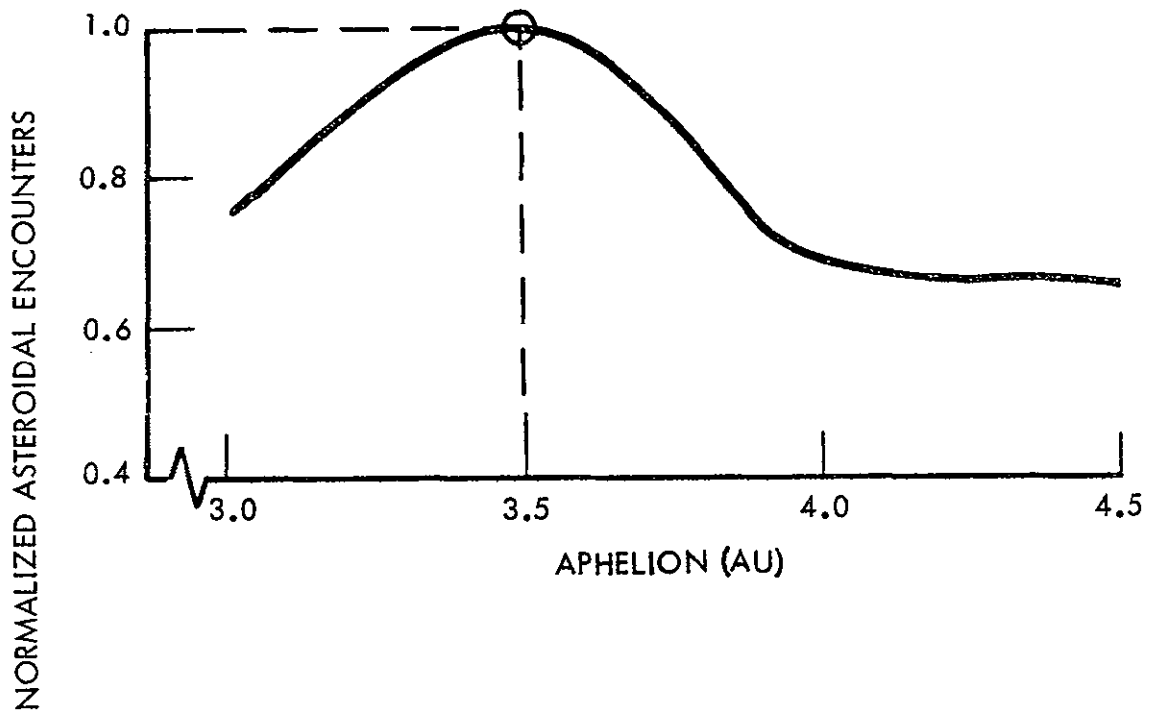
Figure 2-3.   Effect of Trajectory Aphelion on Expected Flux Encounter

Spacecraft Orientation Requirements

The orientation requirements of the science payload may also influence the final selection of the mission trajectory. The meteoroid sensors have more stringent orientation requirements than do the particle and field sensors. Penetration and impact detectors realize maximum efficiency by keeping the sensor surface normal to the relative velocity vector between the spacecraft and the asteroidal flux. It is desired to orient the proximity-type sensor (optical detector) to look away from the sun and also to avoid having the optics being struck by the asteroids. This requires that the optics plane be oriented nearly parallel to the relative velocity vector between the spacecraft and the asteroid flux.

In the interest of design simplicity, it is desirable to fix-mount the sensors on the spacecraft and optimally orient the spacecraft. This, in turn, will influence the power available to the spacecraft. Figure 2-4 shows the asteroid impact angle, $\emptyset$, on the spacecraft versus solar distance for typical trajectories having aphelions of 3.0, 3.5, 4.0 and 4.5 AU. In the region from 2.0 AU to 3.5 AU, the asteroid impact angle varies over 80 degrees. In order to achieve maximum asteroidal encounter data with fixed-mounted sensors, significant power losses will be incurred. Power falls off as the cosine of the angle from normal incidence to sun's rays. In Figure 2-4, it may be also seen that the impact angle is relatively insensitive for small variations in trajectory aphelion, five degrees or less for a ±0.05 AU variation.
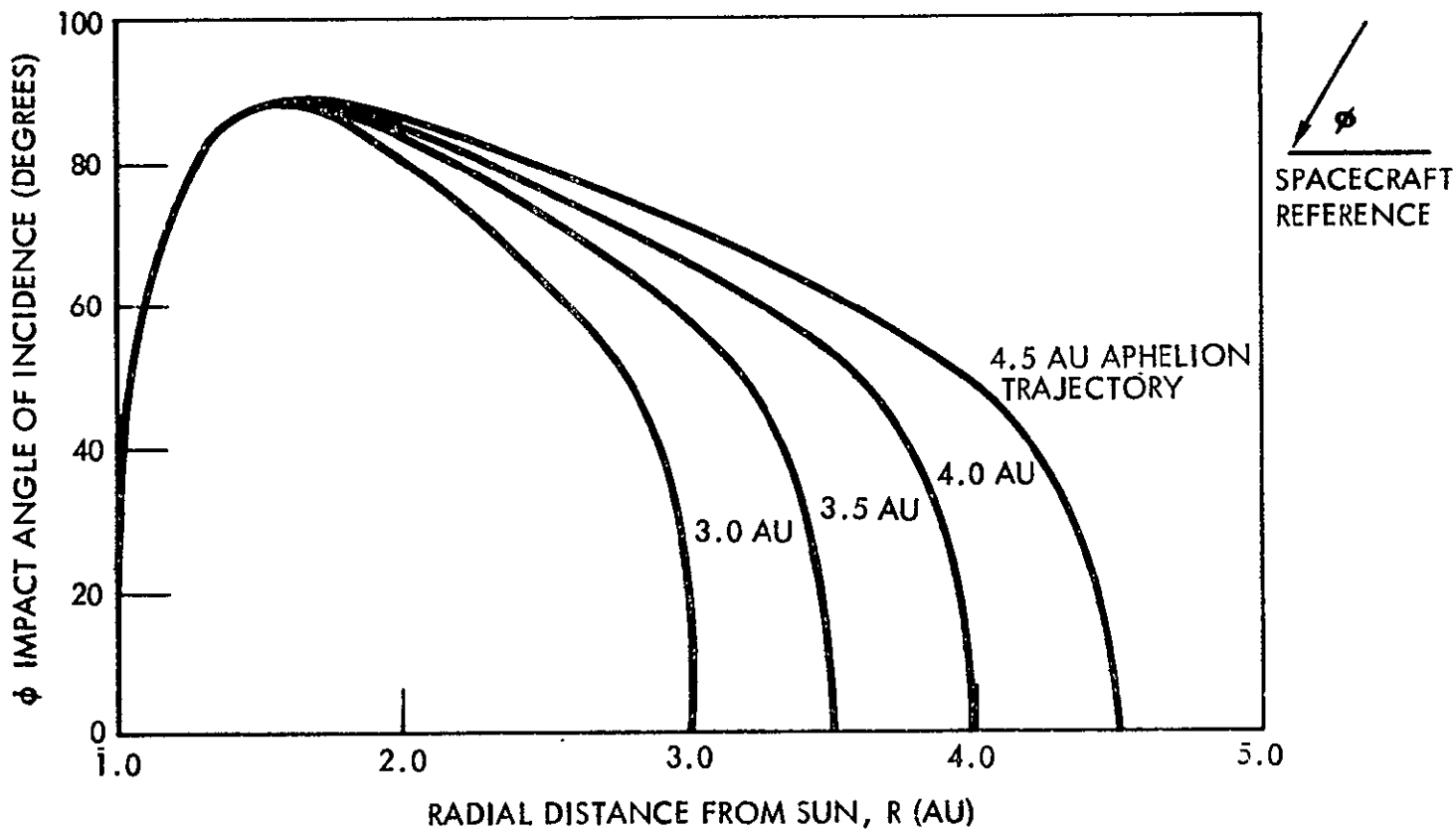
Figure 2-4. Meteoroid Impact Angle of Incidence on Solar Electric
Asteroid Belt Mission

Space Division
North American Rockwell

TRAJECTORY AND PERFORMANCE ANALYSIS

Introduction

Trajectory analysis for the SEP Asteroid Belt Mission Study Contract was conducted to assist in mission definition and in spacecraft and propulsion system design. The first phase of the study was a parametric performance analysis of basic mission considerations from which a set of ground rules for the second phase was derived. The second phase included more detailed performance trade-offs for 3.5 AU aphelion trajectories. A baseline mission trajectory was then selected from these results. Perturbation data for this trajectory was generated to determine sensitivity of the mission to variations in launch booster performance, propulsion system performance, and launch date.

All trajectory analyses were performed using ground rules specified or approved for the study by the Jet Propulsion Laboratory. The definitions of Atlas/Centaur and Titan III-C launch booster performance, the total ion propulsion system efficiency, and the relative power available as a function of heliocentric radius are presented in Figures 2-5 through 2-8. Use of roll-up solar arrays (15.0 kg/kw) was assumed throughout the study. A 15 percent solar cell degradation due to gradiation damage was used as specified. Other losses were determined during the study and are discussed later in this section.

Parametric Performance Analysis

Figures 2-9 through 2-12 illustrate the results of the parametric performance analysis from which the basic ground rules were derived. In Figure 2-9, two different aphelions were considered for the spacecraft's orbit. Values of 3.1 AU and 3.5 AU were examined for their effect on the length of time spent by the spacecraft in the region of greatest scientific interest, about 2.5 AU. This time span is significantly reduced in an orbit having the smaller aphelion, and, therefore, the aphelion of 3.5 AU was recommended. Figure 2-9 also illustrates the insensitivity of the time to aphelion and of time spent near and beyond 2.5 AU to the spacecraft power level. Therefore, this aspect of mission objectives is not sensitive to the propulsion system selection.

Figure 2-10 demonstrates the effect of thrusting time on net mass (defined as total spacecraft mass less propulsion system mass) and the relation between net mass and power for the two launch boosters under consideration, the Atlas/Centaur and Titan III-C. The optimum solar panel output power level with the Atlas/Centaur is about 12 kw; the optimum power level using the Titan III-C is about 26 kw.

Two thrusting times, 250 days and 400 days, were examined for the trajectory with an aphelion of 3.5 AU. For both launch boosters, it can be

2-14
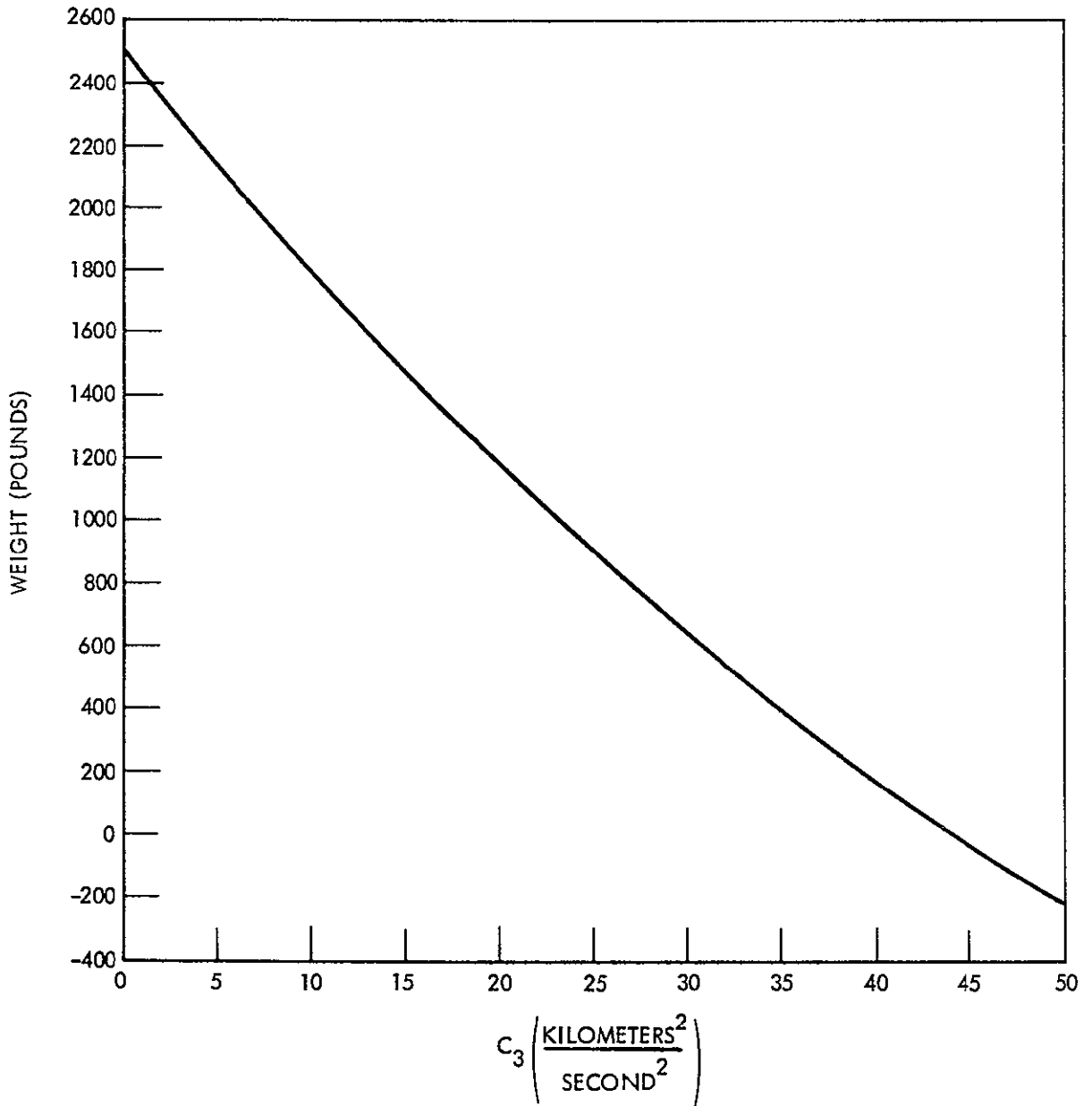
Figure 2-5. Performance of Atlas (SLV 3IC)/Centaur
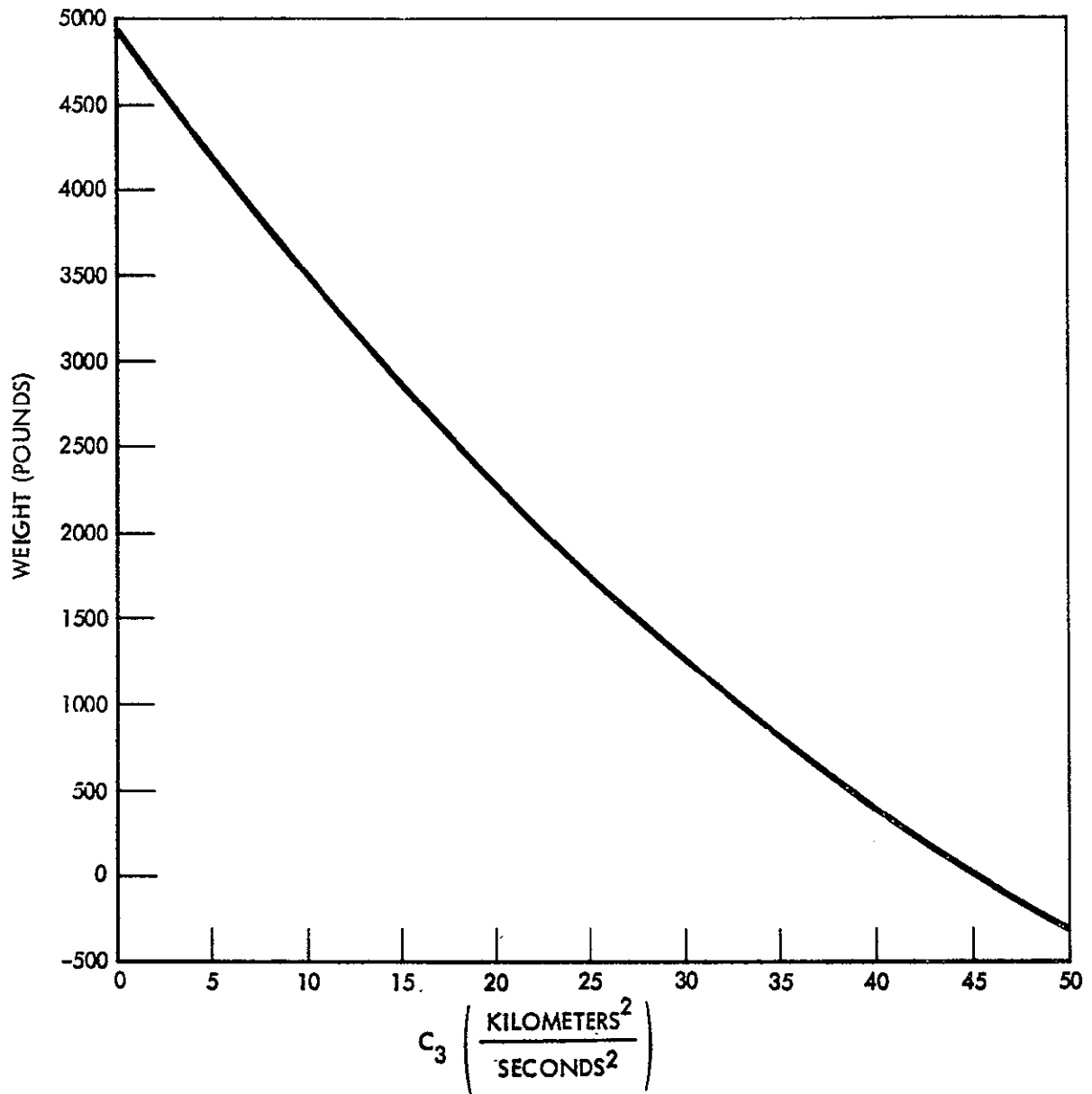
Figure 2-6. Performance of Titan IIIC (1205)
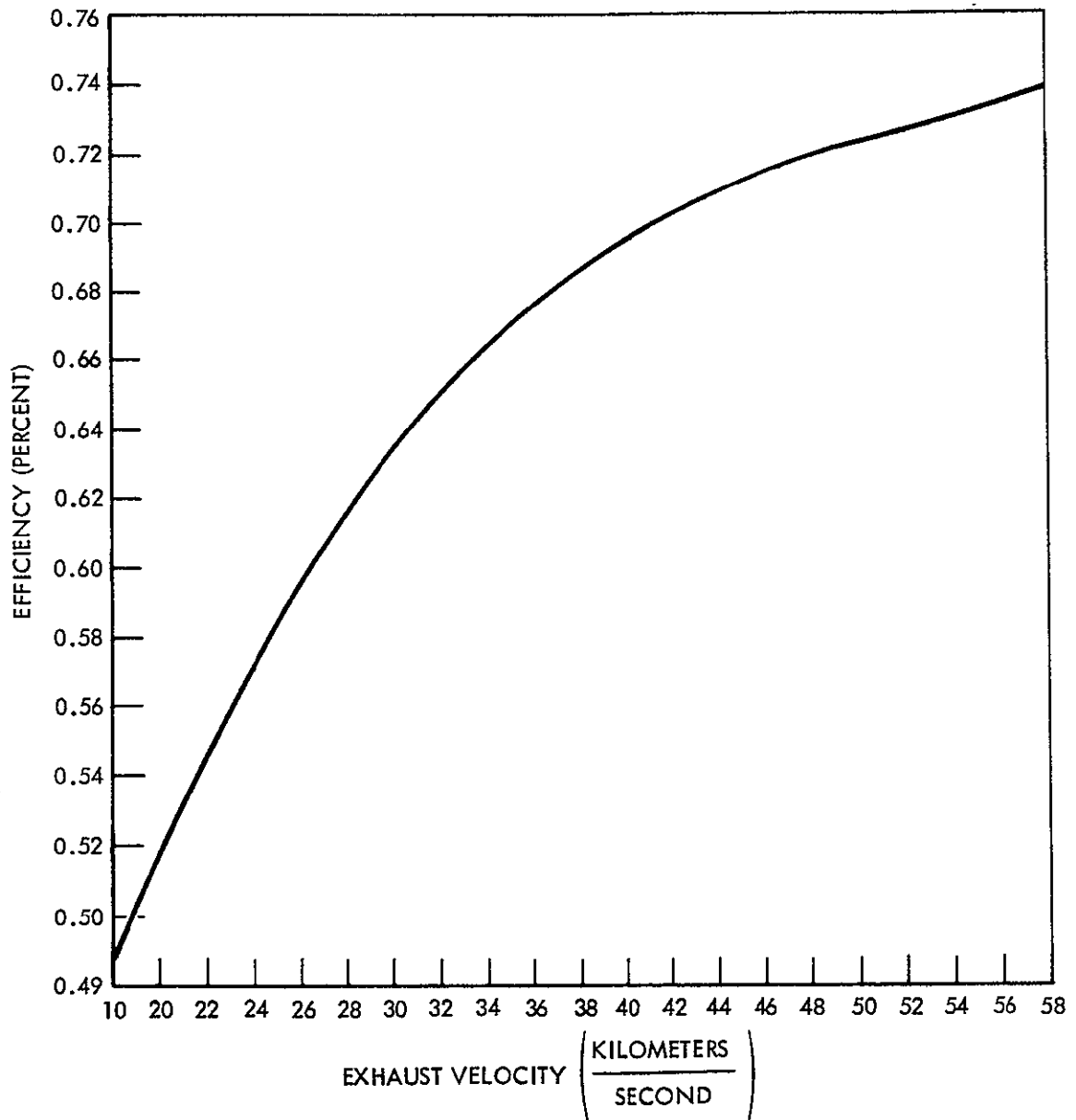
Figure 2-7. Overall Power Efficiency
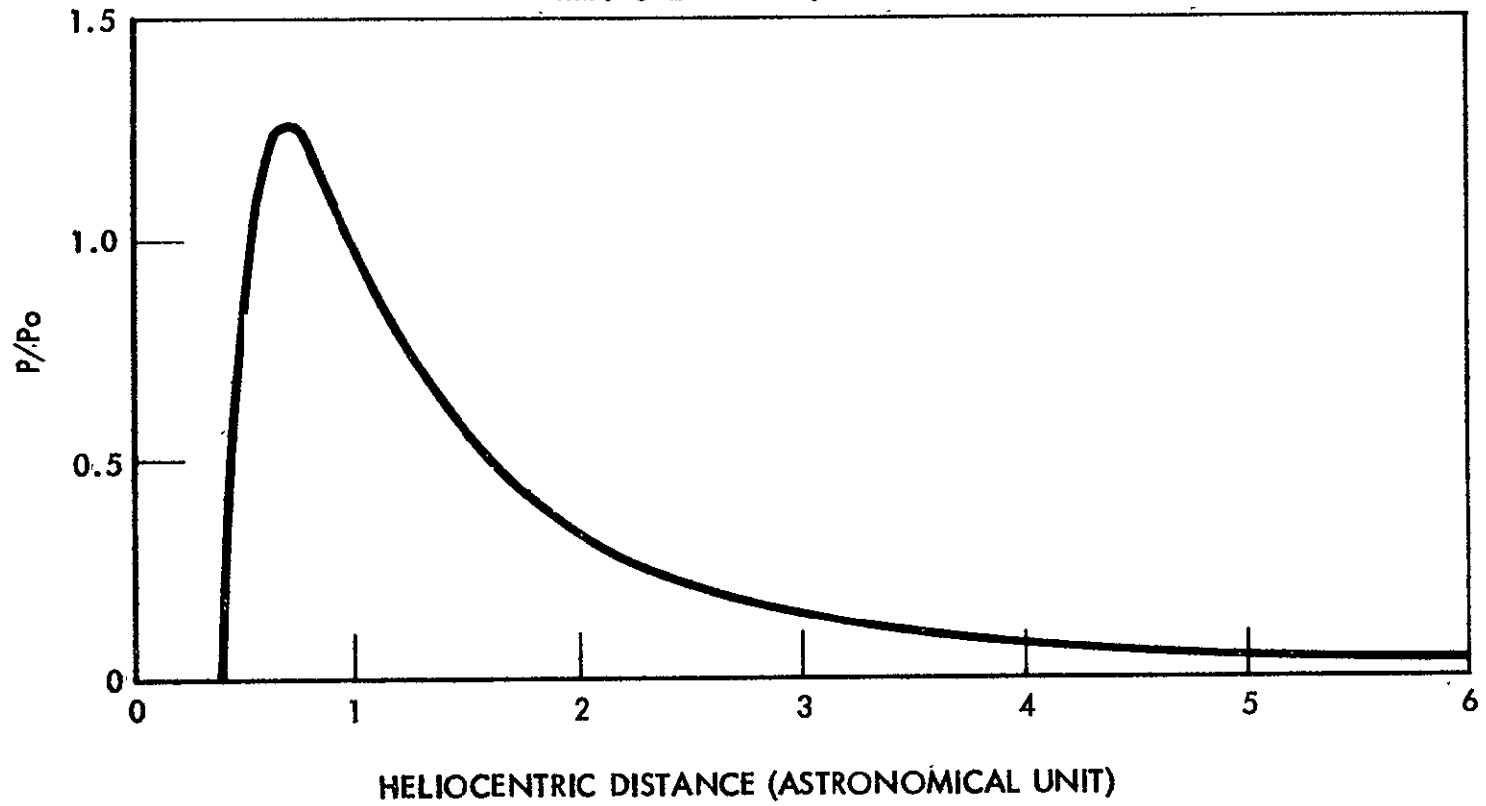
Figure. 2-8. Power. Ratio Versus Heliocentric Distance
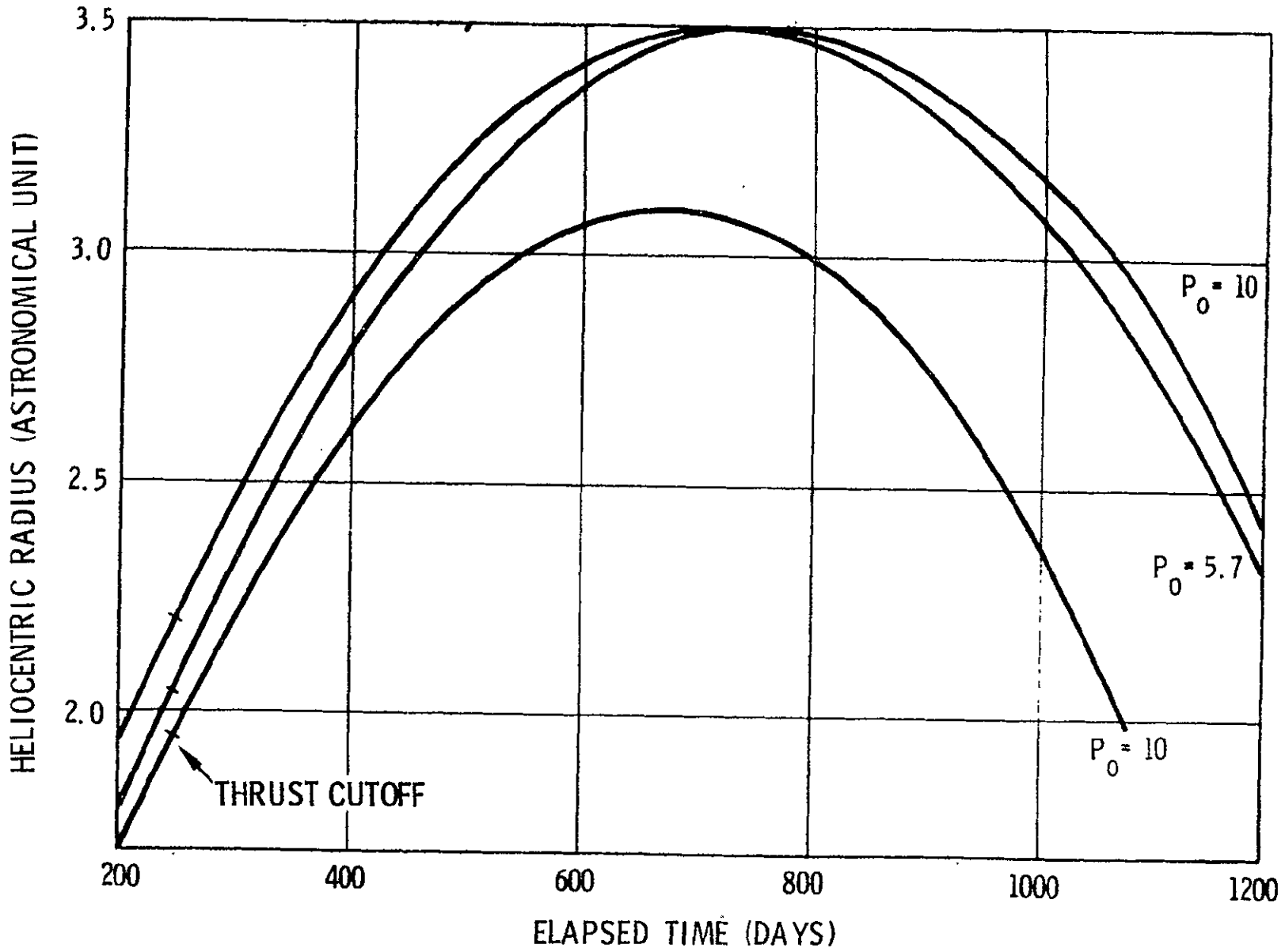
Figure 2-9. Asteroid Belt Mission Trajectory Profiles, Atlas/Centaur
Launch Vehicle

Space Division
North American Rockwell
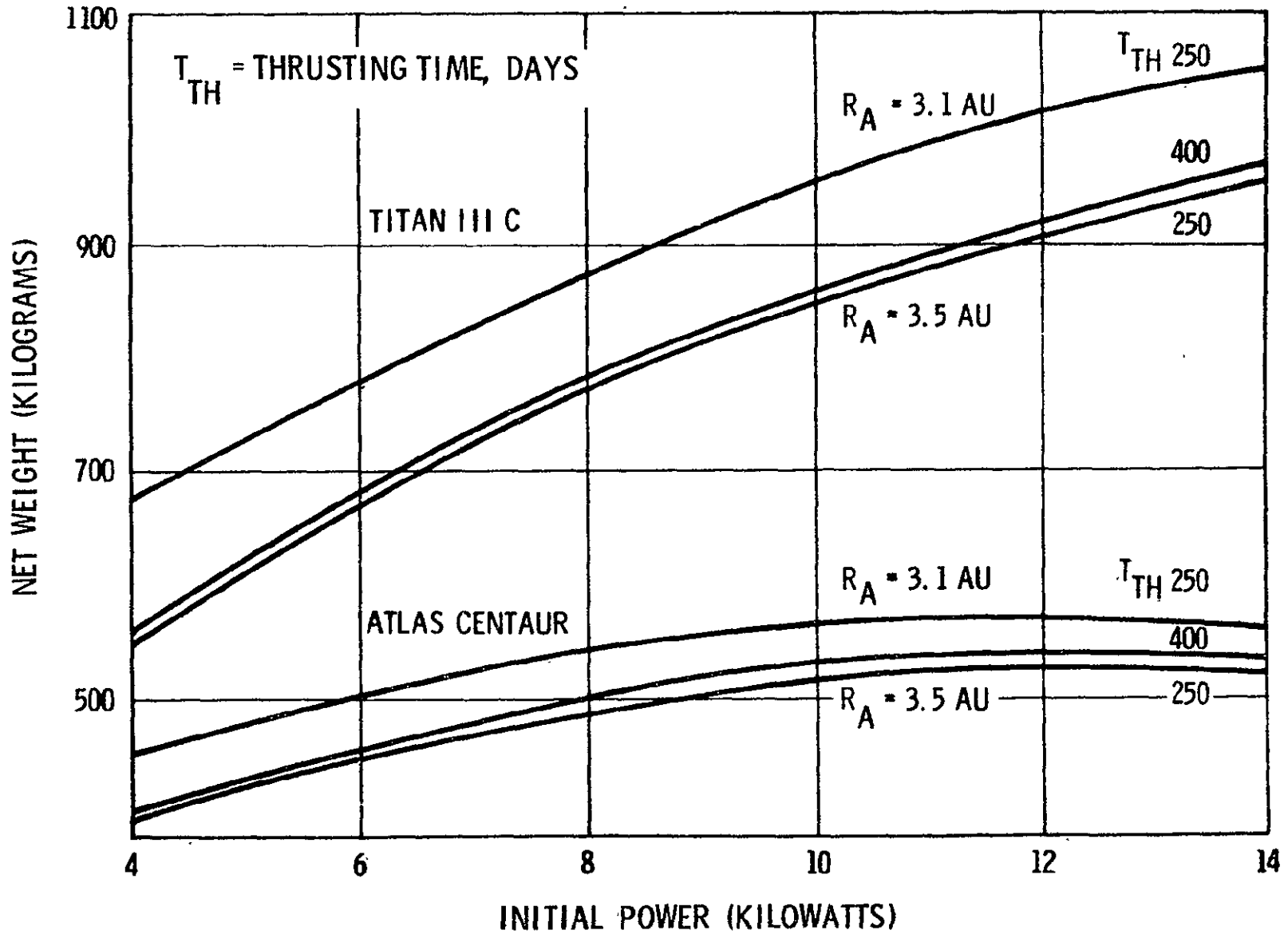
Figure 2-10. Net Weight Versus Level

seen that an increase in thrusting time of 150 days added about 12 kilograms
to net mass. This performance improvement is not deemed worthwhile
because of the reliability degradation resulting from the longer thrusting
time and the desirability of avoiding thrusting during the scientific measure-
ments within the asteroid belt (beyond 2.0 AU).

Trajectories for Figures 2-11 and 2-12 were run with an aphelion of
3.5 AU and thrusting time of 250 days. Figure 2-11 shows the C_3 values
required for different power levels for the two launch boosters, and Figure 2-12
shows the optimized specific impulse values for the same range of power for
both launch vehicles. The optimum specific impulse curve for the Titan III-C
increases near the optimum power point in a manner similar to the Atlas/
Centaur curve, but this optimum point (about 26 kw) is much above the region
of interest in this study.

From the results presented in Figures 2-9 through 2-12 the following
ground rules were adopted: an aphelion of 3.5 AU was selected for the orbit
of the spacecraft; thrust cutoff was to occur at 2 AU, the time for which
varies between 200 and 250 days, depending on the selected spacecraft power.

3.5 AU Trajectory Performance Tradeoffs

Performance tradeoffs for the class of trajectories defined above are
illustrated in Figure 2-13. Figure 2-13 is a contour map illustrating the net
mass as a function of specific impulse and power level. All trajectories were
run with an optimum constant thrust attitude. For increasing power, there
is a marked spreading out of the curves of constant net mass, indicating a
flatness near the peak. The optimum specific impulse on the curves of con-
stant net mass of 500 kilograms and less is about 2500 seconds. The curve
drawn through these optimum points, the points of minimum power for a
given net weight, is a curve of optimum specific impulse versus power. The
shape and range of this curve is given in Figure 2-12 (Atlas/Centaur curve).
The flattening of this curve as it approaches its minimum indicates that in
Figure 2-13 the curves of lower constant net weights would "break" near a
specific impulse of 2500 seconds. Thus, this "hill" describing the optimum
has a sharp cliff for specific impulses below a curve similar to the curve in
Figure 2-12. It is also clear that net weight would decrease again for powers
greater than 12 kilowatts. These higher powers would force the C_3 values
below the optimum, while for values of power well below 12 kilowatts, the
C_3 values are higher than optimum.

The sensitivity of net mass to thrust vector and solar panel orientation
was investigated; spacecraft design problems were considered in the com-
parison of the alternatives. Figure 2-14 shows the angles varied in this
study: γ, the angle between the heliocentric radius and thrust vector, and ϕ,
the angle between the thrust vector and the plane of the solar panels.
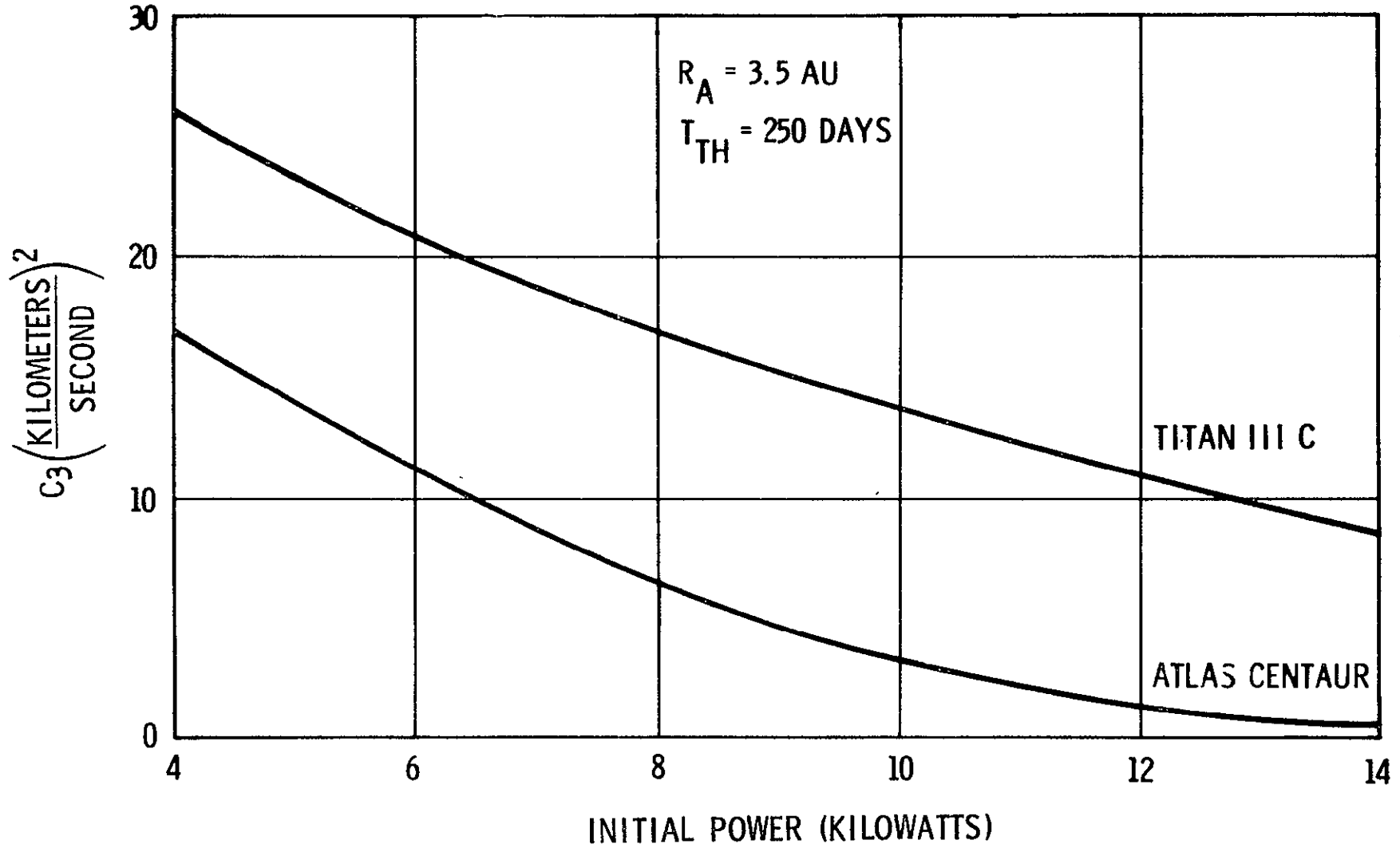
Figure 2-11. C_3 Versus Power, Asteroid Belt Mission

Space Division
North American Rockwell
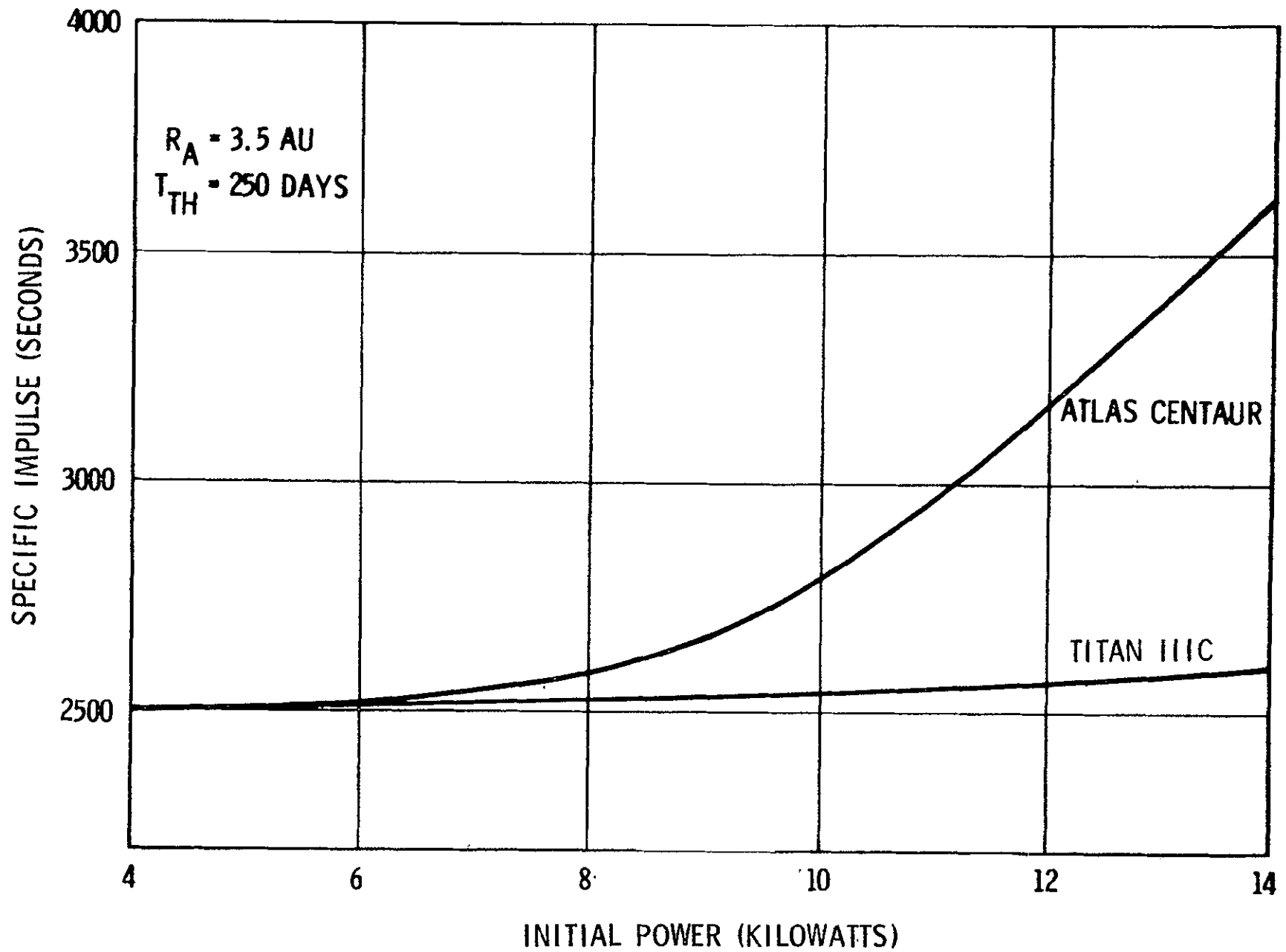
Figure 2-12. Specific Impulse Versus Power
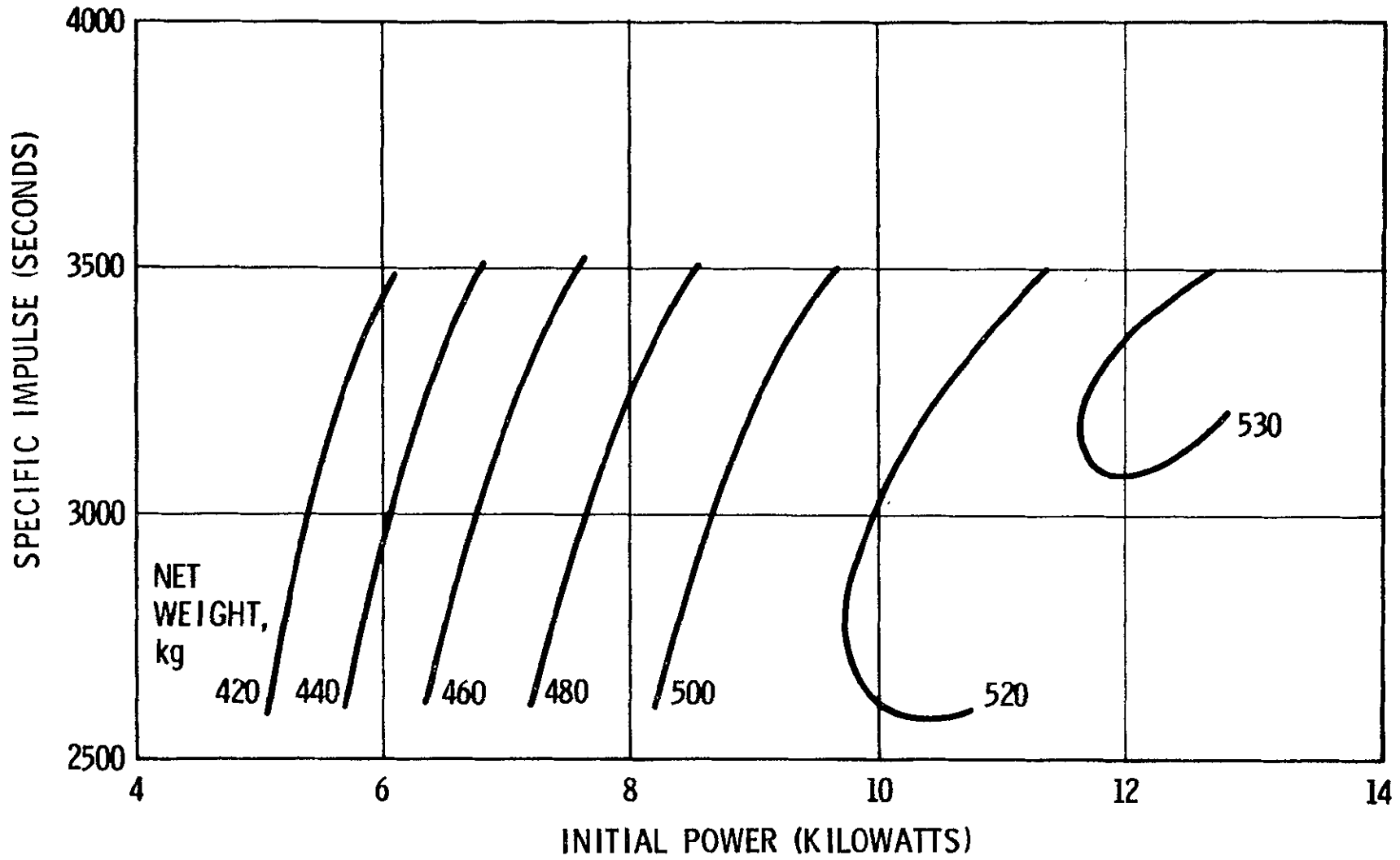
Figure 2-13. Optimum Constant Attitude Trajectories, Asteroid Belt
Mission—Atlas/Centaur

THRUST

NOTE: ECLIPTIC IN PLANE
OF PAPER

γ

ϕ

SOLAR PANEL

HELIOCENTRIC RADIUS
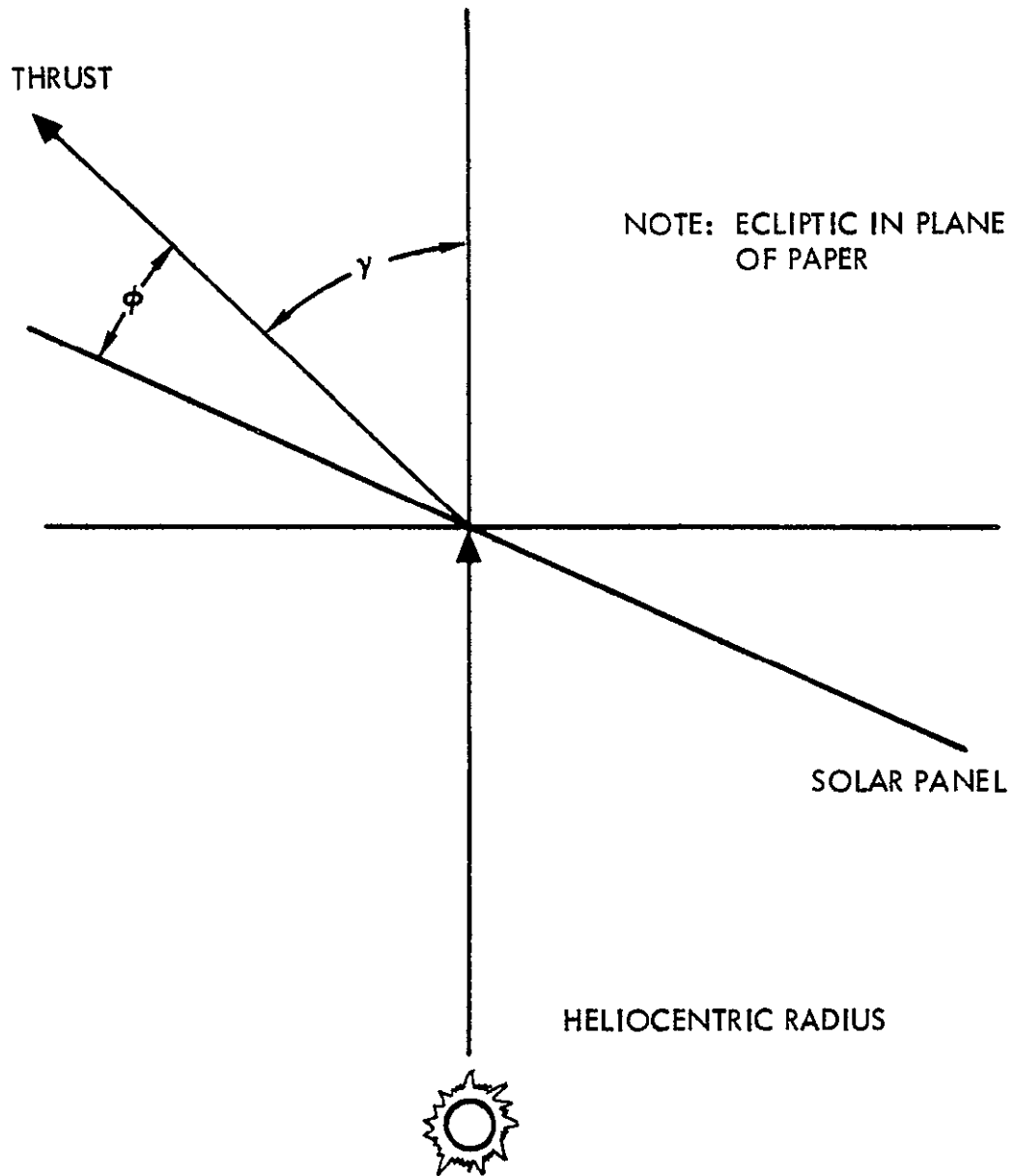
Figure 2-14.   Thrust Vector Geometry

Table 2-1 shows the performance comparison between different control and configuration options for spacecraft having solar panel output of 10 kw at 1 AU (normal incidence). Solar panel power was assumed to vary with the cosine of the angular deviation from normal solar incidence.

Option number 2 was used as the reference. For this option, the thrust vector was held in the plane of the solar panels (ϕ = 0 degrees) and the angle γ was held constant at its optimum, about 84 degrees. Option 1, wherein γ was fixed such that the solar panels would remain normal to the heliocentric radius, would cause a loss of about 4.4 kilograms of net mass. This option would never be chosen as it is no simpler to execute in flight than option 2, and would cause a loss in net mass.
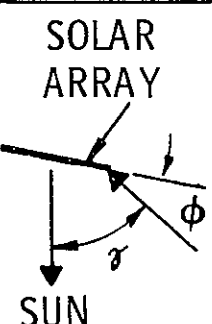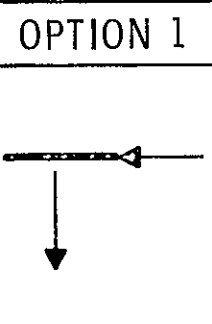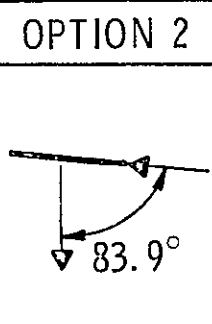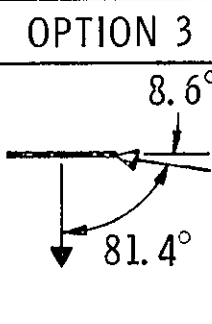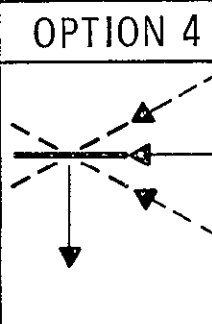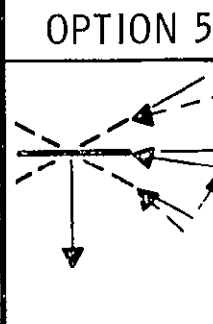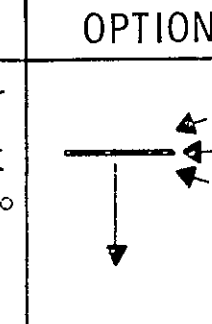
For option 3, both γ and ϕ were optimized, but with γ again held constant. The effect on the solar cells of having the engine ion emission on the sun side of the panels ($\phi > 0$) is not known, but such a configuration is considered undesirable because of the potential problem of mercury deposition on the solar cells. The small increase in net mass (2.4 kilograms) is therefore not considered worthwhile.

Option 4 represents the effect of allowing the angle γ to vary with time while the thrust vector is fixed in the solar panel plane. With the thrust profile optimized, a gain in net mass of 11.5 kilograms is achieved over the nominal. Since maintaining a constant γ would require rotation of the spacecraft inertially during the mission, a varying thrust profile could be implemented without introducing new attitude control problems. Attitude sensing is not significantly more complex (this capability is also desired for the scientific payload during the coast phase of the mission). Figure 2-15 illustrates the shape of this optimum thrust profile. This continuous thrust attitude history can be approximated with a "stair step" history of five steps at a performance loss of about 0.6 kilogram.

Options 5 and 6 show further gains in net mass from first fixing ϕ at its optimum different from zero, and second, from allowing ϕ to vary so that the solar panels are held normal to solar incidence. Both of the options involved the same potential hazard described for option 3 with ϕ greater than zero. Option 6 also requires the ability to rotate the solar panels with respect to the spacecraft body, whereas the other options can be executed by rotating the entire spacecraft in space. The substantial increase in design complexity required for this option and concomitant mechanical, structural, and control penalties have not been included.

From the results of Table 2-1, Option 4 (fixing the solar panels with respect to the spacecraft and using a variable thrust attitude with the thrust vector in the plane of the solar panels) was adopted.

Table 2-1   Spacecraft Configuration and Thrust Orientation Options

SELECTED

SOLAR ARRAY / SUN	OPTION 1	OPTION 2	OPTION 3	OPTION 4	OPTION 5	OPTION 6
		83.9°	8.6° / 81.4°		8°	
γ	90°	FIXED OPT (83.9°)	81.4°	VARIABLE OPTIMUM	VARIABLE OPTIMUM	VARIABLE OPTIMUM
ϕ	0°	0°	FIXED OPT (8.6°)	0°	FIXED OPT (8°)	VARIABLE OPTIMUM ($-18° < \phi < 40°$)
NET WT	-4.4	0	2.4	11.5	13.7	19.9
REMARKS	NO ADVANTAGE		HG DEPOSITION, OFFSET-THRUSTERS		HG DEPOSITION, OFFSET-THRUSTERS	HG DEPOSITION, EXTRA COMPLEXITY

Space Division
North American Rockwell

Figure 2-15. Optimum γ ($\phi = 0$) Versus Thrusting Time

The graph shows a curve of γ (DEGREES) on the y-axis (ranging from 60 to 110) versus TIME FROM LAUNCH (DAYS) on the x-axis (ranging from 0 to 250).

Label on graph: SOLAR PANEL OUTPUT POWER AT 1.0 AU = 10 KW
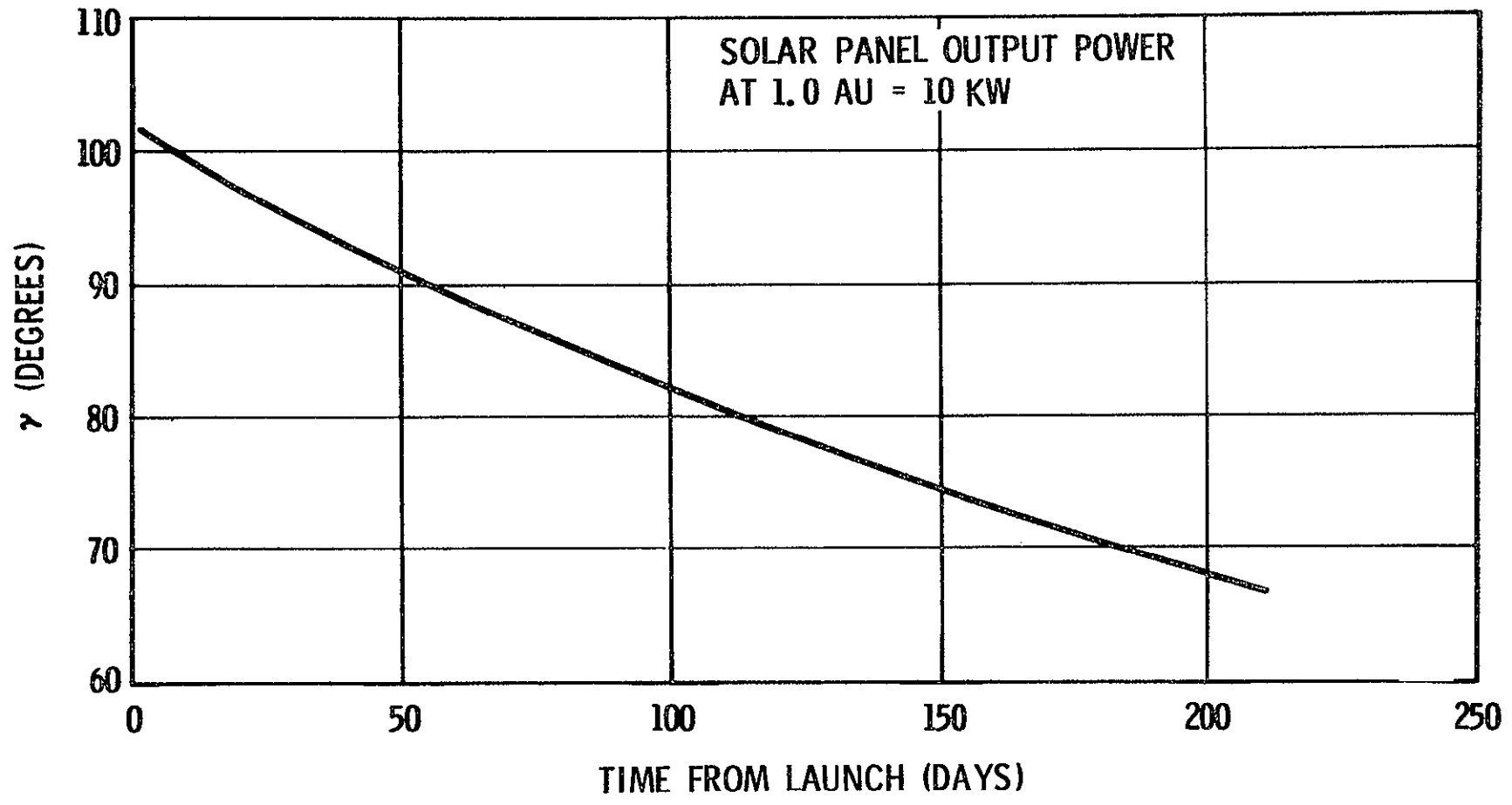
Baseline Mission Trajectory

Baseline Mission Trajectory Parameters

A baseline spacecraft configuration was selected and the propulsion
system and trajectory optimized using the Atlas Centaur launch booster.
The parameters defining this configuration are specific impulse, solar panel
rated power at 1. 0 AU and degradations, heliocentric radius at thrust termi-
nation, and the data of Figure 2-5 through 2-8. Other propulsion system
parameters and trajectory parameters were determined in the optimization
process.

An engine specific impulse of 3500 seconds was chosen because this
selection represents more proven technology and has greater potential
versatility in performing missions other than the asteroid belt survey. The
performance cost of this choice for the asteroid belt survey is indicated in
Figure 2-13. The solar panel rated power is 10. 0 kilowatts, and is assumed
to undergo an 18 percent degradation upon deployment to provide an adequate
allowance for radiation and meteoid impact damage and to account for power
losses between the solar panel output and the power conditioning input. This
18 percent value was determined to be a good approximation for use in the
trajectory analysis. (A more detailed assessment is presented in Section 7,
Electrical Power Subsystem). The spacecraft housekeeping power of 450
watts is deducted from the available solar panel power before thrust is
computed.

The initiation of low thrust propulsion was assumed to occur one day
after launch booster thrust termination. The minimum time required from
high thrust termination before low thrust may be initiated is a function of
the time to solar panel deployment (nine hours have been allocated between
lift-off and thrust initiation.) From a performance standpoint, this minimum
time is optimum; the one day assumed in the trajectory studies therefore
represents a small performance pad.

Termination of low thrust occurs at 2 AU. This selection was based
on the desirability of not thrusting during performance of the scientific exper-
iments, most of which are carried out beyond 2 AU. The time of this thrust
termination is 210 days.

The optimization of the propulsion system defines the thruster module
size and number, and the redundancy required in the power conditioning panels
to achieve the desired mission reliability. The optimum propulsion system
design has two power conditioning panels, and two initially-operating thrusters
and one standby thruster. The rated input power to each power conditioning
panel is 3. 9 kilowatts. The nominal engine diameter is 30 centimers, and
each engine has a rated power of 3. 6 kilowatts.

From the trajectory optimization, the injected mass, net mass, C_3
values and thrust attitude were determined. The value of C_3 for the baseline

trajectory is 12.2 $(km/sec)^2$ with a resulting injected mass capability (using the Atlas/Centaur) of 751 kilograms. A detailed mass statement is given in Section 4.0. The thrust attitude was optimized as a time variable, and Figure 2-16 shows the resulting curve. Note that Figure 2-16 is very similar to Figure 2-15 despite the considerable difference in the power level. Time histories of several trajectory parameters are shown in Figures 2-17 through 2-22. Figures 2-23 through 2-27 provide time histories of the following earth referenced parameters: launch profile, earth-spacecraft range, cone angle, and clock angle. Figure 2-23 indicates that the spacecraft will be in earth shadow for about 20 minutes after launch booster cutoff.

At the beginning of the trajectory, two thrusters are operating at full power. As the spacecraft moves away from the sun, the total available power decreases, and both thrusters operate at less than full power. The total beam power output by these thrusters is evaluated, and when it drops to the amount output by a single thruster at full power, one thruster is turned off, and the other is returned to full power. For the asteroid belt survey baseline trajectory, this module switching occurs after 134 days.

A thruster or power conditioning panel operating at less than full input power undergoes a decrease in efficiency because part of the internal losses are fixed. This power matching loss has not been included in the trajectory studies because it would violate the study ground rules. However, this loss has been evaluated by degrading the efficiency given in Figure 2-7. The HACPOLT-T simulation program continuously computes the propulsion system design being simulated. The loss depends on the trajectory power profile as well as the propulsion system design; for the baseline mission this loss is approximately equivalent to a 1.5 percent loss in total propulsion system efficiency. The thruster modules should operate above 50 percent rated capacity to avoid substantial power losses. The satisfaction of this criteria on the baseline trajectory is responsible for the relatively small 1.5 percent loss.

Baseline Mission Performance Analysis

Mission performance analysis includes an evaluation of both the nominal trajectory and performance disperions. These items are not independent; the latter is one of the inputs to the former during detailed mission evaluation.

Ground rules have been defined for the study (Figure 2-5 through 2-8) which are a primary input to the nominal trajectory; potential changes in these ground rules are discussed briefly. Performance dispersion sources and the effects of these dispersions on both untargeted (area type) and targeted (point type) missions are also discussed.
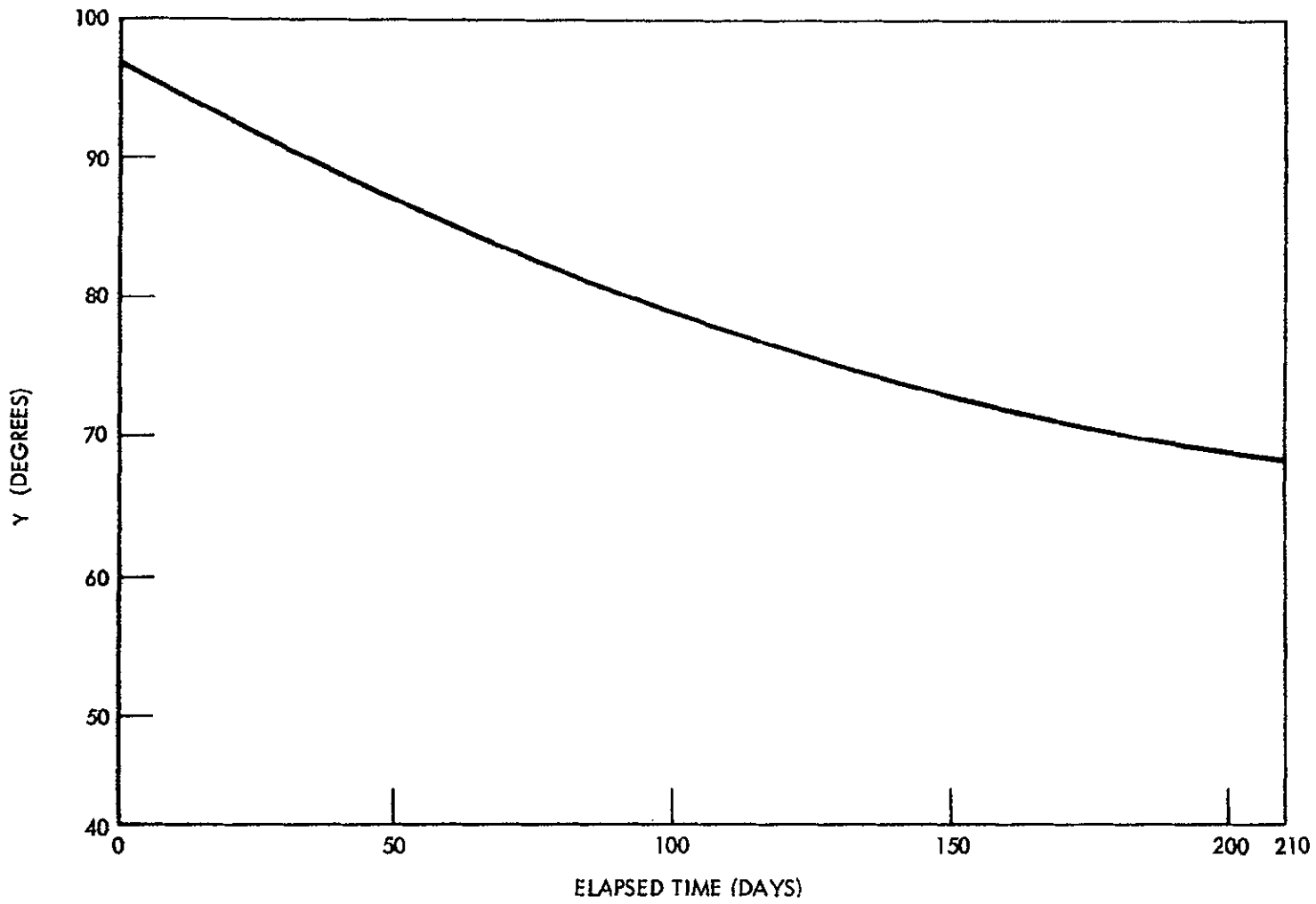
Figure 2-16. Asteroid Belt Mission Baseline Trajectory Thrust Angle

Space Division
North American Rockwell
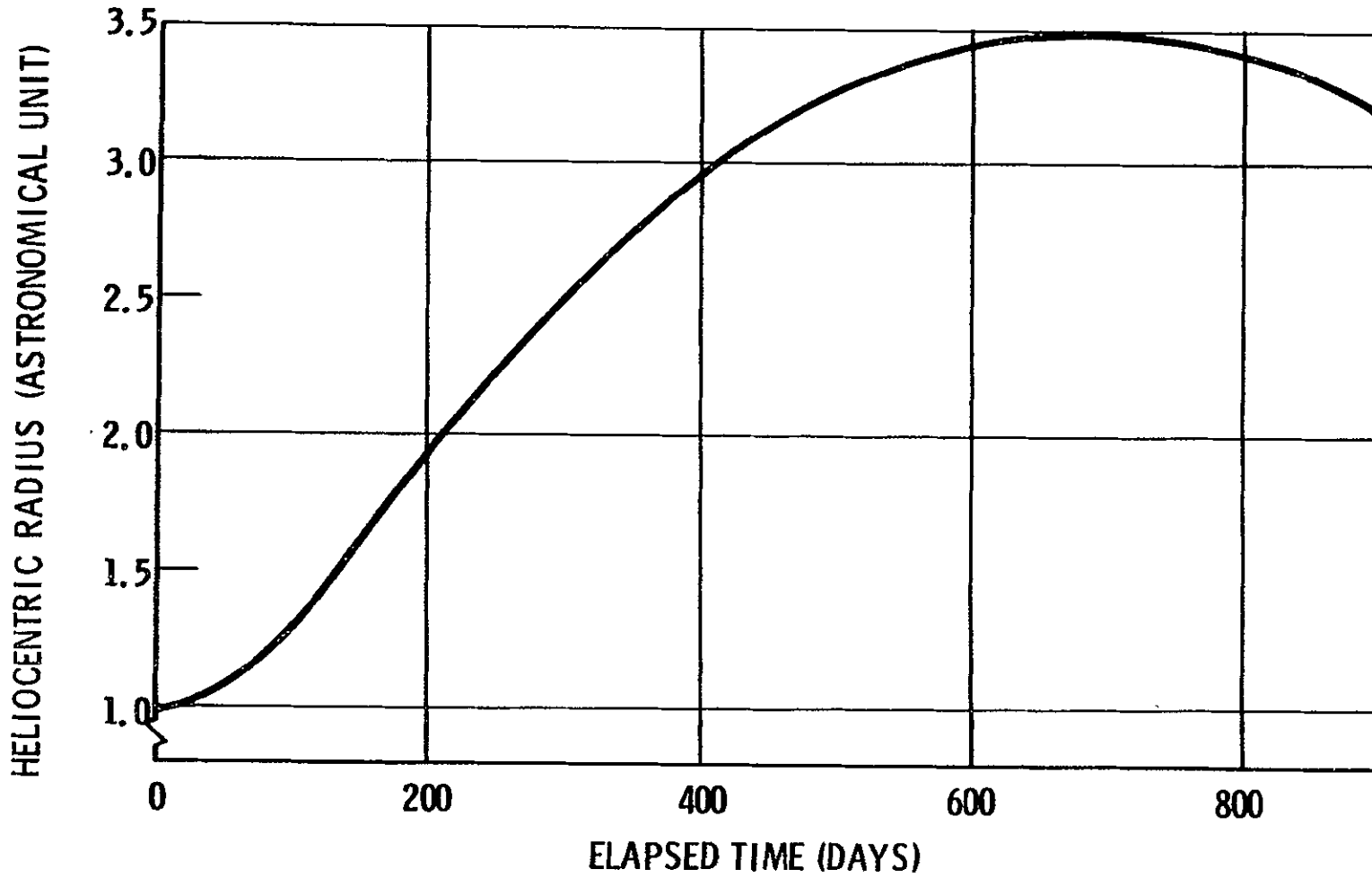
Figure 2-17. Heliocentric Radius Versus Time Baseline Trajectory, Asteroid Belt Mission
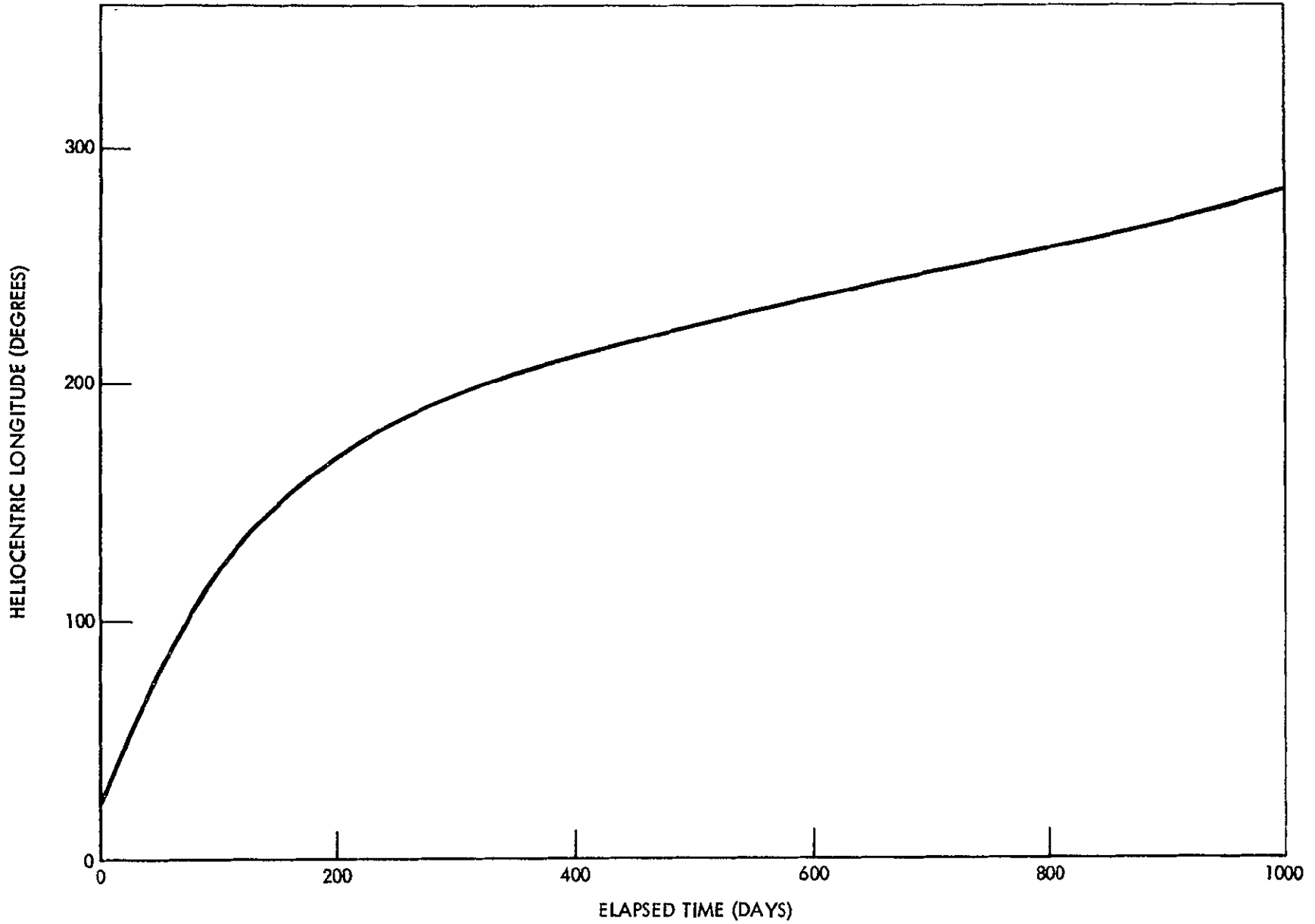
Figure 2-18.   Asteroid Belt Mission Baseline Trajectory Heliocne

Space Division
North American Rockwell
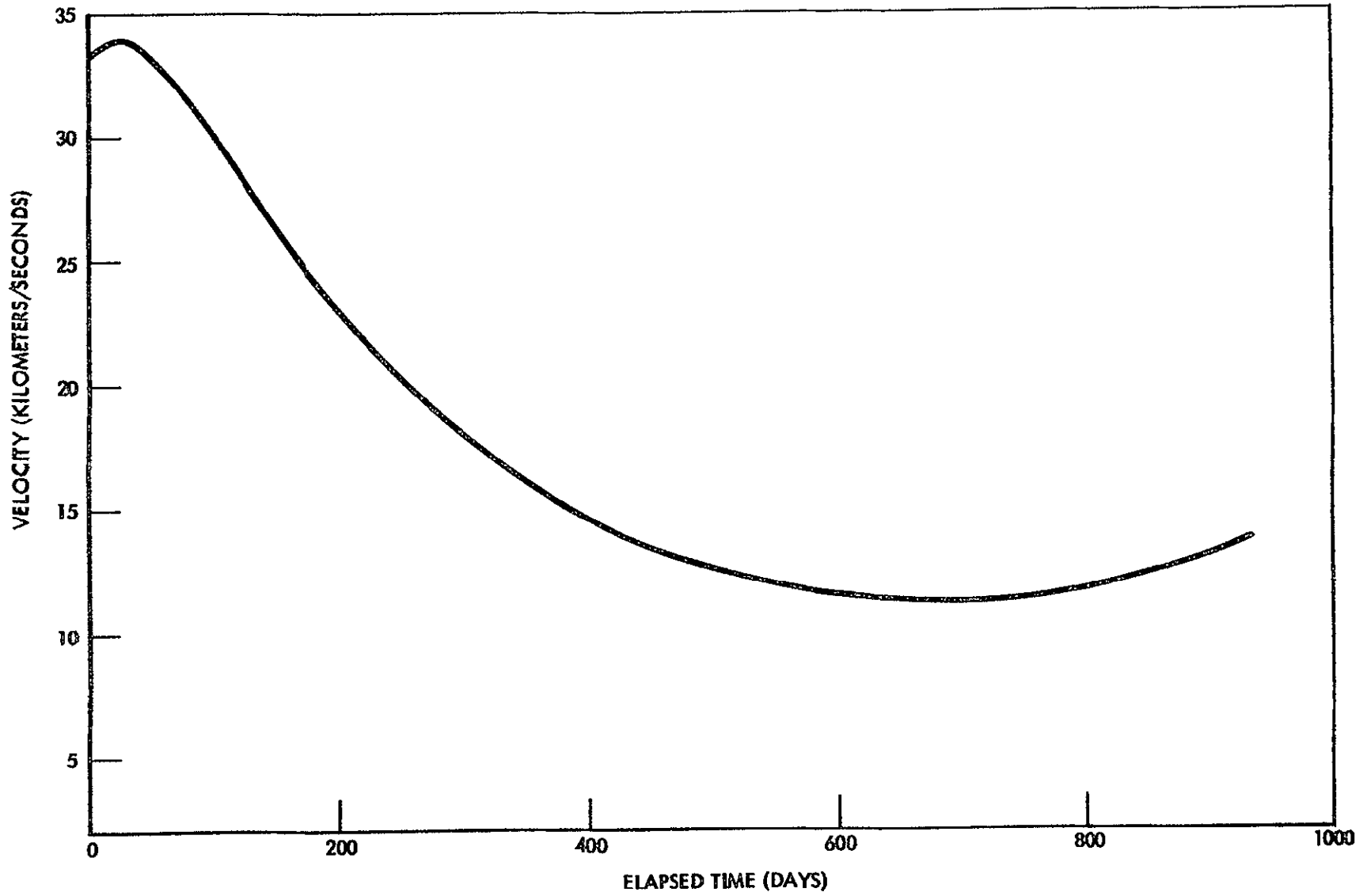
Figure 2-19. Asteroid Belt Mission Baseline Trajectory
Heliocentric Velocity

Space Division
North American Rockwell
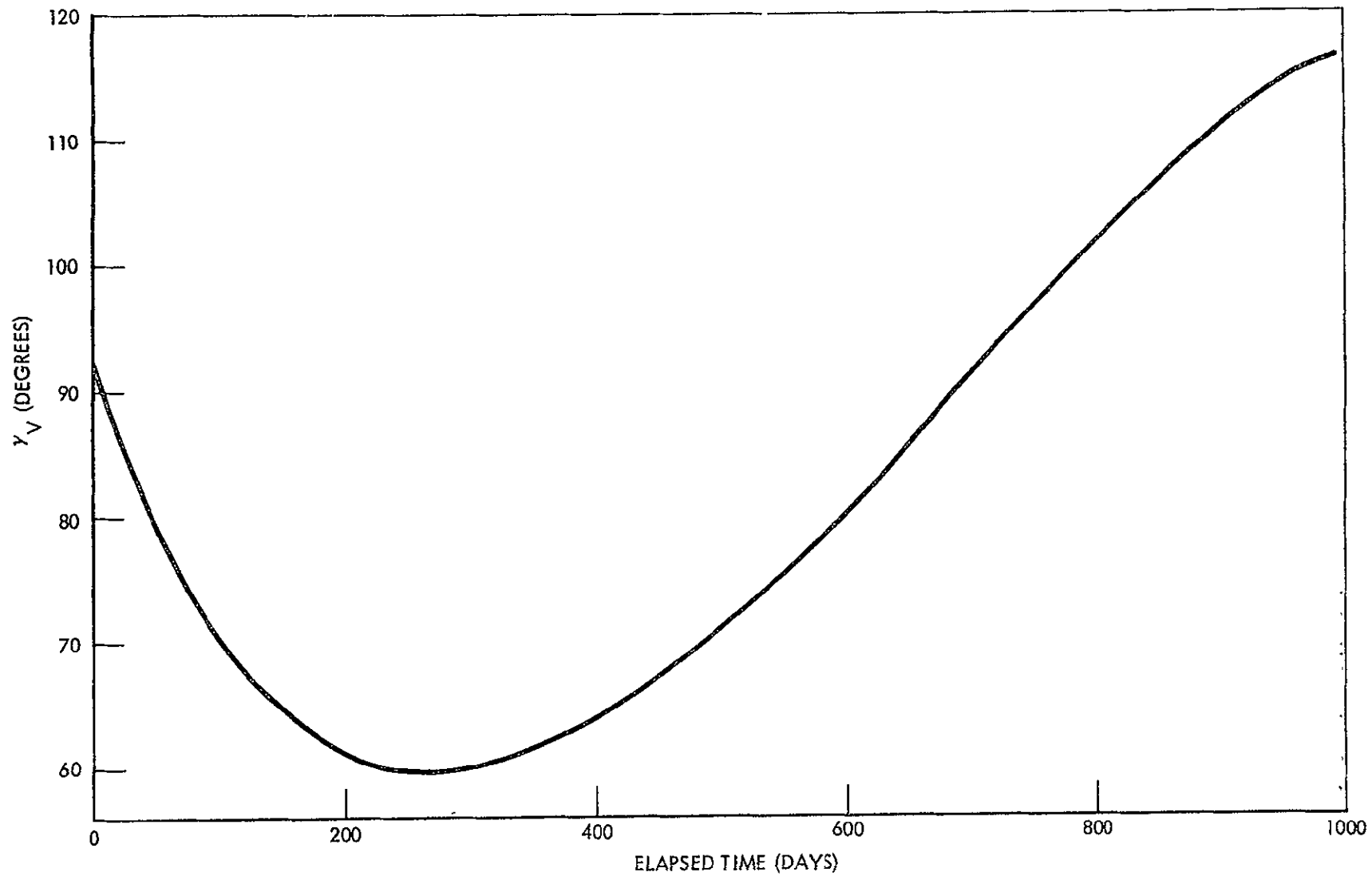
Figure 2-20. Asteroid Belt Mission Baseline Trajectory Angle Between
Heliocentric Radius and Velocity Vector
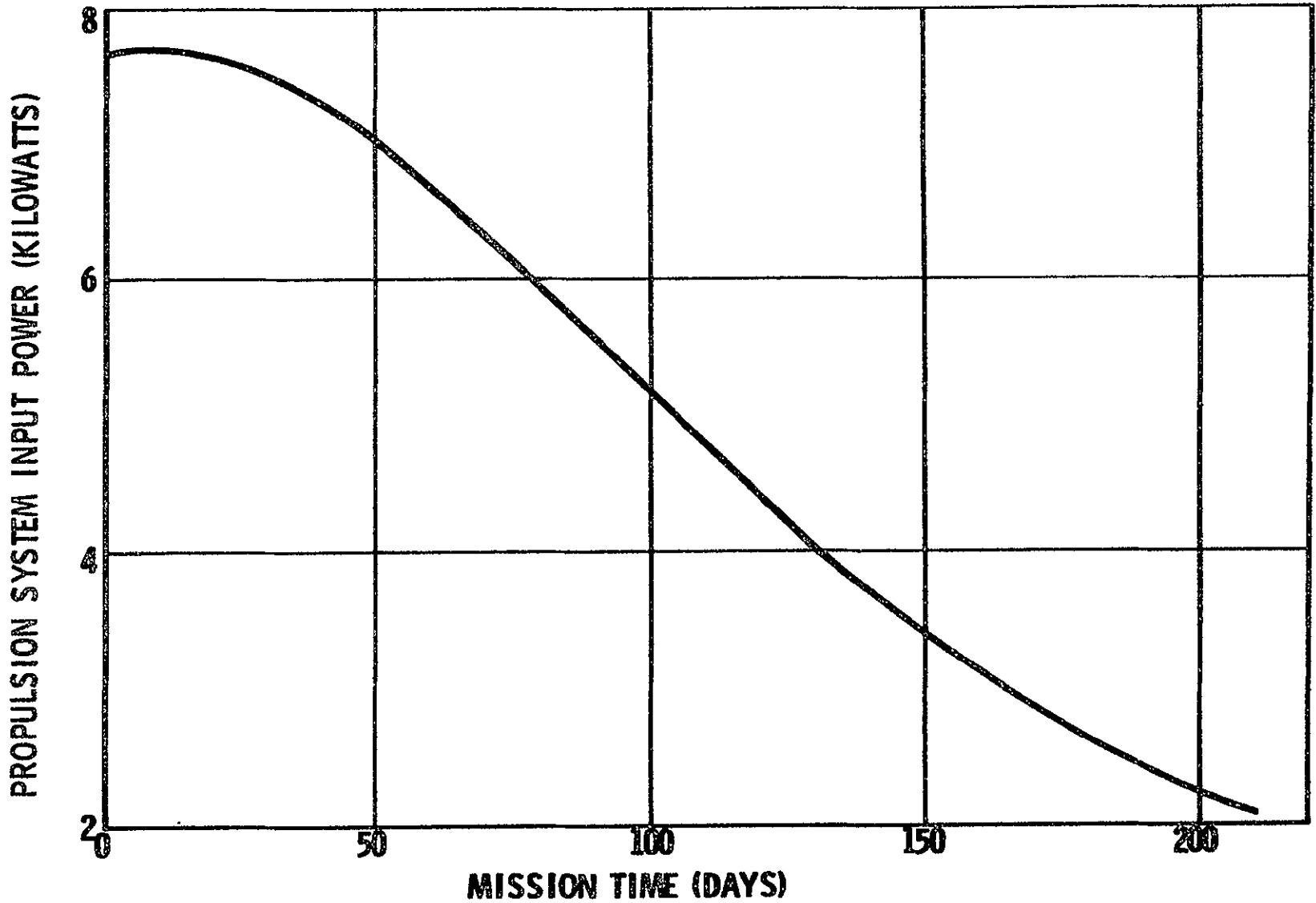
Figure 2-21. Propulsion System Input Power Versus Time
Baseline Trajectory

Space Division
North American Rockwell
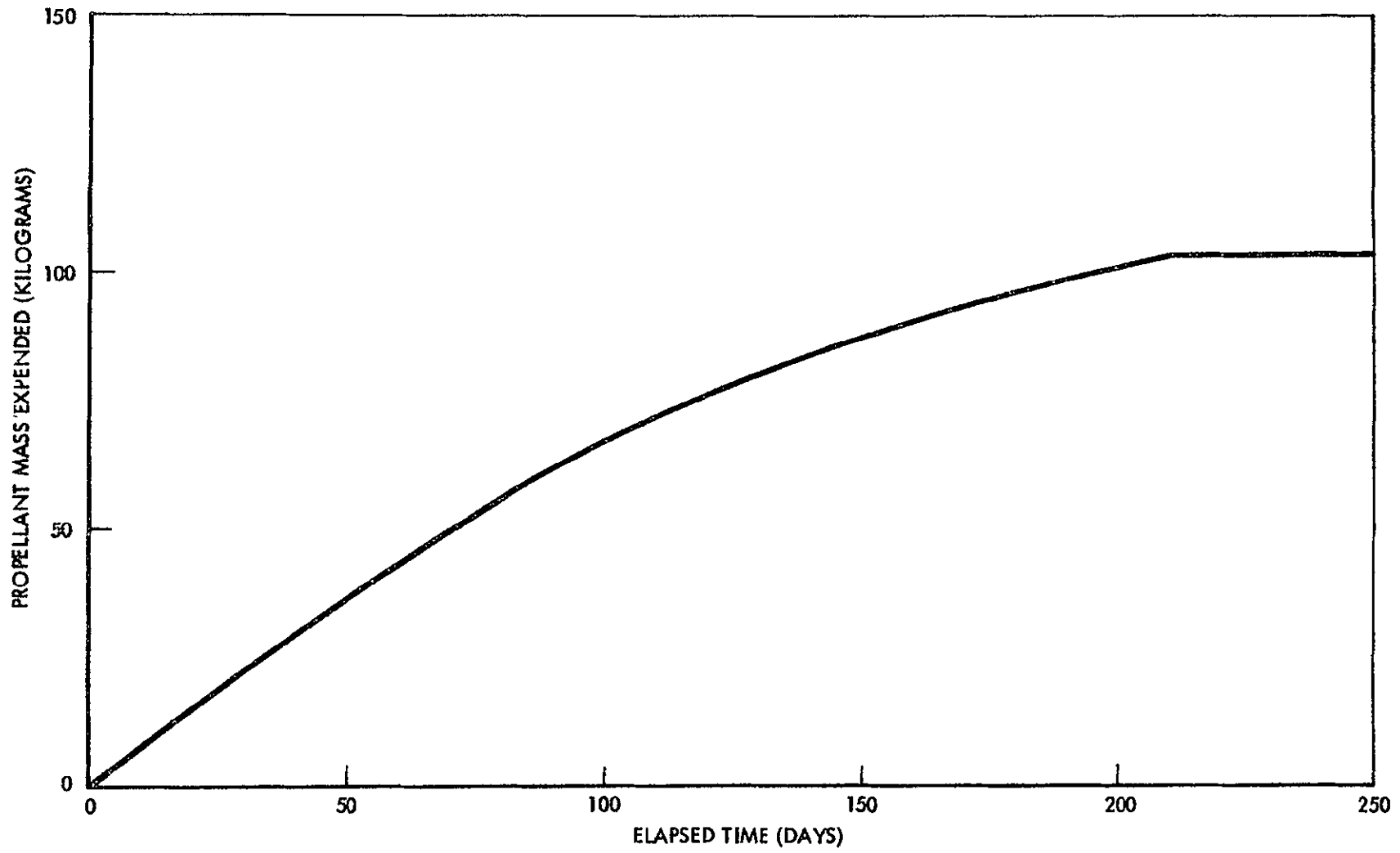
Figure 2-22. Asteroid Belt Mission Baseline Trajectory Propellant
Expended Versus Thrusting Time

Space Division
North American Rockwell
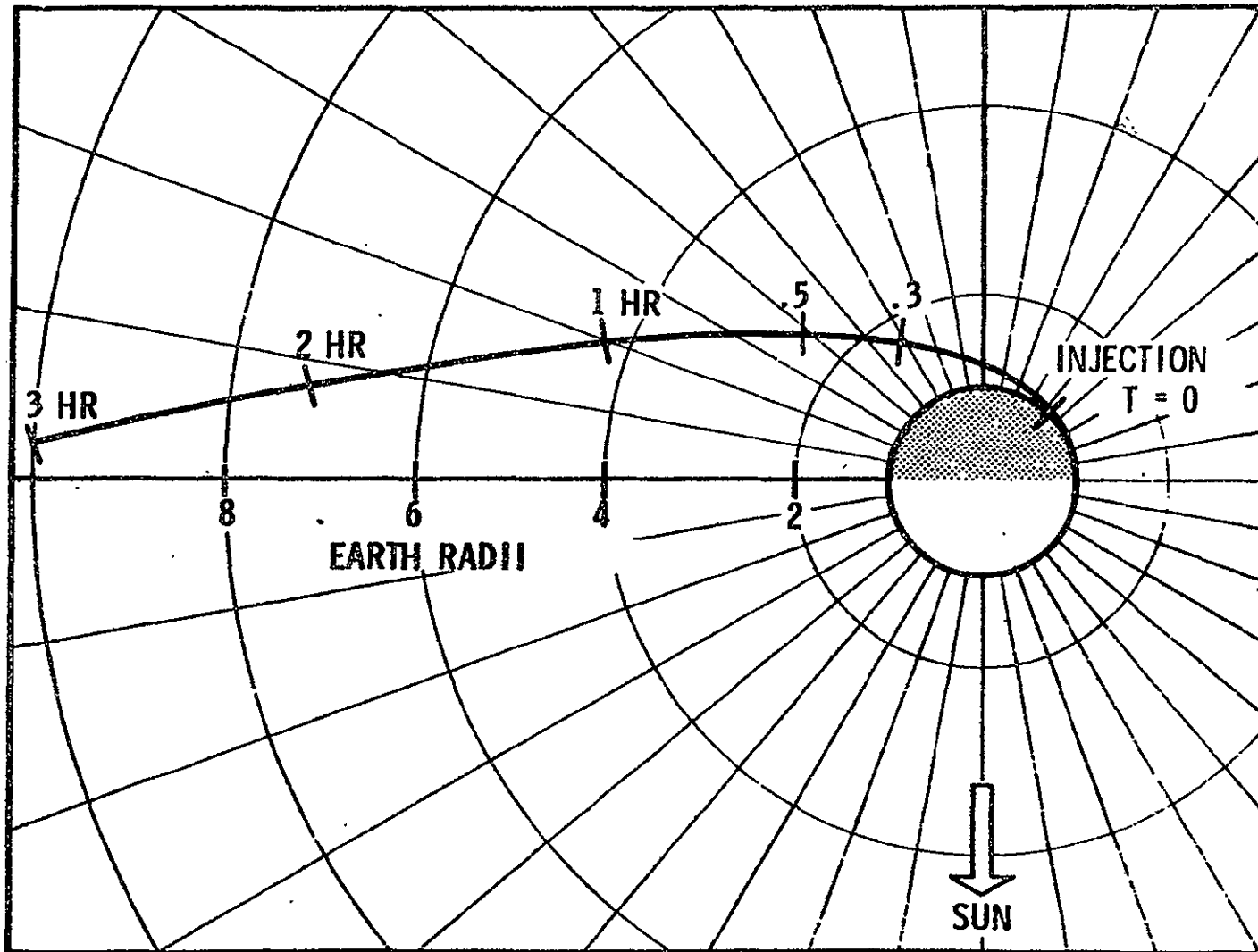
Figure 2-23. Geocentric Launch Profile, Asteroid Belt Mission
Baseline Trajectory
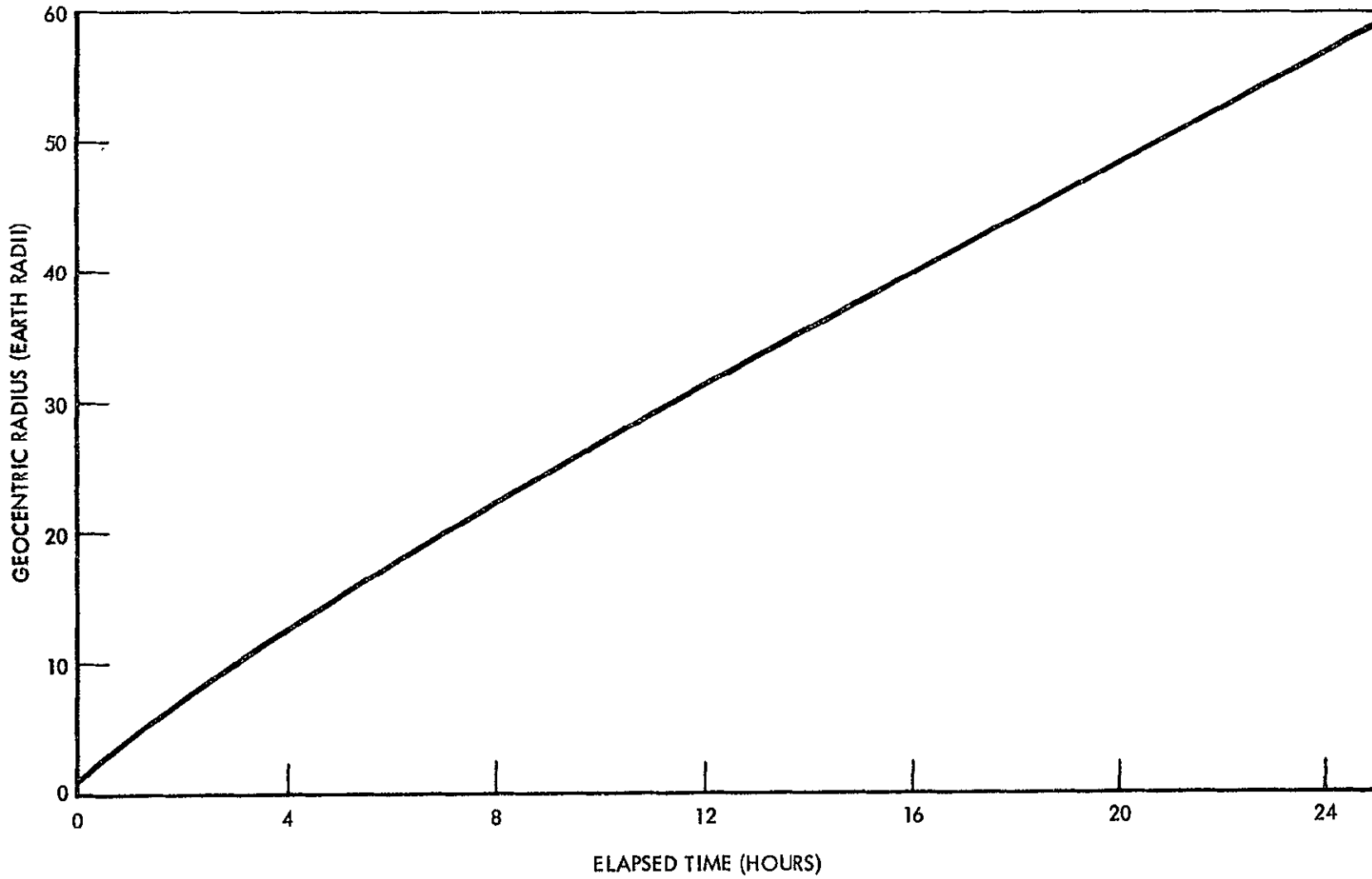
Figure 2-24. Asteroid Belt Mission Baseline Trajectory Geocentric Radius

Space Division
North American Rockwell
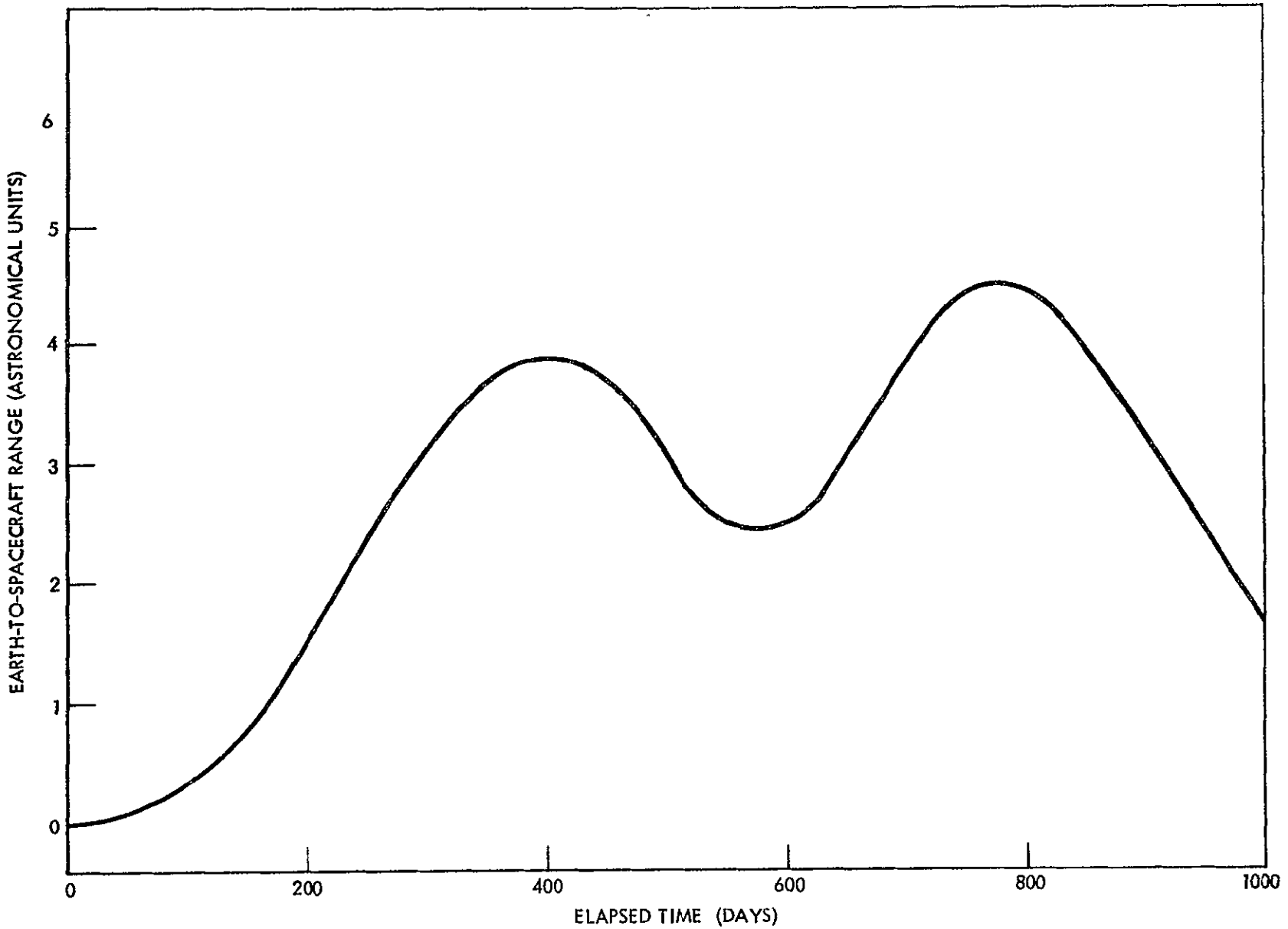
Figure 2-25. Asteroid Belt Mission Baseline Trajectory
Earth-Spacecraft Range

Space Division
North American Rockwell
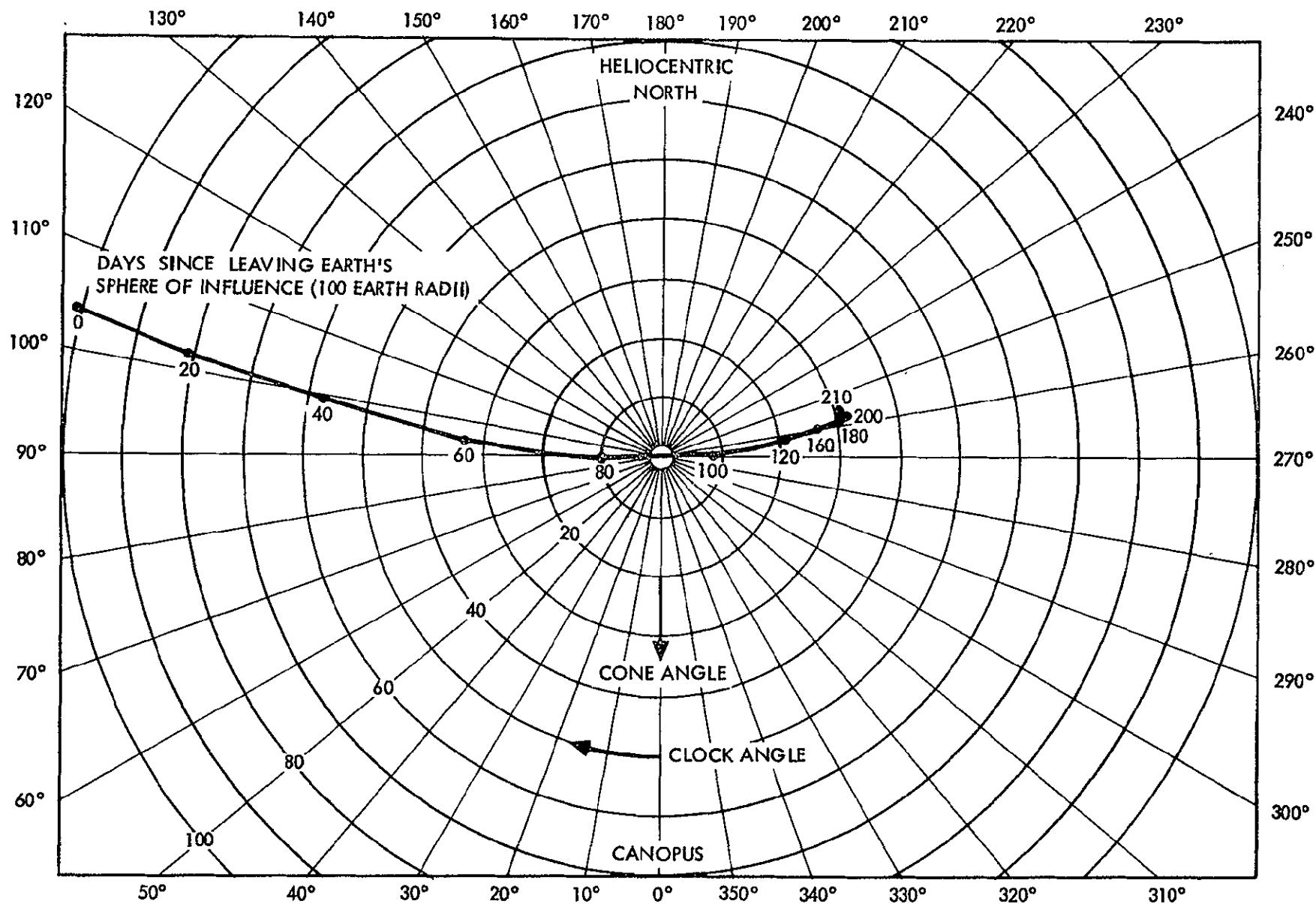
Figure 2-26. Asteroid Belt Mission Baseline Trajectory Cone and Clock
Angles Thrusting Phase of Trajectory
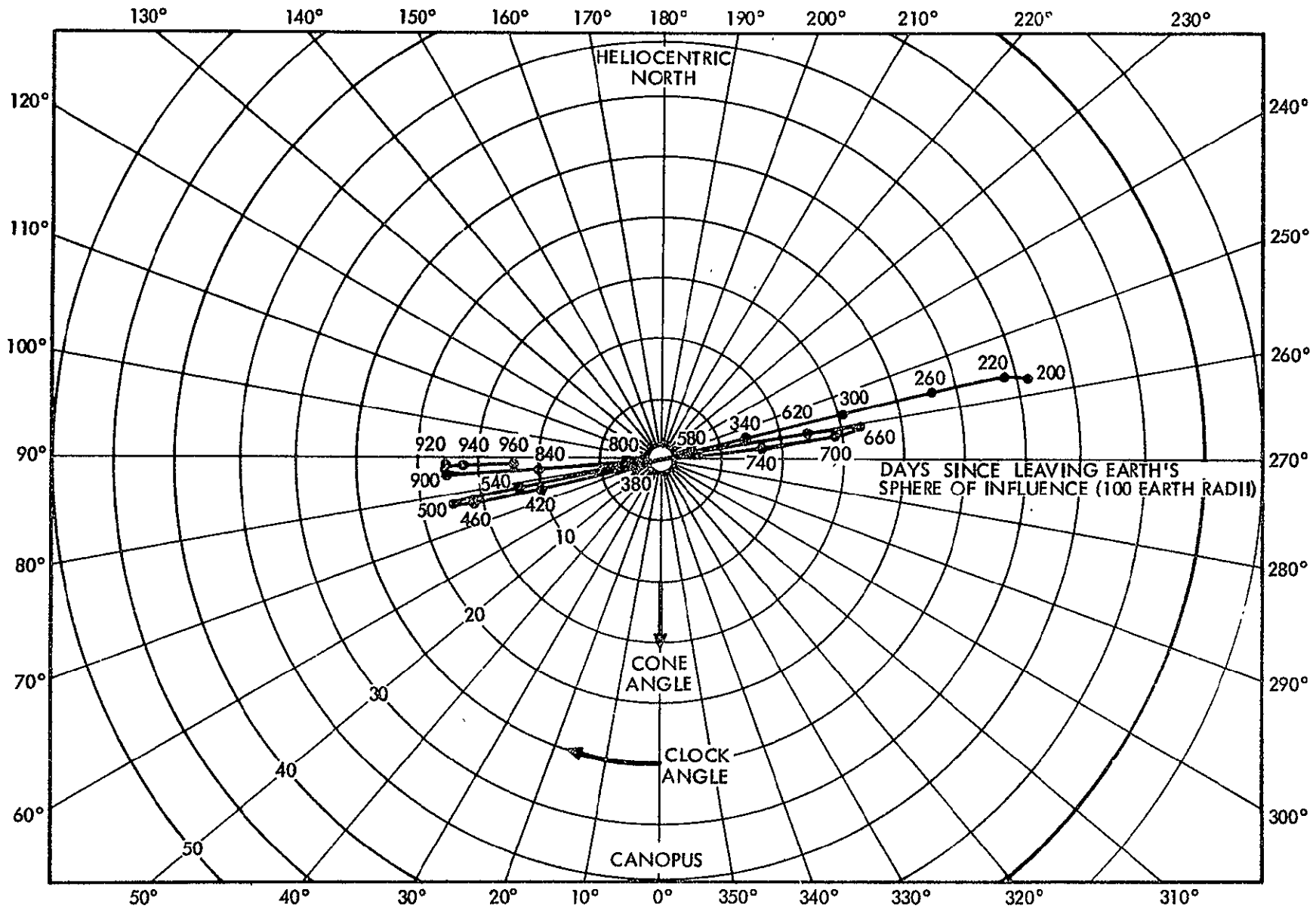
Figure 2-27. Asteroid Belt Mission Baseline Trajectory Cone and Clock
Angles Ballistic Phase

Propulsion System Tradeoffs on the Baseline Trajectory. The trajectory analysis performed heretofore has considered net mass as the payoff function. Net mass has been defined as the injected mass less the masses of the solar panel, the mercury propellant, and the electrical propulsion subsystem. The electrical propulsion subsystem includes the thrusters, the power conditioners, the propellant tank, and approximately 16 kilograms allocation for mechanisms, plumbing, etc. Use of net mass as a variable is very convenient from the standpoint of the interface between the trajectory analyst and the spacecraft designer because it provides a convenient and unambiguous mass breakdown. Unfortunately, however, net mass is not the best payoff function to use in performance optimization; the proper payoff function will be called adjusted net mass and will be defined presently. In most cases, design recommendations from the analysis would not be changed by using adjusted net mass rather than net mass as a payoff function. This insensitivity is fortunate because adjusted net mass is a function of the actual spacecraft design configuration and, therefore, cannot be reliably initially estimated.

Adjusted net mass is spacecraft net mass less those parts of the spacecraft subsystems which need not exist if the low thrust propulsion system were removed. In other words, adjusted net mass is that portion of the spacecraft which is required for autonomous operation if the spacecraft were launched ballistically; it is this mass which should be used when making comparisons to ballistic alternatives to mission implementation. The mass breakdown for the baseline spacecraft design is shown in Table 2-2. The dependence of the various subsystem masses on the propulsion power will be discussed in detail to illustrate the computation of adjusted net mass. Performance changes due to changes in propulsion system size will be presumed to increase or decrease the performance pad rather than change the subsystem masses; although changed performance capability might ultimately affect subsystem masses via spacecraft redesign.

The science payload, the communications and data handling equipment, and the CC &S are not affected by changes in propulsion system power level. Note that in the recommended asteroid survey spacecraft, capacitor type meteoroid impact detectors are bonded to the shadow side of the solar array, therefore the amount of area available is obviously affected by the power level selected. The spacecraft power subsystem has the housekeeping power as an input, and includes regulation and distribution to science, communication, data handling, etc.; this subsystem is also unaffected by changes in propulsion system power.

The masses of the electric propulsion system, the propellant, and the solar panel are subtracted from the total injected mass to derive net mass as previously defined. The thruster mass is computed on the bases of information derived from scaling laws. The power conditioning mass

Table 2-2. Subsystem Masses

Subsystem	Mass- kilograms	Propulsion Power Independent Mass- kilograms	Propulsion Power Dependent Mass- kilograms
Science	80.0	80.0	
Communications and data handling	61.0	61.0	
CCS	10.5	10.5	
Spacecraft power	28.5	28.5	
Electric propulsion	62.5		62.5
Propellant	107.0		107.0
Solar Panel	155.0		155.0
Cabling	54.5	34.5	20.0
Thermal Control	14.5	12.5	2.0
Stability and control	77.0	47.0	30.0
Structure	77.0	55.0	22.0
Total	727.5	329.0	398.5

was assumed to vary linearly with P_o (the input power to the power conditioners at 1 AU). Solar panel specific mass was assumed to be 15 kilograms per kilowatt undegraded (18.3 kilograms per kilowatt based on P_o). Since differential changes to the nominal General Electric Company roll-out type design used in the baseline trajectory will actually occur at somewhat smaller values of specific mass, this assumption favors trajectories utilizing lower power propulsion systems. Note that a significant portion of the solar panel is used for housekeeping power (to the spacecraft power subsystem) but charged to the propulsion system; to do otherwise would greatly complicate the bookkeeping.

Approximately 20 kilograms of the spacecraft cabling will be presumed to be directly proportional to P_o and represents the cabling from the solar panel to the power conditioners and from the power conditioners to the thrusters. Thermal control is utilized primarily for science and spacecraft equipment; 2 kilograms has been assumed to be direct proportional to P_o.

Approximately 75 percent of the cold gas and tankage (30 kilograms; the remaining 25 percent is assumed to be leakage) in the stability and control subsystem is assumed to be linearly dependent upon P_o. The remaining 37 kilograms of this subsystem mass includes items which are essentially independent of spacecraft mass: lines, nozzles, and valves. It should be noted that the power dependent allocation is unusually high for this baseline design because the very long coast period requires much more attitude propellant expenditure than does the usual mission profile. This propellant and tank mass would also be reduced by a large factor if liquid hydrazine rather than cold gas were used in the control system. The use of hydrazine is perfectly feasible for this mission; cold gas was selected solely because 0.1 pound hydrazine thruster assemblies have not yet been space-proven. This choice was the conservative approach; there is in fact reason to believe that suitable space qualified liquid hydrazine thrust chamber assemblies will be available in time for use on this mission.

Only 22 kilograms of structure has been assumed to be directly protional to P_o and this is largely allocated to solar panel support. The propulsion system and propellant tank require little in the way of structural support because these loads are largely supported during launch by the payload interstage for the recommended spacecraft design. This is a configuration dependent item; on other designs, a larger percentage of the structure could be power dependent.

The adjusted net mass on the baseline trajectory is 349.9 kilograms. The adjusted net mass is shown as a function of P_o on Figure 2-28; the thrust termination for all of the trajectories takes place at 2 AU. The variations of P_o in this figure are approximately the "rubberization" limits of the present design. As was indicated in Figure 2-13, the optimum performance trajectory has a P_o slightly in excess of 12 kilowatts; C_3 is approximately 3 $(km/sec)^2$. The fact that the "rubberization" of the present design cannot be validly carried through to this optimum point is of no real concern since the theoretical performance improvement at values of P_o greater than about 10 kilowatts is too small to justify the requisite growth in propulsion system size. On the other end of the scale, values of P_o less than about 7 kilowatts, the reduced solar panel area would not permit the area of capacitors presently assumed to be deployed on the back of the panel. At present, there is a performance pad of approximately 20 kilograms even though conservative mass estimates have been used. An additional 20 kilograms of performance pad could be obtained by increasing P_o to about 10 kilowatts. This change can be considered a backup alternative if performance difficulties are discovered before system development. On the other hand, the present performance pad is so marginal that a reduction
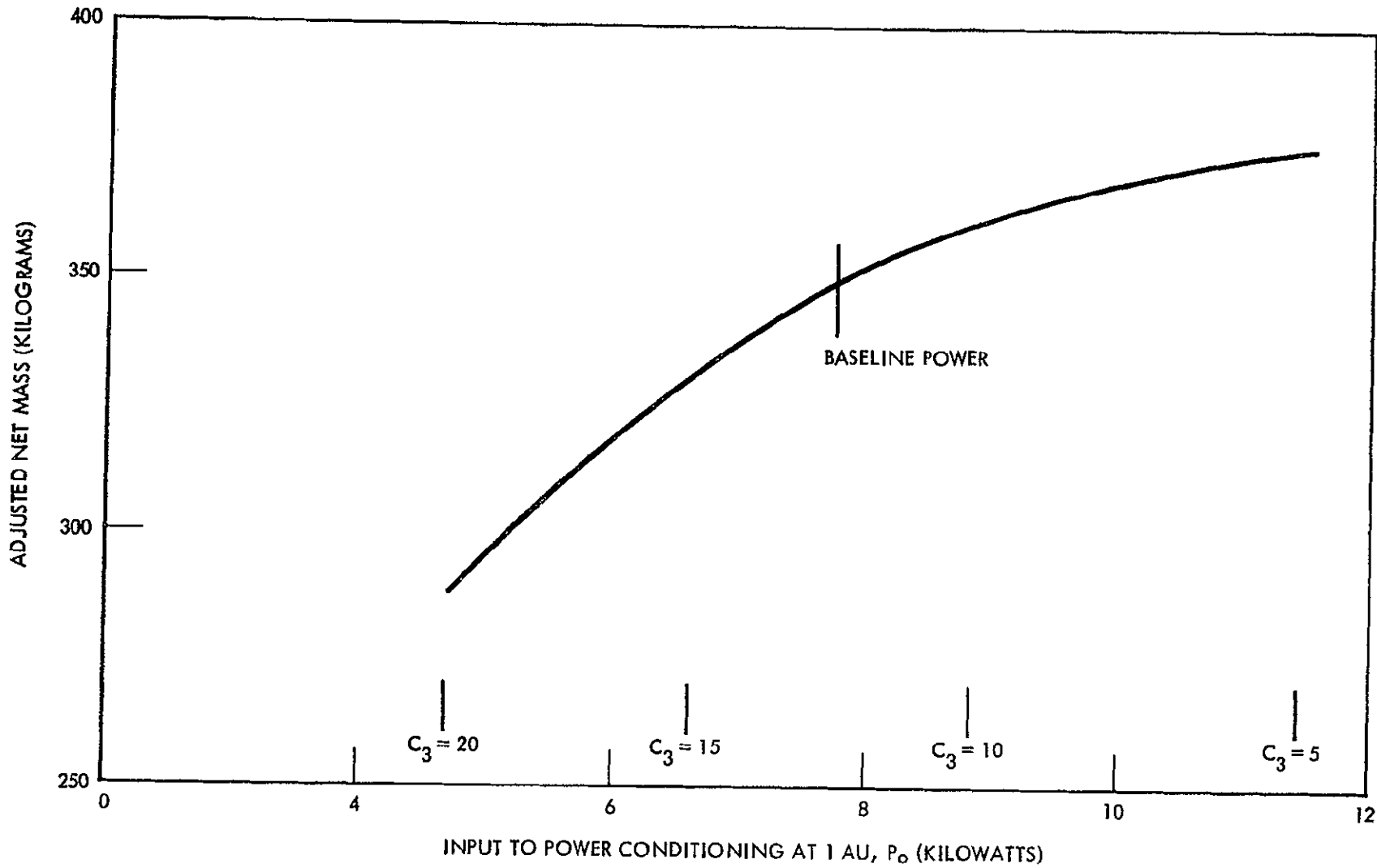
Figure 2-28. Effect of Change in Propulsion System on Baseline Performance

in P_o should not be seriously considered. In summary, the value of P_o (7.75 kilowatts) selected for the baseline trajectory appears to be a reasonable choice.

The problem of estimating adjusted net mass is basically one of estimating adjusted propulsion system specific mass (adjusted to include those parts of the spacecraft subsystems which are not part of the propulsion subsystem but which are required by the propulsion subsystem). The adjusted propulsion system specific mass is approximately 38 kilograms per kilowatt on the baseline trajectory (based on P_o). Since the baseline design utilizes many components which are actually under development, this estimate can be used with confidence. The real question arises as to the proper functional relationship of specific mass as a function of P_o. The values which have been derived and which were used in determining the adjusted net mass of Figure 2-28 are shown in Figure 2-29. For several reasons, including the solar panel specific mass previously discussed, the slope of this curve of specific mass is actually somewhat steeper than that indicated. If this adjustment were made, the performance of the trajectories having higher values of P_o would be improved; those having lower values would be degraded. The situation emphasizes that the true functional relationship of specific mass and P_o usually cannot be available for trajectory analysis unless the trajectory analysis/spacecraft design process is iterated. Fortunately, design decisions are somewhat insensitive to the precise value and functional relationship of low thrust propulsion system specific mass. The effect of variations of ± 5 kg/kw from the baseline of Figure 2-29 is indicated in Figure 2-30. Note that although the adjusted net mass is considerably changed by these large variations, the baseline design is still well below the "optimum" power. The effect of adjusted propulsion system specific mass on optimum C_3 is shown in Figure 2-31.

As mentioned previously, adjusted net mass corresponds to the injected mass for a ballistic spacecraft and, therefore, is the quantity to be optimized. Of course, neither the adjusted net mass nor injected ballistic mass is all science payload. However, an increase in adjusted net mass or injected ballistic mass will always permit an increase in scientific payload. It must be emphasized that any attempt to "optimize" science payload directly is a tactical error because one gets the small payload number by subtracting relatively large assumed subsystem masses from the total injected mass. Because of the small differences of large numbers, this computed science payload is then very sensitive to the assumed subsystem masses; it is possible to obtain almost any result by appropriate scaling assumptions.

Changes in the Nominal. The effect of the launch date on net mass was evaluated and is shown in Figure 2-32. Although the launch date may cause a change in net mass of up to 24 kilograms, this change does not
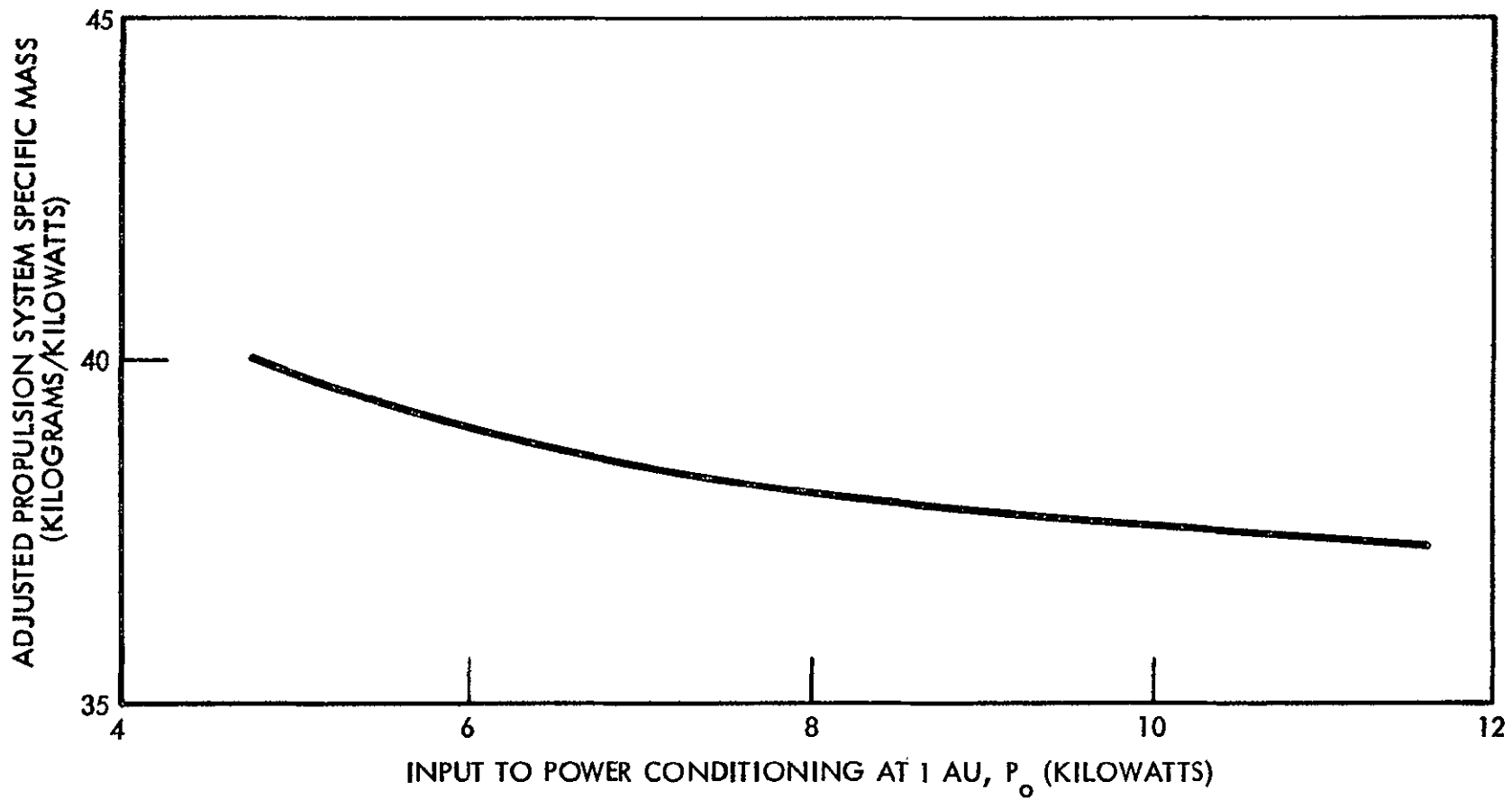
Figure 2-29. Adjusted Propulsion System Specific Mass

Space Division
North American Rockwell
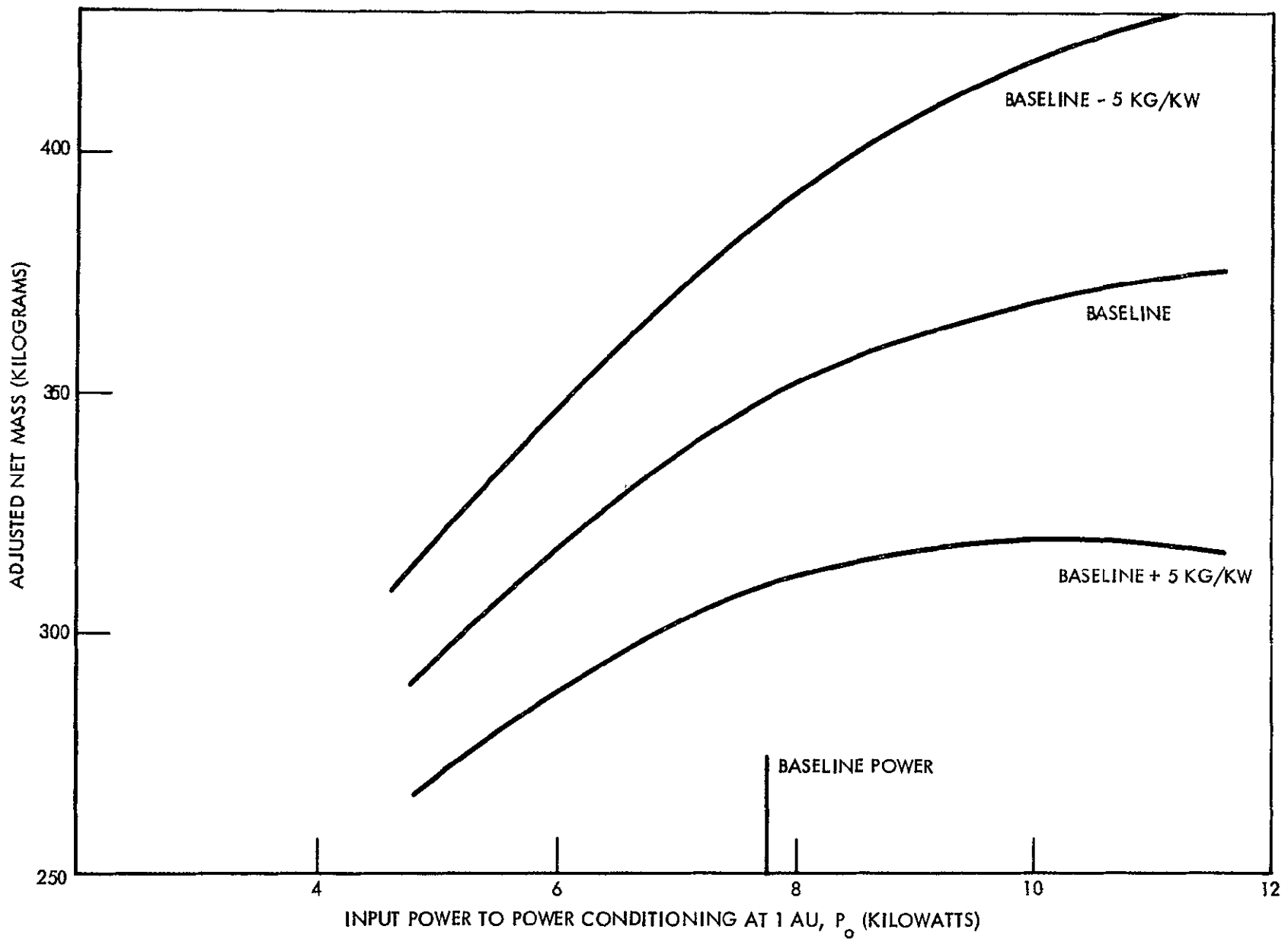
Figure 2-30. Effect of Changes in Propulsion System Specific Mass
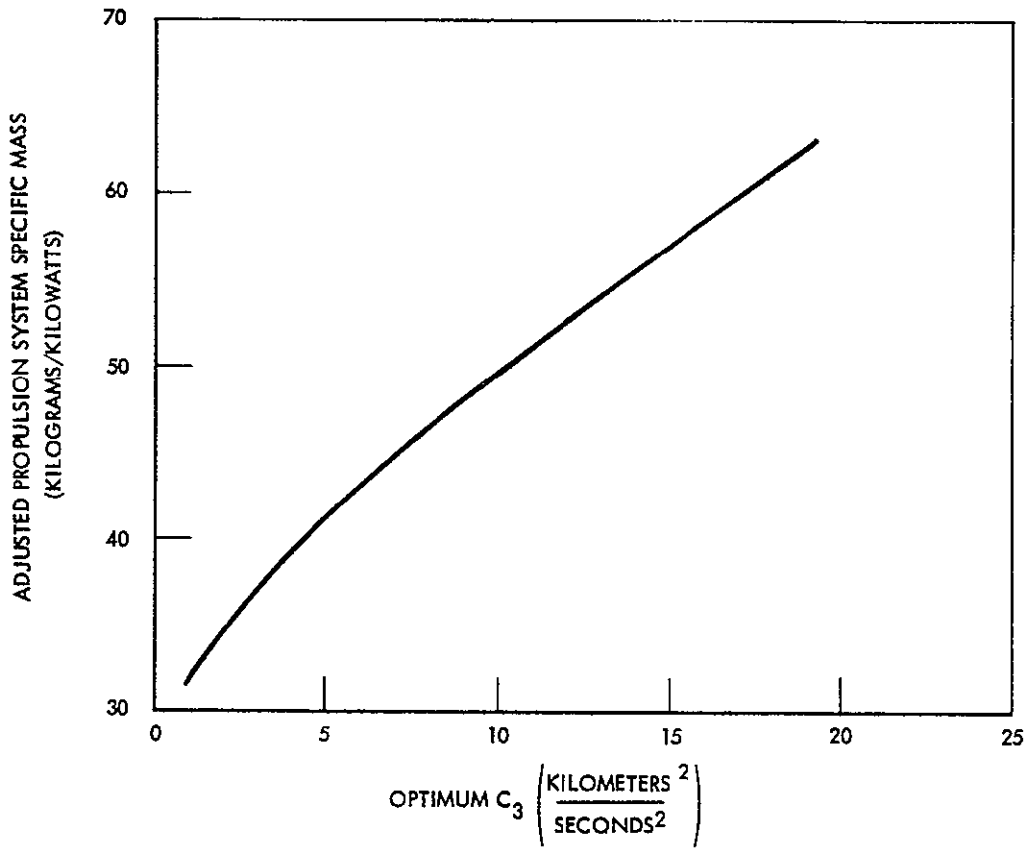
Figure 2-31. Effect of Adjusted Propulsion System Specific Mass on
Optimum C_3 for Asteroid Belt Mission
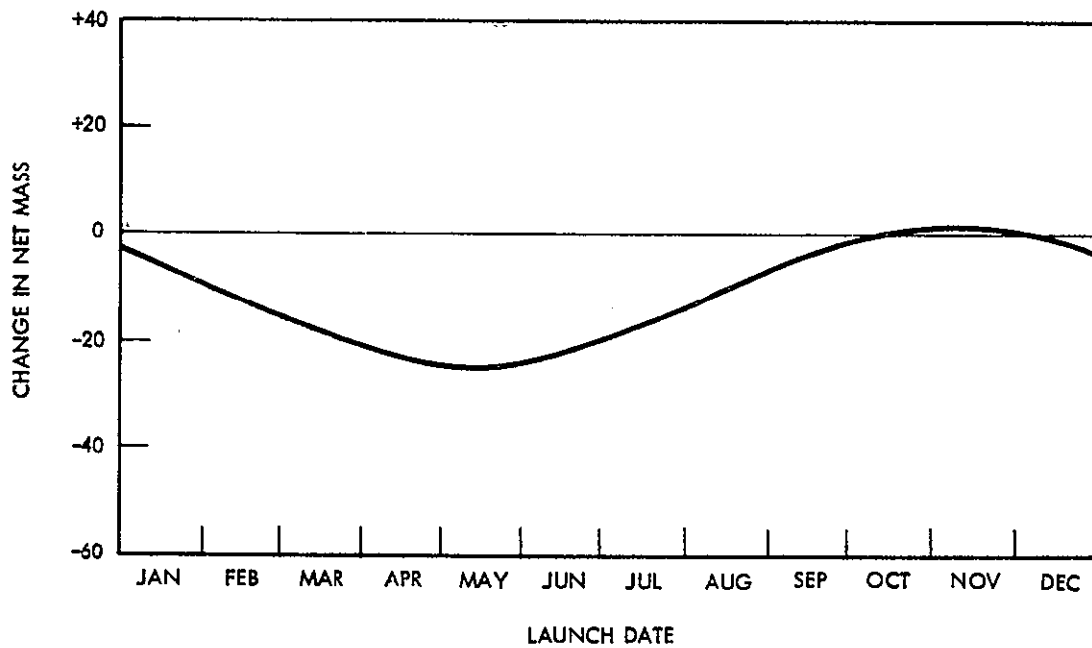
Figure 2-32. Asteroid Belt Mission Baseline Trajectory
Launch Date Performance Changes

2-50

represent a performance dispersion in the usual sense because this effect
can be evaluated before launch.

Estimates of nominal propulsion system mass and performance will
undoubtedly change but can also be reevaluated before launch. Figure 2-33
indicates that potential performance changes are modest for the reevaluations
of propulsion system efficiency which can be reasonably anticipated. Other
possible system changes affecting the nominal include the relative solar
panel power (Figure 2-8) and the effective solar panel specific weight
(including degradation).

One of the important dynamic inputs to any low thrust mission analysis
study is the performance capability of the launch booster. Detailed repre-
sentation of this performance capability is complicated by two factors. In
the first place, ostensibly identical boosters do, in fact, have different
performance characteristics, and the estimated performance capability of
any launch booster relies in part upon statistical analyses and interpretations.
Secondly, the performance capability for any mission depends upon the
launch-time-dependent booster launch azimuth and on-orbit maneuvers. For
example, a specified launch booster may be capable of placing a given pay-
load on an earth escape trajectory with a value of C_3 between 12 and 15
$(km/sec)^2$, this uncertainty being due to unpredictable statistical variations
in the performance and use of the launch booster itself. In order to facilitate
low thrust spacecraft and propulsion system design studies, these statistical
considerations are ignored and a single value is used as an indication of
launch booster performance (12 $(km/sec)^2$), leading to representation of
performance capability as a single curve of injected mass as a function of
C_3 (Figures 2-5 and 2-6). Proper tradeoffs are performed in the optimization
because launch booster statistical considerations do not have a first order
influence on the slope of injected weight versus C_3. However, the nominal
performance of the launch booster (Figures 2-5 and 2-6).will unquestionably
be reevaluated before final spacecraft design and development.

Performance Dispersions. The performance characteristics of the
Atlas/Centaur launch booster (Figure 2-5) are assumed to be a minimum
guaranteed (-3σ); with maximum (+3σ) performance the same mass can be
launched with a C_3 which is about 3.7 $(km/sec)^2$ higher than the nominal.
This is a statistical variation and is not related to the variations in the
nominal previously discussed.

The solar cells have been assumed to degrade 18 percent instantaneously
upon deployment, and remain at this performance level throughout the mis-
sion. This assumption is conservative, particularly at the start of the
mission, and presumably represents worst case (-3σ) performance for this
subsystem.
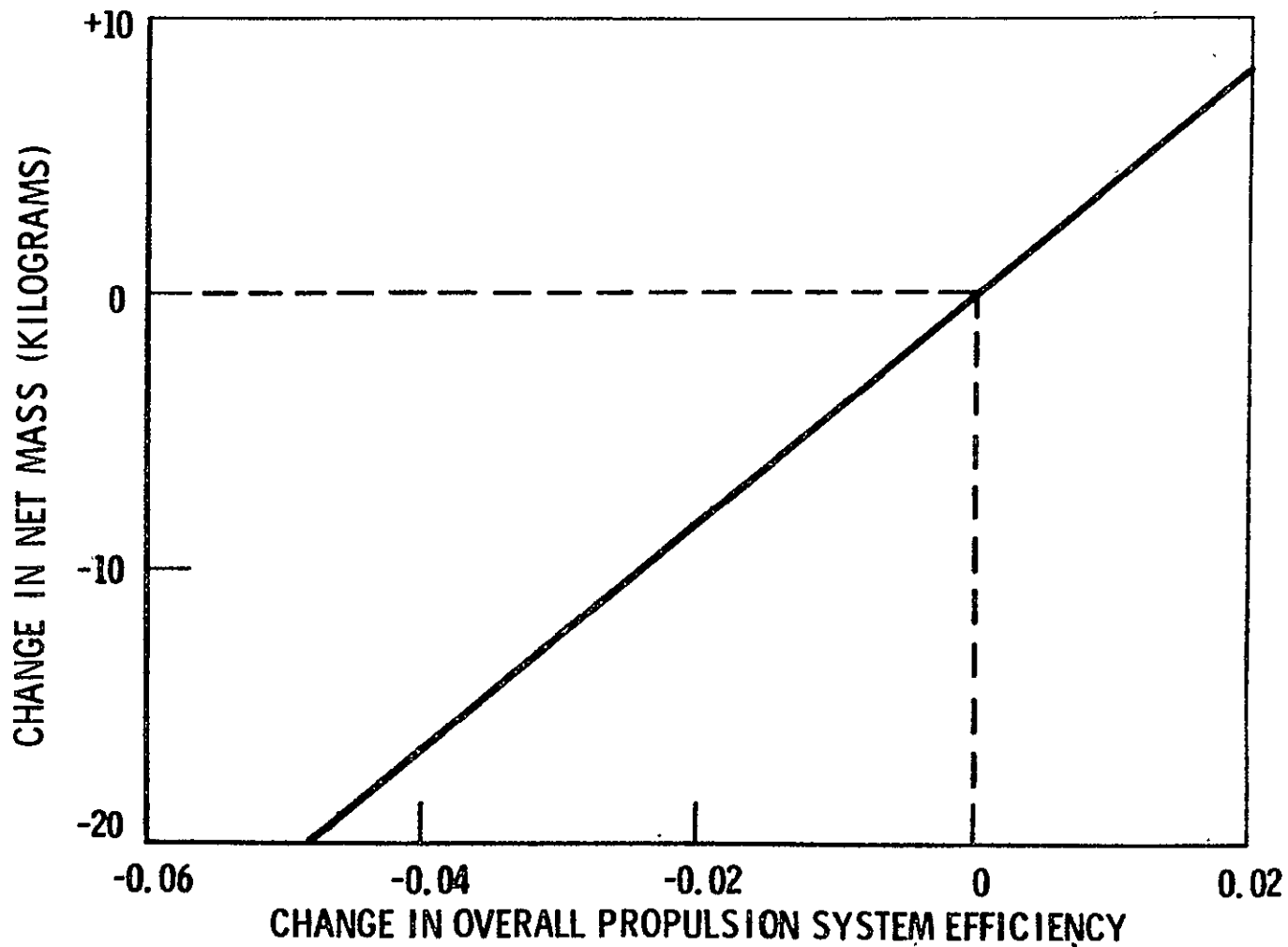
Figure 2-33. Effect of Propulsion System Efficiency on Net Mass Asteroid
Belt Mission Baseline Trajectory

Space Division
North American Rockwell

Propulsion system dispersions are listed in Table 2-3. The source dispersions are the best current estimates; the other table entries are computed from these estimates. The power conditioning efficiency, the discharge chamber losses, and the beam voltage are independent sources of performance anomalies; the total effect on thruster input power is then the root sum square or 1.2 percent (3σ). The control loop accuracy limits represent the excursions experienced in continuous normal limit cycle operation; since the input power must always be available, this requires that the nominal input power be reduced by 0.6 percent (0.5 percent +0.1 percent). The total effect of propulsion system dispersions on thruster input power is then 1.8 percent (1.2 percent +0.6 percent). This dispersion is not related to the power matching losses previously discussed.

It should be noted that performance dispersions given here are for missions during which no subsystem failure occurs.

Performance on Untargeted Missions. The 3.5 AU asteroid belt probe mission can utilize an "untargeted" guidance profile to satisfy all science objectives. In this mode, the spacecraft orbital energy would be increased as rapidly as possible until aphelion is extended to 3.5 AU, at which time low thrust propulsion would terminate. Neither the non-radial position nor time of aphelion or any other trajectory point would be controlled. This procedure has the advantage of maximizing the probability of satisfying the science objectives, but does not provide a demonstration of the capability of low thrust propulsion to perform a targeted mission (planetary flyby).

The solar cell output will probably exceed that assumed in the baseline trajectory throughout the thrusting period; and within the maximum power utilization capacity of the propulsion system, this increased power output can be used to increase the mass flow rate (and thrust). The desired aphelion can then be obtained by using higher values of thrust for a shorter total thrusting time. The change in thrusting time depends on the magnitude and time history of the usable "excess" power; if a constant percentage change were usable throughout the mission (an unlikely circumstance) the effect would be the same as an identical propulsion system efficiency change. Since the assumed solar panel degradation is 18 percent, the actual degradation could easily leave an "excess" power exceeding the magnitude of the effective power changes due to propulsion system efficiency perturbations. The change in low thrust propulsion operating time with perturbations in propulsion system efficiency is shown in Figure 2-34. The 1.8 percent 3σ propulsion system dispersion required a thrusting time change of about 19 days in order to hold aphelion at 3.5 AU. As indicated above, a much larger decrease in thrusting time could be produced by reduced solar panel power degradation.

Table 2-3. Propulsion System Dispersions

Dispersion Source	Source Dispersion (Percent)	Thruster Input Power (Percent)	Ion Mass Flow Rate (Percent)	Neutral Mass Flow Rate (Percent)	Mean Ion Exit Velocity (Percent)
Power conditioning efficiency (3σ)	1.0	1.0	—	—	—
Discharge chamber loss (3σ)	5.0	0.6	—	—	—
Beam voltage (3σ)	1.0	0.4	—	—	0.5
Control loop (accuracy limit)					
Beam current	0.5	0.5	0.5	—	—
Discharge current and vaporizer power	0.5	0.1	—	0.1	—

Space Division
North American Rockwell
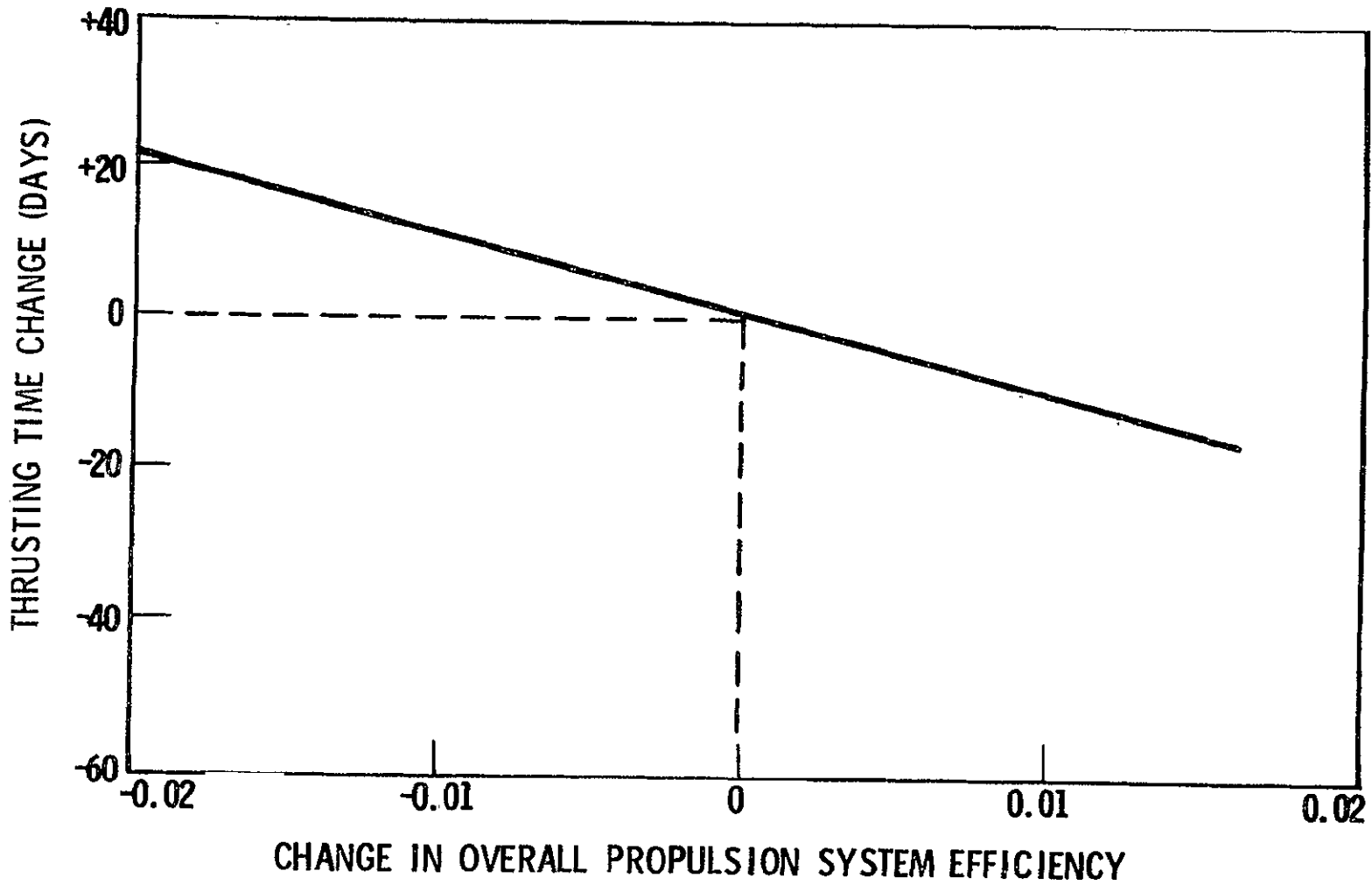
Figure 2-34. Effect of Propulsion System Efficiency on Thrusting Time,
Asteroid Belt Mission Baseline Trajectory

An untargeted mission would usually utilize a soft (propellant depletion) shutdown of the launch booster. Since the asteroid belt probe nominal trajectory assumes -3σ launch booster performance. a significant shortening of the ion propulsion thrusting time (see Figure 2-35) will usually occur as a result of the greater C3 obtained when a soft shutdown of the launch booster is used.

In summary, the baseline mission trajectory is actually more conservative than -3σ in performance (including power matching losses) for an untargeted mission assuming the inputs (Figures 2-5 and 2-7) are valid.

Performance on Targeted Missions. Although the primary science objectives do not require precise trajectory control, the mission could include a requirement for flyby of a pseudo target. The spacecraft has the subsystems required to operate in this mode, and doing so could provide a convincing demonstration of the capabilities of solar powered spacecraft. The performance cost in implementing this experiment is about 20 kilograms relative to the baseline trajectory (the performance pad on the baseline design is reduced about 20 kilograms if a targeted mission is implemented).

On a targeted mission, the actual spacecraft thrust acceleration must conform reasonably closely to the preplanned nominal to avoid a large "miss" of the target. This constraint implies a hard (desired velocity) cutoff of the launch booster and (except for guidance corrections) a preplanned thrust-time profile; therefore, Figures 2-34 and 2-35 are not applicable to a targeted mission.

The 1.8 percent 3σ propulsion system dispersion requires the nominal trajectory performance to be correspondingly reduced to assure that the desired thrust acceleration can always be obtained; from Figure 2-33 this dispersion requires a decrease of about 8 kilograms in launch mass. This performance loss has not been included in the baseline trajectory. Power matching losses (about 6 kilograms) have been previously discussed; these losses must be included in a targeted mission.

Since the 18 percent solar panel degradation used in the nominal presumably represents -3σ subsystem performance, no adjustment of the baseline trajectory is required.

Guidance corrections can probably be implemented with an excess acceleration capability of 1 percent; from Figure 2-33 the concomitant performance loss is about 4 kilograms in launch mass. The excess propellant required for guidance corrections appears to be less than 1 percent (about 1 kilogram); an amount substantially less than tank ullage (about 3 percent). Guidance dispersions are therefore a minor factor in performance estimation.
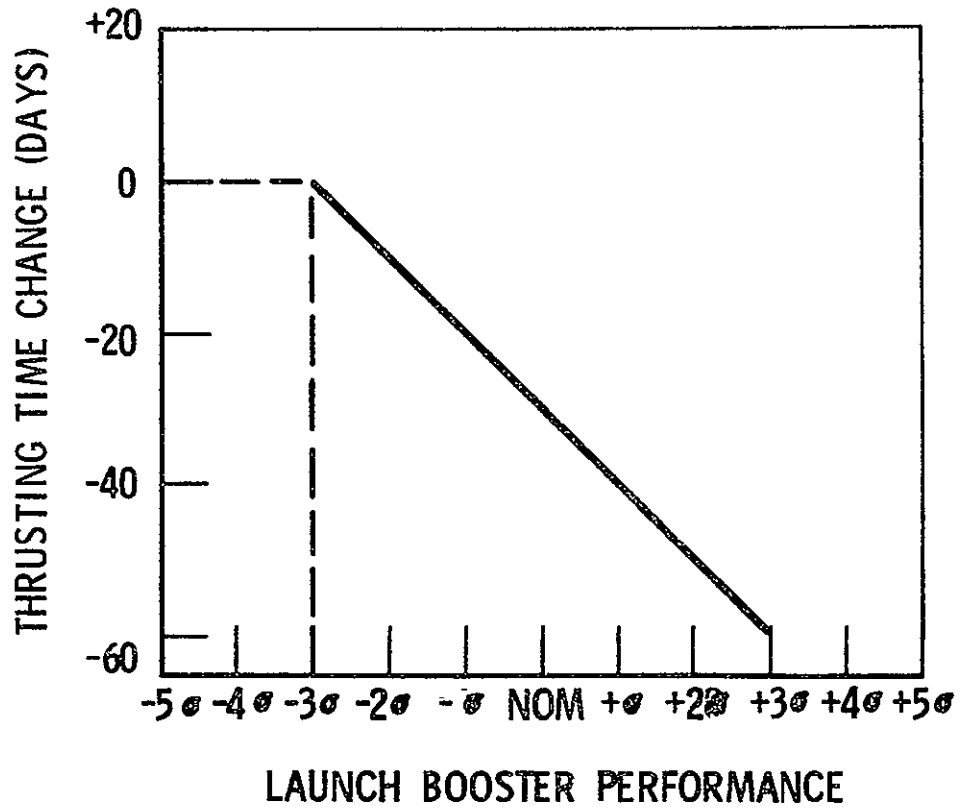
Figure 2-35. Effect of Launch Vehicle Performance Dispersions on Thrusting Time, Asteroid Belt Mission Baseline Trajectory

Trajectory and Performance Analysis for Alternate Missions

Although the primary purpose of this study was to design a spacecraft to probe the asteroid belt, the baseline spacecraft configuration selected is suitable for other missions. The performance of this spacecraft was evaluated for two such missions, a solar probe and an out-of-ecliptic probe. The use of the Titan III-C as a launch booster with the baseline spacecraft has been investigated for both the primary and alternate missions. The ground rules used for the generation of the baseline trajectory were also used in this study. The propulsion systems used in this study are identical to the baseline, except as specifically noted.

Asteroid Belt Probe Mission Using Titan III-C

The use of the baseline ion propulsion system on a spacecraft launched with the Titan III-C provides a net mass of 674. kilograms; 94. kilograms of propellant are required. The thrust termination still takes place at 2 AU, but the time is reduced to 193 days, with a resultant slight increase in propulsion system reliability.

Solar Probe Mission

The net mass, propellant mass, and time to perihelion are shown as a function of perihelion radius for both the Atlas/Centaur and Titan III-C launch vehicles in Figures 2-36, 2-37 and 2-38.

Out-Of-Ecliptic Probe

The net mass and propellant mass are shown as a function of final inclination to the ecliptic for both the Atlas/Centaur and Titan III-C launch vehicles in Figures 2-39 and 2-40. Four thrust periods were used, and the time to maximum distance out of the ecliptic is 680 ±5 days for all the conditions shown in the figures.

Other Missions

The baseline spacecraft and propulsion system designs are versatile and therefore adaptable to other missions. Trips to Venus, Mars, or Jupiter are possible; but an asteroid intercept is perhaps more intriguing because it could be implemented while satisfying the baseline mission objectives if an asteroid with a suitable ephermeris were chosen. A primary requirement is that the intercept point be near the ecliptic plane to avoid a large performance loss.
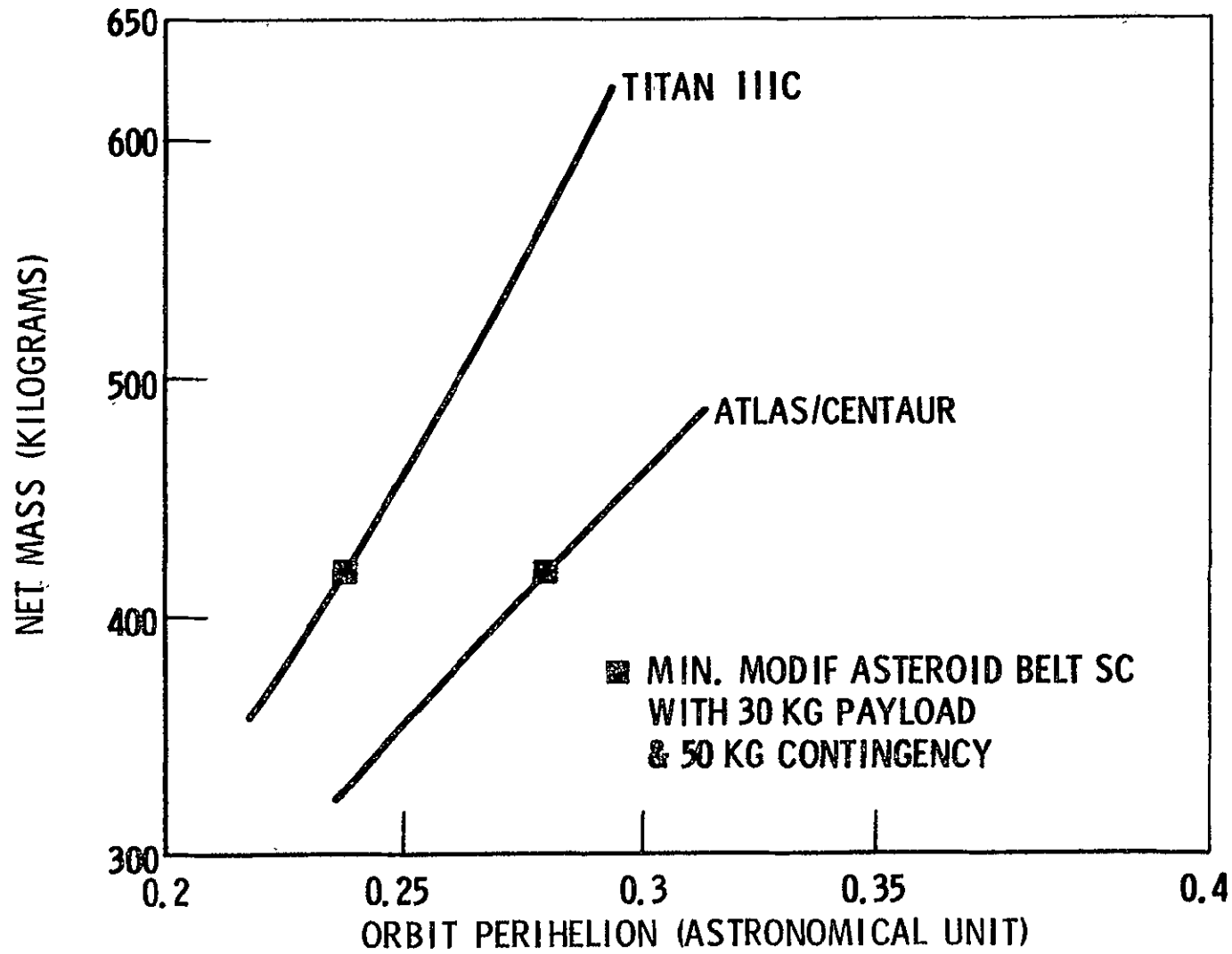
Figure 2-36. Solar Probe Mission Performance (P_O = 7.8 Kilowatts)

Space Division
North American Rockwell
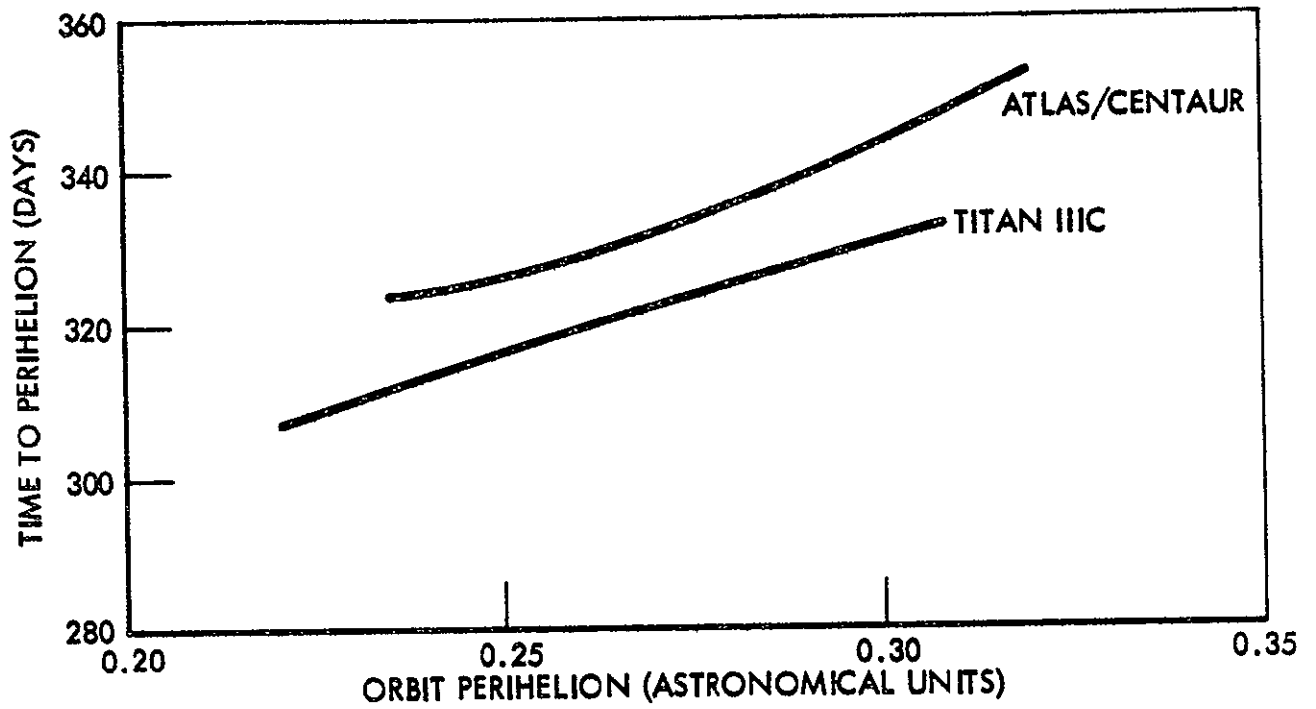
Figure 2-37. Solar Probe Mission
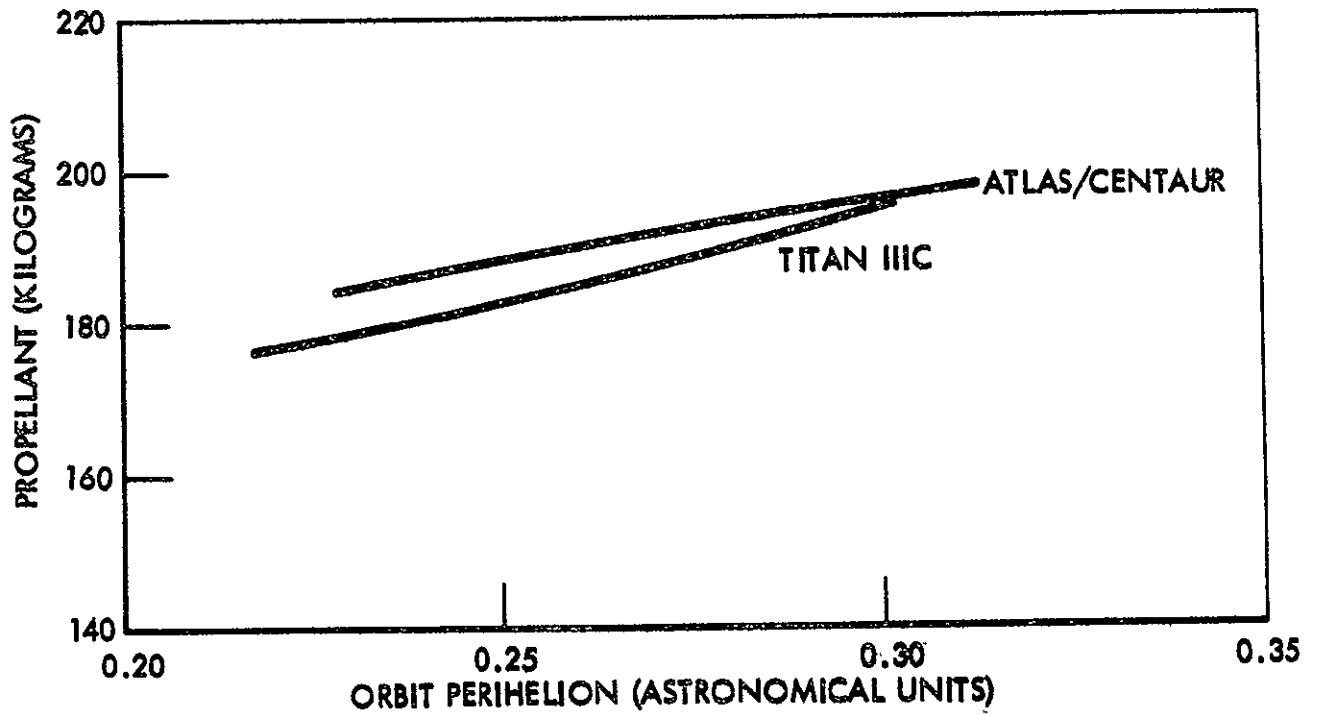
Figure 2-38. Solar Probe Mission
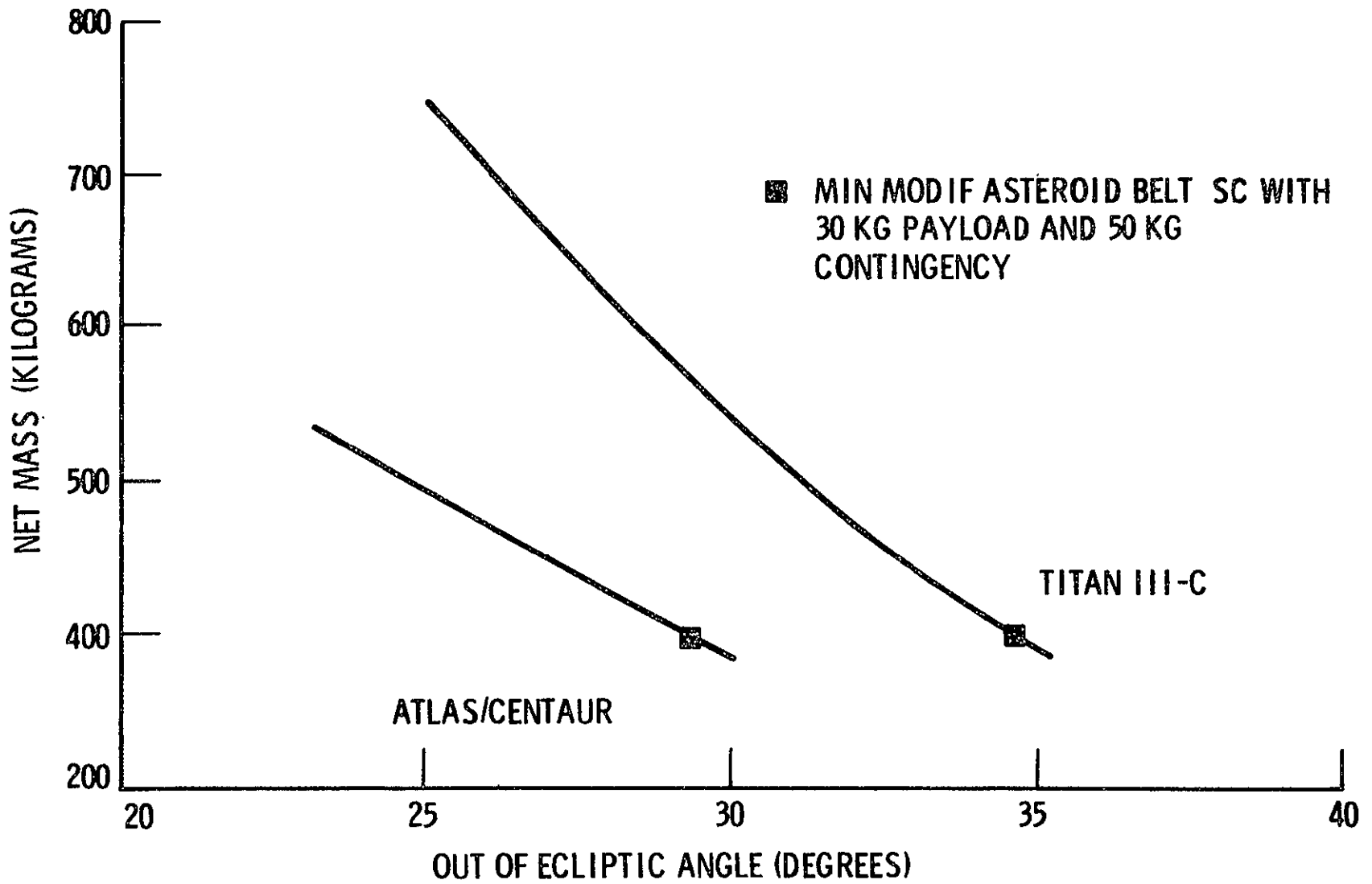
Figure 2-39. Out-of-Ecliptic Probe Mission Performance (P_O = 7.8 Kilowatts)

Space Division
North American Rockwell
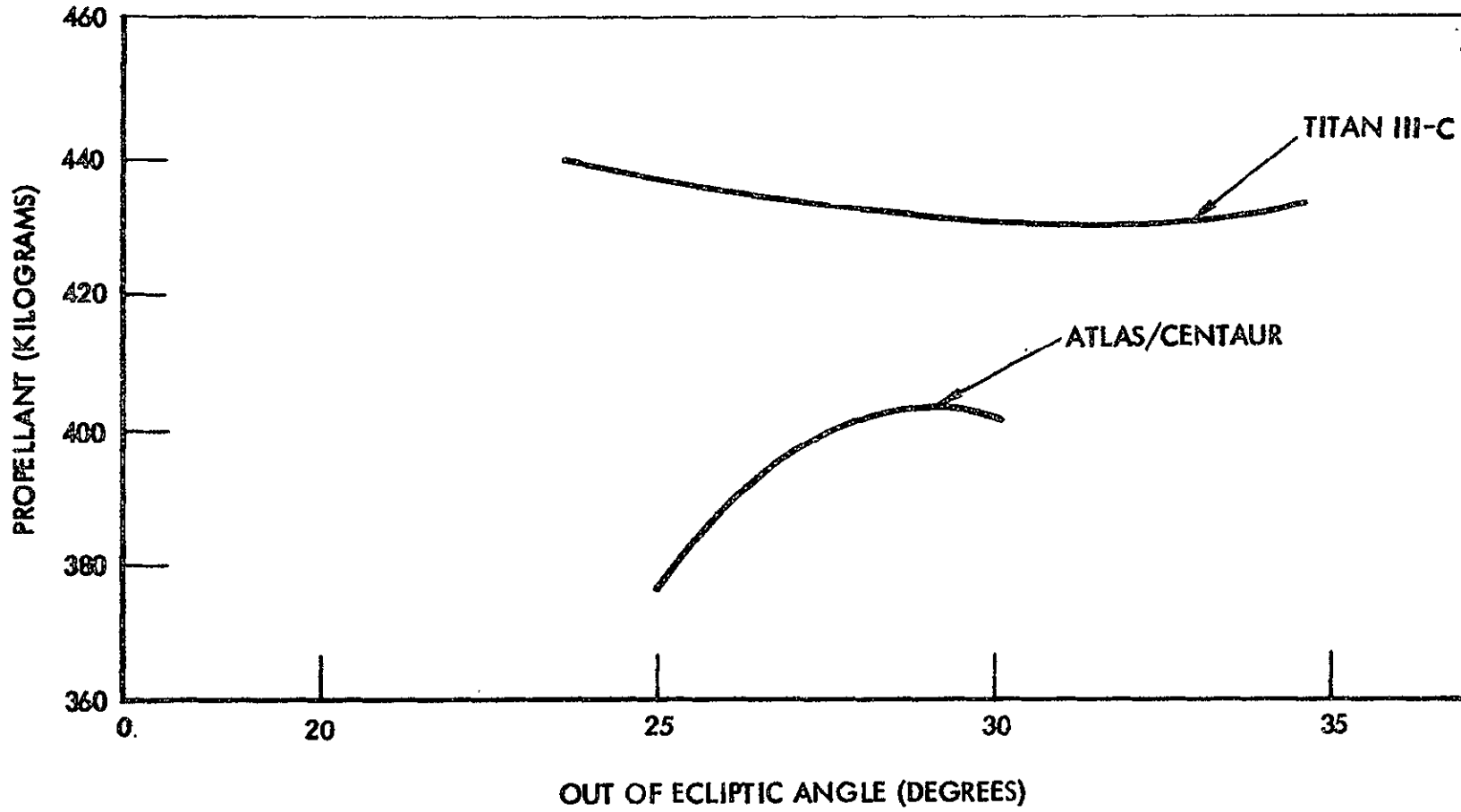
Figure 2-40. Out-of-Ecliptic Probe Mission

GUIDANCE ANALYSES

SEP Trajectory Dispersion Analysis

The primary purpose of this effort is to perform trajectory dispersion analyses for SEP missions. In order to accomplish this task it is necessary to define an error model which determines SEP heliocentric trajectory dispersions (deviations from the nominal) as a function of trajectory initial conditions (heliocentric injection errors) and in-flight random accelerations (thrusting control errors).

The trajectory dispersion time-varying covariance matrix can be computed by a well known, but rather complex, equation for a linear time-varying system excited by a random forcing function; however, this approach requires that the linearized equations of motion be computed numerically by first-order differences of the nominal powered flight trajectories or numerical integration of the state transition matrix, and subsequent numerical integration of the covariance matrix equation. This approach is generally computationally inefficient and would require significant computer running time which could be prohibitive for parametric analyses.

Thus, this effort was devoted to the formulation of a simplified and efficient error model which would be sufficiently accurate for the present problem. Accordingly, an error model was defined on the basis of an osculating ellipse: for small segments of the powered trajectory the first-order sensitivities are computed on the basis of local conic motion for the heliocentric flight phase. Using this approach, the time-varying state transition matrix can be computed without lengthy numerical methods, and a highly efficient error model can be defined by propagating the trajectory dispersion covariance matrix on a discrete basis over small intervals of the powered flight trajectory. A more detailed discussion of this error model is given in Appendix B-1.

SEP Trajectory Dispersion Data

Using the trajectory dispersion error model defined in Appendix B-1, a set of trajectory dispersion data was generated for a typical SEP trajectory as shown in Figures 2-41 and 2-42. The data for heliocentric injection errors and in-flight thrusting control errors are as follows:

1. Heliocentric Injection Errors:

    Position Errors = 500 KM (1σ)

    Velocity Errors = 4 M/S (1σ)
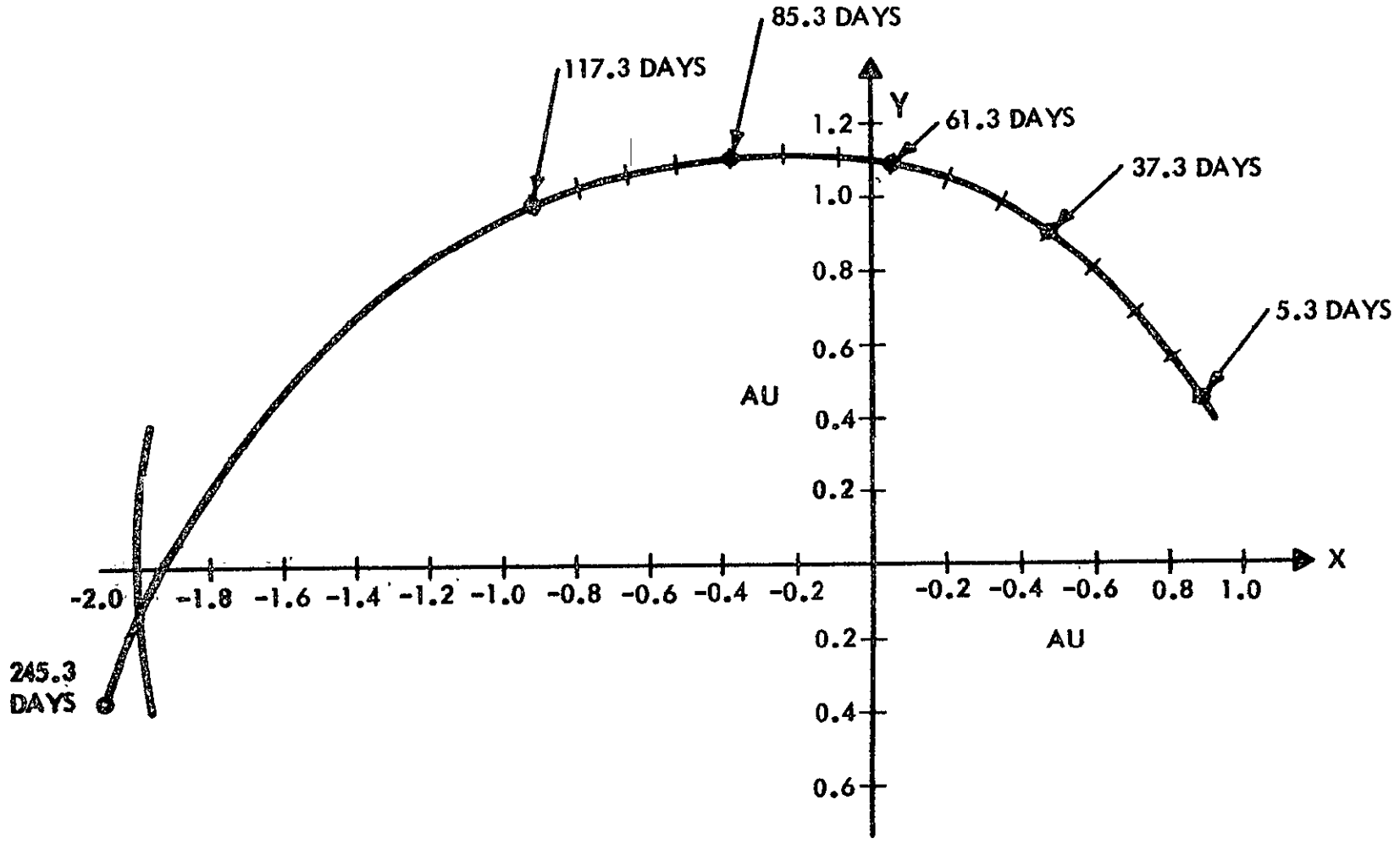
Figure 2-41. Powered Flight Phase Trajectory
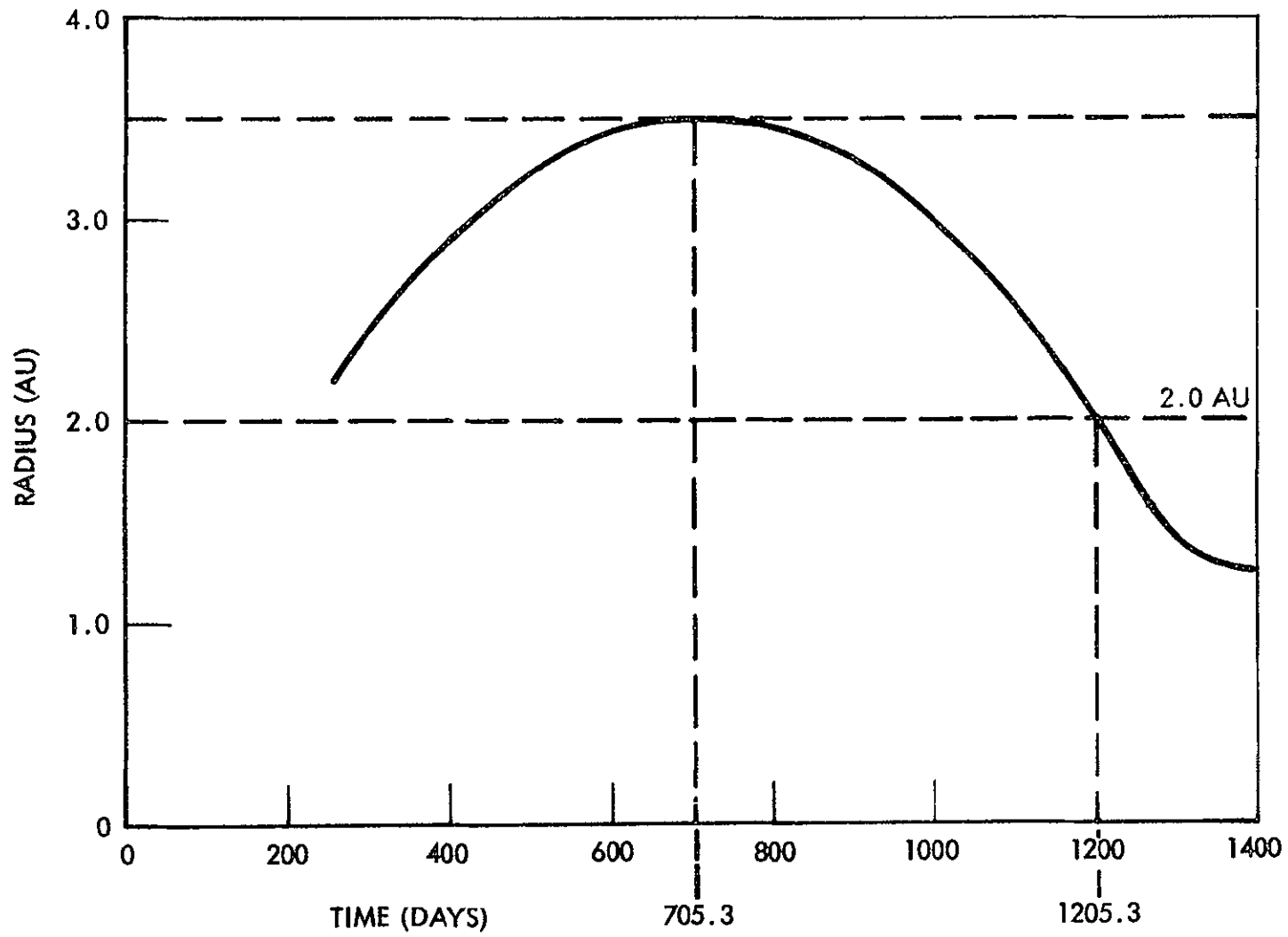
Figure 2-42. Spacecraft Radius for Coast-Flight Phase

Space Division
North American Rockwell

2. In-Flight Thrusting Errors:

1 Percent Spherical Distribution (1σ)

The trajectory dispersion data are presented in Figures 2-43 through 2-47.
(The co-ordinate system used is shown in Figure 2-41.) The total trajectory
dispersions in Figure 2-43 include both heliocentric injection and thrusting
control error contributions. Figures 2-44 through 2-47 present trajectory
disperions due to thrusting control errors for correlation times (τ) of 1, 10,
100 and 1000 seconds, respectively. It is noted that the heliocentric
injection errors dominate the thrusting control errors for all cases
considered, however, for a larger control error correlation time the
contribution of control errors will begin to approach that of the injection
errors. Also, a higher percent control error will increase the contribution
of control errors. It is noted that for the values of thrusting control error
correlation time considered the positional error variances are approximately
proportional to the correlation time.

A compilation of the positional errors is given in Table 2-4, which
includes propagation of the errors at "cutoff" to aphelion of the coast flight
trajectory as shown in Figure 2-42. As noted, the data in Table 2-4 is for
a thrusting control error correlation time of 1000 seconds. The dispersion
errors are tabulated for thrust cutoff and aphelion portions of the trajectory
and although, as absolute values, they are rather large, the asteroid belt
survey mission does not require accurate guidance and therefore may employ
the open loop guidance mode.

Delta-Velocity Guidance Analysis

The primary purpose of this effort is an assessment of the delta-
velocity (ΔV) guidance requirement to correct the trajectory dispersions
considered in the previous section. Specifically, an assessment of the ΔV
requirement to correct the terminal positional errors is of interest.
Genreally, the ΔV requirement is a function of the following:

1. Heliocentric Injection Errors

2. In-flight Thrusting Control Errors

3. Spacecraft State Estimation Errors

4. ΔV Control Errors
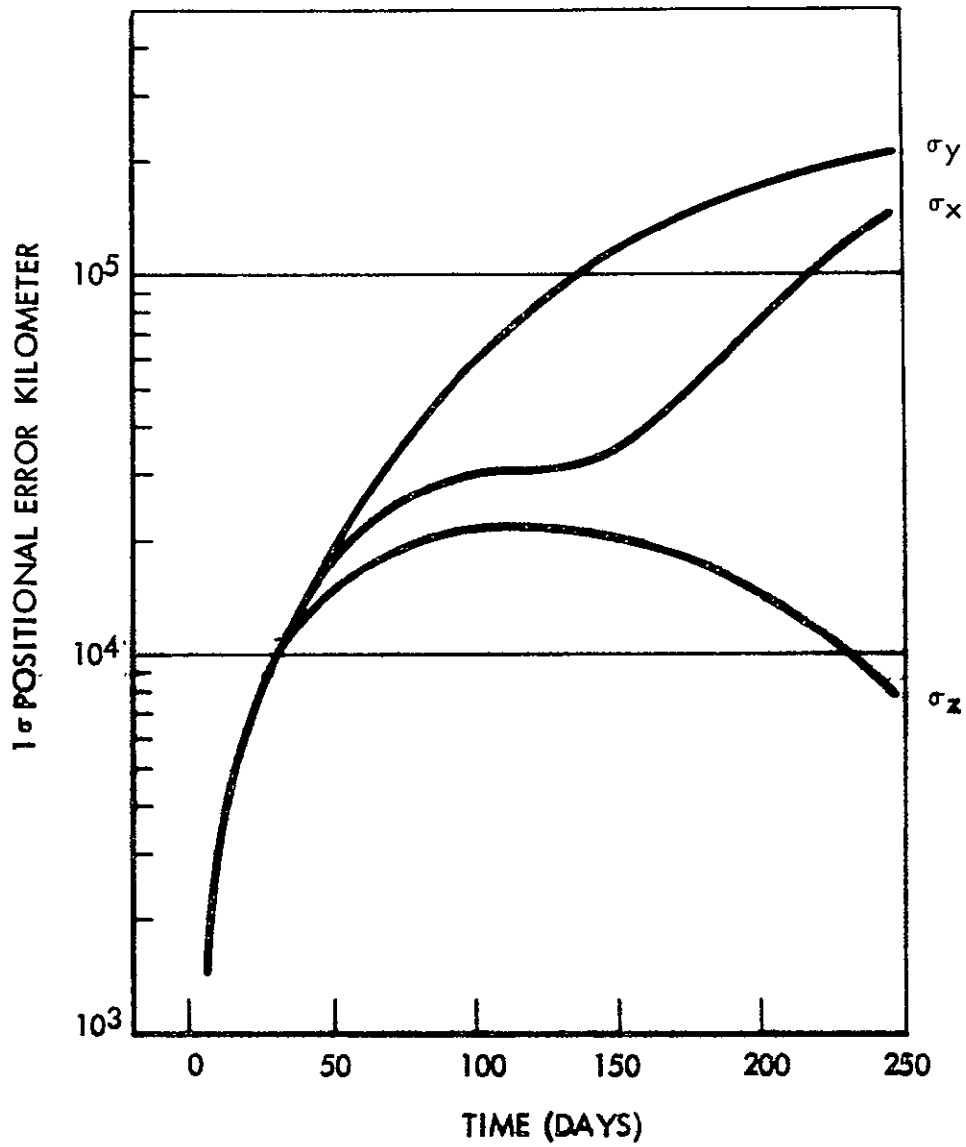
Figure 2-43. Total Trajectory Dispersion,
Including Heliocentric Injection Errors
and Inflight Control Errors, $\tau = 1000$

2-67
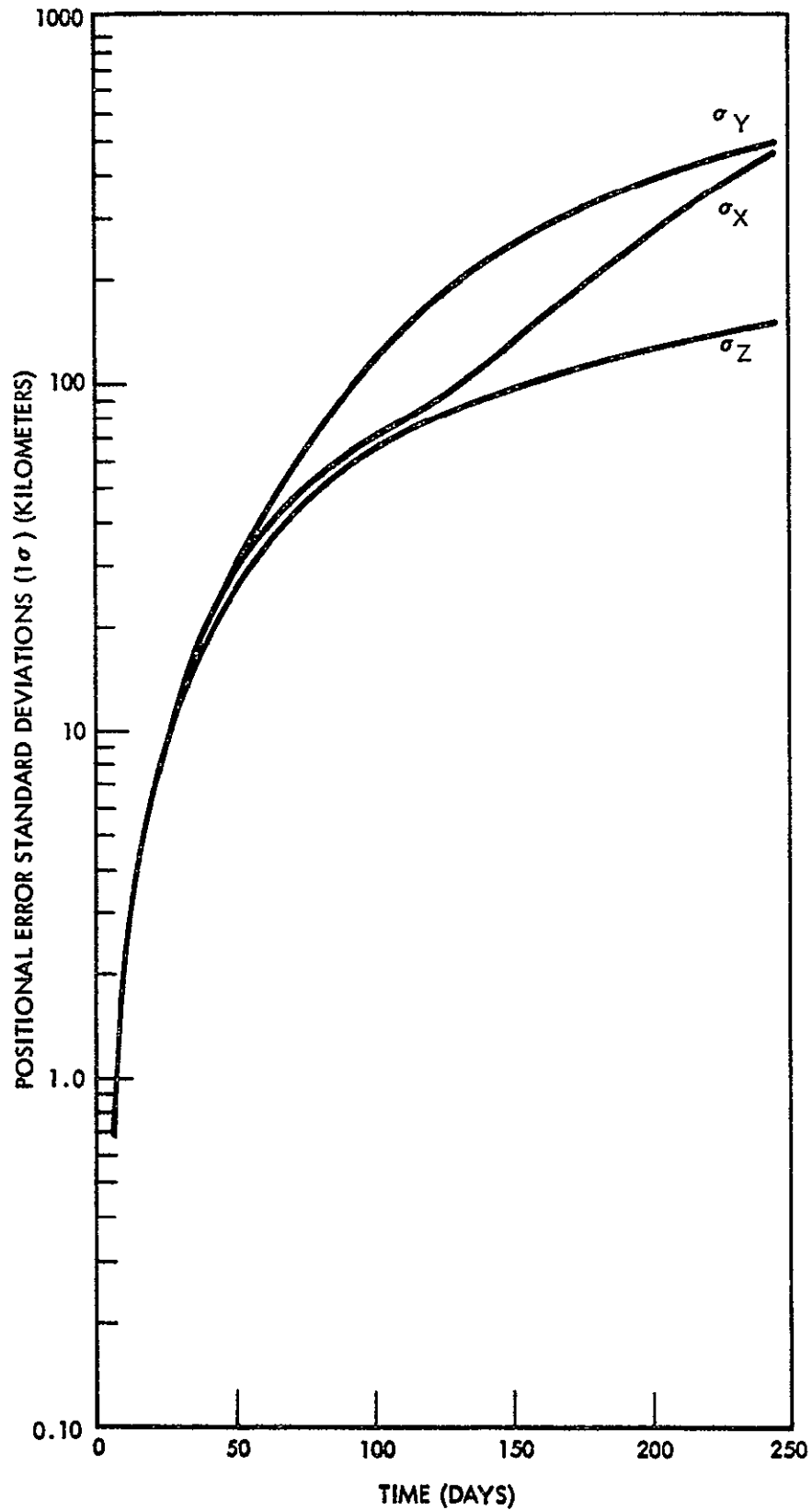
Figure 2-44. Trajectory Dispersion Due to In-Flight Control Errors $\tau = 1.0$
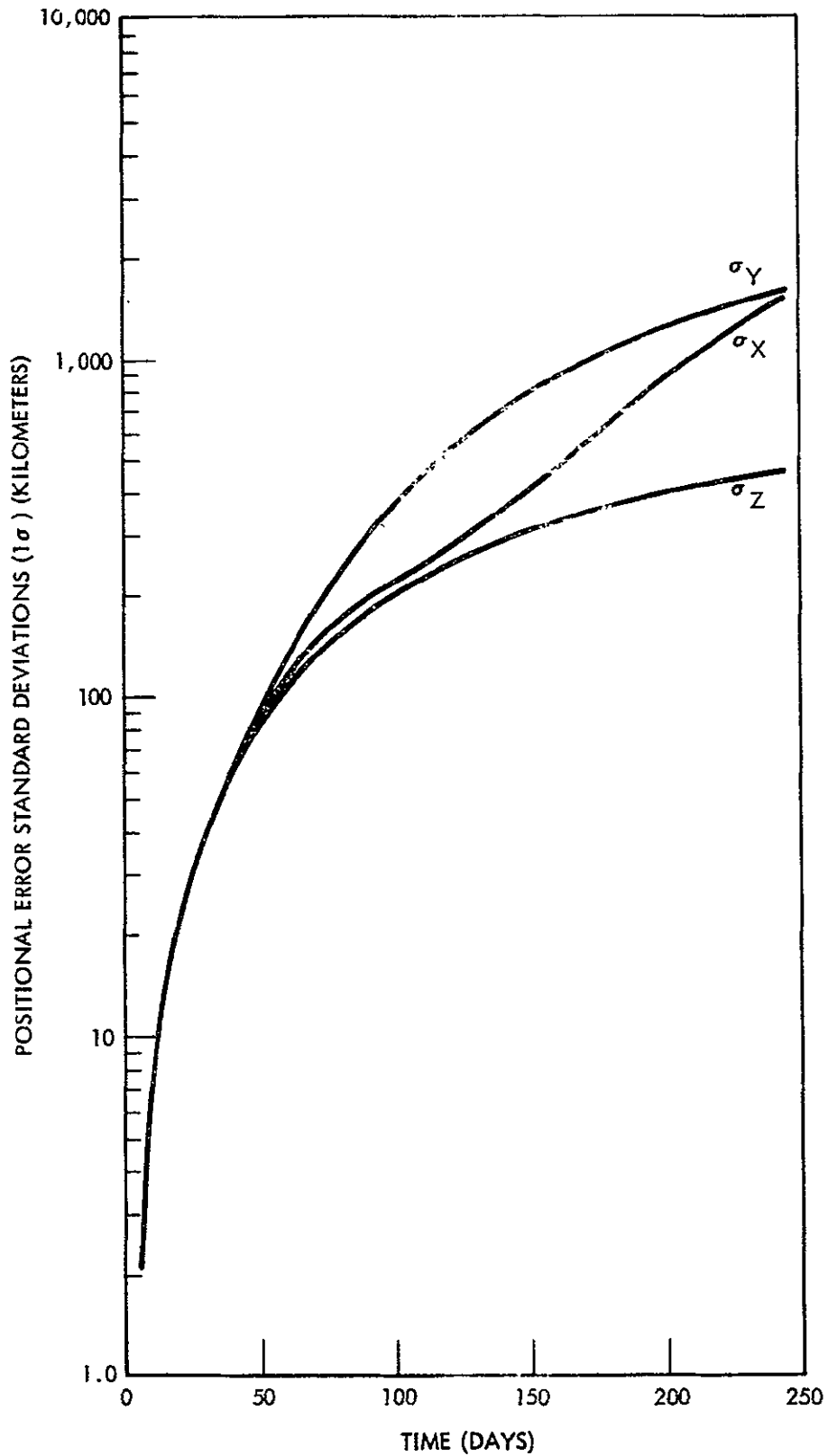
Figure 2-45   Trajectory Dispersion Due to In-Flight Control Errors
$\tau = 10.0$

2-69
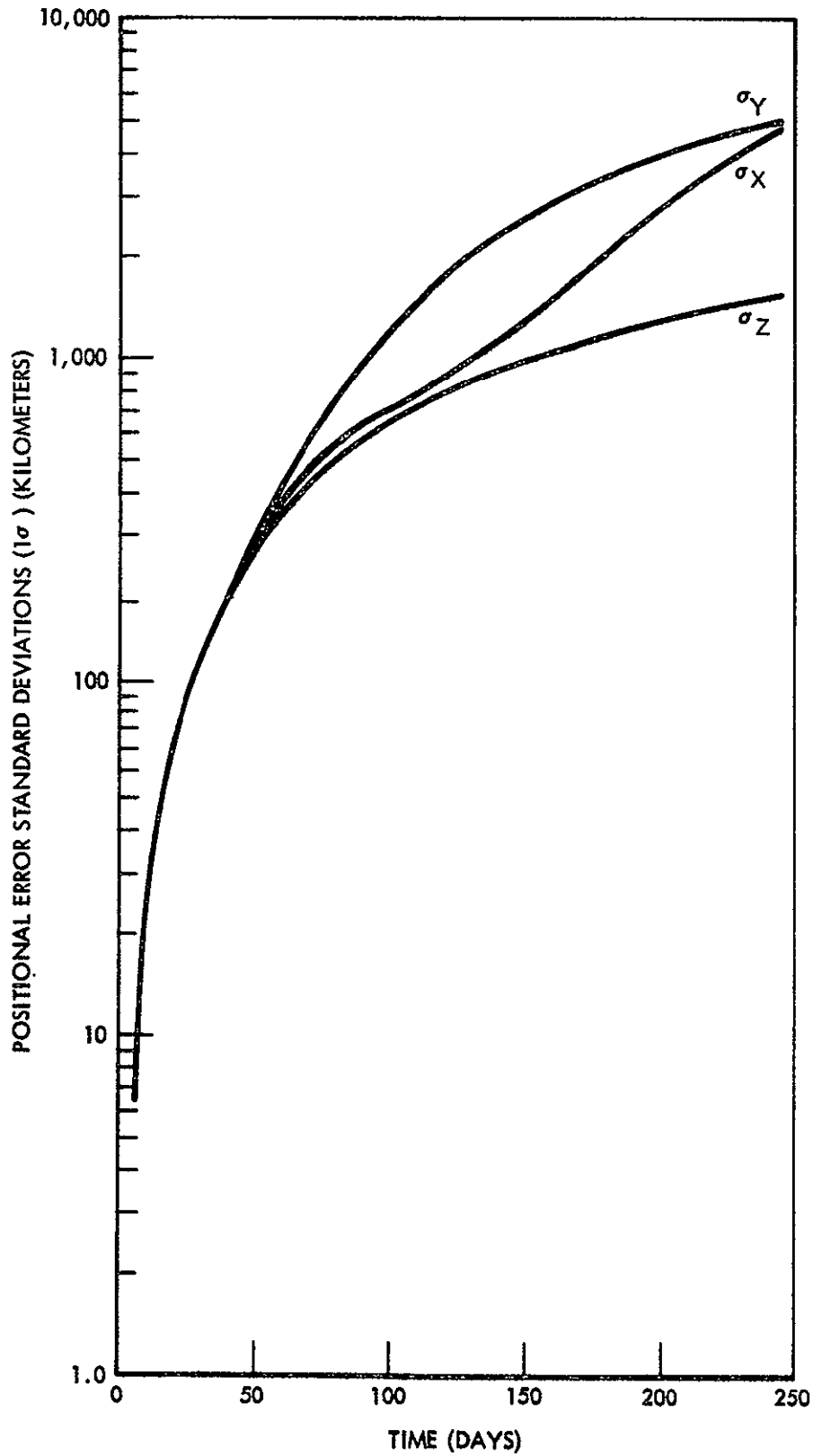
Figure 2-46. Trajectory Dispersion Due to In-Flight Control Errors
$\tau = 100.0$
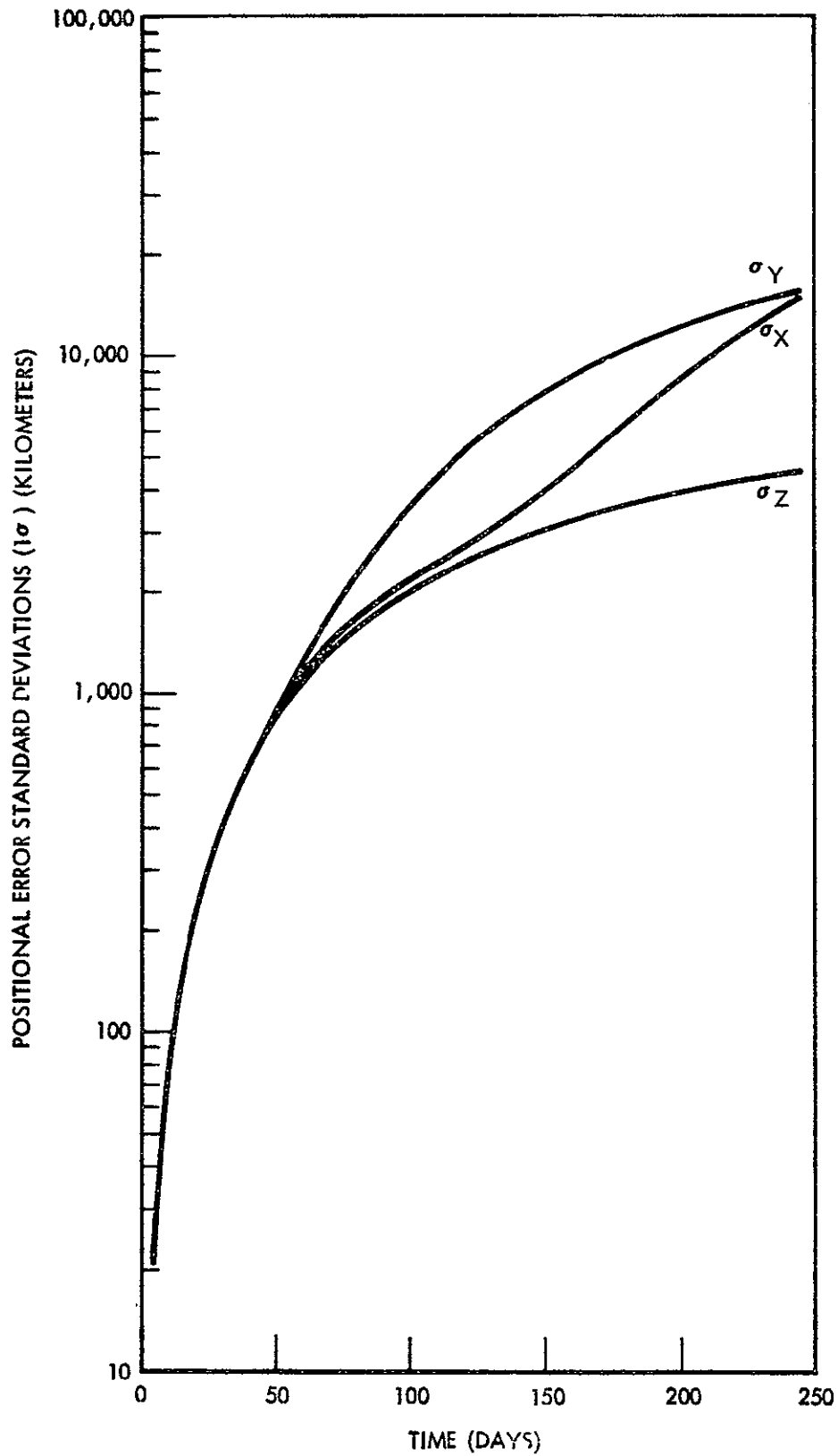
Figure 2-47. Trajectory Dispersion Due to In-Flight Control Errors
$\tau = 1000.0$

2-71

Table 2-4. Trajectory Dispersion Errors (Open-Loop Guidance)

Time	Function		X	Y	Z
At Cutoff	Heliocentric Injection Error	1σ	143,280 km	208,630 km	7,947 km
	Thrust Control Error*	1σ	15,410	15,960	4,781
	Total	1σ	144,110 km (0.000964 AU)	209,240 km (0.001399 AU)	9,274 km (0.000061 AU)
At Aphelion	Total	1σ	945.000 km (0.00633 AU)	308,000 km (0.00206 AU)	50,600 km (0.00034 AU)
* τ = 1000 seconds					

The set of equations (mathematical model) which defines the ΔV requirement as a function of these error sources is presented in detail in Section A of Appendix B-2. The terminal position errors after a ΔV correction are also given in the math model.

In the following section, a set of data is presented as determined from the ΔV guidance mathematical model presented in Appendix B-2.

ΔV Guidance Analysis

Using the ΔV guidance math model defined in Appendix B-2, a set of data was generated for the SEP trajectory depicted in Figure 2-41. The particular error data used in the analysis are as follows:

1.   Heliocentric Injection Errors:

Position Errors = 500 KM (1σ)

Velocity Errors = 4 M/S (1σ)

2-72

2. Inflight Thrusting Errors:

    1 percent Spherical Distribution (1σ)

    1000 Seconds Correlation Time (τ)

3. State Estimation Errors:

    Position Errors = 10 KM (1σ)

    Velocity Errors = 0.5 CM/S (1σ)

4. ΔV Control Errors:

    1 Percent Spherical Distribution (1σ)

In Figures 2-48 through 2-51 the "root-mean-squared" (rms) values of the ΔV requirement due to heliocentric injection errors, in-flight thrusting errors, ΔV control errors, and state estimation errors, respectively, are given as a function of ΔV control time after heliocentric injection. In Figure 2-52, the terminal positional errors after ΔV control are presented as a function of ΔV control time after heliocentric injection. In Figures 2-53 through 2-55, the terminal positional errors after ΔV control due to in-flight thrusting errors, ΔV control errors and state estimation errors, respectively.

From Figures 2-48 through 2-51, it is seen that the ΔV requirement is dominated by the heliocentric injection errors, and the ΔV requirement due to state estimation errors is negligible. Also, it is seen that by delaying the ΔV control, a significant increase in ΔV requirement due to heliocentric injection errors occurs, thus, the ΔV control should be made as early as possible after orbit determination to correct for the heliocentric injection errors with the minimum of ΔV requirement. If the ΔV control is made within the twenty days after heleiocentric injection, the ΔV RMS requirement is approximately seven meters per second.

From Figures 2-52 through 2-55, it is seen that the terminal positional errors after ΔV control is dominated by the in-flight thrusting errors and they decrease significantly by delaying the ΔV control. Therefore, it is seen that in addition to an early ΔV correction to correct for heliocentric injection errors another ΔV correction could be made at a later time to correct for the accumulation of in-flight thrusting errors. If a second ΔV correction is made at approximately 117 days, the terminal position errors would be reduced as shown in Table 2-5.
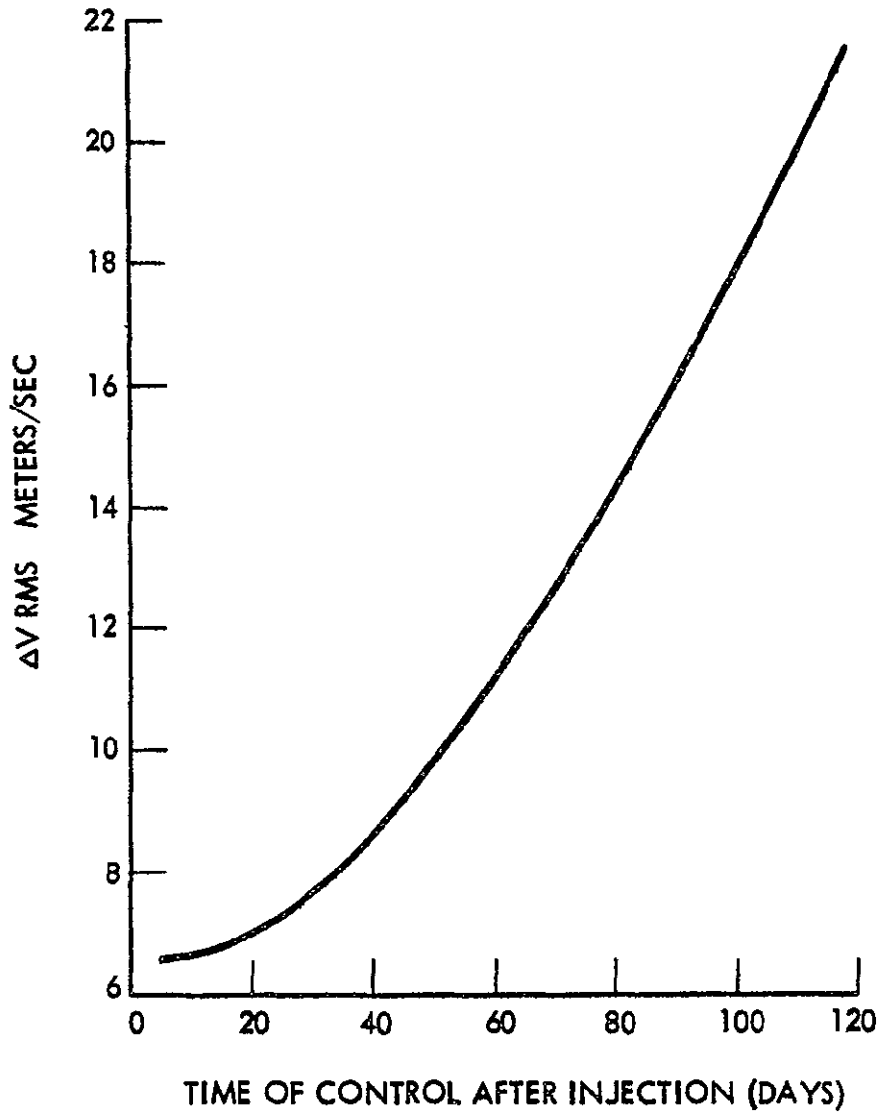
Figure 2-48. ΔV RMS Due to Injection Errors

Figure 2-49. ΔV RMS Due to Inflight
Thrusting Errors

ΔV RMS (METERS/SEC)

TIME OF CONTROL AFTER INJECTION (DAYS)

Figure 2-50. ΔV RMS Due to ΔV
Control Errors

ΔV RMS - METERS PER SECOND

TIME OF CONTROL AFTER INJECTION DAYS

Space Division
North American Rockwell
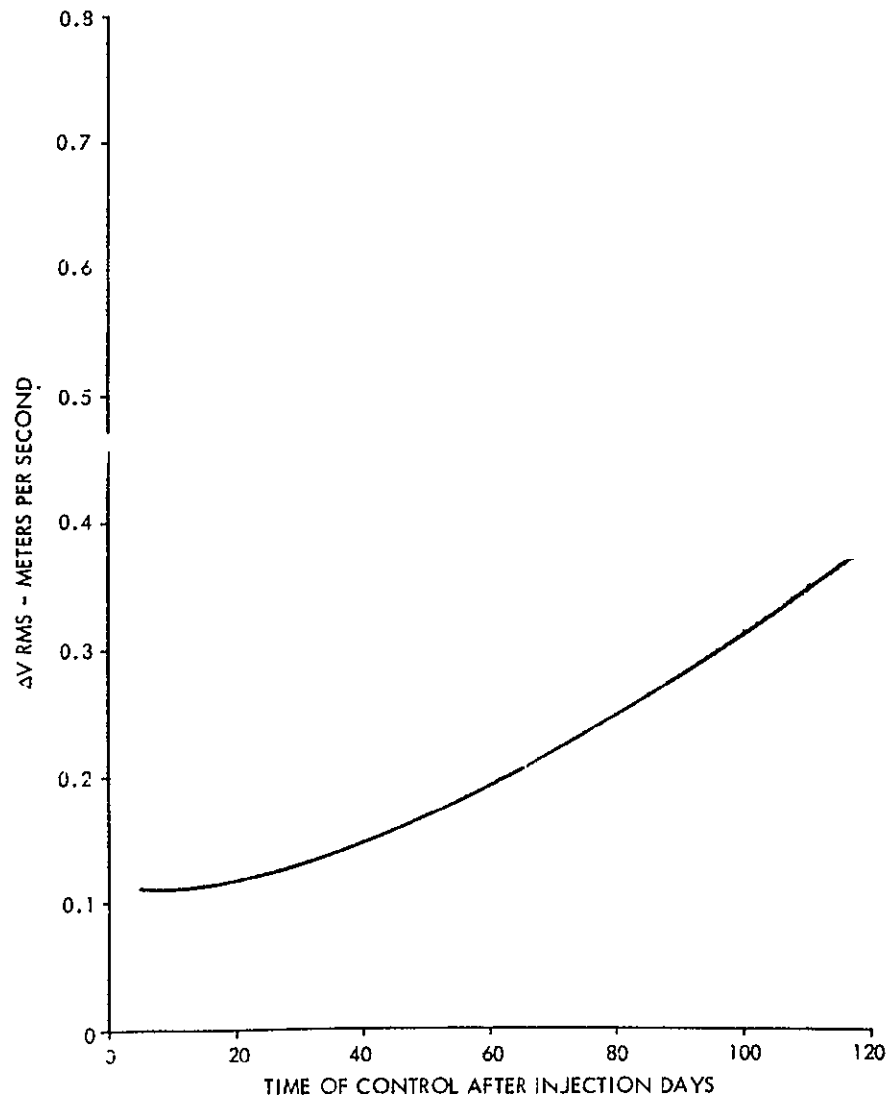
Figure 2-51. ΔV RMS Due to State
Estimation Errors

Figure 2-52. Total Terminal
Positional Errors

Space Division
North American Rockwell
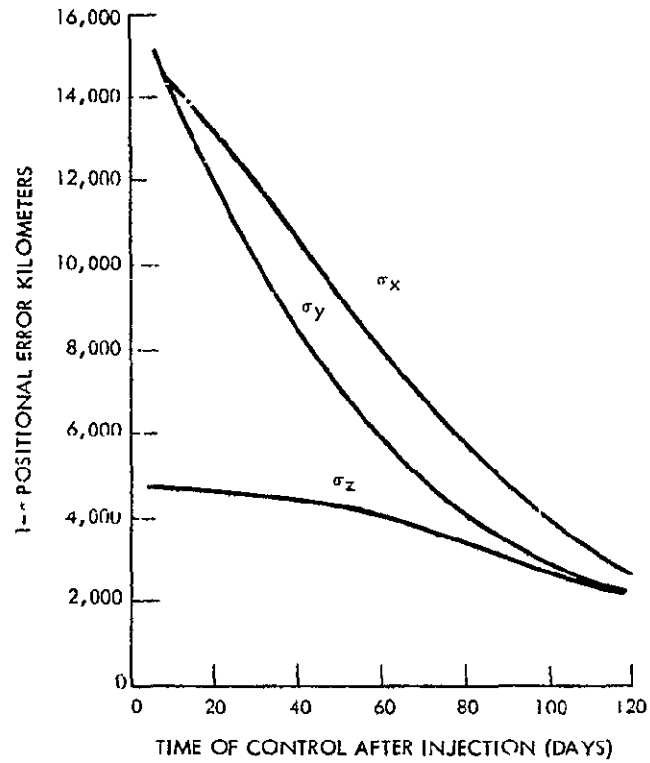
Figure 2-53. Positional Errors After
Control Due to Inflight Thrusting
Errors
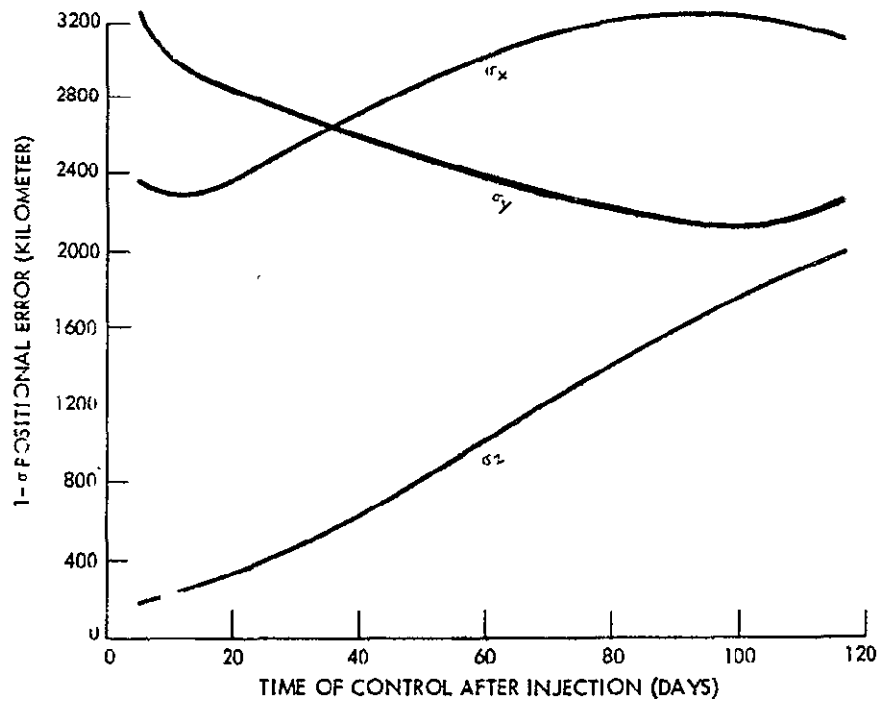
Figure 2-54. Positional Errors After Control
Due to ΔV Control Errors
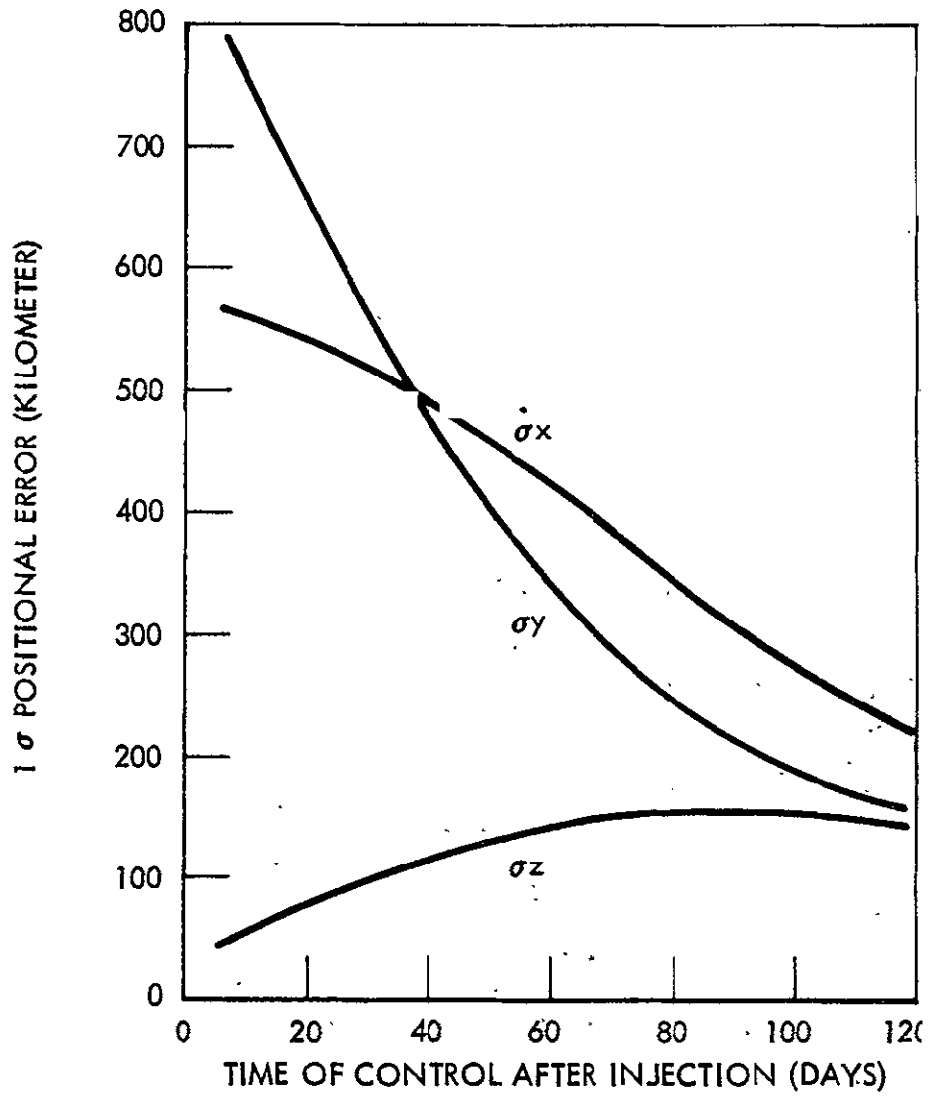
Figure 2-55. Positional Errors After Control Due to
State Estimation Errors

Table 2-5. ΔV Guidance Conclusions

Conditions = Two Impulses

- An early correction to "null" injection errors (after state estimation is completed to estimate terminal error due to injection)

$\sim$ 7 M/S RMS ΔV

- A second correction delayed sufficiently to "null" inflight thrusting errors - e.g., at 117 days $\sim$ 1.8 M/S RMS ΔV

Terminal Errors	Dispersion	X (KM)	Y (KM)	Z (KM)
Thrust Control	1σ	2,835	2,210	2,146
ΔV Control	1σ	775	550	500
Estimation	1σ	229	160	147
Total RMS (Corrected)	1σ	2,948 1.91×10^{-5} A.U.	2,283 1.53×10^{-5} A.U.	2,208 1.45×10^{-5} A.U.
Uncorrected	1σ	144,100 9.64×10^{-4} A.U.	209,240 1.4×10^{-3} A.U.	9,274 6.1×10^{-5} A.U.
Factor Improvement		49	91	4.2

Adaptive Guidance Analysis

The primary purpose of this effort is an assessment of the feasibility of an adaptive mode of guidance wherein the trajectory dispersions are corrected by augmenting the thrust acceleration. In the present analysis the feasibility of this mode of guidance is assessed by considering the acceleration level required to correct the terminal position errors by applying a constant acceleration at some time after heliocentric injection. The equations which define the required accelerations are given in Section B of Appendix B-2.

Adaptive Guidance Data

Using the adaptive guidance mathamatical model as defined in Appendix B-2, a set of data was generated for the SEP trajectory shown in Figure 2-41. The particular error data used for the present analysis are as follows:

1. Heliocentric Injection Errors

   Position Errors = 500 KM (1σ)

   Velocity Errors = 4 M/S (1σ)

2. Inflight Thrusting Errors -

   Spherical Distribution (1σ)

   1000 Second Correlation Time

These error sources are the dominate error sources and are the same values as considered in the ΔV guidance analysis.

Figure 2-56 presents the rms acceleration level to correct the heliocentric injection errors and the inflight thrusting errors as a function of the time after heliocentric injection that the correction is initiated. It is noted that the acceleration level due to heliocentric injection errors dominates that due to inflight thrusting errors by an order of magnitude. In Figure 2-57 the total acceleration level RMS value is shown in comparison with the thrust acceleration as derived from the solar electric engine during the powered flight phase. It is noted that the acceleration level rms value to correct for heliocentric injection and inflight thrusting errors is less than one percent (<1 percent) of the minimum solar electric engine thrust acceleration level.
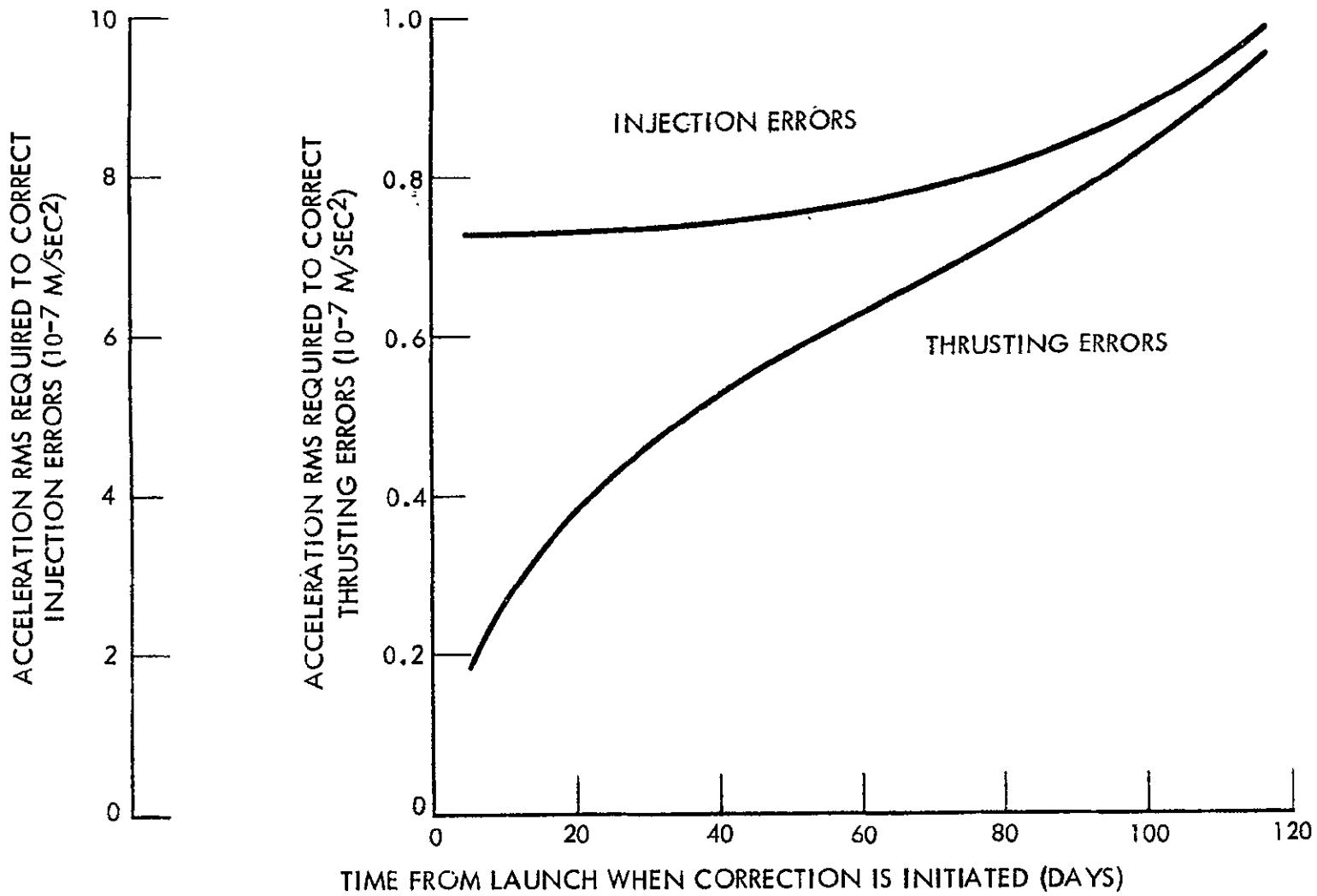
Figure 2-56. Acceleration RMS Requirements

Space Division
North American Rockwell
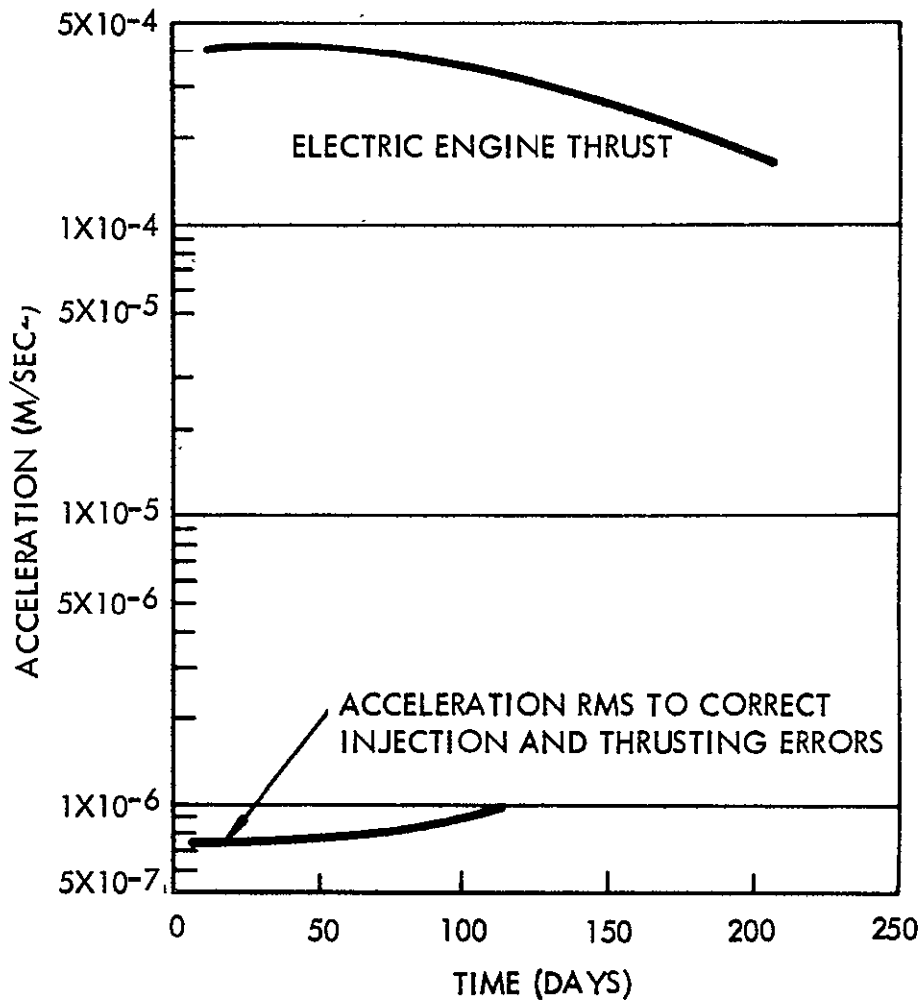
Figure 2-57.   Comparison of Acceleration Levels

Conclusions

The SEP trajectory dispersions (deviations from the nominal) contributions are dominated by the heliocentric injection error as compared to the inflight thrusting control errors for the particular errors considered; one percent thrusting error with a correlation time of 1000 seconds. In general terms, the heliocentric injection contribution is an order of magnitude greater than the contribution of inflight thrusting errors. However, it should be noted that for larger percent error and correlation (~3 percent and 10,000 seconds), the contributions of these two error sources will be comparable. For the asteroid belt mission, it was shown from Figure 2.3 that the aphelion selection could vary ±0.05 AU without an appreciable loss of asteriod encounter data. From Table 2-4, the dispersion from the nominal aphelion selection is less than 0.01 AU due to trajectory dispersion errors. Open loop guidance is adequate for performing the "area" target asteriod belt mission thus negating any need for a complex onboard guidance system.

In the employment of ΔV guidance to correct for terminal position errors more than one impulse should be considered. One correction should be made as soon after heliocentric injection as possible, (after orbit determination) to correct for the effect of injection errors with a minimum ΔV requirement. This effectively reduces the terminal position errors to those caused by the inflight thrusting control errors. A later ΔV correction (117 days) can be used to significantly reduce the terminal position errors due to the inflight thrusting control errors. If trajectory dispersions during coast flight are of concern, a final ΔV correction at the terminal point can be used to correct residual velocity errors.

A total ΔV correction of 10 meters/sec., ≈ 7 m/sec shortly after heliocentric trajectory injection and ~2 to 3 m/sec at 117 days results in an aphelion position error of less than 2×10^{-5} AU.

The adaptive mode of guidance can generally be considered to be feasible from the standpoint of acceleration level requirement. That is, the rms value of acceleration level requirement to correct terminal position errors is less than one percent of the minimum thrust level of the solar electric propulsion engine.

SELECTED MISSION CONCEPT

Trajectory Selection

Selection of the mission trajectory profile is governed by the consideration of mission objectives and launch vehicle and spacecraft

performance capabilities. It becomes obvious that the spacecraft should spend not only a long time in the 2.0 to 3.5 AU region, but also follow a path which maximizes asteroid flux encounter. The cumulative number of meteoroid encounters for a given detector area are functions of both the stay time in the Asteroid Belt and the frequency with which the particles are encountered.

The encounter frequency is dependent on the relative velocity and direction between the spacecraft and the particles. For example, even for long stay times in the center of the belt, few particle encounters will occur if the spacecraft and the particles are traveling in approximately the same direction and velocity. Therefore, it is necessary to select a trajectory which provides the best combination of stay time and particle encounter frequency.

Four representative trajectories were analyzed with aphelions of 3.0, 3.5, 4.0 and 4.5 AU to determine the relative encounter of asteroid particles. Figure 2-58 shows the results which indicate that an aphelion of 3.5 AU provides potential for maximum asteroid encounter.

Although an aphelion of 3.5 AU appears best from the science viewpoint, performance capabilities of the launch vehicle and spacecraft must be considered. Net payload available for science decreases with increasing trajectory aphelion. It becomes necessary to evaluate loss of data (due to less science equipment) against value of maximum flux encounter. Sensitivity of payload to aphelion selection then is a factor to be considered. Associated directly with available payload is the constraints placed on the mission thrust profile.

It is highly desired that the SEP propulsion system not interfere in any way with the science gathering task during passage through the asteroid belt region from approximately 2.0 AU out to 3.5 AU (Figure 2-2). During operation of the SEP thrusters, magnetic fields and the ionized exhaust plume may interfere with the particle and field experiments. To avoid this, the SEP thrusters must be cut off prior to entering the asteroid belt. During the study, it was determined that meteoroid data gathering falls off rapidly below 2.0 AU, as shown later in Section 5, Figure 5-3.

Payload sensitivity to aphelion was determined in this trajectory and performance analysis. Figure 2-58 shows the results of payload sensitivity to aphelion using a 2.0 AU thrust cut off.
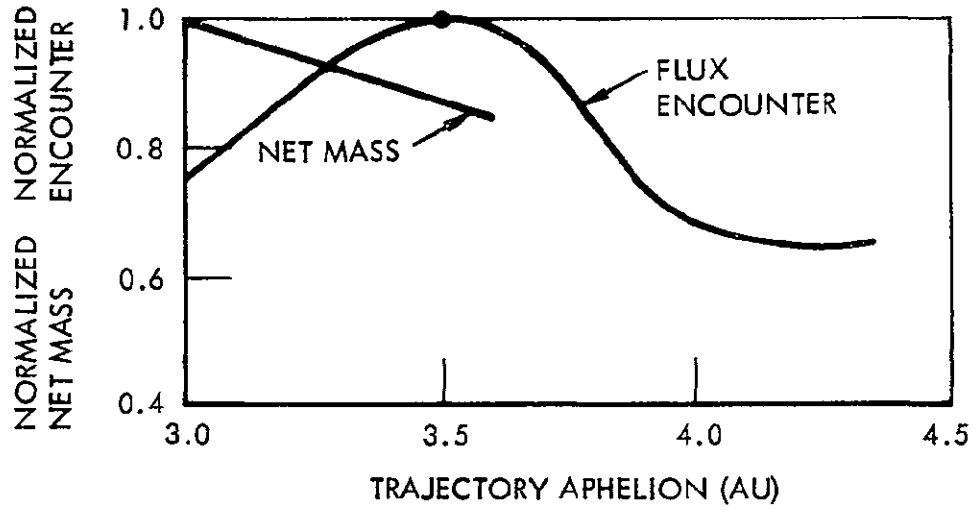
Figure 2-58. Effect of Trajectory Aphelion on Net Mass
and Meteoroid Encounter

The payload is expressed in terms of "net mass," which is defined here as the total spacecraft weight less all elements of the electric propulsion system (ion thrusters, power conditioning and control units, solar cell arrays, mercury propellent, tankage, and feed, and miscellaneous equipment). As shown, appreciable increases in net mass can be gained by selecting trajectories with lower aphelion distances. However, selecting an aphelion much less than 3.5 AU results in a significant reduction in asteroid encounter.

Selection of thrust termination at 2 AU was based on the following considerations: thrust termination at 2 AU, before entering the main region of the asteroid belt, is desirable to preclude unforeseen interference of the scientific measurements by the electric engine operation; the penalty in net mass is almost negligible (approximately 10 kg) for thrust termination at 2 AU as compared to an optimum thrust time of approximately 400 days, as shown in Figure 2-59; and the resulting short thrusting time of 210 days (see Performance Analysis, Section 2.3), reduces the SEP system development and mission risks to a minimum.

In summary, a trajectory aphelion of 3.5 AU was selected for the asteroid belt mission. Figure 2-60 shows the detailed trajectory profile. Thrust cut off of the SEP system occurs 210 days after launch at 2.0 AU. From 210 days to mission termination (a total of 980 days), the spacecraft remains in the 2.0 to 3.5 AU region.

Spacecraft Flight Orientation

Special significance must be given to spacecraft orientation for the Asteroid Belt mission. In the trajectory and performance analysis, it was determined that payload performance capability is dependent upon the thrust vector and solar array orientation. During the data gathering coast phase above 2.0 AU, it is desirable to orient the science for maximum efficiency.

Thrust Vector Considerations

It becomes apparent that maximum performance capability is achieved when the thrust is optimally oriented and the solar arrays are maintained normal to the sun for maximum useable power (option 6 in Table 2-1). This operational concept involves design complexity for continuously orienting the solar arrays with respect to the spacecraft and the SEP thrust angle. With respect to complexity of design, simpler operational concepts worthy of consideration included fixed-mounted solar arrays with either an optimum constant orientation angle for both the spacecraft and the thrust (Option 2) or an optimum variable orientation of the solar-arrayed thrust (Option 4).
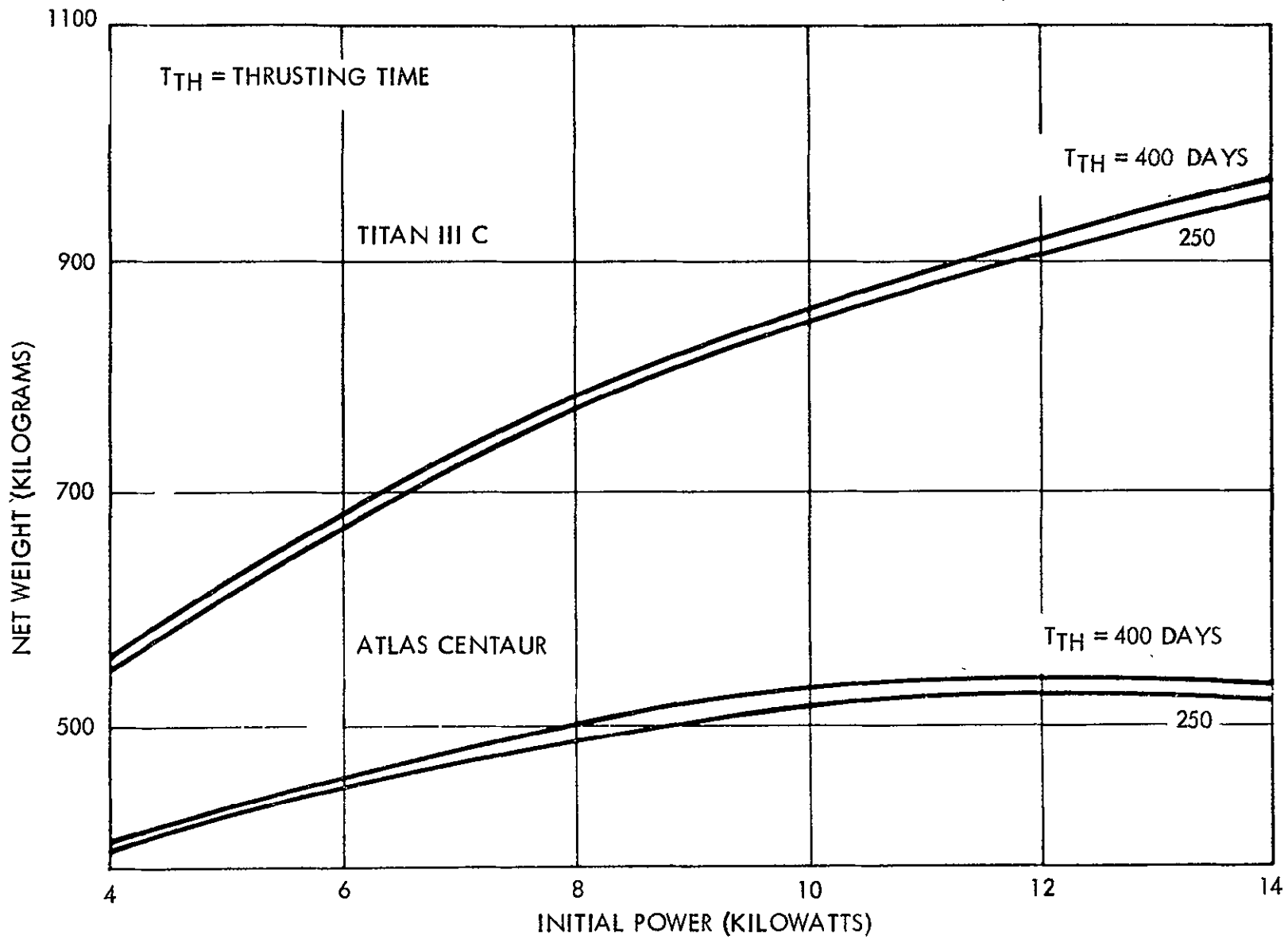
Figure 2-59. Relative Insensitivity of New Weight to Thrust Time for 3.5-AU Trajectory
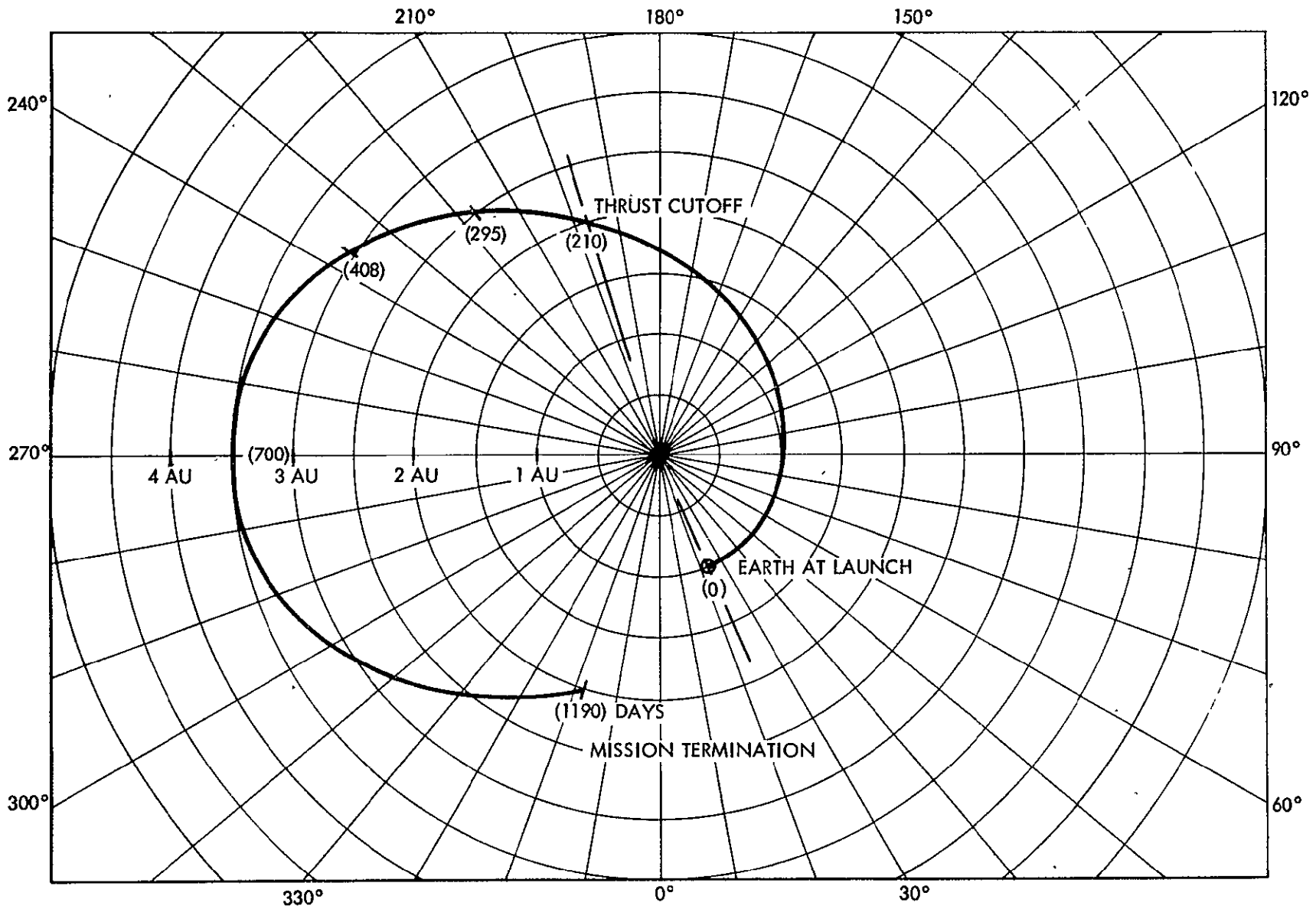
Figure 2-60. Selected Mission Trajectory

Space Division
North American Rockwell

Referring to Table 2-1, relative performance in terms of payload weight differential shows that Option 6 provides a gross gain of 19.9 kilograms and Option 4 a gross gain of 11.5 kilograms over that for Option 2.

Spacecraft design for Options 2 and 4 are virtually identical from a complexity viewpoint. The solar arrays are fixed-mounted and the thrust vector is oriented in the solar array/spacecraft mounting plane. In both cases, the vehicle must rotate with respect to the heliocentric reference system. Figure 2-60 shows that during thrust, the spacecraft traverses through a 172 degree rotation about the sun. For this reason, Option 4 is preferable to Option 2 with its payload weight advantage of approximately 11.5 kilograms. The additional complexity in spacecraft design required for Option 6, weight penalty for orientation drive mechanisms and controls, would more than offset the net payload gain. For this reason, the thrust orientation of Option 4 was selected for the asteroid belt mission. Power requirements are most demanding during the thrust phase of the mission. The spacecraft orientation requirements during thrust for Option 4 were used to size the solar arrays.

Science Equipment Considerations

Orientation requirements imposed on the spacecraft during passage through the asteroid belt region are dictated by the asteroid encounter direction. Figure 2-61 shows the asteroid encounter direction for the selected trajectory assuming a reference plane normal to the sun. It is desired to have the science sensors fixed-mounted to the spacecraft and present maximum sensing area normal to the asteroid encounter direction. Obviously, this ideal condition cannot be achieved throughout the mission. Looking at Figure 2-61, it may be seen that the solar arrays would be oriented up to 90 degrees from the normal plan to the sun at aphelion, thus total power loss would result. After aphelion, the asteroid particles will strike the sun-lit side of the spacecraft rendering the large area meteoroid detectors on the back of the solar arrays useless, except for cometary impacts. To alleviate this condition, two of the solar arrays are oriented 180 degrees to provide asteroid impact data during descent from aphelion.

The high power requirement of the SEP system dictated a solar array sizing which provided far more power than is necessary during the coast phase. Figure 2-62 shows the effect of orienting the spacecraft during asteroid encounter. The cumulative encounter was normalized to the selected trajectory for the region from 2.0 AU up to 3.5 AU. As may be seen, for the selected trajectory with meteoroid sensors facing normal to and away from the sun, 85 percent of the maximum number of asteroids will be encountered. A further reduction in recorded events is anticipated due to the obliqueness of the incidence of impact. Larger particle sizes
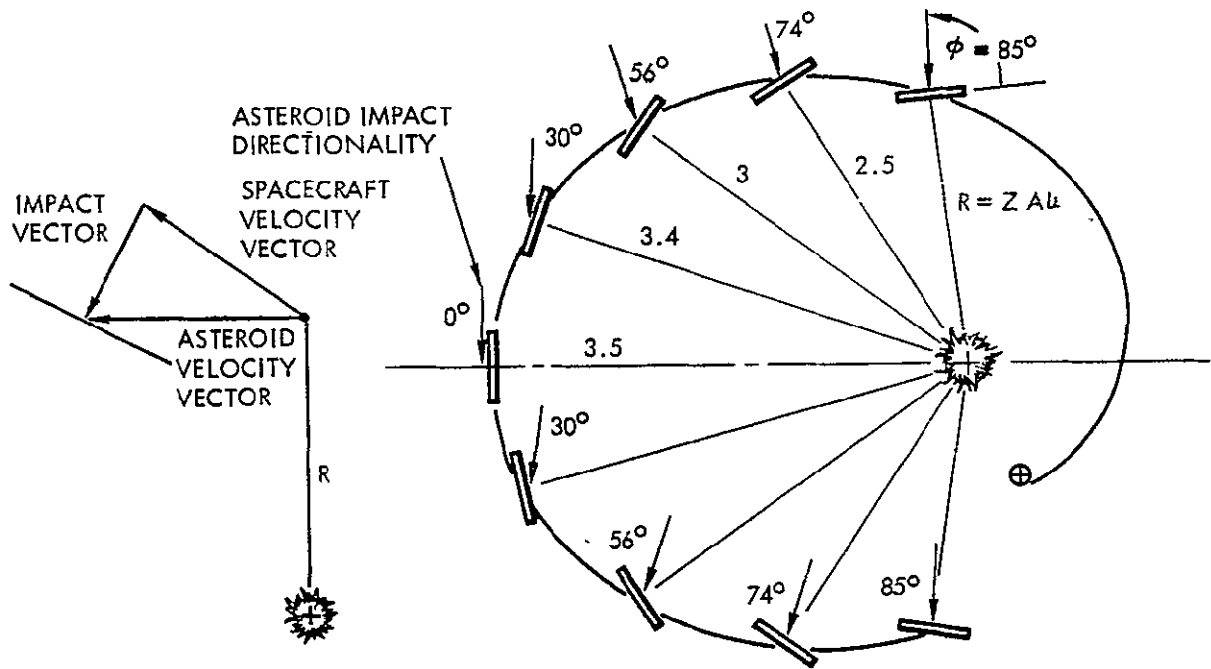
Figure 2-61. Asteroid Encounter Direction
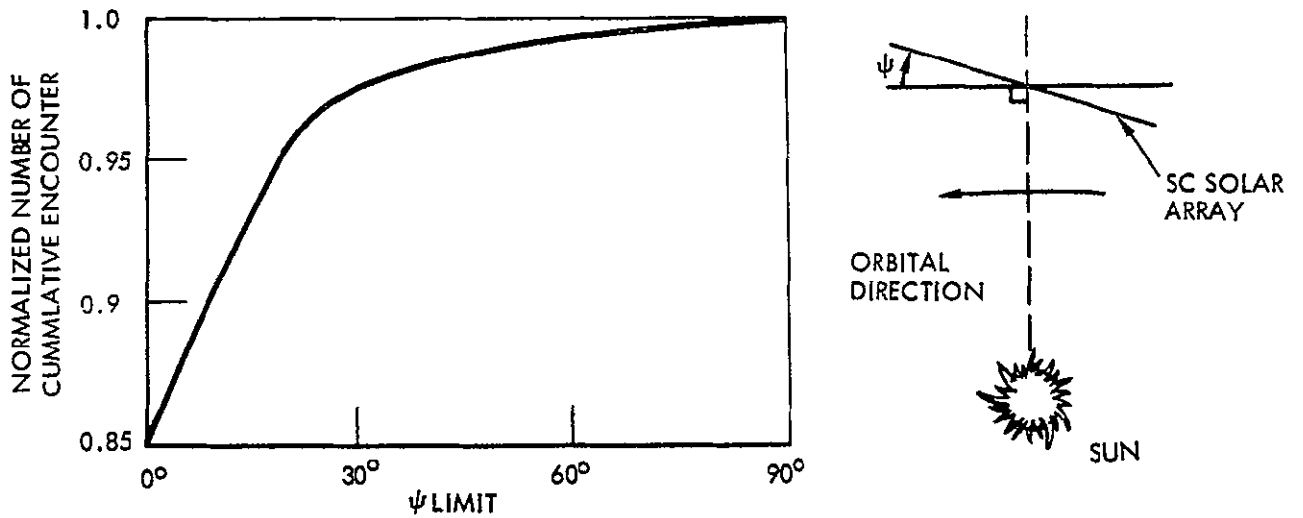
Figure 2-62. Effect of Variable Orientation
Limit on Meteoroid Encounters

(greater particle momentum) are required to penetrate the meteoroid capacitor sheets as the angle of impact becomes less. In Figure 2-62, it may also be seen that very little increase in the number of events is obtained after the first 30 degrees orientation maneuver. For sizing, the spacecraft and science payload, a maximum orientation angle of 30 degrees from the normal to the sun was used.

Mission Flight Sequence

The flight sequence may be divided into five major phases as follows:

1. Prelaunch

2. Launch/injection and separation

3. Deployment/prethrust

4. Thrust

5. Coast

The major events which occur, time of occurrence, and subsystems which are involved are presented in Table 2-6. A brief discussion of the major events during each mission phase is presented below. This mission definition was used as the basic guideline for determining subsystem operations and, subsequently, performance requirements.

1. Pre-launch Phase. As indicated in Table 2-6, the prelaunch phase consists of the six-hour period prior to launch during which last minute preparations for launch are made. Adjustments in the systems due to variation of launch time include adjusting the mercury fuel supply and updating the stored guidance program in the computer controller and sequencer (CC&S). This program is used as the backup mode only in event of a system failure, such as tracking, command distribution, etc. Prior to launch and switch over to battery power, the gyros are brought up to speed thus reducing on-board battery requirements.

2. Launch, Injection and Separation Phase. The spacecraft is launched on the Atlas/Centaur into a parking orbit, if required, to compensate for launch time variation. The optimum launch time for direct heliocentric injection occurs once each 24 hours when the launch site is on the dark side of the earth opposite the sun. During this period, the shroud is jettisoned and the space-craft is maintained in a fixed attitude such that the solar electric power conditioning and control panels face the earth.

2-91

At the proper time, the Centaur burns a second time to inject the spacecraft on the desired transfer. After separation, the low gain antennas are deployed, transmission via the low gain antenna is initiated, solar panel boost tie-downs are released, and spacecraft rotation rates are reduced to zero. The spacecraft is oriented such that the electric propulsion power conditioning and control panels face the sun during a coast period lasting up to 4.0 hours after launch for passage through the Van Allen Belt.

3. Deployment/Prethrust Phase. After passage through the Van Allen belt, the solar panels are deployed and sun acquisiton is initiated. Switch over from battery to solar power is initiated. A 360-degree roll maneuver is executed for star (Canopus or Vega) acquisition. During the star acquisition maneuver, the magnetometer is calibrated. At 4.5 hours maximum time after launch, the spacecraft is on full solar power.

During the period after full solar power is achieved, but before thrust, the Group B experiments are calibrated and left operational. The Sisyphus and electrostatic ballistic pendulum are also activated. Prior to electric propulsion thrust initiation, the magnetometer and Faraday cup experiments are turned off.

4. Thrust Phase. At nine hours after launch, which allows time for determination of heliocentric injection conditions, thrust initiation begins. During the next 210 days the spacecraft attitude is maintained by thrust vector control by the ion engines. At 134 days after launch, the available power is switched to one ion engine until thrust termination. During this phase, signals from the attitude reference sensors (sun and Canopus or Vega trackers) are biased with signals from the CC&S to provide control signals to the closed loop gyro, translator, and engine gimbal system and, if necessary, the cold gas valve controls. Three axis attitude control of the spacecraft is provided throughout the thrust periods, as well as thrust vector control. During this period, it may be necessary to shift from Canopus to Vega or vice versa to maintain a star reference signal.

5. Coast Phase. At a distance of 2.0 AU, some 210 days after launch, ion engine thrust is terminated. The magnetometer and the Faraday cup experiments are activated and a roll maneuver is executed for experiment calibration. The large area meteoroid detectors (capacitor-sheets) are activated and the spacecraft is oriented in an optimum attitude to obtain on the asteroid belt environment. During this period, the spacecraft is oriented in

Table 2-6. Mission Events and Timeline - SEP Asteroid Belt Mission

LCE - Launch Complex Equipment
CC&S - S/C Central Computer & Sequencer
SIC - Separation Interface Connector
SIT - Separation Initiated Timer
DC - Direct Command
SCS - Stabilization and Control Subsystem

Group A Experiments

Geiger Muller Computer
Cosmic Ray Spectrometer
Triaxial Spectrometer

Group B Experiments

Magnetometer
Faraday Cups

Group C Experiments

Sisyphus
EBP
Capacitor - sheet

Flight Phase	No	Event	Time	Time From Launch	Source	Destination	Thruster and Pwr Cond, Propellant Tank & Feed	Structure	Lo Gain Antenna & Mount	HI Gain Antenna & Mount	Radio	Flight Telel Flight Telemetry	Flight Command	CC&S, SIT, and SIC	Data Automation	Data Storage	G&C Electronics	Gyro Package	Canp Canopus or Vega Sensor	Sun Sensors	GN₂ A/C Jet System	Translator & Gimbal	Solar Array	Pwr Electronics & Cabling	Batteries	rmal Control	Pyrotechnics & Mechanisms	Group A Field & Part Exp	Group B Field & Part Exp	Sisyphus	Eect-Bat Data EBP
PRELAUNCH	1.1	Adjust Hg propellant supply	L-6 hrs	-6 hrs			x																								
	1.2	Update and verify CC&S programs	L-30 min	-30 min	LCE									x																	
	1.3	Turn on gyros	L-17 min	-17 min	LCE													x													
	1.4	Switch to SC internal power	L-7 min	-7 min	LCE																			x x						
	1.5	Release LCE relay hold	L-4 min	-4 min	LCE									x																	
	1.6	Release CC&S real-time inhibit	L-3 min	-3 min	LCE									x																	
	1.7	Clear relay release	L-1 min	-1 min	LCE																										
LAUNCH, INJECTION AND SEPARATION	2.1	Lift-off (Atlas-Centaur)	L=0	0																											
	2.2	Nose-shroud jettison (≈300,000 ft altitude)	L+3 4 min	3 4 min																											
	2.3	Parking orbit insertion	L+10 min	10 min																											
	2.4	P.O Stay Time (up to 65 min)	L+75 min (max)	75 min (max)																											
	2.5	Heliocentric injection (≈3 min Centaur burn)	L+75 min (max)	L+75 min (max)																											
	2.6	Spacecraft Separation	S=0	78 min	Centaur Timer																										
	3.1	Remove relay hold and enable CC&S	S=0		SIC	CC&S								x																	
	3.2	Arm pyrotechnics	S+1 min	79 min	SIC	Pyrotechnics		x						x														x			
	3.3	Deploy low gain antenna (2)	S+1 min	79 min	SIT	Comm		x						x											x x						
	3.4	Initiate transmission via low gain antenna (125 milliwatt exciter output)	S+1 min	79 min	SIT	Comm		x	x x					x	x x									x x						
	3.5	Activate SCS (except translator and gimbal closed loop)	S+1 min	79 min	SIT	SCS								x				x x x x x						x x						
	3.6	Release solar panel boost tie-downs	S+1 min	79 min	SIT	Pyrotechnics								x									x				x			
	3.7	Perform events 2.7 through 2.12 (back-up to SIC and SIT)			CC&S	Applicable Destination																									
	3.8	Reduce rotation rates	S+4 min	82 min	CC&S	SCS								x			x x		x			x x x	x					
	3.9	Spacecraft orientation command and cruise (beyond Van Allen Belt)	S+4 min	82 min	CC&S	SCS								x			x x		x			x x x	x					

Table 2-6. Mission Events and Timeline - SEP Asteroid Belt Mission (Cont)

LCE - Launch Complex Equipment
CC&S - S/C Central Computer & Sequencer
SIC - Separation Interface Connector
SIT - Separation Initiated Timer
DC - Direct Command
SCS - Stabilization and Control Subsystem

Group A Experiments

Geiger Muller Computer
Cosmic Ray Spectrometer
Triaxial Spectrometer

Group B Experiments

Magnetometer
Faraday Cups

Group C Experiments

Sisyphus
EBP
Capacitor - sheet

Flight Phase	No	Event	Time	Time From Launch	Source	Destination	Thruster and Pwr Cond.	Propellant Tank & Feed / Structures	Lo Gain Antenna & Mount	Hi Gain Antenna & Mount	Radio	Flight Telemetry	Flight Command	CC&S, SIT, and Sic	Data Automation	Data Storage	G&C Electronics	Gyro Package	Canopus or Vega Sensor	Sun Sensors	GN2 A/C Jet System Translator & Gimbal	Solar Array	Pwr Electronics & Cabling	Batteries	Thermal Control	Pyrotechnics & Mechanisms	Group A Field & Part. Exp	Group B Field & Part. Exp	Sisyphus	Elect-Bal Pend. (EBP)	Capacitors on Solar Array
LAUNCH, INJECTION AND SEPARATION	3 10	Initiate solar array deployment	S+2L2 m	3L20 m	CC&S	Power	X							X			X X					X X X	X								
	3 11	Initiate sun acquisition (1st 180° roll) low gain antenna switching	S+2L2 m	3L20 m	CC&S	SCS			X					X			X X X X X					X X X	X								
	3 12	Group B experiments on, switch to 10 watt xmtr mode	S+2L32 m	3L52 m	CC&S	Science comm			X	X X			X	X X								X X						X			
	3 13	Initiate 360° roll maneuver for Group B experiment calibration (low gain antenna switching)	S+2L32 m	3L52 m	CC&S	SCS			X					X			X X X X X					X X X	X				X			
	3 14	Switch from battery to solar power	S+3L12 m	4L30 m	Solar Array Voltage Monitor	CC&S, Power								X								X X X	X							
	3 15	Initiate roll reference star acquisition (Canopus or Vega)	S+3L12 m	4L30 m	CC&S	SCS								X			X X X X X					X X X	X							
	3 16	Release and deploy high gain antenna (orient as required)	S+3L42 m	5L	CC&S	Comm Pyrotechnics				X			X				X X	X			X X			X						
	3 17	Release translation and thruster boost tie-downs	S+3L42 m	5L	CC&S	Propulsion	X	X					X								X			X					
	3 18	Gyros to standby mode	S+3L42 m	5L	CC&S	SCS								X			X													
	3 19	Activate all science (except capacitor sheet) for calibration at IAU	S+4L12 m	5L30 m	CC&S	Science																X X				X X X X X
	3 20	Update CC&S (as required)	S+7L32 m	8L50 m	DC	CC&S					X		X	X																
	3, 21	Group B Experiments power off	S+7L42 m	8L58 m	CC&S	Science								X								X X				X
THRUST	4 1	Initiate electric propulsion thrust phase	T 0 m	9 hr	DC	CC&S							X	X															
	4 2	Energize translator and gimbal circuitry (open loop)	T+1 min	9L1 m	CC&S	SCS								X						X									
	4 3	Position translator and orient thrusters to initial position	T+4 min	9L4 m	CC&S	SCS	X						X		X				X	X X						
	4 4	Turn-on propellant feed system	T+14 min	9L14 m	DC	Propulsion	X	X	X	X																		
	4 5	Electric propulsion power conditioning and control (PCC) power on - units 1 and 2	T+24 min	9L24 m	DC	Propulsion	X	X	X	X										X X			X				

Table 2-6. Mission Events and Timeline - SEP Asteroid Belt Mission (Cont)

Legend:

LCE – Launch Complex Equipment
CCS&S – S/C Central Computer & Sequencer
SIC – Separation Interface Connector
SIT – Separation Initiated Timer
DC – Direct Command
SCS – Stabilization and Control Subsystem

Group A Experiments
  Geiger Muller Computer
  Cosmic Ray Spectrometer
  Triaxial Spectrometer

Group B Experiments:
  Magnetometer
  Faraday Cups

Group C Experiments:
  Sisyphus
  EBP
  Capacitor – sheet

Flight Phase	No	Event	Time	Time From Launch	Source	Destination	Thruster & Pwr Cond	Propellant Tank & Feed	Structures	Lo Gain Ant & Mount	Hi Gain Ant & Mount	Radio	Flight Telem	Flight Cmd	CC&S/SIT/SIC	Data Auto	Data Storage	G&C Elec	Gyro Pkg	Canopus/Vega	Sun Sensors	GN2 A/C Jet	Translator & Gimbal	Solar Array	Pwr Elec & Cabling	Batteries	Thermal Control	Pyro & Mech	Grp A Exp	Grp B Exp	Sisyphus	EBP	Capacitors
THRUST	4.6	Pre-heat outboard thrusters	T+34 min	9L34 m	DC	Propulsion	X			X				X										X	X								
	4.7	Increase GN2 SCS dead band to ±3 degrees to allow translator and gimbal control to take over	T+34 min	9L34 m	CC&S	SCS										X					X												
	4.8	Activate flight control system, translator and gimbal (closed loop)	T+40 min	9L40 m	CC&S	SCS										X							X	X	X								
	4.9	Thrusters on full power	T+40 min	9L40 m	DC	Propulsion	X			X				X										X	X								
	4.10	Gyro power off	T+45 min	9L45 m	CC&S	SCS										X				X				X	X								
		During thrust phase, sun sensor, star tracker switching occurs as required closed loop and/or CC&S control																															
	4.11	Switch 10 watt smtr to high gain antenna (200 bps – 6 hrs every 5 days to 85 ft DSN)	T+100 D	100 D	CC&S	Comm						X	X	X	X	X	X							X	X								
	4.12	Gyros in stand-by mode	T+134 D	134 D	CC&S	SCS										X				X				X	X								
	4.13	Gyros on (back-up during thruster switching)	T+134 D	134 D	CC&S	SCS										X				X				X	X								
	4.14	Outboard thrusters power off – preheat center thruster, switch all power to one PCC	T+134 D	134 D	DC	Propulsion	X	X		X				X				X						X	X								
	4.15	Center thruster to full power	T+134 D	134 D	DC	Propulsion	X	X		X				X				X							X	X								
	4.16	Gyros off (cold gas system provides roll control during remaining thrust phase)	T+134 D	134 D	CC&S	SCS										X				X				X	X								
	4.17	Update CC&S (as required)	T+134 D	134 D	DC	CC&S							X	X	X																		
	4.18	Gyros to stand-by mode	T+210 D	210 D	CC&S	SCS										X				X				X	X								
	4.19	Gyros on	T+210 D	210 D	CC&S	SCS										X				X				X	X								
	4.20	Power off – thruster, translator, gimbal turn-off propellant feed	T+210 D	210 D	DC	Propulsion	X	X		X				X											X	X						X	

Table 2-6. Mission Events and Timeline - SEP Asteroid Belt Mission (Cont)

LCE - Launch Complex Equipment
CC&S - S/C Central Computer & Sequencer
SIC - Separation Interface Connector
SIT - Separation Initiated Timer
DC - Direct Command
SCS - Stabilization and Control Subsystem

Group A Experiments
  Geiger Muller Computer
  Cosmic Ray Spectrometer
  Triaxial Spectrometer

Group B Experiments
  Magnetometer
  Faraday Cups

Group C Experiments
  Sisyphus
  EBP
  Capacitor - sheet

Flight Phase	No.	Event	Time	Time From Launch	Source	Destination	Subsystems Affected
COAST	5.1	Initiate coast phase	C-0	210 D			
	5.2	Switch to 20 watt xmtr mode (200 bps to 270 days, 80 or 40 bps for mission duration - 85' DSN)	C=0	210 D	CC&S	Comm	Radio X, Flight Command X; CC&S/SIC X, Data Auto X, Data Storage X; Solar Array X, Pwr Elec X
	5.3	Magnetometer on	C+1 min	210 D	CC&S	Science	Data Auto X; Group B Exp X
	5.4	Conduct (360°) roll maneuver for magnetometer calibration	C+2 m	210 D	CC&S	SCS	Data Auto X; G&C Elec X, Gyro X, GN2 A/C Jet X; Solar Array X, Pwr Elec X
	5.5	Star reacquisition maneuver	C+32 min	210 D	CC&S	SCS	Data Auto X; G&C Elec X, Gyro X, Canopus X, Translator X; Solar Array X, Pwr Elec X
	5.6	Gyros off	C+37 min	210 D	CC&S	SCS	Data Auto X; Gyro X; Pwr Elec X
	5.7	All science on	C+37 min	210 D	CC&S	Science	SCS X; Solar Array X, Pwr Elec X; Group A Exp X, Capacitors on Solar Array X
		During coast phase sun sensor and star tracker switching as required					
	5.8	Spacecraft orientation commands (γ = angle from sc sun line in counter clockwise direction)			CC&S	SCS	Comm \; Data \; SCS \ \ X X X \
		Y = 85°		210 D			
		77.5°		265 D			
		72.5°		305 D			
		67.5°		346 D			
		62.5°		380 D			
		60° (max limit)		410 D			
	5.9	Rotate 2 solar arrays 180° at aphelium passage		700 D	CC&S	Science Power	Data X; SCS X X; Solar Array X, Pwr Elec X; Capacitors on Solar Array \
	5.10	Spacecraft orientation commands (post aphelion)			CC&S	SCS	Comm \; Data X; SCS X X X X X
		Y = 124° to 102°		990 D			
		117.5°		1020 D			
		112.5°		1055 D			
		107.5°		1095 D			
		102.5°		1135 D			
		95°		1190 D			
	5.11	Possible electric propulsion restart if Hg fuel is available		1190 Days	DC	Propulsion	Thruster X, Prop Tank X; Radio X, Flight Command X; CC&S X; SCS X X; Solar Array X, Pwr Elec X; Science \
	5.12	Mission termination - all power off		1190 Days (nominal)	DC (CC&S back-up)	All systems	Radio X; CC&S X

an optimum attitude until the solar array spacecraft mounting plane is oriented 30 degrees away from the normal to the sun. This orientation takes place in five steps of 5, 7.5, 5, 5, and 7.5 degrees up to aphelion and in reverse order back down to 2.0 AU (see Table 2-6 for mission times). At aphelion or shortly after aphelion passage, two of the solar arrays are reoriented 180 degrees so that asteroid particles lifting from the sun side of the spacecraft can be detected.

3. SYSTEMS ANALYSES AND DESIGN CONCEPT SELECTION

APPROACH

The intent of this solar electric propulsion asteroid belt mission spacecraft study was to determine a baseline system at the midpoint of the study program. This was desirable from the standpoint that the last half of the program could then be fully devoted to the detailed subsystem analyses and definition of the spacecraft. This scheduling was also desirable to provide sufficient time to define in detail, the major elements of the Program Development Plan. The basic philosophy used in the baseline selection approach was unique in that a number of candidate concepts were available. "Candidate concepts" in this context are taken to be combinations of power level, specific impulse, and launch vehicle configurations; these parameters have a major impact on the design of an SEP spacecraft. The following paragraphs describe the evaluation methods used in assessing the candidate concept capabilities and comparing these capabilities with the science payload requirements for the mission.

CAPABILITIES AND REQUIREMENTS ANALYSIS

Capabilities Evaluation

The system evaluation technique used to arrive at a spacecraft design selection required the careful evaluation of the scientific payload requirements for the asteroid belt survey mission. These requirements were then compared to the capabilities of the launch vehicle and electric propulsion system power level chosen. The science payload sizing and selection rationale are discussed in Section 5.0. Based on the results of trajectory analyses and preliminary subsystem sizing, the payload performance capabilities of candidate spacecraft design points (power level, specific impulse, and launch vehicle) were established. This being the first potential application of solar electric propulsion for primary thrust on an unmanned space exploration spacecraft, it is highly desired to use modest propulsion system power levels, (a power level at 1.0 AU less than 10.0 kilowatts). Consequently, the following candidate concepts were evaluated in terms of their science payload capabilities: Propulsion system power levels (at 1.0 AU) on the order of four, six, and eight kilowatts were considered for the Atlas/Centaur/SEP spacecraft. These propulsion system power levels imply a total spacecraft power of approximately 5, 7.5, and 10.0 kilowatts, respectively, when a 15 percent radiation degradation factor, spacecraft

3-1

housekeeping power, and losses are considered. For the range considered
in this study, these power levels could be considered candidates for a small,
medium, and large variety SEP spacecraft. Only propulsion system power
levels of 4 and 6 kilowatts were considered for the Titan III C/SEP space-
craft since going to any higher power levels for the Titan III C yields
extremely high payload capabilities (weight available for science) that
could not be effectively used. Figure 3-1 shows the relationship of science
payload weight capability versus propulsion system power level for the
candidate concepts considered. The data also indicate the variation in the
available science payload weights to the engine specific impulse selected.
It can be seen that for the Atlas/Centaur/SEP spacecraft the penalty
(decrease in payload capability) associated in using 3500 seconds versus
specific impulse values which are closer to optimum (see Trajectory and
Performance Analysis, for the discussion of specific impulse selection)
are rather insignificant at the higher power levels.

Requirements Evaluation

The next step in the system evaluation of the candidate concepts was
to establish the science payload requirements so that a direct comparison
of the requirements could be made against the candidate capabilities. In the
preceding Science Payload section, a requirement for 70 square meters of
meteoroid penetration detectors was established to obtain a ten-percent
standard error or better for data on 10^{-7} gram meteoroids. Table 3-1
shows an important relationship between the weight of 70 square meters of
capacitor detectors and the total spacecraft power. As shown, the detector
weight increases with decrease in power. The reason is that, for example,
a 10-kilowatt solar array has enough substrate area to mount 70 square
meters of detectors, while a 5-kilowatt array can only mount 35 square
meters of detectors. Therefore, for a 5-kilowatt spacecraft, a separate
structural array is required to mount the remaining 35 square meters, thus
the weight is increased.

In Figure 3-2, the science payload requirements have been super-
imposed on the capabilities for the Atlas/Centaur and Titan III-C concepts.
Two payload requirements curves are indicated; the lower curve considers
utilizing independent capacitor meteoroid detector panels, and the upper
considers independent pressure-cell detector panels. For propulsion power
levels below 7.75 kilowatts, insufficient area is available on the backside of
the solar panels for bonding 70 square meters of capacitor detectors.
Furthermore, the heavy penalty of independent panels pushes the science
payload weight beyond the capability of the spacecraft at lower power levels.

As a result of the evaluation, the study efforts concentrated on 10 kilo-
watts of total power and about 8 kilowatts of propulsion system input power.
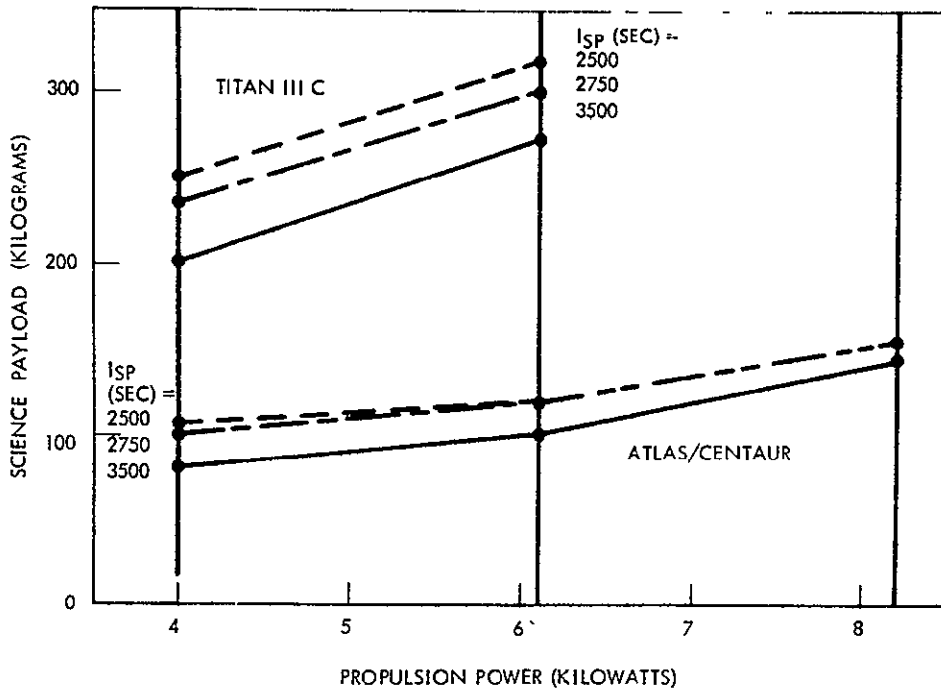
Figure 3-1. Science Payload Capability
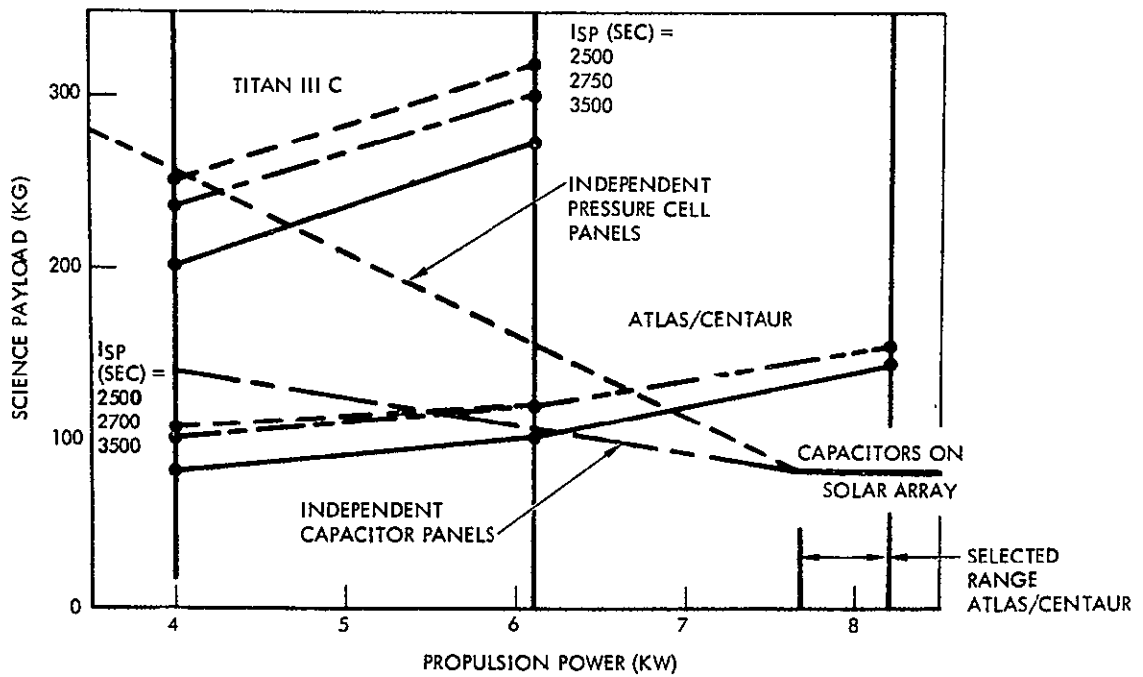
Figure 3-2. Science Payload Capability Versus Requirements

Table 3-1 Science Payload Requirements

Required capacitor area - 70 M^2 $\geq 10^{-7}$ GM particle 10 percent standard error from 2.4 to 2.6 AU Order of magnitude contingency		Spacecraft Power		
		5 KW	7.5 KW	10 KW
Capacitor on back of solar array (75 percent array substrate covered)	Area	35 M^2	52 M^2	70 M^2
	Weight	15.5 KG	23 KG	31 KG
Independent capacitor array	Area	35 M^2	18 M^2	-
	Weight	63 Kg	32.4 KG	-
Total Capacitor Weight		78.5 KG	55.4 KG	31 KG
Sisyphus, electrostatic ballistic pendulum, particle and field experiments	Weight	49 KG	49 KG	49 KG
Total Science Weight		127.5 KG	104.4 KG	80 KG

A 3500-second specific impulse was selected because of the state-of-the-art thruster design and suitability for other potential missions; i.e., an out-of-ecliptic mission where the specific impulse optimizes in the 4000-second regime.

DESIGN CONCEPTS ANALYSIS

Upon selection of the propulsion system input power level (on the order of 8 kilowatts) and specific impulse (3500 seconds), meaningful evaluation of the influence of the major design considerations on the spacecraft configuration can be determined. Initiation of the detailed electric propulsion system design was also contingent upon the selection of these parameters.

The Atlas/Centaur launch vehicle was selected for two main reasons:

1. Adequate payload capability

2. Lower cost versus the Titan III-C.

This selection does not preclude the possibility of launching the Atlas/Centaur - design spacecraft with the Titan III-C inasmuch as the payload envelopes are very similar (both use 120-inch diameter shrouds) and the Titan III-C shroud is capable of accommodating various payload lengths by incorporating five-foot long shroud-extension cylinders.

Major Design Considerations

With the incorporation of solar electric propulsion on a scientific exploration spacecraft there exist novel design constraints and considerations not previously facing the designers of all-chemical (ballistic) space vehicles. These considerations are brought forth primarily because of the very large area solar arrays that must be deployed from the vehicle and because of ion expulsion from the electric engine thrusters. In the overall spacecraft configuration there exist four major design considerations that must be satisfied by the general arrangement of the vehicle:

1. Provision for spacecraft appendage clearance from the exhaust plume

2. Incorporation of multi-kilowatt roll-out solar cell array system

3. Unobstructed field-of-view for star tracker(s) and other attitude reference sensors

4. Provision for science equipment location, orientation, and field-of view

The impact of these design considerations on the spacecraft configuration is discussed below.

Ion Engine Exhaust Clearance

Due to the uncertainty of the problems associated with the prevention of mercury propellant deposition on spacecraft appendages and components, a ground rule imposed in the spacecraft configuration studies was that all spacecraft elements would be kept forward of an imaginary plane defined by the ion exit plane of the thrusters. This ground rule automatically rejected any consideration of using a cruciform solar panel arrangement such as the Mariner spacecraft. Such arrangements have been considered in past

SEP design studies where the ion engines are mounted so their exhaust is directed through a corridor between adjacent solar panels (Figure 3-3). As shown, this particular arrangement does offer a convenient, unobstructed location for viewing the southern celestial sphere, and Canopus, which makes it very desirable for spacecraft designs for missions in the plane of the ecliptic. However, in such a configuration, the solar panels protrude aft of the ion engine plume and may be contaminated by the exhaust. For this reason, further consideration of these configurations were precluded from this study.

Rollout Solar Cell Arrays

In this study the JPL contractual guidelines dictated consideration of both the roll-out or fold-out types of large area solar cell arrays. The present technology level in the development of these arrays has indicated that a specific mass of 15 kilograms per kilowatts and 21 kg/kw are attainable for the roll-out and fold-out type of mechanizations respectively. Since no significant advantages were identified for using fold-out types rather than the roll-out array, based strictly on the weight advantage alone, the roll-out arrays were chosen. In addition to this significant weight advantage, the roll-out arrays occupy less stowage space for the power levels under consideration.

Another consideration in the selection of the roll-out solar array was the adaptability of placing meteoroid impact detectors on the backside of the panels. It was found that bonding capacitor sheet impact detectors directly to the substrate causes no degradation to the performance of the panels. This concept of integrating the meteoroid impact detectors on the panels was adopted as the selected concept (Figure 3-4). Alternate techniques of integrating impact detectors with the fold-out type solar array are also shown in the figure. As indicated, pressure cell type impact detectors placed behind the solar panels may significantly degrade their performance (11 percent reduction in power output) if the pressure cells are not directly in contact with the substrate. This power degradation is due to the temperatue increase of the cells caused by degrading the backside radiating surface of the panels.

In the trajectory and performance analyses section, the decision was made to orient the entire spacecraft in order to optimize the thrust vector orientation throughout the thrusting phase of the mission. This decision was made on the basis that the weight and complexity penalties of a spacecraft designed to accommodate a mechanical orientation capability for the thrusters while maintaining the solar panels always normal to the sun are greater than the theoretical performance increase. Consequently, a fixed solar panel/spacecraft bus concept was adopted.

3-6
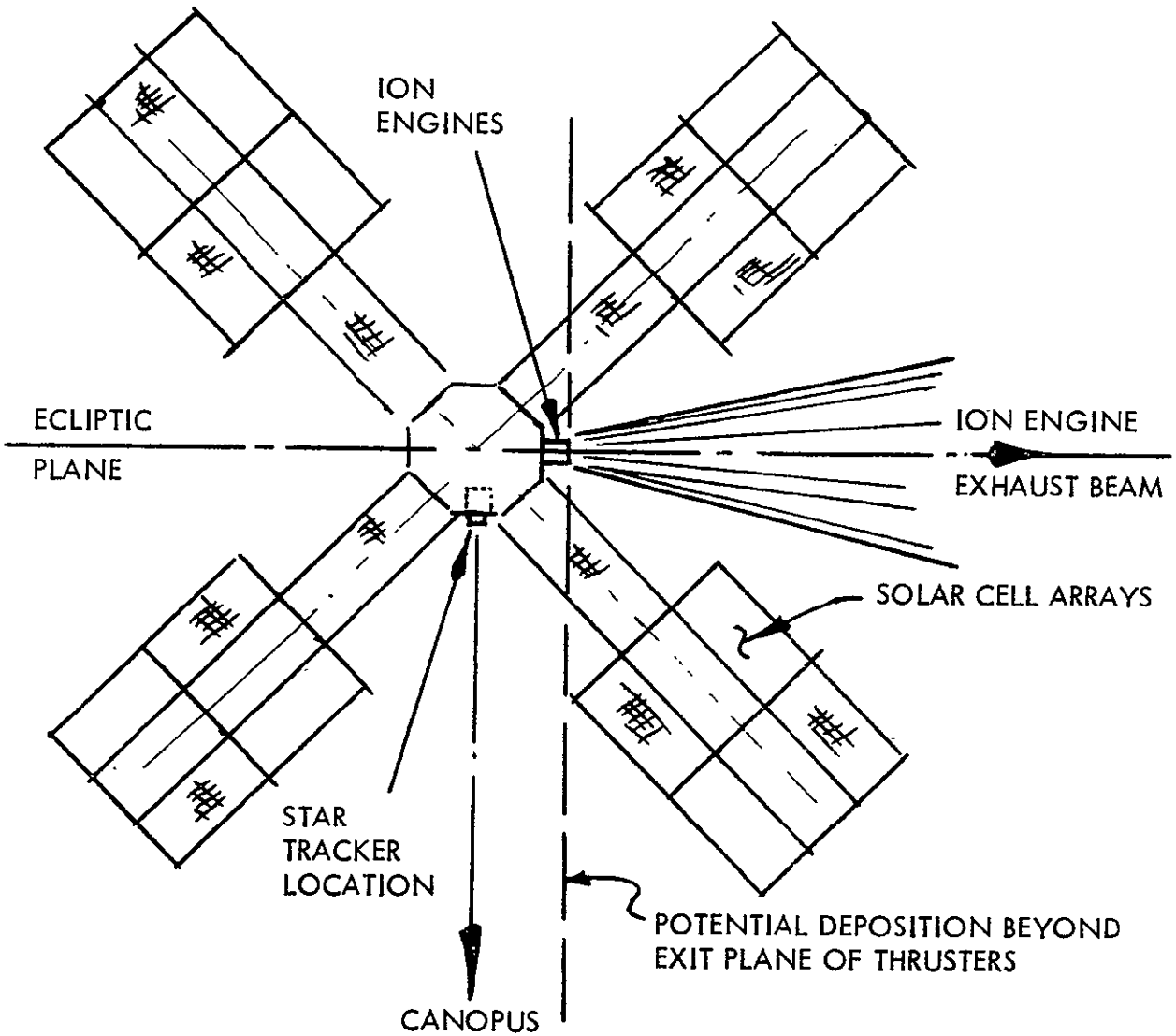
Figure 3-3. Mariner-Type Solar Array Arrangement

GE ROLL-UP ARRAY

BOEING FOLD-UP ARRAY

LONGITUDINAL
INTERCOSTAL

SOLAR CELLS

LEADING EDGE
MEMBER

OUTBOARD SPAR

SEE CROSS SECTIONS

FOAM BUTTONS

LRC PRESSURE CELL

LONGITUDINAL
INTERCOSTAL

CAPACITOR DETECTOR-
PEGASUS TYPE

OUTBOARD
SPAR
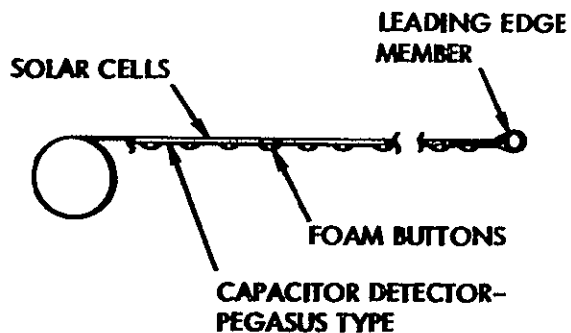
SOLAR CELLS

THICKNESS MICRONS	WEIGHT	
	KG/M^2	(LB/FT^2)
65	0.36	0.074
125	0.53	0.109

$\Delta T_{sc} = 28°C$ (11% POWER DEGRADATION)

$W = 5.254 \, KG/M^2 = 1.08 \, LB/FT^2$

EXPLORER PRESSURE CELL

SOLAR CELLS

NO TEMPERATURE INCREASE
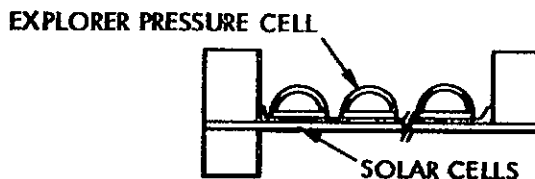
$\Delta T_{sc} = 14°C$ (5% POWER DEGRADATION)

$W = 7.239 \, KG/M^2 = 1.5 \, LB/FT^2$

Figure 3-4. Integrated Solar Cell and Meteoroid Detector Array

The selection of roll-out type solar arrays also imposes some limitations to the manner in which they are attached on the spacecraft body. Since the arrays are long, cylindrical bodies in the stowed configuration they generally must be aligned parallel to the longitudinal axis of the payload envelope. The spacecraft configurations possible, therefore, take on the appearance of a flying wing.

Star Tracker Field of View

Providing a clear field-of-view throughout the entire mission for the attitude reference star tracker(s) proved to be one of the major considerations in the evolution of the spacecraft configuration. During the design evolution, several approaches to solving the problem were investigated. The spacecraft is continuously oriented throughout the trajectory with the solar array facing the sun, with the exception of being slightly off normal to accommodate thrust vector attitude and meteoroid encounter geometry requirements. For the asteroid belt mission, the vehicle makes almost one complete revolution about the sun; therefore, for a single star in the southern or northern celestial sphere, a fixed mounted tracker on the spacecraft would detect the reference point as though it were moving in a circular pattern. Figure 3-5 shows four configuration approaches (A, B, C, and D) which could be implemented to accommodate fixed - mounted star tracker field-of-view requirements.

These configurations also satisfy the design constraint adopted of keeping all spacecraft appendages forward of the thruster ion exit plane. In configuration A, the choice of using the star Canopus required that the solar panels (in the plane of the paper) be deployed forward to provide an unobstructed field of view throughout the mission. For missions in the ecliptic plane, where the ion engines operate throughout most of the life of the mission, this approach would be acceptable since the thrust vector could be used to compensate for solar pressure disturbance torques resulting from such an arrangement. For missions that involve long coast periods, the inherent large non-alignment of the center of pressure and the center of gravity requires a substantial amount of fuel to compensate for the disturbing torque (approzimately 40 Kg of GN$_2$). Deploying the top solar panel to the rear could be considered so that the center of pressure would remain centered, but this would violate the ion exhaust beam clearance criterion adopted. In configuration B the approach taken was to consider a symmetrical arrangement of the solar panels, but to orient the entire vehicle so that the lower panels would be outside of the tracker's field of view. This approach causes the thrust vector to be tilted out of the ecliptic plane and consequently sacrifices some of the thrust for in-the-ecliptic thrusting.
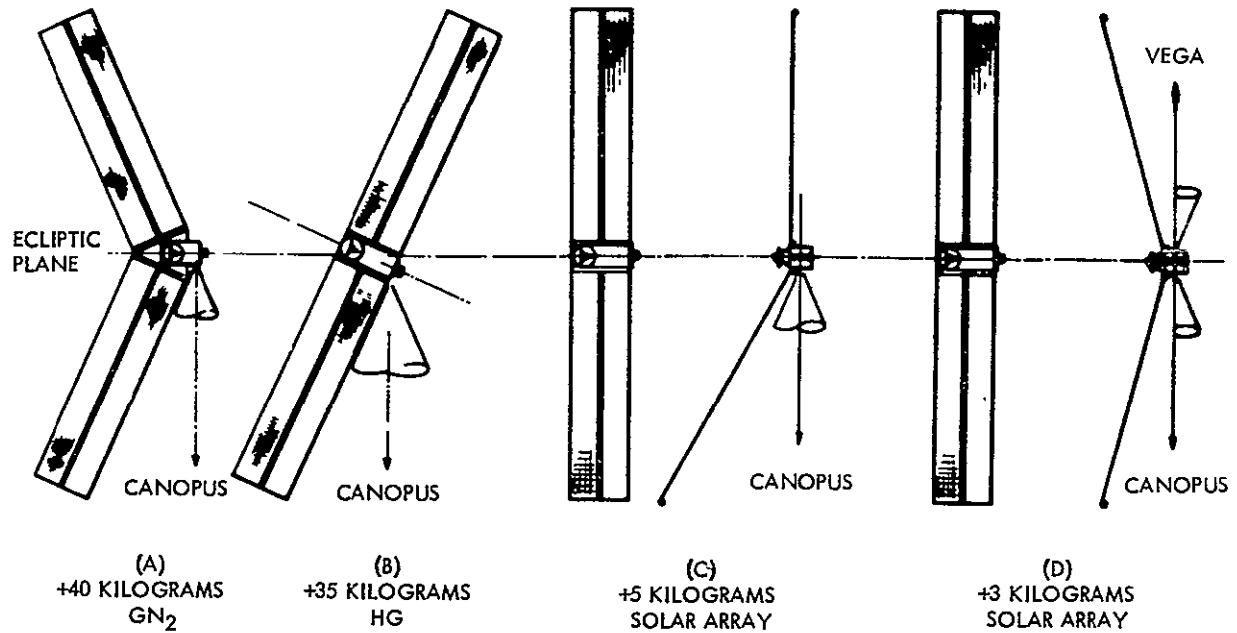
Figure 3-5. Spacecraft Configuration Concept Evaluation
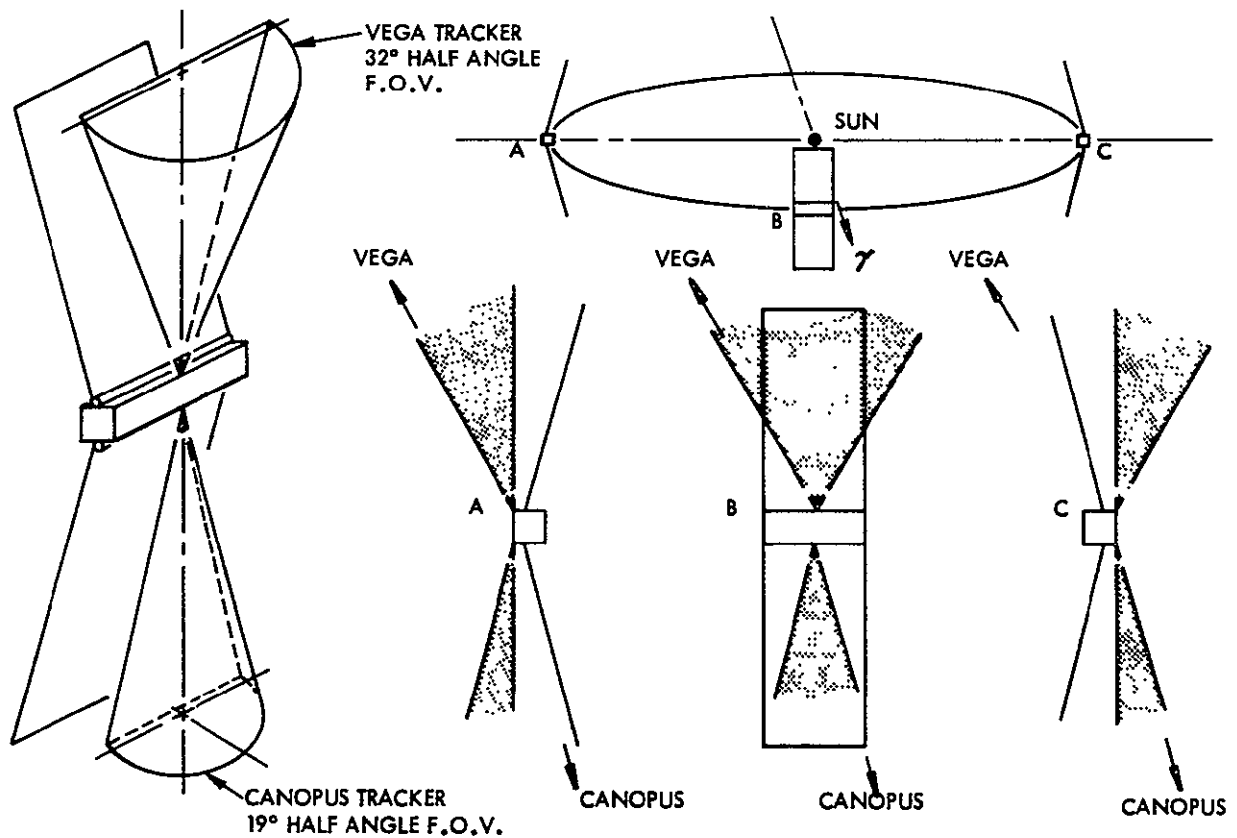
Figure 3-6. Canopus and Vega Tracker Geometry

3-10

The affect on the trajectory is rather insignificant in terms of causing the trajectory to become inclined with the ecliptic plane. The resultant trajectory would be inclined to the ecliptic by less than 5 degrees, but the Mercury fuel penalty to compensate for the performance loss is approximately 35 Kg.

In configuration C only the lower solar panel was canted toward the sun providing an esthetically unattractive, unbalanced, and nonsymmetrical configuration. For a modest array weight penalty of 5 kg, configuration C could be designed to accommodate the resultant shift in center of gravity caused by the single canted panel, but it is necessary to provide two different panel designs (length, cell arrangement, and thermal properties for the canted array is different from the non-canted array). Configuration D utilized two star references in addition to the sun. The two stars chosen were Canopus in the south and Vega in the north. The selection of these two start permits the spacecraft to view one or the other during any portion of the trajectory with only a minor amount of symmetrical canting of the top and bottom solar panels toward the sun. Canting the panels at 15 degrees will ensure that the panel extremities will never enter the field of view of either tracker viewing Canopus or Vega. The panels are expected to deflect away from the sun due to thermally-induced bending of the extension boom members. Bending back to the vertical by as much a five degrees at 1 AU can be expected. Should this occur, a sufficient clear field of view would still exist for the trackers so that the coverage of the reference stars would never become obscured. The field-of-view geometry is shown in Figure 3-6. As one star moves out of the field of view of its tracker during the mission, the second star will already have entered the field of view of the other. In this way, the necessity for going into a roll reference search at the time of switching from one star tracker to the other is not required and the chances of losing roll reference lock are minimized. The use of the dual fixed-mounted trackers is also significantly less complicated than gimbaling a single image dissector-type star sensor which would be used to pickup alternate star references along the trajectory.

SELECTED DESIGN CONCEPT

The systems analyses and design selection of the SEP asteroid belt mission spacecraft encompassed a multitude of interrelated considerations and tradeoffs in the areas of trajectory analyses and mission profile, science payload selection, spacecraft configurations and subsystem design. Only the highlights of the selected design will be briefly discussed here, as the remainder of this technical volume and related appendixes cover each of the spacecraft subsystems in depth.

The four design concepts presented in Figure 3-5 meet all the major design considerations required. Concepts A and B require a minimum

solar array area, but incur significant weight penalties. Concept A requires 42 kg of GN_2 to compensate for the misalignment of the space-craft center of gravity and the center of solar pressure. Concept B requires an additional 35 kg of mercury to overcome the loss of thrust in the ecliptic plane. Based on these weight penalties along, these two concepts were eliminated for further consideration in the design concept selection. Concepts C and D cannot be evaluated on the basis of weight panelty, a difference of a few kilograms, but the symmetrical appearance of Concept D and the cost advantages of using identical solar arrays makes Concept D the preferred design concept.

The recommended solar electric propulsion spacecraft design (Figure 3-7) features the utilization of four identical 2.5 kilowatt roll-up solar cell arrays with capacitor type particle impact detectors bonded to the anti-solar side of the panels. The spacecraft configuration is symmetrical with the arrays deployed initially to be canted 15 degrees sunward to provide an adequate field of view for the Canopus and Vega star trackers. The star trackers are rigidly mounted to the spacecraft and do not require mechanical or electronic scan capability. One pair of the rollup solar cell arrays are mounted to a rotatable base which permits these two panels to be reoriented away from the sun after aphelion passage to maintain proper encounter geometry of the capacitor sheets with the asteroidal particles during the coast phase back to 2.0 AU.

The electric propulsion system designed for the spacecraft is rated as a 7.8 kilowatt system at 1.0 AU. Its major elements consist of three 30 centimeter mercury electron bombardment ion thrusters rated at 3.6 kw each. Two thrusters operate initially with one in standby. Two 3.9 kw rated modular designed power conditioning and control panels provide the thrusters with the required operating voltages and currents. A single mercury propellant reservoir is provided and is capable of feeding all thrusters. Dual-axis translation is provided for the thruster array and each thruster is individually single-axis gimbal mounted. This mechanization not only insures that the resultant thrust vector is always aligned with the vehicle's center of mass, but also provides three-axis attitude control capability during the thrust phase of the mission. A three-axis cold gas (GN_2) control system is also provided for other mission phases. An SEP upper stage approach has been utilized in the design of the electric propulsion system: the entire electric propulsion system, exclusive of the solar arrays, has been designed as a distinct entity and requires a minimum interface with the rest of the spacecraft subsystems. The spacecraft has been designed into three separate modules, the electric propulsion module, the spacecraft sub-system equipment compartment module, and the science payload module. All of the science payload is easily accommodated in the forward science section, with the exception of the capacitor sheet particle penetration detectors on the solar arrays (Figure 3-8).

3-12
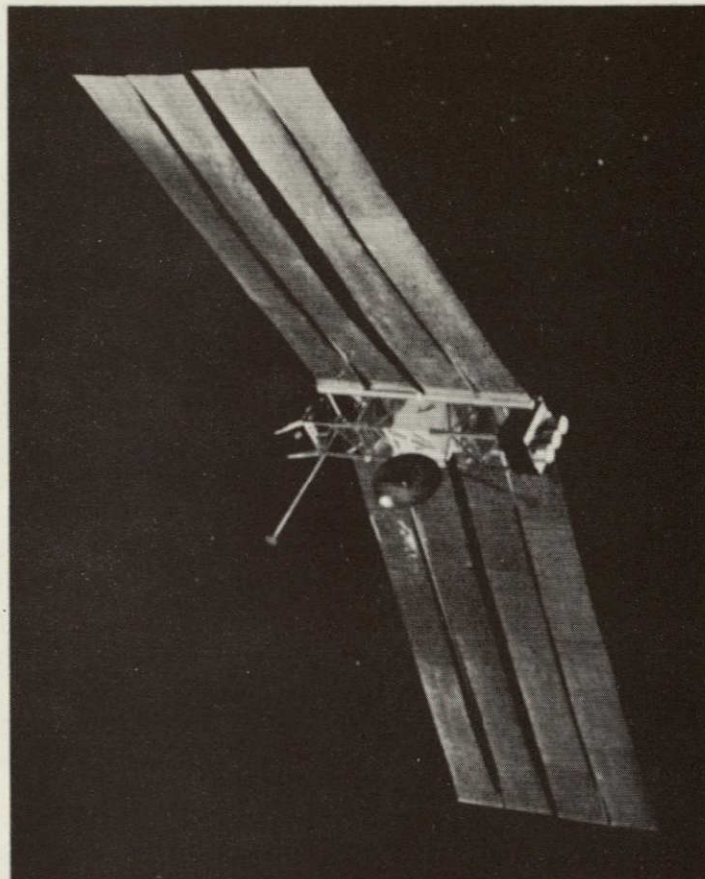
Figure 3-7. Selected Spacecraft
Configuration

HELIUM
MAGNETOMETER

TRIAXIAL PARTICLE
SPECTROMETER

ELECTROSTATIC BALLISTIC PENDULUM ~ 1 MODULE
FARADAY CUP ~ (2-REQD)
COSMIC RAY SPECTROMETER

ELECTROSTATIC BALLISTIC PENDULUM ~ 6 MODULES

$X_{SEP} = 0.00$ (REF)

GEIGER-MUELLER COUNTER (2-REQD)

FARADAY CUP (2-REQD)

SISYPHUS OPTICAL DETECTOR

SUN
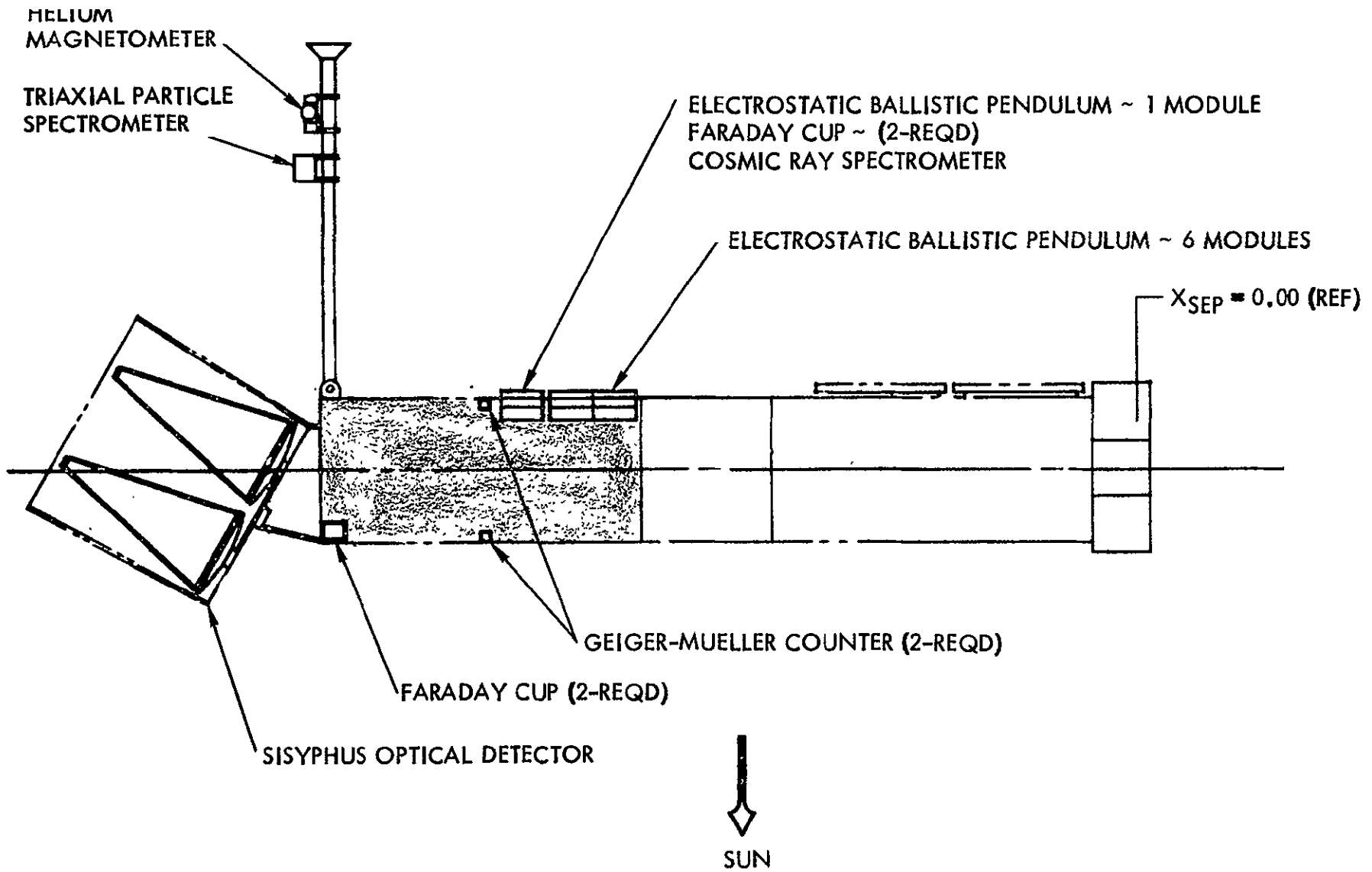
Figure 3-8.   Science Equipment Location

The spacecraft has been designed to be compatible with the Atlas Centaur or Tital III C launch vehicles. A weight summary of the recommended spacecraft is given in Table 3-2. A detailed weight breakdown is provided in the following Spacecraft Design section of this report.

The spacecraft may accomplish alternate missions with only minor changes to the rest of the vehicle. For an out-of-ecliptic mission the position of the Canopus and Vega star trackers are changed so that they may view out along the forward longitudinal axis of the spacecraft to accommodate the unique thrust vector orientation required for this mission-thrust orientation is essentially normal to the orbital plane. Additionally, a second degree of freedom is incorporated in the high-gain antenna gimbal mount to adequately maintain earth-spacecraft telemetry contact. For an alternate mission, major modifications to the science payload are not unlikely, but with the spacecraft modular design concept this is not expected to significantly alter the recommended SEP spacecraft design.

A complete detailed description of the recommended SEP spacecraft design and associated subsystems is the subject of the remainder of this Technical Volume.

Table 3-2. Spacecraft Weight Summary

System	Weight in Kg (lb)
Science payload (incl 755 ft^2 of capacitors)	80 (176)
Electric engine subsystem	62.5 (138)
Mercury propellant	107 (236)
Solar cell array (less capacitors)	155 (341)
Spacecraft power subsystem	28.5 (63)
Cabling	54.5 (120)
Communications and data handling subsystem	61 (135)
Spacecraft control subsystem	77 (170)
Central computer and sequencer	10.5 (23)
Thermal control subsystem	14.5 (33)
Spacecraft structure	77 (170)
Total Spacecraft Weight	727.5 (1604)
Atlas/Centaur capability at $C_3 = 12.2$ km^2/sec^2	751 (1656)

4. SPACECRAFT DESIGN

RECOMMENDED SPACECRAFT CONFIGURATION DESIGN

The recommended spacecraft configuration concept was the result of the configuration tradeoff studies in Section 3.0. A detailed design definition was performed on the recommended configuration in five major areas: a detailed mass properties analysis was performed to define the center of gravity offset problem due to the 15-degree canted solar arrays and the location of scientific equipment; the spacecraft structural concept was defined and a preliminary structural analysis completed. A detailed definition of the scientific experiment payload installation, the subsystem equipment compartment, and the electric propulsion system design were performed.

RECOMMENDED CONFIGURATION

The overall configuration is shown in Figure 4-1. The recommended configuration is shown in the completely deployed mode. The stowed mode limitations are indicated by the Centaur boost fairing outline (shown in phantom). The fairing system shown consists of the standard OAO nose fairing attached to the jettisonable OAO Agena mid-fairing. These two are then attached to an Intelsat IV adapter stub fairing. All of these fairings are existing or will be shortly "off-the-shelf" fairings. The Atlas/Centaur fairing system is shown rather than the Titan III-C fairing system, because the con- constraints are greater for this system concerning the use of existing hardware. Both fairing systems have a nominal 120-inch outside diameter and similar payload envelope diameters. The Centaur system is somewhat more constrained in length than the Titan III-C, which has the capability of incorporating cylindrical fairing sections to the standard fairing in 5-foot long increments.

The spacecraft structure as shown on the drawing is 1.0 meter (40 inches) square by 5.4 meters (212 inches) long. Most of the subsystem equipment is located in the central portion of the spacecraft structure and is designated the equipment compartment section. The ion engines, mounted on the aft end of the structure on a translator assembly, translate on the Y and Z axis to provide thrust vector alignment capability during the thrusting

phases of the mission. The mercury propellant tank and feed system along with the electric propulsion system power conditioning panels are located on the spacecraft near the engines. Such a location minimizes long power lines between the electric propulsion system components and the electrical power system. The aft section of the structure where the electric propulsion system is located is designated the electric propulsion module.

The four identical roll-up solar arrays (total of 10 kilowatts at 1 AU) are mounted symmetrically about the Z axis. All four arrays are canted 15 degrees toward the sun to provide sufficient clearance for the star tracker field of views. The solar arrays are modified versions of the General Electric Company 2.5 kilowatt arrays presently under development and test at GE, with capacitor meteoroid penetration detectors bonded to the dark side. The two arrays which extend along the -Y axis are mounted on rotary mounts which allow these arrays to be rotated 180 degrees about the Y axis after aphelion. These arrays are rotated so as to allow the capacitor meteoroid penetration detectors on the normally dark side to encounter the meteoroid environment after aphelion, when the meteoroids impact the spacecraft on the sun illuminated side. Figure 4-2 shows this meteoroidal impact geometry during the cruise (science-gathering) phase of the mission.

The Viking high gain antenna is mounted on the sun side of the spacecraft equipment compartment. The antenna mount is folded during launch to a position aft of the equipment compartment and is held in this position by pyrotechnically actuated boost tiedown fittings attached to the electric propulsion module structure. After deployment, the antenna is held in position by a combination deployment damper locking mechanism. Since the spacecraft X-axis remains in the ecliptic or trajectory plane during all mission phases the high gain antenna is required to hinge only about an axis parallel to the Y-axis to maintain earth pointing. One Mariner 1971-type low gain antenna is mounted parallel to the Z-axis facing the positive direction and is located near the forward end of the spacecraft. A second Mariner 1971-type low-gain antenna is similarly located on the opposite side of the spacecraft to provide omnidirectional coverage over 4π steradians. Once the spacecraft is properly oriented to the sun for SEP thrust and cruise phases of the mission, only the sun-facing low-gain antenna is utilized.

The structure forward of the equipment compartment (Figure 4-1) is discussed later in the scientific experiments payload section. The Sisyphus optical meteoroid detector is fixed mounted to the forward end of this structure. It is oriented 30 degrees from the X-axis toward the -Z-axis, which offers a sufficient field of view for the sensor. The Sisyphus detector is surrounded by a solar shade and glint shield to protect the mirrors from stray or glint light. The dark side area of this science payload section houses or provides mounting for the bulk of the scientific experiment
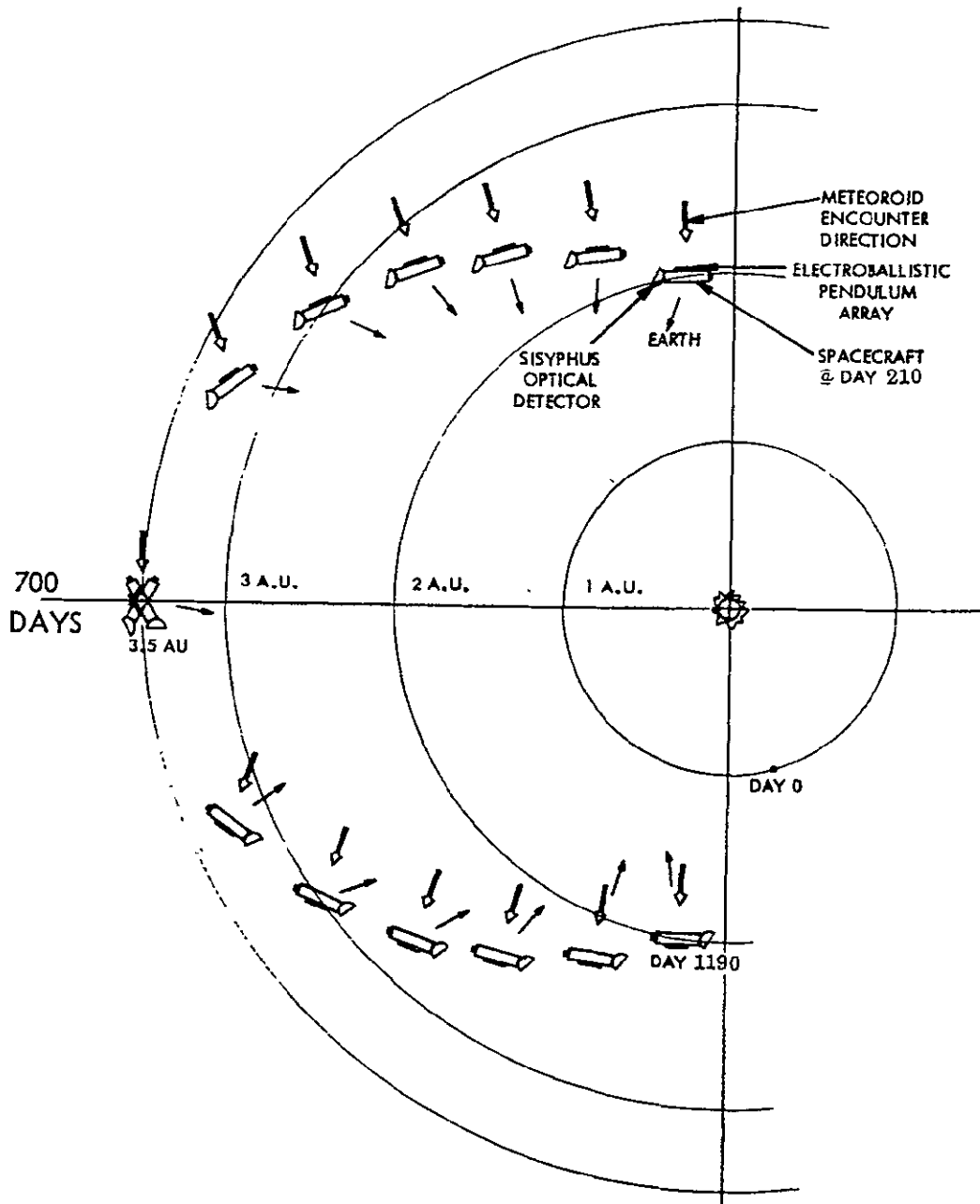
Figure 4-2. Meteoroid Encounter and Spacecraft Orientation Direction

payload. The seven electrostatic ballistic pendulum modules, a cosmic ray spectrometer, two Faraday cups and one Geiger-Mueller counter are accommodated in this area. The helium magnetometer and the triaxial particle spectrometer are mounted to the low gain antenna facing the dark side. Two additional Faraday cups and a Geiger-Mueller counter are mounted to the payload science section on the sun-facing side.

Dual Canopus and Vega star trackers are shown mounted on the dark side. One of the tracker pairs is located just aft of the equipment compartment and one forward of the scientific experiments. These locations were chosen to allow the solar array panels and drums in these areas to offer additional shading for the trackers, and to reduce the possibility of stray or reflected light from entering the optical field of view.

The two electric propulsion system power conditioning panels are also located on the dark side of the spacecraft. They are located between the aft end of the electric propulsion module structure and the aft set of star trackers. The electric propulsion module shown in the sun side view has a compartment at the aft end which houses the mercury propellant reservoir and feed system. The ion engines are individually hinged and mounted to a dual-axis linear translator assembly. Power to the electric propulsion system power conditioning panels comes from the equipment compartment.

The equipment compartment contains the spacecraft subsystem equipment. The dark side area of the compartment contains thermal control louvers. Attitude control cold gas jet valve assemblies are located on the equipment compartment flats about the 3 axes. The clear area around the equipment compartment offers maximum accessibility to the equipment.

MASS PROPERTIES ANALYSIS

The canting of the roll-up solar arrays 15 degrees toward the Sun has the net result of shifting the spacecraft center of gravity in the same direction. This condition is undesirable since the center of gravity is shifted off the spacecraft longitudinal axis. The solution to this potential center of gravity offset is to configure the spacecraft such that with all appendages deployed (solar arrays, low gain antennas and high gain antenna) the center of gravity is on the longitudinal axis. The required resultant center of gravity location for all equipment on the spacecraft, with the exception of that which is symmetrical about the longitudinal axis or that which is located for reasons of field of view or isolation, is 0.27 meters (10.8 inches) along the -Z axis, as shown in Figure 4-3. Obtaining this center of gravity location proved to be simple: within the electric propulsion system it was found that the power conditioning panels, if mounted outboard of the spacecraft on the dark or -Z side, would perform ideally. This location would reduce to a minimum the addition of thermal control equipment to the units. Also most of the

DESIRED SC C.G.

REQUIRED C.G. FOR ALL SC EQUIPMENT EXCEPT SOLAR ARRAYS, Hg TANK, A/C THRUSTER ARRAY & HIGH GAIN ANTENNA

+Z

SUN

+Y

Y	0
Z	-10. 8"
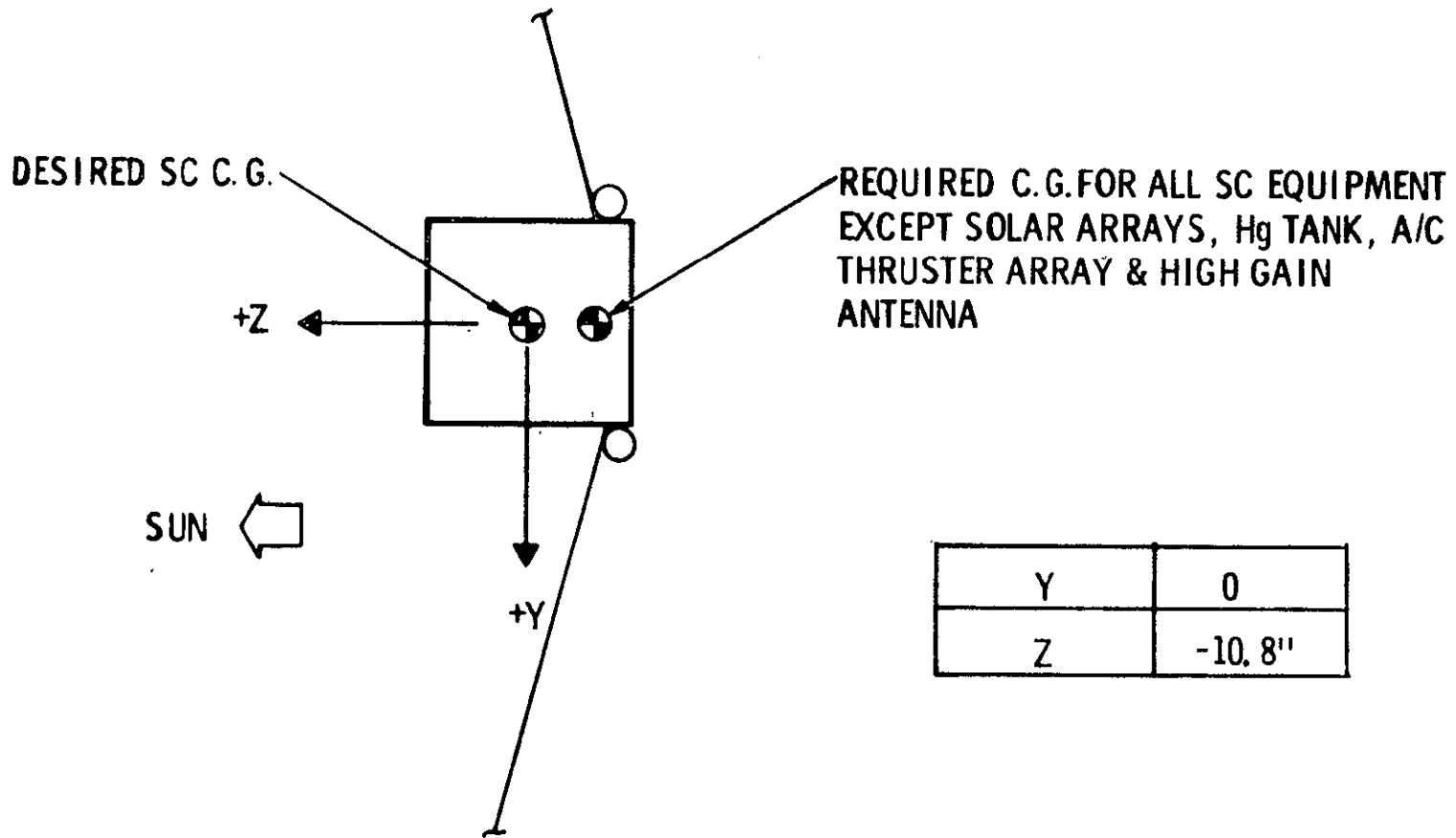
Figure 4-3. Center-of-Gravity Offset Analysis

scientific experiments viewing requirements were such that most of the equipment was mounted on the dark side of the science payload section. All of these factors aided in obtaining the required center of gravity location; the requirement was easily met.

The verification of having met this requirement can be seen in the spacecraft center of gravity summary shown in Figure 4-4. At spacecraft injection (separation from launch vehicle) with the solar arrays and antennas in the stowed configuration (array blankets not deployed and antennas folded) the spacecraft total weight is 727.5 kg (1604 pounds) and the center of gravity is located 42.6 centimeters (16.8 inches) aft of the spacecraft center of pressure and 22.8 centimeters (9.0 inches) along the -Z axis. When the ion engines are started the solar arrays and antenna appendages have been deployed and the spacecraft total weight remains at 727.5 kg (1604 pounds). Since no mercury has been used, the center of gravity remains at 42.6 centimeters (16.8 inches) aft of the center of pressure and lies on the longitudinal axis (arrays are deployed and equipment has been arranged to balance their canting effect). When the engines are shut down after the thrusting phase the mercury propellant has been almost completely depleted and the total spacecraft weight reduces to 620.5 kg (1368 pounds) and the center of gravity assumes a position which is coincident with the center of pressure of the spacecraft. Therefore, the possibility of a solar pressure disturbance torque due to a center of gravity and center of pressure offset is virtually eliminated during the post SEP-powered phase of the mission.

The spacecraft moments of inertia are presented in Figure 4-5 for the three conditions listed in the center of gravity summary (injection, ion engine start-up, and shutdown). As can be seen, the moments of inertia about the roll and pitch axes at ion engine start-up are roughly twice that of yaw, with the roll moment being roughly 20 percent larger than the pitch moment. At injection with all appendages stowed the roll and yaw moments are roughly equivalent and 15 times the pitch moment. The yaw moment is essentially constant during injection through ion engine start-up, and decreases 15 percent from ion engine start-up to shutdown. The roll moment decreases 8 percent from ion engine start-up to shutdown, but increases 130 percent when the appendages are deployed from injection to ion engine start-up. The pitch moment increases 22 times when the appendages are deployed from injection to engine start-up, but then remains unchanged through ion engine shutdown.

The spacecraft weight summary (Table 4-1) presents the major subsystem weight breakdown of the spacecraft along with the mass fraction of the four major subsystems. The contingency listed is based on using an Atlas/Centaur with a launch injection energy (C3) of 12.2 km^2/sec^2. A more detailed weight breakdown of each subsystem is given in Table 4-2.

SPACECRAFT C.G. SUMMARY				
	WT (LB)	C.G. (IN.)		
		X	Y	Z
INJECTION (STOWED SOLAR ARRAY)	1604	−16.8	0	−9.0
ENGINE START UP	1604	−16.8	0	0
ENGINE SHUT DOWN	1368	0	0	0
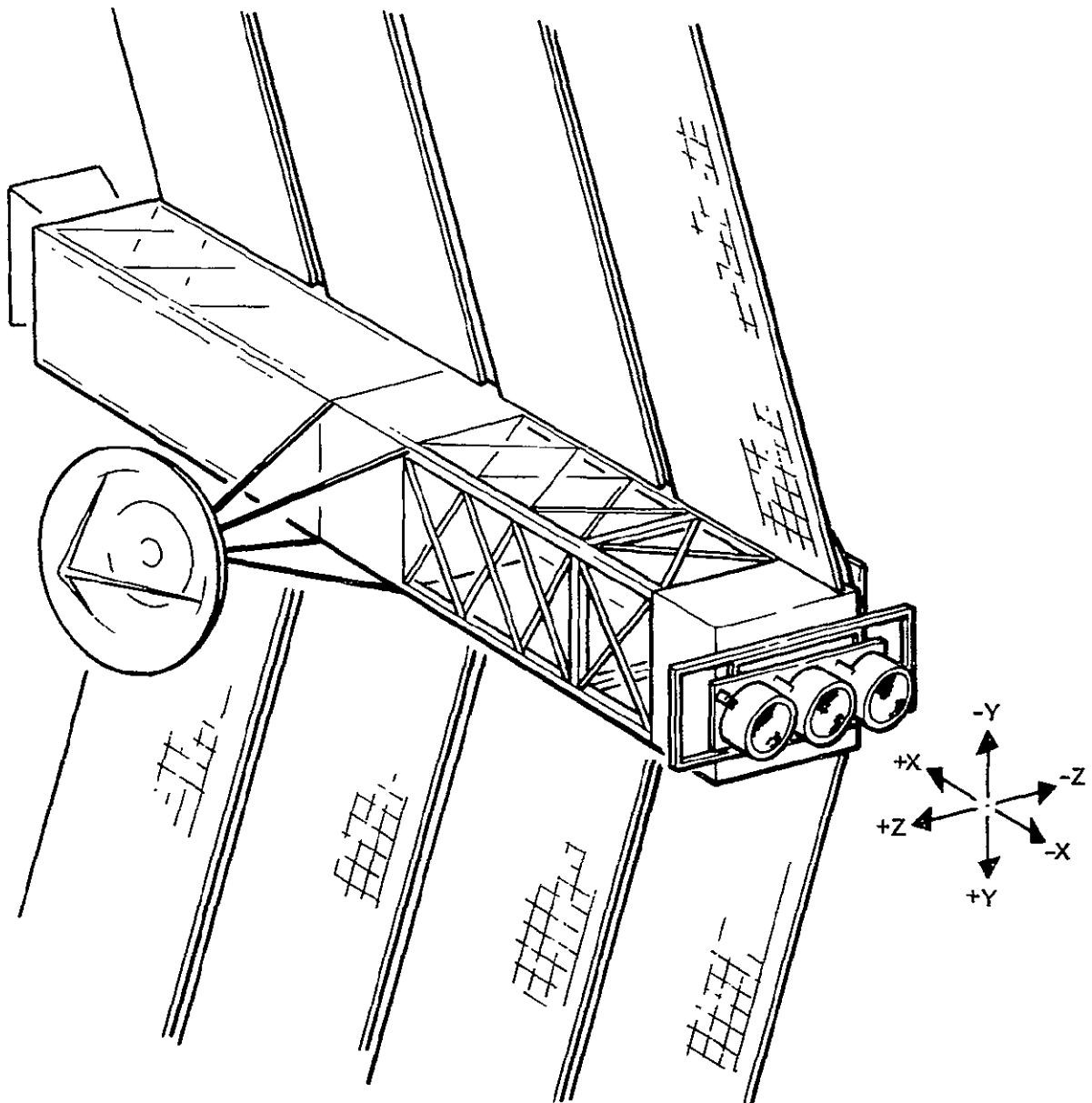
Figure 4-4. Spacecraft Center-of-Gravity Summary

MOMENT	INJECTION (SLUG FT^2)	ENGINE START-UP (SLUG FT^2)	ENGINE SHUTDOWN (SLUG FT^2)
I_{XX} (PITCH)	185	4050	4050
I_{YY} (YAW)	2815	2820	2380
I_{ZZ} (ROLL)	2840	6500	5950
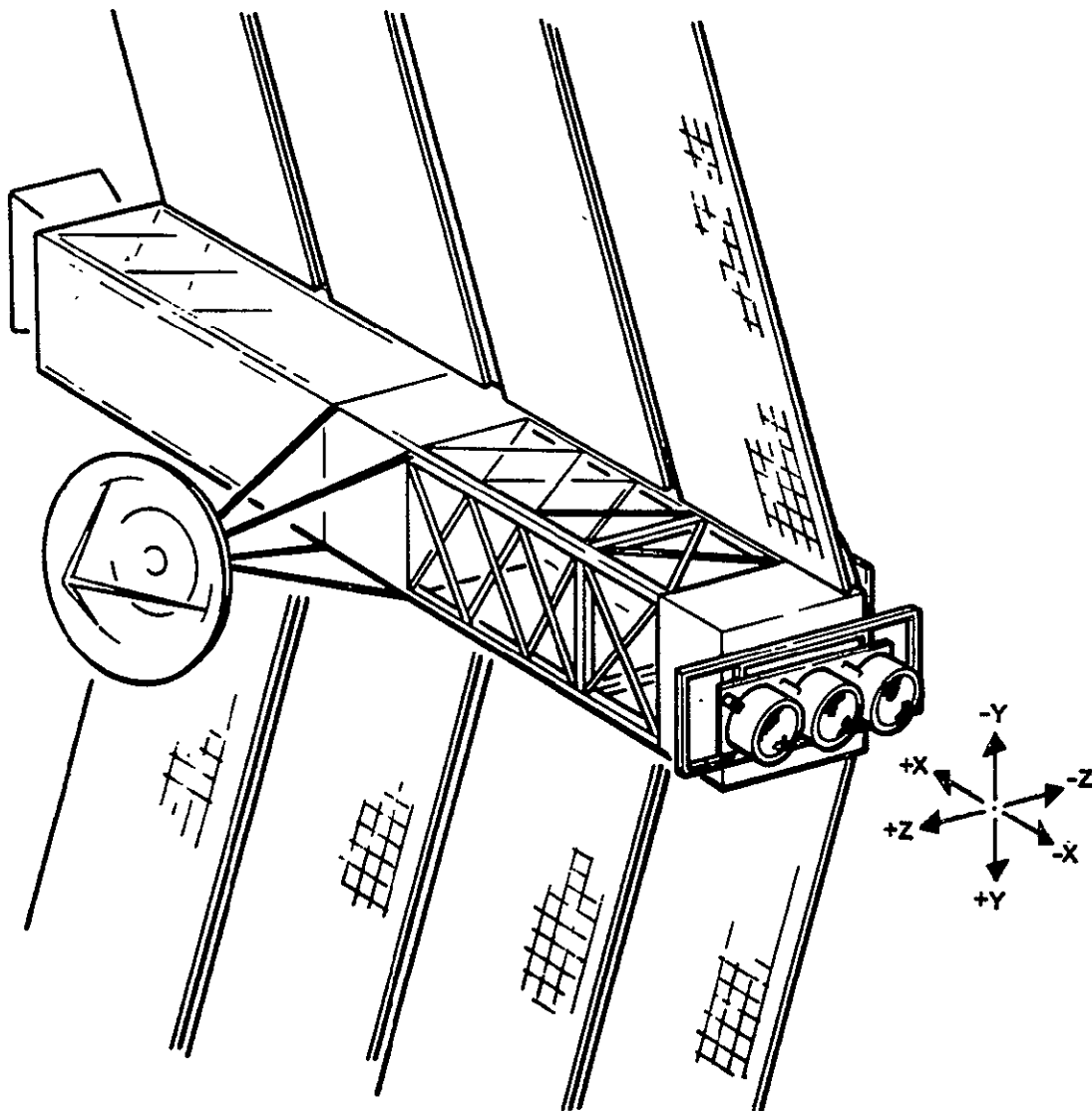
Figure 4-5. Moments of Inertia

4-10

Table 4-1. Weight Summary

Component	Weight kilograms (pounds)		Percent Mass Fraction
Electric Propulsion System		169.5 (374)	23
Electric Engine Subsystem	62.5 (138)		
Propellant	107 (236)		
Solar Array System		155 (341)	21
Payload			
Scientific Experiments		80 (176)	11
Engineering Systems		323 (713)	45
Electrical Power Subsystem	28.5 (63)		
Electrical Cabling Subsystem	54.5 (120)		
Communication and Data Handling Subsystem	61 (135)		
Stabilization and Control Subsystem	77 (170)		
Central Computer and Sequencer Subsystem	10.5 (23)		
Thermal Control Subsystem	14.5 (32)		
Structure Assembly	77 (170)		
Total Injected Weight		727.5 (1604)	100
Atlas/Centaur capability at C_3 12.2 km^2/sec^2	751 (1656)		
Contingency	23.5 (52)		

SPACECRAFT STRUCTURAL CONCEPT

Maximum simplicity and minimum cost were of primary concern in determining the structural concept to be employed by the recommended configuration. A brief comparison of unitized structural design versus modular design resulted in the selection of a modular design approach. This modular approach simplifies manufacture and test and checkout operations as well as providing minimum influence on overall structural design due to design changes in any modular section.

Table 4-2. Subsystems Weight Breakdown

Component	Weight in kilograms (Pounds)	
Electric Propulsion Subsystem		169.5 (374)
Thrusters	11.91 (26.25)	
Power Conditioner Panels	31.8 (70)	
Propellant Tank	2.27 (5)	
Propellant Feed System	0.9 (2)	
Power Distribution System	1.8 (4)	
Translator and Gimbal Mechanisms	10.8 (24)	
Propellant	110 (243)	
Solar Array Subsystem		155 (341)
Basic Solar Array (4)	150 (330)	
Strengthening to Support Capacitors	5 (11))	
Payload		80 (176)
Faraday Cup (4)	6.0 (13.2)	
Helium Magnetometer	3.4 (7.3)	
Geiger-Mueller Counter (2)	0.3 (0.6)	
Cosmic Ray Spectrometer	3.4 (7.3)	
Triaxial Particle Spectrometer	3.4 (7.3)	
Sisyphus	15 (33)	
Electrostatic Ballistic Pendulum	17.5 (38.3)	
Capacitors	31 (69)	
Engineering Subsystems		323 (713)
Electrical Power System	28.5 (63)	
Batteries	18 (40)	
Power Conditioning and Control Set	10.5 (23)	
Stabilization and Control Subsystem	77 (170)	
Gyro Package	5 (11)	
Canopus Sensor (2)	8.6 (19)	
Vega Sensor (2)	8.6 (19)	
Fine Sun Sensor (4)	0.9 (2)	
Coarse Sun Sensor (2)	0.2 (0.4)	
Electronics	9.1 (20)	
GN_2 Tanks (2)	19.4 (43)	
Fill Valves (2)	0.1 (0.2)	
Relief Valves (2)	0.2 (0.6)	
Squib Values (3)	0.5 (1.2)	
Filter (2)	0.1 (0.2)	
Regulator (8)	4.3 (9.6)	
Solenoid Valves (24)	4.3 (9.6)	
Nozzles (12)	0.5 (1.2)	
Plumbing Lines	1.7 (4.0)	
GN_2	13.5 (30)	
Central Computer and Sequencer Subsystem	10.5 (23)	
Thermal Control Subsystem	14.5 (32)	
Insulation	6.3 (14)	
Surface Coatings	1.8 (4)	
Louvers	4.1 (9)	

Table 4-2. Subsystems Weight Breakdown (Cont)

Component	Weight in kilograms (Pounds)	
Heaters	2.3 (5)	
Structure Assembly		77 (170)
Electric Propulsion Module	30.4 (67)	
Equipment Compartment	16.3 (36)	
Payload	19 (42)	
Bracketry and Fittings	11.3 (25)	
Electrical Cabling Subsystem		54.5 (120)
Comm and Data Handling Subsystem		61 (135)
Radio Frequency Subsystem (less antennas)	17.8 (39)	
High Gain Antenna	4.5 (10)	
Low Gain Antenna (2)	3.2 (7)	
Flight Command Subsystem	2.7 (6)	
Flight Telemetry Subsystem	11.8 (26)	
Data Storage Subsystem (2)	15.5 (34)	
Data Automation and Processor Subsystem	5.9 (13)	

It has long been the desire in solar electric propulsion spacecraft design to isolate the propulsion section from the spacecraft subsystem and science. Using the modular approach, the electric propulsion module can be considered as a separate entity. The equipment compartment and the scientific payload section can also be treated as separate entities. The equipment compartment may be manufactured, tested, and checked out without requiring physical attachment to the other modules. The science payload section can be manufactured and tested and checked out as various experiment payloads are received from the experimenters. The solar arrays are treated as a separate subsystem since they would first interface with the equipment compartment even though most of the power they produce is delivered to the electric propulsion module.

Each of these modules, after modular checkout, is mated and spacecraft final integrated tests and checkout operations are conducted. This approach enables each module to be completely tested and checked out separately in a much smaller facility than would be required if the entire spacecraft were used while testing or checking only a small portion of it. As a result, the modular approach offers the potential for maximum simplicity of development, manufacture and test, and minimum cost.

Several candidate construction methods were investigated fully to determine which would be simplest and reflect minimum cost. The selected concept is shown in Figure 4-6. The four longerons of each module are aluminum angle and the diagonals are aluminum tees. These members are mechanically fastened together and in turn the equipment supports are mechanically attached to the structural frame. The modules are then mechanically attached to each other. This technique allows each module to be treated as an entity, and creates a minimum impact on the spacecraft integration and checkout procedures and handling. This structural concept is considered to be a simple state-of-art construction (airframe) utilizing available standard materials (aluminum) and components (standard size angle and tee sections). The mechanical fastener concept allows the spacecraft structure to be built with a minimum of tooling and eliminates the need for any expensive manufacturing developments. Other structural concepts were also considered and rejected as discussed below.

The first concept considered welding the entire structure. This method would require large and expensive welding fixtures as well as requiring special heat treatment of the metal structure after welding to relieve welding induced stresses. Once the structure had been completely assembled it could not be dismantled. Maintaining tolerance within acceptable levels for a structure of this type also would be very difficult. A slight weight advantage (approximately 10 percent) is realized when using the welded structure instead of the mechanically fastened approach. The welded type structure was rejected because of its manufacturing complexity and cost.

EQUIPT COMPT SECTION

ELECT. ENGINE SECTION

SCIENCE SECTION

THERMAL CONTROL LOUVERS

ELECTRIC PROPULSION POWER CONDITIONING PANELS

SOLAR ARRAY

STRUCTURAL
SUBASSEMBLIES

MAIN STRUCTURE ASSEMBLY

LOW-GAIN ANTENNA

HELIUM MAGNETOMETER

TRIAXIAL PARTICLE SPECTROMETER

ION ENGINE CLUSTER &
TRANSLATOR ASSEMBLY

ELECTRO-STATIC BALLISTIC
PENDULUM MODULE-7

HIGH-GAIN ANTENNA

SISYPHUS OPTICAL DETECTOR

FARADAY CUP

SOLAR ARRAY

LOW-GAIN ANTENNA

SYSTEMS INSTALLATION & CHECKOUT

COMPLETE ASSEMBLY

Figure 4-6. Solar Electric Spacecraft - Exploded View

The use of a tubular structure was considered because of the initial weight savings over the angle and tee structure. However, tubular structure requires many special fittings for joining and providing adequate mounting flanges and surfaces. The added weight of these fittings plus the added complexity of their shapes and attachments indicated a significant increase in machining cost. For these reasons the tubular structure concept was also rejected.

The use of lighter and more exotic materials was also discarded because the added complexity to the structure and the increased cost of manufacturing processes involved were not conducive to minimum cost and maximum simplicity. An enclosed box or essentially the recommended truss approach with skins around the periphery did not offer any significant advantage. The addition of the skins would have offered meteoroid penetration protection for some of the exposed experiment packages, but it was found that it was lighter to provide this protection to each package on an individual basis rather than completely enclose the truss network. A honeycomb type of box construction was considered but rejected because of the size of the structure and the heavier structure weight required for hard point attachment of equipment and transmission of the launch loads to the booster interface. Although the honeycomb approach was rejected as the recommended concept, it would offer advantages for a smaller spacecraft and might have been recommended if a lower power level spacecraft were used.

Once the recommended structural concept was selected, a cursory structural analysis was performed which gave credibility to the selected modular truss concept. The analysis was also used to arrive at the structural weight and to evaluate the alternative construction concepts. The modular design shown in Figure 4-6 is considered to be both the simplest design and representative of a minimum cost spacecraft.

SCIENTIFIC EXPERIMENTS PAYLOAD

The payload for the asteroid belt mission solar electric propulsion spacecraft is basically composed of scientific equipment designed to investigate the meteoroid (asteroidal and cometary) and radiation environments of space within the asteroid belt. The payload consists of field and particle experiments and meteoroid experiments. Each experiment sensor has its unique field-of-view requirement and many have critical location and isolation requirements. As a result of these requirements the payload section of the spacecraft is configured to accommodate all of the experiments without sacrificing any of the initial viewing or location requirements. The number of experiments, their field-of-view requirements, and their location and isolation requirements are discussed in detail in the Science discussion (Section 5.0) in this report and in Appendix   A brief summary of these science equipment requirements is presented below to explain the general location of the science equipment as shown in Figure 4-7.

4-16
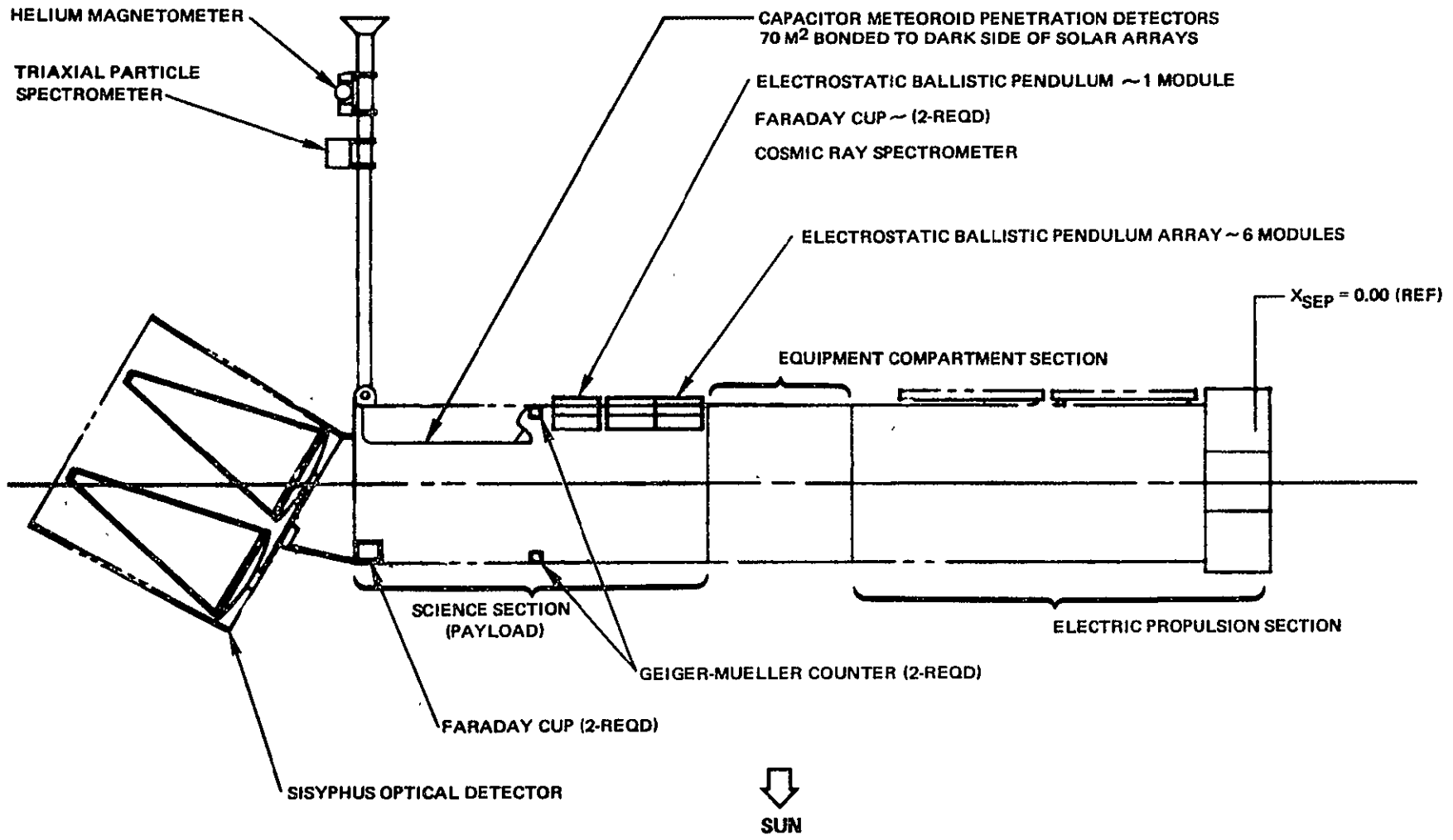
Figure 4-7. Science Equipment Location

Space Division
North American Rockwell

Field and Particle Experiments

The field and particle experiments are conducted by five experiment sensors. The first is a helium magnetometer which requires no specific orientation with respect to the spacecraft, but does require that its orientation be known at all times during the mission. The helium magnetometer requires isolation from the spacecraft which indicates a boom mounting. Consequently, a fixed position near the outermost part of the dark side-facing low-gain antenna boom was chosen. The second is a triaxial particle spectrometer which requires an unobstructed 10-degree conical field-of-view in three orthogonal directions. One of the sensor elements views away from the sun; one normal to the sun-spacecraft line, in the ecliptic plane, facing in the direction of posigrade helicentric orbit; the third one is normal to the ecliptic plane. This instrument was also mounted on the low gain antenna boom just below the helium magnetometer. This location satisfies the field-of-view requirements. The third sensor consists of four Faraday cups with 45-degree conical field of views. Two cups face the sun and two face away from the sun. The fourth sensor type consists of two Geiger-Mueller counters having 90-degree fields of view with one facing the sun and one facing away from the sun. The fifth sensor is a cosmic ray spectrometer which completes the field and particle experiments list. This instrument faces away from the sun and requires a 60-degree conical field of view.

Meteoroid Experiments.

There are three meteoroid experiments. The first consists of 70 square meters of capacitor meteoroid penetration detectors, that require facing the meteoroid encounter direction. The capacitors have been bonded to the dark side of the roll-up solar arrays. The second experiment is seven modules of electrostatic ballistic pendulums. These have a 60-degree square field of view and also require facing the meteoroid encounter direction. The last experiment is the Sisyphus optical detector. This instrument has a very narrow field of view requirement (2 degrees) but its large size and pointing requirements make it one of the forcing elements in the payload section design. The Sisyphus is required to point away from the sun and normal to the meteoroid encounter direction.

The direction of meteoroid encounter was shown in Figure 4-2 for the cruise phases of the mission. Also shown is the direction of the earch at different points along the trajectory, the orientation of the spacecraft, and location of the electrostatic ballistic pendulum array and the Sisyphus detector. As was discussed in preceding sections (and shown in the figure), the spacecraft is step-oriented during the cruise phases to optimize the encounter direction. Before reaching 3.5 AU the asteroidal meteoroids encounter the spacecraft from the dark side where the ballistic pendulum modules and the capacitors are facing. After aphelion the asteroidal meteoroids encounter the front or

sun side of the spacecraft. During these post aphelion phases, the two solar arrays extending into the northern celestial hemisphere are rotated 180 degrees to expose the capacitor meteoroid penetration detectors (bonded to the dark side) to the encounter direction. The ballistic pendulum array will record cometary impacts during these phases and the Sisyphus will continue to operate as it did in the pre-aphelion phases.

The integrated scientific experiments payload installation is shown in Figure 4-8. The main view of this drawing gives the general location of individual experiments on the payload section of the spacecraft. As can be seen, all of the experiments can be mounted to the payload section structure and checked out before integrating with the total spacecraft. Details A and E in the figure give the location of the equipment mounted on the low-gain antenna. The helium magnetometer is mounted farthest out on the antenna to isolate it as far as possible from the spacecraft. The triaxial particle spectrometer is mounted inboard of the magnetometer far enough to allow field-of-view clearance for the sensor element facing away from the sun. The magnetometer is mounted over 100 inches from the spacecraft center-line. The sensor elements of the triaxial particle spectrometer are located approximately 15 inches inboard of the magnetometer. The spectrometer should be of sufficient magnetic cleanliness to assure that its operation does not interfere with that of the magnetometer.

Detail B in Figure 4-8 shows the installation of the Sisyphus optical detector. The primary mirrors are 67 centimeters in diameter and 72 centimeters between centers in a square pattern. A tubular truss support structure is provided on the forward end of the payload section to mount the detector. The truss allows for final alignment of the detector assembly with respect to the spacecraft axis. Once mounted, the detector maintains a constant angle of 30 degrees with the spacecraft longitudinal axis. A combination solar shade and glint shield surrounds the detector to protect the secondary mirrors which are approximately 131 centimeters forward of the primary mirrors. This shade is 1.5 meters square and 1.5 meters long, which made the Sisyphus a forcing element in the design of the payload section. As previously mentioned, the spacecraft is oriented throughout the cruise phases of the mission to maximize the asteroidal meteoroid flux impact on the penetration sensors. The Sisyphus sensor was fixed oriented to the spacecraft to provide maximum data based on the spacecraft orientation in the region from 2.0 to 3.0 AU. The resultant attitude angle was approximately 30 degrees from the X-axis in the -Y-axis direction.

Several experiments are shown mounted to the payload section structure in Detail C of Figure 4-8. These instruments are mounted forward of the payload section/equipment compartment interface. The experiments shown are grouped into two subassemblies. The first assembly, located just

forward of the equipment compartment, consists of six modules of electro-
static ballistic pendulums. This array faces the encounter direction in the
pre-aphelion phases of the mission. The 60-degree square unobstructed
field of view requirement is easily provided in the location shown. A second
subassembly is mounted forward of the ballistic pendulum array. This
assembly consists of two Faraday cups, a cosmic ray spectrometer, and one
electrostatic ballistic pendulum module. The ballistic pendulum module is
mounted in a manner similar to the ballistic pendulum array and also faces
the encounter direction. A 60-degree conical unobstructed field of view for
the cosmic ray spectrometer is provided at the location of the sensor as
shown. The two Faraday cups and their 45-degree conical unobstructed
fields of view are accommodated as shown. The Faraday cups and the cosmic
ray spectrometer are fixed-mounted to the payload structure and face away
from the sun (mounted on the dark side of the spacecraft). The ballistic
pendulums are also fixed-attitude mounted to the payload structure, limiting
their use for obtaining asteroidal meteoroid encounter data up to mission
aphelion. After aphelion, only cometary data will be obtained.

The location of the two Sun-facing Faraday cups and the two Geiger-
Mueller counters is shown in Detail D of Figure 4-8. The fields of view of
the two Faraday cups were provided by mounting them at the forward edge
of the Sun side of the payload structure. The two-Geiger-Mueller counters
are mounted at about the mid point of the payload structure with one counter
mounted in front of the solar array drum (facing the sun) and one counter
mounted behind the solar array drum (facing the dark side). This location
satisfies the 90-degree conical field of view requirement for these instru-
ments. The capacitor meteoroid penetration detectors are also shown in
this detail mounted to the dark side of the solar arrays. After reaching
aphelion the arrays extending into the northern celestial hemisphere, -Y
axis, are rotated 180 degrees to detect asteroidal meteoroids now encountered
on the sun side of the spacecraft.

SUBSYSTEM EQUIPMENT COMPARTMENT DEFINITION

All of the spacecraft subsystems equipment is located within the equip-
ment compartment. The compartment is a modular entity and interfaces aft
with the electric propulsion module and forward with the payload section.
This compartment is centrally located on the spacecraft (Figure 4-9). In
addition to accommodating all of the subsystem equipment, the compartment
also provides hard points for the attachment of the Viking high-gain antenna
support truss and the roll-up solar array end support fittings. The compart-
ment flats provide mounting for the twelve cold gas (GN$_2$) stabilization and
control jets.

In defining the equipment compartment there are four items of major
concern. The first item is the location of the equipment within and around

VEGA

EQUIPMENT COMPARTMENT SECTION

ELECTRIC
PROPULSION SECTION

SUN

ELECTRIC
PROPULSION
SECTION

+X

+Z

ECLIPTIC
PLANE

FLIGHT
DIRECTION

SCIENCE
EXPERIMENTS
SECTION

X_{SEP} = 0.0 REF

EQUIPMENT COMPARTMENT
SECTION (HIDDEN LINE)

+Y

CANOPUS
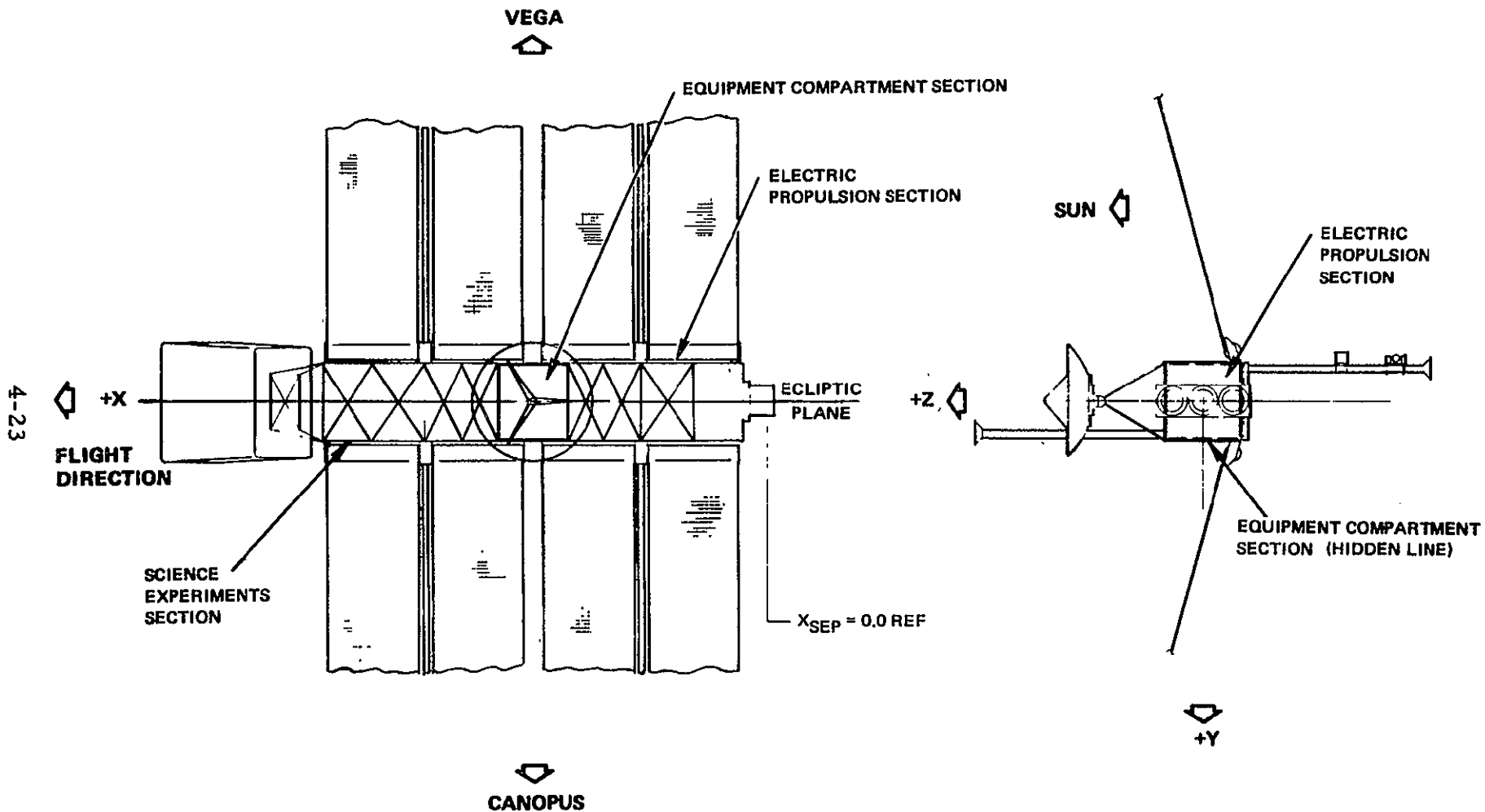
Figure 4-9. Equipment Compartment Location

the periphery of the compartment. Of primary importance is that the equipment be arranged within the compartment to eliminate the possibility of a center-of-gravity offset due to the canted solar arrays. Meeting this requirement dictates that the equipment be located on the dark side of the compartment. The GN_2 tanks should also be located to avoid creating a center-of-gravity shift as the fuel is depleted. The equipment should also be arranged to minimize interconnecting wire bundle lengths and separate or shield equipment which could be electrically disturbed by high power cables or other equipment. Second, thermal control requirements to provide a comfortable thermal environment for the equipment should be minimized by suitable equipment arrangement. The arrangement should be such that hot spots and cold spots do not exist. The third item of concern is protection for the subsystem equipment from meteoroid damage. The equipment compartment will be subjected to the same hazard the spacecraft is designed to investigate since the purpose of the asteroid belt mission is a long-duration stay within the belt to gather information on the environment. To ensure mission survivability, the equipment compartment must be protected sufficiently from this meteoroid environment. The last consideration is that of equipment accessibility. Since meteoroid protection as well as thermal insulation is required within the compartment, a means must be implemented to remove the equipment easily and efficiently during assembly, checkout, and prelaunch maintenance.

The equipment compartment is shown in Figure 4-10. The compartment is basically one meter (40 inches) square and 0.9 meters (36 inches) long. The 0.9-by-1.0 meter area which faces away from the Sun is covered with approximately 0.7 m^2 (7.6 ft^2) of thermal control louvers. All of the electronic equipment is mounted a short distance inboard of the louvers. The cold gas jets are located around the periphery of the compartment such that their moment arms are equal. The jets are located longitudinally at the location of the spacecraft center of gravity after depletion of the mercury propellant. As seen in Section B-B, the two 14-inch diameter GN_2 tanks are mounted on cylindrical support skirts, which are of skin stringer construction, and are located on the spacecraft longitudinal axis. The depletion of the cold gas then offers minimum, if any, center of gravity shifts. The subsystem electronic equipment is shown mounted on the -Z side of the compartment. This location accommodates two requirements of the equipment location. The first is that the equipment be located so that the center of gravity of the spacecraft is coincident with the center of solar pressure once the solar arrays are deployed and the Hg fuel is expended. Coincident center-of-gravity and center-of-solar-pressure conditions should be maintained throughout the coast phase of the mission. For center-of-gravity shift requirements, see Figures 4-3 and 4-4. The second requirement deals with the thermal control of the electronic equipment. The location of the equipment, mounted to a cold plate (shear plate), is maximized for viewing through the louvers out the dark side of the compartment.

All sides of the equipment compartment with the exception of the louver side are insulated on the inside with 25 layers of aluminized mylar. These same sides are covered with an external meteoroid bumper skin for protection against the possibility of meteoroid damage to the equipment. The thickness of the meteoroid bumper skin and its spacing or stand-off distance from the compartment outer skin is based on the meteoroid impact damage analysis discussed in Section 12. Figure 12-13 of this analysis indicated that for a 90-percent probability of no meteoroid damage, the total thickness of both the bumper skin and the equipment compartment outer skin should be 0.12 inches. Since the compartment structure outer skin is 0.06 inches thick, the bumper skin is 0.03 inches and the remainder of the required protection thickness is provided by the 25 layers of aluminized mylar insulation.

Meteoroid protection for the louver side of the equipment compartment is provided by a unique bumper concept. The equipment within the compartment is mounted on a structural shear plate which also serves as a radiating cold plate for heat dissipation. This plate faces the louvers. The shear plate is 0.12 inches thick to meet structural and thermal requirements. This shear plate provides the second sheet protection for the equipment and its thickness, based on the meteoroid damage analysis of Appendix A is of sufficient thickness (0.12 inches) for both sheets. This indicates that the outer bumper sheet need only be of minimum thickness to meet the ratio of outer sheet-to-inner sheet thickness of 0.25. The outer bumper is unique in that it consists of an aluminum screen material with approximately 50 percent open area (Figure 12-14 of Section 12). The closed area does not increase the area of louvers required by the same 50-percent percentage, but only requires a 33 percent increase in total louver area. If a solid skin had been used the required louver area would have been doubled.

With the installation of the meteoroid protection bumpers on the outside and aluminized mylar insulation on the inside, it is undesirable and inefficient to require removal of this protection to gain access to the electronic equipment. A concept was therefore adopted which allows removal of the electronic equipment from the louver side of the equipment compartment only. This concept is similar to that used in several of the subsystem equipment bays on the Mariner 1969 spacecraft.

The installation of a subsystem is initiated with the attachment of the subsystem chassis into the equipment compartment. The chassis contains racks for the push-pull installation of the subsystem electronic subassembly units. It also has all of the intra- and inter-subsystem wiring attached to its external surface. The chassis is mounted to the structure through thermal isolation mounts (Sections B-B and C-C of Figure 4-10). The electronic subassemblies are then inserted into the chassis from the louver side. The electrical connections are made through push connectors which are mounted

to the chassis and received by the subassembly as it is inserted. A mechanical attachment is made between the subassemblies and the chassis (Section C-C of Figure 4-10). The chassis is of varying depth to accommodate the various subassemblies. The subassemblies, once installed, however, are parallel to the dark face of the compartment. This condition is required so that the subassemblies can be mounted to a combination structural shear plate and thermal control cold plate (Section B-B, Figure 4-10). The shear plate is then attached to the equipment compartment structure through thermal isolator mounts. This concept enables any electronic subassembly to be removed easily and efficiently through one side (louver side) of the equipment compartment without risking damage to either the mylar insulation or the external meteoroid bumper skins.

The location of each subsystem is shown in Section D-D in Figure 4-10. As can be seen, the available mounting area has been divided into four sections, and utilizes four chassis. Each chassis combination shear plate and cold plate faces a set of thermal control louvers (View E-E). The equipment has been arranged for minimum wire lengths, minimum electrical interference, balanced weight and thermal loads, sufficient meteoroid protection, and maximum accessibility.

ELECTRIC PROPULSION MODULE DEFINITION

The electric propulsion module is located aft of the equipment compartment and requires only mechanical and electrical interfaces with the rest of the spacecraft. The location of the electric propulsion module is shown in Figure 4-11. The structure of the module is similar to that of the payload section. An enclosed portion is provided forward of the ion engines for the tankage and electrical and propellant feed systems. The structure provides hard points for the central mounting fitting and end-supports for two of the roll-up arrays. The ion engines are attached to the module structure through a dual-axis linear translator. Two power conditioning panels are mounted to the external part of the structure area facing away from the sun. As was the case in the design of the equipment compartment, the electric propulsion module also has four areas of concern to its detailed definition.

The first area is that of the location of the various elements in the propulsion system. The liquid mercury propellant tank should be located on the longitudinal axis to minimize stabilization and control requirements. The power conditioners should be attached to the module structure to keep wire lengths at a minimum. The location and mechanization of the electrical and propellant feedlines across the translator must also be accommodated.

The second area is the thermal control of the propulsion module. The thermal control requirements are different from those of the remainder of

VEGA

SPACECRAFT STRUCTURE

ELECTRIC PROPULSION MODULE

ELECTRIC PROPULSION
MODULE

SUN

ECLIPTIC PLANE +Z

FLIGHT
DIRECTION

+Y

CANOPUS

Space Division
North American Rockwell
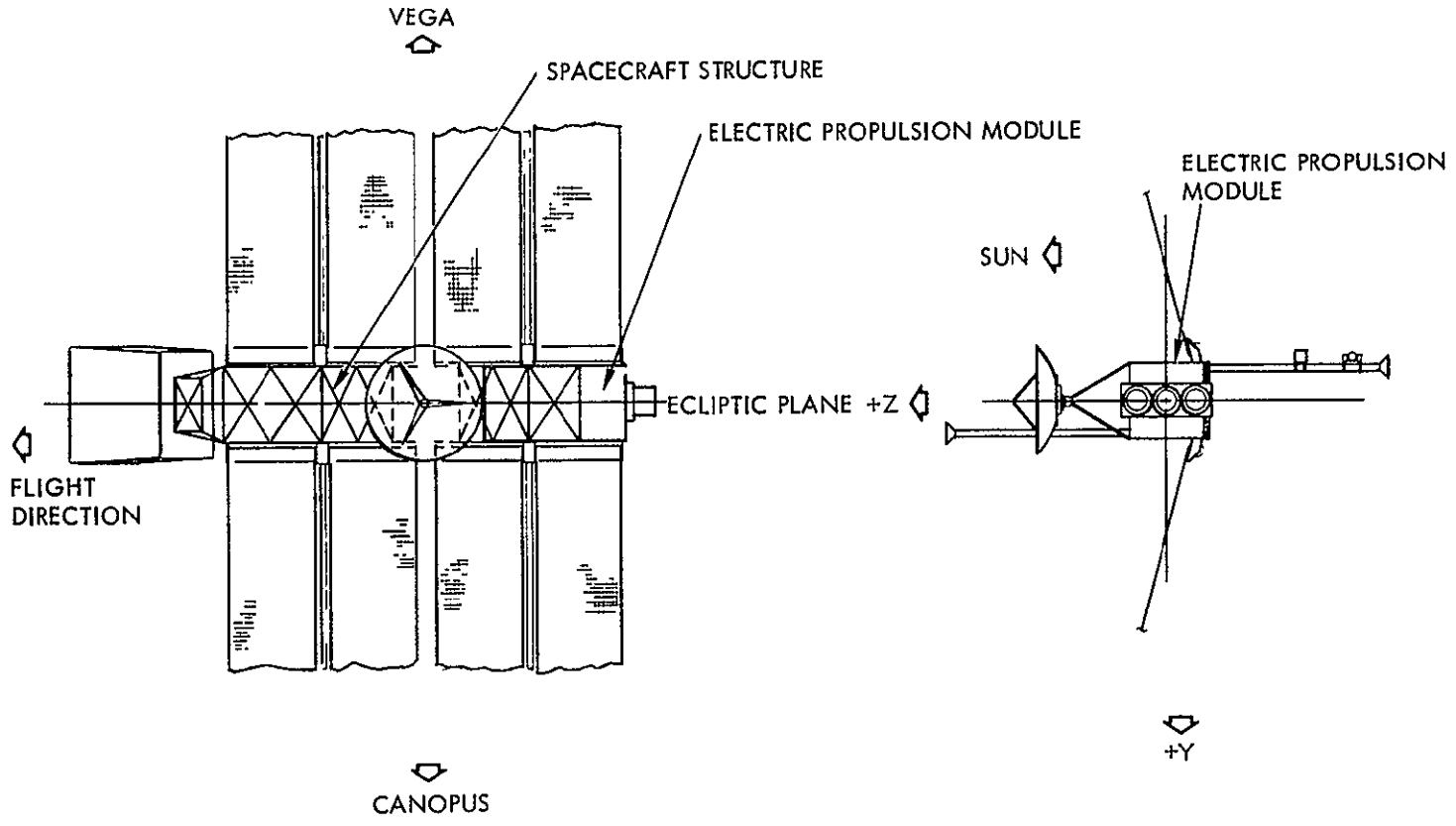
Figure 4-11.   Electric Propulsion Module Location

the spacecraft systems since the electric propulsion module operates for the first 210 days of the 1190-day mission. The requirements are such that the ion engines must be maintained at a warm temperature before they can be turned on. The power conditioning panels must also be kept warm before turning them on. Equipment within the enclosed compartment must also be provided with an acceptable thermal environment.

The third area of concern involves protecting the equipment from meteoroid damage until the end of thrusting. It would also be desirable to protect the equipment sufficiently to enable the propulsion system to be used or started again after the completion of the mission (1190 days) as an engineering test of the electric propulsion modules survivability in the space environment, providing that sufficient fuel remains.

The last area of concern is associated with maintaining thrust vector alignment with the center of gravity and also providing thrust phase attitude control by use of the thrust vector alignment capability. For a single row of thrusters, the thrust vector control requirements can be achieved through the use of either a single-axis linear translator with single-axis gimbaling of each thruster or a dual axis linear translator with hinged thrusters. Perhaps of greater influence on the selection of the approach for thrust vector control is the consideration given to the performance of these two approaches when applied to missions other than those requiring a single row of thrusters. Using a single-axis translator with single-axis gimbaled thrusters for control of 2 or more rows of thrusters, failure of a single thruster necessitates the shutdown of at least one normally operating thruster. This is necessary as the thrusters are operated in pairs (or groups) to maintain balanced thrust through the center of gravity. This problem is not faced when using a dual axis translator with hinged thrusters as the second axis motion of the translator enables the thruster array to always thrust through the center of gravity, independent of the number of engines operating. Because of this decided performance advantage, the dual-axis linear translator with hinged thrusters design concept was utilized.

The electric propulsion module configuration is shown in Figure 4-12. The module structure is one meter (40 inches) square and 2.23 meters (88 inches) long. The enclosed compartment near the aft end of the module is 24 inches long. The ion engines extend aft of the structure an additional 16 inches; the entire module is 104 inches in length from tip to tip. As can be seen in Detail A, the structural arrangement is basically the same as that of the payload section.

The two power conditioning panels are mounted outboard of the dark facing side structure. They are attached to the structure through thermal isolation mounts. The basic power conditioning panels are covered on the sun facing side with eight layers of aluminized mylar insulation and an

aluminum cover skin for meteoroid protection as shown in Section D-D. The dark facing or radiating area of the panels is also covered with meteoroid protection skin. Both surfaces of the power conditioning panels are provided with an $\alpha/\epsilon = 0.6$ thermal control coating. They are also provided with internal heaters to maintain their temperature limits during the power conditioning and control standby mode of operation. Locating the power conditioning panels on the -Z side of the spacecraft also helps to eliminate the possibility of a center-of-gravity offset from the canted solar arrays.

The enclosed compartment at the aft end of the propulsion module structure contains the liquid mercury propellant/pressurant tank, the mercury feed system, and the electrical feed system. The detail of the propulsion section shown in Section B-B of Figure 4-12 is presented again in Figure 4-13, enlarged for clarity of detail. The 10-inch-diameter mercury propellant/pressurant tank is shown supported on a conical skin stringer support. The tank is located on the longitudinal axis to minimize center-of-gravity shifts resulting from propellant usage. A squib valve and flow control orifice are located on the aft end of the tank to prevent hammering of the ion engine vaporizer screens by the liquid mercury during launch vehicle boosting. Mercury leaves the tank through the orifice and enters the feed system manifold from which it is distributed to the engines. The electrical power for the engines enters the switching network, attached to the translator, which directs the power to the operating engine or engines. The switching network receives both low and high voltage power from each power conditioning panel. The enclosed compartment utilizes a double skin to provide meteoroid protection. The skins are the same thicknesses and spacing as required on the equipment compartment (Figure 12-13 of Section 12). Sufficient protection is provided for the electric propulsion equipment so that the potential exists for restarting the thrusters at the end of the mission to provide data on the systems survivability in the space environment.

The ion thrusters and translator assembly are mounted to the aft surface of the propulsion module. Three ion thrusters are mounted to an engine mount side by side in the ecliptic plane. The propellant feed system manifold and the electrical switching network assembly are mounted to the opposite side of the engine mount. The thrusters are mounted to single axis gimbal mounts which allow the thrusters to hinge ±10 degrees from the nominal to provide attitude control about the longitudinal axis during two-thruster operations. The gimbal mounts are then attached to the engine cluster mount through thermal isolators. The engine cluster mount is the first component of the dual axis translator. The attachment of the thrusters to the mount is illustrated in Section C-C of Figure 4-12.

The engine cluster mount translates ±3 inches along the Y axis. It translates within a carriage which translates within guide rails ±17 inches
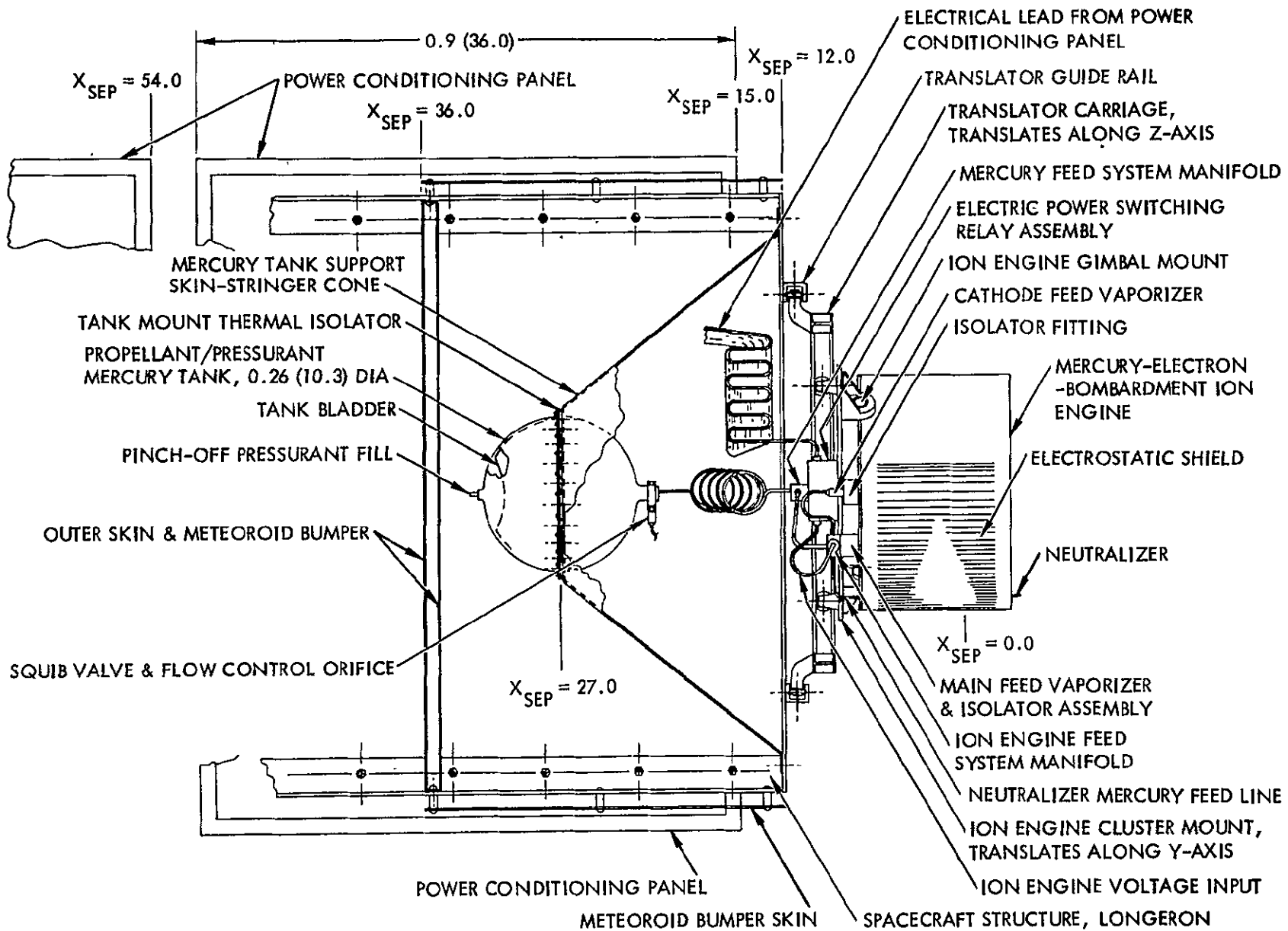
Figure 4-13.   Detail of Electric Propulsion Module

along the Z axis. The guide rails are rigidly attached to the propulsion
module structure. Both the cluster mount and carriage translate by use
of a stepper motor-gear reduction unit which utilizes a band to provide the
necessary motion. The mount and carriage are guided by self aligning
V-groove rollers at four points on each structure. The mount and carriage
translate 0.005 inches per motor step which when coupled with the 100 step-
per-second rate of the motor yields a translation rate of 1/2-inch per second.
The selection of this translator concept was based on an analysis of several
methods of providing dual axis translation to an ion thruster array. This
analysis was performed by the Space Division of North American Rockwell
Corporation, as an internal research and development program. The results
of the study are presented in Appendix D-2. The selection is based mainly
on the simplicity of the mechanism and its lower weight. The concept
selected overcomes rolling friction only and contains no sliding members.

The translator was designed for minimum weight, and consequently
requires boost tiedown and load support to maintain structural integrity.
The boost tiedowns are released after separation and before thruster
operation.

A significant item of concern in the design of the translator system
is the method employed to transfer the mercury propellant and electrical
power feed system lines across the translator element. The translator
concept selected offers the maximum of clear area within the translator
members. A hard-line mercury propellant feed line system is very desir-
able from the standpoint of state-of-the-art components and technology and the
outgassing experienced by flexible lines in a space environment. At the
present time flexible lines are being replaced with coiled hard lines in many
aircraft hydraulic applications. This same approach is recommended for
the mercury propellant feed system where the small diameter feedline to
the feed system manifold from the tank will be coiled in a manner to allow
the large flexing necessary. The extreme translation is only required in the
event of a thruster failure. The attitude control translations are relatively
small when compared to that required for a thruster failure mode. Since the
large translation should at most only be required a few times, the coiled
hard line approach offers high reliability.

Two candidates exist for the electrical power feeds to the thrusters
across the translator. The first is a flat wire design resembling a ribbon.
The other concept is the common round cable. The argument used for the
selection of a coiled tube feed system for the propellant system could also
be used for the electrical feed system, but a coiled electrical cable requires
the use of the round cable and adds considerable weight over the flat ribbon
cable. The flat ribbon cable concept uses a loop-upon-loop approach for the
translation and minimizes weight. The flat ribbon concept also gives more
efficient heat dissipation than the round cable. The flat ribbon cable concept

is recommended for use with the selected mercury feed system concept and the translator selected. It is possible that the electric power cable and the mercury propellant line could be coiled and looped in a manner so as to nearly occupy the same volume. In other words, with proper insulation between the mercury line and the power line the two could be coiled and looped as a single system resulting in total design simplification.

CONCLUSIONS

The recommended spacecraft configuration which has been discussed in detail above has effectively utilized the large area solar arrays for mounting the capacitor meteoroid detectors. The roll-up solar arrays selected are modified versions of the standard, or presently under development, 2.5 kilowatt General Electric Company array. A hemisphere of clearance has been provided aft of the ion thruster exit planes. The spacecraft is 3-axis-stabilized and uses both Vega and Canopus star trackers which are fixed mounted to the spacecraft structure. The spacecraft structure utilizes a modular design which allows the configuration to be divided into three discrete modules: electric propulsion section, a compact and protected equipment section, and the science payload section (scientific experiments). The science payload section provides adequate mounting area for science payload growth for the asteroid belt mission. The use of state-of-the-art construction (mechanically fastened airframe) materials (aluminum structure) and components (subsystem equipment) has resulted in a minimum cost spacecraft which meets all of the solar electric propulsion asteroid belt mission and system requirements. The modular design approach is such that the scientific experiments payload unique to the asteroid belt mission may be removed and other mission payloads substituted with no required changes to the configuration of the solar electric propulsion section.

5. SCIENCE PAYLOAD

INTRODUCTION

This section discusses applicable methods for obtaining scientific and engineering data on the asteroid belt covering both the radiation and meteoroid environment. The work statement for the study states that the spacecraft design must be consistent with the following science instrumentation:

1.   Charged particle detector

2.   Interplanetary fields monitor

3.   Particle/asteroid proximity detector

4.   Particle size and velocity detector

The specific instrumentation (hardware type and design) and supporting requirements were determined during this study.

In accordance with the mission objectives and knowledge requirements defined in Section 2.0, the science measurement objectives and applicable sensors are defined and candidate experiments are identified. Selected experiment concepts (sensor experiments) for the asteroid belt mission are identified with the rationale and justification for selection. Design requirements are developed for the selected sensors, and sensor interface with the spacecraft and influence on mission operations are presented.

SCIENCE MEASUREMENT OBJECTIVES

In Section 2.0, the mission objectives and scientific knowledge requirements were defined which determine the science requirement objectives. In summary, these requirements are to obtain knowledge on the origin of the asteroids and comets, to define the interplanetary plasma and to investigate the interstellar medium. Associated with these knowledge requirements are specific measurement objectives.

Measurement objectives for the asteroid belt region include the following:

1.   The determination of the velocity distribution of meteoroids, and distinguishing asteroidal from cometary particles

2. The determination of the flux and mass distribution of the asteroidal meteoroids

Measurement objectives for the interplanetary plasma and interstellar medium include:

1. Dependence on solar distance of solar charged particle and magnetic field environments at different levels of sunspot activity

2. Infer, if possible, the extent of the solar wind and high-energy charged particle and field environments in interstellar space.

More specifically, the particle and fields measurement objectives can be identified in greater detail (Table 5-1). Influencing the selection of these measurement objectives was the overall contribution to scientific knowledge which could be gained by comparing data obtained on the Asteroid Belt Mission with previous and planned Pioneer, Mariner, and Viking missions and future outer planet missions. Table 5-1 also briefly indicates the integration of the asteroid belt mission science data with the other planetary space exploration programs.

The experiments for the asteroid belt mission fall into two categories: meteoroid (asteroidal and cometary), and particle and fields. In this study, meteoroid experiments were given priority over the particle and field types. The primary reason for this decision is that the basic objective of the mission is to learn about the asteroid belt. As such, the mission trajectory was selected to spend a long time (approximately 1000 days) in the 2.0 to 3.5 AU region to measure meteoroid data. Interplanetary particle and fields measurements may be made on probes and spacecraft headed toward the outer planets with desired accuracy, but these missions are not ideal for meteoroid data gathering. As such, only a reasonably adequate set of particle and fields experiments was considered for the asteroid belt survey spacecraft.

METEOROID EXPERIMENTS

Space meteoroid measurement systems may be classified according to the method of measurement and the objective of the measurement. Four classes of meteoroid measurement systems employed in space experiments will be described.

In the first category are the mass and velocity measurement systems. This category will determine the distribution of mass, the distribution of velocities, and the estimation of the density of the meteoroids in the space

Table 5.1. Particles and Fields Measurement Objectives for SEP Missions

	Asteroid Belt Mission 2.0 to 3.5 AU	Viking, Pioneer, Mariner Missions	Outer Planet Missions
1.0 Magnetic Fields Objectives 1.1 Radial Dependence of Flux 1.2 Directional Map of Field Vector 1.3 Determine strength of solar activity-produced disturbances. 1.4 Determine distant variations correlated with disturbances of field due to presence of large bodies such as Earth, Mars, asteroids, Jupiter, and cometary debris clouds. 1.5 Search for evidences of galactic magnetic field, field transition, and regions of antisolar field directions.	Measure with Helium and flux-gate magnetometers Study correlation of increases with solar activity. Correlate flux variations with locations of spacecraft relative to planets and asteroids. Requires extreme magnetic cleanliness and stability of spacecraft so that weak field flux and direction can be measured.	Compare with 0.7 to 1.5 AU. Correlate with increases in space and near Earth. Compare with data taken when passing thru and out of Earth's magnetospheric tail (Mariner IV).	Compare and extend with 3.5 to 4.0 AU radial dependence at later time period Remeasure variation on later OPM mission to help remove temporal variations Compare and extend with 3.5 to 4.0 AU measurements at later time period.
2.0 Solar-Interplanetary Plasmas (electron and proton) 2.1 Correlation of plasma flux with magnetic field strength for each particle type. 2.2 Energy spectra for each particle type, and radial dependence. 2.3 Determine directional dependence of plasma. 2.4 Is the plasma related to a particular plasma temperature?	Measure flux versus energy and particle type using Faraday Cups. Measure flux, energies, and particle types using electrostatic analyzer. Compare Faraday cup and electrostatic analyzer directionality data. Extend Mariner and Pioneer data to regions of low turbulent fields.	Is behavior an extension of Venus-to-Mars-plasma characteristics?	Does particle flux density vary in proportion to field strength far from sun? Is there a deep space acceleration mechanism? Does plasma flow back to the sun or always outward '
3.0 Solar Corpuscular Radiations 3.1 Distant flux and energy spectra of solar protons, electrons and alpha. 3.2 Directional dependence of flux associated with solar activity. 3.3 Perturbations of flux due to presence of bodies in space.	Measure flux and energy spectrum of radiations correlated with solar activity. Do all increases detected near Earth propagate as far as 3.5 AU? Measure flux per steradian versus angle from sun using directional monitor. Is flux radial or along field lines for each energy and particle type. Monitor flux and direction and correlate with locations of bodies between probe and sun.	Compare with responses with Pioneer nearer the sun at same time.	Extend into deep space at later time period. How far away from sun can solar flux be distinguished from galactic flux? Compare with distant behavior. Separate directionality into sun-oriented flow as opposed to field-dominated flow. Compare flux and spectra in magnetospheric tails from planetary bodies with solar and galactic flux.
4.0 Galactic Corpuscular Radiations 4.1 Continuous measurement of galactic flux, particle type and energy spectrum to determine spatial and temporal behavior. 4.2 Determine variations with short-term solar activity. 4.3 Determine variations with long-term solar activity. 4.4 Determine isotopic composition of galactic spectrum. 4.5 Beyond the point where the solar field no longer varies with intense short-term solar activity, determine the 0.1-to 0.5-Bev proton flux out of the ecliptic relative to other directions.	Monitor 10- to 1000-Mev protons, alphas, electrons, and heavy ions with GM counter, and cosmic ray sensors, pointed away from sun. Monitor low energy flux of protons and find correlations with solar activity (flares). Is flux in solar direction? Over the duration of the mission, study variations of galactic flux between periods of solar flares to determine long term variation. Is same isotopic composition found for each energy region above 0.1 Bev? (0.1-0.5), (0.5-1), (1-5 Bev). Use directional monitor or rotate spacecraft to point cosmic ray spectrometer out of the ecliptic, and later perpendicular to the sun-spacecraft line.	Compare with similar sensor on Pioneer and Mariner IV. Compare and extend with Pioneer measurements over 5- to 10-year period. Compare with near-earth data	Extend to 4.0 AU on later flights. Does solar activity influence deep space galactic spectrum? Are Forbush decreases observed beyond 1.5 AU? At what solar radius does solar modulation of galactic flux become independent of sun-spot number cycle? Is there a boundary to the solar field? Compare with deeper space probes carrying cosmic ray spectrometers of same type plus spare chamber types. Repeat measurements with larger area sensors on later flights.

environment and the frequency of encounter of a space vehicle within each range of mass and velocity. Sensors within this classification are primarily designed for determination of the characteristics of the meteoroid environment in space, without particular reference to the effects of the impacts of particle members of this environment. A second category includes the large area perforation detectors. These detectors are designed for the purpose of determining the rate at which specific thicknesses of specific materials are punctured by the impact of meteoroids in the space environment. The data so obtained will contribute valuable information for designers of later generation space vehicles. Included in the third category are the remote meteoroid detection systems which will attempt to determine the appearance and external characteristics of meteoroids. The third category is relatively new, and sensor systems within this classification have not been flight qualified. In the fourth category are a series of miscellaneous detectors which do not make direct measurements on either mass, velocity, density, or perforation characteristics of impacting meteoroids. Sensors of this category make quantitative measurements on individual or cumulative impact events whose measurements might be used to infer, by indirect means, the characteristics of the impacting micrometeoroid. Some sensors within this category fail to supply meaningful information for any other purpose other than to determine how often that specific sensor generates a signal of a specific magnitude. Others which purport to measure momentum or energy of impacting meteoroids do not uniquely determine either mass or velocity and therefore cannot discriminate between impacts produced by low mass particles at high velocities for high mass particles impacting at low velocities. The majority of all micrometeoroid space experiments have been in this latter category. In interpretation of the resulting data, an assumption was made that all impacting micrometeoroids had the same velocity. The mass estimates were based not only on the uncertainty of the actual velocity of impact, but also on the uncertainty of the performance characteristics of the sensors themselves which have never been calibrated in the laboratory over the full range of velocities of meteoroids which may be encountered in space. Calibration has usually been conducted below meteoritic velocities.

Large Area Perforation Detectors

The large area perforation detector systems comprise those sensors which are designed to determine the rate at which specific thickness of typical materials may be perforated by impinging micrometeoroids in the space environment. Individual sensors may have active sensing areas ranging from many square centimeters to several square meters, and capable of being operated in arrays of tens to hundreds of square meters in total area. Since the perforation sensors count only perforations in a specific thickness of a specific material, they provide no information as to

the mass, velocity, or density of the impinging micrometeoroids. It is not possible to translate the perforation rate data reliably into meteoroid environmental data since perforations may be caused by low mass micrometeoroids of high velocity as well as high mass micrometeoroids of low velocity. The exposure of large areas of a thin sheet material with a range of different thickness may allow, by extrapolation, predictions as to the rate at which other specific thicknesses of the same material might be perforated by micrometeoroids during a space mission.

Pressurized Cell Perforation Detectors

The pressurized cell perforation detector is one of the oldest sensor systems for perforation rate data flown in satellite experiments, and still remains the most reliable sensor for obtaining perforation rate data. The basic sensor type consists of a hermetically sealed pressurized container filled with helium gas at about one atmosphere pressure and containing a pressure sensing element that responds to a loss of pressure due to the escape of the pressurized gas after a perforation of the thin skin by an impacting micrometeoroid. The pressurized cell detectors flown in Explorers XIII, XVI, and XXIII, consisted of hemicylindrical cans 17.5cm in length, 4.2cm in diameter, with a mass of approximately 0.07 kg. A large number of such pressurized cells were mounted in clusters on each of these micrometeoroid measurement satellites. The hemicylindrical skins were of beryllium copper, or stainless steel of thicknesses of 40 and 8 micrometers. Each cell was pressurized with helium at one atmosphere and contained a simple barometric switch which closed an electrical contact when the internal helium pressure dropped to about 0.5 atmosphere following perforation of the skin. The cells, although simple and reliable, have the disadvantage of being "one time only" devices, after cell penetration, the cell depressurizes and ceases to function. A further disadvantage from the standpoint of obtaining information leading to estimates as to the rate at which the outer skin of spacecraft might be expected to be perforated lies in the relatively thin sheet thicknesses employed in these pressurized cell perforation detectors. Since the perforation rate decreases with increasing material thickness, to obtain meaningful perforation rate data on materials of greater than about 100 micrometers, much larger areas of pressurized cells must be exposed to the space environment during the satellite mission life.

The technique for the fabrication of larger area pressurized cells was developed by the Martin Marietta Corporation under contract from the Langley Research Center (LRC). None of these larger area cells has yet been flown in a space experiment. The larger area cells are essentially flat rather than hemicylindrical. A typical pressurized cell would have an area of several square feet with physical appearance of a quilt. Two sheets of metallic material, bonded at the edge, are bonded at several locations

within the area of the cell. Application of pressure to these cells expands and separates the sheets except at the edge and at the internal weld points. A plan was developed by LRC for a large area micrometeoroid measurement satellite containing a total of several thousands of square feet of flat pressurized cells with skin thicknesses up to 0.1 cm.

A pressurized cell meteoroid bumper experiment has been authorized, and will be flown during 1970. The pressurized cell perforation sensor has a total area of 2 m^2. Each panel is launched in a rolled up condition. For deployment, the cell is pressurized in orbit and the sensor panel unrolls to its full extent. The 2-m^2 panel consists of a number of parallel pressurized cells consisting of two parallel compartments. The outer sheet exposed to the space environment is a skin of 80 μm of stainless steel. Located 1.27 cm behind this sheet is a second sheet with thickness of 40 micrometers of stainless steel. Barometric switches are present in each of the cell compartments. The objective of the experiment is to determine at which rate impacting micrometeoroids not only perforate the outer sheet but at what rate the fragments resulting from the outer sheet perforation perforate the second sheet. This experiment will be launched by a Scout vehicle. The data to be obtained in the form of perforation rate data for both sheets will be used to confirm certain meteor bumper design principles. The total mass of the sensor system is not appreciably higher than the mass of the three thin sheet facings comprising the pressurized cells.

Capacitor Perforation Sensors

The large area capacitor perforation sensor is essentially an electrical capacitor consisting of a metallic sheet, adhesively bonded to a very thin dielectric sheet, and backed by a vapor deposited coating of either aluminum or copper. The thickness of the facing sheet may run 0.01 to 0.1 cm in thickness while the total thickness of the dielectric and back conductor does not exceed about 20 micrometers. A perforation by a particle at meteoritic velocities is sufficiently violent to produce an ionized plasma in the hole in the capacitor produced by impact. The electrically charged capacitor then discharges through the transient arc appearing in the perforation. The discharge of the capacitor is recorded as a perforating event. The capacitor perforation detector is usually self-healing since, during the electrical discharge, the extremely thin vapor deposited back conductor is vaporized by the arc discharge over an area around the perforation. The capacitor then may be recharged and is then sensitive to a succeeding meteoroid perforation.

Capacitor-type perforation detectors have been flown in a large number of satellite systems. The largest were on the Pegasus satellites micrometeoroid measurement system, which incorporated a total of 200 m^2 of capacitor panels, each with dimensions of 0.5-by-1 m. Two such capacitors

were adhesively bonded on the opposite faces of a 2.54-cm thick slab of plastic foam. In the Pegasus system three thicknesses of capacitors were exposed to the meteoroid environment with facing sheets of 60-, 320-, and 640-micrometer thickness, respectively. Smaller capacitor detectors have been flown in other satellites.

The capacitor detectors are simpler than the pressurized cell detectors but not as reliable, but they do have the capability of responding to successive perforations in the same sensor panel. A reliability figure of about 85 percent has been assigned to the capacitor detectors in the Pegasus system. Extensive laboratory tests of Pegasus capacitor panels, subjected to hypervelocity impact of artificial micrometeoroids, has disclosed several types of failure in response to meteoroid impact. Occasional non-perforating impacts may induce violent spalling of the dielectric material with initiation of the arc discharge even though the facing sheet had not been perforated. This type of response causes false indications of meteoroid perforation. Cases have been observed where perforation did not lead to an arc discharge in low velocity impacts although above the minimum meteoritic velocity. During the recharge cycle of an impacted capacitor panel, occasions arise where a second electrical discharge is initiated in the initial perforation site, leading to a double count. Failure to clear the transient short in the panel will inactivate a complete panel. Many of the inherent shortcomings to the capacitor "sheet" perforation detector have been over come by continued development since the Pegasus flight. Operation at higher voltage levels has solved many problems. In the event of a short, the capacitor is surge-impacted with a high voltage charge much greater than that for normal operation, thus burning out the short.

The major attractiveness of this type of detector is its extremely light weight. This becomes especially true when the capacitor "sheet" is integrated with the roll-out solar array. Appendix D-3 presents a detailed configuration analysis of the integrated design concept with the capacitor sheet bonded to the solar cell substrate. Space radiation, in the form of high energy electrons, occasionally produces an intrinsic electrically charged region within the dielectric material which sometimes leads to a spontaneous discharge signal of low amplitude. Voltage discrimination of the apparent discharge signal must be incorporated in the recording electronics to avoid counting these low level discharges which simulate perforation.

A novel type of large area perforation detector is under development in the Meteor Physics laboratory of the North American Rockwell Space Division Advanced Research Branch. The principle of the perforation detector technique is based on a discovery of unusual electrical and electromagnetic phenomena generated by the hypervelocity impact of artificial micrometeoroids upon certain materials. These phenomena give

rise to effects that can be detected by simple antenna systems remote from the point of impact. As applied to the problem of the perforation of thin metallic materials, a metallic sheet of the desired thickness is exposed to the impact of artificial micrometeoroids or other hypervelocity particles. If the metallic sheet is electrically grounded with respect to the antenna system, non-perforating impacts produce no detectable signals in the antenna system. Perforating impacts produce a high velocity spray of fragments of the impinging micrometeoroid and of the target material which then impact upon a thin dielectric sheet positioned behind the target material sheet. The antenna system responds to the appearance of the hypervelocity spray particles by the production of a characteristic electrical pulse sensed by the antenna. The appearance of these characteristic signals is an unambiguous indication that the target sheet had been perforated. An extremely simple antenna system consists of a dielectric sheet coated upon the rear surface by a vapor deposit of thin aluminum. The aluminum layer is directly coupled to the recording system. Many other antenna types have been used with equal success, including parallel wire arrays or metallic grids. Perforation detector panels of this type can be assembled with masses of about 0.1 kg m^{-2}.

The particular advantage of this type of detector is its extreme simplicity and reliability. The panels will continue to respond to successive impacts. A large number of laboratory tests have been conducted with perforation detectors of this type, although no spare operational systems have been constructed. At this time, the SD perforation detector system must be considered to be in developmental status.

Of the three large area sensor types, the flexible capacitor system offers the maximum in weight advantages over the pressurized cell system and the incompletely developed SD perforation detector.

Mass and Velocity Detectors

The measurement of the velocity of meteoroids entering a sensor system is relatively unambiguous. Such measurements are made by determining the transient time between two detector stations. The direct determination of mass of a meteoroid entering a sensor system has not yet been accomplished. However, there are types of sensors capable of determining the momentum of a meteoroid impacting the sensor. When the two types of sensors are combined into a single instrument, it is possible to measure both velocity and momentum, and thereby calculate the mass of the meteoroid from the velocity and momentum values.

Time of Flight Measurements

Two types of velocity measurement sensors employing time-of-flight techniques have been developed. Both of these involve the impact of a meteoroid on an extremely thin film of detector material to start a timing circuit. At meteoritic velocities the meteor is fragmented by contact with

For impacts at meteoritic velocities, a correcting factor must be applied to the momentum values as determined by the piezoelectric microphone. The magnitude of the correction factor is of the order of two, and appears to vary with velocity. No experimentally determined correction factors are available for velocities above 30 km per second. The source of error in impacting microphones is the generation of spurious electrical pulses appearing in the piezoelectric material during temperature cycling. Errors of this type have invalidated all earlier space experiment measurements on the momentum of impacting micrometeoroids. GSFC has employed a combination time of flight measurement and acoustic momentum detectors in OGO-2. Only those microphone responses which are associated with time of flight measurements on individual micrometeoroids are valid.

Momentum measurements are also possible with a ballistic pendulum. The electrostatic ballistic pendulum (EBP) is in a high state of development. Momentum determination is derived from piezoelectric elements bonded to two cantilevered beams supporting the pendulum element. Sensitivity as low as 10^{-5} dyne-seconds have been achieved. The electroballistic pendulum is employed in the MSC mass and velocity measurement system. In the 12-by-12 array of thin film capacitor detectors, one ballistic pendulum is situated behind each subset of four capacitor detectors (Figure 5-1). Particular attention is paid to the design of the pendulum element to trap all of the ejecta particles and eliminate the possibility of recording ejecta momentum as well as impacting meteoroid momentum. In the Rogallo-designed EBP, the pendulum element is covered by a thin plastic film and is in the form of a hollow cone. The meteoroid's impact is the base of the cone. Ejected particles normally have neither sufficient energy or momentum to escape from the pendulum through the base film.

An alternate form of electroballistic pendulum is that developed by LTV and is incorporated in the NASA-MSC T-021 mass and velocity sensor system. Here the momentum sensor consists of a movable impact plate, supported at a central point by a restoring force element, and containing one capacitor plate in an electrical circuit. A rigid non-moving plate constitutes the other element of the capacitor. Transfer of momentum to the forward plate upon meteoroid impact imparts a differential movement so the rate of change of capacitance is directly related to meteoroid momentum.

0.50 IN.
1.27 CM

17.8 CM
7.00 IN. 6.00 IN.
15.3 CM

6.00 IN.
15.3 CM 7.00 IN.
17.8 CM

UPPER BANK
CAPACITOR (36)

3.00 IN.
7.6 CM

0.50 IN.
127 CM

1.00 IN.
2.54 CM

4.00 IN.
10.2 CM

0.88 IN.
2.24 CM

PENDULUM
FACE (9)

ELECTRONICS

LOWER BANK
CAPACITOR (36)

7.00 IN.
17.8 CM

7.00 IN.
17.8 CM
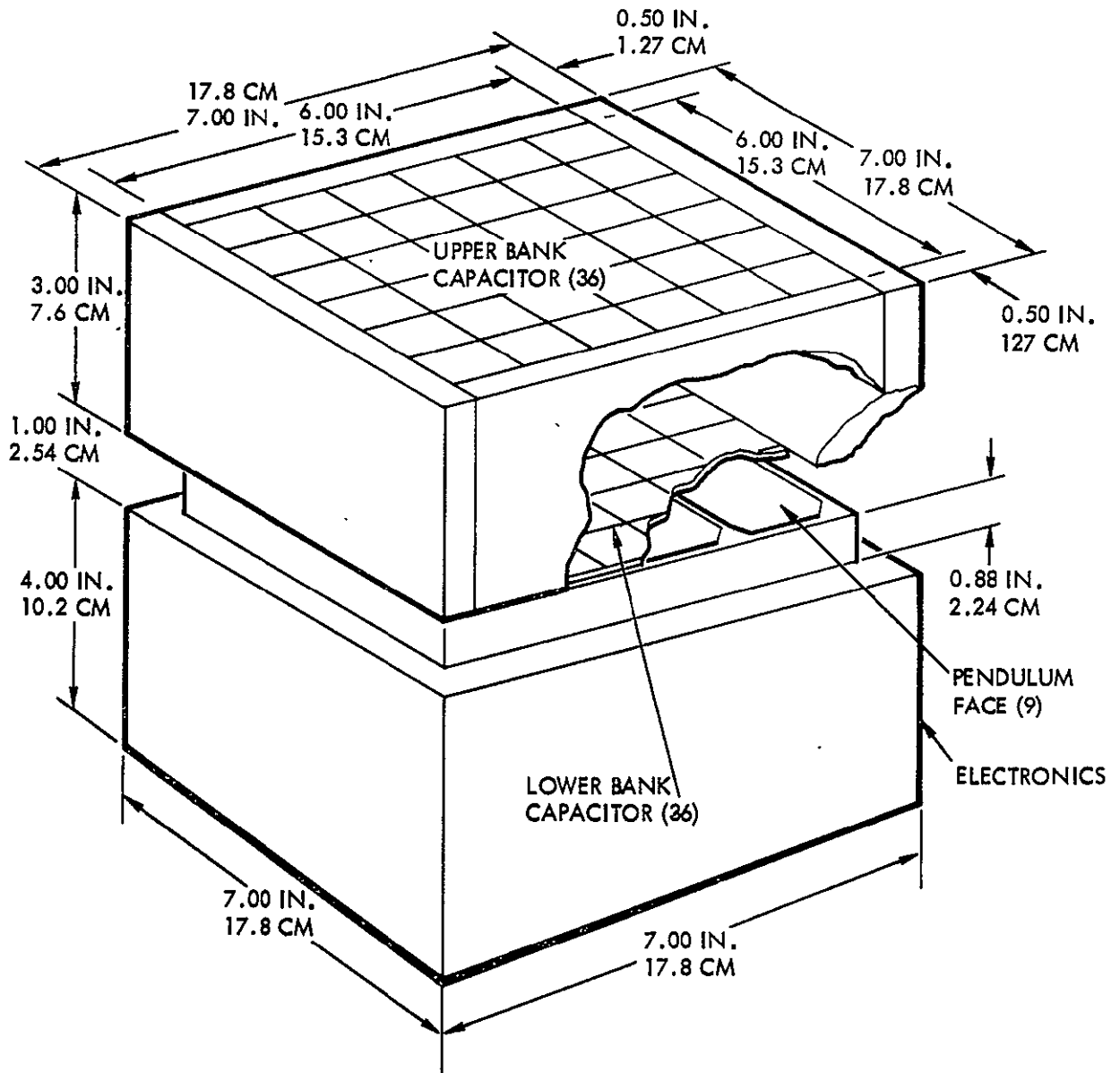
Figure 5-1.   Electrostatic Ballistic Pendulum (One Unit)

5-10

even films of thickness about 0.5 micrometer. The fragments pass over a
fixed distance and impinge upon a second detector panel which generates a
pulse stopping the timing circuit. Individual detector panels may have areas
ranging from 5 to 100 cm^2 and spacings typically about 10 cm. Therefore,
the angle of acceptance of a time of flight measurement device is limited to
a relatively small solid angle. The first detector panel, as developed by
MSC and LRC, is an extremely thin film capacitor. The perforation of the
capacitor film produces an electrical pulse generated as a result of the
discharge of the capacitor through the perforation. A second type of panel
developed by GSFC consists of a very thin plastic film, to the front and rear
of which are pairs of electrically charged grids. The impact of the micro-
meteoroid on the film generates a plasma; a positively charged grid attracts
the generated electrons and a negatively charged grid attracts the positive
ions. Appearance of the plasma burst starts the timing circuit. In the MSC
version, the impact fragments pass to a second thin film capacitor to pro-
duce the second timing pulse. The LRC version permits the fragments that
are produced by impact on the first capacitor film to impact on a second
capacitor of relatively large total thickness, but of very thin dielectric and
rear conductor thickness. The MSC version employs a large number of
capacitor films of approximately 2.5 by 2.5 centimeters in the first
array, and an equal number in a second array located behind the first.
Meteoroids arriving at a relatively oblique angle may impact one of the thin
film capacitors and the fragments arrive at another thin film capacitor not
situated directly behind the first but offset in one dimension. By recording
which pair of capacitors detect the impingment of the meteoroid and its
fragments, it is possible to obtain rough values of the angle of incidence
of the meteoroid on the total sensor array. An array containing about 144
small area capacitors can be contained in an area of approximately 0.1 m^2.

Momentum Measurements

Momentum measuring sensors are also of two types. The oldest is
the acoustic microphone type. An impact plate whose thickness is great
eough to be considered semi-infinite, with thickness several times greater
than the depth of the largest expected crater, is affixed to a piezoelectric
microphone. The impact microphone response is a function of the momentum
of the impacting particle. Unfortunately, the impact microphone is subject
to an uncertainty and an error source. The uncertainty results from the fact
that the microphone response under impact and extremely high velocities is
not the same as the response under low velocities. Microphone calibration
in terms of mementum is usually performed by subjecting the microphone
and impact plate to elastic impacts of known mass and low velocity particles.
At meteoritic velocities, however, not only is the momentum of the impacting
meteoroid delivered to the impact plate, but also the recoil momentum due to
the crater ejecta.

Optical Detectors

All other meteoroid measurement systems and techniques discussed in this report depend upon the actual impact of a micrometeoroid in space with the active area of the sensor system. There are several other techniques for estimating the velocity and apparent size of a micrometeoroid by remote sensing of meteoroids in the space environment. Not considered among these are those techniques employed in meteor astronomy wherein a meteoroid passes through the atmosphere of the earth or other planet and measurements are made of such atmospheric effects as luminous trails and ionized trails detectable by photographic, photoelectric, or radar techniques. One system remains to be discussed: the passive optical technique under development by the General Electric Corporation (GE).

The passive optical system, named Sisyphus by GE (Reference 5.1) consists of four parallel optical systems, each with a conical field of view, with photomultiplier detectors and associated electronics (Figure 5-2). The fields of view overlap in a central region. The four collectors are located at the corners of a square. The entire optical system would generally be pointed in the antisolar direction. Any meteoroid illuminated by the sun and passing within the field of view of one or more of the three telescopic systems would be detected by the photomultipler associated with that individual system. Range and velocity information can be obtained on meteroids which pass through any three sensor field-of-views. The three photomultiplier timing and duration outputs are used for the estimation of the range and velocity of the meteoroid passing through the spatial detection region. Preliminary estimates as to the capability of an operational system suggested the possibility of detecting the appearance of meteoroids with a mass raise from 10^{-8} to 10^{-3} gm at an event rate ranging from 0.1 to 50 events per day in an assumed asteroid belt meteoroid environment. These estimates are subject to uncertainty as to the actual albedos of meteoritic particles in this region of space. Mass assumptions are based on the assumed abledo, an average density, and spherical shape.

Under a contract with NASA's Manned Spacecraft Center, the GE Space Science Laboratory has conducted a series of studies on the expected false alarm rate and sensitivity of such a system. Laboratory models have been constructed and tested. The capability of an operational system depends to a great degree on successful solutions to the problems of the accurate determination of the transit times of the solar illuminated meteoroids through the three fields of view in the presence of system and optical noise due to both the electronics and the stellar background. Because the actual reflectivities for albedos of the meteoroids being observed will be unknown, the system will have a low reliability for the estimation of meteoroid masses.
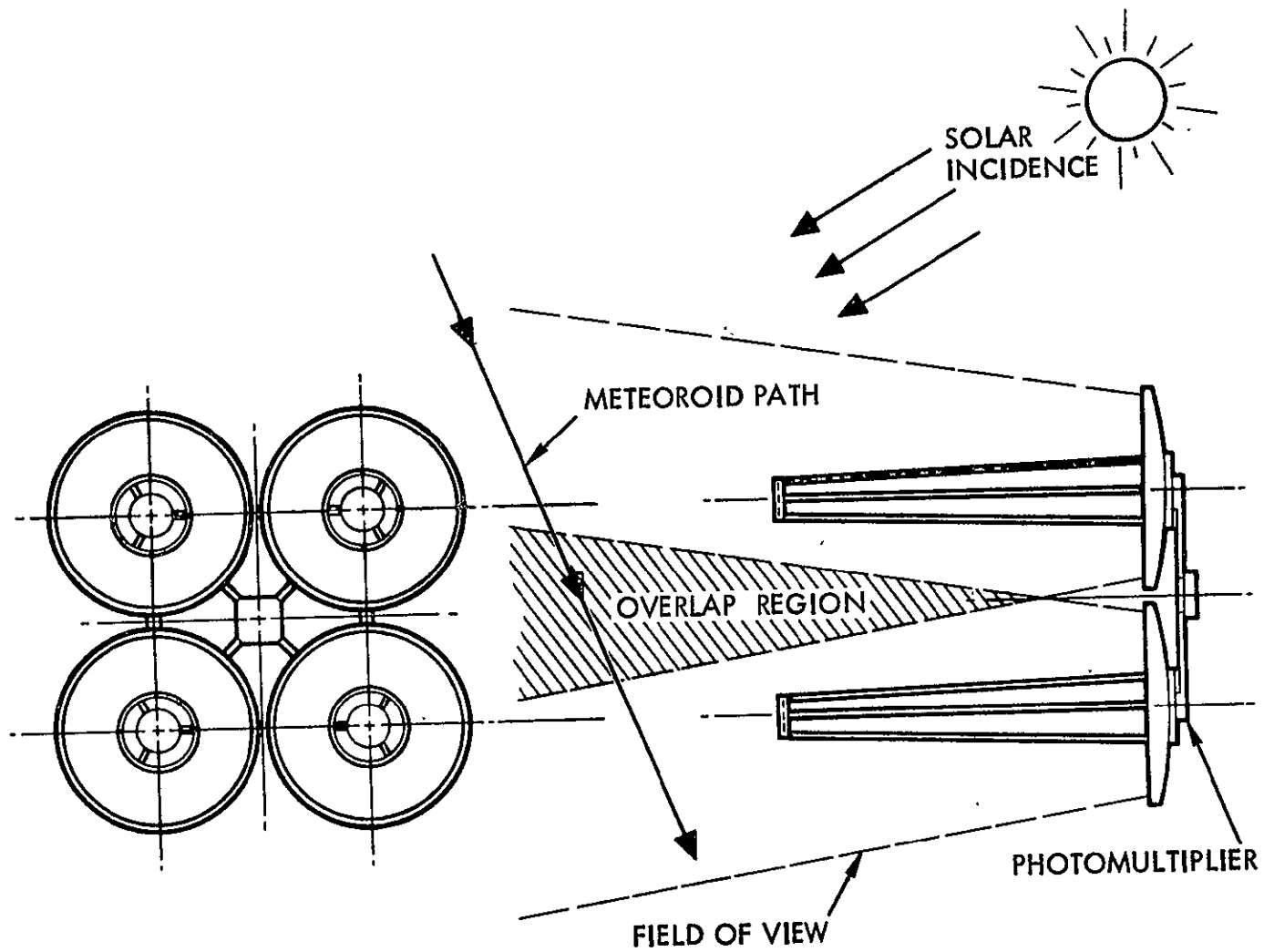
Figure 5-2. Sisyphus Optical Detector

Meteoroid Experiment Concepts Selection

The selection of the meteoroid experiments was governed principally by the requirement to show that the selected spacecraft design is consistent with the use of a particle/asteroid proximity detector and particle size and velocity detector. This requirement was stipulated by the JPL contract statement of work. At least one of each of these types of detectors will be included in the selection of meteoroid detectors.

As mentioned previously, both scientific and engineering knowledge requirements are of concern during the asteroid belt mission. Of greatest concern is the requirement to gather adequate data on the meteoroid flux (mass density versus solar distance) to determine environment protection requirements. Outer planetary mission (OPM) explorations require all spacecraft to pass through the asteroid belt. Since weight is a premium on these missions, it is mandatory that adequate protection against meteoroid damage be provided for a minimum weight penalty.

This scientific knowledge requirement for the asteroid belt mission is to determine the origin of asteroid and comets. The meteoroid experiments selected for the SEP spacecraft must provide data that may contribute to the achievement of the engineering and scientific requirements. The following measurement objectives dictated the ultimate selection of the meteoroid experiments:

1. Meet environment protection requirements

2. Match asteroid and zodiacal light data

3. Distinguish cometary versus asteroidal particles

4. Infer composition from density

To provide data appropriate to these measurement objectives it is necessary to obtain repetitive measurements of meteoroid impact (temporal/spatial distribution); obtain data on particles of mass as large as possible yet still achieve valid statistical information (desirable to measure 10^{-6} to 10^{-3} gram particles, 10^{-9} to 10^{-7} gram particles less acceptable); determine both velocity and direction of the particles.

The experiments may be grouped into two categories: those designed to obtain data on the nature of the particles (size, mass and composition), and those designed to determine the asteroid belt mass/density characteristics.

It is obvious that some type of large area detector is required to achieve the measurements objectives in a satisfactory manner. The leading candidates for these types of sensors are "capacitor sheets" and pressure cells. For the reasons discussed in the paragraph on candidate meteoroid experiments, the "capacitor sheet" detector was selected for the SEP spacecraft. Its primary advantages are ability to make repetitive measurements and light weight-to-area ratio. The pressure cells, although very reliable, are "one-shot" devices and are relatively heavy. The "capacitor sheet" detector provides only data on particle spatial density and on the momentum of a particle above a certain threshold. Directionality is determined only in the hemispherical sense (detector is protected by solar cells on one side). To meet the measurement objectives, it is necessary to include detectors which may determine velocity, direction, and mass.

When mentioning velocity and direction, radar appears an obvious method for direct measurements. A ranging radar would also provide data on the mass (inferred from radar cross-section area, particle shape, and density assumption). A radar to achieve the demands of the asteroid belt mission satisfactorily would be heavy, require high power, and would require an extensive development program. Reliable performance and calibration (tuning) problems would exist throughout the mission.

Since the requirement exists to employ a proximity detector, the General Electric optical detector, named Sisyphus, is the obvious choice. This sensor is currently planned for the Pioneer F and G missions and is under extensive development. Utilization on the SEP spacecraft requires a design modification from the 20 cm (8 inch) diameter primary collector currently being developed. (See discussion in following paragraph on meteoroid sensor requirements.) A much larger size collector diameter is required (67 cm) and the spacing for the telescopes is altered, but no significant design problems are involved and the design changes are considered to be of a routine nature. The Sisyphus determines analytically the velocity and direction based on solar reflected energy from the particle.

Mass of the particle must still be inferred by the assumption of a general shape of the particle, its composition, and its albedo.

The electrostatic ballistic pendulum, as described previously, provides the greatest potential to determine accurately the mass of a particle by measuring the particle velocity and momentum in the most direct manner. The velocity is determined from time of passage through two capacitor sheets and the momentum is measured by pendulum displacement. This detector is also under development by MSC and currently represents the best choice for mass measurements. Acoustic microphones could also be used, but the uncertainty of perforation (inherent in the design) precludes their selection.

The selection of the meteoroid experiments, in summary, are governed by: requirement to use both a proximity detector and a particle size and velocity detector; supporting requirements and weight penalty; interrelationship of measured data; and state of development.

Sensor Configurations for Selected Meteoroid Experiments

Most, if not all, of the meteoroid investigations whether conducted in the past or currently planned for the future (such as Pioneer missions F and G) provide data of low statistical validity. Since the basic mission objective is to gather data on the asteroid belt, the design goal was established to achieve a 10 percent or less standard error deviation in the most dense region of the belt. Referring to the reference asteroid belt model in Appendix A (Figure A-2), dividing the region from 2.0 to 3.5 AU in belts 0.2 AU wide appears to be reasonable for establishing the number of meteoroid detection events required to achieve the desired statistical validity. The region from 2.4 to 2.6 AU was selected as the base for determining the meteoroid sensor sizing in order to provide the equivalent ≥ 100 events (necessary to achieve a 10 percent or less standard error of measurement).

The following approach was used for sizing the three selected meteoroid sensors: the uncertainty of the asteroid belt model was defined, and the reference trajectory was used to determine the asteroid environment relative to the particular space path being traversed. These data were used to establish the expected incidence of hits per unit area (spatial and temporal density) as a function of particle mass. Area and/or volume coverage required for the sensors is then determined based on the 10 percent standard error deviation measurement in the 2.4 to 2.6 AU region.

The asteroid environment model Appendix A, is subject to considerable uncertainty as to the accuracy of the analytical expressions. The nominal environment uncertainty may be as much as three orders of magnitude low and two orders of magnitude high.

For an oriented spacecraft the meteoroid flux may be expressed as:

$$F_a = S_a V_i$$

5-16

where:

F_a = flux of impacting particles of mass (m) grams and greater (impacts/sec per square meter)

S_a = number of asteroid per cubic meter of mass m grams and greater at a distance R (in AU) from the sun

$\log_{10} S_a$ = $-15.79 - 0.84 \log_{10} m + f(R)$, where $f(R)$ is obtained from Figure A-2, Appendix A.

Large Area Detector

Using the reference trajectory in Figure 2-60 and the asteroid model equations, the area requirements for the "capacitor sheet" detector may be determined. The capacitor detector area required to meet the measurement criteria (10-percent individual error in 2.2 to 2.4 AU) for different meteoroid sizes are shown in Figure 5-3. It is evident from this figure that the area required to measure 10^{-6} gram meteoroids is too excessive and that 10^{-7} grams meteoroid size represents a more reasonable selection. With no contingency factor consideration in the environment model, $28m^2$ is sufficient to obtain valid statistical data (10 percent standard error for 10^{-7} gram particles in the 2.2 to 2.4 AU region). If the nominal environment is low by an order of magnitude, then the area required to adequately record 10^{-7} gram particle impacts must be increased by a factor of 10. This is clearly not possible unless independent detector arrays are employed at increased weight penalties. A more appropriate consideration is to provide $28m^2$ designed for 10^{-7} gram particles and $28m^2$ designed for 10^{-8} gram particles. This allows a design safety factor to compensate for an order of magnitude lower environment. If the environment is lower than the nominal by a factor of 10, the detector designed for the 10^{-7} gram particle would record only 12 impacts during transit through the 2.4 to 2.6 AU region (equivalent to a 25.8 percent standard error deviation). The 10^{-8} gram particle detector would record 100 hits, or 10 percent standard error deviation. If the nominal environment is higher by an order of magnitude or more, no problem exists in obtaining adequate statistical validity.

Due to the existing uncertainty in the assumed model environment (five orders-of-magnitude in asteroid flux density), the above contingency design was selected. This 58 M^2 minimum area is required. The area to weight ratio of the "capacitor-sheet" detector (2.25 M^2/Kg) is the lowest of the meteoroid detectors selected for use in the spacecraft. Thus it becomes very desirable to obtain maximum data at lowest penalty by utilizing the maximum available area on the back of the solar arrays. Allowing for capacitor-sheet design, cabling (for the capacitor-sheet and solar cells)

Figure 5-3. Large Area Detector Requirements--2.2 to 3.2 AU (10 Percent)
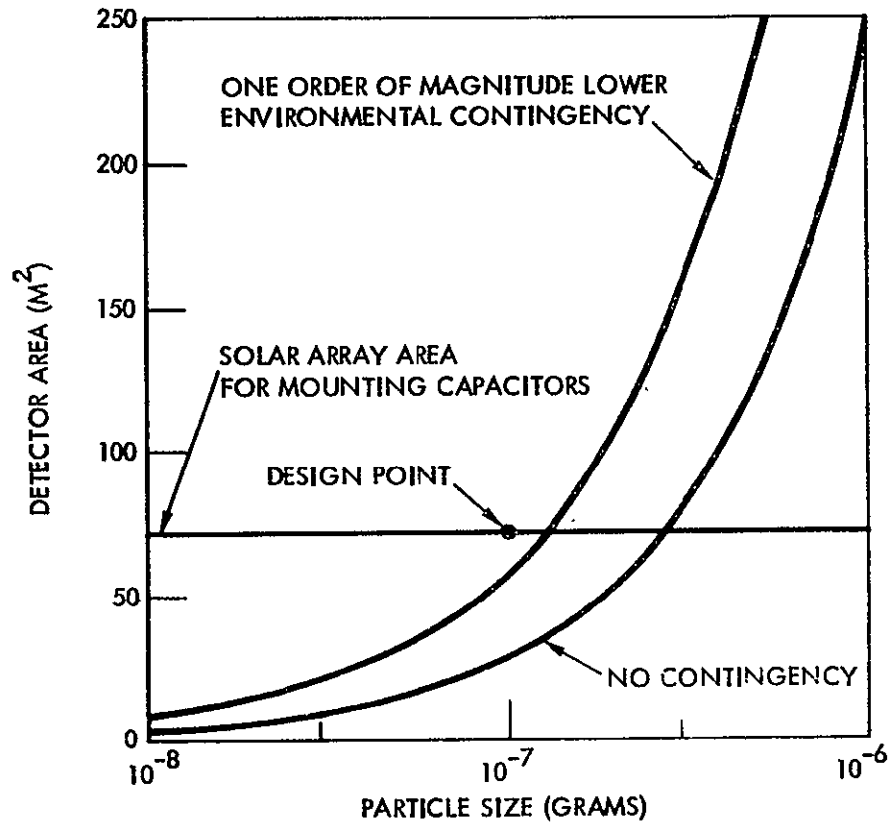
| | STANDARD ERROR (PERCENT) | |
| | DETECTOR AREA | |
	27.8 M^2	35 M^2
2.0 - 2.2	14.6	13.0
2.2 - 2.4	10.63	9.5
2.4 - 2.6	10	8.9
2.6 - 2.8	9.84	8.76
2.8 - 3.0	10.8	9.62
3.0 - 3.2	10.9	9.71
3.2 - 3.4	12.81	11.4

70 M^2 was assumed as a reasonable effective area for the meteoroid detector and was used as the design point for the spacecraft.

Selecting the 70 M^2 detector area results in better than 10 percent standard error measurement data for the 2.2 to 2.4 AU region (see Figure 5-3). Statistically valid data may be obtained in 0.2 AU increments over the 2.2 to 3.2 AU region that covers the major portion of the asteroid belt.

The detector characteristics are detailed in Appendix C. A 4 mil (65 micron detector is used for detecting the 10^{-8} gram particles, and an 8-mil (125 micron) for detecting the 10^{-7} gram particles, resulting in a total detector weight of 31 kilograms.

Electrostatic Ballistic Pendulum (EBP)

The electrostatic ballistic pendulum (EBP) has a mass threshold sensitivity down to 3×10^{-12} grams; the same unit can measure all particle sizes 3×10^{-2} grams with an upper limit greater than 10^{-8} grams (Reference 5-2).

Figure 5-4 shows the 4-unit module construction for the EBP as used on the SEP spacecraft. The effective surface area of 900 cm^2 was used for determining the number of modules required. Six four-unit modules will provide data on 10^{-9} gram particles with a statistical validity equivalent to that for the capacitor sheet detector (10^{-7} gram particles). Since less is known regarding the reliability of the EBP, an additional four-unit module was utilized to improve the reliability of the system. Each of the four units in each module operates independently of each other; loss of one unit does not affect the other three units in the module. Shown in Figure 5-5 is the effective surface area covered by the detectors and the total weight versus the asteroid particle size. As may be seen, the weight penalty becomes unacceptable to achieve a 10 percent standard error for detection of particle sizes larger than 10^{-9} grams.

Optical Detector (Sisyphus)

The Sisyphus uses an optical system focused on a photomultiplier to gather reflected or scattered solar radiation from a meteoroid particle for detection and velocity measurement (Figure 5-6).
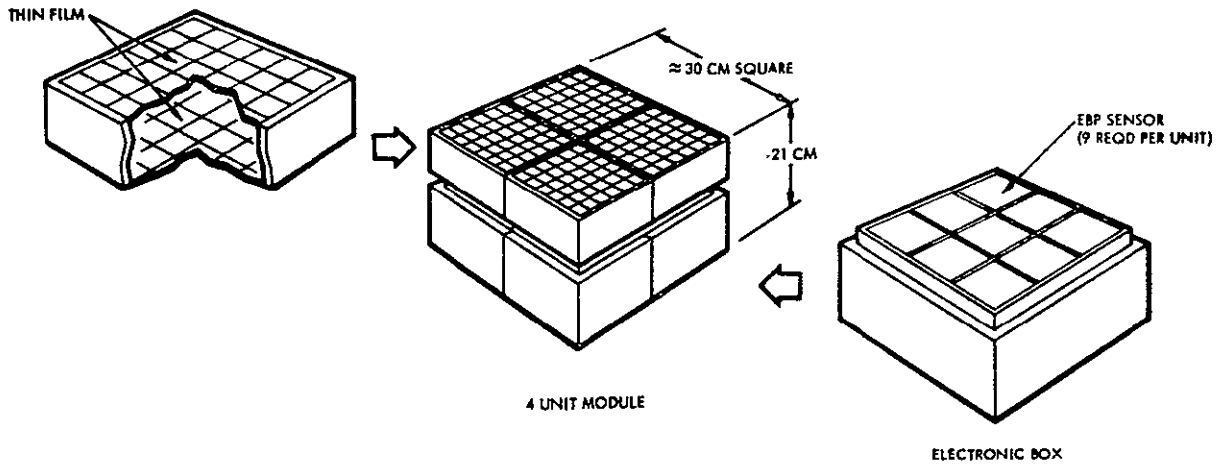
Figure 5-4. Electrostatic Ballistic Pendulum Configuration
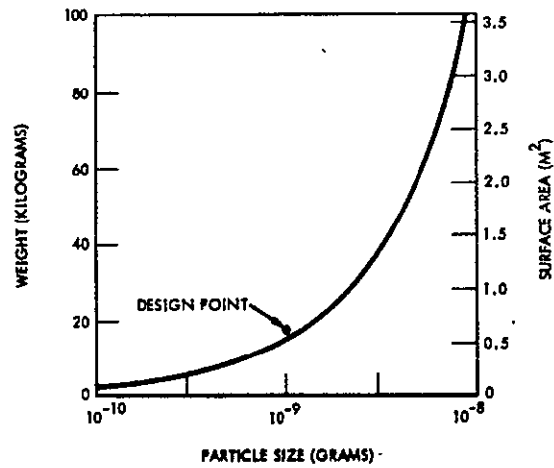
Figure 5-5. Electrostatic Ballistic Pendulum 2.4--2.6 AU 10 Percent
Standard Error
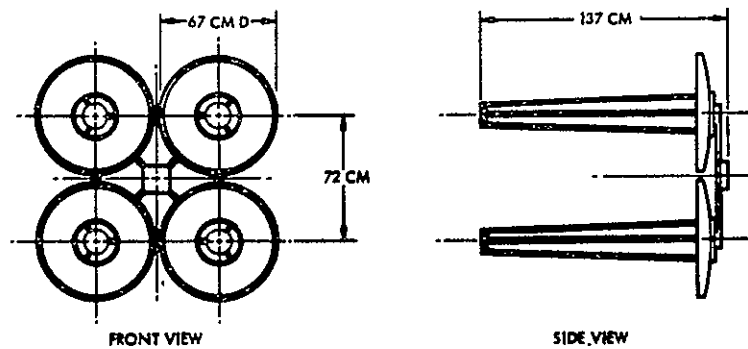
Figure 5-6. Sisyphus Optical Detector Configuration

SD 70-21-2

The amount of light incident on a collector from reflected or scattered solar radiation from a particle (assuming the collector is looking away from the sun) is given by the expression:

$$I = \frac{I_o r\; a^2}{2s^2\; R^2} = \frac{I_o r}{2s^2}\; \left(\frac{a}{R}\right)^2$$

where

I is intensity of reflected sunlight on the optics

I_o is solar illumination at the particle

r is reflectivity coefficient of the particle

a is the radius of the particle - cm

R is distance from particle to optics - cm

s is heliocentric distance to particle - AU

In sizing the Sisyphus system, data obtained from General Electric were used as the basis for all calculations. An S-20 photocathode surface response characteristic was used for determining the minimum signal level for a 31-cm effective aperture with a 2-degree cone half angle field-of-view. At 2.5 AU the mean background level was taken as 120 tenth magnitude stars per square degree. The S-20 photocathode is sensitive to 59 percent of sunlight. The amount of light in lumens (L) collected by the optics of diameter (D) from a star of magnitude (M) is given by

$$2.5 \log_{10} L = 7.57 - 30.00 + 5 \log_{10} (2.54\; D) - M$$

Assuming a solar type spectrum giving about 67 lumens/watt results in a star background intensity of $I_B = 3.5 \times 10^{-14}$ watt-cm^{-2}-deg^{-2}. The rms noise from this steady-state background noise is given by

$$I_n = \left[2I_B \eta \left(\frac{\pi a^2 D^2}{4}\right)\left(\frac{e}{\pi \tau}\right)\right]^{1/2}$$

5-21

where

I_B is the star background light per square degree

η is the luminous sensitivity of the photomultiplier in amp/watt

α is the view cone half-angle in degrees (for angles 56 degrees)

D is the opticics aperature

τ is the time constant of the electronics, and

e is the electron charge in coulombs

The signal intensity from a meteoroid of radius a is given by

$$I_s = \frac{\pi(0.59)\, I_0 r a^2 D^2 \eta}{8\, S^2 R^2}$$

For a minimum acceptable signal-to-noise ratio of $\sqrt{12}$, the maximum range for a given particle becomes

$$\frac{\pi(0.59)\, I_0 r a^2 D^2 \eta}{8\, S^2 R^2} = \sqrt{12}\left[2 I_B \eta \left(\frac{\pi \alpha^2 D^2}{4}\right)\left(\frac{e}{\pi \tau}\right)\right]^{1/2}$$

or

$$R = 4.6 \times 10^7\ (a/s)\ (r I_0 D/\alpha)^{1/2}\ (0.59)^{1/2}\ (\eta \tau)^{1/4}\ \text{cm}$$

The effective cross-sectional area of the cone defined by the Sisyphus optics is approximated in the following manner. The cross-section of the cone is an isosceles triangle, with an apex angle of 2α and a height of R. The base of the triangle is equal to $2 R \tan\alpha$ and the area is equal to $R^2 \tan\alpha$. For small angles of α, $\tan \alpha$ can be approximated by $\pi \alpha/180$ with α expressed in degrees.

The cross sectional area can then be expressed as

$$A' = \frac{\pi \alpha R^2}{180}$$

The effective cross-sectional area is dependent not only on the maximum range R, but also on a minimum range R_0. R_0 is defined as that range from the optics required for the particle to remain at least 2 to 200 microsecond

in the overlapping region of the field of view (FOV) of the four-optics array.
The effective cross-sectional area becomes

$$A = \frac{\pi \alpha}{180} (R^2 - R_o^2)$$

The upper limit on the size of the Sisyphus optics was determined by
the envelope constraint of the launch vehicle shroud (assuming a fixed mount-
ing of Sisyphus to the spacecraft structure). The maximum aperture was
found to be 67 cm, with a distance between centers of 72 cm. Due to the
orientation of the spacecraft during the science gathering period, the
Sisyphus may be oriented a maximum of 30 degrees away from the space-
craft sun line. This means that the minimum range that particles can be
seen is greater than approximately 1.5 meters from the optics. Thus,
$R_o = 1.5$ meters.

According to the range equation, the following detection ranges,
probable number of units in the 2.4 to 2.6 AU region, and time constants
result for various size particles:

Particle Mass (gram)	Maximum Detection Range (cm)	Expected Number of Counts in Coincidence	Expected Total Number of Counts	Lighting Required
10^{-7}	1200	20-25	100	Sunlight at 2.5 AU
10^{-8}	500	50-60	230	Sunlight at 2.5 AU
10^{-9}	25	None*	460	Lamp* Illumination

*Note: 25 cm range is too close to the detectors for coincidence counting.
Lamp (~20 to 100 watts) illumination may be required if the
detectors cast a shadow over the region as close as 25 cm

A count rate of 100 particles per mission leads to a 10-percent
standard error. For a 50-day exposure in the 2.4 to 2.6 AU region,
5 meteoroids/m^2 at 10^{-7} gram are expected. Assuming a density of 3.5 g/
cm^3, the 10^{-9}-gram meteoroid would be about 1.9×10^{-3} cm in radius.
Assuming an albedo of 0.07, each Sisyphus detector unit could detect a
10^{-7} gram meteoroid at 12 meters range, giving 100 counts in 50 days, with
25 counts from each detector. Indication of velocity would be achieved by
observing the pulse width for each passing meteoroid. More accurate veloc-
ity information would require coincidence analysis between 2 and 3 detector

units, but only 20 to 25 coincident 10^{-7} gram meteoroid counts would be expected, with just enough light collected from the average particle to indicate order of magnitude of velocity. To determine velocity still more accurately, smaller particles than 10^{-7} gram could be counted to improve the statistics. Detection of smaller particles is possible close to the detector.

The detection range for 10^{-8} gram is about 5 meters. During the mission about 50 particles would be counted in coincidence, and 230 counted by individual detectors. The above numbers are based on a 200-microsecond time constant, which is comparable to the transit time of the particle across the field of view. Earlier studies indicated a 2-microsecond time constant which would lead to better velocity data, but would drop the coincident count by an order of magnitude.

The detector casts a shadow in the sunlight which would interfere with the detection of smaller than $\sim 3 \times 10^{-9}$ gram meteoroids close to the detector units. A 50-to-100 watt quartz-iodine lamp could be used to allow detection of meteoroids in the shadow zone as well as to extend the useful range of detection slightly. The 100-watt lamp with a 2-degree collimator would double the illumination of 5 meters.

The Sisyphus will also detect larger particles, but very few events are expected. The above calculations have been based on the mean environment as a worst case analysis. If the meteoroid hazard is larger, good statistics will result.

It is advantageous to use as large a Sisyphus as possible within the payload envelope constraint in order to obtain adequate measurements on larger size meteoroids; hence, the 67-centimeter aperture optics configuration was selected. The total weight of the system is estimated at 15 kilograms.

PARTICLE AND FIELDS EXPERIMENTS

Particle and fields sensors having potential application to the asteroid belt mission are discussed in detail in Appendix C. For each sensor, the principle of operation is presented, the use on previous/planned spacecraft is identified, and operational response, constraints, and problems associated with the asteroid belt mission are discussed.

The magnetic field sensors considered in Appendix C include the following types of magnetometers:

1. Spin coil or search coil

2. Motor driven spin-coil

3. Proton precession

4. Flux gate

5. Rubidium vapor

6. Helmholtz coil array plus rubidium vapor

7. Helium vapor

8. Helmholtz coil array plus null-field helium vapor

9. Helmholtz coil array plus total field helium

The plasma measurement sensors considered in Appendix C include:

1. Langmuir probe

2. Electrostatic analyzers (Faraday cups)

3. Curved plate analyzers

4. Channel multiplexer type

5. Faraday cup plasma

The solar and cosmic corpuscular radiation sensors considered in Appendix C include the following types of spectrometers:

1. Geiger-Mueller counters

2. Ion chambers

3. Proportional counters

4. Scintillation and Cerenkov counters

5. Semi-conductor charged particle

6. Charged particle telescope (cosmic ray)

7. Triaxial particle

Particle and Fields Experiment Concepts Selection

The primary particles and fields experiments objectives are to measure the corpsucular radiation environments, and solar-interplanetary magnetic field structures between 2 and 3.5 A.U. Short and long-term time variations are expected in the temporal and spatial distributions of particles and fields that will be measured. Some difficulties in separating long-term temporal variations from spatial dependence of the environments are expected. These difficulties may be at least partially overcome by comparing the long-term behavior of similar sensors on other space probes at the same time at different regions of space, and also with later probes in the same region.

To make these comparisons more valid, identical or at least similar instruments will be required on these various probes. Although standardized instruments have not yet been developed, the sensors have been tailored for specific missions, and are representative of state-of-the-art advances.

Using only the very latest instruments on such long-duration deep space missions, great difficulty in comparison of responses may be encountered, without considering the possibly lower reliability associated with these most recent sensor types. It may be desirable, therefore, that the solar electric mission spacecraft carry both new as well as older types of sensors, providing overlap in spectral sensitivity. The payloads on Mariners II and IV were exemplary in the above considerations. Two different types of plasma probes were carried: a newer electrostatic analyzer type and an older Faraday cup type. Both newer and older types of high energy corpsucular radiation spectrometers were also flown. The JPL ion chamber and a number of Geiger-Mueller counters are available for which a great deal of flight

experience has been accumulated. Overlapping sensitivity was provided with the newer type of semiconductor telescope from the University of Chicago. An advanced magnetometer was used by JPL on Mariner IV. The older type used on Mariner II could have been flown as well, with improvements, had the additional payload been available.

For the solar electric mission, the above ideas used in selecting the Mariner payloads should be followed to provide for high reliability and to permit comparison with earlier as well as later flights into deep space. Fortunately, older sensors are often light in weight.

As indicated in Table 5-1, consideration in selecting the particle and fields experiments should also be given to the similarity of measurements made by other previous and planned space flights, thereby extending or verifying results in a integrated manner throughout the interplanetary space region.

Another factor in the selection of experiments is the interrelatedness (correlation) of the various measurements.

Table 5-2 presents eight leading candidate experimental sensor types, showing briefly what experiments may be performed and the correlation of measurements. Each of the sensors has been described in Appendix C. Included are two types of magnetometers, two types of plasma spectrometers, two charged particle spectrometers, and an array of GM counters with an ion chamber as flown on Mariners II and IV. Similar sensors have been flown on Pioneer and also on several spacecraft in earth orbit giving considerable experience on performance, reliability, degradation, and failure modes.

Using the criteria that low weight, long-lived sensor types should be selected for an asteroid belt mission the set of representative instruments in Table 5-3 were selected as prime candidates.

Each of these candidate sensors was futher evaluated in terms of supporting requirements, value of data obtained and hardware status. This resulted in eliminating three of the candidates for the reasons summarized in Table 5-3. The sensors selected for use on the SEP spacecraft for the asteroid belt mission are identified by enclosure in boxes.

5-27

Table 5.2. SEP Sensors and Measurements (Excluding Meteoroids)

Potential Sensors for SEP	Measurements								
	Magnetic Fields		Solar Plasma			Corpuscular Radiation			
						Solar		Galactic	
	Magnetic	Direction	Protons	Electrons	Direction	Spectrum	Direction	Spectrum	Isotopes
Flux-Gate Magnetometer	Gives 3 components of field	Direction from component ratios	Correlated with magnetic field			Is flux field oriented			
Helium vapor Magnetometer	Absolute measurement	Requires Helmholtz coils							
Faraday Cups	Correlated with magnetic field	Correlated with fields	Spectral determinations	Best statistic	Wide angle sensor	Low energies only			
Electrostatic Spectrometer	Correlated with magnetic field	Correlated with fields	Spectral determinations	Low count rate	Narrow angle sensor	Low energies only			
Tri-axial Particle Spectrometer	Correlated with magnetic field	Correlated with fields	Overlaps at high plasma energies	Overlaps at high plasma energies		Determine flux, spectrum particle type	Gives dir. to ±10 degrees	Low energies detected	Disting. protons alphas electron
Geiger-counter Array						Ion rate versus shield for 2-3 sensors			
Ion Chamber						Ion rate versus shield for 2-3 sensors			
Cosmic Ray Spectrometer	Indicates extent of galactic fields					High energies		High energies	Disting. particle type

Table 5.3. Particle and Field Experiments Selection

Measurement Objectives	Measurements	Sensors	Reason for Elimination
Solar wind versus solar distance and activity	Magnetic field vector	Helium magnetometer Triaxial fluxgate magnetometer	Not absolute measurement
	Plasma 100 EV-20 Kev	Faraday cup Curved plate spectrometer	Requires scan platform
Penetration of galactic protons Propagation of solar flare particles	Protons and electrons 1-1000 MEV	Cosmic ray spectrometer Triaxial spectrometer Geiger-Mueller counters Ion chamber	Limited data

SEP SCIENCE PAYLOAD

A total of 80 kg of science payload was selected for the SEP space-craft, with approximately 17 kg devoted to particle and field sensors and 63 kg devoted to meteoroid particle detectors. Table 5-4 identifies the selected list of sensors with their associated weight, power, and data support requirements.

Orientation and mounting requirements imposed on the spacecraft by the selected experiments are also summarized in the table. The meteoroid sensors dominate the spacecraft mounting provisions. The "capacitor sheet" meteoroid penetration detectors are mounted on the anti-solar side of the solar panels. The Sisyphus detector is mounted at the forward end of the spacecraft looking away from the sun. A further restriction is that the sensor be placed such that the field of view covers a region not shaded by the spacecraft. The electroballistic pendulum sensors must be mounted for external, unobstructed exposure to the meteoroid flux impacting direction.

All particle and field sensors could be mounted on a boom. Several of the sensors that could be mounted at the spacecraft wall are indicated in the last column of Table 5-4. The magnetometer is to be mounted at the end of the boom pointed approximately perpendicular to the spacecraft trajectory. Mounting to the antenna may be used, but this type of mount could place the instrument close to magnetic components in the telemetry power output stage. The plasma spectrometers are to point into the ecliptic plane in the general direction towards the sun. The cosmic ray spectro-meter should point in the ecliptic plane looking away from the sun. The other sensors have loose pointing requirements if on the boom.

Each of the three meteoroid detector types selected for the SEP asteroid belt mission have peculiar advantages and disadvantages, but no one sensor obtains all of the data necessary to determine particle size, mass, velocity vector, density, and composition. The capacitor sheet detects events based on a momentum threshold. The electrostatic ballistic pendulum determines velocity vector and mass. The Sisyphus provides velocity vector and inferred size based on albedo cross section (reflected brightness of object).

From an engineering viewpoint, the larger particles (10^{-6} grams and greater) are of primary interest to determine the degree of protection (shielding) required for the spacecraft. From a scientific viewpoint, it is desired to provide valid statistical data for a wide range of particle sizes to shed light on the origin of the asteroids and gain a better understanding of the asteroid belt. Based on the previous sensor performance analyses, a 10^{-7} gram particle represents an upper limit on which measurement

Table 5-4. Selected Sensors Support Requirements

Sensor	Mass (kg)	Weight (lb)	Power (watt)	Data (bits per second)	Dimensions Area	Development Problem Area	Mounting
Cosmic ray spectrometer	3.4	7.7	8	1	1-2 cm x 10 cm head plus 10 x 10 x 10 cm box	detector drift	at S/C wall or on boom
Triaxial charged particle spectrometer	3.4	7.7	8	3	3-1 cm x 3 cm heads plus 10 x 10 x 10 cm box	detector drift	on boom, one sensor points to sun, one out of ecliptic, and one 90° to sun
Shielded Geiger-Mueller counter array small ion chamber (2 required)	0.3	0.66	< 0.2	0.1	10 x 10 x 10 cm box plus 3-10 cm spheres	burn out at 10^7 counts	on boom or on S/C wall looking away from the sun
Helium magnetometer	3.4	7.5	7.3	1	16-cm sphere plus two boxes	stability S/C fields noise	on end of boom
Faraday cup plasma spectrometers (4 required)	6.0	13.2	2.0	1	2 (10 cm diam x 10 cm)	sputtering	on boom, pointed 10 degrees away from the sun
Sisyphus optical detector	15	33	9.0	0.1	4 (67-cm aperture) reflectors	star background & scattered light	pointed away from sun
Electrostatic ballistic pendulum micrometeoroid sensors (7)	17.5	38.5	42.0	2	$7 \times (1000 \text{ cm}^2 = 1 \text{ m}^2$ $6300 \text{ cm}^3)$	proof test sensi sensitivity to spacecraft no noise sources	--
Capacitor penetration panel micro-meteoroid detectors	31	69.0	1.4	0.1	70 m^2	shorting out of panel sections	Rear of solar panels

data (ten percent standard error or better) can be obtained during passage through the 2.4 to 2.6 AU region. This particle size upper limit is dependent upon the available payload and is representative for the SEP spacecraft only. For larger particle sizes, the area coverage requirements and weight of sensors increases very rapidly (Figures 5-3 and 5-7).

The sensor designs selected for the SEP asteroid belt region provides valid statistical data (ten percent standard error) for particle sizes ranging from less than 10^{-10} to 10^{-7} grams. Each sensor complements data gathered by the other sensors. The capacitor sheet provides flux data for particles generally greater than 10^{-8} grams and 10^{-7} grams, giving good correlation of particle mass distribution. The electrostatic ballistic pendulum provides velocity vector and particle momentum data for particle sizes ranging from 10^{-9} to 3-by-10^{12} grams. The Sisyphus sensor provides velocity vector data and inferred size (albedo cross section) for particle sizes less than 10^{-9} to 10^{-7} grams.

Correlation of the velocity, momentum, and size data obtained from the EBP and Sisyphus for the 10^{-7} to 10^{-9} gram particles with the statistically significant flux data obtained from the capacitor sheet should provide a sound basis for verifying and improving asteroid belt analytical models. Correlation of particle velocity, momentum, and inferred size also enables scientific judgments on particle composition.

6. ELECTRIC PROPULSION SYSTEM

The electric propulsion system is one of the most important and unique spacecraft subsystems to be considered during this study program. It not only provides energy for the heliocentric transfer trajectory for the asteroid belt survey mission, but also constitutes the major technology experiment. Because of its importance, it is appropriate that the general design guidelines employed during the electric propulsion system design effort be stated and justified. The guidelines used for this study are as follows:

1. To establish system design credibility, state-of-the-art components and performance estimates were used wherever possible. The contract statement of work stipulated the use of the Hg bombardment thruster as the propulsion device. The state-of-the-art guideline resulted in the choice of a 40v - 80v transistorized (and modularized) power conditioning and control system and a positive expulsion reservoir system. Performance estimates of the complete propulsion system, in terms of efficiency versus specific impulse, were reviewed and approved by JPL. (These performance estimates were subsequently met by the proposed final design.)

2. To lend confidence to the final design, system reliability was established as an important design criterion; the design techniques by which high reliability was achieved (and determined) is described in detail.

3. To minimize system complexity and maximize mission success (asteroid belt science objectives) only those technology experiments were proposed which are necessary to evaluate system performance (including failure modes) or which might indicate a need for basic system design change. Experiments which have been or will be performed in the laboratory or on other spacecraft (NASA's SERT or ATS flights) should be seriously questioned.

4. To minimize spacecraft program cost risks, technology development and test program was designed which insures successful development of the proposed asteroid belt survey electric propulsion system.

6-1

Along with the development of a set of study guidelines, such as given above, initiation of the design of an electric propulsion system depends on the establishment of the overall design point by the trajectory analysis. The design point information required includes specification of the following:

1. Trajectory. The specific trajectory employed determines the variation of the initial design point with time and affects thermal design considerations.

2. Power Level. The power level at 1 AU determines propulsion system size; its variation with time affects both reliability and power matching considerations. This variation for the asteroid belt mission is shown on Figure 6-1.

3. Solar Panel Bus Voltage. The bus voltage at 1 AU affects the basic power conditioner design; its variation with time affects voltage regulation requirements and reliability considerations

4. Propellant Mass. The amount of propellant required affects the number and size of the propellant reservoirs employed

5. Specific Impulse. The specific impulse chosen determines the ion beam voltage (screen electrode voltage) and affects the choice of thruster electrode system.

The design points for the proposed asteroid belt spacecraft as well as for out-of-the-ecliptic and solar probes are summarized in Table 6-1.

Table 6-1. Propulsion System Design Points

| | Mission | | |
Trajectory	Asteroid Belt (Figure 6-1)	Out-of-Ecliptic Constant Power	Solar Probe Constant Power
P (1 AU), KW V (1 AU) V Propellant Mass, Kg I_{sp}, sec	7.75 40 104 (229 lb) 3500	7.75 40 400 (882 lb) 3500	7.75 40 200 (441 lb) 3500
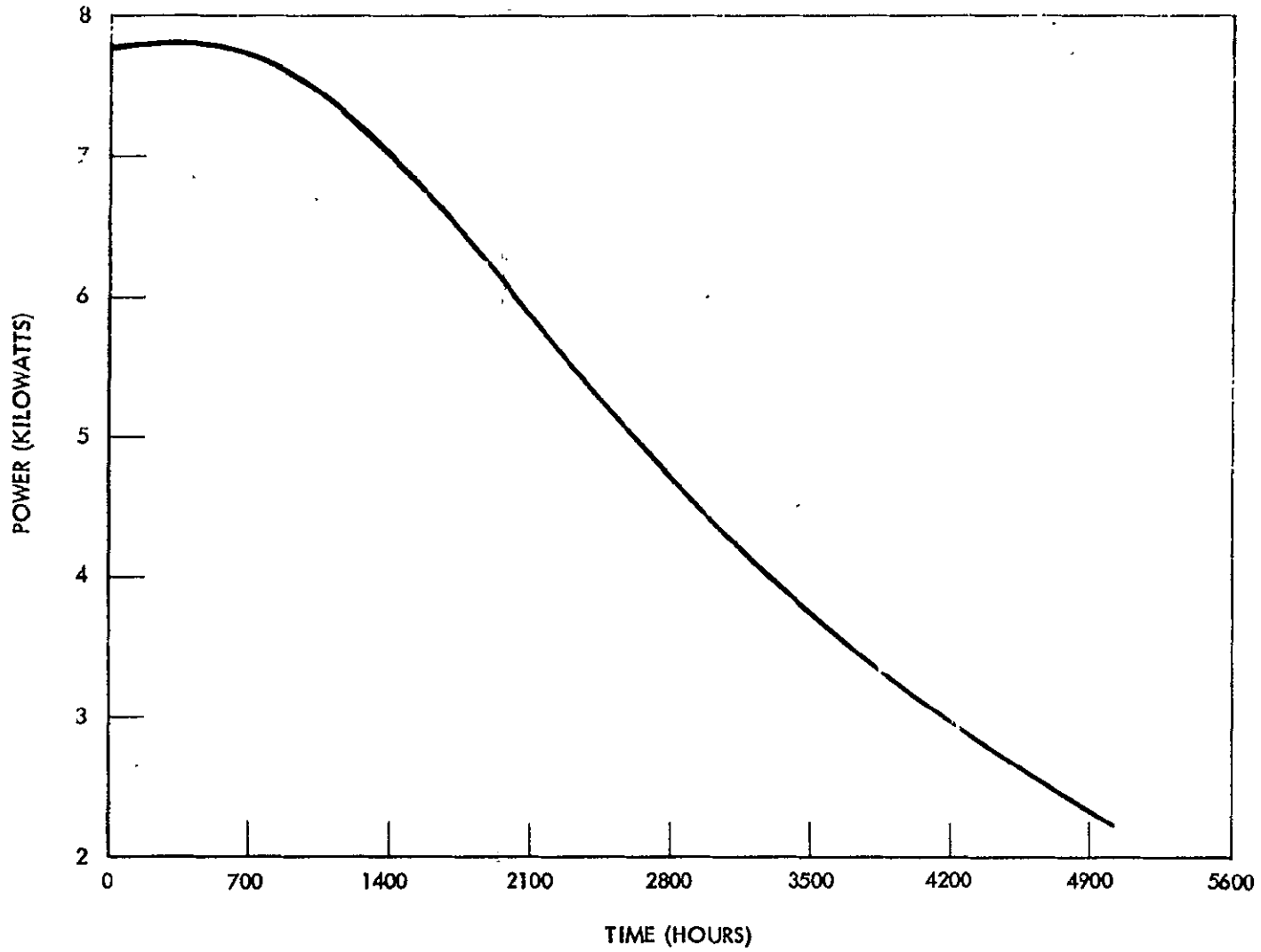
Figure 6-1.   Maximum Solar-Panel Power Available to Propulsion System

GENERAL SYSTEM DESIGN CONSIDERATIONS

An approach (or methodology) based on extensive analyses and system design considerations has been developed for the purpose of designing electric propulsion systems for interplanetary spacecraft. It is based on the design concept of seeking a minimum mass system while maintaining the system reliability at or above a given level. The methodology will be briefly reviewed here since it forms the basis of the propulsion system design definition.

Figure 6-2 summarizes the basic design approach described more completely in Reference 1. The methodology indicated leads to a detailed electric propulsion system design which has been optimized for a specific mission and integrated into a specific spacecraft. The effort performed to obtain the final designs is divided into two general tasks:

1. Computer simulation, design optimization, and sensitivity analysis of the major propulsion subsystems

2. Propulsion system integration and propulsion system/spacecraft integration

[The system design methodology described in Reference 1 has been extended, during this study, to include iteration between the trajectory and propulsion system optimization programs (the "dashed line" loop in Figure 6-2). This extension allows for a more complete and accurate simulation and optimization of both propulsion system and trajectory.]

Basic Design Tradeoffs

Because interplanetary missions require long duration component operation, it is obvious that system reliability is a major factor in system design. In general, reliability requirements are such that such techniques as redundancy are necessary to increase the probability of mission success to acceptable levels. Redundancy techniques can, of course, lead to severe system mass penalties. Since increased mass is undesirable in any space system, it is important that these penalties be minimized.

Where redundant components must be employed to increase system reliability, an effective means of reducing the concomitant system mass penalty is the use of a modularized system concept: the replacement of a single large component with a number of smaller subsystem components. In such a subsystem the incorporation of a redundant component for reliability purposes will, in general, result in a relatively small mass

TRAJECTORY
OPTIMIZATION

INPUT STUDIES

COMPONENT WEIGHT
vs.
POWER LEVEL
SCALING LAWS

SOLAR ARRAY
POWER PROFILE

COMPONENT
RELIABILITY
vs
POWER LEVEL
SCALING LAWS

COMPUTER PROGRAM

COMPUTE
PROPULSION SYSTEM
WEIGHT

COMPUTE THRUSTER AND
POWER SUPPLY
MODULE SWITCHING TIMES

COMPUTE
PROPULSION SYSTEM
RELIABILITY

TRIAL
SYSTEM
DESIGN

OPTIMIZATION
PROCEDURE

COMPUTER STUDIES

OPTIMUM
SUBSYSTEM
DESIGNS

• OPTIMUM
MODULE
SIZES

• SENSITIVITY
ANALYSIS

FINAL
ELECTRIC
PROPULSION
SYSTEM
DESIGN

INTEGRATION STUDIES

PROPULSION SYSTEM INTEGRATION AND DESIGN
THRUSTER LOCATION ANALYSIS
SYSTEM INTEGRATION STUDIES
THERMAL
MECHANICAL
ELECTRICAL

PROPULSION SYSTEM/SPACECRAFT INTEGRATION EFFECTS
MAGNETIC AND ELECTRIC FIELDS
ION BEAM IMPINGEMENT
POWER CONDITIONING COMMONALITY
THRUST VECTOR/ALTITUDE CONTROL SYSTEMS
SPACECRAFT THERMAL CONTROL

Figure 6-2.   Propulsion System Design Methodology

penalty. For modularization to be considered, this reduction in mass penalty must compensate for the increase in initial system mass which normally results when a system is modularized.

A unique factor in the design of a solar-electric propulsion system for interplanetary spacecraft is the nature of the output characteristics of the solar panel power source. First, the I-V characteristic and, thus, the maximum amount of power available from the panel is a function of distance from the sun and, therefore, variable with time. Second, the maximum power available will be delivered only when the ion engine load is properly matched to the solar panel characteristic. Thus, it is apparent that the ion engine system load must be continually and properly programmed during the flight.

Reference 1 shows that the optimum procedure for programming an ion engine load is a combination of varying the ion beam current (throttling propellant flow rate) at constant beam voltage (constant specific impulse) and switching ion engine modules. In general, the throttling of ion thrusters can introduce a decrease in thruster efficiency, (Figure 6-3). The degree to which a thruster must be throttled for a given application is a function of the number of thruster modules employed. Thus, the penalty associated with power matching requirements is also determined by the degree of thruster subsystem modularization.

The above identifies two basic tradeoffs involved in the design of a solar-electric propulsion system: system reliability versus system mass, and power matching versus system performance (the latter can be effectively related to system mass). In each case the number of modules employed in the system becomes the major design variable. Therefore, to minimize the system weight for a given application, the optimum number of modules must be determined.

System Configurations

In designing a modularized propulsion system, there are several ways in which the major subsystems (thrusters, power conditioners, and reservoirs) can be integrated. For example, each thruster could have its own reservoir and power conditioning and control system. In the other limit, by incorporating the proper cabling and switching matrix and manifolding and valving system, an individual thruster could be operated by any power conditioning panel and could be supplied with propellant by any reservoir. Between these two limiting designs several other possible configurations exist.
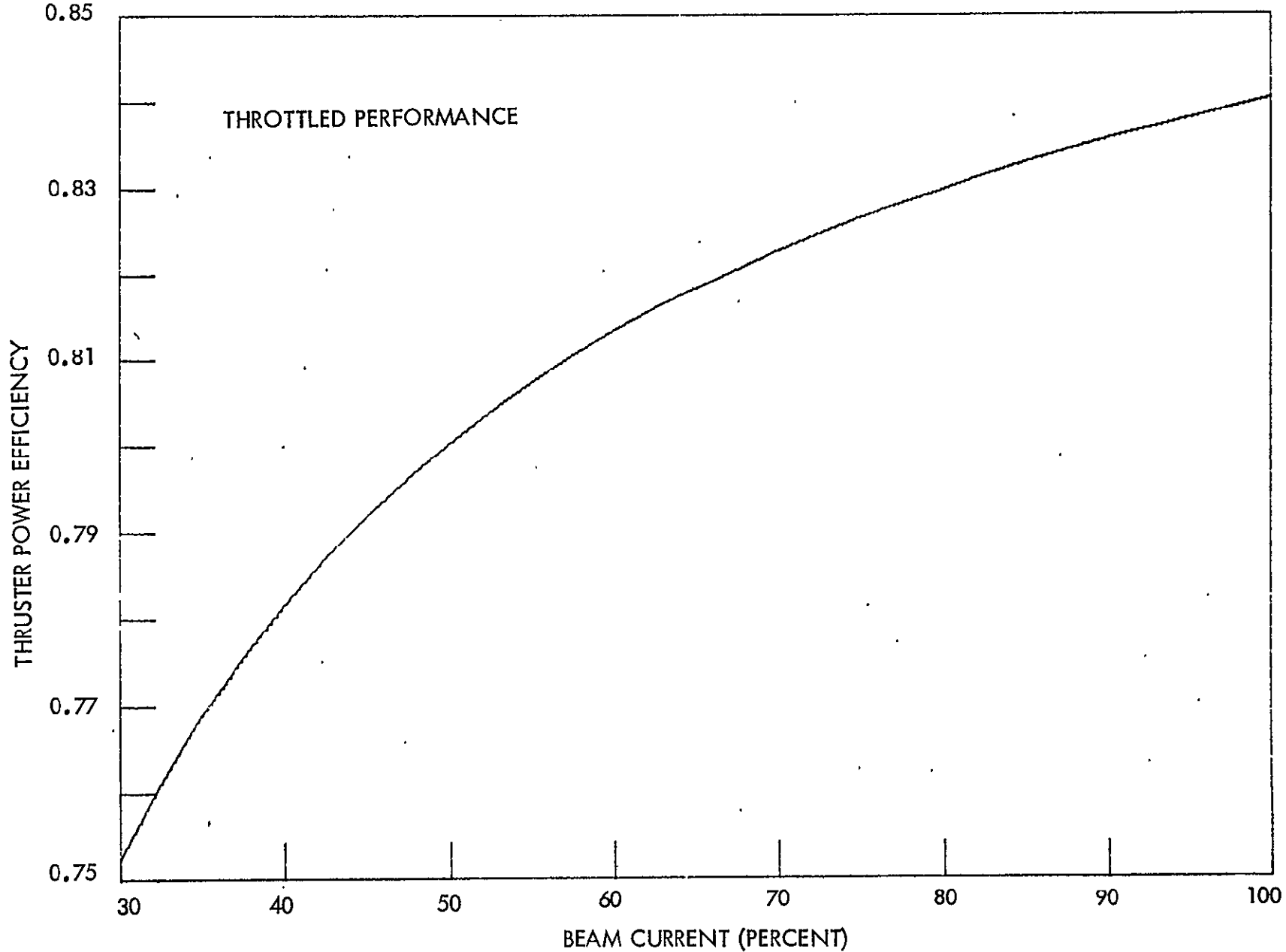
Figure 6-3. Throttled Thruster Power Efficiency

Space Division
North American Rockwell

In this study, the two limiting configurations and one which appears to be the most attractive compromise design were reviewed. For each of the three configurations, the general propellant reservoir subsystem layout was identical: a single reservoir feeds propellant to a common manifold through which propellant is distributed to all operational engines. Because of the extreme penalty for the additional propellant involved, redundancy in the reservoir system is undesirable. Thus, it is assumed that the reliability of the reservoir subsystem is increased internally (without reservoir redundancy) and does not become part of the tradeoff studies discussed above.

Block diagrams of the three configurations are shown in Figure 6-4. The first configuration is composed of O_T operating thrusters and power conditioning and control (PC&C) panels and S_T standby thrusters and PC&C panels. No switching network is provided in this design. Thus, each PC&C panel operates only the one thruster to which it is originally connected. In the second configuration a switching and cabling network is provided so that any of the $O_T + S_T$ PC&C panels can be connected during flight to any of the $O_T + S_T$ thruster modules. The third configuration shown consists of a number O_T of operating thrusters and power conditioning and control panels and a number S_T of standby thrusters. The switching and cabling network, in this case, is limited to connecting a PC&C panel to any standby thruster if the engine normally operated by the panel fails.

A brief qualitative comparison of the three configurations is given in Table 6-2. (A more quantitative comparison between configurations 1 and 3 for the asteroid belt mission is given in a later Section.) Configuration 3 was chosen for this study, since for a given system reliability goal, it is the lightest. The switching network required by this system concept should not constitute a reliability problem, since the relays involved represent a minimal requirement and need only function once during the mission.

Thruster Switching Criteria

The thruster modules associated with a solar electric propulsion system must be both throttled and switched to provide the proper power (or impedance) matching capability. The throttling schedule for each module is obtained directly from the power-time relationship for a given mission and the switching times associated with the thruster system number of thruster modules) under consideration. The choice of the times at which thrusters are switched also affects system reliability.

Two different criteria were considered for determining the switching time. Using criterion 1 the decreasing available maximum power is followed by throttling the thrusters until the power drawn by the thruster array and power conditioning system drops from the starting value by an

THRUSTERS

POWER CONDITIONING
PANELS

PROPELLANT TANKS

CONFIGURATION 1

SOLAR PANEL POWER BUS

THRUSTERS

POWER CONDITIONING
PANELS

PROPELLANT
TANKS

CONFIGURATION 2 AND 3

SOLAR PANEL POWER BUS

SWITCHING
ASSEMBLY

NOTE: SWITCHING ASSEMBLY CONNECTS A
PANEL TO ITS DESIGNATED THRUSTER
AND:
a.   IN CONFIGURATION 2 – ANY OTHER
THRUSTER
b.   IN CONFIGURATION 3 – ANY STANDBY
THRUSTER ONLY

Figure 6-4.   System Configurations

Table 6-2. System Configuration Comparison

Configuration	Advantages	Disadvantages
1	No switching network PC&C panel redundancy Highest reliability	Additional PC&C panels Additional cabling Heaviest system
2	Most versatile system Minimum number of PC&C panels Lightweight High reliability	Most complex switching and cabling network System reliability depends on relay operation
3	Versatile system Minimum number of PC&C panels Minimum cabling requirements Lightest weight High reliability	Switching network required (of minimal complexity) System reliability depends on relay operation

amount equal to the nominal power drawn by one PC&C-thruster operating unit. At this point one of the thruster and PC&C panels is switched off and the remaining thrusters returned to their nominal power (100 percent beam current). As the available power continues to decrease, the thruster array is again throttled until the maximum power available again decreases by an amount equal to the nominal rating of one PC&C-thruster unit at which time

a second-thruster and PC&C panel is switched off. This process of throttling the thruster array and switching thrusters is continued until the end of the mission.

The second switching criterion and its advantage over the first are shown in Figure 6-5. The solid curve represents the beam power as it would appear with the first switching criterion if there were no efficiency penalties associated with throttling. The dashed curve represents the actual beam power with the throttling penalties included when switching according to criterion 1.

Switching criterion 2 differs from criterion 1 in that the switching time is selected by reference to ion beam power rather than to PC&C-thruster unit power. Note the dashed curve shows that the beam power (thrust) immediately before switching is lower than that immediately after switching, even though the available power is greater before switching. This anomaly occurs because the thruster power efficiency is lower when the engine has been throttled. A switching criterion which would never allow the beam power to fall below that attainable immediately after switching would, thus, be better. Such a condition can be accomplished by switching off a PC&C-thruster unit when the total throttled thruster array beam power equals the nominal beam power of an array minus one thruster (criterion 2). Since the thrusters cannot be operated at greater than their nominal power, switching at these times (points A and B in Figure 6-5) will result in the available power being larger than that which the thruster array can handle. The PC&C subsystem is designed, however, to allow the thruster array to operate under such conditions. The dotted curve in Figure 6-5 represents the beam power (throttling penalties included) when switching criterion 2 is used.

By using this latter switching criterion, any penalty associated with power matching is minimized. Furthermore, a slight system reliability gain is realized since PC&C thruster units are switched into standby at the earliest possible time. For these reasons, switching criterion 2 was used in the system reliability modeling and design.

Computer Simulation

A computer program was developed which establishes an optimum electric propulsion system design by evaluating the design tradeoffs discussed below to obtain a minimum mass system while maintaining the system reliability at a predetermined high level. The system mass and reliability were formulated in terms of variables representing numbers of operating or standby modules. The formulations were made using system configuration 3 shown in Figure 6-4. (Configuration 1 was also formulated and evaluated for quantitative comparison purposes.) Baseline subsystem configurations
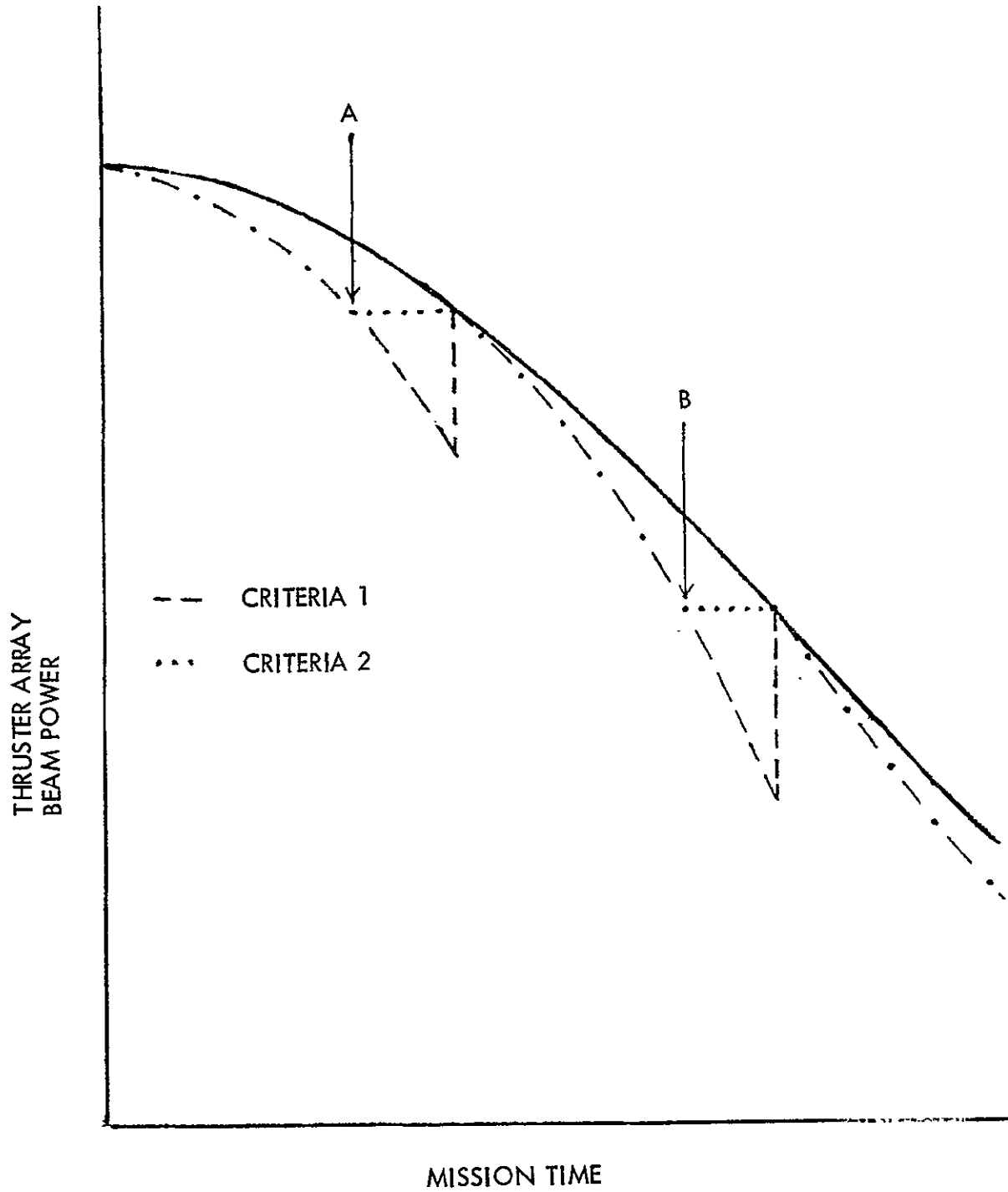
Figure 6-5. Comparison of Switching Criteria

developed for key supplies in the PC&C subsystem were also formulated:
Figure 6-6 illustrates the baseline configuration for the screen supply in a
PC&C panel. Methods discussed earlier for using the maximum available
power according to switching criterion 2 were assumed in the formulation.

The system mass is simply expressed as a sum of subsystem masses;
the subsystem masses are given by the sum of the masses of their com-
ponents. The masses of the components are obtained from scaling studies
which give the mass of real component hardware as a function of parameters
affected by the choice of a particular detailed system design (by a particular
choice of the variables and parameters used in the optimization process).
The scaling studies form the bridge between the analytical system descrip-
tion and real hardware.

Similarly, but in a much more complex manner, system reliability is
expressed as a function of the component failure rates. The component
failure rates are also obtained from scaling studies which relate the failure
rate of real component hardware to such parameters as power, and are
affected by the choice of a particular detailed system design. The reliability
formulation is inherently complex, especially for decreasing power missions
such as the asteroid belt survey. For example, define T to be the length of
the decreasing power mission and S_i to denote state i. In addition, let

$$P'_{pc}(S_i, T) = \text{the probability that the combined thruster and power}$$
$$\text{conditioning subsystems successfully complete a mission}$$
$$\text{in which exactly i \underline{panel} failures occurred.}$$

The reliability $R_{th, pc}(T)$ of the combined thruster and power conditioning
systems is formuated as the sum

$$R_{th, pc}(T) = P'_{pc}(S_o, T) + P'_{pc}(S_1, T) + \ldots + P'_{pc}(S_{k-1}, T)$$

The first three terms $P'_{pc}(S_o, T)$, $P'_{pc}(S_1, T)$ and $P'_{pc}(S_2, T)$ are given in
Table 6-3 to illustrate the complexity of the formulation required to model
properly a solar-electric propulsion system. An extrapolation technique is
used to obtain the remaining terms: $P'_{pc}(S_1, T)$, for $i = 3, \ldots \ldots k-1$.

The system mass and reliability formulation were mechanized in a
computer program (Figure 6-2). The program also incorporates an optimi-
zation technique developed to solve the electric propulsion system design
optimization problem.

In an optimization many trial designs are compared to find the one with
minimum mass. This comparison procedure is carried out automatically by
the optimization subroutine. Various levels of system optimization,

6-13

Screen Inverter-Transformer Rectifier Module

Screen
High Voltage
Filter

Parallel Redundancy   Internal Redundancy
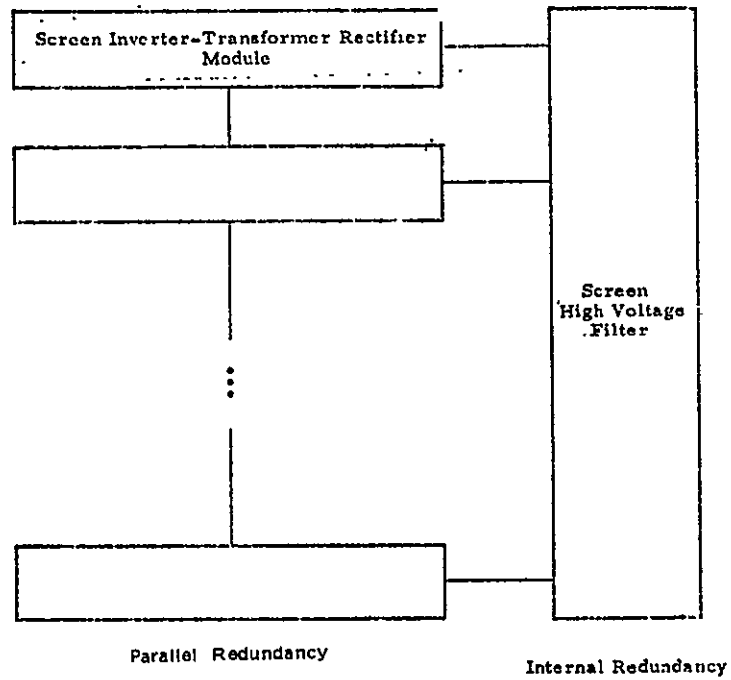
Figure 6-6. Screen Supply Block Diagram

Table 6-3. System Probabilities

$$P'(S_0, T) = r_0(t_1)r_0(t_2)\ldots r_0(t_k) \left[r_0(t_k) \right]^{O_T - k} R_{th}(O, O, T)$$

$$P'(\hat{S}_1, T) = \sum_{i=2}^{k} \left\{ (O_T - i + 1)\frac{P(S_0, T)}{r_0(t_1)r_0(t_i)} \int_{t_{i-1}}^{t_i} r_1(\tau) r_0(t_i + t_i - \tau) \, d\tau \right\} R_{th}(\Delta t_i, O, T)$$

$$P'(\hat{S}_2, T) = \sum_{i=2}^{k-1} \sum_{j=i+1}^{k} \left\{ \frac{O_T + 1 - i)(O_T + 1 - j)}{r_0(t_1)r_0(t_i)r_0(t_j)} P(S_0, T) \int_{t_{i-1}}^{t_i} \int_{t_{j-1}}^{t_j} r_1(\tau_1) r_1(\tau_2) r_0(t_1 + t_i + t_j - \tau_1 - \tau_2) \, d\tau_2 \, d\tau_1 \right\} R_{th}(\Delta t_i, \Delta t_j, T)$$

$$+ \sum_{i=3}^{k} \left\{ \frac{(O_T + 1 - i) \, P(S_0, T)}{r_0(t_1)r_0(t_2)r_0(t_j)} \int_{t_{i-1}}^{t_i} \int_{\tau_1}^{t_1} r_1(\tau_1) r_1(t_1 + \tau_2 - \tau_1) r_0(t_2 + t_1 - \tau_2) \, d\tau_2 d\tau_1 \right\} R_{th}(\Delta t_i, \Delta t_j, T)$$

$$+ \sum_{i=3}^{k'} \left\{ \frac{(O_T + 1 - i)(O_T - 1) \, P(S_0, T)}{r_0(t_1)r_0(t_2)r_0(t_i)r_0(t_1)} \int_{t_{i-1}}^{t_i} \int_{\tau_1}^{t_i} r_1(\tau_1) r_1(\tau_2) r_0(t_1 + t_i - \tau_1) r_0(t_2 + t_1 - \tau_2) \, d\tau_2 d\tau_1 \right\} R_{th}(\Delta t_i, \Delta t_j, T)$$

$$k' \equiv \min(k, O_T - 1), \quad i' \equiv \min(k, i + 1), \quad t_k = T$$

$k - 1$ = Number of thruster and PC&C panels switched into standby

t_j = Time at which thruster and PC&C panels are switched (except t_k)

$r_0(t_j)$ = The probability that a subsystem does not fail in (O, t_j)

$r_1(t_j)$ = The probability that a subsystem operates in (O, t_j) then fails once in $(t_j, t_j + dt_j)$

$R_{th}(\Delta t_i, \Delta t_j, T)$ ≡ The reliability of the thruster subsystem for a mission on which panel (PC&C) failures occurred in time intervals Δt_i and Δt_j.

depending on the number of quantities to be varied simultaneously, can be performed. Either independent subsystem optimizations or system optimization based on proper reliability allocation among the subsystems can be obtained.

Table 6-4 summarizes the major aspects of the computer simulation of the electric propulsion system design problem. The computer program accepts inputs relating to the trajectory and scaling studies. It then performs an optimization of the system design according to the design tradeoffs listed. The resulting outputs then describe the "optimum" propulsion system design. Since the scaling laws used as inputs to the computer program are based on detailed subsystem analysis, the resulting outputs can immediately be related to specific subsystem designs.

Table 6-4. Computer Simulation Summary

Inputs	Design Tradeoffs	Outputs
Trajectory information Scaling	Reliability Weight Power matching	Number of modules Module size Amount of redundancy Thruster switching times Thruster beam current variation System mass and reliability Allocation of reliability

MODULE SIZE DETERMINATION

Using the overall design points obtained by the trajectory analysis (Table 6-1), it is necessary to design an electric propulsion system which meets these requirements while satisfying such additional constraints as those imposed by reliability and power matching considerations. Because of the availability of detailed scaling studies, such a design definition is reduced to the determination of the number and size of the various subsystem modules.

Since only state-of-the-art hardware is to be considered, thrusters with anode diameters larger than 30 cm were excluded from this study.

6-16

System Design Optimization

The number and size of the subsystem modules were chosen according to the optimization criteria that a minimum weight system be obtained while maintaining system reliability (defined as consisting of the thruster and power conditioning and control subsystems) greater than or equal to a chosen value R_g. (As discussed earlier, the reservoir subsystem is not included in the optimization process in this study.) The variables used in the optimization are given in Table 6-5.

Although the system is to be optimized for the asteroid belt probe mission, an evaluation of system reliability and weight for both solar and out-of-the-ecliptic probes is to be provided to indicate multimission capability.

Table 6-5 Variables or Parameters in System Optimization

Symbol	Definition
O_T	Maximum number of thruster modules in operation during the mission
S_T	Number of standby thruster modules
O_B	Number of required beam supply modules
S_B	Number of standby beam supply modules
O_A	Number of required or operating accelerator supply modules
S_A	Number of standby accelerator supply modules
S_D	Number of standby discharge supply modules
S_{L1}	Number of standby line regulator 1 modules
S_{L2}	Number of standby line regulator 2 modules
S_I	Number of standby 5 kc inverter modules
R_g	Minimum reliability allowed the electric propulsion system

System Mass-Reliability Tradeoff

The initial computer studies were performed with all design variables being allowed to change. Optimum system designs were obtained for a range of values of desired system reliability, R_g. Figure 6-7 shows the electric propulsion system mass variation with R_g, illustrating the tradeoff between system mass and reliability. From these data, it is apparent that the propulsion system mass increases rapidly as R_g approaches a value near 0.99, indicating the severe mass penalty for designs with higher reliability. Using the data in Figure 6-7 with an estimate of allocation of reliability among all spacecraft subsystems, a value of R_g equal to 0.99 was chosen for the propulsion system (thruster and PC&C subsystems).

The system designs corresponding to points on the curve of Figure 6-7 are, in general, not physically realizable because the design variables, which denote "numbers" of modules, can take on non-integer values (continues functions are required in the computer simulation). Thus, the next step in the design optimization is to determine the optimum design with integer values for the variables when R_g is equal to the chosen value: $R_g = 0.99$. The optimum system design for integer variable values is found using the computer optimization program in a slightly modified way, as described below.

System Reliability Limits

The power conditioning system considered in this study does not incorporate arbitrary amounts of redundancy in every individual element. If it did, the overall system reliability (neglecting switching) could be made as high as desired. Instead, optional amounts of redundancy are provided only for key elements. For example, the beam supply allows for any number S_B of redundant beam inverter modules, whereas the screen filter mass and failure rate depend only on the power level. As a result, the presently modeled thruster power conditioning configuration has implicit upper limits to which the reliability can be raised. These limits can be evaluated as a function of O_T for a given mission. The maximum attainable system reliability is plotted versus O_T in Figure 6-8 for the asteroid probe mission. The curve was obtained by evaluating the system reliability with O_T set equal to 2, 3, 4, etc. ($O_T = 1$ is not considered, since this implies a thruster larger than 30 cm) and the redundancy in each power supply set high enough to raise its reliability to one. From the curve, it is obvious that only with O_T equalling 2 will it be possible to obtain a system with reliability 0.99. Regardless of the redundancy used, system designs with O_T greater than 2 are less reliable than 0.99.
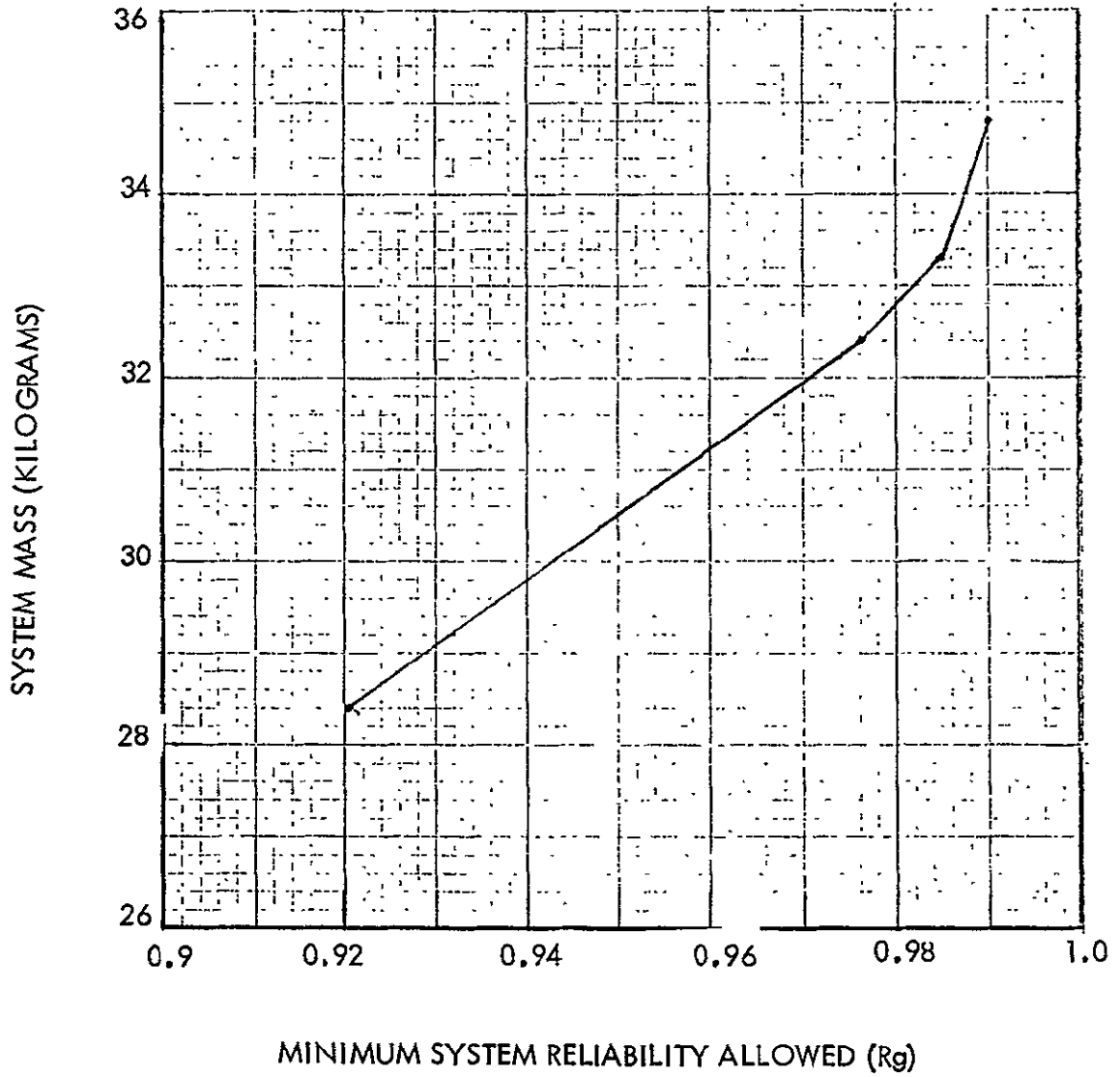
Figure 6-7. System Mass Reliability Tradeoff
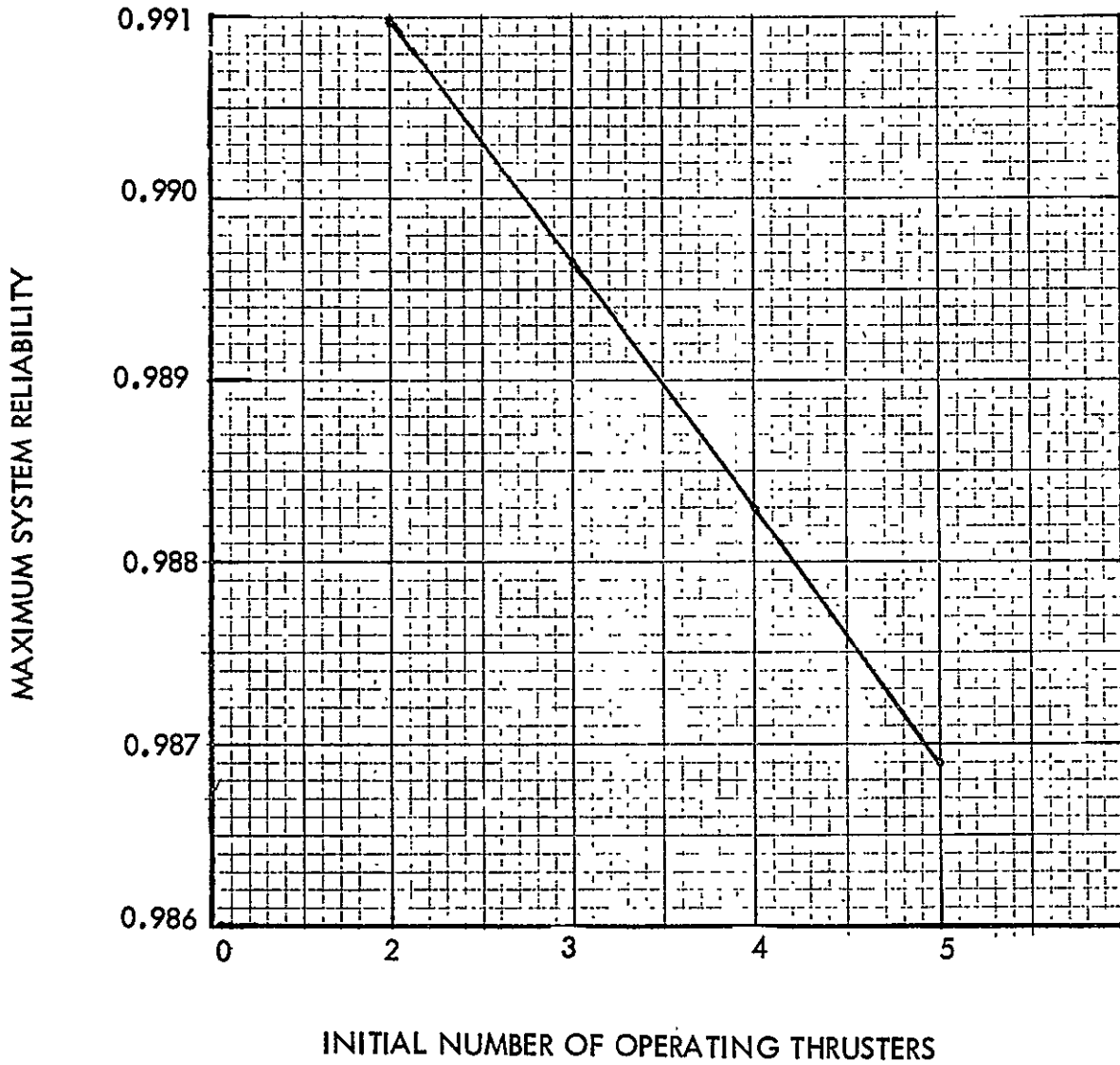
Figure 6-8. System Reliability Limit

Optimum Module Sizes

The optimum value for O_T has been determined by the choice of a system reliability constraint ($R \geq 0.99$). If there had been more than one value for O_T which satisfied this constraint, the optimization program would have been run with O_T held fixed at each of those values. The value of O_T which gave the lowest mass would then have been the optimum.

By point evaluation of the system reliability, determining the system reliability for a given set of the variables, it was determined that the reliability constraint could not be satisfied with S_T equal to 0 even with unlimited redundancy in the power conditioning panel. Therefore, the lower limit of the allowed S_T range can be set to the smallest integer value which satisfies the reliability constraint. In this case, the lower limit, which was found to be one, was also the optimum.

The choice of O_T = 2 indicates a thruster power of 3.62 kW. For this power level a line regulator 2 is not used in the power conditioning design. Thus, the variable S_{L2} is removed from consideration.

Point evaluation of the system reliability shows that the remaining redundancy variables, i.e., S_B, S_A, S_{L1}, S_I, need to be at least one for the reliability constraint to be satisfied. Subsequent optimization shows that the lower limit on the ranges of these variables is also their value at the optimum.

The remaining variables to be specified are O_B and O_A, the respective required number of screen and accelerator inverters. All variables except O_B and O_A were fixed at the previously found values and the system optimization was performed with O_B and O_A as the only variables. Point evaluations were then made of the system mass and reliability at the nearest integer values for O_B and O_A: O_B = 10, 11 and O_A = 2, 3. The results are shown in Table 6-6. The system design with O_B = 10 and O_A = 2 is seen to provide the 0.99 reliability requirement while minimizing the weight penalty.

Table 6-6. Determination of O_B and O_A

Variables O_B, O_A	System Mass, kg (lb)	System Reliability
10.3, 2.26	35.29 (77.79)	0.990083
10, 2	35.36 (77.95)	0.990085
11, 2	35.37 (77.98)	0.990073
10, 3	35.41 (78.06)	0.990082
11, 3	35.42 (78.09)	0.990070

Design Summary and Implications

The values of the variables for the optimum system design are summarized in Table 6-7. Characteristics of the optimum electric propulsion system design for the asteroid belt mission are shown in Table 6-8.

The thruster array has a total of three 3.62-kilowatt thruster modules, one of which is a standby. As shown in the thruster beam power profile (Figure 6-9), thrusting begins with two thrusters operating at their nominal power. As the mission progresses, the solar array power decreases and the propellant flow rate and the resulting beam current are decreased (at constant voltage) until the total beam power output of the two thrusters is equal to the beam power that one thruster would deliver if run at full power. At this point (3218 hours), one thruster is shut down and the other thruster brought back to full power. The mission is continued with this remaining thruster being throttled to follow the available solar array power until the end of the thrusting period (5014 hours). The beam current variation schedule for the thruster in operation for the entire thrusting period is shown in Figure 6-10. The beam current variation for the other operating thruster is the same until at the switching point it is shut off.

Two power conditioning panels are provided: one for each operating thruster. Since there are no standby panels, power conditioning redundancy is built up within each of the supplies which comprise a panel (the numbers of operating and redundant power supply modules explicitly optimized in the panel design are shown in Table 6-7).

Table 6-7. Summary of Propulsion System Design

Module	Number
Thruster-initial operating	2
Thruster-initial standby	1
Beam supply-operating	10
Beam supply-redundant	1
Accelerator supply-operating	2
Accelerator supply-redundant	1
Discharge supply-standby	1
Line regulators-standby	1
5 kc inverter-standby	1
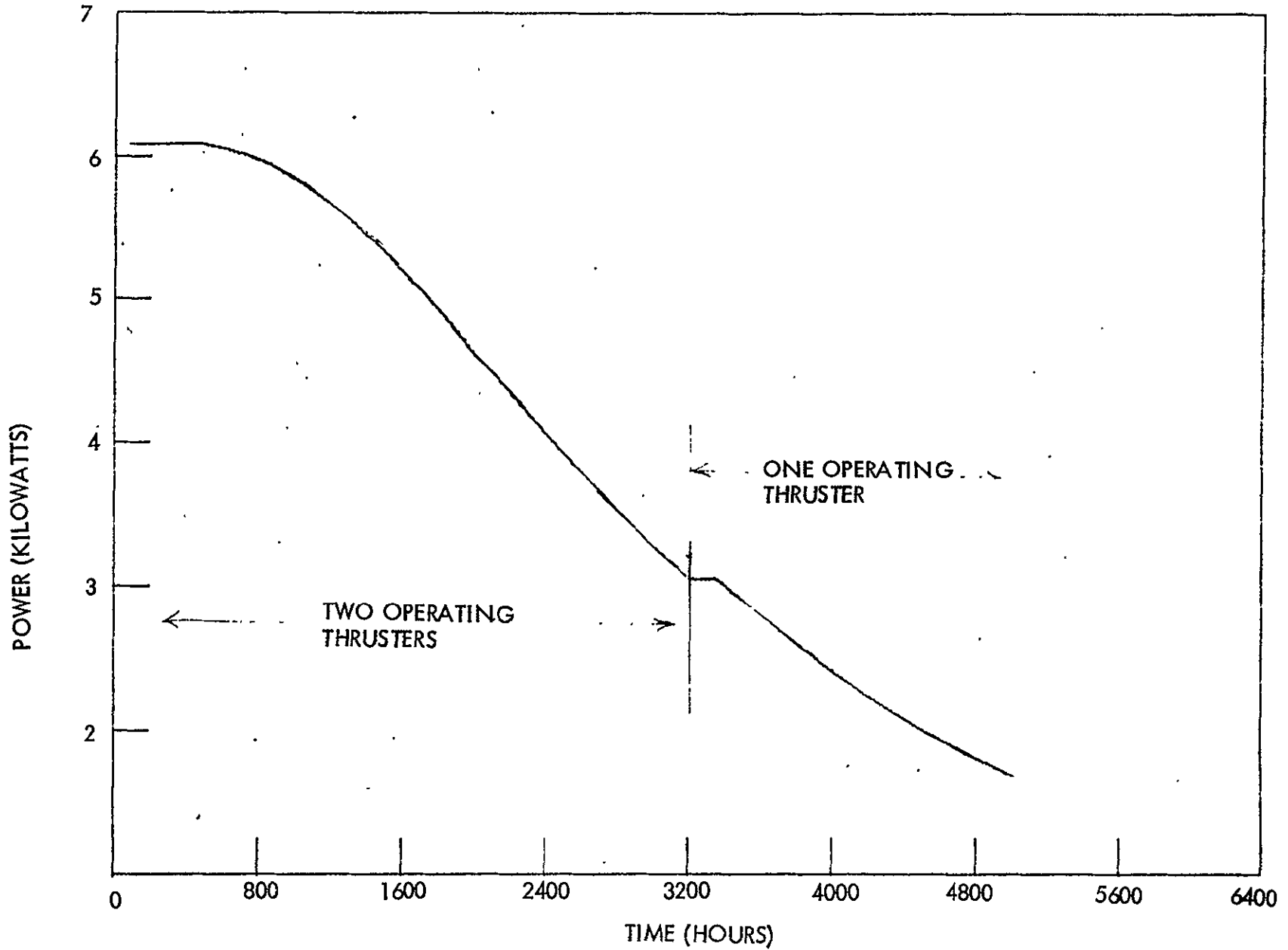
Figure 6-9. Thruster Array Beam Power Profile

Space Division
North American Rockwell
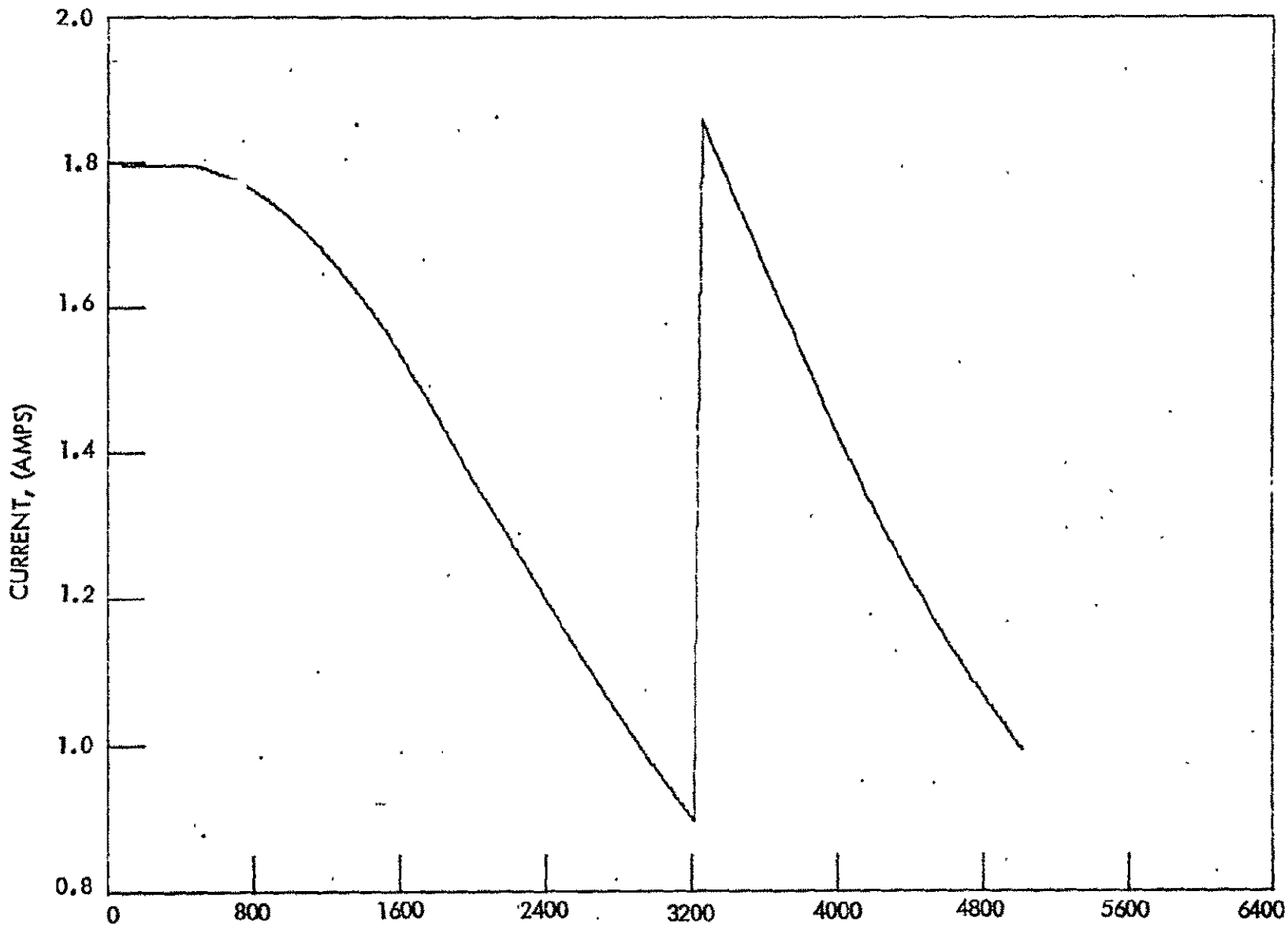
Figure 6-10.   Thruster Beam Current

Table 6-8. Electric Propulsion System Design Characteristics

Item	Characteristics
Maximum system input power	7.75 kw
Specific impulse	3500 sec
Thruster power, nominal	3.62 kw
Thruster beam current, nominal	1.8 amps
Beam potential	1696 volts
Thruster diameter	30 cm
Thruster mass	3.97 kg (8.75 lb)
Number of thrusters	3
Thruster array mass	11.91 kg (26.25 lb)
Number of PC& C panels	2
Power conditioner panel mass	15.9 kg (35 lb)
Power conditioner system mass	31.8 kg (70 lb)

While the failure rates of the power conditioning panel elements could be accurately assessed because of available data, thruster failure rates were more difficult to determine. The absolute value of the thruster failure rate was arrived at by considering the failure rates of its component parts. To obtain this estimate, the construction of a thruster was reviewed. A thruster was figuratively divided into its constituent parts and assembly features (such as welds). Failure rates for each of the component parts and assembly features were then obtained from various failure rate references (References 6-2, 6-3, 6-4, 6-5 and 6-6). For components for which failure rate data did not exist, component failure rates for similar equipment adjusted to a space environment were used. Using this technique, the failure rate of the proposed thrusters was estimated to be 6.35 failures per 10^6 hours.

While convenient, and in fact the only current practical method to determine the thruster failure rate, this method can only provide an estimate which can be used as a lower bound for the failure rate. For this reason, provision was made in the reliability simulation to include a constant (with beam current) multiplying factor, α, for the thruster failure rate. The effect that the thruster failure rate has on the system reliability can then be assessed by computing the system reliability for a given system design as a function α. Figure 6-11 shows the reliability versus α for the proposed optimum system design given in Table 6-7. The graph illustrates that even if the thruster failure rate is five times that assumed (32 failures per 10^6 hours), the system reliability is still a relatively high 0.9725.
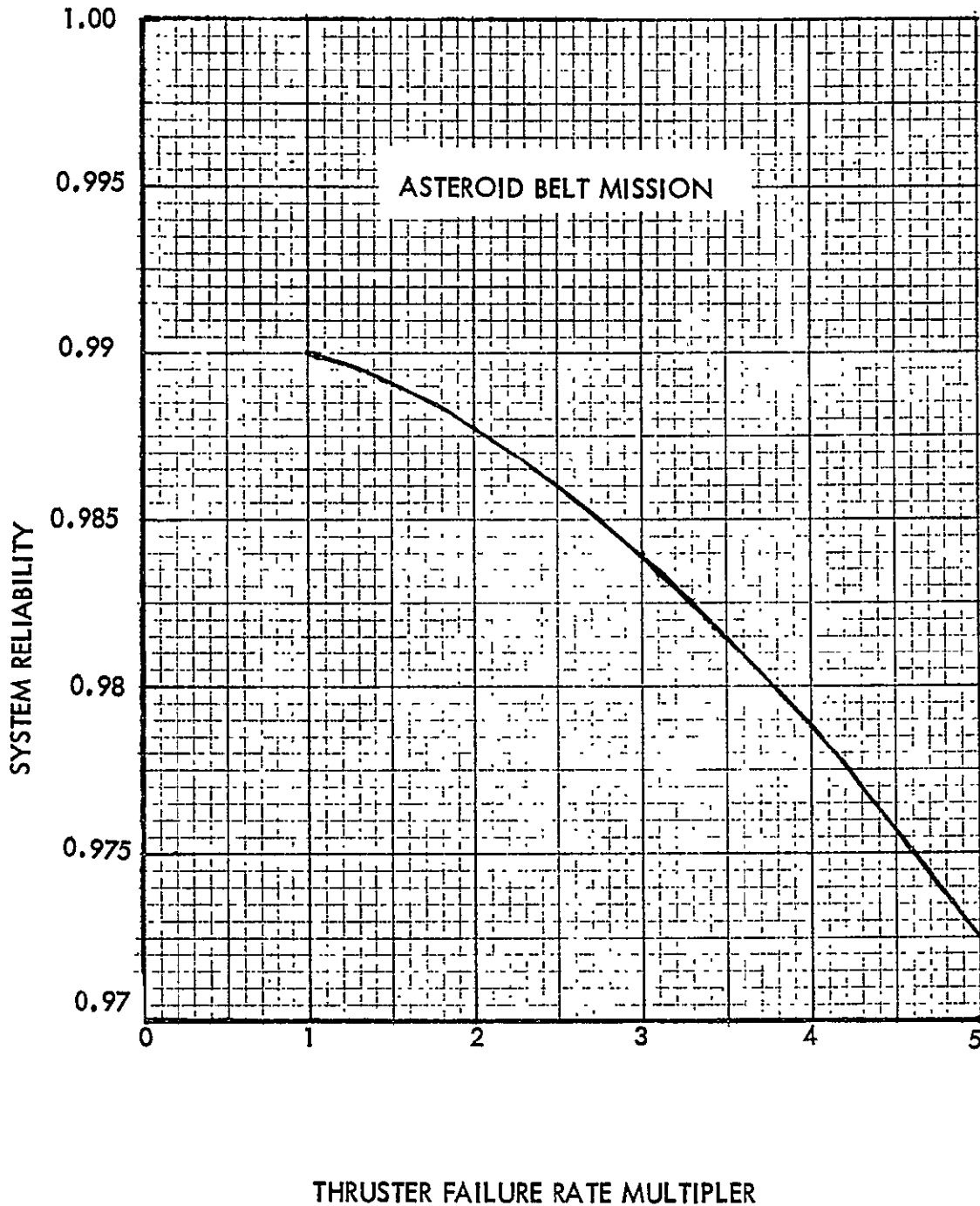
Figure 6-11. System Reliability Sensitivity to Thruster Failure Rate

6-26

In the proposed optimum system design, if a thruster fails during the asteroid belt mission the standby thruster is connected to the PC&C panel of the failed thruster by a switching matrix; no standby PC&C panel is provided. Because there was a need to demonstrate the value of having a switching matrix for the standby thruster (rather than providing a standby PC&C panel), the proposed optimum system design was compared with two other system designs. Each of these two additional designs negate the switching requirement. Thruster sizes and ratings for all three systems are those established for the optimum system design. PC&C panel redundancy was also assumed to be the same as for the optimum design. Propellant reservoir, cabling, and standby switching matrix data were included in the comparison. Block diagrams of the three compared systems are shown in Figure 6-12. System 1 has two initially-operating thrusters and negates the switching requirement by having no standby thrusters. System 1 can be considered representative of both configurations 1 and 3 (Figure 6-4) since the two configurations are equivalent when there are no standby thrusters. System 2 is the proposed optimum system design based on configuration 3. It differs from System 1 by the addition of the standby thruster and switching matrix. System 3 based on configuration 1, differs from System 2 in that a standby power conditioning panel is furnished (in place of the switching matrix) for the standby thruster. Table 6-9 contains a summary of the pertinent features of each system design. The reliability of System 1 is not acceptable for the present study and indicates the need for a standby thruster. Systems 2 and 3 present two means for including such a standby; System 2 has the obvious advantage of having less mass for the same reliability as System 3. This equivalence is due to the switching matrix having a low mass and a reliability sufficiently high (0.99999) to have negligible effect on the reliability of System 2.

Table 6-9. Comparison of System Designs

System Number	Switching Matrix Mass, Kg (lb)	Reliability	Cabling Mass, Kg (lb)	Thruster and PC&C Mass, Kg (lb)	Reliability	Propellant Tank Mass, Kg (lb)	Reliability	System Mass, Kg (lb)	Reliability
1			0.214 (0.472)	39.74 (87.4)	0.949	2.27 (5)	0.993	42.24 (92.9)	0.942
2	0.724 (1.6)	0.999 (99)	0.295 (0.65)	43.71 (96.2)	0.990	2.27 (5)	0.993	47.01 (103.4)	0.983
3			0.399 (0.88)	59.61 (131.1)	0.990	2.27 (5)	0.993	62.31 (137.08)	0.983
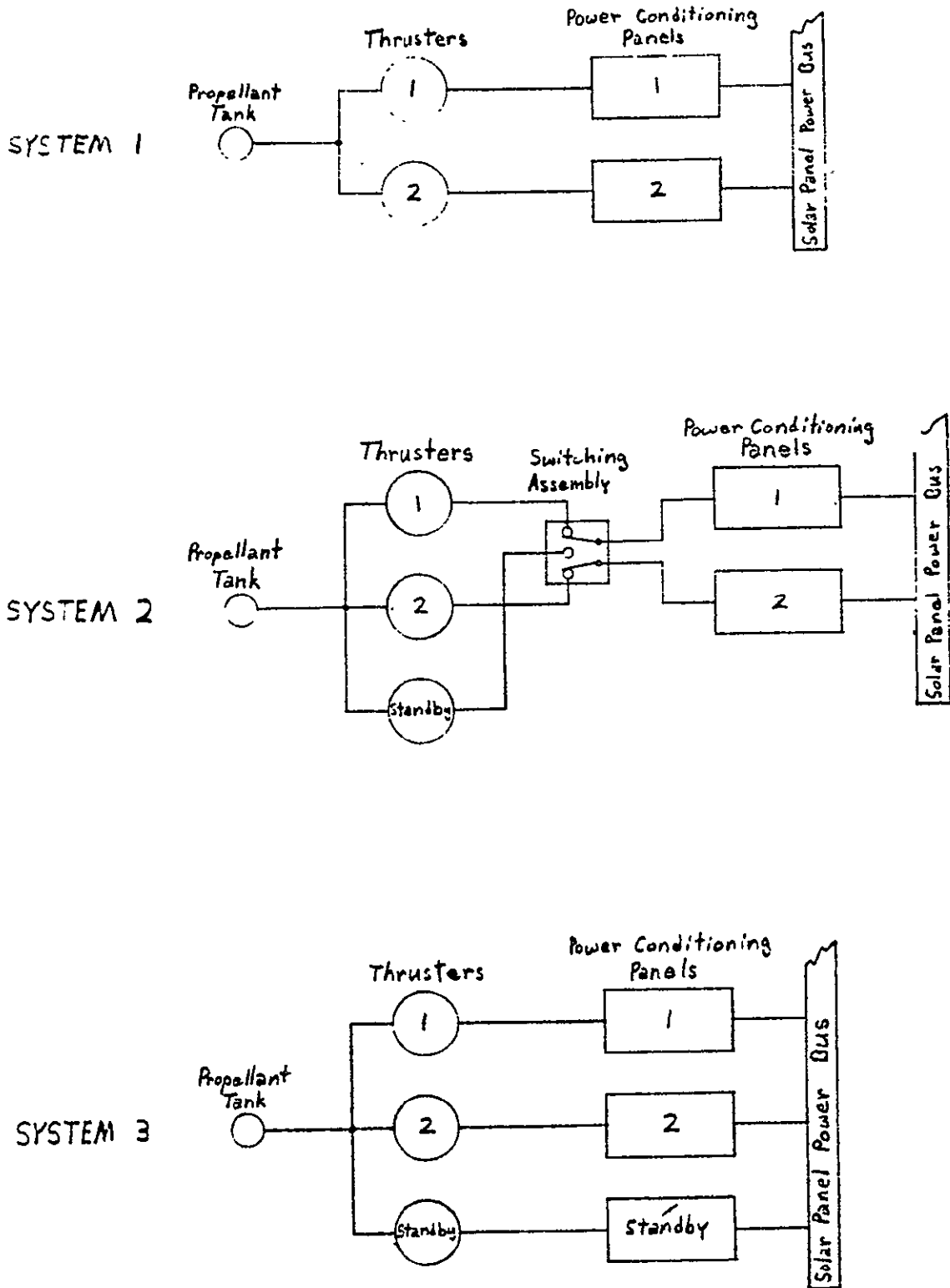
Figure 6-12. Comparison of System Designs

Multimission Capability

Although the proposed electric propulsion system design has been optimized for the asteroid belt mission, its multimission capability is also of great interest. In particular, the design may be applied to both solar and out-of-the-ecliptic probes. For these latter missions the thruster array is designed to operate at constant (nominal) power throughout the mission.

For these two constant power missions, the reliability of the proposed propulsion system will be somewhat lower than that calculated for the asteroid mission. There are two basic reasons for this difference. First, the thrust period is longer for both the solar probe (6360 hours) and the out-of-the-ecliptic (13,440 hours) missions. Second, on constant power missions both thrusters operate for the full duration of the mission, while on decreasing power missions (such as the asteroid belt mission) thrusters turned off for impedance matching purposes are available as standbys. Table 6-10 summarizes the features of the electric propulsion system for solar probe and out-of-the-ecliptic missions. The standby switching relays and the propellant reservoir are included in the system characteristics summarized in Table 6-10.

Table 6-10. Multimission Characteristics - Asteroid
Belt Probe System Design

Characteristic	Solar Probe	Out-of-Ecliptic Probe
Thrust Period (hours)	6360	13440
System Reliability	0.968	0.925
System Mass, Kg (lb)	48.1 kg (105.8 lbs)	53.5 kg (117.7 lbs)

The propulsion system reliability for the solar and out-of-the-ecliptic probes can be increased by including extra redundancy in the system; there is a mass penalty involved. Table 6-11 reviews the increases in system mass and reliability when an additional standby thruster is included (the system now has two operating and two standby thrusters) in the electric propulsion system. The system features shown in Table 6-11 also reflect the additional switching necessary to connect the power conditioning panels to the two standby thrusters. Comparing the system reliabilities with one and two standby thrusters shows the use of two standby thrusters to be of questionable value because of the small reliability increase, especially for the solar probe mission. Figures 6-13 and 6-14, illustrating the variation of the system reliabilities with thruster failure rate, show the value of the extra redundant

6-29
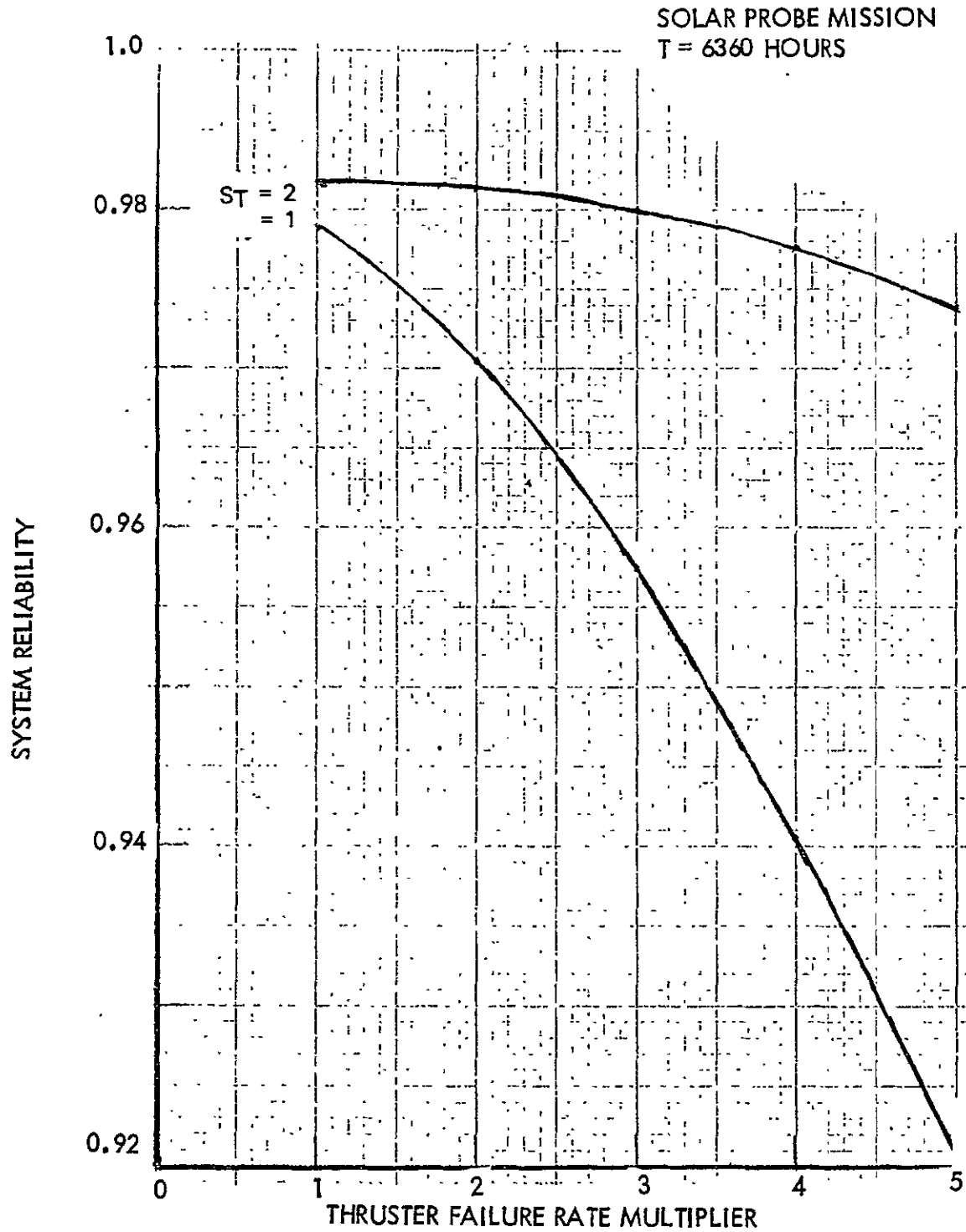
Figure 6-13. System Reliability Sensitivity to Thruster Failure-Rate
Multiplier - Solar Probe

6-30
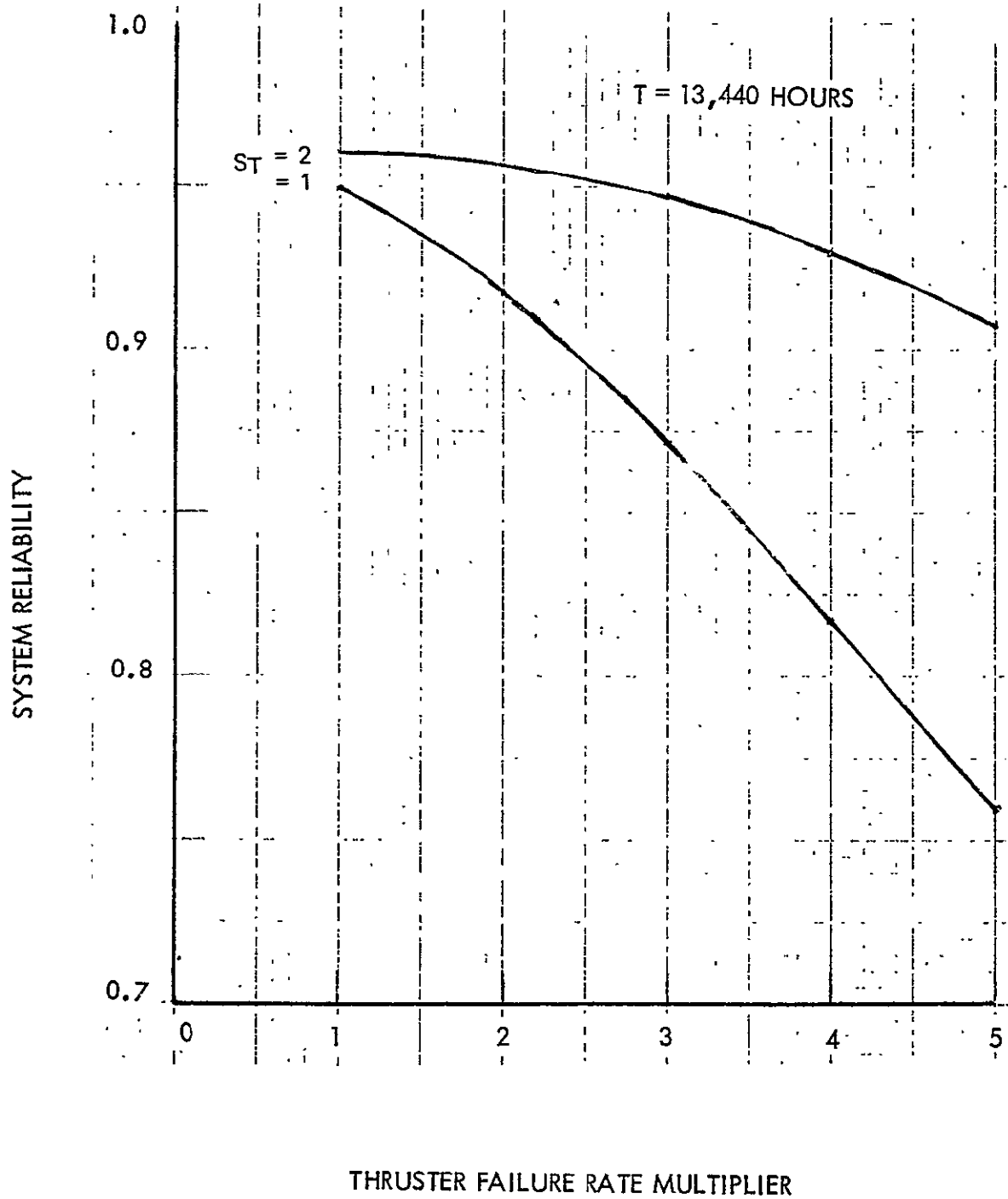
Figure 6-14. System Reliability Sensitivity to Thruster Failure-Rate
Multiplier - Out-of-Ecliptic Probe

6-31

thruster. For both the solar probe and the out-of-the-ecliptic missions, employing two standby thrusters ensures that the system reliability remains high even if the thruster module reliability is less than expected.

A means of achieving still higher system reliability than that shown in Table 6-11 is to carry a standby power conditioning panel (in addition to the two standby thrusters). This panel would be connected to one of the standby thrusters and be switchable to the other (as are the two normally operating power conditioning panels). The corresponding system features for a system with this design are summarized in Table 6-12. High reliability is achievable using this method, but a sizeable mass penalty is paid.

Table 6-11. System Characteristics With an
Additional Standby Thruster

Characteristic	Solar Probe	Out-of-Ecliptic Probe
Thrust period (hours)	6360	13440
System mass, kg (lb)	52.3 kg (115.1)	57.7 kg (126.9)
System reliability	0.971	0.936

Table 6-12. System Characteristics With a Standby
Power Conditioning Panel

Characteristic	Solar Probe	Out-of-Ecliptic Probe
System mass, kg (lb)	68.2 kg (150.0)	73.6 kg (161.9)
System reliability	0.989	0.972

MODULE DESIGNS

As a result of the computer studies described, the number, sizes, and designs of the subsystem modules to be used in the electrical propulsion system have been specified (with the exception of the reservoir subsystem, which was not included in the optimization). These module descriptions were based on the present scaling information used as an input to the computer program. To ensure that the final system design accurately reflects the

current state-of-the-art in hardware, the proposed module designs were reviewed and modified where appropriate. The weights and reliabilities of these final subsystem and module designs (those designs which satisfy the current state-of-the-art hardware criterion) were then reevaluated and reestimated. It is felt that although future improvements in subsystem designs are possible the credibility of the final results is presently established.

Thruster and Feed Subsystem

The thruster and feed subsystem module consists of a thruster module, three propellant vaporizers, and two high-voltage isolators. A schematic of the thruster and feed system module is shown in Figure 6-15. Two of the vaporizers supply mercury vapor to the hollow cathodes employed in the discharge chamber and neutralizer, while the third controls the main mercury flow to the discharge chamber. The two isolators, both of which are employed in the feedlines to the discharge chamber, are required to isolate the propellant reservoir electrically from the high-voltage thruster.

The isolator enters a plenum at the back of the thruster discharge chamber and passes through holes in the plenum into the discharge chamber. The hollow cathode, located on center in the rear of the discharge chamber, emits electrons and some neutral mercury atoms. The permanent magnets placed around the periphery of the thruster cylinder and the magnetic end plates produce a diverging axial magnetic field in the discharge chamber. The electrons spiral around these field lines and are electrostatically reflected from the ends of the discharge chamber. They can thus only reach the cylindrical anode by scattering collisions with residual gas (mercury) atoms, ions, or other electrons. These collisions ionize the mercury atoms in the discharge chamber creating the plasma from which the ions are extracted by the electrode system to form the beam. A mercury vapor hollow cathode neutralizer is used to neutralize the beam.

Figure 6-16 shows a 30-centimeter hollow cathode thruster. This thruster, like the proposed design, employs permanent magnets to produce the required discharge chamber magnetic field. The advantages of using permanent rather than electromagnets include weight, power efficiency, and reliability as well as a fully developed and proven 30-centimeter thruster design. Its main disadvantage is the resulting residual magnetic field which can potentially interfere with scientific measurements. Incorporation of electromagnets in the thruster could probably be accomplished without difficulty. Such a decision should include consideration of the results of specific propulsion system/spacecraft interaction studies.

The detailed operating characteristics and performance of the proposed thruster module are listed in Table 6-13, the physical description in Table 6-14.

6-33
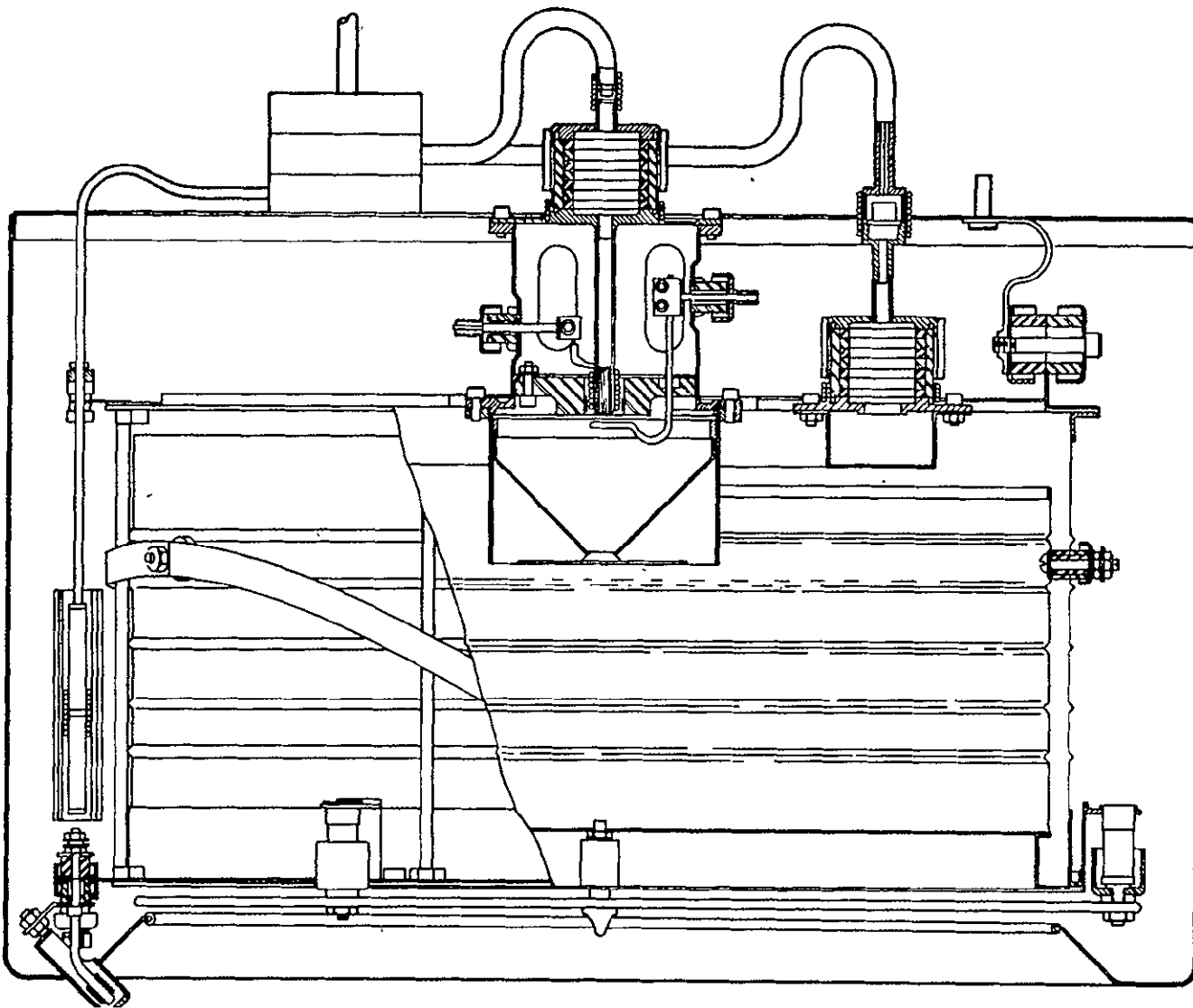
Figure 6-15.   Thruster and Feed Subsystem Module

Space Division
North American Rockwell
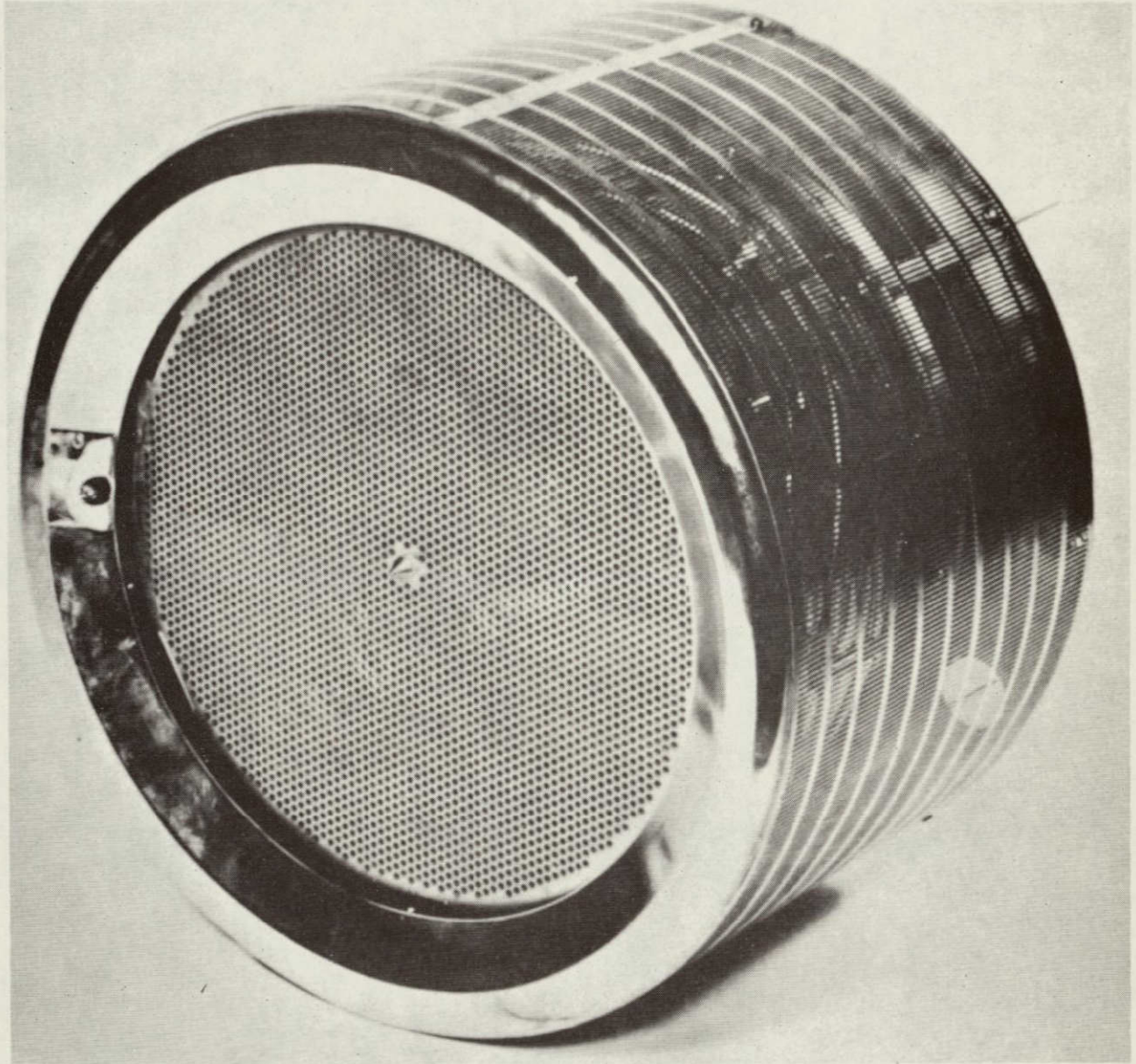
Figure 6-16.   Thirty-Centimeter Thruster

Table 6-13. Thruster Operation Parameters

Characteristic	Value
Specific impulse, sec	3500
Input thruster power, watts	3623
Thruster beam power, watts	3046
Power efficiency (at rated power)	85.3
Discharge losses (at rated power), eV/ion	200.
Propellant utilization efficiency	85
Acceleration-deceleration ratio	2.5
Beam current, amps	1.8
Beam potential, volts	1696
Thruster power losses, watts	
Discharge	360.0
Cathode and isolator heaters	54.9
Cathode keeper	2.2
Accelerator	77.0
Neutralizer heater and vaporizer	22.8
Neutralizer keeper	2.2
Vaporizer	9.7
Cathode vaporizer	5.2
Neutralizer bias	44.9

Table 6-14. Thruster Physical Description

Measurement	Value
Thruster and feed system mass, kg (lb)	3.97 (8.75)
Anode diameter, cm (in.)	30.0 (11.8)
Outside diameter, cm (in.)	40.0 (15.7)
Thruster length, cm (in.)	27 (10.6)
Accelerator electrode thickness, cm (in.)	0.128 (.0504)

The cathode vapor isolator and the main thruster vapor isolator are shown in Figure 6-15, the thruster and feed system schematic. The two isolators are identical except for slight differences in mounting requirements. The isolator design for the main thruster mercury vapor flow has been adopted for convenience for the cathode isolator. However, because of the smaller flow required by the cathode, it should be possible to design a slightly smaller isolator for it. Pertinent physical dimensions of the isolators are given in Table 6-15.

Table 6-15. Isolator Dimensions

Characteristic	Number
Number of potential dropping screens	10
Inside diameter, cm (in.)	2.00 (.787)
Outside diameter (except mounting flange), cm (in.)	3.3 (1.3)
Isolator chamber outside length, cm (in.)	3.99 (1.57)

Figure 6-17 is a schematic of the vaporizer furnishing the main mercury flow to the discharge chamber; its physical dimensions are given in Table 6-16.

Table 6-16. Vaporizer Dimensions

Dimension	Size
Chamber length, cm (in.)	1.78 (.7)
Top hat length, cm (in.)	0.625 (.25)
Chamber diameter, cm (in.)	1.40 (.55)

Figure 6-18 is a schematic of the design used for the neutralizer vaporizer and the thruster cathode vaporizer. These two vaporizers are identical except for length. Pertinent dimensions summarizing the physical design are also given in Figure 6-18.
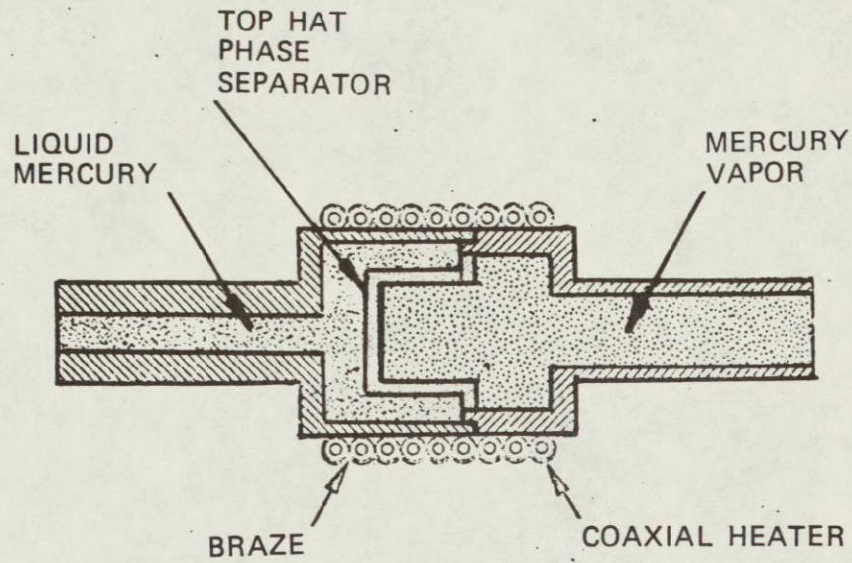
Figure 6-17. Vaporizer
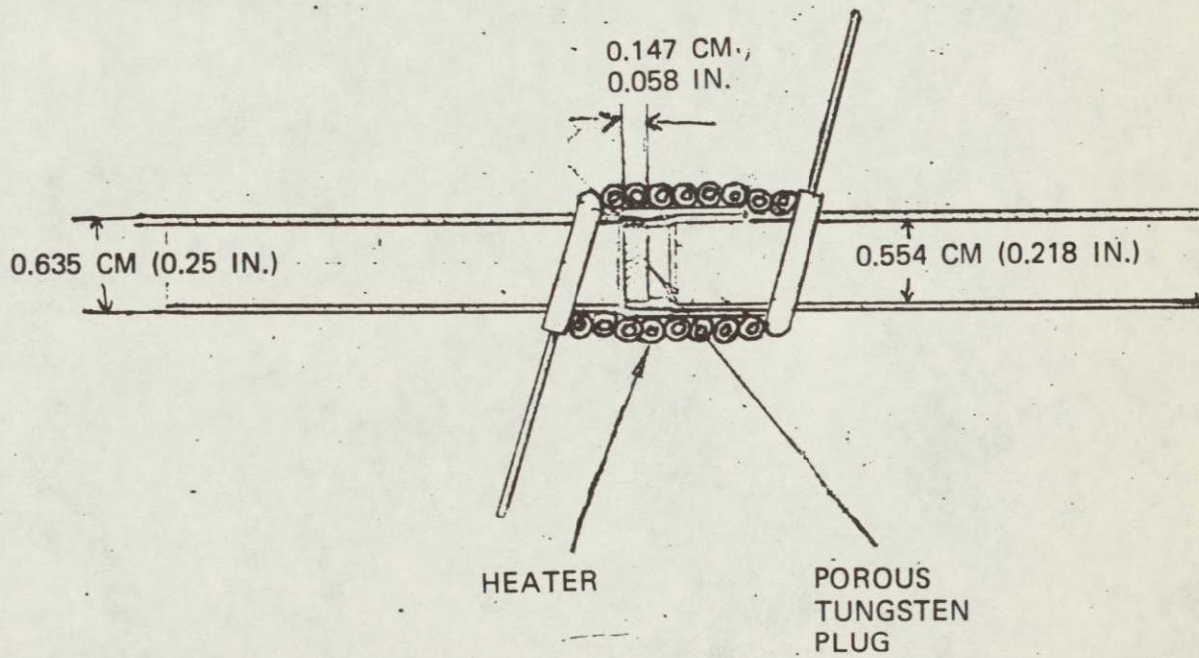
Figure 6-18. Neutralizer and Thruster Cathode Vaporizer Design

6-38

Mercury Propellant Reservoir

The reservoir tanks must store liquid mercury reliably under controlled pressure (approximately two atmospheres) for the duration of the mission including the launch phase. The mercury requirement for the asteroid probe mission is 104 kilograms. A single tank is proposed to hold the propellant in the present application, since use of multiple tanks to contain the required propellant would impose a reliability penalty. Analysis of the spacecraft structure indicates that this amount of propellant may be carried in a single tank without structural problems.

Figure 6-19 illustrates the configuration chosen for the propellant tank. This design is representative of the reservoir concepts employed for the NASA/LRC SERT II test flight scheduled for early 1970 and for the JPL propulsion system development programs. The design consists of a spherical metal tank divided into two compartments by an elastomeric bladder. One side is filled with mercury, and the bladder is deformed so as to leave a relatively small void on the other side. This void is then filled with a liquid (typically freon) in equilibrium with its vapor, and sealed. The pressure is then determined by the ambient temperature and the vapor pressure behavior of the driving liquid provided some material always remains in the liquid phase. The temperature may be artificially controlled if necessary. However, the operating pressure range over which the feed system will give satisfactory performance is such that it is possible a driving fluid may be chosen so that the ambient vehicle temperature will be sufficient.

A valve is placed on the propellant tank to avoid launching with propellant lines loaded with mercury. This valve (squib activated) would be opened before thruster on commands. An orifice restricts the propellant flow to prevent the momentum of the pressurized mercury from hammering and damaging the porous refractory metal vaporizer. (There will be no gas cushion in the propellant feedlines because of bleedout in space through the porous vaporizer).

Jet Propulsion Laboratories has reported tests of a reservoir system similar to the one shown in Figure 6-20. Figure 6-21 shows the JPL reservoir. A positive expulsion-type tank design was developed utilizing a hemispherical neoprene bladder. The pressurization system was formed by attaching a small reservoir of liquid Freon 113 on the gas side of the bladder. The mercury side of each tank was connected to a common manifold through valves.

A neoprene bladder was used to satisfy compatibility requirements with mercury and Freon 113. Tests were performed to verify mercury compatibility by submerging stretched neoprene samples in a pan of mercury
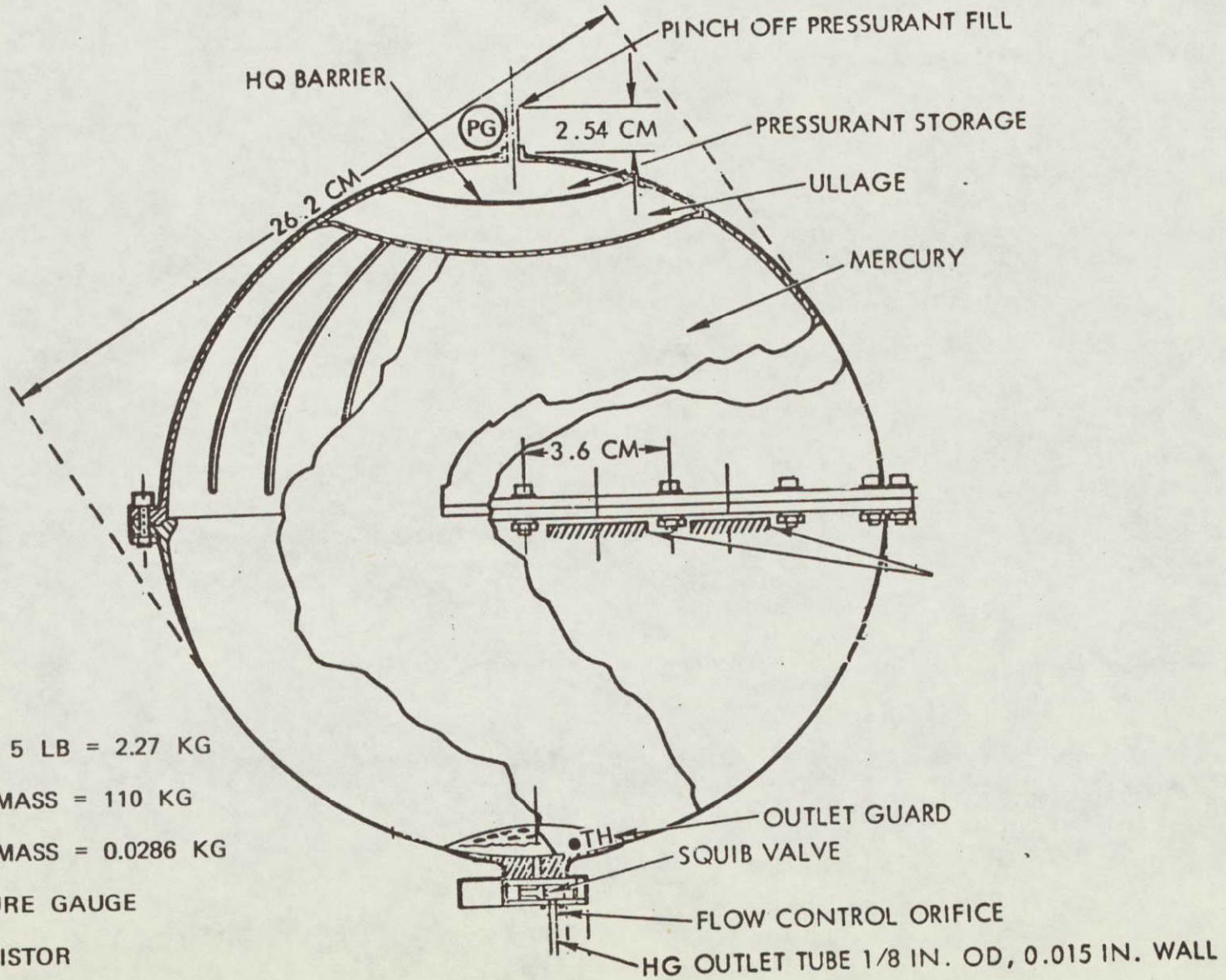
PINCH OFF PRESSURANT FILL

HQ BARRIER

PG

2.54 CM

PRESSURANT STORAGE

26.2 CM

ULLAGE

MERCURY

3.6 CM

TANK MASS = 5 LB = 2.27 KG

PROPELLANT MASS = 110 KG

PRESSURANT MASS = 0.0286 KG

PG = PRESSURE GAUGE

•TH = THERMISTOR

•TH

OUTLET GUARD

SQUIB VALVE

FLOW CONTROL ORIFICE

HG OUTLET TUBE 1/8 IN. OD, 0.015 IN. WALL

Figure 6-19. Mercury Propellant Reservoir
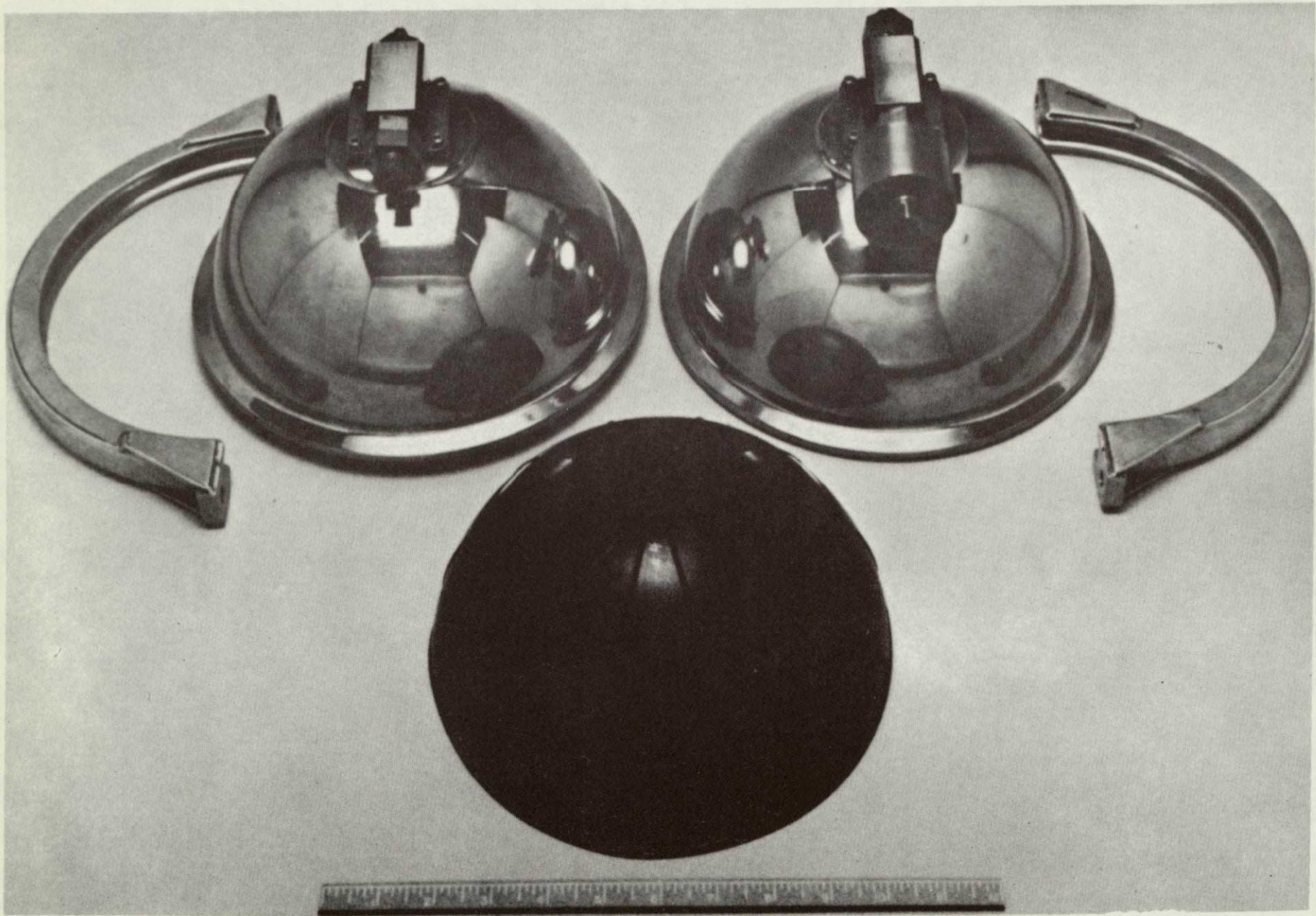
Figure 6-20.   Mercury Propellant Tanks
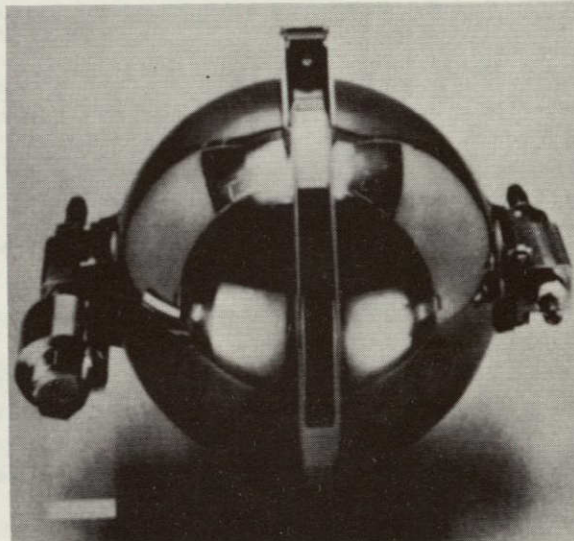
Figure 6-21.   Mercury Reservoir

for 2800 hours. No sample failures occurred and, after initial stretching, no further change in elongation occurred during the test period.

To check the permeability of neoprene to Freon 113, a rough test was performed. A 0.060-inch-thick neoprene sheet was clamped to a 3-inch-diameter hemisphere. A halogen detector was used to test for leakage, but no Freon was detected. The hemisphere was still pressurized after about 4000 hours, indicating that the Freon-neoprene combination is suitable.

The pressure supplied by the Freon 113 depends on the temperature. For vaporizers typically used at this time, the useful pressure ranges from 1 to 3 atmospheres at temperatures of approximately 100 to 200 F. If necessary, the useful pressure range can be modified either by choosing a different material for the vaporizer or for the pressurizing gas.

The proposed propellant tank was designed assuming an operating pressure of 45 psi with 43 percent safety factor. Analysis of prospective tank materials showed that lightweight propellant tanks could be made of 6061 aluminum, 304 LC stainless steel, or 6A1-4V titanium. Stainless steel has been chosen for the present application because of reported attacks on both aluminum and titanium by mercury.

Table 6-17 lists dimensions of the propellant tank. The actual amount of propellant carried on the mission is that required for the mission (104 kilograms) plus a 2 percent contingency for guidance and a 3 percent contingency for tank propellant expulsion. The total propellant mass is then 109.2 kilograms. The propellant tank was sized to carry a 10 percent larger propellant load to allow for possible growth in propellant requirements (dispersion allowance). The tank mass is 2.04 percent of the mass of the tank and propellant. This relatively low tank-to-propellant ratio is made possible by the high density of mercury.

Table 6-17. Tank Dimensions

Dimension	Value
Propellant mass, kg (lb)	109.2 kg (241 lb)
Tank mass, kg (lb)	2.27 kg (5.0 lb)
Tank volume, cubic meters (cu. in.)	0.00944 (576)
Mercury volume, cubic meters (cu. in.)	0.00806 (492)
Ullage (percent)	5
Misc (percent)	1
Dispersion allowance (percent)	10
Tank diameter, meters (in.)	0.262 meter (10.3 in.)
Tank reliability	0.9926

Power Conditioning and Control System

The proposed 30-centimeter thruster nominally requires approximately 3.62 kilowatts of conditioned power, from low ac voltage to high dc voltage, regulated for wide variation of solar array voltages, and controlled over large ranges to maintain and vary thrust. In addition, some of the thruster circuits may make short-term demands (on the order of minutes) in excess of their nominal requirements, and the supplies furnishing power to these circuits must be sized to handle these demands. The power conditioning is therefore designed for an electrical capability of 3.9 kilowatts. As a conservative design measure, the thermal design of the panels is also based on this higher number. The solar panel bus voltage range specified for this study was 40-80v.

Analogous to the thruster and feed system, the design of a PC&C panel was reviewed and modified where appropriate to ensure that design reflects the state-of-the-art. As a result, slight differences exist between the panel design described in this section and the design given as an output of the computer program.

The high premium in mission performance of high efficiency, low weight, and long-term reliability has resulted, in previous contracts with NASA and JPL, in the development of the modular-inverter technique now proposed for the asteroid mission. The modular-inverter technique is characterized by the use of electrically and mechanically discrete, intermediate-power inverters (300-500 watts), connected together to provide power in the multikilowatt range. The advantages accruing from this technique are as follows:

1. Limited power per inverter permits use of high-speed power transistors, permitting high frequency (10 KHz) inversion with acceptable switching loss, thereby allowing use of lightweight transformers

2. Limited power per inverter permits use of low core-loss, ferrite transformers, for high frequency compatibility

3. Limited power per inverter permits low heat-loss density, with associated low weight heat conduction paths to radiating area (each module is self-sufficient in radiating area)

4. Low weight inverter modules and associated distributed mass in total structure permits a low weight supporting frame

5. Multiple inverters in a single supply permit high reliability by fractional redundancy, whereby one redundant or standby inverter may replace any failed inverter, at low cost in weight

6. Multiple inverters in a single supply permit use of staggered phase summation of outputs for low ripple, low weight filters, low EMI

7. Low complexity per module permits convenient replacement, using functional isolation technique, rather than component isolation, during the test phase

The solar array voltage, varying from 40 to 80 volts on a typical mission (only 40 to 60 volts for the asteroid probe), must be converted to miscellaneous high and low voltages. The output voltages must be held to within 1 percent for varying line and load. The method of voltage conversion for dc-dc supplies, proposed for this mission, is based on extensive successful experience on previous NASA and JPL thruster systems. It is that of the parallel transistor, pulse-width modulated, fixed-frequency inverter. This technique is used for the high power dc-dc supplies, such as the screen and arc (discharge) supplies, with 10 KHz inverter frequency. For the low-power dc-ac supplies, where a multiplicity of regulated and controlled outputs in the 5 to 50 watt range are required, the lower efficiency is justified by the lower complexity of a single series pulse-width-modulated dc regulator and square-wave 5 KHz inverter, supplying multiple magnetic-amplifier controllers. The choice of 5 KHz is made here since it is the maximum frequency compatible with acceptable inductive ac line drops between power conditioner and thruster.

Control logic is provided for operating the thruster in a mode which gives maximum fuel utilization and controllable thrust, but which requires closed-loop coupling between various supplies. The necessary sequencing and programming for turn-on and recycle after high-voltage arcs and the use of a staggered phase technique place a high premium on the use of integrated microcircuits in the control section. This technique permits a high degree of circuit complexity with minimum parts, maximum reliability, and minimum weight. Experience in previous development contracts has shown that microcircuits may be adequately protected against transients due to high voltage arcs. Therefore, this circuit technique is proposed for the control logic on the asteroid mission.

A block diagram of the PC&C panel design is shown in Figure 6-22. Parallel redundancy is used in the arc and screen supplies; no redundancy is furnished for the remaining supply modules. Two functional subgroups can be distinguished in the panel: a high-power, high-voltage group, and a low-power, low-voltage group.

The low-power, low-voltage group consists of the various heater and keeper supplies. During thruster start-up all supplies in this group are

6-45
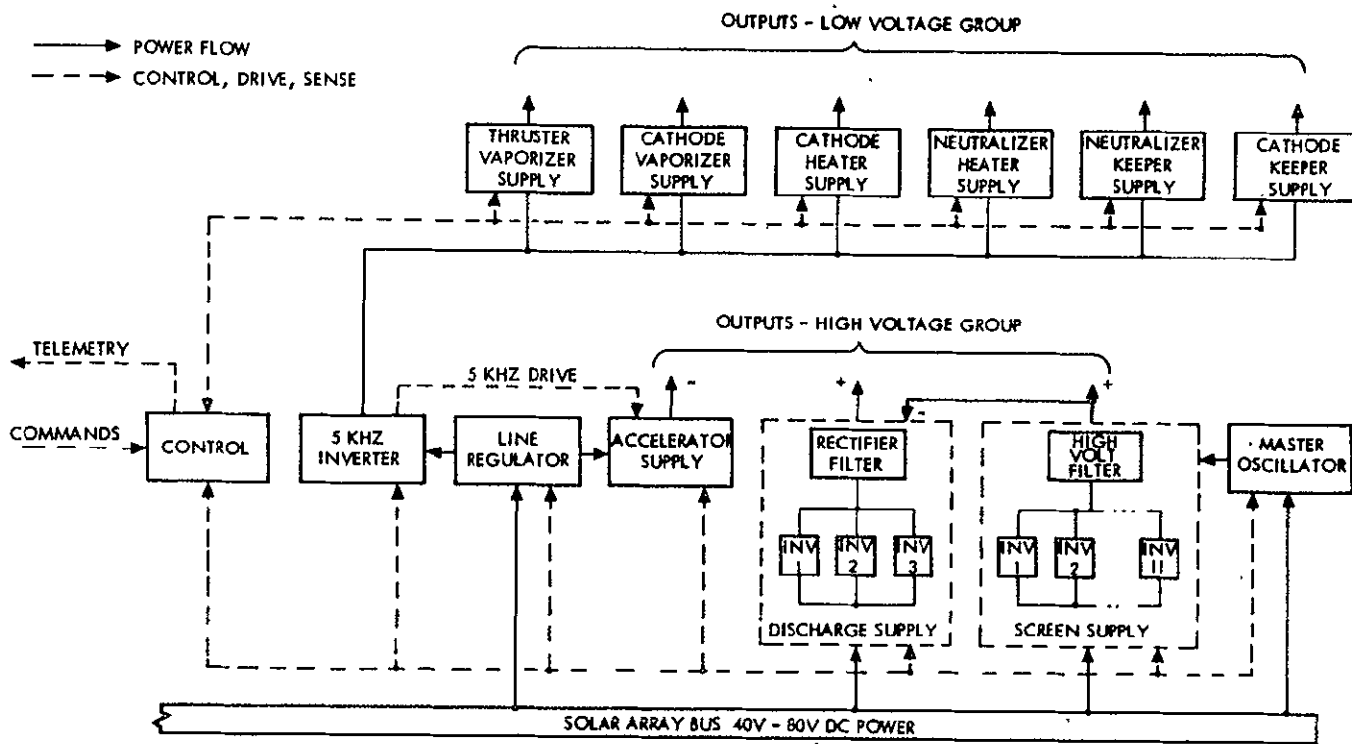
Figure 6-22. Power Conditioning Panel Electrical Block Diagram

Space Division
North American Rockwell

turned on before the high-voltage group. These supplies are all on the regulated 5 KHz bus from the 5 KHz inverter, supplied in turn from the dc-dc line regulator. The various heater supplies are magnetic-amplifier controlled to provide programmed ac currents (rms-controlled, pulse-width-modulated). The two keeper supplies are reactor current-limited to provide 300 volt dc starting voltage at no load, dropping to zero volts at 1 ampere.

The high-voltage group consists of the screen, accelerator, and arc (discharge) supplies. The screen supply provides 1700 volts at 1.2 amperes, the accelerator supply provides 2540 volts at 40 milliamperes, and the arc supply provides 36 volts at 15 amperes, referenced to the screen. The accelerator supply is a single, square-wave converter, converting regulated 35-volts dc to 2540-volts dc, with a drive switching frequency of 5 KHz supplied from the 5 KHz inverter. On an overload due to arcs, the 5 KHz drive is cut off and recycled on automatically. The arc (discharge) supply consists of three 10 KHz inverters, supplied in parallel from the solar array bus, with ac outputs in series to a rectifier-filter. The inverters are pulse-width modulated synchronously at a fixed frequency, controlled by output voltage and current feedback to maintain constant output with variable solar array voltage. Voltage is held constant up to a programmed current, at which value the supply delivers constant current. One of the three inverters may fail without loss in output, since the remaining two inverters will advance in pulse-width to compensate. The output transformer of the failed inverter is shorted automatically on failure by a relay contact to bypass the failed inverter. The screen supply has eleven dc-to-dc converters, supplied in parallel from the solar array bus, with unfiltered dc outputs in series to a high-voltage filter. The total voltage is sensed, compared to a fixed reference, and the difference applied to a single pulse-width modulator driving all inverters through a staggered 22-phase delay network. At the start of the mission (low solar array voltage), one inverter may fail without loss of output voltage. At the end of the mission, two inverters may fail.

The total system, as shown, is programmed on and off, recycled after overload trips, and programmed for commanded screen current by variation of heater currents, by the control module.

The master oscillator provides the square-wave drives for all inverters, supplying the system with synchronized 5 KHz, 10 KHz, 20 KHz, together with the pulse-wave modulated staggered-phase drive for the screen system.

Schematics for the major power circuits utilized in the power conditioning panel are shown in Figures 6-23 through 6-33.
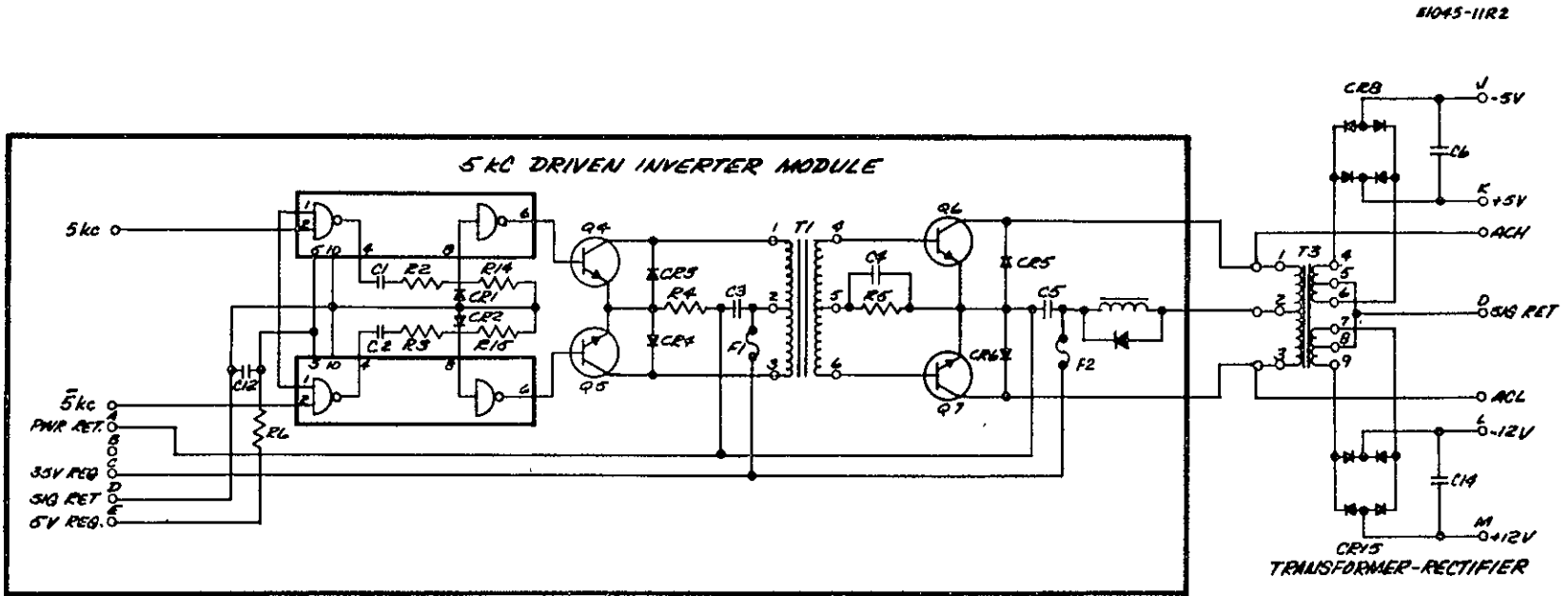
Figure 6-23. KiloHertz Converter

Figure 6-24.   Line Regulator

E1045-8R1
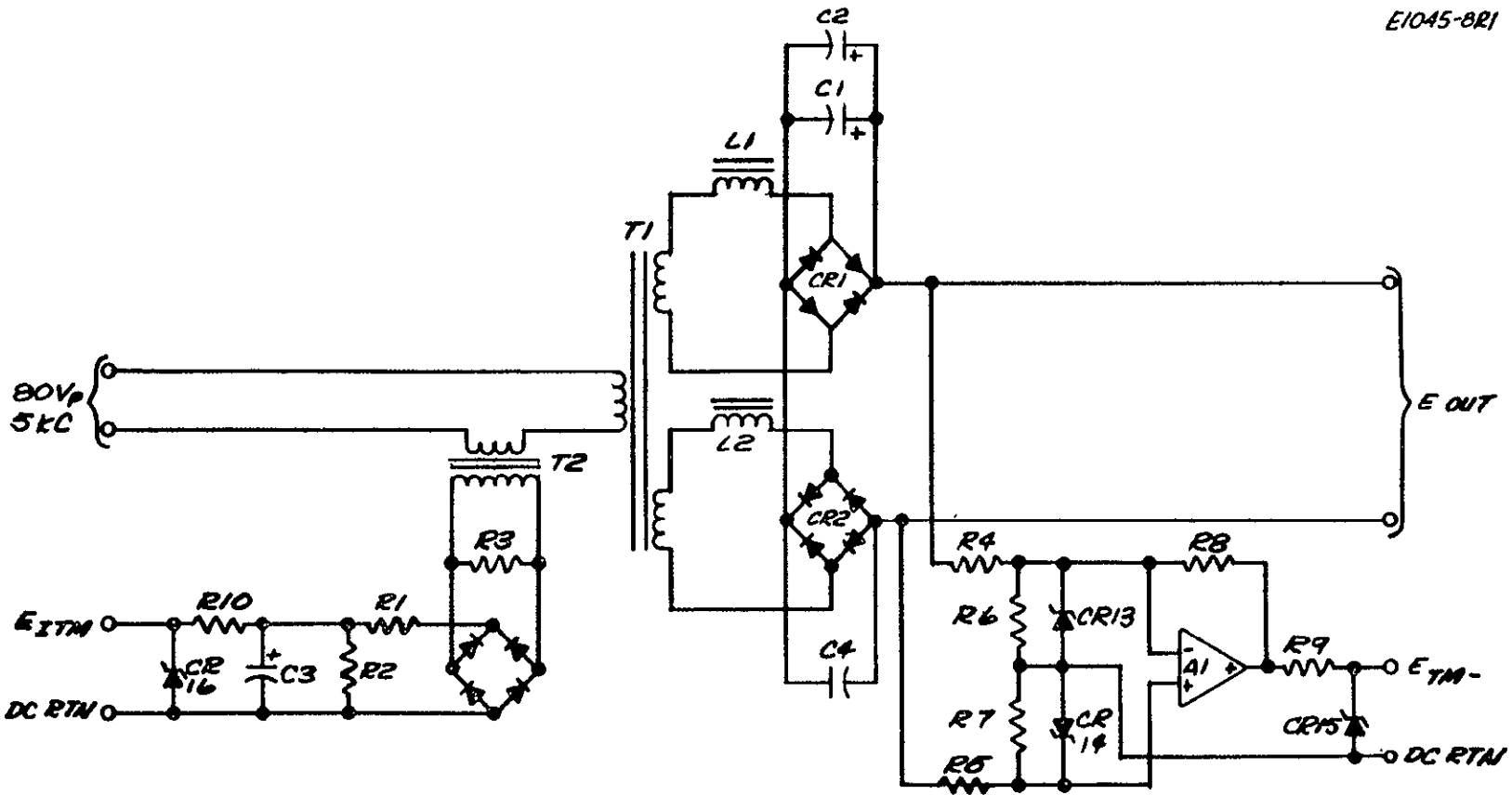
Figure 6-25. Cathode and Neutralizer Keepers

Space Division.
North American Rockwell
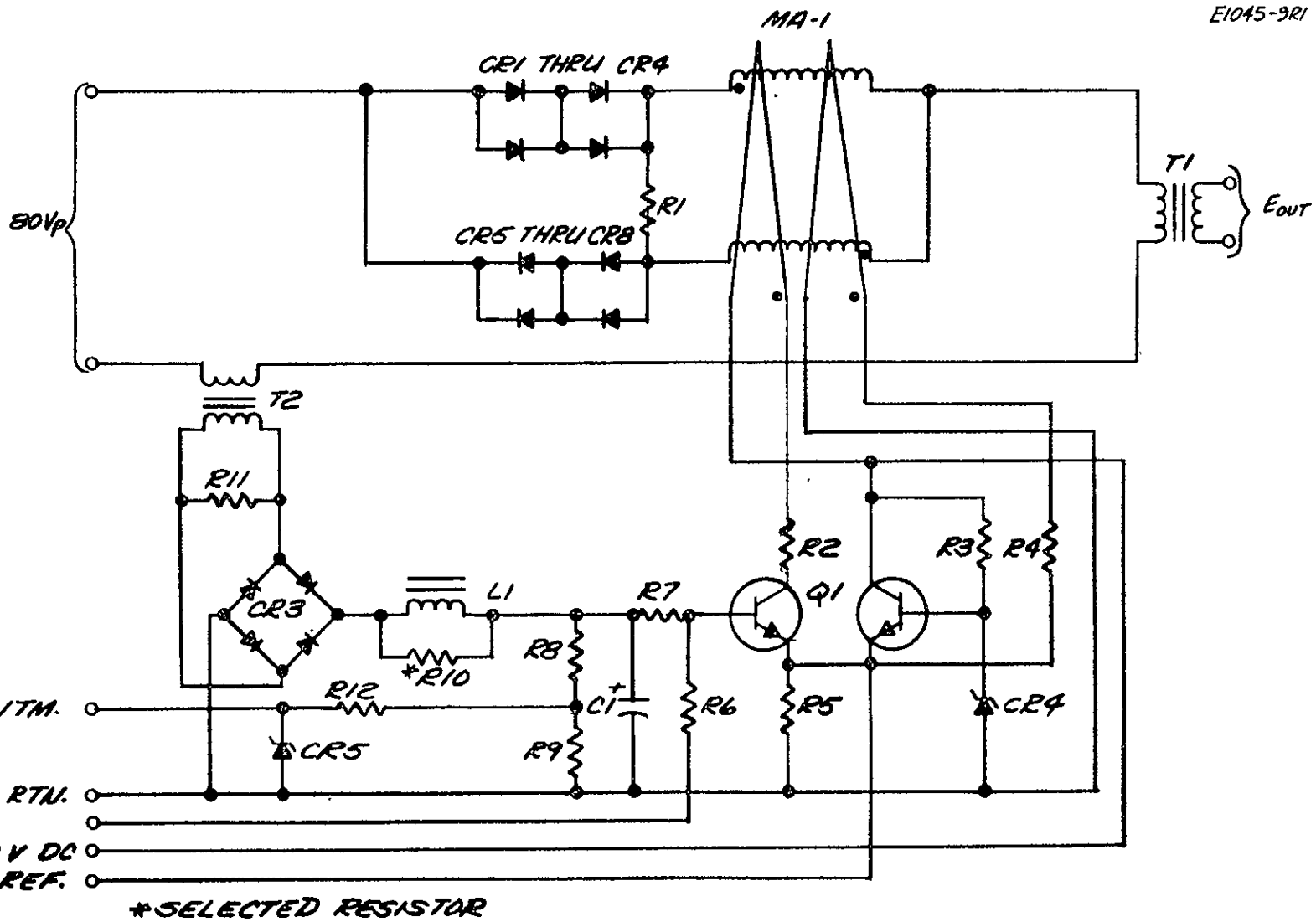
Figure 6-26. Vaporizer, Isolator, Neutralizer, and Cathode Heaters
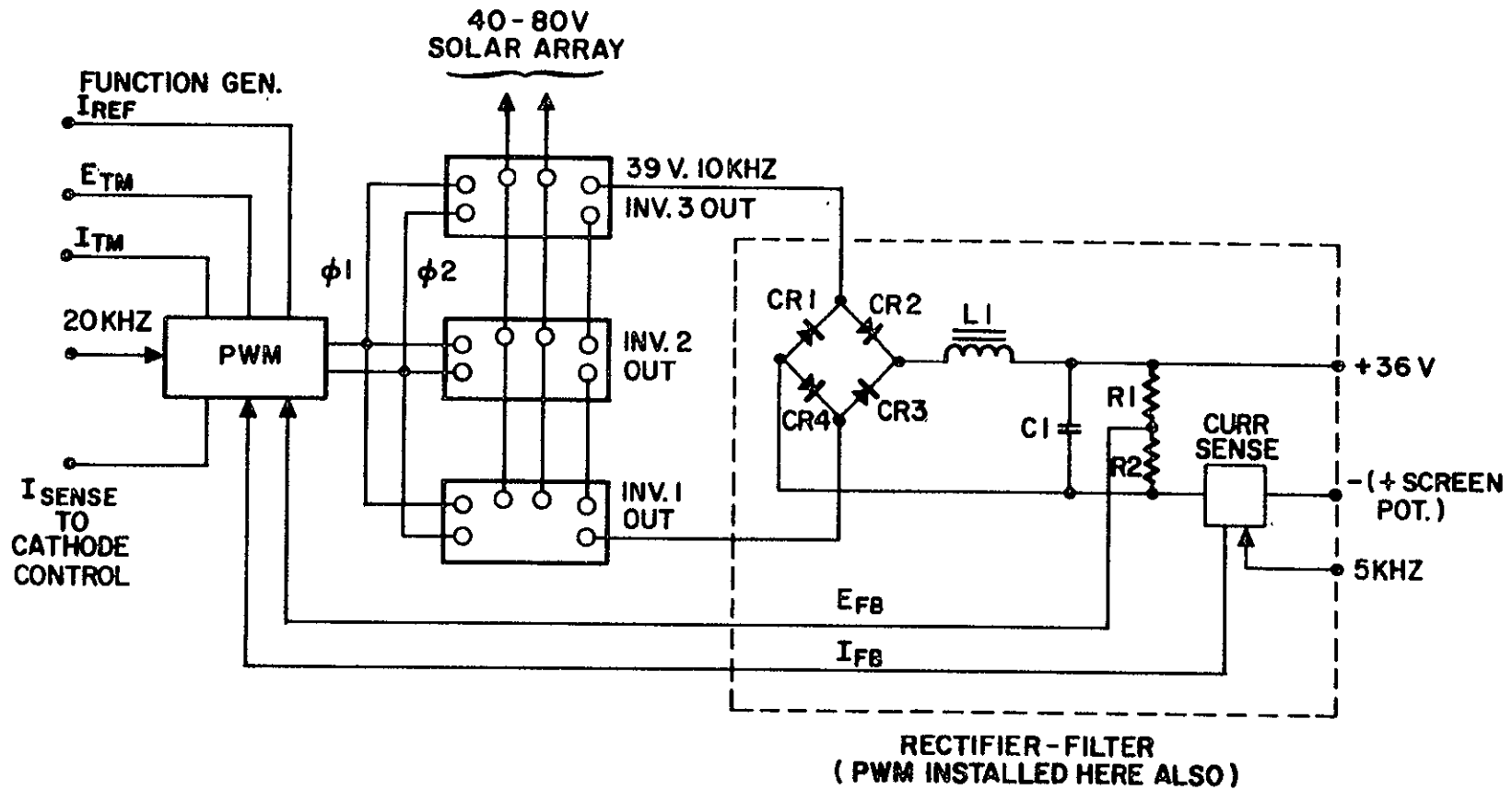
Figure 6-27. Arc (Discharge) Supply
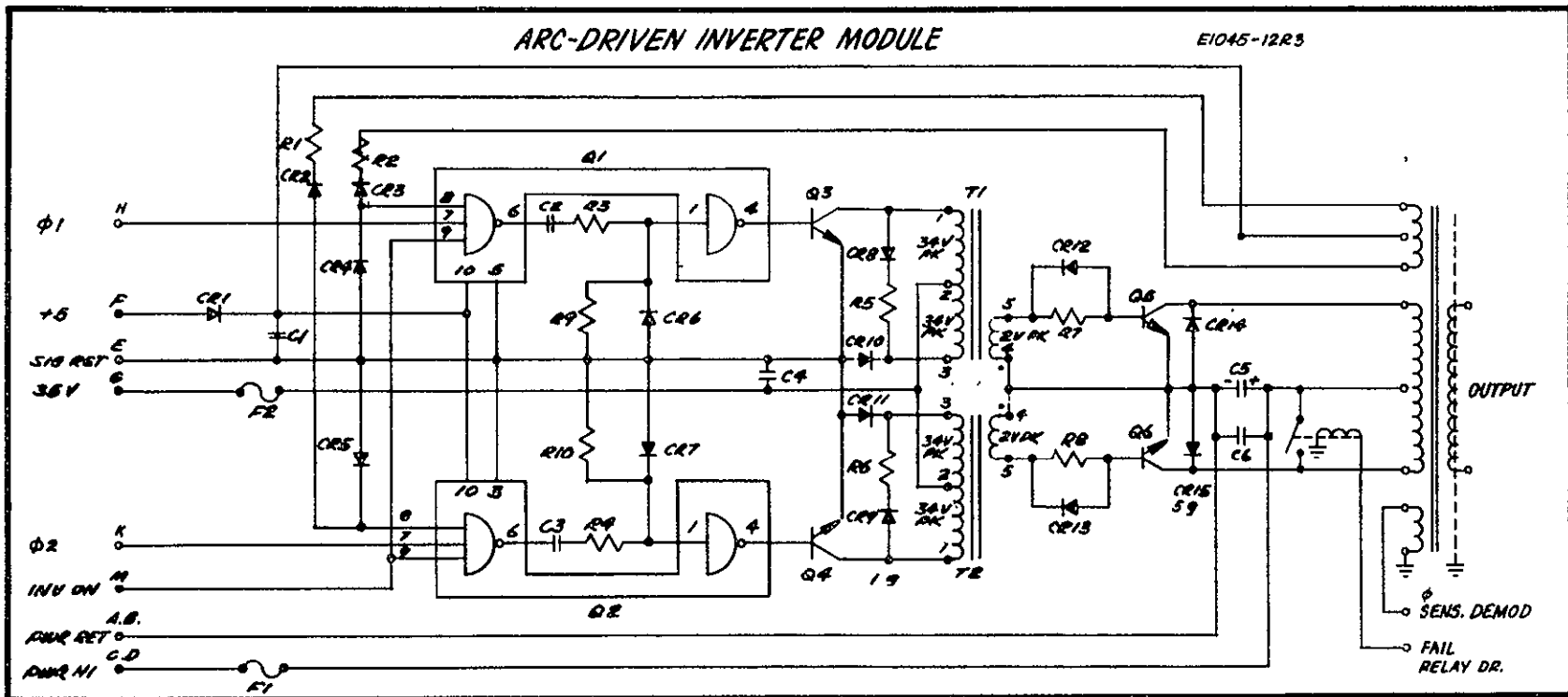
Figure 6-28. Arc (Discharge) Inverter Module
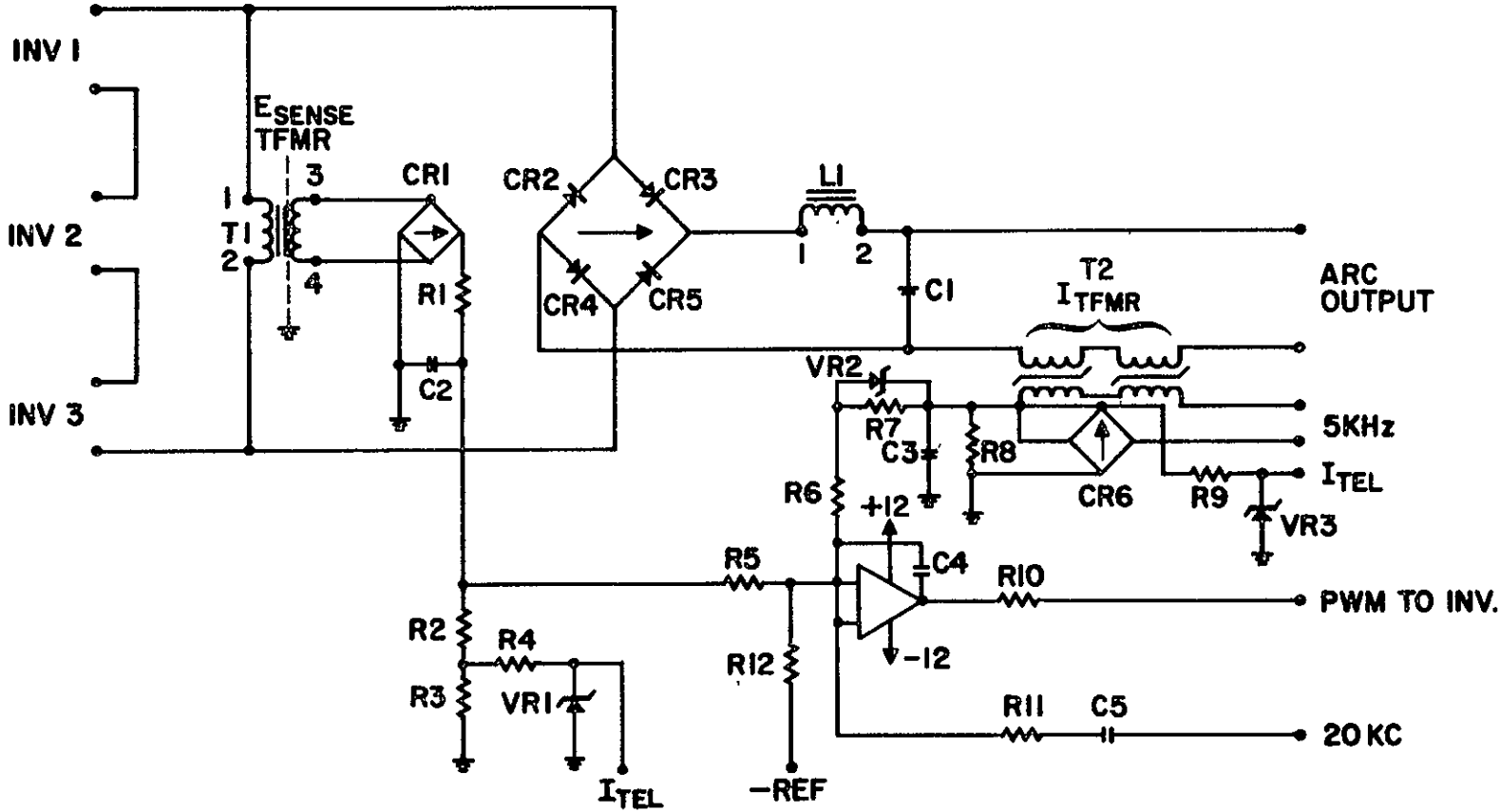
Figure 6-29. Arc Rectifier Filter
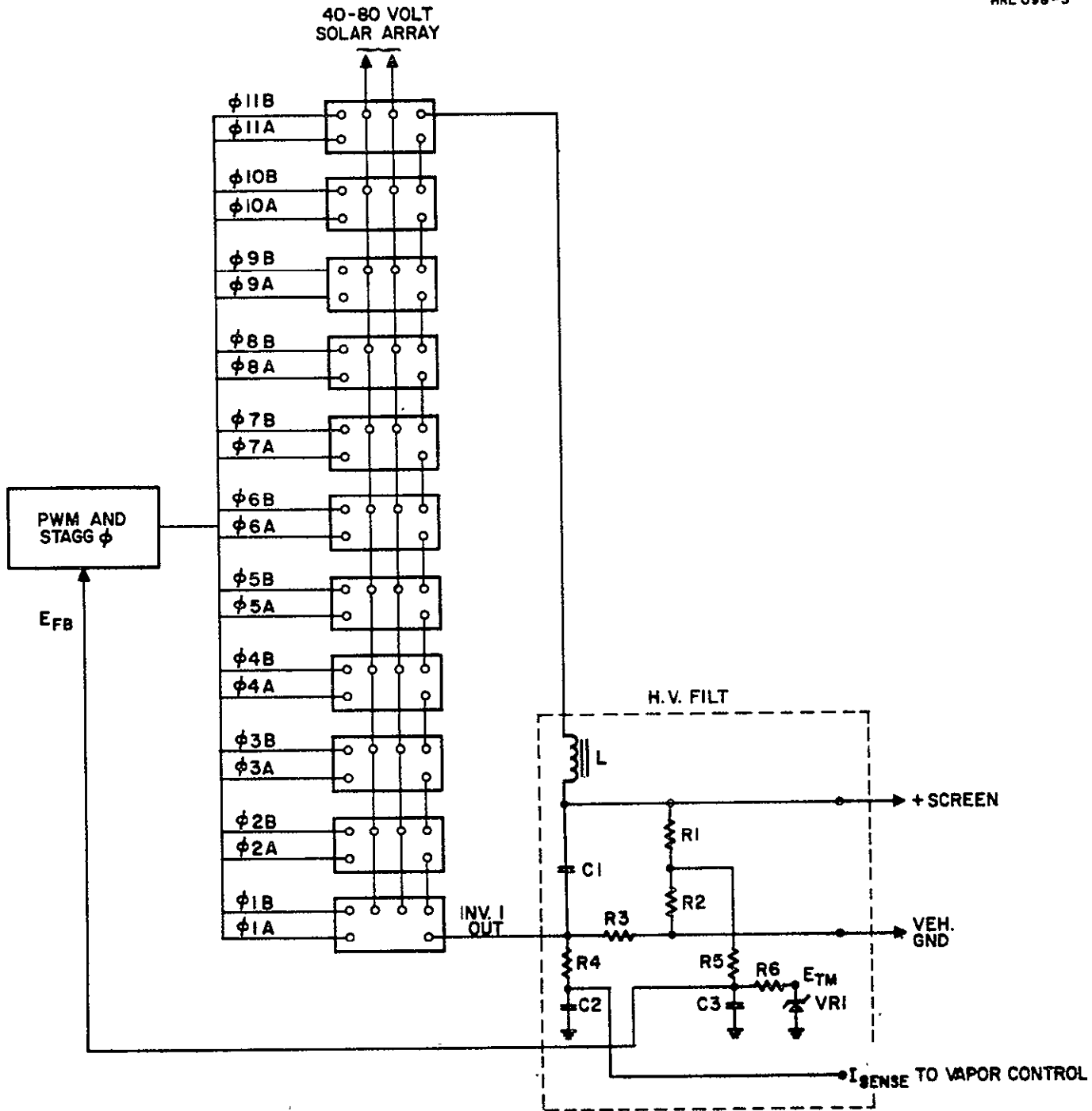
Figure 6-30. Screen Supply
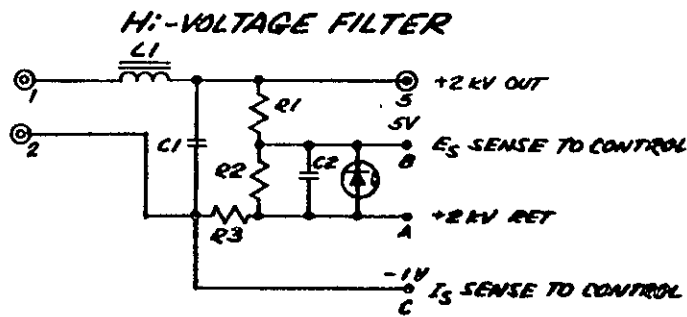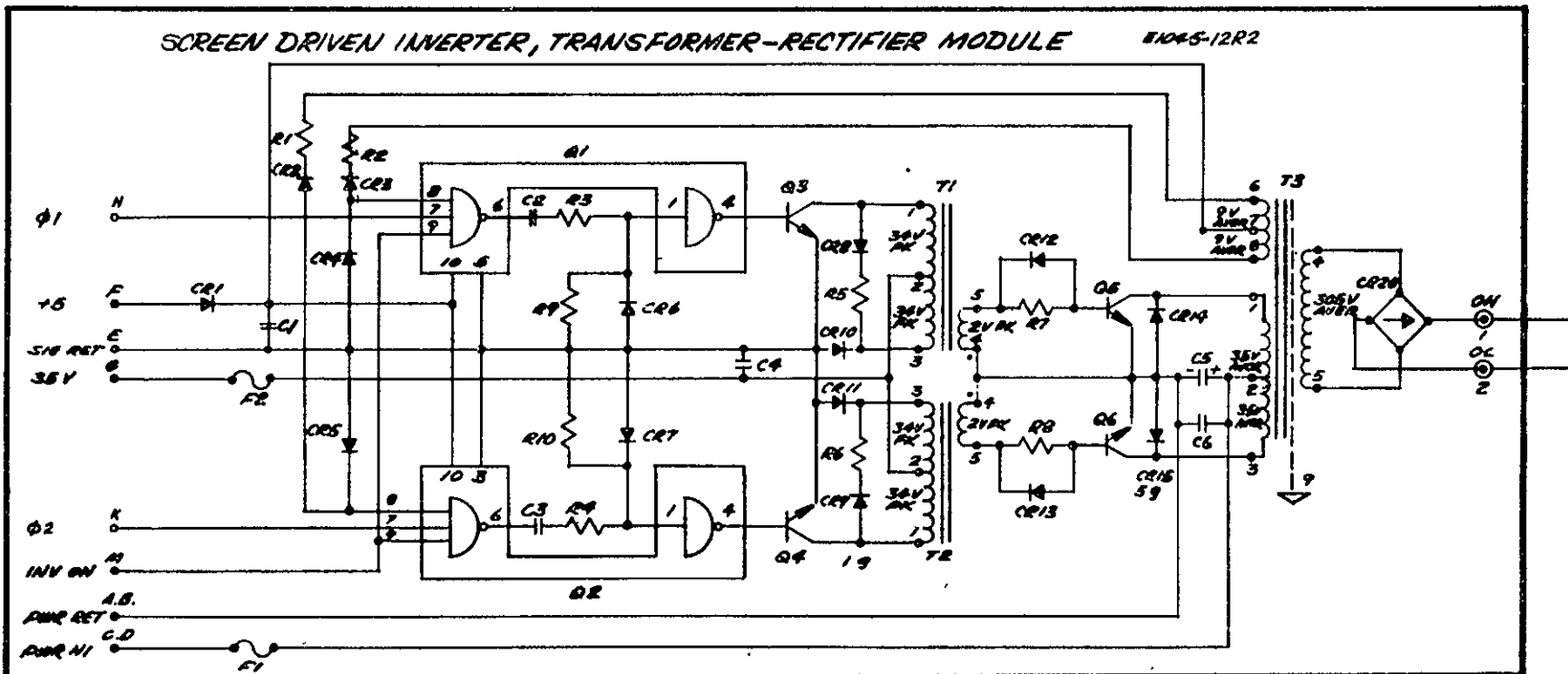
Figure 6-31. Screen Filter and Inverter Module

HRL 098-5
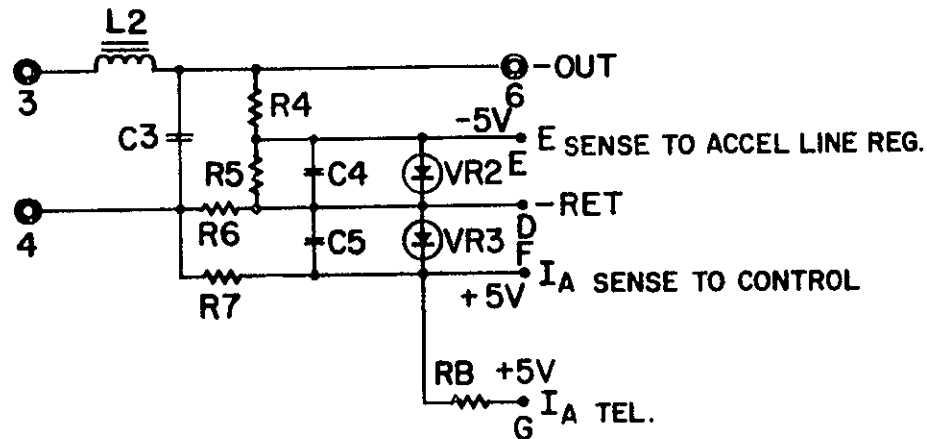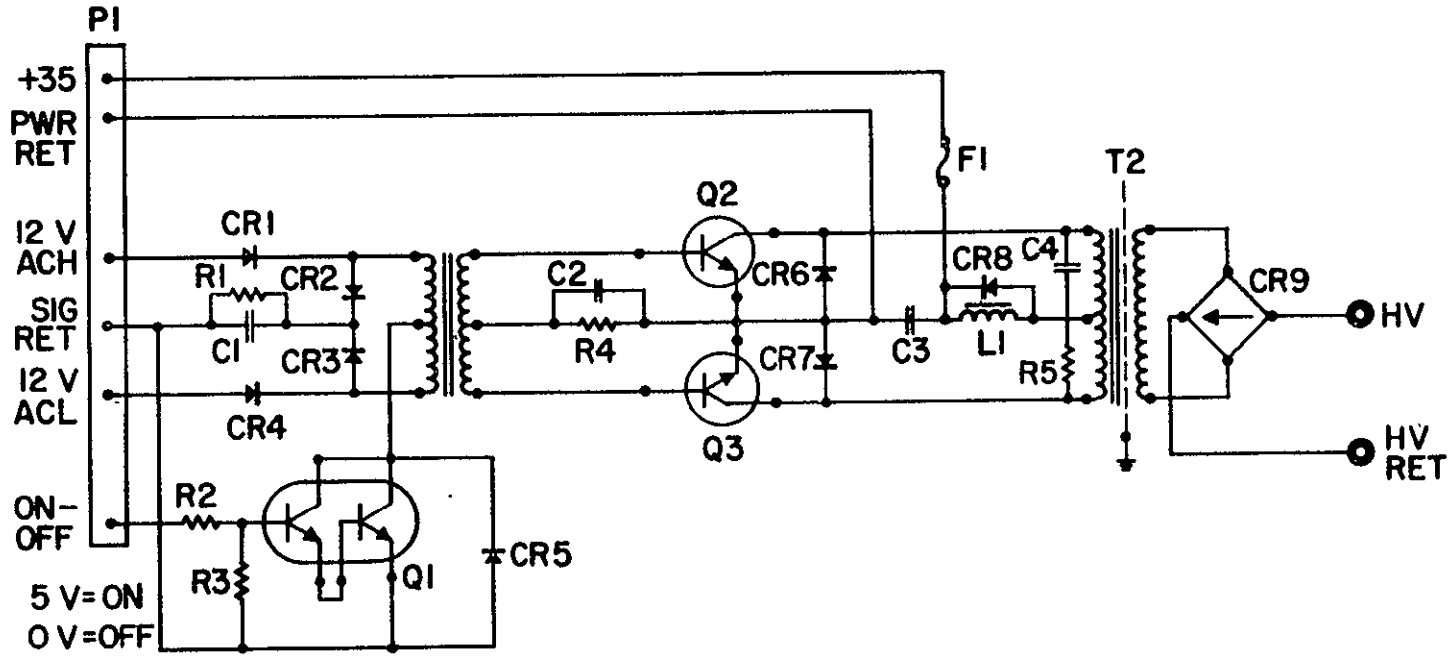
Figure 6-32. Accelerator Supply

Space Division
North American Rockwell
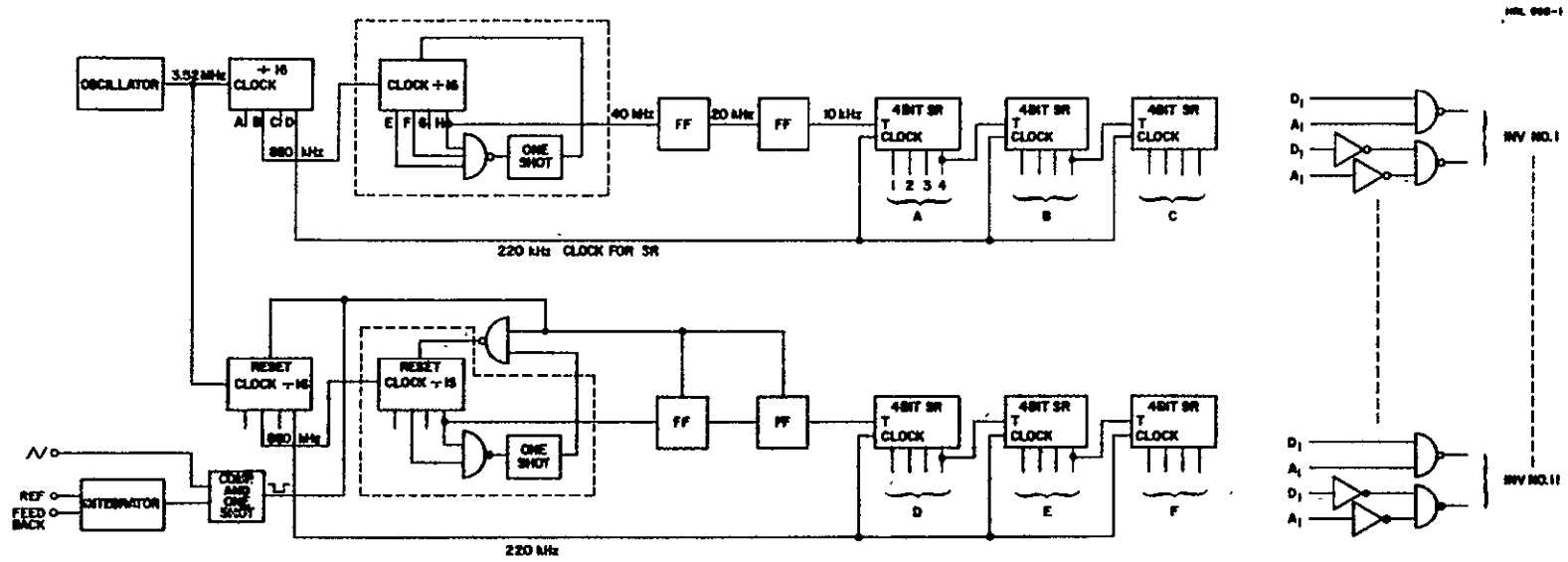
Figure 6-33. Master Oscillator and Phase Shifter

Space Division
North American Rockwell

Figure 6-34 outlines the physical construction of a PC&C panel. The required thickness of the module array with cover is only four inches, since almost all components may be mounted directly on the radiating chassis plates, and the largest component is less than 2-1/2-inches high. To minimize vehicle and power-conditioner wiring weight, input commands, telemetry, and power are brought into one edge of the assembly, and output voltages out from the opposite edge. Twenty-four discrete module assemblies are used in the array, mounted on an "egg-crate" type frame, made up of a lightweight I-beam section behind module edges, and to which the modules are fastened by screws for replacement during test. This arrangement also permits a high degree of repetitive manufacturing steps which also may take place in parallel. The individual modules are sized for self-sufficient radiating area, eliminating the need for good thermal interface with structure. The entire assembly is mounted to the vehicle structure with screws along four edges, and with two screws on center-line of rear face. The completed assembly, with its rear cover, is electrically "dead" in accessible areas for personnel protection during testing. The enclosed structure also minimizes EMI, yet has sufficient open area in the grilled cover to permit free out-gassing, preventing intermediate pressures from producing a Paschen type voltage breakdown. The completely opaque radiating face acts as a nuclear-radiation shield for the modest radiation incident to an interplanetary mission.

Based on experience with similar systems recently built, the following performance is anticipated with a solar array voltage varying from 40 to 80 volts:

Weight - 34 to 36 pounds
Efficiency - 90-91 percent
Reliability - 0.96 for 10,000 hours
Regulation - ±1 percent on outputs for 40 to 80 volt line
Control - ±1 percent of command value on outputs
Telemetry - 5 volts full scale, 10 kilowatt-ohm source
   impedance, ±2 percent of full scale on all measured parameters,
   ±1 percent over limited range
Commands - 28 volt, 10 milliamps, 20 millisecond pulse into
   latching relays for "preheat," "low-voltage on," "high-
   voltage on," "off." 0-5 volts, 10 kilowatt load, for screen
   current command.

Recent experience with best available power transistors and optimized magnetic core materials indicates that an improvement in efficiency and weight could be made if higher solar array voltages were used. For the intended mission of an asteroid survey, expected solar array voltage varia-tion is not 2-to-1 as previously used for power conditioning design, but

6-59
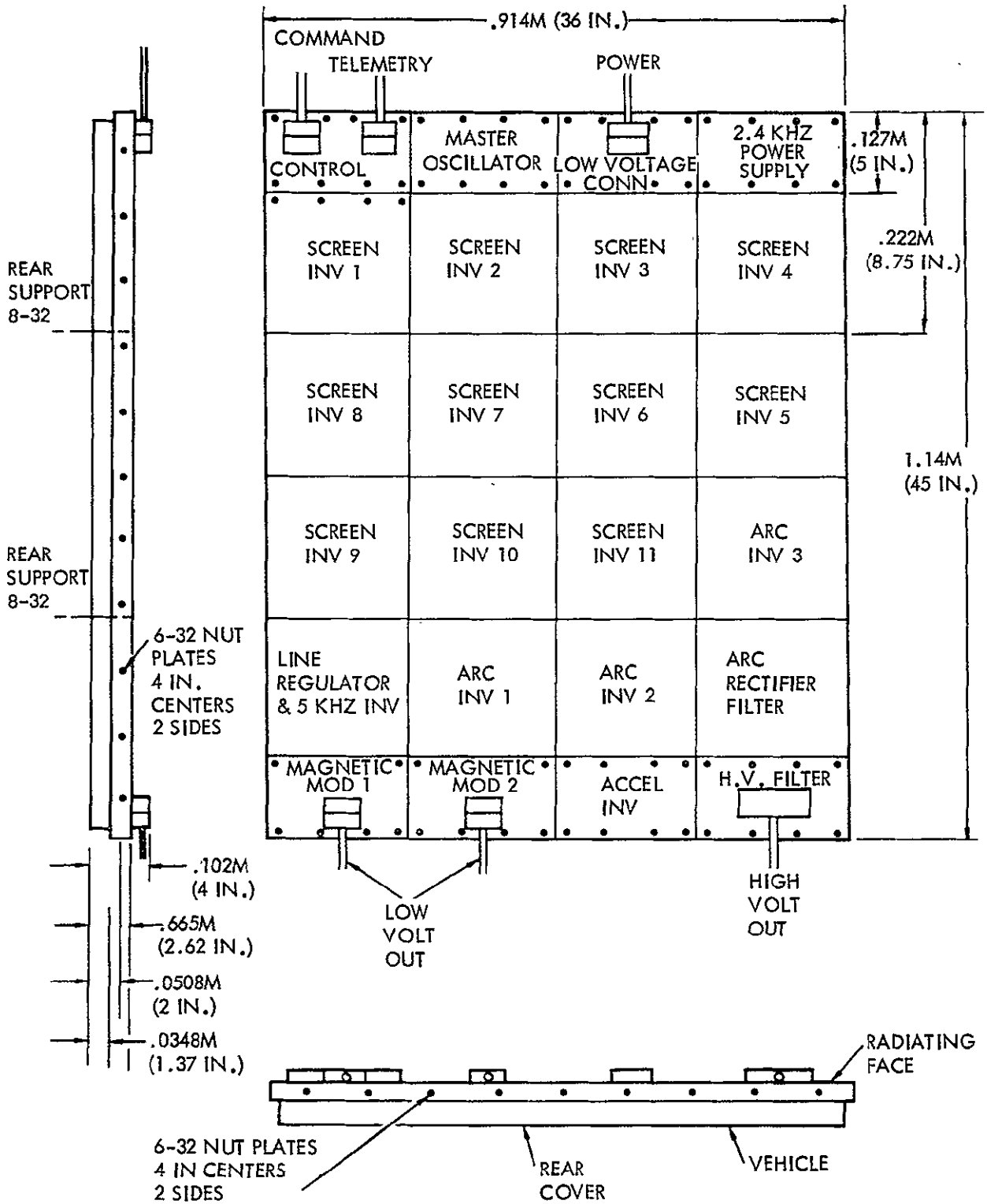
Figure 6-34. Panel Physical Construction

1.5- to -1. Therefore, a suggested solar array voltage range is 120 to 180 volts, with which transistor bridge inverters with approved type transistors operating at one half ratings on voltage and current could be used. A gain in efficiency between 1 and 1.5 percent may be expected with a possible weight reduction of 2 pounds. Such a line voltage would also significantly reduce the weight of wiring from the solar array, or reduce line drops and increase overall efficiency of the power conditioner and vehicle wiring.

Three power conditioners very similar to that required for this mission have been previously developed. One system, developed under JPL Contract 952229, was designed to operate a 20-centimeter thruster with a line voltage varying from 72 to 80 volts. Total power output was approximately 2.9 kilowatts. Over 700 hours of particularly stringent time was experienced with a thruster load during a development period, to optimize the thruster mode of operation. Many thousands of high-voltage arcs were experienced with no failures due to normal operation. This system used center-tap inverters as now proposed for the 40-80 volt array.

Another, more recent system (Figures 6-35 and 6-36) was developed under JPL Contract 952297, for the 20 centimeter thruster, but was designed for operation with a solar array varying from 40 to 80 volts. Over 1200 hours with thruster was experienced, the last 500 hours of which was "hands-off," the first 700 hours being used to optimize the thruster mode of operation. No failures were experienced not attributable to operator error, except for inadvertent standby switching, which was overcome with a few small RF filter chokes on logic supply buses. This system also used center-tap inverters.

A third system has been recently developed for testing a 30-centimeter thruster, requiring 3 kilowatts in the main beam and 1200 watts maximum for experimental purposes in the arc (discharge) supply. These supplies operate on line voltage which may vary from 250 to 500 volts. This system uses bridge inverters such as would be proposed if the solar array voltage range were 120 to 180 volts. (The 250 to 500 volt inverter uses a power transistor made by Delco, which is not an approved source for flight hardware. This transistor is rated at 1000 volts V_{CE}, and 3-1/2 amps collector current. Each inverter delivers 500 watts.)

PROPULSION SYSTEM/SPACECRAFT INTEGRATION AND INTERACTION STUDIES

The integration of the thrusters, PC&C panels, and reservoir into a complete spacecraft propulsion system is dependent on an evaluation of the various subsystem interfaces and potential interactions involved in the design of a solar-electric spacecraft. The most important of these considerations

6-61
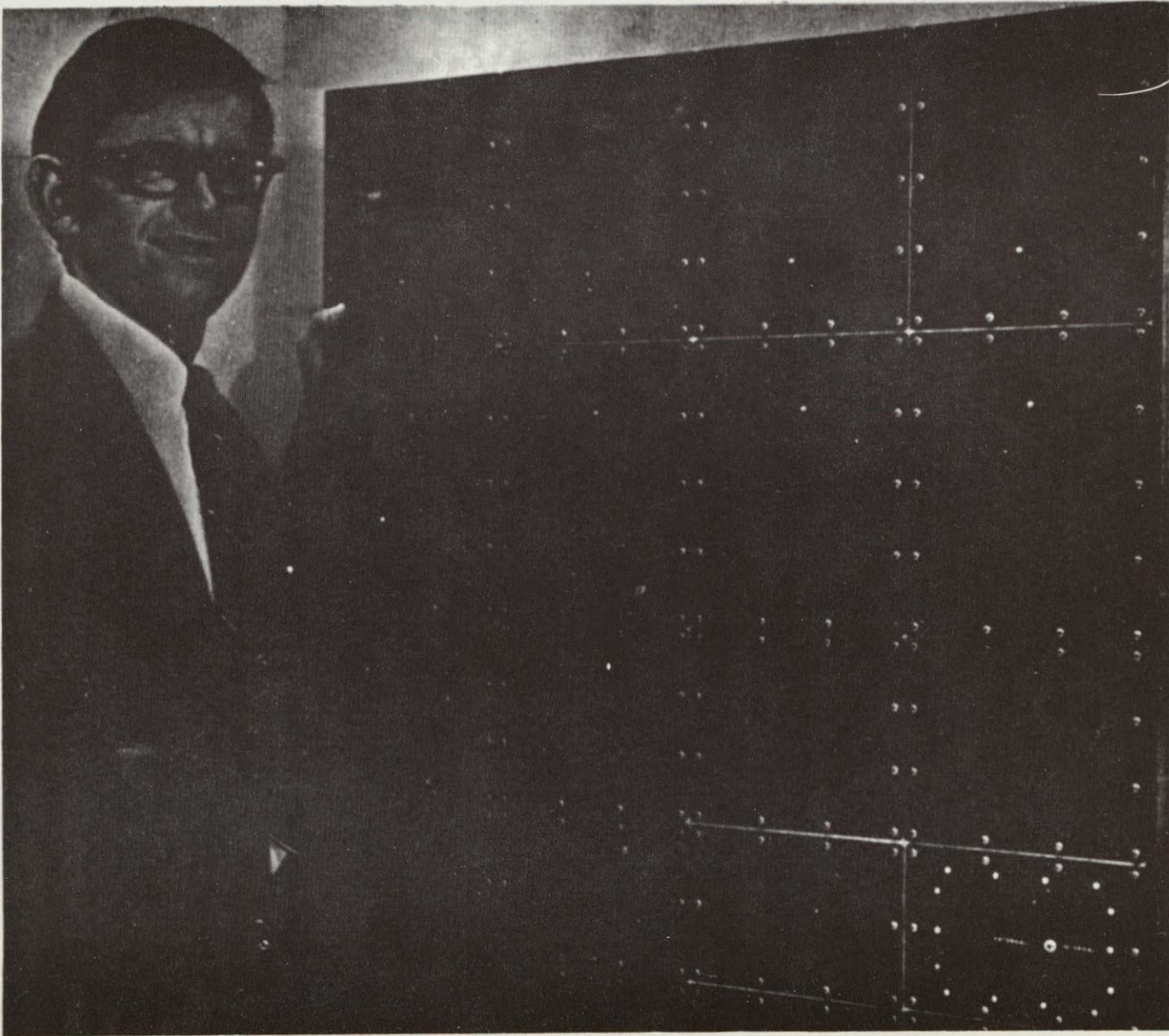
SD 70-21-2

Figure 6-35. Power Conditioning Panel
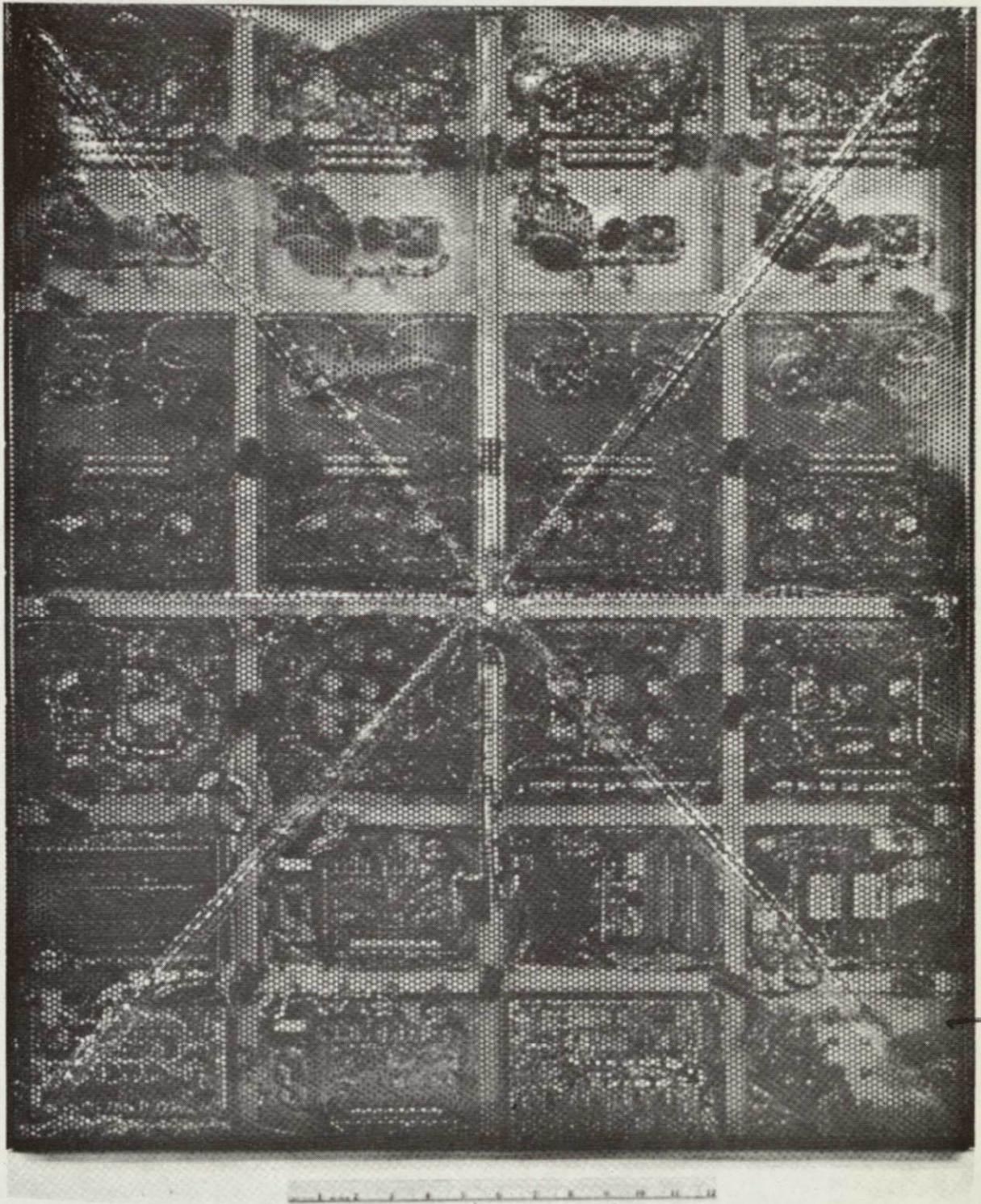
Figure 6-36. Rear View of Power Conditioning Panel

include the requirements imposed on the prime propulsion system by its involvement in the spacecraft guidance and control functions, the effects of propulsion system generated particles and fields on other spacecraft subsystems, and the mechanical, thermal, and electrical constraints associated with the integration of an electric propulsion system into a specific spacecraft envelope.

Guidance and Control Interfaces

Three functions to be performed during any mission are navigation, guidance, and control. The complexity of these functions is mission-dependent; at the level of detailed implementation, these separate functions are sometimes interrelated. These functions are nonetheless conceptually independent and are defined as follows:

1. Navigation is the process of determining the ephemeris of the spacecraft orbit to the present time

2. Guidance is the process of selecting the spacecraft acceleration vector which will produce the most satisfactory ephemeris for the spacecraft trajectory from the present time forward

3. Control is the process of implementing the desired guidance commands (desired spacecraft acceleration)

For the Asteroid mission both the navigation and guidance functions are performed on the ground; the output of these computations will be desired thrust acceleration magnitude and thrust acceleration orientation programs. On the baseline spacecraft and propulsion system design configuration, the thrust acceleration magnitude is controlled by specifying the thruster and power conditioning on/off switching and by specifying the desired beam current. The desired acceleration orientation is obtained by specifying the appropriate spacecraft attitude. The guidance output is then the thruster and power conditioning switching, the desired beam current, and the spacecraft attitude. The selection of the best values for these functions (the guidance function) does not interfere with the spacecraft or propulsion system design and will not be discussed.

The guidance commands computed on the ground must be implemented by the spacecraft; implementation of these commands for vehicle attitude and propulsion system operation imposes requirements on the propulsion system design and on the interface between the propulsion system and the spacecraft. The variation in solar panel power throughout the mission and the requirements for a standby thruster to obtain satisfactory mission reliability both require the capability to perform power conditioning/thruster

switching. It must be possible to align the thruster vector through the spacecraft center of mass for any possible combination of operating thrusters, and to obtain moments about this stable point which are large enough and responsive enough to stabilize and control the spacecraft.

On/off control, thruster switching, and thrust termination are provided by direct commands from the ground. Thrust vector control is provided by programmed thrust magnitude and attitude stored in the central computer and sequencer (CC&S). It is entirely possible to control all of the functions associated with the solar electric propulsion subsystem from the ground via direct command. This approach has the advantage over a fully automated spacecraft of allowing spacecraft reaction to each command in the sequence of thruster operation from initiation to termination to be analyzed and evaluated for correct procedure before the next sequential command is given. It appears that this approach would provide a maximum capability to ensure correct operation of the SEP subsystem: providing maximum control from the ground in essentially real time. Since this mission represents the first use for SEP as a prime thrust source, it seems desirable to provide that at least those commands associated with the thruster on/off control, thruster switching, and thrust termination be controlled by direct command from the ground.

The above approach does not demonstrate a fully automated spacecraft which may be a design requirement for the multi-mission applications, in particular those applications involving point targets. Point targets are distinguished from area targets by the specific requirement to arrive at a point in space at the correct time with the right velocity vector. The area target mission merely requires the spacecraft to arrive at a region in space within a reasonable transit time. Demonstration of the automated space-craft concept is partially fulfilled by storing thrust magnitude and attitude programs for SEP control in the central computer and sequencer on-board the spacecraft. The stored programs are determined before launch, based on the mission trajectory requirements and the expected power availability profile.

After launch and solar panel deployment, the solar array power output is measured. If necessary the power availability profile is revised and the stored thrust magnitude and attitude programs are updated. Throughout the duration of SEP thrust, these stored programs in the CC&S are subject to update from ground command.

Figure 6-37 is a functional schematic of the SEP system showing the interface with the spacecraft stabilization and control subsystem. Thruster and power conditioner on/off control and thruster switching is provided by direct command through the command distribution logic (the power conditioning switching and control includes logic to protect the propulsion
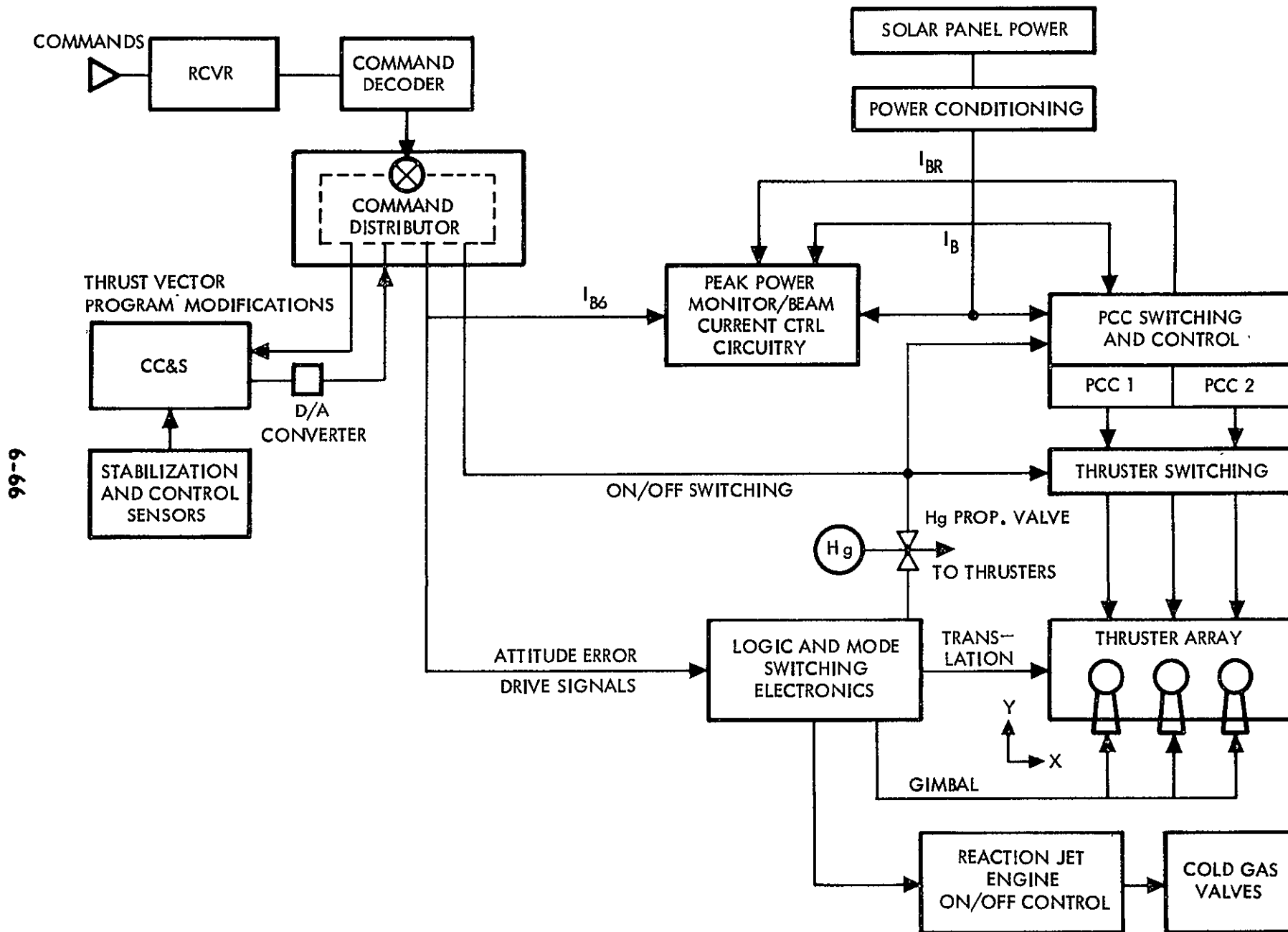
Figure 6-37. Functional Schematic - SEP Interface with Spacecraft
Stabilization and Control

subsystem in the event of thruster failure or other malfunction). Thrust vector control is provided by onboard computation.

The available solar panel power is continuously examined by the peak power monitor. If adequate solar panel power is available, the beam current requested from the thrusters (I_{BR}) is identical to the command beam current (I_{BC}). If the peak power monitor indicates that beam current (I_B) cannot be increased to I_{BC}, then I_{BR} is commanded to be the maximum attainable value. In either case, beam current is regulated to equal I_{BR} by closed loop control.

Spacecraft attitude is sensed by sun and star position trackers and compared to the attitude program stored in the CC&S. Thrust magnitude and attitude error signals are distributed to the proper end points (beam current control circuitry for thruster control and logical mode switching electronics for attitude control). At the start of the mission, when two thrusters are operating, the attitude error is nulled by translation and/or gimbaling of the thruster array. When only one thruster is operating, roll control is implemented by the cold gas system. During coast the cold gas system is used for attitude control in all three axis. This approach to satisfying the spacecraft stabilization function is based on a comparative analysis presented in Section 9.0. However, since the required mechanisms and integration constraints affect the propulsion system design, the results of this analysis will be reviewed here.

The solar electric propulsion spacecraft designed to survey the asteroid belt region uses the low thrust propulsion system for more than 200 days. Throughout this entire period of time, the resultant thrust vector must be oriented so that it passes through the center of mass of the space-craft. To ensure that this does occur in the presence of center-of-mass uncertainty, resultant thrust vector position uncertainty, and potential individual thruster module failure or intentional shutdown, a means of physically moving the thrust vector is required. One could conceive of mechanizing a ballast device to displace the center of mass, but the weight penalty and mechanization complexity would be unwarranted for the space-craft proposed. To accept even small misalignments (less than 1 inch) between the thrust vector and the vehicle's center of mass throughout the thrusting phase of the mission would require an extremely large amount of auxiliary fuel (cold gas or hydrazine) to compensate for the disturbance torques this misalignment would produce. Thus, the conclusion reached is that some type of thrust vector control mechanization is required based on strictly a fuel weight penalty standpoint. The utility of a mechanism to perform thrust vector orientation for alignment purposes is logically extended to provide attitude control of the spacecraft during thrusting. Such a mechanism is, therefore, dual purpose.

A number of possibilities were investigated during this study (e. g. , see Appendix D). The mechanism selected for the recommended spacecraft design requires the following characteristics:

1. Two-degree-of-freedom translation capability with a ±17-inch stroke along the inline axis of the three thrusters and a ±3-inch stroke normal to the inline axis

2. Single-axis hinge gimbaling of each thruster with a stroke limit of ±10 degrees. The hinge axis should be oriented so that the thrusters may be directed in or out of the ecliptic (or trajectory) plane

3. Locking or latching provisions to sustain the boost environment should be provided so that severe loading conditions are not imposed on the positioning devices

Particle and Field Interactions

The application of electric propulsion to interplanetary spacecraft presents some potential problem areas that are not present with conventional high thrust propulsion systems. Among the more important of these areas are the generation of magnetic and electric fields by the thruster-ion beam system and its associated electrical circuitry, and the possible impingement on the spacecraft of neutral atoms and ions from the ion beam. The magnitude of the above effects must be determined, and minimized, before the propulsion system design is fixed.

Magnetic Fields

The primary sources of the remnant magnetic fields on the spacecraft are the axial permanent magnets mounted on each thruster. These magnets produce an axial field strength of 5-10 gauss in the plane of the ion extraction grids over approximately the full 30-centimeter thruster diameter. The resulting dipole moment was experimentally measured and found to be approximately 5 amp-M^2. This dipole moment produces an axial magnetic field strength of ~1000γ ($1\gamma = 10^{-5}$ gauss $= 10^{-9}$ W/M^2) at a distance of 1 meter from the extraction grids. It has been estimated that at distances of 1 meter from the power conditioning or solar array, the field strength would be limited to 1^{-3} by employing normal field cancellation wiring technique. Thus, assuming that these precautions are taken, the contributions from the currents flowing in the power conditioning and solar cells can be neglected.

For the asteroid belt mission, the only science experiment requiring
a very low background magnetic field is the helium magnetometer. For
this instrument, backgrounds of less than ~0.1 Y are desired. The magnetic
field at the magnetometer produced by the three thrusters under consideration
was calculated by assuming that the magnetic field of each thruster was
equivalent to a magnetic dipole with axis parallel to the thrust axis of each
engine. It was assumed that each thruster had a magnetic moment of
$5A-M^2$ for these calculations. The magnetic field components produced by
a magnetic dipole at the origin and pointing in the +X direction are given by

$$B_x = \frac{\mu M}{4\pi r^3} \left(3 \frac{x^2}{r^2} - 1 \right) (W/M^2)$$

$$B_y = \frac{\mu M}{4\pi r^5} \frac{xy}{r^5}$$

$$B_z = \frac{\mu M}{4\pi r^5} \frac{xz}{r^5}$$

where

$r = 4\pi \times 10^{-7}$ (H/M)

M = magnetic moment $(A - M^2)$

$r^2 = x^2 + y^2 + z^2$ (M^2)

The resultant field of the three thrusters was partially canceled by
alternating the sense of the dipole moments of the two outboard thrusters.
The thruster array and co-ordinate system used for the calculations are
shown in Figure 6-38. The thrusters are mounted in the x = 0 plane with
the following coordinates:

Thruster	Y coordinate	Z coordinate	Sign of dipole moment
1	0	0	+
2	0	+15.3	+
3	0	-15.3	-

The resultant magnetic field at the helium magnetometer (located a
x = 225 inches, y = 16.5 inches, z = -102 inch) was calculated using the
previous expressions and was found to be

$B_x = 1.9$
$B_y = -0.3$
$B_z = -2.4$

HELIUM MAGNETOMETER
LOCATION:

X = 225. (INCH)
Y = -16.5
Z = -102.

LOCATION OF THRUSTERS (3):

X = Y = 0
Z = 0
Z = ±15.3 INCH

THRUSTER DIPOLE
MOMENT SENSE
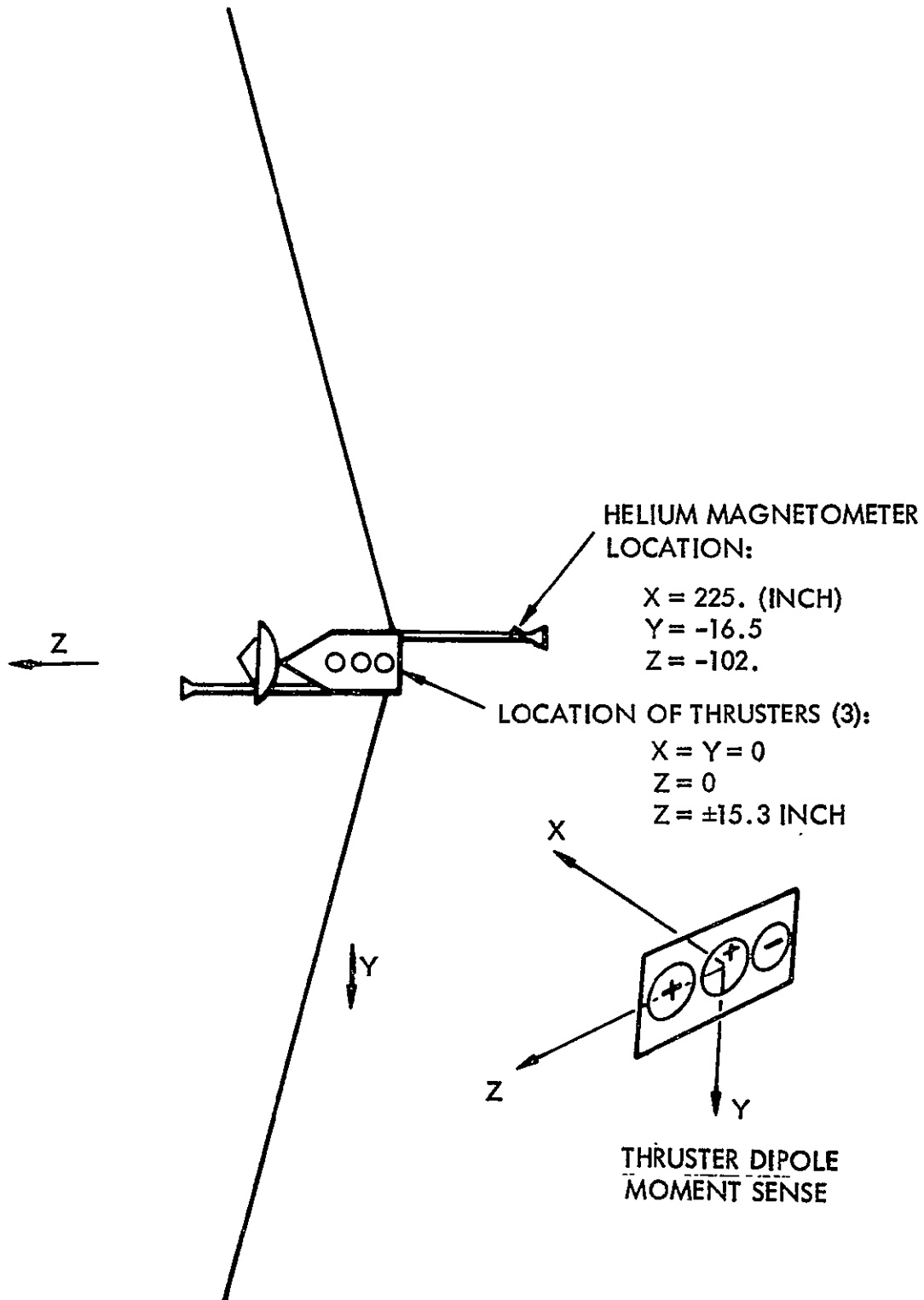
Figure 6-38. Thruster Array Configuration

6-70

Since the above values are above the desired background level of 0.1Y, some field cancellation is required to reduce the background to the low level required. One possible method found by trial and error numerical calculations was to place a permanent magnet having a magnetic moment of 1.9 A-M^2 at x = 69 inch, y = -4.5 inch, z = 0 and having a negative moment to oppose the center thruster. The resultant field at the magnetometer with this extra source is

$$B_x = .02Y$$
$$B_y = .02Y$$
$$B_z = .03Y$$

These values are well below the background required. This method of field cancellation requires that the thruster's magnetic moment does not change more than ±5 percent. Any more than a 5 percent change in the moment of one thruster would raise the background above the desired 0.1Y level.

Should the above approach to minimizing the residual magnetic field due to the permanent magnet thrusters prove unacceptable in a particular spacecraft configuration, a thruster employing electromagnetics could be substituted.

Electric Fields

All the electric potentials and hence electric fields associated with an interplanetary spacecraft are determined by the equilibrium condition in which no net current leaves the vehicle. The two equilibrium potential differences of particular interest in evaluating the electric field environment of the SEP asteroid belt spacecraft are those between the ion beam itself and the spacecraft, and between the ion beam-spacecraft system and the space plasma. The former determines the current flow between the beam and spacecraft while the latter determines the current flow to the beam-spacecraft from the space plasma.

Experiments using the plasma bridge neutralizer have shown that the potential between the ion beam and the neutralizer (neutralizer coupling voltage) depends primarily on the physical placement of the neutralizer and on the neutral flow rate to the hollow cathode. These experiments have indicated that this voltage is typically of the order of +25 to +30 volts (the ion beam is positive with respect to the neutralizer by 24 to 30 volts). If the neutralizer was connected to the spacecraft ground, the electric field produced by the voltage difference would be in a direction to sweep slow charge exchange ions to the spacecraft from the ion beam and to attract any photoelectrons to the beam from the spacecraft. While the power loss caused

by these currents is negligible and no interference with science measurements anticipated, they could be eliminated by simply biasing the neutralizer negatively 25 to 30 volts with respect to spacecraft ground, thus making the ion beam and spacecraft the same potential.

The potential difference between the ion beam and space plasma is certainly less than 20-30 volts for a well-neutralized ion beam. Thus, the only science experiment that could possibly be affected by either of these characteristic potential differences of 20-30 volts is the measurement of low energy particles. Since the only measurement of particle energies proposed during the thrust phase is the cosmic ray and triaxial spectrometers measuring particle energies of 1-1000 Mev, no deleterious effects can be expected from the characteristic electric fields produced by the ion beam.

Beam Impingement and Mercury Deposition

For a spacecraft propelled by an ion engine, the exhaust presents some special problems. The velocity of this exhaust relative to the spacecraft is high, typically ranging from 30 to 100 kilometers per second (Figure 6-39). While the exhaust is theoretically electrically neutral, the limitations of the neutralization process and the low ionization potentials of its constituent atoms (~4 volts, which means solar ultraviolet photons can ionize them) mean that there will be both plus and minus ions as well as neutral atoms present. In addition, the low thrust capabilities of ion engines require that they be operated for long periods of time (weeks to years) to effect appreciable incremental velocities. This, in turn, requires that the communications equipment and environmental sensors, on board the spacecraft be able to function while the ion engine is operating.

In the vacuum of free space, the exhaust plume of an ion engine will expand to fill essentially the half space aft of the exit plane. Any portion of the spacecraft in this area will become coated with some of the exhausted material and the ion engine thrust will be reduced by this intercepted fraction. While the buildup of material will typically be on the order of mils to tens of mils (depending upon the remoteness from the exhaust source). This deposited material will become opaque to visible and infrared radiation within a few minutes after the start of ion engine operations (Figure 6-40). Table 6-18 gives the properties of mercury and cesium used in the following analysis. Solar cells and optical sensors will be made inoperative, and exposed electrical conductors will be shorted. It will take somewhat longer (hours to weeks) for the buildup of the deposited exhaust material to become opaque to radio-frequency radiations, due to the longer skin depth of rf ($\sim 10^{-4}$ cm for 10^{10} cycles per second, $\sim 10^{-6}$ cm for visible light—Figure 6-41).

$$\text{VELOCITY} = \sqrt{\frac{2E}{M}}$$

E = ION ENERGY
M = ION MASS

ACCELERATING POTENTIAL (KILOVOLTS)

EXHAUST VELOCITY (KILOMETERS/SECOND)
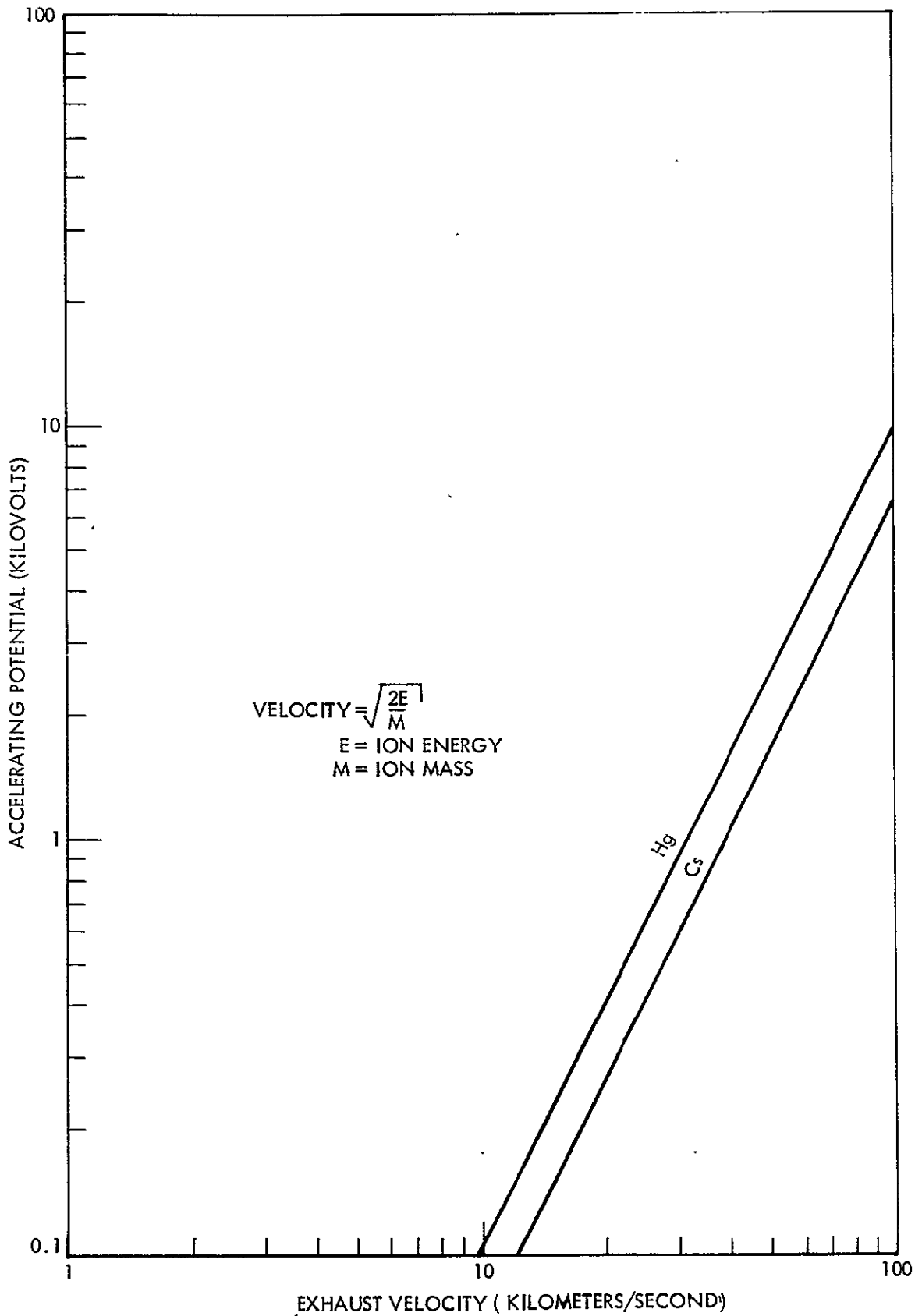
Figure 6-39.   Ion Exhaust Velocity for Mercury and Cesium as a Function
of Accelerating Potential

6-73
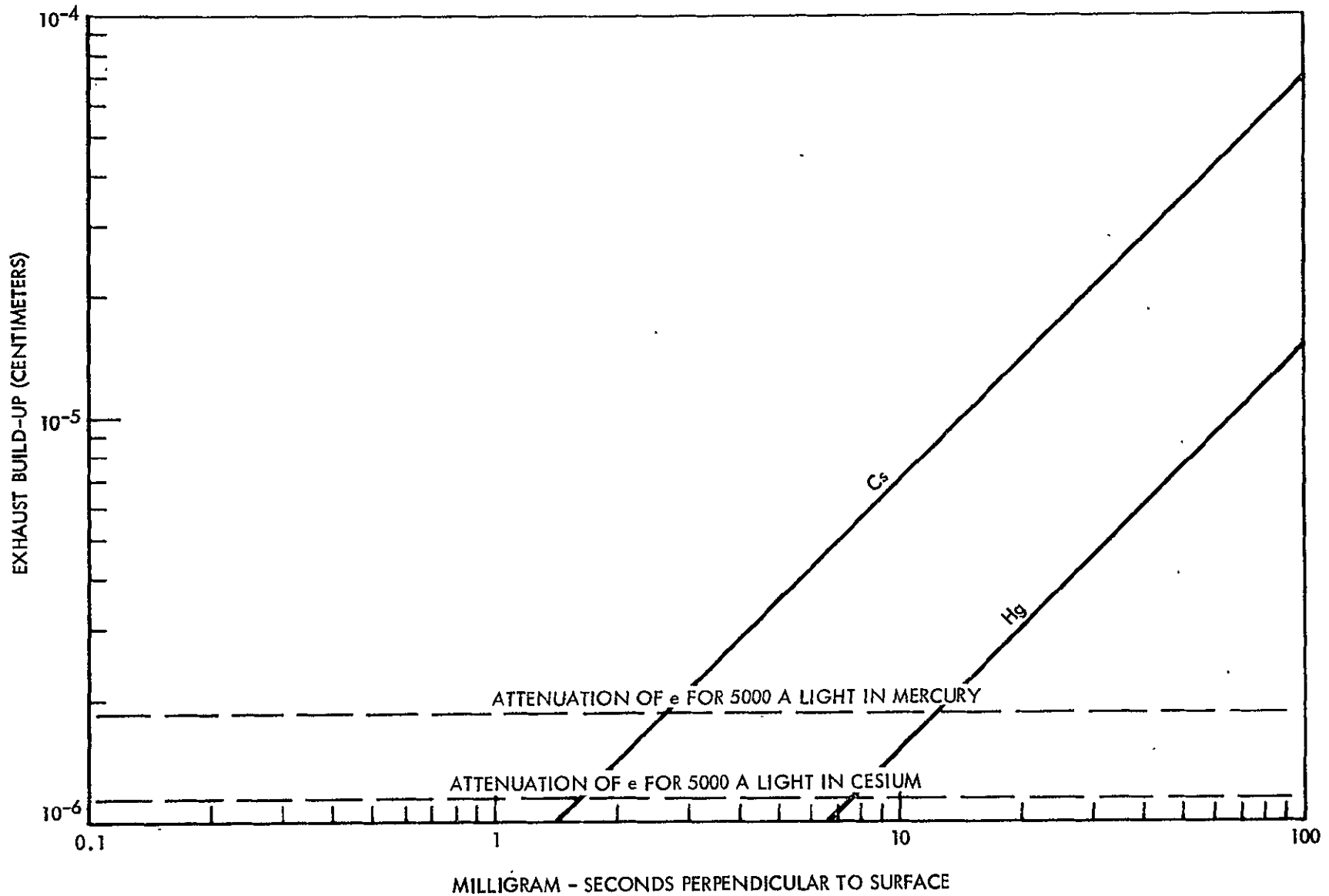
Figure 6-40.   Exhaust Buildup of Mercury and Cesium on Exposed Surfaces,
Assuming 100-Percent Sticking Probability

The chart shows:

$$\text{SKIN DEPTH} = \sqrt{\frac{2}{\omega \sigma \mu}}$$

$\omega = 2\pi \times$ FREQUENCY

σ = ELECTRICAL CONDUCTIVITY

μ = MAGNETIC PERMEABILITY

Y-axis: RF SKIN DEPTH (CENTIMETERS)

X-axis: RF FREQUENCY (CYCLES/SECOND)

Curves labeled: MERCURY, CESIUM
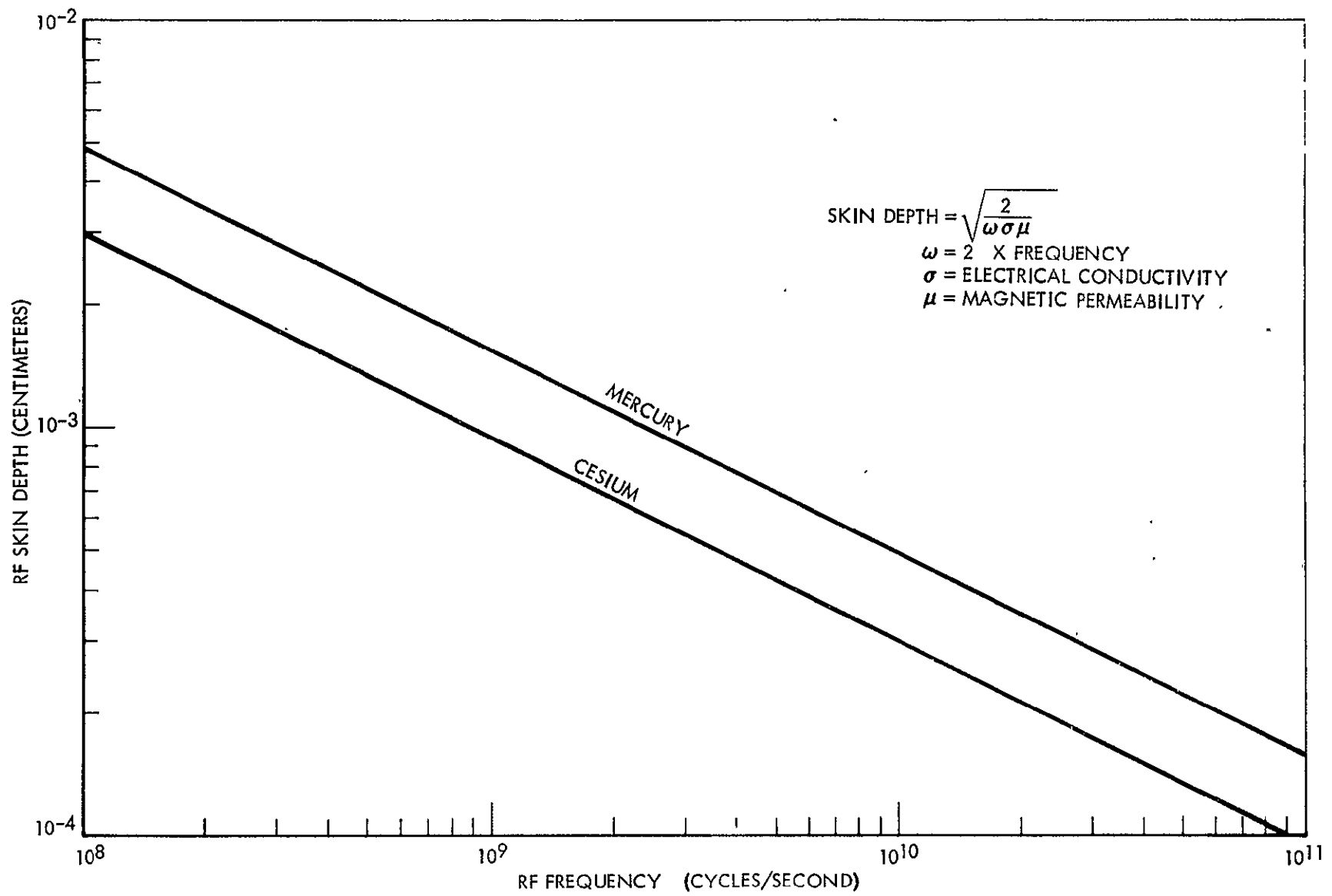
Figure 6-41. Radio-Frequency Skin Depth in Mercury and Cesium as a Function of Frequency

Table 6-18. Properties of Cesium and Mercury

Cesium	Property	Mercury
132.91 amu 55 (100 percent Cs^{133})	Mass Atomic number	200.61 amu 80 (29.72 percent Hg^{202}, 23.1 percent Hg^{200}, etc.)
+1	Valence	+1 or +2
1.873 gm/cm^3	Density (20 C)	11.546 gm/cm^3
28.5°C	Melting point (STP)	-38.87 C
670°C	Boiling point (STP)	356.9 C
2.55 Å	Atom radius	1.47 Å
1.67 Å (+1)	Ion radius	1.11 Å (+2)

The impingement of exhaust material on exposed spacecraft surfaces aft of the ion engine may cause some secondary effects. The original spacecraft surface material will tend to be sputtered off if the exhaust material does not stick, which may wear away thin members in a few weeks. If the exhaust material does stick, chemical interactions will change the properties of the exposed spacecraft surfaces to a depth of several tens of atom diameters ($\sim 10^{-6}$ cm). These chemical interactions may liberate gaseous products and produce minute electric currents, in addition to changing the physical properties of the original surface. However, because of the very short range of the ion exhaust products in matter, the properties of the bulk material will not be affected. Only if the affected surface material were being continually lost (exposing fresh material to be irradiated) would the exhaust impingement pose a problem to the bulk properties of the exposed spacecraft material.

The exhaust plume (consisting of free electrons and ions as well as neutral atoms) will act to attenuate radio frequency signals transmitted through it. The plasma frequency determines the low frequency cutoff. Below this frequency the radio frequency is attenuated because the electrons can move fast enough to be accelerated by the rf energy. Above this frequency the electrons cannot move this fast. This cutoff frequency is approximately

$$V_{cutoff} \simeq 9 \sqrt{N} \text{ cps}$$

where N is the electron density in m^{-3}. However, due to the exhaust velocity of $\sim 5 \times 10^4$ m/sec, even if there is one free electron per exhaust ion, N will be on the order of 10^{12}. Consequently, the radio frequency cutoff frequency will be $\sim 10^7$ cps, over two orders of magnitude below the S and X bands. Consequently, no difficulty in transmitting radio frequency signals through the ion engine exhaust is expected.

The spatial distribution of the ion engine exhaust is composed of two parts. The charged exhaust (ions) is emitted with an approximated gaussian distribution with a half-intensity of ~45 degrees (full angle). Thus, the streamlines of flow are essentially conical. The neutral exhaust (atoms) is emitted with an approximately cosine distribution. The spatially integrated neutral exhaust comprises approximately 15 percent of the total.

For a 3.9-kilowatt mercury ion engine with a 30-centimeter diameter exit plane, the spatial distributions of these two exhaust components have been calculated (Figures 6-42 and 6-43). The accelerating voltage used for these calculations was 3 kilovolts, yielding an exhaust current of 1.3 amps. These spatial distributions show that any surface aft of the ion engine exhaust exit plane will be exposed to neutral atoms and surfaces lying within ~60 degrees of the beam axis will be exposed to some ions as well.

From Figure 6-42 and Figure 6-40, the buildup of surface coating can readily be determined for conducting surfaces, assuming 100 percent sticking of the impacting ions. From Figure 6-42, assume an r (distance from exhaust plume centerline) of 100 centimeters and a distance aft of the exit plane $z = 100$ centimeters, the ion current density is approximately 10^{-2} ma - sec^2. From Figure 6-40 it may be seen that 1000 sec exposure (equivalent to 10 ma-sec) results in a coating thickness of Hg of 1.5×10^{-6} cm. Similar calculations may be made to determine the coating problem for any point in the plume (any values of r and z). Coating due to neutral particles may be approximated in the same way.

The buildup of exhaust material on insulating spacecraft surfaces will act to raise them to a high positive potential. However, the electrons in the solar wind will rapidly increase with potential, limiting it to less than a kilovolt (the solar electron wind current at 1 AU to a body with a positive voltage V is $\sim 3 \times 10^{-7} e^{V/10}$ amps/m^2). Once equilibrium is reached, material should build upon an insulating spacecraft surface similar to that on a conducting spacecraft surface.

Due to the uncertainty of the effects of the exhaust plume on surface coating and erosion, and the magnitude of the problem as indicated in the previous discussion, the decision not to allow any spacecraft protrusion beyond the exhaust exit plane was used as a basic design ground rule.

Mechanical, Thermal, and Electrical Integration

The integration of modularized electric propulsion must be guided by an evaluation of the mechanical, thermal, and electrical interface between propulsion subsystems and between propulsion system and spacecraft.
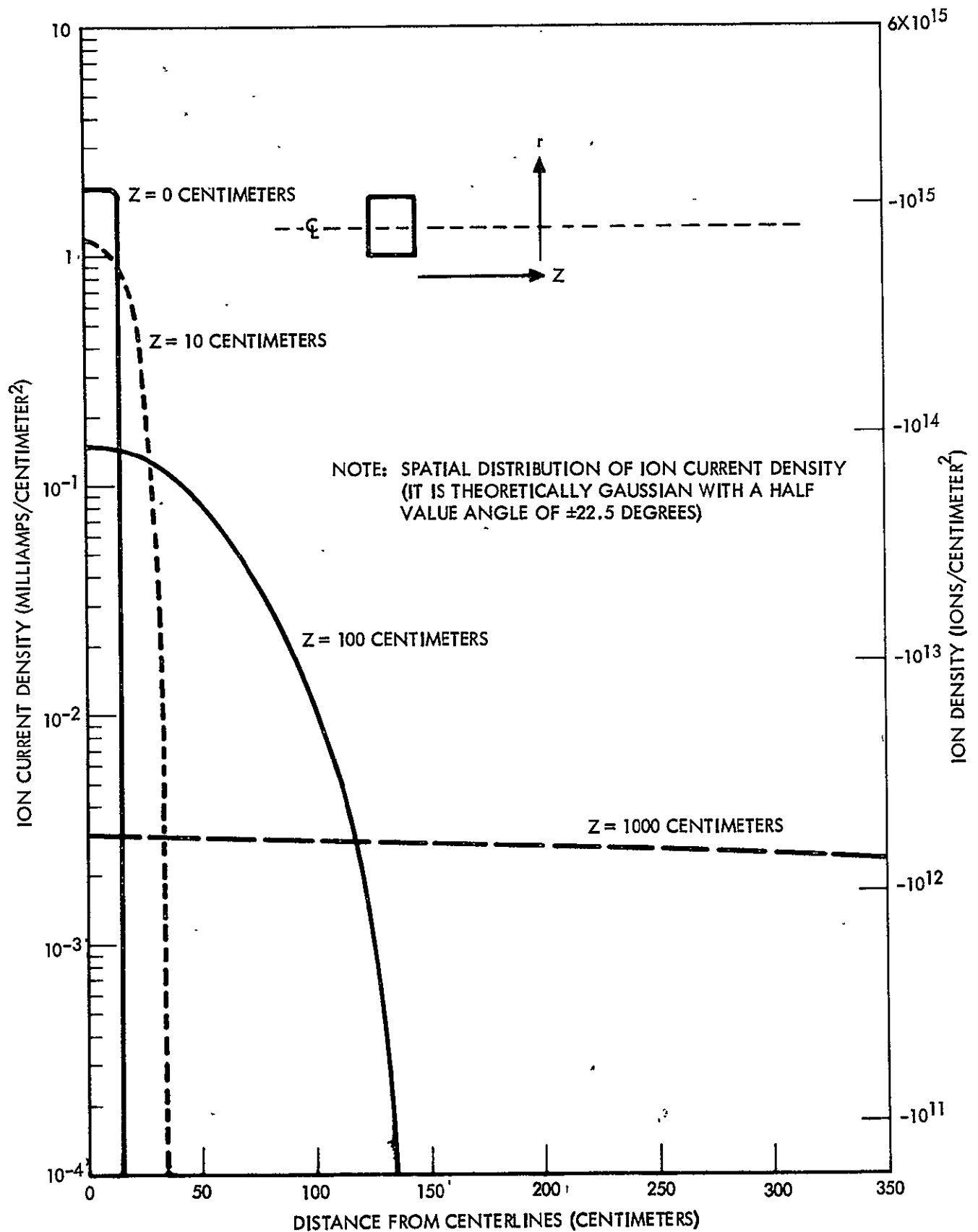
Figure 6-42. Spatial Distribution of Ion Current Density
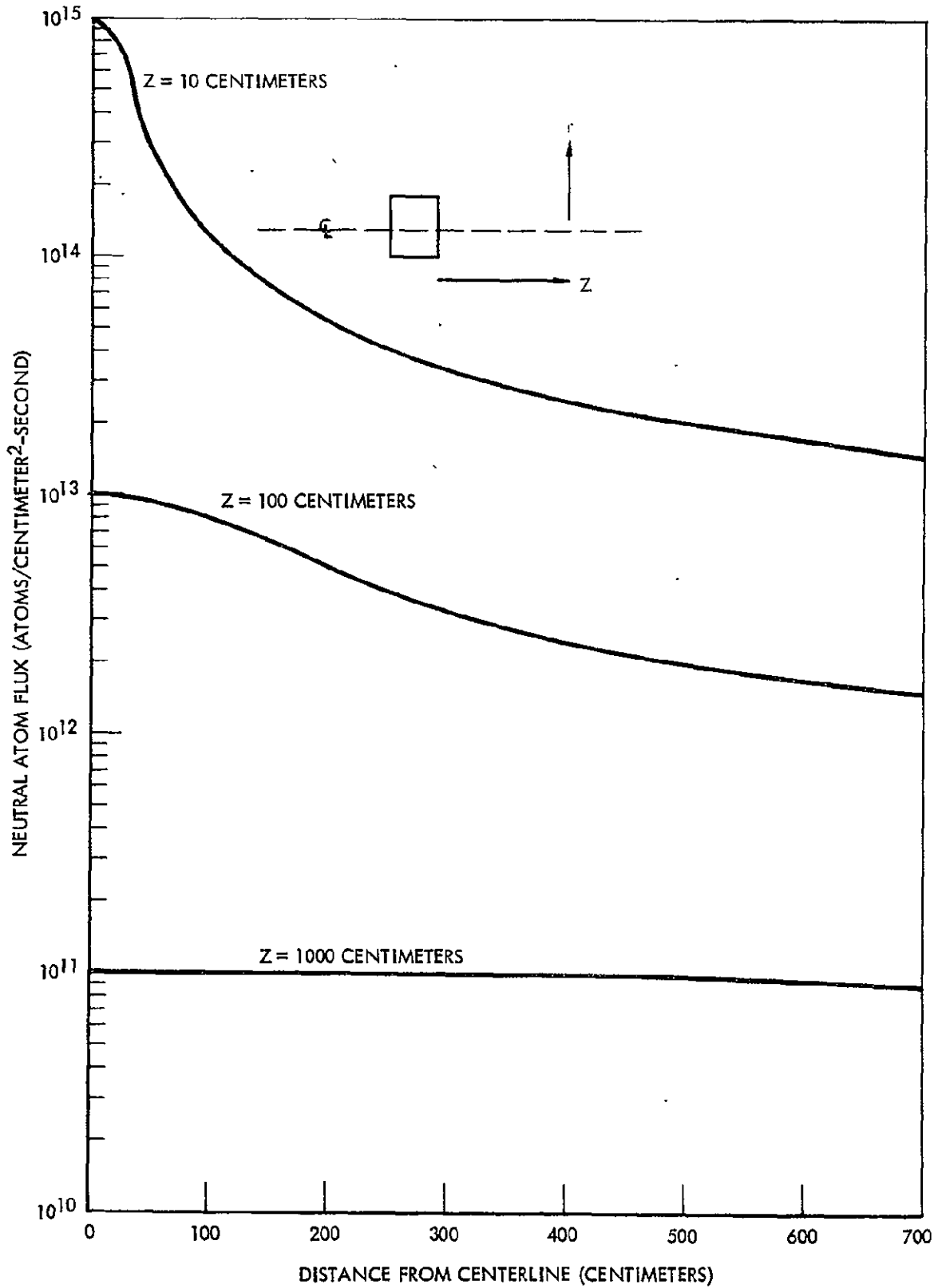
Figure 6-43. Spatial Distribution of Neutral Atom Flux

6-79

SD 70-21-2

Mechanical Integration

This section discusses the Mechanical Integration aspects of the thruster array positioning device (translator), individual engine gimbal mounts, tiedown feature, and propellant transfer mechanization for the propulsion system design.

Mechanisms. During this study a number of techniques of manipulating the ion engine array were investigated. Gimbaling of the entire thruster array as well as gimbaling each thruster module was briefly considered, but rejected due to the mechanical complexity and poor capability to compensate for an engine failure or shut-down. Linear (screw-type) actuators were also considered for translation of the entire engine array, but were also rejected due to their inherent sliding friction characteristics. A number of conceptual designs performed during the early phase of this study, before the selection of the recommended propulsion system configuration of three 30 centimeter diameter mercury electron bombardment ion engines, are presented in Appendix D-2.

The mechanization recommended for the spacecraft engine system consists basically of a translation device capable of moving the entire engine array in two orthogonal directions and single-hinges (gimbals) for each of the thruster modules. These combined provide complete three-axis control torques for the spacecraft. During the portion of the thrusting phase when only one thruster is operating, attitude control about the thrust vector is provided by the auxiliary cold gas system. For a linear arrangement of thrusters, such as in the basic design for the asteroid belt spacecraft which uses three thruster modules, complete three-axis control could be provided by gimbaling each engine and only providing one axis translation along the axis of the in-line engines. The incorporation of the additional degree of freedom (cross-translation) does allow for future growth (addition of more thrusters in the array) where a linear arrangement would be awkward. In addition, the provision of the cross-translation capability serves as a back-up mode of operation in the event of gimbal failures.

The thruster array translation mechanism consists of the following elements:

1. A structural tray to which the thruster gimbal mounts are attached

2. Guide rail assembly which rigidly mounts to the spacecraft structure

3. A carriage which attaches the tray to the guide rail assembly

4. Four 90-degree permanent magnet stepper motors (two-drive tray on carriage and two drive carriage on guide rail assembly)

5. Four gear reduction units

6. Roller and band suspension units (Rolamite devices)

The thruster gimbal mechanism hardware consists of the following elements:

1. A trunnion mount adapter plate that attaches to the base mounting studs of the thrusters

2. Two bearing angle brackets with thermal and electrical isolator pads

3. A stepper motor and gear reduction drive assembly

The spacecraft dynamics aspect associated with the use of the translator-gimbal mechanism is treated in detail in the Stabilization and Control section of this report.

It should be noted that a higher degree of alignment precision can be obtained by using the two-degree-of-freedom translation for thrust vector-center of mass alignment over the single degree of freedom translator and gimbals. This is caused primarily by the center of mass of the spacecraft being approximately ten feet from the thruster array: small errors in the gimbal increments would be amplified at the center of mass. A five-arc minutes error in the gimbal position would result in an approximate 3/16-inch misalignment error between the thrust vector and vehicle center of mass.

The drive mechanism for the two degree-of-freedom translator is designed to traverse the ±17 inch or ±3 inch strokes at 0.005-inch increment per pulse of the stepper motor. The stepper motor is capable of 100 steps per second which results in a translation rate of the engine array of 0.5-inch per second. This rate may be readily changed by modifying the gear reduction unit. Such a modification will not result in a change of the stepper motor or rollers in the assembly.

The overall dimensions of the translation mechanism support framework are 27.5 by 69 inches (Figure 6-44). The size of the translator support structure is primarily based on the packaging diameter of the thrusters and the thruster arrangement. The selection of three nominal 30-centimeter diameter thrusters arranged inline accounts for the lengthy stroke along one axis.

GUIDE RAIL   ION ENGINE (REF)

GEAR REDUCTION UNIT

A

STEPPER MOTOR

DRIVE ROLLERS

ENGINE MOUNT

0.5

4.1

1.2

1.6

CARRIAGE

A

STEPPER MOTOR

GEAR REDUCTION UNIT

ROLLER DRIVE BANDS

CARRIAGE

DRIVE ROLLERS

SECTION A-A
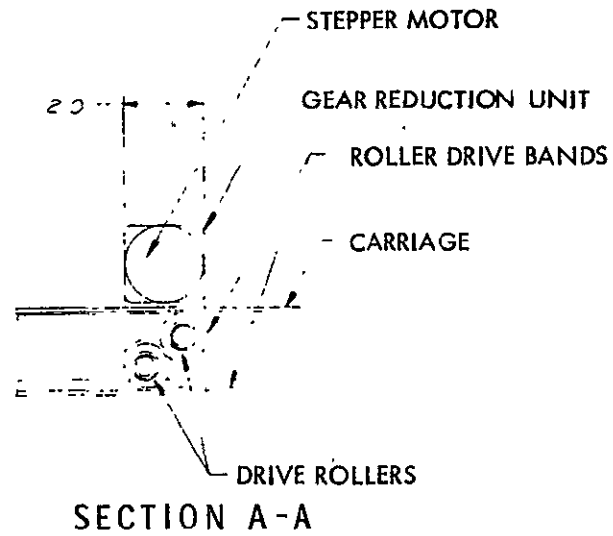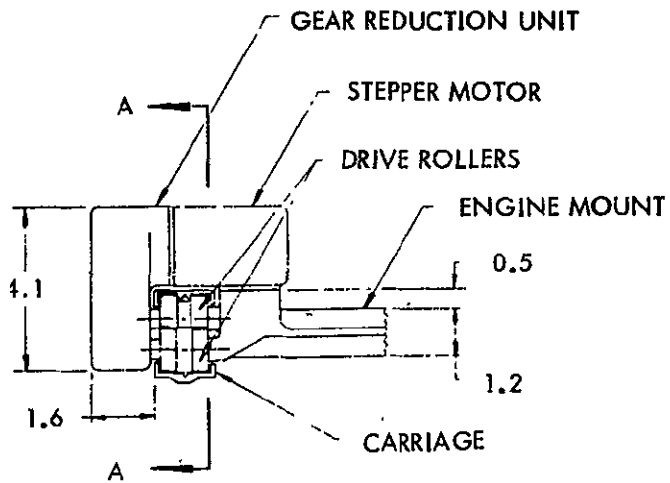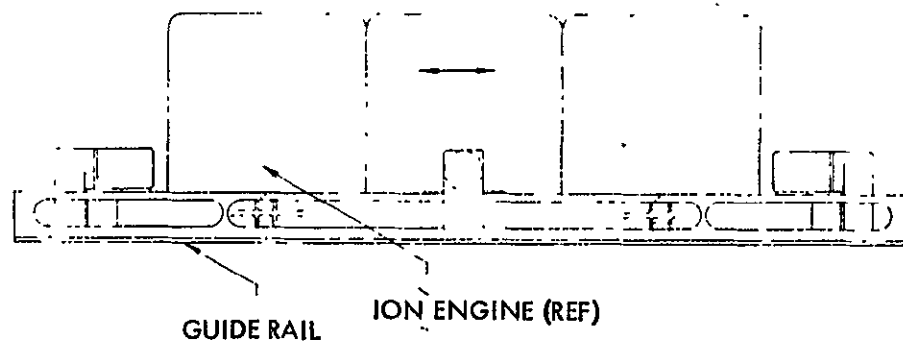
Figure 6-44.   Gear-Reduction Unit and Related Hardware

Each of the three thrusters are single-axis gimbaled with the hinge axes oriented at 45 degrees to the ecliptic plane. The placement of the hinge axes in this position is primarily to minimize the space requirements and consequently to minimize the extent of translation along the inline thruster axis. Placement of the gimbal mounts in this manner does reduce the moment arm that is effective in producing control torques with the thrusters about the vehicles' longitudinal axis, but not to unacceptable levels. With the gimbal hinge axes at 45 degrees and the combined long-axis translation capability, a three-axis control backup mode is available in the event of failure of the cross-axis translation device.

The engine array carriage is secured to the spacecraft base structure with four tie-down latching clamps. These tie-down latches are pyrotechnically actuated to unlatch the carriage when the spacecraft is in a zero-g environment. The hinged latches are spring-loaded to swing clear of the translator for translator motion clearance.

The total weight allocated for the translator and gimbals is 24 pounds.

Propellant Lines. A significant item of concern in the design of the translator system is the method employed to transfer the mercury propellant and electrical power feed system lines across the translator elements. The translator concept selected offers the maximum of clear area within the translator members. A hard line mercury propellant feed line system is very desirable from the standpoint of state-of-the-art components and technology and the outgassing experienced by flexible lines in a space environment. At the present time flexible lines are being replaced with coiled hard lines in many aircraft hydraulic applications. This same approach is recommended for the mercury propellant feed system where the small diameter feedlines to the thrusters will be coiled to allow the large flexing necessary. The extreme translation is only required in the event of a thruster failure. The attitude control translations are relatively small when compared to that required for a thrust failure mode. Since the large translation would only be required a few times, the coiled hard line approach offers a higher reliability since hard lines usually outlast the system to which they are connected.

Thermal Integration

In the thermal integration studies conducted for the electric propulsion section of the spacecraft, the temperature control of the power conditioners, mercury propellant reservoir and feed system, and thrusters was considered. The temperature limits of the propulsion system equipment considered in the thermal control analyses were as follows:

Equipment	Temperature Limits (F)	
	Non-Operating	Operating
Power conditioners	-50 to 140	32 to 140
Mercury reservoir	-22 to 212	86 to 212
Thrusters		32 to 500

The electric propulsion module of the spacecraft is shown in Figure 6-45 in its relative location to the rest of the spacecraft. In this figure the normal thrusting and coast phase orientation of the spacecraft are indicated with the power conditioners facing away from the sun. Before engine startup and operation of the propulsion system the power conditioners would undergo a severe temperature drop, to approximately -108 F, if they were not heated. During the early phase of the mission, before the availability of solar power, approximately 100 watts of heater power would be required to maintain each of the power conditioning panels at a 0 F level. During this phase of the mission, battery power is at a premium and providing such heater power would be unrealistic. Consequently, the recommended flight mode, before the availability of solar power, is to orient the entire spacecraft so that the power conditioning panels face the sun (Figure 6-46). Sun oriented, the panels can be maintained at 130 F. The effect of this orientation on other spacecraft compartments does not present problems and is discussed in the Thermal Control Subsystem (Section 10.0) of this report. The temperature variation of the power conditioners during a parking orbit phase about earth is also minimized by the sun orientation mode (Figure 6-47).

When power becomes available from the deployed solar panels, power can then be supplied to heaters for the power conditioning panels, mercury reservoir, and thrusters for prestart warmup of the propulsion system.

During the sun acquisition phase of the mission when the panels are oriented away from the sun and before solar power is available to power the heaters, the thermal inertia of the power conditioners would maintain the units above the minimum nonoperating temperature limits. Data for the panel temperature decay as a function of time is shown in Figure 6-48.

In the course of the mission when the second operating thruster is shut down (approximately 134 days), and a single thruster is reinstated to operate at full power, the nonoperating power conditioner would drop in temperature below survivable limits. To maintain acceptable standby panel temperatures, a 100-watt heater is provided for each conditioner. With this exception, the power conditioners are temperature controlled completely passively. As shown in Figure 6-49, the panels are isolated from the spacecraft structure by fiberglass mounts and superinsulation. The external surface of the power

VEGA

SPACECRAFT STRUCTURE

ELECTRIC PROPULSION MODULE

ELECTRIC PROPULSION
MODULE

SUN

SPACECRAFT STRUCTURE

FLIGHT
DIRECTION

ECLIPTIC PLANE   +Z

THRUSTER

POWER
CONDITIONER
PANELS

MERCURY PROPELLANT
RESERVOIR

CANOPUS

+Y

129PD98306

Space Division
North American Rockwell
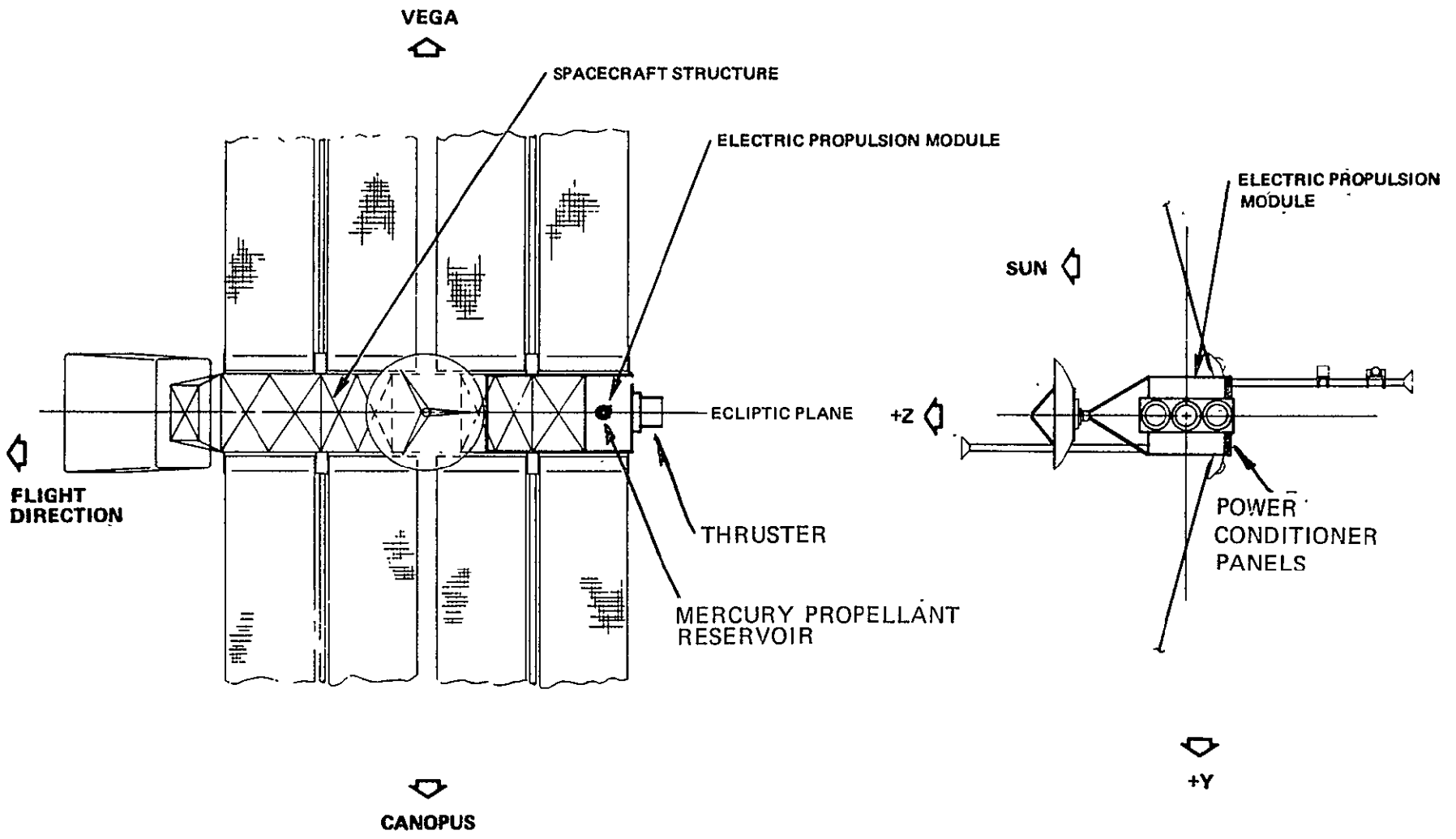
Figure 6-45.   Electric Propulsion Module Location
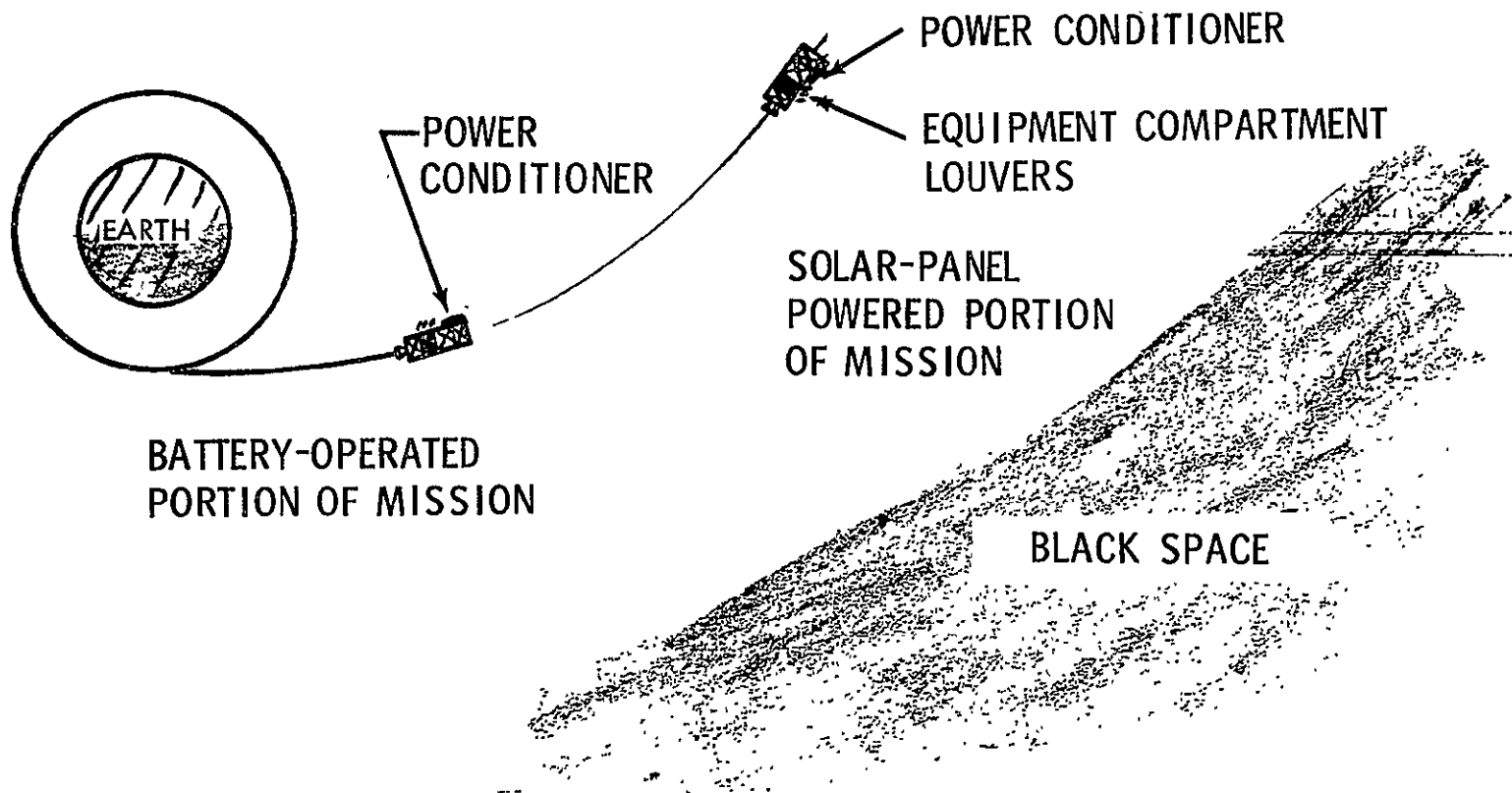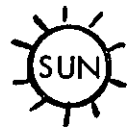
Figure 6-46. PCC Thermal Control Using Solar Energy
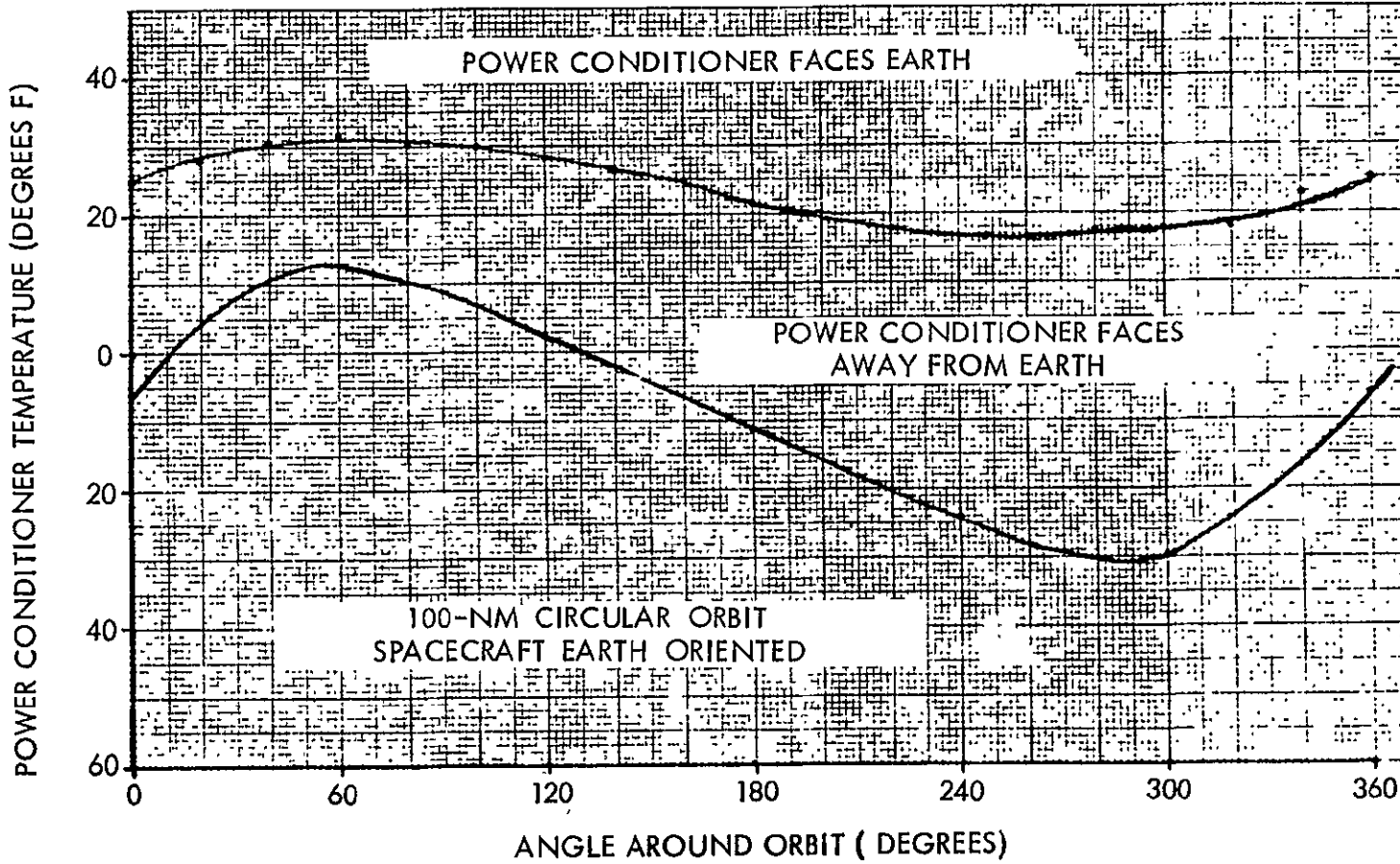
Figure 6-47. Temperature-Time History of Power Conditioner
During Parking Orbit
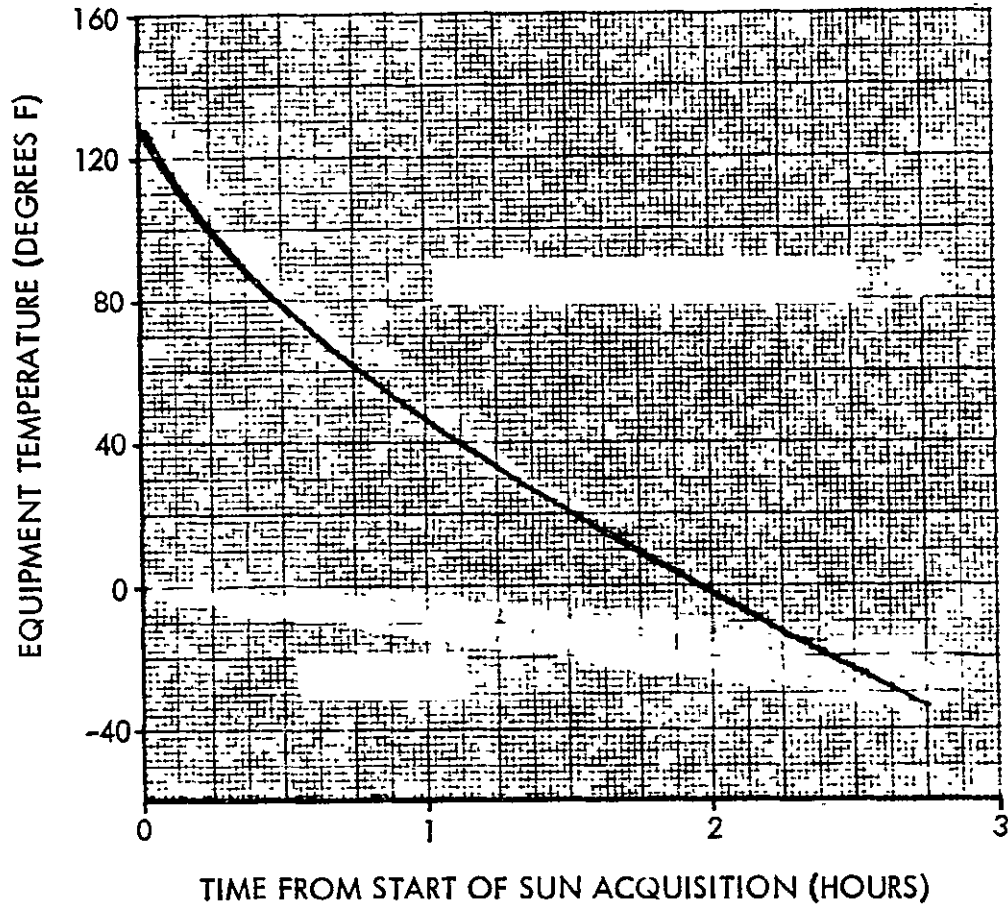
Figure 6-48.   Temperature-Time History of Power
Conditioners and Science During Sun Acquisition
and Solar Array Deployment

6-88
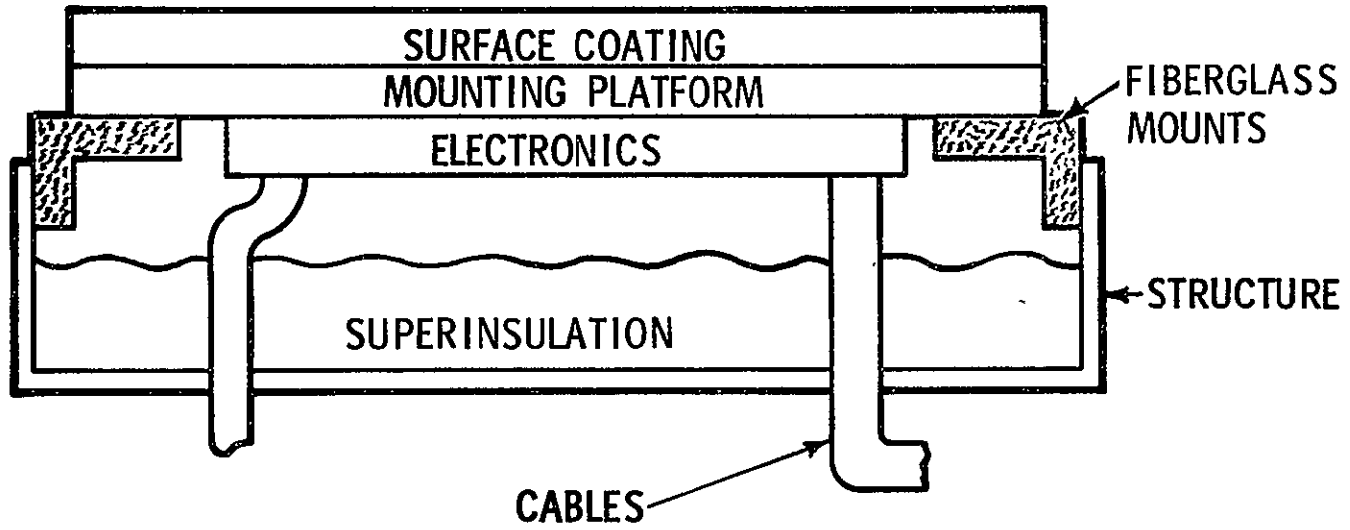
Figure 6-49. Schematic Diagram of Power Conditioner Mounting

conditioners are treated with a surface coating with an α/ϵ equal to 0.6. The inner surface of the power conditioners with the exception of the temperature control surfaces, are covered with 15 layers of aluminized mylar separated by nylon netting.

The mercury propellant reservoir and freon pressurization feed system is mounted centrally in the propulsion section of the spacecraft (Figure 6-44). As discussed in the section describing the electric propulsion system/spacecraft assembly, the mercury tank is supported by a frustum type mount. Thermal isolator flanges are used to isolate the tank from the support structure. A heater is provided for the reservoir to maintain the proper pressurization of the freon gas which expels the mercury in the zero-gravity environment. This heater requires less than 10 watts of power and would maintain the reservoir temperature within 90 to 120 F. Surrounding the spherical mercury reservoir is the propulsion module with the inside surface polished.

The thrusters mounted to the aft end of the propulsion section do not pose a thermal control problem. Heaters are provided to ensure that warm up/start up operation temperatures should not drop below 32 F. To decouple the wide dynamic range of the heat source provided by the thrusters, the thrusters are isolated from the aft end of the spacecraft by thermal isolator mounts. An aluminized kapton blanket is provided on the aft surface of the propulsion module.

During the mission phase, when only one thruster is operating, the other two thrusters in standby are maintained above the freezing temperature of mercury by thermal energy from the operating module.

Electrical Integration

Provision must be made in the electric propulsion system design to transfer power from the PC&C panels to the three thrusters. A switching assembly is also required to allow switching of each PC&C panel to the standby thruster. There are two candidates for the electrical power feeds to the thrusters across the translator. The first is a flat wire design resembling a ribbon. The other concept is the traditional round cable. The argument used for the selection of a coiled tube feed system for the propellant system could also be used for the electrical feed system, but a coiled electrical cable requires the use of the round cable and adds more weight than the flat ribbon cable. The flat ribbon cable concept uses a loop upon loop approach for the translation and minimizes additional weight. The flat ribbon concept also gives more efficient heat dissipation than the round cable. The flat ribbon cable concept is recommended for use with the selected mercury feed system concept and the translator selected. It is possible that the electric power cable and the mercury propellant line could be coiled and looped in a manner

6-90

so as to nearly occupy the same volume. With proper insulation between the mercury line and the power line the two could be coiled and looped as a single system. This approach would simplify the concept greatly and offer greater reliability for the entire system.

Switching Circuitry. The electric propulsion system contains two operating thrusters (each with its own power conditioning panel) and one standby thruster. No power conditioning panel is furnished for the standby thruster. Instead, provision is made to switch the power conditioning panel from a failed thruster to the standby thruster. Panel reliability is built up through the use of internal redundancy. Either one of the two power conditioning panels may be connected to the standby thruster (but not to the other operating thruster). If one of the operating thrusters fails, its power conditioning panel will automatically shut off power to the thruster. Subsequently, this power conditioning panel will be disconnected from the failed thruster and switched to the standby thruster where the panel power will be again turned on. Table 6-19 lists the switching requirements; Figure 6-50 shows the generalized switching circuitry to be used.

Table 6-19. Switching Requirements

Circuit No.	Circuit	Contact Requirements	
		Current (amps)	Standoff Potential (volts) (across open contacts)
1	Screen	17.1	+1700 dc
2	Accelerator	0.040	-2550 dc
3	Discharge	15	+1740 dc
4	Thruster cathode keeper	1	+2000 dc
5	Thruster cathode, heater, isolator and thruster isolator	2.9	18.8 ac on top of +1700 dc
6	Neutralizer keeper	1	+300 dc
7	Neutralizer vaporizer and cathode heater	1.6	14.2 ac
8	Thruster cathode vaporizer	0.525	10.0 ac
9	Thruster vaporizer	0.97	10.0 ac

POWER CONDITIONING
PANELS

SWITCHES
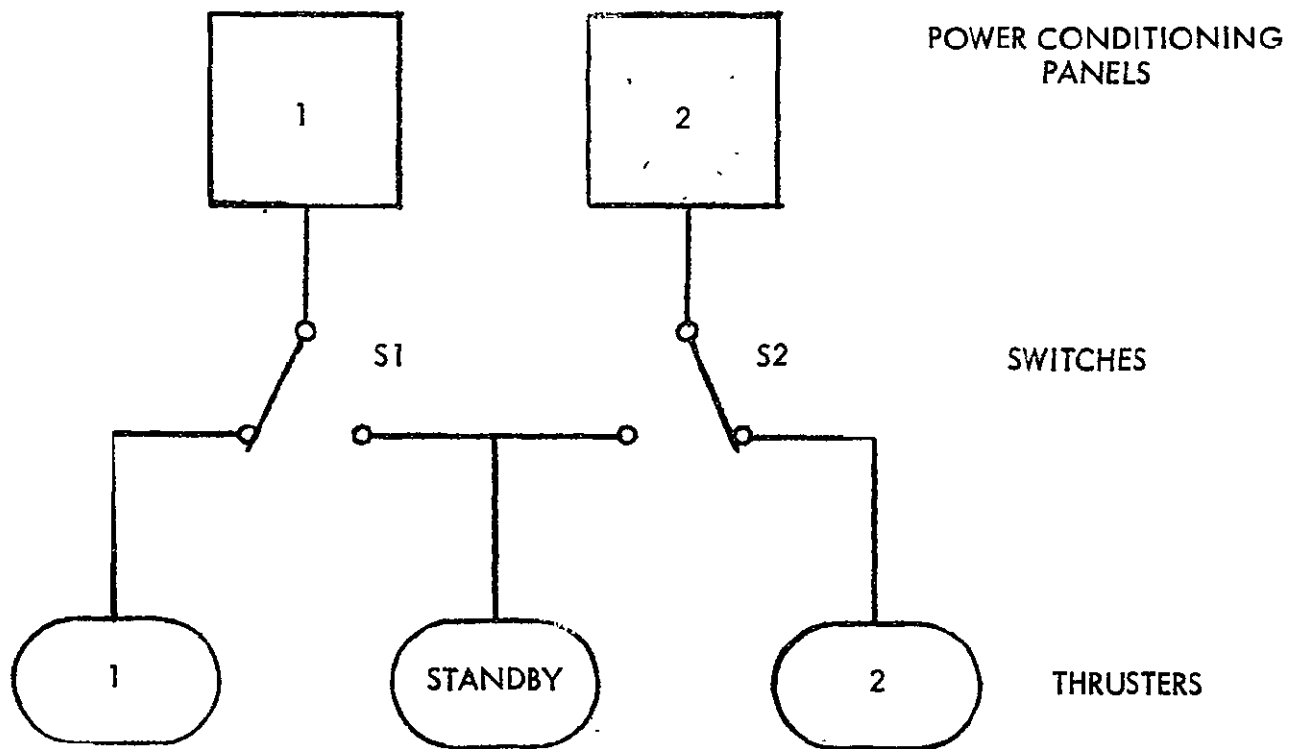
THRUSTERS

Figure 6-50.   General Standby Switching Circuitry

SD 70-21-2

A thruster requires nine different circuits for operation. This implies that the switching function S1 (or S2) represents a nine-pole double-throw switch. The switching functions represented by S1 or S2 will be accomplished using magnetic latching relays. These relays do not require continuous power for operation; a single pulse is given to the proper coil so that the correct contacts are closed, the contacts are then held closed by a magnet. The fact that the switching action takes place with the circuits (and PC&C panel) dead eases the requirements placed on the relays. Since no nine-pole double-throw latching relays were found which would perform the necessary switching functions, the use of multiple relays was considered.* Four-pole double-throw latching relays exist (Table 6-20) which will satisfy the switching requirements for the four low-voltage circuits. The series 9228 relay is an older relay which has seen extensive use in aircraft and space environments. Much test data is available for this relay. Its reliability for a single operation (one operation is all that is required for the standby switching function) has been conservatively estimated to be 0.999999. The KL series relay is a new product which offers substantial improvement in rating and mass over the older 9228 relay. Because of its newness, less test data are available for it. In particular, an estimate has not yet been made of the reliability for a single operation. However, a classified reliability investigation is presently under way for the 2 PDT version of this relay.

Table 6-20. Low Voltage Magnetic Latching Relay Characteristics

Manufacturer	Type	Rating	Mass, gm (oz)	Coil Characteristics
Leach Relay	Series 9228 (4 PDT)	28 v, 5 amp 1000 v test	158.8 (5.6)	28 vdc, 20 millisec, 200 Ω coil
Leach Relay	Series KL (4 PDT)	28 vdc, 15 amp 1250 v test	70.9 (2.5)	28 vdc, 20 millisec, 450 Ω coil

Single-pole double-throw magnetic latching ceramic vacuum relays that can be used to switch the high voltage circuits are summarized in Table 6-21. Jennings ITT is the major manufacturer of this type relay. The vacuum ceramic relay's advantages are small size and weight and the capability of withstanding baking at high temperatures during its construction. This ensures thorough outgassing of the relay initially, which tends to prevent contamination of the contacts due to later outgassing during operation. Single operation reliability for these relays is not known but is expected to be at

---

*The use of vacuum magnetic latching reed relays to satisfy the switching requirements has been considered in the past. They will not be considered further here because such relays would have to be developed specifically for the present specialized application and, if developed, would not necessarily improve upon existing relays.

least as good as the Series 9228 low voltage relay. Both relay types listed
in Table 6-21 may require hermetic sealing of the exposed actuator portion
to be usable in a space environment.

Table 6-21. High Voltage Magnetic Latching Relay Characteristics

Manufacturer	Type	Rating	Mass, gm (oz)	Coil Characteristics
Jennings ITT	RFI-J (1PDT ceramic enclosed vacuum relay)	2 kv, 8 amp (4 kv test)	14.2 (0.5)	26.5 v, 1 amp for 10 millisec. Maximum pulse length is 50 millisec for 26.5 v.
Jennings ITT	RF3B (1PDT ceramic enclosed vacuum relay)	10 kv, 25 amp (11 kv test)	49.6 (1.75)	26.5 v, 4 amp for 10 millisec. Maximum pulse length is 500 millisec.

The switching function S1 (or S2) is proposed to be accomplished by
using one KL series low-voltage relay to switch circuits 6 through 9, four
RF1-J high-voltage relays to switch circuits 2 through 5, and one RF3B relay
to switch circuit 1, the screen circuit. Table 6-22 summarizes the relay
characteristics and their use to perform the switching function. Figure 6-51
illustrates the use of the relays as a switch (S1 or S2) to connect a power
conditioning panel to the standby thruster as well as the thruster the
PC&C panel normally services. Assuming all relays have the same reliability
for single operation (i.e., 0.999999) as the series 9228 relay, the reliability
of the relays in performing switch function S1 (or S2) is 0.999994.

Table 6-22. Relays Used for Standby Switching

Manufacturer	Type	Mass, gm (oz)	Number Used (per PC&C panel)	Total Mass, gm (oz)
Jennings ITT	RF1J (1PDT ceramic enclosed vacuum relay)	14.2 (0.5)	4	56.7 (2)
Jennings	RF3B (1PDT ceramic enclosed vacuum relay)	49.6 (1.75)	1	49.6 (1.75)
Leach Relay	Series KL (4PDT)	70.9 (2.5)	1	70.9 (2.5)
Total Switch Mass (S1 or S2)				177 (6.25)
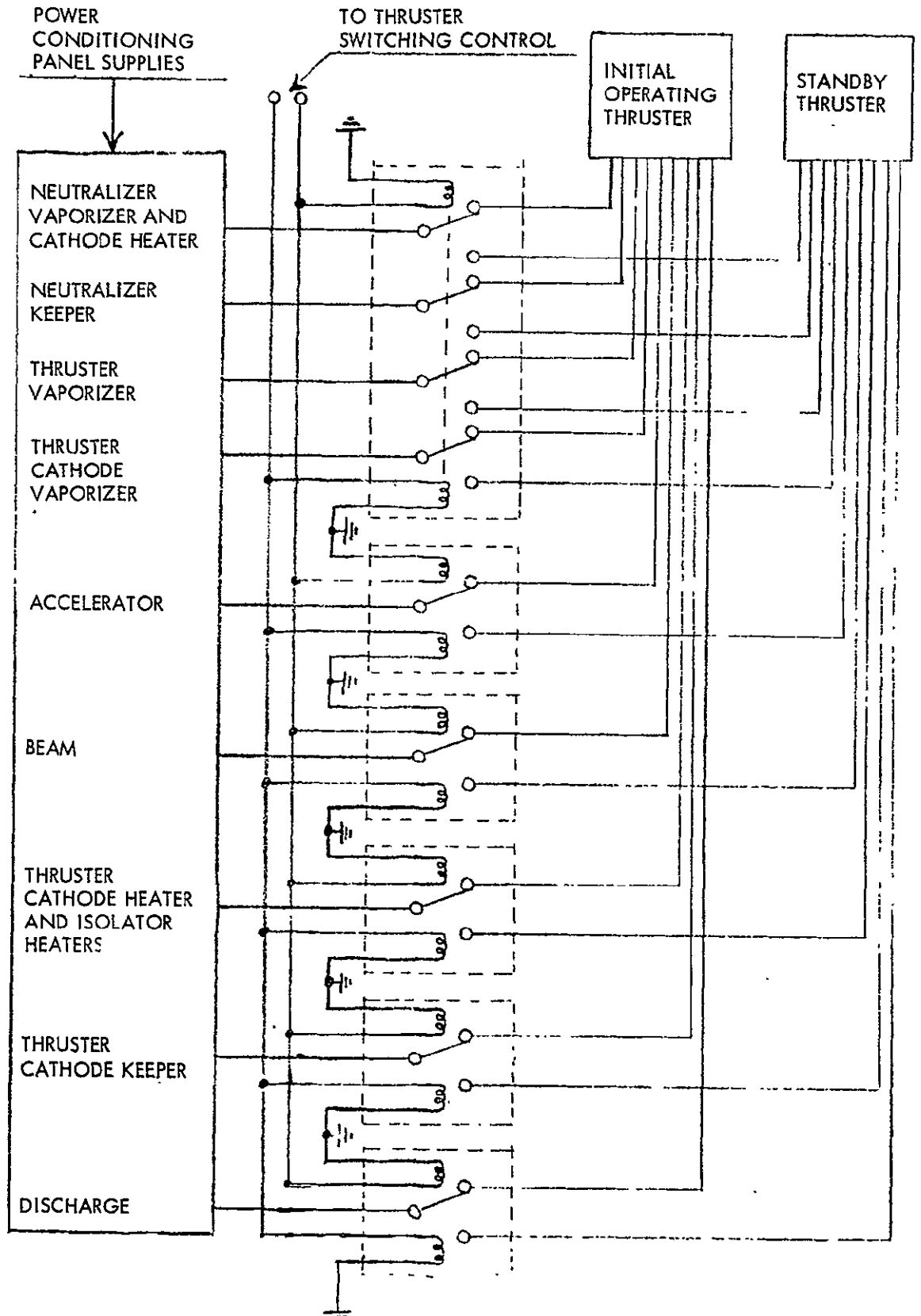
Figure 6-51. Standby Switching Logic

6-95

0.254 M (10")

O

KL RELAY

KL RELAY

MOUNTING HOLE

RF3B RELAYS

0.133 M (5.25")

RF1-J RELAYS

O
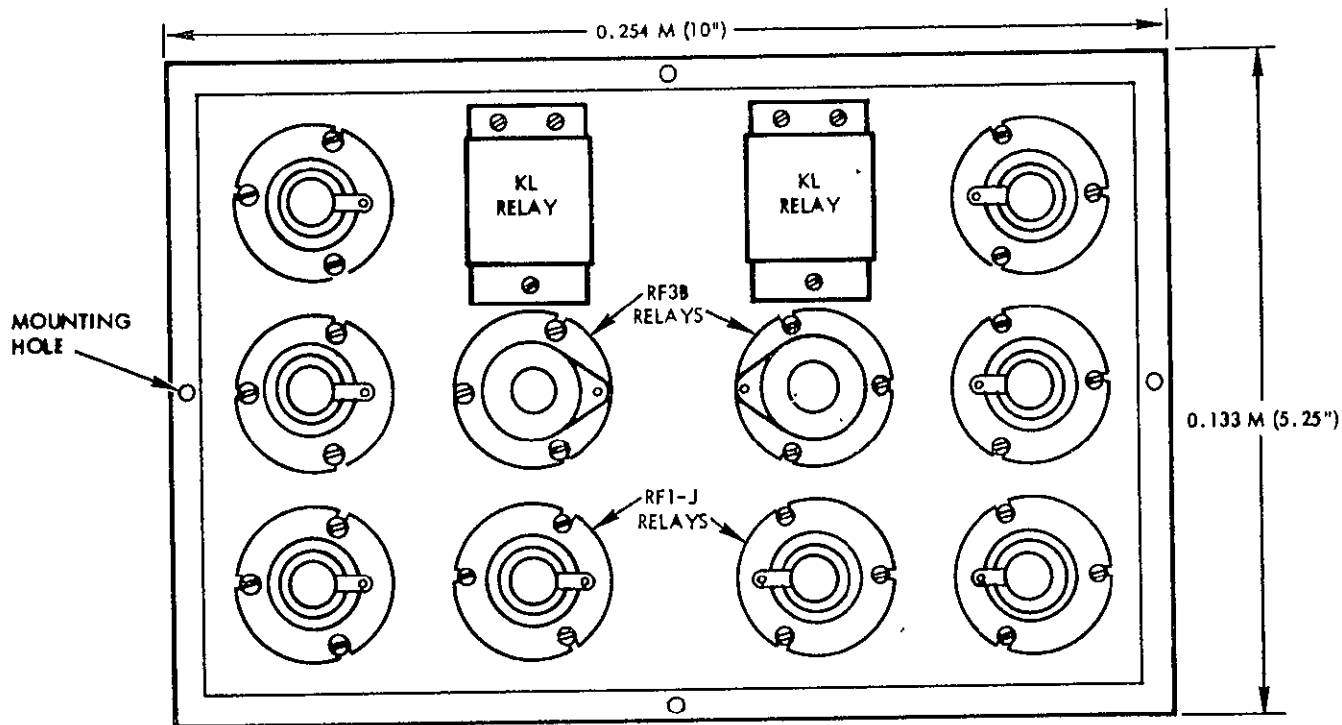
Bottom View

Figure 6-52.   Switch Assembly

7.1 CM (2.8")

6.6 CM (2.6")

5.83 CM - 2.3" (24 CONDUCTORS ON 0.1" CENTERS)

1 MIL ALUMINUM COATED KAPTON SHIELD

.0254 CM (.01") APPROX.

2 MIL KAPTON INSULATION

SHIELD GROUND

SCREEN

DISCHARGE

CATHODE ISOLATOR HEATERS

THRUSTER CATHODE VAPORIZER

GROUND

NEUTRALIZER HEATERS

NEUTRALIZER KEEPER

CATHODE KEEPER

THRUSTER VAPORIZER
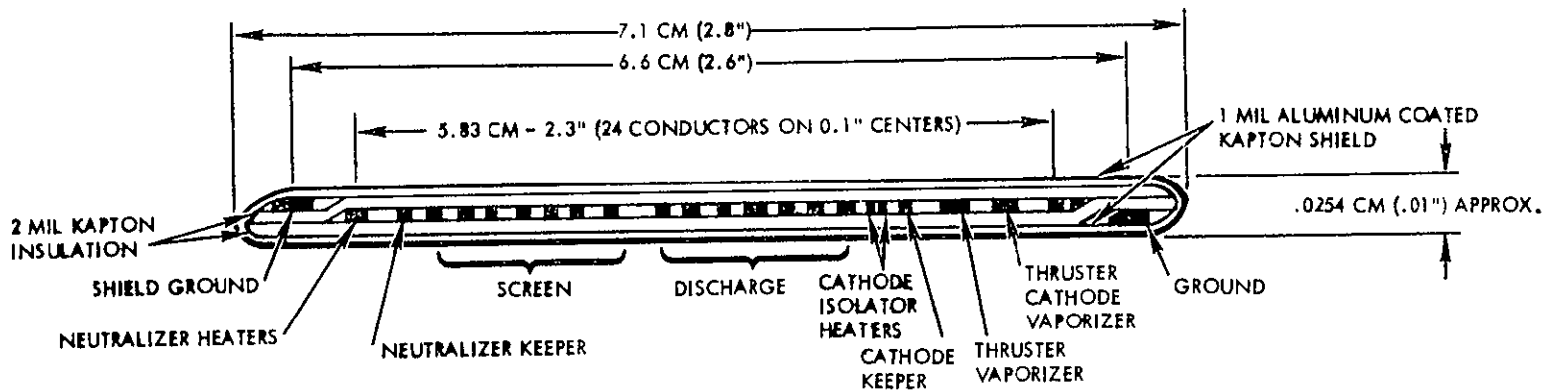
Figure 6-53.   Ribbon Cable Cross-Section

Space Division
North American Rockwell

The switch assembly for the proposed system design consists of the following set of relays for each of the two PC&C panels: four RF1-J relays, one RF3B relay and one KL series relay. A schematic of the switch assembly mounted in its enclosure is shown in Figure 6-52. The switch assembly enclosure is estimated to have a mass of 368 grams (13 ounces). The total mass of the switching assembly is then 0.724 kilogram (1.60 pounds).

Transmission Cable. An electrical power transmission cable is required by the propulsion system to connect the PC&C panels to the switching assembly and this assembly to the thrusters. Each cable must transmit the power (nominally 3.6 kilowatts but up to 3.9 kilowatts under certain conditions) drawn by an operating thruster. Desirable features of such a cable are flexibility, low mass, and high transmission efficiency. Cable flexibility is necessary to allow the thrusters to be translated and gimbaled. Flat, flexible ribbon cable of the type used on the Surveyor spacecraft is suitable for use as the propulsion system power transmission cable. The cable is fabricated from strips of rectangular cross section copper wire sandwiched between two 2-mil layers of insulating material (Kapton). For electrical shielding, the cable is sandwiched between two aluminum coated one mil layer of Kapton. Figure 6-53 shows a cross-section and the dimensions of the cable.

Nine thruster circuits require transmission of power. Table 6-23 lists cable conductor requirements. This requirement will be met by using a 24 conductor cable. The arc (discharge) circuit will use seven conductors to accommodate the high current in this circuit. Similarly, the screen circuit will require seven conductors; two conductors will be used to furnish power to the isolator heaters and the thruster cathode heater. The remaining six circuits will use single conductors in the cable. The number and size of conductors used in the cable are summarized in Table 6-24. The specific mass of the cable is 0.0378 pound per foot (0.0562 kilograms per meter).

Table 6-23. Cable Conductor Requirements

Conductor Purpose	Current Carried (amps)	Potential to Ground (volts)
Screen	17.1	+1700 dc
Accelerator	.040	-2550 dc
Discharge (arc)	15	+1740 dc
Neutralizer keeper	1	+300 dc
Thruster cathode keeper	1	+2000 dc

6-96

Table 6-23. Cable Conductor Requirements (Cont)

Conductor Purpose	Current Carried (amps)	Potential to Ground (volts)
Neutralizer vaporizer and cathode heater	1.6	14.2 ac
Thruster cathode heater, heaters for isolators	2.9	18.8 ac on +1700 dc
Thrusters cathode vaporizer	0.525	10.0 ac
Thruster vaporizer	0.97	10.0 ac
Ground line	9.1	0

Table 6-24. Ribbon Cable Conductor Sizes

Circuit	Number of Conductors	Conductor Width, (in.) (all conductors 0.005 in. thick)
Screen	7	0.062
Discharge	7	0.062
Neutralizer heaters	1	0.062
Cathode vaporizer	1	0.025
Main thruster vaporizer	1	0.025
Isolator, cathode heaters	2	0.042
Acceleration	1	0.025
Neutralizer keeper	1	0.042
Cathode keeper	1	0.025
Ground	2	0.062

The cable will be connected to the thruster as shown in Figure 6-54. It will be clamped in two places to the thruster mounting plate which forms the back of the electrostatic shield. One of the clamps also fastens the cable to a printed circuit board. The conductors from the cable are lap-soldered to conductors on the printed circuit board. Wire leads connected to the printed circuit board conductors then carry power to points inside the thruster.
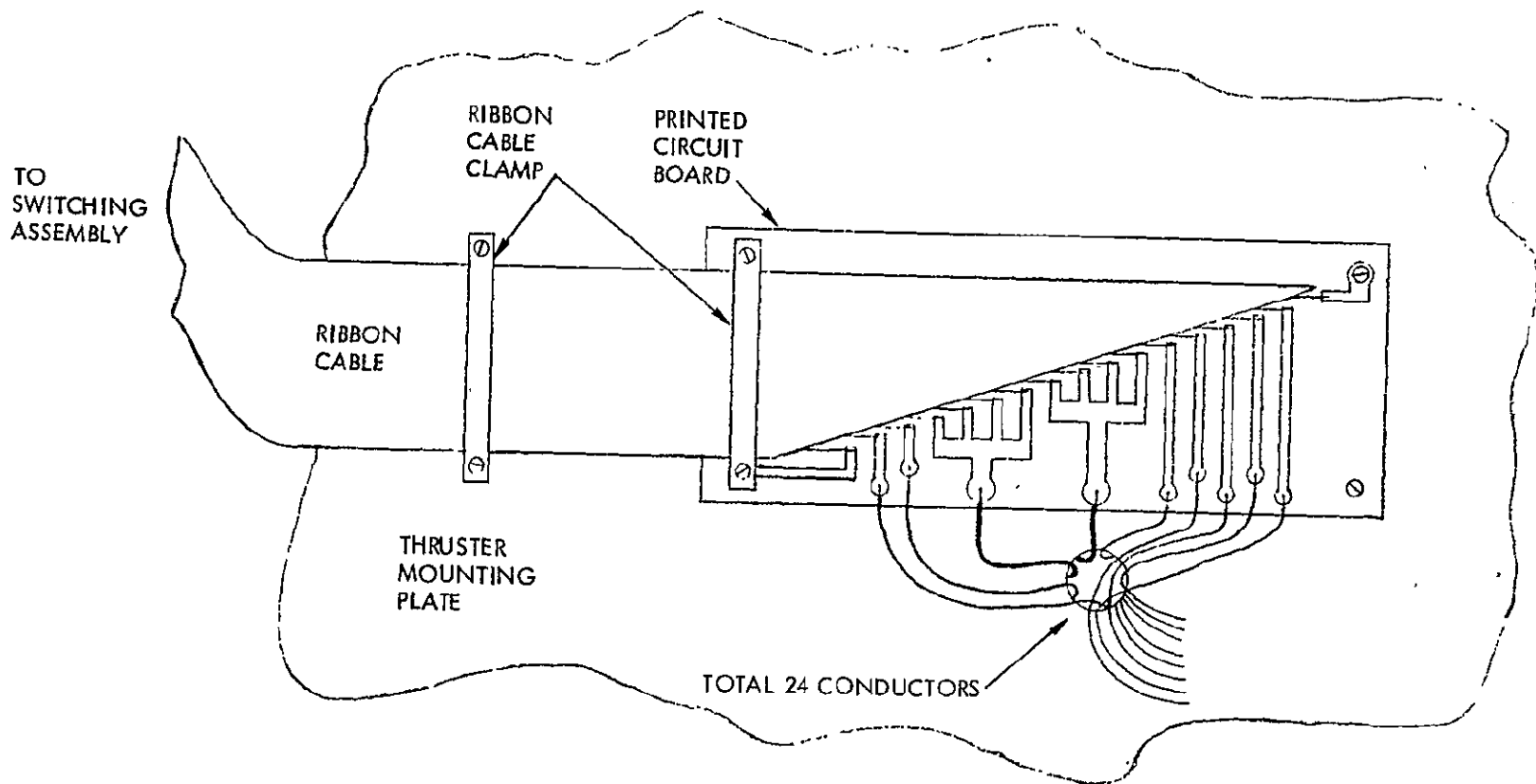
Figure 6-54. Ribbon Cable Termination at a Thruster

Space Division
North American Rockwell

The ribbon cable is similarly connected to circuits in the standby switching assembly enclosure. Two cables enter the enclosure, one from each power conditioning-panel, and three cables leave the enclosure, one to each thruster. Figure 6-55 shows the cable connection to the enclosure. The cable conductors are lap-soldered to printed circuits which carry power between the cables and circuits in the standby switching assembly enclosure.

ELECTRIC PROPULSION SYSTEM/SPACECRAFT ASSEMBLY

In the design of the electric propulsion section of the spacecraft, a major effort was placed on developing a modular design concept: minimizing the interfaces between the electric propulsion system and the remainder of the spacecraft subsystems and science modules. In this way, the design of the propulsion system would be negligibly affected and would be easily adapt-able for use on missions other than an asteroid belt survey. A minimum interface design approach also lends itself to systems testing and checkout simplicity in comparison to an integrated spacecraft-electric propulsion system approach, the philosophy adopted in previous solar electric propulsion spacecraft·design studies.

The electric propulsion section of the recommended spacecraft is shown in Figure 6-56 in its relative location to the entire spacecraft: at the aft end. This module has been designed as an entity, and requires only mechanical and electrical interfaces with the remainder of the spacecraft. An enclosed portion is provided forward of the ion engines for the mercury propellant tankage and electrical and propellant feed systems. The structure provides hard points for the central mounting fitting of the two rearward mounted roll-up arrays. The structure also provides end supports for the cantilevered portion of the solar array drums. The ion engines are attached to the module structure through a dual-axis linear translator. Two power conditioning panels are mounted to the external part of the structure area facing away from the sun.

In the design of the electric propulsion section of the spacecraft, emphasis was placed in arriving at a design concept which satisfied four major considerations. The first is that of the arrangement and relative locations of the various elements in the propulsion system. The liquid mercury propellant tank should be located on the longitudinal axis to minimize stabilization and control requirements. The power conditioners should be attached to the module structure to keep cable lengths to a minimum. The location and mechanization of the electrical and propellant feed lines across the translator are also of concern. The second item is the thermal control of the propulsion module. The thermal control requirements are different from those of the remainder of the spacecraft systems, since the electric propulsion module operates for the first 210 days of the 1190 day mission. The requirements

TOP VIEW
SWITCHING ASSEMBLY

TO PC&C
PANEL NO. 1

TO PC&C
PANEL NO. 2

RIBBON
CABLE

ACTUAL TOTAL
24 CONDUCTORS
FOR EACH
RIBBON CABLE

RIBBON
CABLE

TO THRUSTER
NO. 1

TO STANDBY
THRUSTER

TO THRUSTER
NO. 2
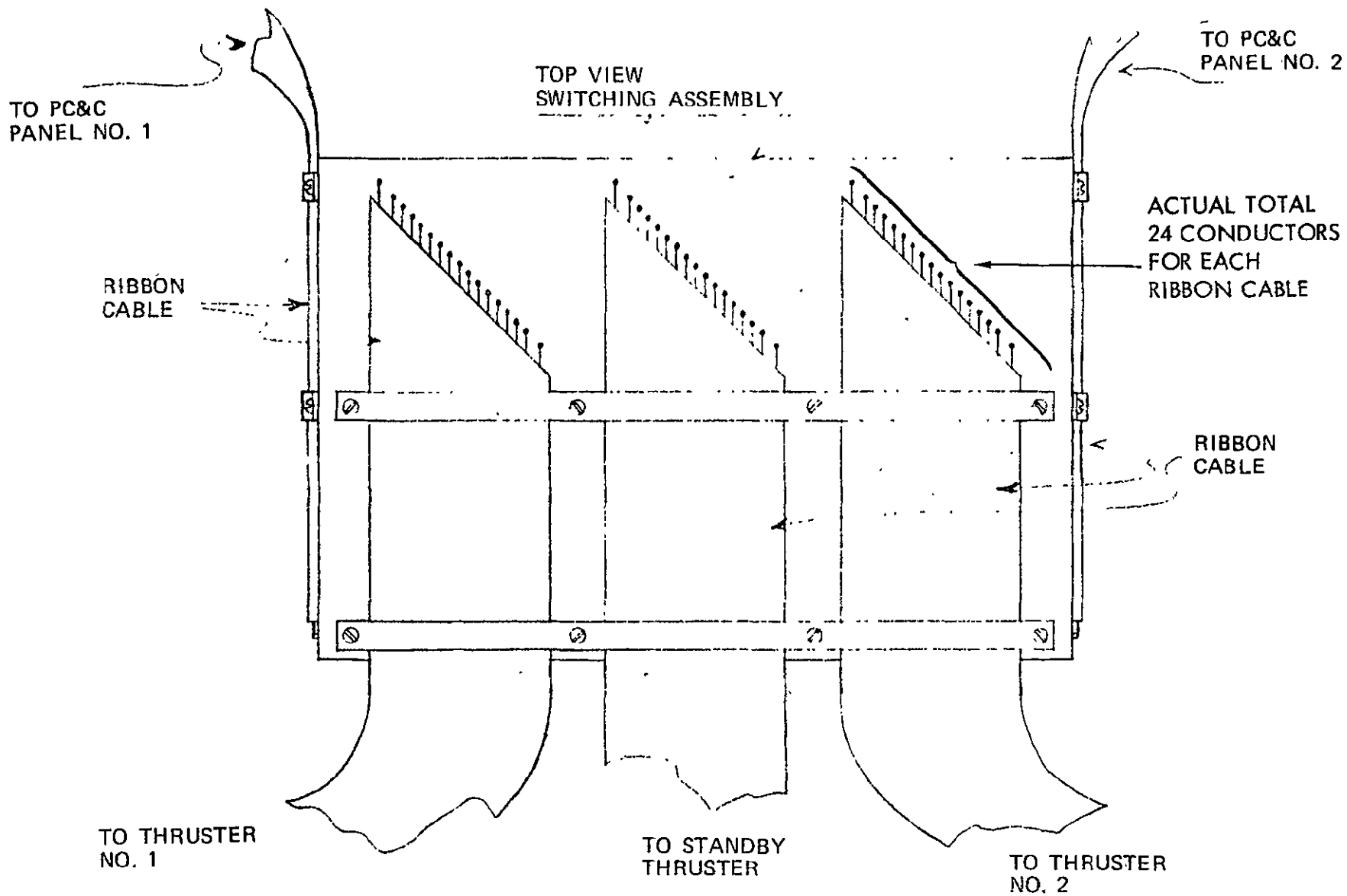
Figure 6-55. Ribbon Cable Termination at the Switching Assembly Enclosure

are such that the ion engines must be maintained at a warm temperature
before they can be turned on. The power conditioning panels must also be
kept warm before turning them on. Engine control and switching equipment
within the enclosed compartment must also be provided with an acceptable
thermal environment. Third, all of the equipment must be protected from
meteoroid damage until the end of thrusting. It is also desirable to protect
the equipment sufficiently to enable the propulsion system to be used or
started again after the completion of the mission (1190 days) as an engineering
test of the electric propulsion module survivability in the space environment.
The last item concerns maintaining thrust vector alignment with the center
of mass of the vehicle and providing thrust phase attitude control by use of
thrust vector displacement. Satisfying this requirement requires the imple-
mentation of mechanical translation of the engine array. The individual
engines must also be hinged to provide attitude control torques about the
thrust vector axis.

The electric propulsion module configuration is shown in Figure 6-57.
The module structure is one meter (40 inches) square and 88 inches long.
The accelerated grids of the thrusters are 16 inches from the aft end of the
structure. The structural arrangement shown on Figure 6-57 is basically
the same as that of the forward payload section of the spacecraft.

The two power conditioning panels are mounted outboard of the dark
facing side structure. They are attached to the structure through thermal
isolation mounts. The basic power conditioning panel is covered on the sun-
facing side with 15 layers of aluminized mylar insulation and an aluminum
cover skin for meteoroid protection as shown in Figure 6-58. The dark facing
or radiating area of the panel is also covered with a meteoroid protection
skin. They are provided with internal heaters to warm them when they are
in a standby mode. Locating the power conditioning panels on the dark side
of the spacecraft also helps to eliminate the center-of-gravity shift from the
solar arrays canted toward the sun.

The enclosed compartment at the aft edge of the propulsion module
structure contains the liquid mercury propellant/pressurant tank, the mercury
feed system, the electrical switching network between thrusters and power
conditioning panels and the electrical feed system. The 10-inch diameter
mercury propellant/pressurant tank is supported on a conical skin stringer
support. The tank is located on the longitudinal axis to minimize center of
gravity shifts resulting from propellant usage. A squib valve and flow control
orifice is located on the aft end of the tank to prevent hammering of the ion
engine vaporizer by the liquid mercury during boost. Mercury leaves the
tank through the orifice and enters the feed system manifold, from which it
is distributed to the engines. The electrical power lines from the power con-
ditioners to the engines enter the compartment and are routed to the switching
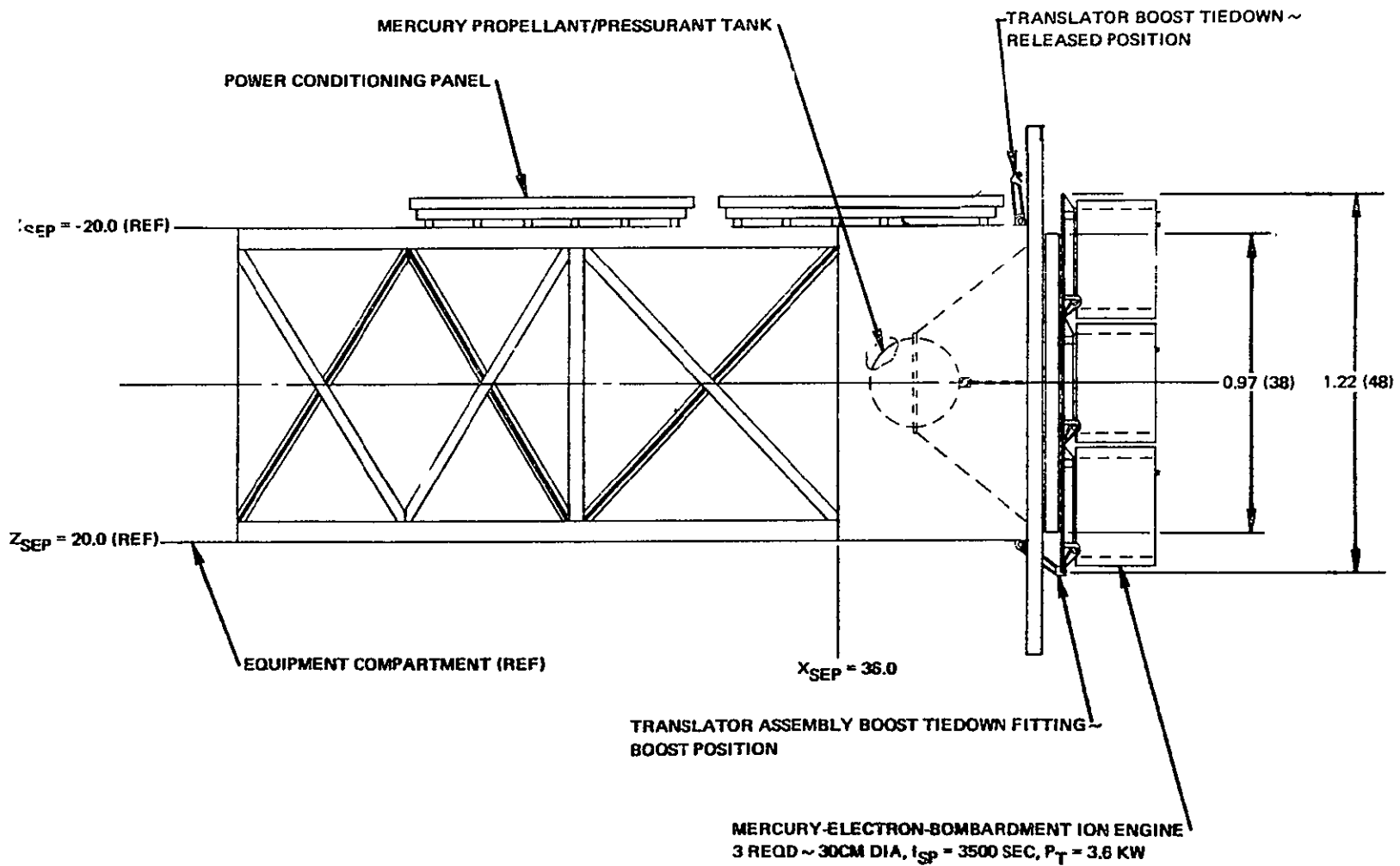
Figure 6-57. Electric Propulsion Module Installation

HIGH AND LOW VOLTAGE OUTPUT
TO ION ENGINES

THERMAL ISOLATOR MOUNT (TYP)

POWER CONDITIONING PANEL
RADIATING SURFACE AND METEOROID BUMPER

POWER CONDITIONING PANEL COVER
AND METEOROID BUMPER

ALUMINIZED MYLAR INSULATION

POWER INPUT
FROM ELECTRICAL POWER SYSTEM

LONGERON (REF)

STRUCTURE (REF)
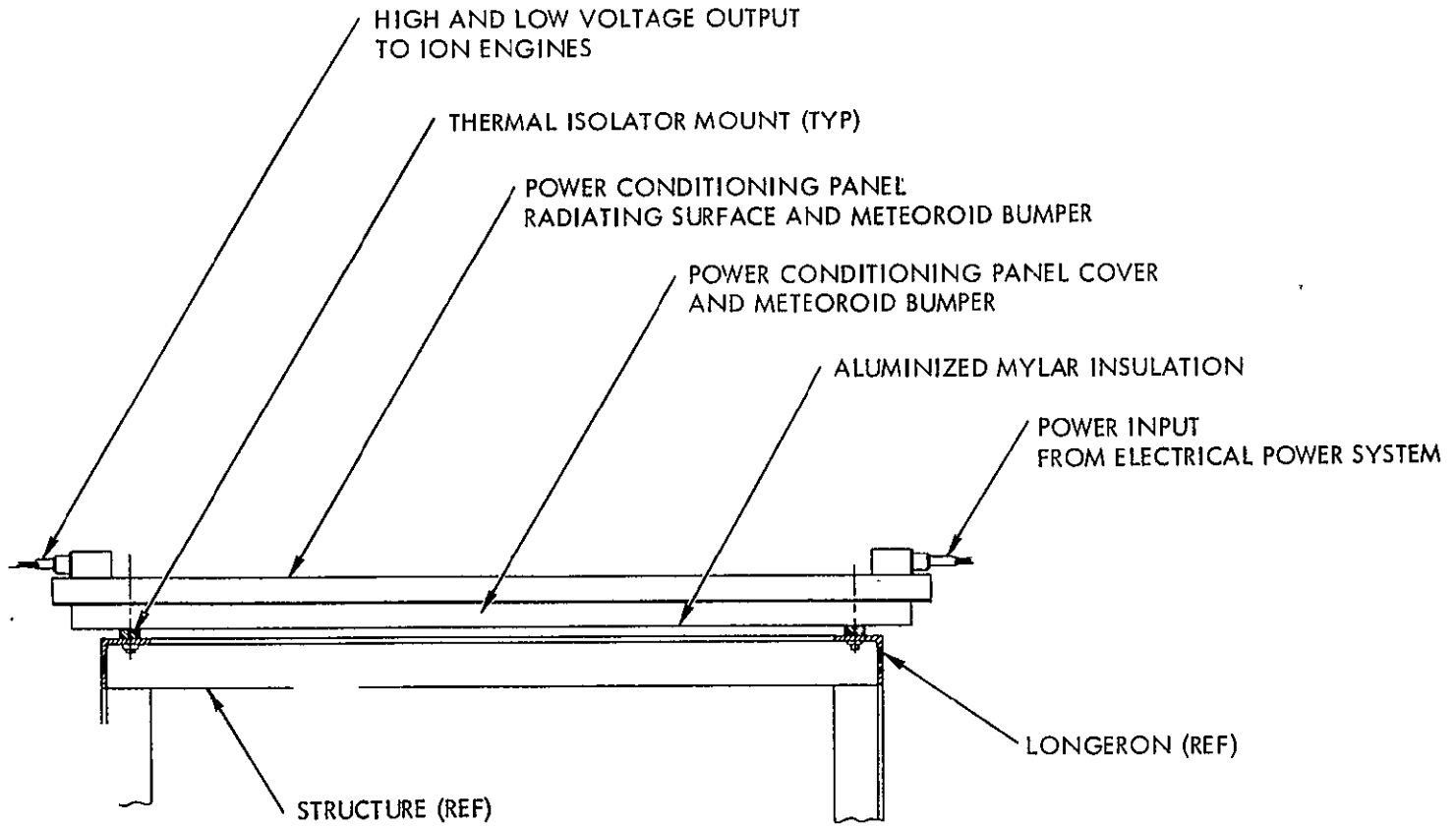
Figure 6-58.   Power Conditioning Panel

network which directs the power to the operating engine or engines. The switching network receives both low and high voltage power from each power conditioning panel. The enclosed compartment utilizes a double skin to provide meteoroid protection. The skins are the same thicknesses and spacing as required on the equipment compartment of the spacecraft. Sufficient protection is provided for the electric propulsion equipment to survive the coast phase through the asteroid belt. At the end of the mission an attempt to restart the engines would provide some additional and valuable engineering data on the system survivability in the space environment.

The ion thrusters and translator assembly are mounted to the aft surface of the propulsion module. Three ion thrusters are mounted to an engine mount side by side in the ecliptic plane. The thrusters are mounted to single-axis gimbal mounts which allow the thrusters to hinge ±10 degrees from normal to provide attitude control about the longitudinal axis during two thruster operation. Gimbal mounts are attached to the engine cluster mount through thermal isolators. The engine cluster mount is the first component of the dual axis translator. The attachment of the thrusters to the mount is illustrated in Figure 6-59.

The engine cluster mount translates ±3 inches normal to the ecliptic plane. It translates within a carriage which translates within guide rails ±17 inches in the ecliptic plane. The guide rails are rigidly attached to the propulsion module structure. Both the cluster mount and carriage translate by use of a stepper motor gear reduction unit which utilizes a band to provide the necessary motion. The mount and carriage are guided by self aligning V-groove rollers at four points on each structure. The mount and carriage translate 0.005 inches per motor step, which when coupled with the 100 step per second rate of the motor yields a translation rate of 1/2-inch per second.

To keep the weight and size of the translator at a minimum, it was designed deliberately not to support the engine array during the boost phase. Consequently, the ion thruster mount is held during boost by tiedowns which carry the launch loads of the thrusters directly to the spacecraft base structure. After separation, and before thruster turn-on, the boost tiedowns are released.

To ensure high reliability for the propulsion system for higher energy missions requiring longer thrusting times, such as an out-of-ecliptic probe that requires a total thrust time of approximately 680 days versus 210 days for the asteroid belt survey, the addition of one standby thruster is recommended. Providing additional carriage mounting length to accept an additional thruster to the existing row of three thrusters is a feasible solution, although not recommended because of the increased envelope and attendant spacecraft-launch vehicle adapter space considerations. An arrangement of the four

10°

10°

ELECTROSTATIC SHIELD

ENGINE MOUNT (REF)

ION ENGINE GIMBAL FITTING

0.4 (15.8) DIA.

0.3 (11.8) DIA.

0.25 (10.0)

THERMAL ISOLATOR

NEUTRALIZER

CATHODE ISOLATOR

CATHODE MERCURY FEED VAPORIZER

GIMBAL DRIVE MOTOR AND MECHANISM

MERCURY INLET FROM MANIFOLD

ION ENGINE FEED SYSTEM MANIFOLD

ION ENGINE VOLTAGE INPUT

NEUTRALIZER MERCURY FEED LINE

MAIN FEED SYSTEM VAPORIZER AND ISOLATOR ASSEMBLY

Figure 6-59.   Thruster Attachment

thrusters in a 2- by-2 square pattern (Figure 6-60) is proposed. In this pattern the thrusters can be single-hinge gimbaled with the hinge axis oriented diagonally across the square pattern. In this arrangement the operation of any two thrusters can produce control torques about the thrust vector, or longitudinal axis of the spacecraft. The arrangement of four thrusters in this fashion does require two-degree-of-freedom translation to provide center of mass and thrust vector alignment. Since in the recommended design 2-degree of freedom translation is proposed, the reduction of stroke length along the in-line thruster axis and the extension of the stroke in cross translation does not offer a major design modification to the translation technique proposed. For future solar electric missions where, probably, more than three thrusters would be integrated into an array, adoption of the two-degree-of-freedom translation concept would benefit from the development experience and subsequent flight demonstration of the asteroid belt survey spacecraft.

For missions other than the asteroid belt survey, the removal of all of the particle impact and momentum sensing equipment (electrostatic ballistic pendulum modules) from the shadow side of the spacecraft bus will provide more than adequate space for the addition of a third power conditioning panel Expansion of the size of the electric propulsion system therefore does not appear to be a potential design problem for the recommended spacecraft design.

POWER CONDITIONING
PANELS

SUN
SIDE OF
SPACECRAFT

HG. RESERVOIR

30 CM DIAMETER
THRUSTERS

HINGE
AXIS

HINGE
AXIS

STEPPER MOTOR AND
GEAR REDUCTION UNITS
(1 REQ'D EACH THRUSTOR)

Space Division
North American Rockwell
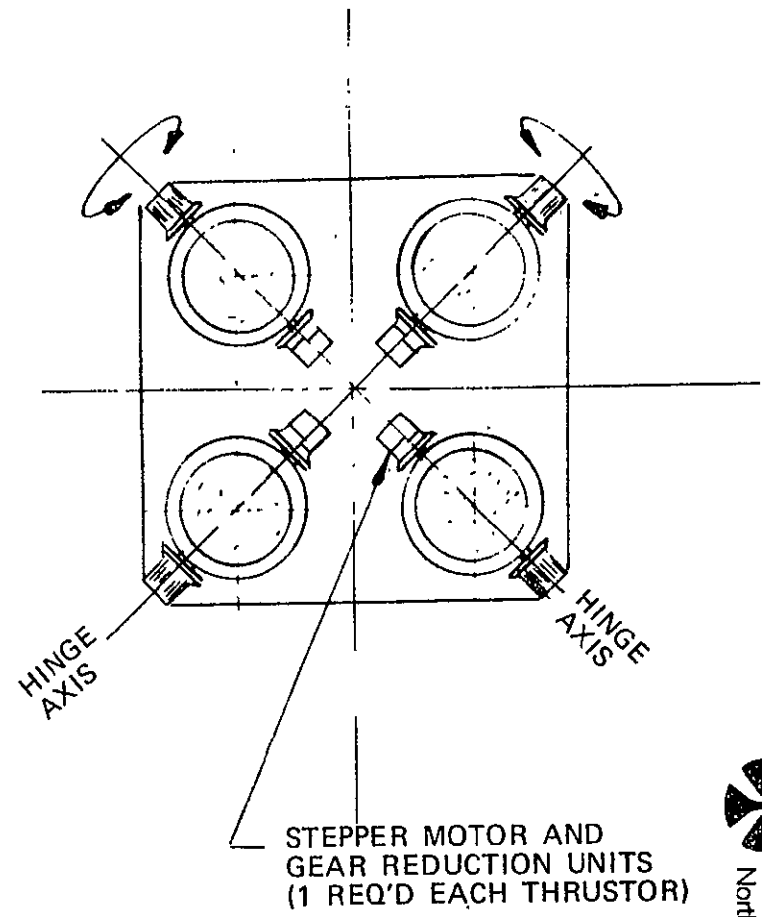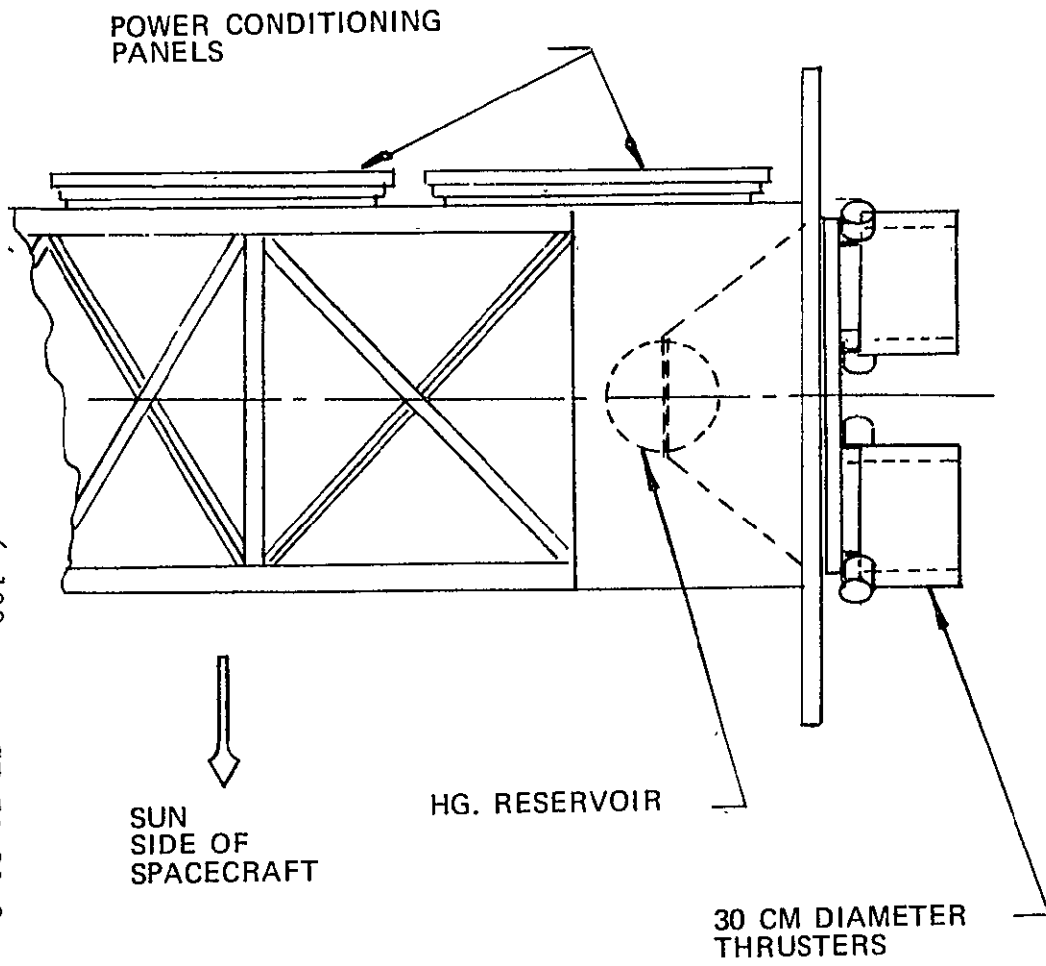
Figure 6-60.   Four-Thruster Array Configuration

TECHNOLOGY EXPERIMENTS

It is evident that the proposed spacecraft must incorporate tests, or experiments, which during the mission yield information about the operational characteristics of the propulsion system. The information to be gained should include housekeeping data for all vital components of the propulsion systems, data which permit identification of failures, parametric performance data on the extended capabilities of the propulsion system, and data on the interaction of the propulsion system with the spacecraft and with the space environment. In selecting appropriate experiments for these tasks, it must be remembered that the prime purpose of the mission is to perform a number of space science experiments. In other words, technology type experiments should be incorporated only to the extent that they are essential to the safe performance of the mission, provied important information for future electrically propelled missions, or improve knowledge about electrically propelled spacecraft without compromising the scientific payload. Division of all conceivable technology experiments into these categories (and an additional category defined below) provides a logical priority rating system whereby experiments are considered so essential that they sould be incorporated at all costs. Informational experiments are considered desirable and they should compete with the planned space science experiments for spacecraft space, weight and power. General knowledge-seeking experiments are understood to be optional and they should be considered only to the extent that space, weight and power are available beyond the needs of the scientific mission. A last category consists of those conceivable experiments which can be or are conducted eleswhere, for example, on the ground or aboard the SERT or ATS spacecraft. Experiments of the latter type will not be recommended for this mission.

A number of conceivable technology type experiments are described below and rated in accordance with the described priority system.

Housekeeping Tests

Table 6-25 lists some 40 types of tests which should be conducted periodically during the thrust phase of the mission to provide up-to-date information on the operational status of the propulsion and power systems. Most of these tests are based upon familiar measuring principles (bleeder resistors, series resistors, dc current transformers, thermistors, and thermocouples). However, some of the proposed tests require development of suitable sensing devices. This applies in particular to a propellant reserve gauge and a flow meter.

Table 6-25. Housekeeping Tests

Parameter	Measuring Device	Number Measured	Measurement Range	Resolution	Measurement Frequency	Test Priority
		THRUSTER AND FEED SYSTEM				
Main propellant flow	Flowmeter	3	$0-5 \times 10^{-3}$ gr/sec	1	1/hr	A
Cathode propellant flow	Flowmeter	3	$0-5 \times 10^{-4}$ gr/sec	5	1/hr	A
Neutralizer propellant flow	Flowmeter	3	$0-5 \times 10^{-4}$ gr/sec	5	1/hr	A
Main vaporizer temp	Thermistor	3	$T_{oper} \pm 20$ C	± 1 C	1/hr	A
Cathode vaporizer temperature	Thermistor	3	$T_{oper} \pm 20$ C	± 1 C	1/hr	A
Neutralizer vaporizer temperature	Thermistor	3	$T_{oper} \pm 20$ C	± 1 C	1/hr	A
Hollow cathode temperature	Thermocouple	3	-50 to + 1200 C	± 60 C (5%)	1/hr	A
Thruster shell temperature	Thermistor	3	-50 to 400 C	+ 20 C (5%)	1/day	B
Main isolator temperature	Thermistor	3	-50 to + 350 C	± 2 C	1/day	A
Cathode isolator temperature	Thermistor	3	-50 to + 350 C	± 20	1/day	A
		POWER CONDITIONING AND CONTROL SYSTEM				
Beam supply volt	Bleeder resistor	2	1500-2000 V	1%	1/hr	A
Accelermeter voltage	Bleeder resistor	2	1500-2000 V	5%	1/hr	A
Discharge voltage	Dc current transformer	2	30-50 V	5%	1/hr	A
Main vaporizer voltage	Bleeder resistor	2	0-5 V	1%	1/hr	B
Cathode vaporizer voltage	Bleeder resistor	2	0-5 V	5%	1/hr	B
Neutralizer vaporizer and neutralizer cathode heater voltage	Bleeder resistor	2	0-5 V	5%	1/hr	B
Cathode keeper voltage	Dc current transformer	2	0-400 V / 0-20 V	5%	1/hr	B
Neutralizer keeper voltage	Bleeder resistor	2	0-400 V / 0-20 V	5%	1/hr	B
Main isolator, cathode isolator heater voltage	Bleeder resistor	2	0-20 V	5%	1/day	B
Valve activation		1	On/off		once	B
Ion beam current	Series resistor	2	0-2A	0	1/hr	A
Accel current	Resistor	2	0-200 mA	10	1/hr	A
Discharge current	Dc current transformer	2	0-20A	0.5	1/hr	A
Magnet current (Required only if electromagnet thrusters are used instead of permanent magnet thrusters)	Dc current transformer	2	0-20A	1.0	1/day	A
Cathode keeper current	Dc current transformer	2	0-1A	1.0	1/day	A
Neutralizer keeper current	Series resistor	2	0-1A	1.0	1/day	A
Main vaporizer heater current	Series resistor	2	0-3A	0.5	1/hr	A
Cathode vaporizer heater current	Series resistor	2	0-3A	0.5	1/hr	A
Neutralizer vaporizer heater current	Series resistor	2	0-3A	0.5	1/hr	A
Main isolator, cathode isolation and cathode heater current	Series resistor	2	0-5A	1.0	1/day	A
Various temperatures	Thermistors	10	-50 to +150 C	± 1 C	1/day	A
		RESERVOIR				
Propellant Reserve	Volume gauge	1	0-10 ℓ	2	1/day	A
Propellant pressure	Pressure gauge	1	0-15 psi	5	1/day	A
Propellant temperature	Thermistor	1	-50 + 150 C	5	1/day	B
		MECHANISMS				
Gimbal position indicator	Shaft encoder	1	± 10 deg	1%	1/day	A
Translator position indicator	Synchro-trol transformer	1	17 in	1%	1/day	A

Failure Diagnostics

Desirable failure sensing tests are listed in Table 6-26. These tests use exclusively sensing devices that are similar to those required for housekeeping tests. The list reflects concern about failure modes which have been observed in present state-of-the-art thrusters. Future technological advances may minimize the probability for some of these failure modes. On the other hand, new hazards may appear during continued thruster tests and appropriate diagnostic tests must then be devised.

Extended Propulsion System Tests

During the proposed mission, not all functions which an electric propulsion system can perform may be executed. Table 6-27 lists a number of propulsion exercises intended to provide in-flight information about the dynamic behavior of electrical thruster systems. For mission safety it is proposed that these exercises be performed at the end of the thrusting phase.

Interactions of the Propulsion System with Spacecraft and Space Environment

Table 6-28 lists interactions of fields and particles generated by the propulsion system with spacecraft components and with environmental fields and particles.

With proper design and ground testing, the danger of radio frequency interference resulting from switching surges as well as corona can be practically eliminated. The danger of interference of the ion beam with the communication system is quite remote. The frequency range in which ion beam instabilities may be expected (close to the plasma frequency) is below 100 KHz. This range is too far from the communications band (2000 MHz) to lead to interference. Even if the microwave beam were passed directly through the ion beam, random refractive deflections associated with ion beam instabilities would be much too small to be noticeable as noise. The refractive index of the ion beam at 2000 MHz does not exceed 1.0001.

Determination of the potential difference between spacecraft and ion beam is of interest, since this difference affects thrust to a small degree. It is anticipated that hot probe measurements aboard SERT II will give the required information. For this reason, ion beam probe measurements are not considered necessary aboard the mission under discussion. Changes of the spacecraft potential (with respect to space potential) due to the thrust beam would interfere with the collection rates of solar wind

Table 6-26. Failure Diagnostics

Failure Mode	Evidence	Measuring Device	Measurement Range	Test Priority
Feed system leak	Pressure drop or propellant volume change	Pressure gauge Volume gauge	0-15 psi 0-10ℓ	A A
Valve inoperative	No discharge and keeper currents	Dc current transformer	0-20A 0-1A	A
Main vaporizer stoppage	Low discharge current normal keeper current	Dc current transformers	0-20A 0-1A	A
Cathode vaporizer stoppage	No discharge and cathode keeper currents normal neutr keeper currents	Dc current transformers and resistors	0-20A 0-1A 0-1A	A
Neutralizer vaporizer stoppage	Normal discharge and cathode keeper currents no neutralizer keeper current	Dc current transformers and resistors	0-20A 0-1A 0-1A	A
Main vaporizer punch-through	Excessive discharge and beam currents	Dc current transformers and resistors	0-20A 0-2A	A
Cathode vaporizer punch-through	Excessive cathode keeper and discharge currents	Dc current transformers	0-20A 0-1A	A
Neutralizer vaporizer punch-through	Excessive accel currents	Current sensing resistors	0-200mA	A
Grid erosion	Apparent increase in propellant utilization	Current sensing resistors	0-2A 0-3A	A
HV Arcs				
1 Thruster to ground	Beam current surges	Arc counters	0-10 arcs/min	A
2. Thruster to accelerometer	Beam and accel current surges	Arc counters	0-10 arcs/min	A
HV Leakage				
1. Thruster to ground	Apparent increase in propellant utilization	Current sensing resistors	0-2A 0-3A	A
2 Thruster to accelerometer	Increase in accel currents	Current sensing resistors	0-2A	A

Table 6-26. Failure Diagnostics (Cont)

Failure Mode	Evidence	Measuring Device	Measurement Range	Test Priority
HV Short				
1 Thruster to ground	HV supply shorted	Bleeder resistors	1500-2000V	A
2. Thruster to accelerometer	HV and accel supplies shorted	Bleeder resistors	1500-2000V 1500-2000V	A .
Heaters (all)				
1 Open circuit	No current and lower temperature	Current sensing resistors		A
2. Short circuit	Excess current and lower temperature	Thermistors, thermocouples		
Power conditioning failure				
1. Open circuit	No output voltage	Bleeder resistors		A
2. Short circuit	No output voltage high temperature	Bleeder resistors thermistors		A
Array Failure				
1 Deterioration	Reduced voltage under load	Test load	0-100V	A
2. Shorts	Reduced voltage under load	Bleeder across subpanels	0-100V	A
3 Open circuit	Reduced voltage under load	Test load and bleeder across subpanels	0-100V	A
Gimbal arrest	No change in encoder output	Shaft encoder	±10	A
Translator arrest	No change in encoder output	Synchro-trol transformer	17 in., 3 in.	A

Table 6-27. Propulsion System Exercises

Test	Activation	Test Range	Sensing Method	Accuracy (percent)	Test Priority
Throttle thruster	Change of set point	0.5-1 (full thrust)	Beam current	1	B
Change direct of thrust	Gimbal	±10°	Amount of counter action required with cold gas jets		B
Change thruster position	Translate	±17 in., ±3 in.	Amount of counter action required with cold gas jets	1	B
Stop and restart thrusters	Vaporizer heater	0-1 (full thrust)	Beam current	5	B
Change thrusters	Vaporizer heater		Beam current		B

Table 6-28. Propulsion System Interactions With Spacecraft and
Surrounding Space

Type of Interactions	Components (or Quantity) Affected	Evidence	Magnitude	Test Procedure	Test Priority
RF Interference					
From shorting surges (in presence of ground loops)	Command and communication system	Erratic performance.	Unimportant with careful design		D
From corona along insulators and from vacuum prebreakdown	Command and communication system	Erratic performance	Unimportant with careful design	Turn-off HV	D
From ion beam instability	Command and communication system	Erratic performance	Unimportant with careful design	Turn-off ion beam	C
Dc E-Fields and Potentials					
Elevated spacecraft potential associated with beam ejection	Ejected ions and Faraday Cup	Thrust and changes	Small, <1%	Plasma probe in beam	D
		Change in collection rates and energies	Large	Turn-off ion beam	C
Array potentials	Ejected ions and Faraday Cup	Thrust and changes	Small, <1%	Short circuit array	C
		Change in collection rates and energies	Large		

Table 6-28. Propulsion System Interactions With Spacecraft and
Surrounding Space (Cont)

Type of Interactions	Components (or Quantity) Affected	Evidence	Magnitude	Test Procedure	Test Priority
B-Fields					
Thruster fields	Faraday Cup and	Change in collection rates	Large	Turn-off thruster coils	C
B Fields associated with bus currents	Gaussmeter	and erroneous B-fields	Very large	Short circuit array in many places	C
Thrust Beam Particle	Faraday Cup	Change in collection rates	Severe	Turn-off ion beam	C
	Array surface	Current leakage detection	Small	-	D
		Breakdown	Small	-	D
		Decrease in transparency	Unknown	-	D
f electromagnets are employed					

particles by the Faraday cup collectors. The only reliable way to eliminate this effect is to turn off the propulsion system during solar wind measurements. This turn-off procedure is necessary also because thrust beam particles will find their way in to the Faraday collectors.

B-fields associated with the propulsion system are of a magnitude where they can interfere strongly with measurements of the solar wind B-field. At 3 AU the solar field is on the order of 0.5γ. B-fields associated with the thruster system can be expected to be comparable to or exceed this amount anywhere on the spacecraft, except on the outboard edges of the solar array. As indicated previously, it may be desirable that the thrusters use electromagnets which can be switched off. B-fields associated with the currents carried by the array buses can be made relatively small by suitable bus layout. Buses also may be shorted during solar wind B-field measurements.

Finally, thrust beam particles (electrons, ions and charge exchange ions, slow and fast propellant atoms) can be expected to land upon various spacecraft surfaces. Of main concern is the interaction of these particles with the array surfaces. Electrons landing there may constitute current leakage. However, it can be shown that this hazard is negligible. Impacting beam ions may charge up insulating converslides and thereby cause dielectric breakdown problems. Actually, with ion energies less than 2000 volts, this danger is remote. Finally, coverslide surfaces may be sputter-damaged, resulting in reduced light transmission and thereby in reduced power output. An experiment will be performed aboard SERT II which should provide pertinent information about such damage. For this reason, a cell deterioration experiment is not proposed at this time for the mission.

A review of the proposed technology experiments shows that all high priority (categories A and B) tests are listed in Tables 6-25, 6-26 and 6-27. The experiments listed in Table 6-28 are considered optional. In many cases the measuring device and technique are included as part of the PC&C system electronic circuitry. For cases where other types of instrumentation are required, Figures 6-61, 6-62, and 6-63 indicate the device required and its position on the thruster, PC&C panel, and reservoir, respectively.

TECHNOLOGY DEVELOPMENT AND TEST PROGRAM PLAN

Prototype thrusters and associated power conditioning and control systems have been constructed in 15-, 20- and 30-centimeter diameters at nominal power levels of 1 to 4 kilowatts. The data used to design the

FM = FLOW METER

•TH = THERMISTOR

•TC = THERMOCOUPLE
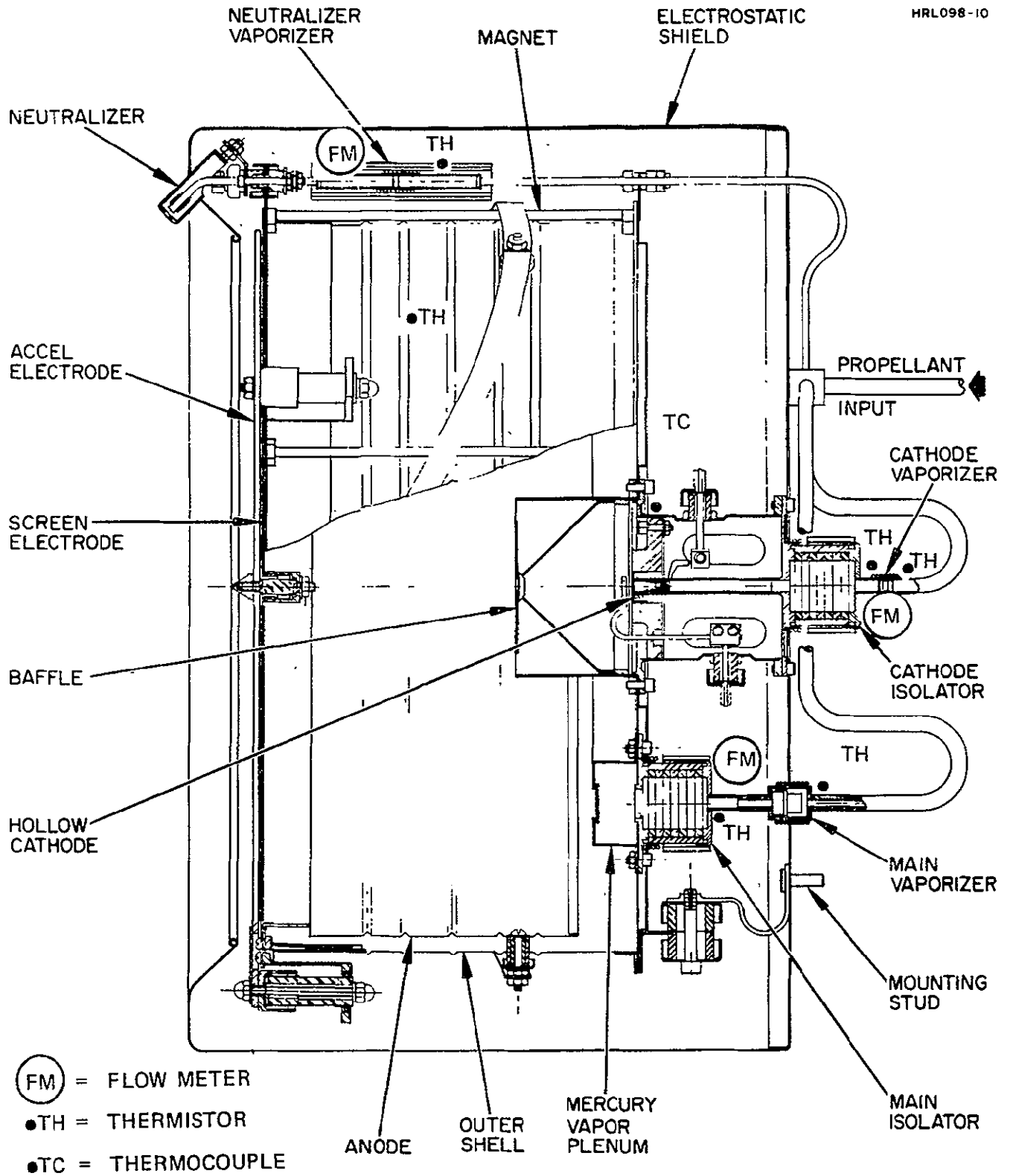
Figure 6-61. Location of Measuring Devices on Thruster
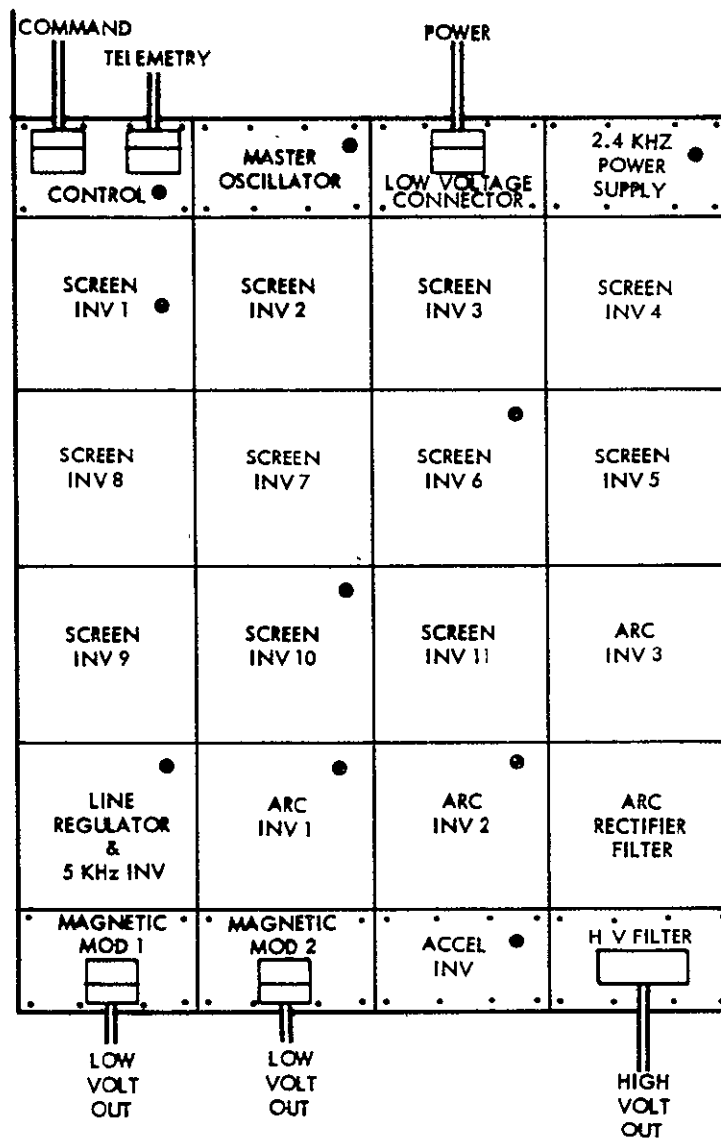
Figure 6-62. Location of Measuring
Devices on Power Conditioning Panel
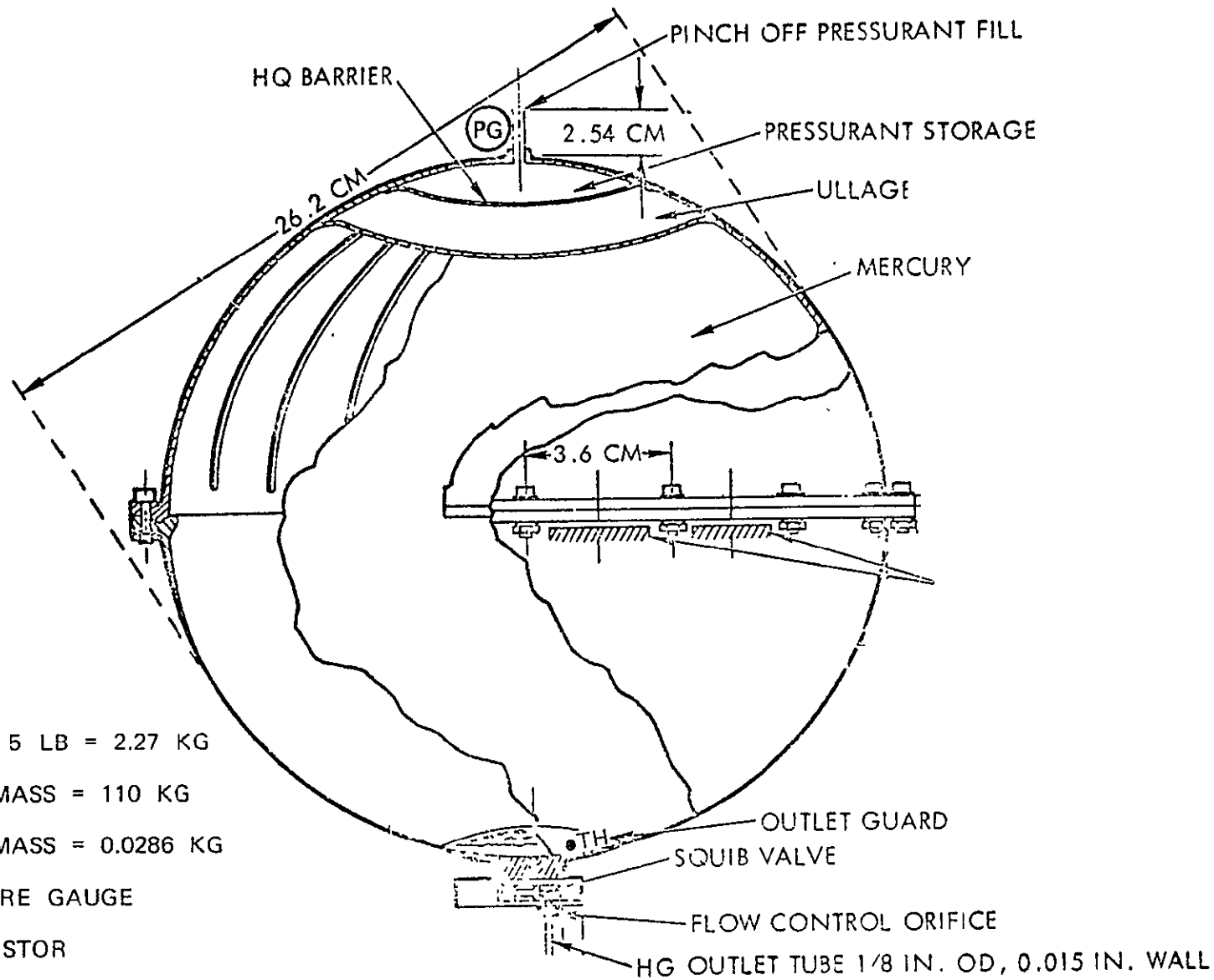
PINCH OFF PRESSURANT FILL

HQ BARRIER

PG

2.54 CM

PRESSURANT STORAGE

ULLAGE

26.2 CM

MERCURY

3.6 CM

TANK MASS = 5 LB = 2.27 KG

PROPELLANT MASS = 110 KG

PRESSURANT MASS = 0.0286 KG

PG   = PRESSURE GAUGE

•TH = THERMISTOR

OUTLET GUARD

•TH

SQUIB VALVE

FLOW CONTROL ORIFICE

HG OUTLET TUBE 1/8 IN. OD, 0.015 IN. WALL

Figure 6-63.   Mercury Propellant Reservoir

electric propulsion system for this study have been interpolated or extrapolated from the characteristics of these experimental systems. This background provides a firm basis for predicting the characteristics, performance, requirements, constraints, and all other aspects of the proposed propulsion system design. However, final confirmation of the proposed design requires the development, integration, and test of all major elements into a flight type configuration. For example, flight type (or their equivalent) circuit components must be found for the power supplies; the gains, time response, and set points for the control circuitry must be established; a detailed structural thruster design must be completed. After final design and fabrication, the performance of each subsystem must be verified experimentally. Finally, these subsystems must be integrated for complete system evaluation and life testing. These combined tasks constitute the Technology Development and Test Program to be discussed here and include a complete failure modes and effects analysis study to aid in subsequent test planning and test result interpretation.

Since life testing for electric propulsion systems consumes extended periods of real time (at least equal to the operating times required for the mission), it is necessary to initiate the development and test program well in advance of phase C (Volume III, Program Development Plan, for asteroid belt mission program schedule definition). In this way no major changes in propulsion system design need be expected during the critical Phase C and D design specification and fabrication efforts. The details of a program which will fulfill these goals are presented in this section.

Prototype Phase

This phase of the program is the fabrication (and development, where necessary) of prototype hardware representative of those designs proposed as a result of the design analysis present earlier. The prototype phase will start with a complete and detailed specification of the system including the following subsystem definitions:

Thruster and Feed Subsystem

Power level
Effective specific impulse
Thrust level
Throttling range
Lifetime
Reliability
Size
Launch environment
Weight
Thermal constraints
Stability requirements

Power Conditioning and Control Subsystem

Nominal thruster operating parameters
Input voltage and current ranges
Control logic
Recycle transient demands (high voltage arc energy
  requirements)
Recycle PC&C programming and timing
Thruster - PC&C loop gain
Switching requirements
EMI specifications
Thermal constraints
Reliability requirements
Size
Launch environment
Weight

Reservoir Subsystem

Capacity
Valving
Thermal environment
Launch environment
Location w. r. t. thrusters

Overall System

System constraints and configuration

From these specifications, prototype hardware will be designed and
subsequently fabricated. Individual subsystem performance will be verified
experimentally with a series of relatively short (100-hour) tests. During
these tests, critical voltages, currents, temperatures, and other measure-
ments will be monitored for correlation with results from previous failure
modes and effects analyses. These tests will also be used to establish the
interface specifications which exist between the thruster and feed and the
power conditioning and control subsystems.

Following verification of the individual subsystems, they will be
integrated into a single system for further testing. Integration will begin
first with manual control to evaluate the overall system transfer functions
(loop gains, time constants, etc.). The automatic control and startup cir-
cuitry will be introduced as rapidly as practical to provide a prototype
system which is as nearly representative of the flight system as possible.
This system will be exercised over the full range to establish limits of
performance, stability, transient response, etc.

This prototype phase of the program will end with a life test of the system. The test should be of 500 to 1000 hours duration and be heavily instrumented to determine small drifts in performance characteristics, temperatures, and transient response, related to the failure modes which might be expected to present a major problem in longer tests. These "indicator" parameters will also be used to interpret degradation during final system reliability tests.

Design Verification Phase

The objective of the design verification phase of the program is to quantitatively verify all performance goals, including lifetime, of a single array. in a vehicle configuration. Three thrusters, two power conditioners and control systems, the reservoir, and the auxiliary equipment will be fabricated. The subsystems will satisfy the specifications provided by the prototype development phase including the life test. These subsystems will be assembled into an array similar to that currently proposed for the flight vehicle. Sufficient hardware will also be provided to run a preliminary evaluation of the ability to withstand launch vibrations.

The array will be exercised in a thermal vacuum environment which as closely as possible matches that of the flight spacecraft. One possible. exception may be the necessity to isolate the power conditioning in a vacuum chamber separate from the thrusters to assure that the power conditioning is not contaminated by the mercury effluent from the thrusters and back-sputtered material from the ion beam collector. All conditions of operation anticipated on the mission will be simulated with the array. If desired, interactions with the science and communication subsystems on the vehicle could, to a degree, be simulated with a minimum of additional effort during this phase.

In particular, the experiments with the array will include measurements of the following:

1. Switching procedures

2. System stability

3. Startup/shutdown procedures

4. Effects of input power variation (i.e., throttling)

5. Effect of cold soak

6. Interaction between adjacent thrusters (neutralizers, heat transfer, etc.)

7. Effects of simulated arcing

8. System transients and response time

9. EMI levels

Reliability Testing Phase

Following successful completion of the prototype and design verification phases of the technology development and test programs, the reliability of the complete propulsion system must be verified. Since the reliability testing of components or systems which must operate for long periods (such as is the case for electric propulsion systems) can be costly, an attempt was made to develop the simplest and least expensive test plan which will yield reasonable confidence in the test result.

Since portions of the proposed propulsion system are in standby during normal operation, the total system reliability of 0.983 can be apportioned to one series set of 1 thruster module, 1 PC&C panel, and 1 reservoir assembly for reliability purposes. The amount of hardware to be tested and the mean time between failures to be established is therefore minimized. This series set will hereafter be considered the test system. The results of the reliability apportioning are shown in Table 6-29 where, from the complete system estimate of R = 0.983, the equivalent series set is R = 0.955. This latter reliability figure converts to a mean time between failure (MTBF) of 110,000 hours. Table 6-29 also shows the comparable reliability and MTBF for the series set when the minimum acceptable level is considered. This minimum acceptable figure is shown to be MTBF $\cong$ 30,000 hours. The reliability test plan is devised to prove with high confidence that the actual MTBF is greater than 30,000 hours and with lower confidence that the MTBF could be as high as the 110,000 hour goal. Although the costs would be prohibitive to prove with high confidence that the MTBF is at least 110,000 hours, it is believed possible to prove with a high confidence that the MTBF is not a small fraction of the 110,000 hour goal and with at least 60 percent confidence that the actual MTBF is greater than the minimum 30,000 hour level. To augment the statistical confidence from the full system (series set) test, two parallel phases of the test will be performed to derive engineering confidence in the capability and inherent reliability of the devices. The results of these ancillary test phases can be summarized to support the test conclusions, but cannot be translated into statistical confidence figures. It is believed that on the basis of this combined test plan no real advantage could be gained by going to the much more expensive tests required to obtain higher statistical confidence in the test results.

6-125

Table 6-29. Propulsion System Reliability Estimates

| System | Reliability (Mean Time Between Failures) | |
	Predicted	Acceptable*
Asteroid Belt Propulsion System	0.983 (290,000 hours)	0.966 (145,000 hours)
Thruster Module	0.969	0.853
PC&C Panel	0.993	0.993
Reservoir	0.993	0.993
Series Set System (1 Thruster, 1 PC&C, 1 Reservoir)	0.955 (11×10^4 hours)	0.841 (3×10^4 hours)
*Based on a thruster failure rate multiplying factor of 5		

Test Plan

To achieve the planned high engineering confidence in the system reliability, a three phase test has been developed. The three phases are as follows:

Phase 1 - Accelerated Tests on Critical Mechanical Devices
Although it is not considered feasible to accelerate the stress conditions in the final system tests, it is very desirable to perform accelerated condition tests on the critical mechanical devices. Such items as valves, gimbals, and translators can be exercised through the equivalent of many missions and performance cycles to evaluate their life and failure characteristics fully. Actual failure density distribution curves can be plotted from these test results which can be interpreted directly into mission failure probability for these portions of the system. The quantities of these devices tested will depend on the device types and their individual costs. Generally speaking fairly large numbers (8 to 15) will be tested for relatively short times at accelerated conditions. From reliability physics studies into the mechanisms of degradation with stress and life, fairly accurate predictions can be made of mechanical system longevity and failure rate under normal mission conditions.

Phase 2 - Special Functional Tests on Assemblies and Subsystems

These tests will be performed on relatively small quantities of such assemblies and subsystems as power conditioning modules and switching assembly. The objective of these tests is to evaluate the system interaction effects and the capability of redundant circuitry. The effects of minor degradation on performance will also be studied so as to assess acceptable limits related to possible degraded operation. All failures will be analyzed as a part of the failure modes and effects analysis. Existing data from supplier and designer testing will be reviewed and correlated to provide a basis for realistic interpretation of system test results. Degradation analysis and mathematical modeling will be employed where needed to give assurance and direction to the test operation.

Phase 3 - Full System (Series Set) Tests

The search for an optimum test plan providing the greatest confidence in the shortest time at the least cost resulted in the Test Plan VI of MIL-STD-781B. This is a standard sequential test plan based on 10 percent risk that the test conslusions will be in error (90 percent confidence that the desired test objectives will be proven) as shown in Figure 6-64.

One way of interpreting the results of this test plan is the statement that, if zero failures occur in 30,000 system test hours, there is demonstrated with almost 90 percent confidence that the actual MTBF is between 6,000 and 30,000 hours. Likewise, the best estimate (or nearly 60 percent confidence) is that the MTBF is equal to 30,000 hours (the minimum acceptable MTBF: Table 6-29). Thus, this test plan can be performed economically using six series sets tested for 5,000 hours under simulated operational conditions. If a failure occurs during the 30,000 hours, the test can be continued (an advantage of the sequential test) until a valid conclusion can be reached. For example, if a second failure does not occur before 1.25 times 30,000 hours or 37,000 test hours, the test plan says that the test can be successfully concluded. Thus, with one failure and the six series sets, the test could be concluded in $\frac{37,000}{6} = 6,160$ hours.

Other quantities of failure events can be evaluated as discussed in the following section.

Interpretation of Test Results

Without considering the practical engineering confidence which can be placed on the systems inherent reliability as a result of Phases 1 and 2 of the test plan, the results of Phase 3 can be evaluated from the standpoint of best estimate interpretation.

Figure 6-64. Accept-Reject Criteria for Test Plan VI (MIL-STD-781B)
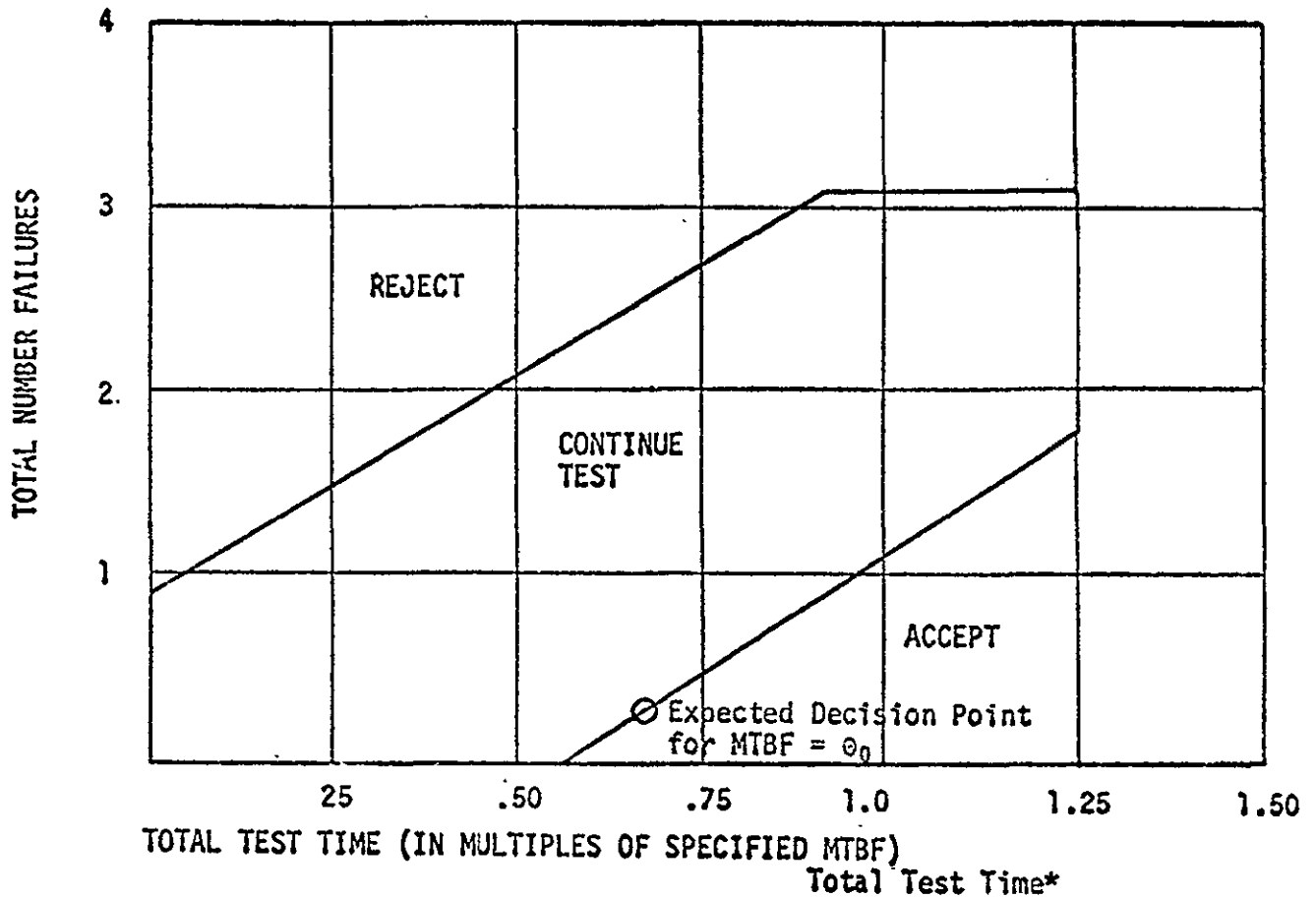
No. of Failures	Reject (Equal or less)	Accept (Equal or more)
0	N/A	0.55
1	0.04	0.95
2	0.44	1.25
3	0.85	1.25
4	1.25	N/A

*Total test time is total unit hours of "equipment on" time and is expressed in multiples of the specified MTBF.

LEGEND	
DECISION RISKS	10 Percent
DISCRIMINATION RATIO	5.0 : 1

28

Values of MTBF demonstrated in the 30,000 hour test for various numbers of failure can be derived from Table 6-30.

Table 6-30. Mean Time Between Failure Forecasts

Number of Failures	Mean Time Between Failures (hours)	
	~90 Percent Confidence Level	~60 Percent Confidence Level
0	13,000	32,000
1	7,800	15,000
2	5,800	9,800
3	4,500	7,200

The MTBF figures can be plotted as shown in Figure 6-65. These data show that the lower limit probable reliability near zero failures is rising abruptly. If the upper possible limit for the same test based on the chi^2 cumulative probability is plotted as shown by the dashed line and extrapolated to zero failures, the demonstrated reliability could approach or even exceed the goal of 110,000 hours. (The upper dashed curve indicates that there is a 60 percent chance with one failure that the MTBF might be as high as 134,000 hours.)

Program Schedule

The phasing schedule for the proposed technology development and test program is given in Figure 6-66, which shows that the total program duration approaches 30 months. As indicated previously, this program should be completed before initiation of Phase D of the Asteroid Belt Spacecraft Program.
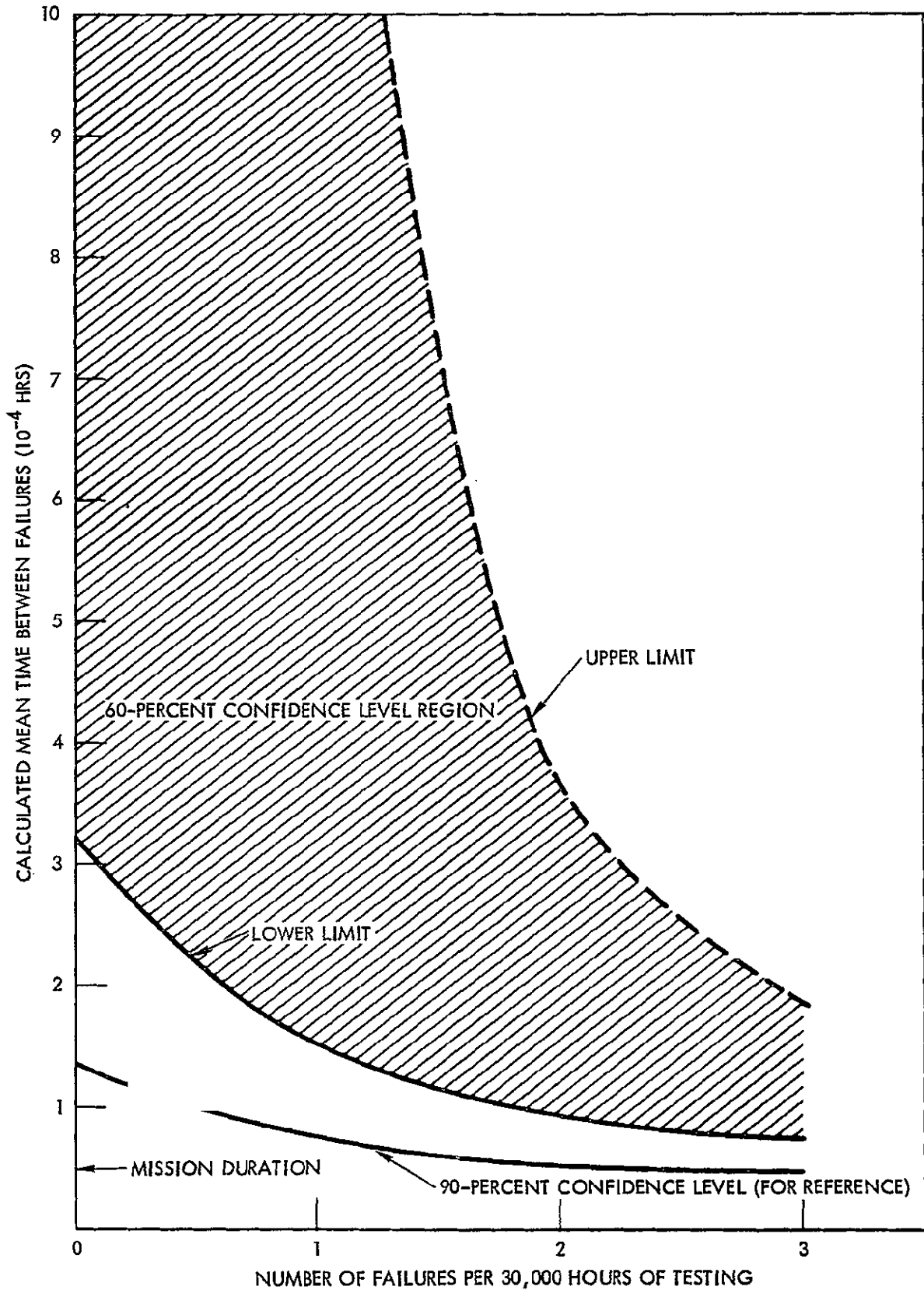
Figure 6-65. Interpretation of Results of Reliability Testing

PHASE	MONTHS FROM PROGRAM GO-AHEAD
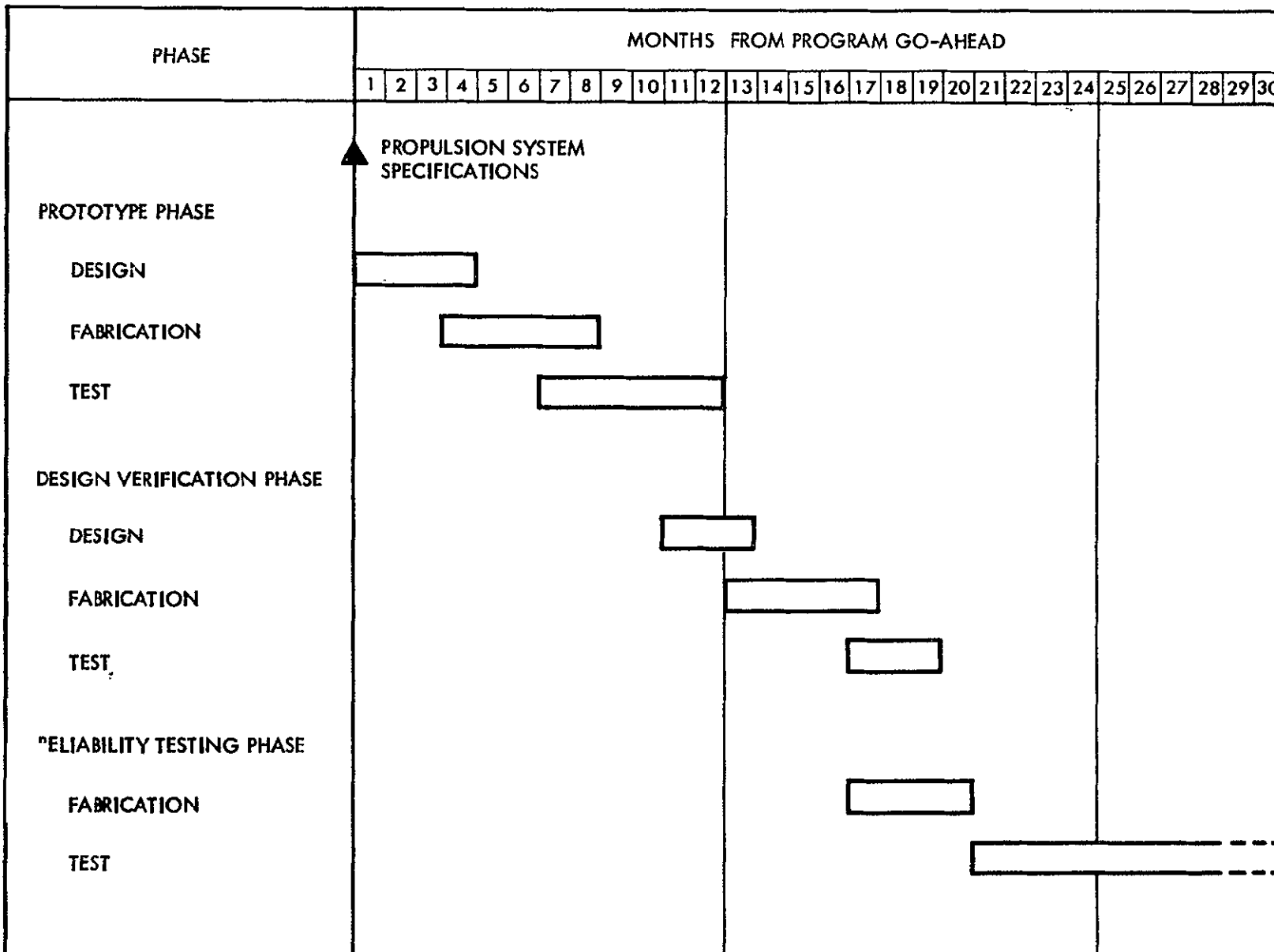
Figure 6-66. Program Phasing Schedule

Space Division
North American Rockwell

7. ELECTRICAL POWER SYSTEM

The spacecraft power generation, distribution, and control are discussed in this section. Design considerations influencing the selection of the system concept are defined, functional operation required during the various phases of the mission is specified, and spacecraft systems power requirements are determined. System design concepts are evaluated and a detailed description of the selected design concept is provided.

DESIGN CONSIDERATIONS

System design is strongly influenced by the selection of ground rules and constraints which determine priority of importance in the decision making process. The following program guidelines were specified in the study work statement:

1. State-of-the-art technology with off-the-shelf components given first priority

2. Solar arrays have the following specific/mass characteristics:

> Fold-up array   21 kg/kw
> Roll-up array   15 kg/kw

3. Thin film arrays will not be considered

4. Variation in solar array performance with solar distance shall be in accordance with Exhibit "A", dated 30 July 1968, Jet Propulsion Laboratory Contract 952566

5. A 15 percent degradation will be used for radiation degradation at start of mission

6. Minimum cost commensurate with accepted design practices.

In addition to these program guidelines, the following design requirements also influence the power system design process:

1. Mission lifetime of 3.5 years

2. Solar arrays are deployed such that they are canted 15 degrees from the normal to the sun

7-1

3. Micrometeoroid damage may be considered negligible (Section 12)

4. Micrometeoroid penetration sensors (capacitor sheets) are bonded to the anti-solar side of the array

5. Auxiliary power is required for 4.5 hours after launch prior to solar array deployment

6. Solar electric propulsion power conditioning and control equipment automatically provides load matching to available power. Power cutoff occurs at 35 vdc

POWER SYSTEM FUNCTIONAL OPERATION

Prelaunch (Phase 1)

System checkout and testing of the spacecraft power system will be accomplished using launch complex power. It is anticipated that the battery will be exercised also during prelaunch events; consequently, battery charging or at minimum a topping charge will be accomplished shortly before launch.

Launch Through Array Deployment (Phases 2 and 3A)

Before solar array deployment (a period of 2.5 to 4.5 hours maximum), the spacecraft is powered solely by means of batteries. Deployment of the array after L + 4.5 hours is preferred in order to avoid damage to the arrays by Van Allen belt trapped radiation. As depicted by the power profile (Figure 7-1) except for the last half hour, during which array deployment motors are activated, power requirements remain essentially constant at approximately 125 watts. Before array deployment, power is supplied solely from the batteries in the indicated voltage range; then, as the array is deployed and the solar panels accept solar energy, the panels automatically take over as the primary power supply. Takeover is essentially instantaneous since the bus regulators raise the bus voltage slightly above the maximum working potential established by the battery.

Significant voltage variations may occur during the initial stages of solar array operation due to differential panel temperatures caused by unequal orientation of the panels to the sun. The regulator is designed to compensate for these voltage variations automatically. In the event of near perpendicular panel orientation to the sunline at time of deployment, take over can occur at one-quarter extension of the panel. At this stage of deployment, the panel capability will be twice the spacecraft load requirement, and the solar array bus voltage will be in the range of 55 to 60 volts.
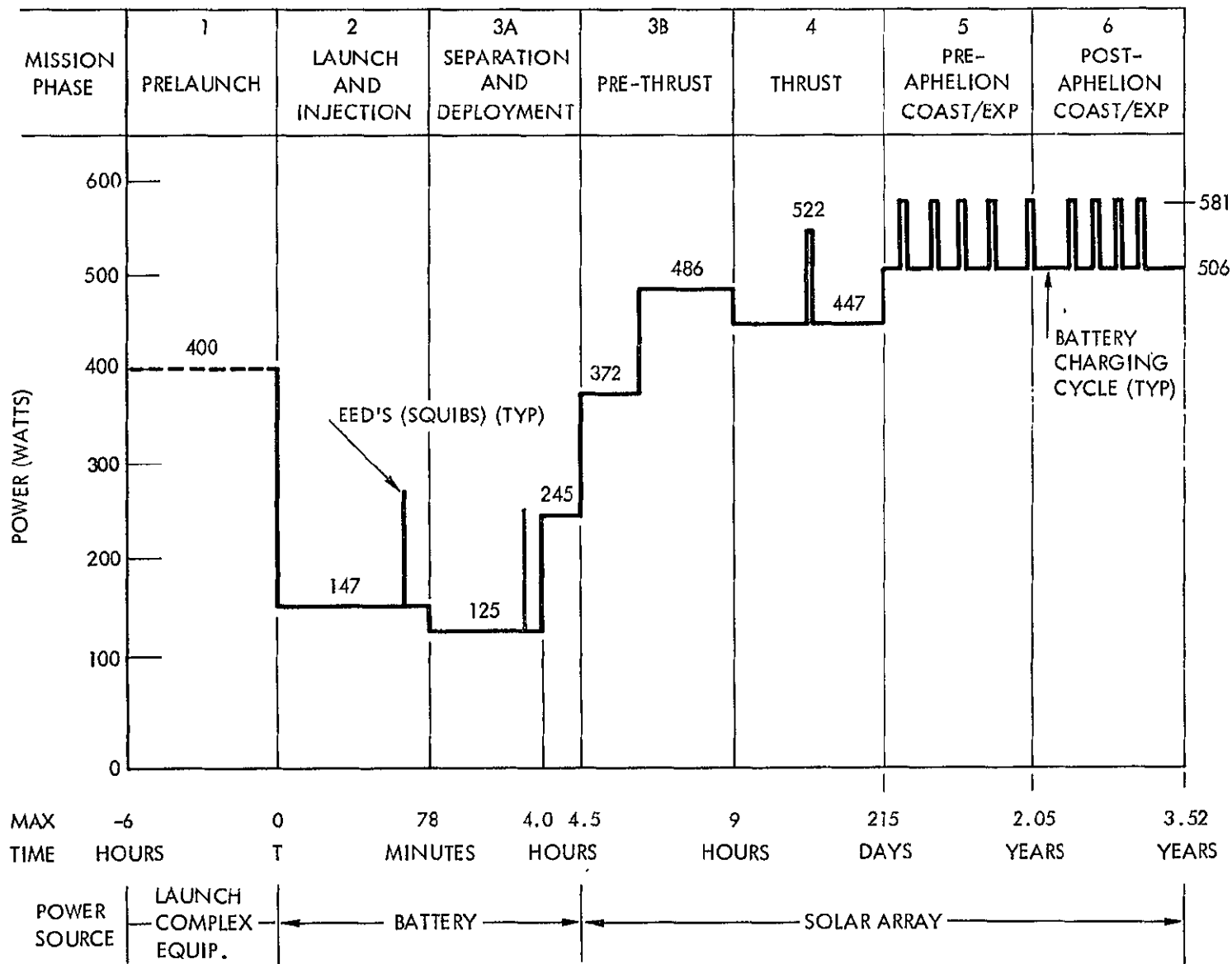
Figure 7-1. Spacecraft Subsystems Power Requirements Profile (Excluding
SEP Engine Subsystem)

Space Division
North American Rockwell

Pre-Thrust (Phase 3B)

Following sun acquisition and panel deployment, additional power is required for communications and data handling and activation of remaining spacecraft systems. During this 4.5-hour period, the solar array is expected to supply almost 500 watts of power. This demand is about 5 percent of array capability; thus, solar bus voltage will be slightly less than panel open circuit voltage. The distribution system is designed to handle voltage variations from 50 to 70 volts without effect on normal subsystem operation.

Thrust (Phase 4)

The Electric Propulsion system requires a maximum of 7.8 kilowatts of power at thrust initiation, gradually diminishing to approximately 2.2 kilowatts at thrust termination at 2.0 AU after 210 days of continuous operation. Engine power demand is limited by on-board controls at a level approximately 18 percent below array nominal output capability, less 450 watts for spacecraft subsystems. Power output of the solar array decreases as heliocentric distance increases. Array temperatures also decrease resulting in an increase in output voltage. Engine controls are designed to accept power with a wider range of voltage (40-80 vdc) than is anticipated from the solar array (50 to 70 vdc). The engine control system regulates the engine load, matching the decreasing array power output capability. A peak power monitor regulates power demand to the engine control system which in turn regulates the engine load to avoid power system overload. At minimum, one battery charging cycle will be performed during the latter period of this phase depending upon actual battery temperature profiles and charge states, and availability of power.

Coast/Experiment (Phases 5 and 6)

After thrust termination, the spacecraft follows a ballistic trajectory from 2.0 AU to an aphelion of 3.5 AU. During this period, science data gathering in the asteroid belt dictates load demand. An average power of approximately 506 watts is required. At aphelion, this represents about 57 percent of the available power with the spacecraft oriented 30 degrees to the sun. Maximum damage to solar panels due to micrometeoroid penetration will occur after aphelion; however, the total combined losses are negligible, being on the order of 1 percent.

Battery charging operations will be required at least once each six months during the mission to assure full charge state. Emergency operation under battery power may be sustained for approximately two hours in the

region beyond 2 AU, provided that all non-essential loads are disconnected. Random operation of spacecraft component heaters will be required throughout these phases.

POWER REQUIREMENTS

A detailed power requirements profile is given in Table 7-1 for ac and dc operation. Before solar array deployment, the power requirements are quite nominal: a maximum of 100 watts ac and 140 watts dc. The highest power requirements occur during the SEP thrust phase, the spacecraft systems power exclusive of SEP is 169 watts ac and 188 watts dc. The SEP power requirements are presented as a function of mission time in the Trajectory and Performance section of this report.

CONCEPT TRADES

The major tradeoff considerations of concern in concept selection are the penalties associated with the various methods of conditioning primary source power to provide regulated power and auxiliary battery power insertion. Inherent in the concept trades analysis is the requirement to provide both ac and dc power to the spacecraft while on auxiliary (battery) power operation. Obviously, battery power distribution efficiency is of primary concern to avoid unnecessary weight penalty. Three basic power system design concepts were investigated as shown in block diagram form in Figure 7-2. Concept A is a parallel ac-dc system characterized by independent ac and dc buses. The battery insertion is required at the solar bus resulting in a loss in battery power distribution efficiency due to the fact that the dc power is distributed through the primary power source regulation and inverter circuits to provide ac power. An additional dc bus regulator is required for control when on solar panel power. Also buck-boost regulation rather than just straight buck regulation is required to accommodate low voltage insertion at the solar bus. Battery power insertion could be accomplished at the dc bus, but this would require complex switching and additional power inversion components which would not be used except when on battery power.

Concept B utilizes an ac main bus and through transformer-rectification provides dc power to a sub-bus. As for concept A, the preferred battery insertion point is at the solar bus. Essentially the same penalties are incurred for this concept as for concept A. Insertion of the battery power on the dc bus requires switching and inversion equipment to provide ac power. Again, this inverter would be inoperative except when on battery power.

Concept C utilizes a main dc bus with an ac sub-bus. This concept allows the battery to be inserted directly to the dc bus and the use of the

Table 7-1. Subsystem Power Requirements

Mission / Subsystem	Watts													
	1 Prelaunch		2 Launch/ Injection		3 Separation/Deployment A (Battery)		3 B (Array)		4 Thrust		5 Coast/ Experiment		6 Coast/ Experiment	
	AC	DC	AC	DC	AC	DC	AC	DC	AC	DC	AC	DC	AC	DC
Comm & data handling	42	54	42	5	42	5	108	54	108	54	108	90	108	90
CC&S	42		42		23		23		23		23		23	
SCS	16	23	16	23	16	23	29	23/0	29	(23)	29	(23)	29	(23)
Payload	11	67					11	0/66	9	60	11	67	11	67
Actuators						0/112		14		42		14		14
Thermal control										32		63		63
Subtotal	111	144	100	28	81	28/140	171	91/134	169	188	171	234	171	234
Battery charger		75						75		75		75		75
Engines (HRL)				HTR		HTR		HTR		7800/ 2200				

NOTE: Ac is 2.4 KHz only
SCS/dc is 400 Hz equivalent
( ) for SCS indicate requirement during gyro operation only

Space Division
North American Rockwell

CONCEPT A

CONCEPT B

CONCEPT C (SELECTED DESIGN)

λ

BUS REG

BATTERY

REG / INV

BUS (TYP)

DC

28 VDC

50 VRMS SQ

AC

L_{DC}
45/155w
(TYP)

L_{AC}
105w
(TYP)

λ

BATTERY

PREFERRED

ALTERNATE

INVERTER

REG / INV

DC

TR

AC

L_{DC}

L_{AC}

λ

ALTERNATE

BATTERY

BUS REG

PREFERRED

DC

INV

AC

L_{DC}

L_{AC}
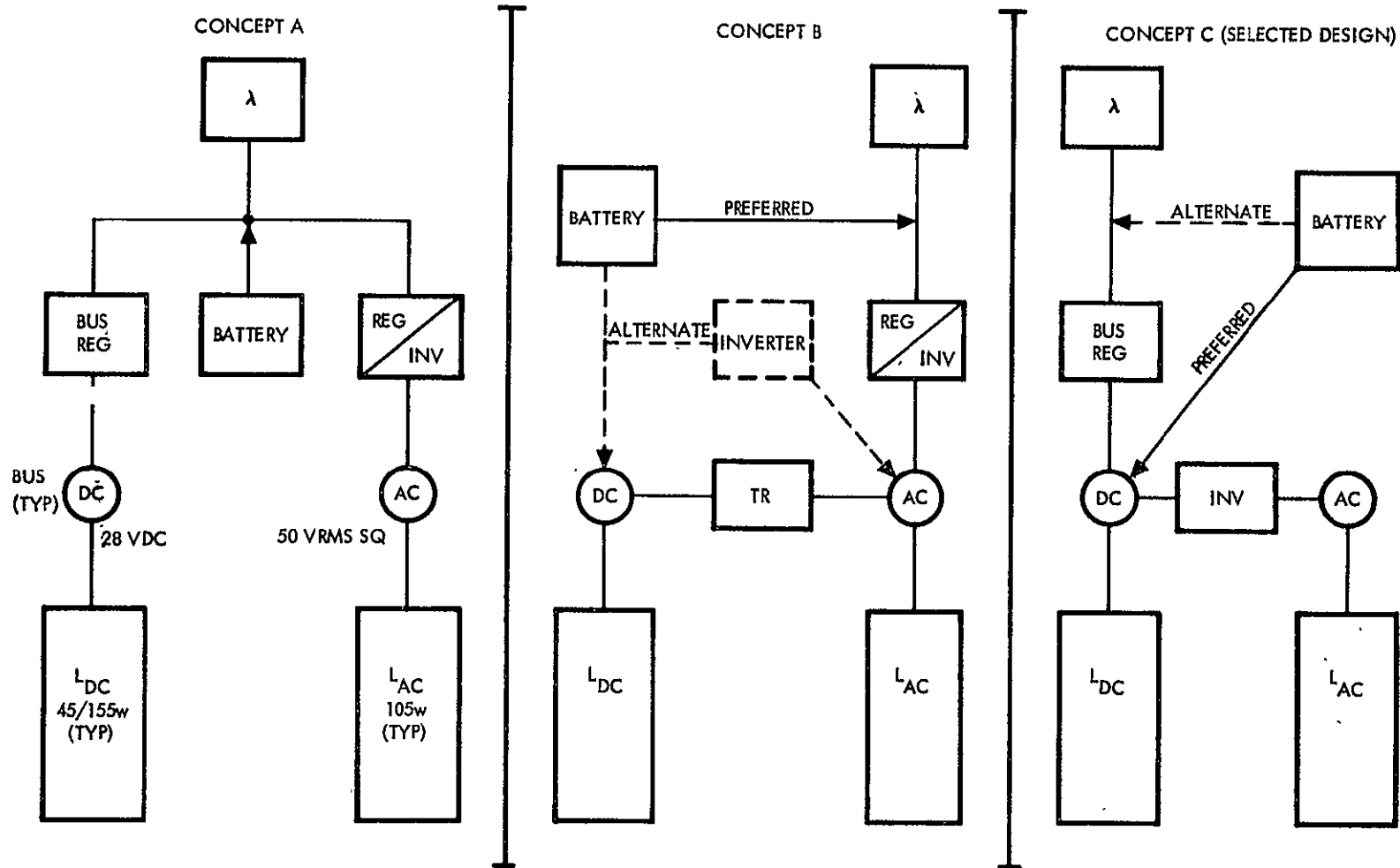
Figure 7-2. Electrical Power System Mechanization Concepts

primary power source inversion components to provide ac power, thus avoiding redundant, unnecessary equipment. This concept also avoids the undesirable solar array/battery load-sharing condition which is inevitable whenever the battery power is inserted at the unregulated solar bus, as is the case for concepts A and B.

An analysis of system operating electrical efficiencies revealed no significant advantage to any one concept. Concept C, however, eliminates the need for additional components during battery operation and provides the most efficient battery power distribution, thus reducing battery energy requirements and, subsequently, battery weight. A summary of the advantages and disadvantages of the basic design concepts is presented in Table 7-2.

Concept C is selected as the preferred design concept, as it requires fewer system regulation and conditioning components, provides more efficient battery power distribution and affords the use of the more desirable low-voltage batteries with their inherently higher reliability.

SELECTED CONCEPT DESCRIPTION

Summary Description

A block diagram of the selected power system design concept is shown in Figure 7-3. The design consists of three major subsystems, the functions of which are as follows:

1. A photovoltaic power source converts solar energy into unregulated electric power

2. A distribution system supplies unregulated power to the propulsion system power conditioner and control (PC&C) for conversion to required voltage and current levels. A peak power monitor provides an electrical signal that may be utilized with engine load matching capabilities to extract maximum power from the photovoltaic source

3. An auxiliary power subsystem supplies power for the various spacecraft functional subsystems. This subsystem includes battery, battery charger, voltage regulator, power conditioning and control equipment. The battery supplies power only during the early part of the mission prior to solar panel deployment; after solar power operation is initiated, the battery is used for emergency operation when solar power is lost

Provisions are included for the utilization of ground power (supplied through Launch complex equipment) for spacecraft checkout and prelaunch

7-8

Table 7-2. EPS Tradeoff Analysis

Concept	Battery	System Weight	Advantages	Disadvantages
A. Parallel ac-dc	On input	H	• Power efficiency/array operation	• Lower efficiency/battery operation • Weight • Reliability/regulator input • Independent buses
B. Ac main bus (dc sub-bus)	On input	M	• Mariner type • Simplified switchover to battery operation	• Lower efficiency/battery operation • Battery and array load sharing
	On dc bus	M	• Better efficiency/battery operation	• Additional inverter • Reliability/TR switch-out controls
C. Dc main bus (ac sub-bus)	On input	M	• Simplified switchover to battery operation	• Buck boost/regulator • Lower efficiency/battery operation
	On dc bus	M	• Better efficiency/battery operation • Reliability/fewer components	• Selected concept

ENGINE
POWER
CONTROL
AND
LOAD-
MATCHING
SYSTEM

POWER SOURCE
PEAK POWER
MONITOR

50 TO 70 VDC

LAUNCH
COMPLEX
POWER

24 TO 29 DC

400 Hz
INVERTER

26 V 3φ

SPACECRAFT
LOADS

SOLAR
PHOTOVOLTAIC
POWER SOURCE

UNREGULATED

45 TO 86 VDC

SC BUS
REGULATOR

28.5 VDC
± 1%

2.4 Hz
INVERTER

50 V RMS SQ

24 TO 28 VDC

BATTERY
CHARGER

BATTERY
CHARGE AND
DISCHARGE
CONTROL

25 TO 29 VDC

BATTERY
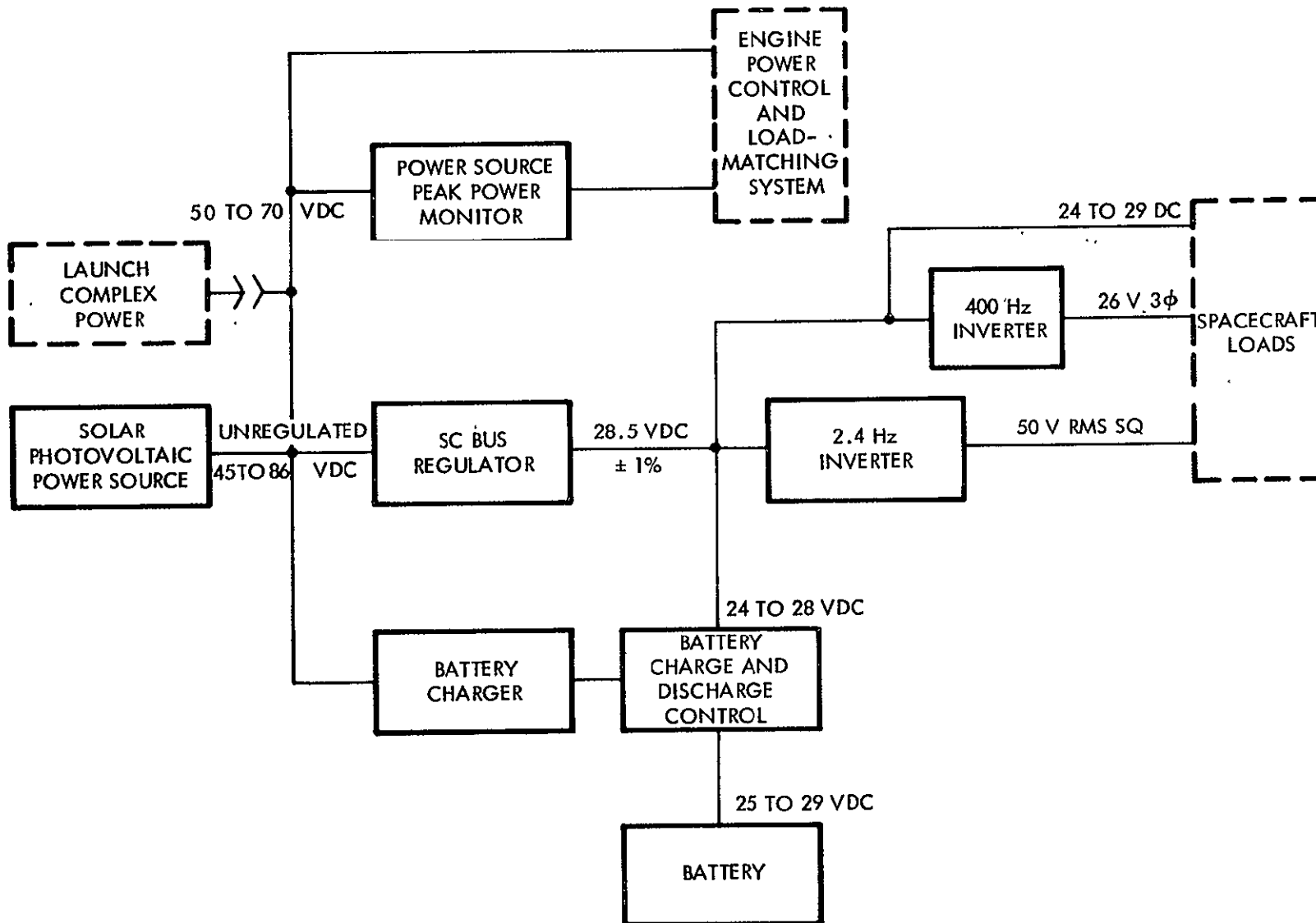
Figure 7-3. Power System Block Diagram

operations. Voltage conditions noted in Figure 7-3 describe normal operating conditions during the planned mission, and, consequently, do not include transient conditions.

System Mechanization

A functional block diagram for the overall electrical power system, including the interface with the SEP thruster control system, is shown in Figure 7-4.

Raw power derived from four solar photovoltaic panels is applied to an unregulated spacecraft solar bus for distribution to the engine PC&C equipment, and the auxiliary power subsystem including battery charger. Load matching and control of the raw power for the engine loads is incorporated in the design of the thruster PC&C equipment. Power cutoff to the PC&C is automatically accomplished whenever solar bus voltage is lower than 35 volts. A peak power monitor with redundancy is applied to the thruster power line and provides signals for load control to demand maximum power from the solar array.

The auxiliary electrical power subsystem is designed to supply a maximum 506 watts of continuous power to operate the spacecraft functione subsystems and science payloads.

Individual bus regulators supply the total auxiliary power subsystem load through independent operation to the regulated dc buses. Each regulator has the capability to provide total auxiliary power requirements in event of regulator malfunction through appropriate switching control. The regulator supply potential, when on solar power, is maintained above battery potential to inhibit battery drain except in event of power system malfunction. The isolation diodes shown in Figure 7-4 represent series parallel quad arrangement for highly reliable operation.

During normal operation, the main loads supplied by dc bus 1 include those essential to maintaining contact with the spacecraft from the ground and spacecraft control.

Two independent single-phase inverters are used to supply 2.4 KHz square wave ac power to the two ac distribution buses. In event of failure, either inverter has the capacity to supply total load requirements to both ac buses. Bus ties and redundant distribution control circuits are provided for flexibility in fault isolation and spacecraft load redistribution.

System Performance

The spacecraft subsystem power requirements given in Table 7-1 represent delivered, conditioned power to the subsystem components. To these values it is necessary to add distribution and regulation losses to determine the power demand as the solar bus (see Figure 7-4). For the ac loads, distribution, inverter, and regulator losses are experienced. For the dc loads, only distribution and regulator losses are incurred. When on battery operation, the ac load losses consist of distribution, inverter, and battery isolation. The dc load losses consist of battery isolation and distribution. Depending upon the mode of operation, the power requirements given in Table 7-1 must be divided by the following load loss factors:

Operation Mode	Type Load	Load Loss Factor
Battery power	Ac	0.85652
	Dc	0.931
Solar power	Ac	0.76636
	Dc	0.8330

The resultant sum of the ac and dc loads from Table 7-1, compensated for the above mentioned losses, is presented in Figure 7-1. The 50 AH AgZn battery provides the power for the first 4.5 hours of flight, discharging to approximately 47 percent of capacity. The SEP thrust phase of the mission is the most demanding, requiring the highest total power. The required spacecraft power, excluding SEP operation, is 447 watts.

In Figure 7-5, the solar array performance power profile for the thrust phase is given. In order to determine the power available to the SEP system it is necessary to subtract power losses due to spacecraft orientation-associated with SEP thrust (Figure 7-6), radiation losses, meteoroid damage, and distribution losses (see discussion on solar array performance). Figure 7-7 shows the power availability to the SEP subsystem during the thrust phase. A point design diagram for a mission time of 75 days is shown in Figure 7-8 to illustrate the procedure used to determine curves C and D in Figure 7-7.

Little or no design margin exists for the thrust phase of the mission. However, the power availability curves in Figure 7-7 are probably conservative. As previously mentioned, no allowance for increase in power due to thermal bending was considered. Also, during the early phases of the mission, the radiation degradation will probably be somewhat less than the 15 percent assumed. Deployment of the solar arrays beyond the inner Van Allen Belt also help to reduce the radiation damage during the first few months of the mission.
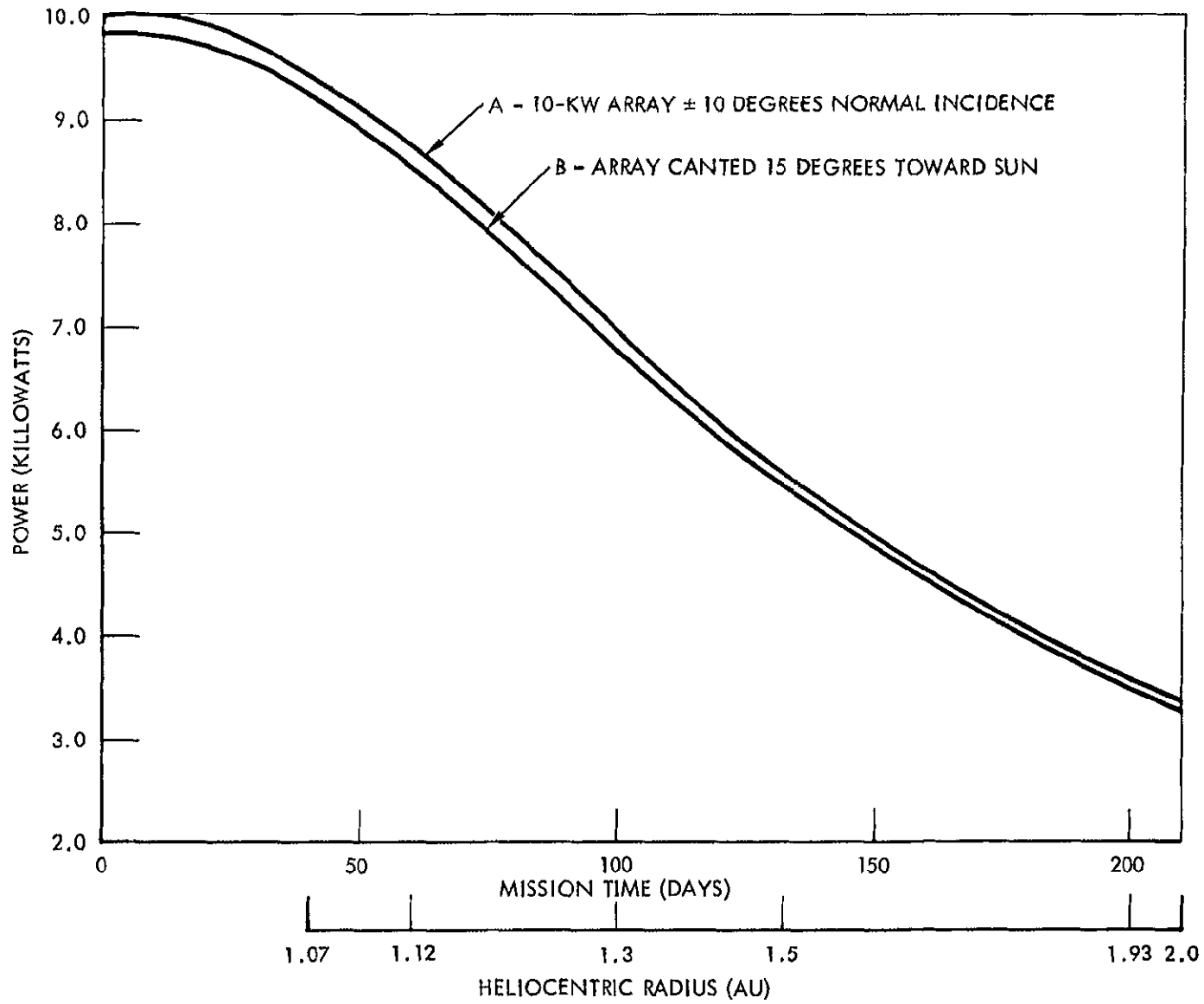
Figure 7-5. Spacecraft Power Availability Profile for Baseline Asteroid
Belt Mission
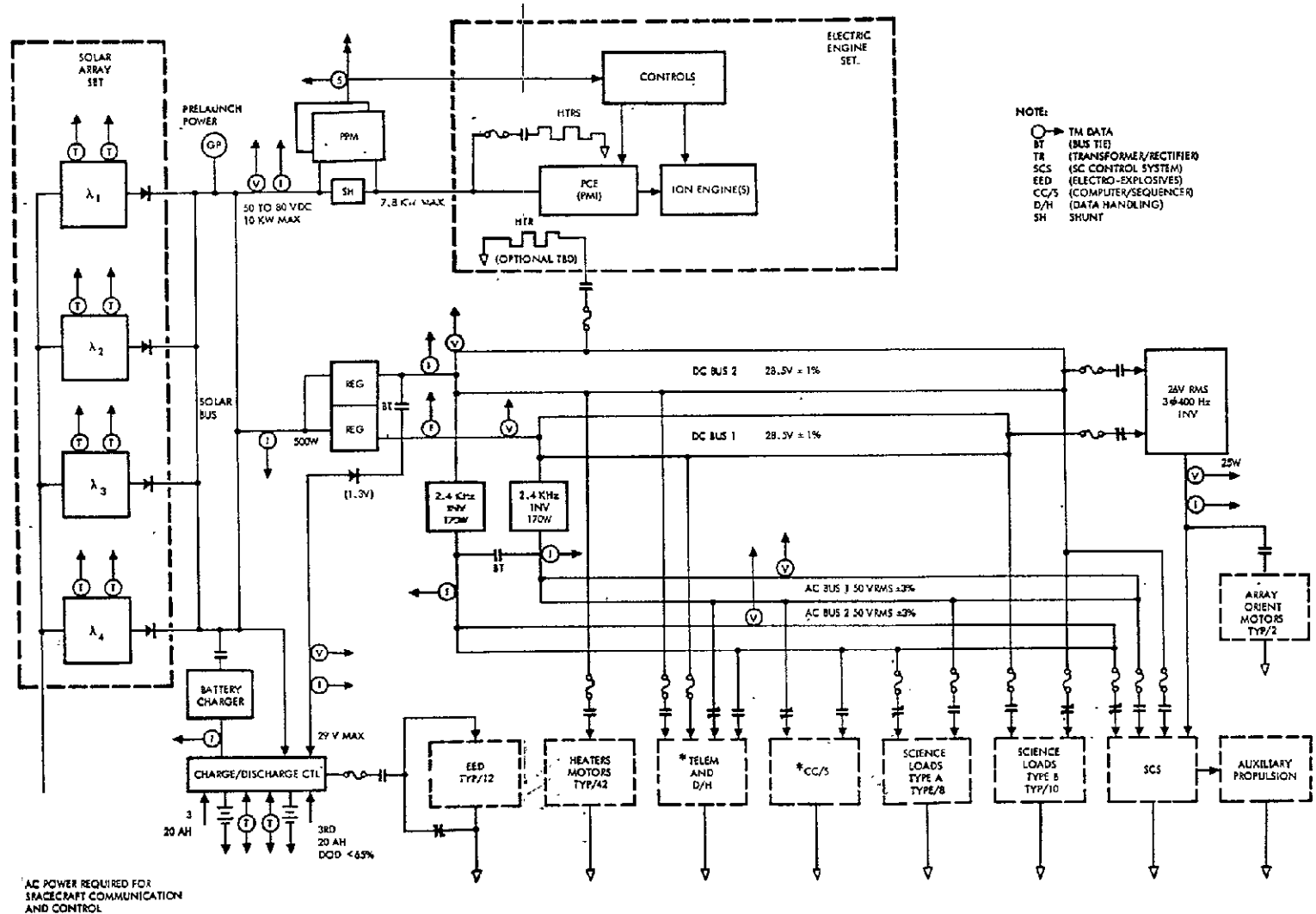
Figure 7-4. SEP ABMS Electrical Power System Functional
Schematic
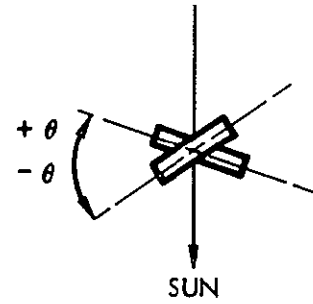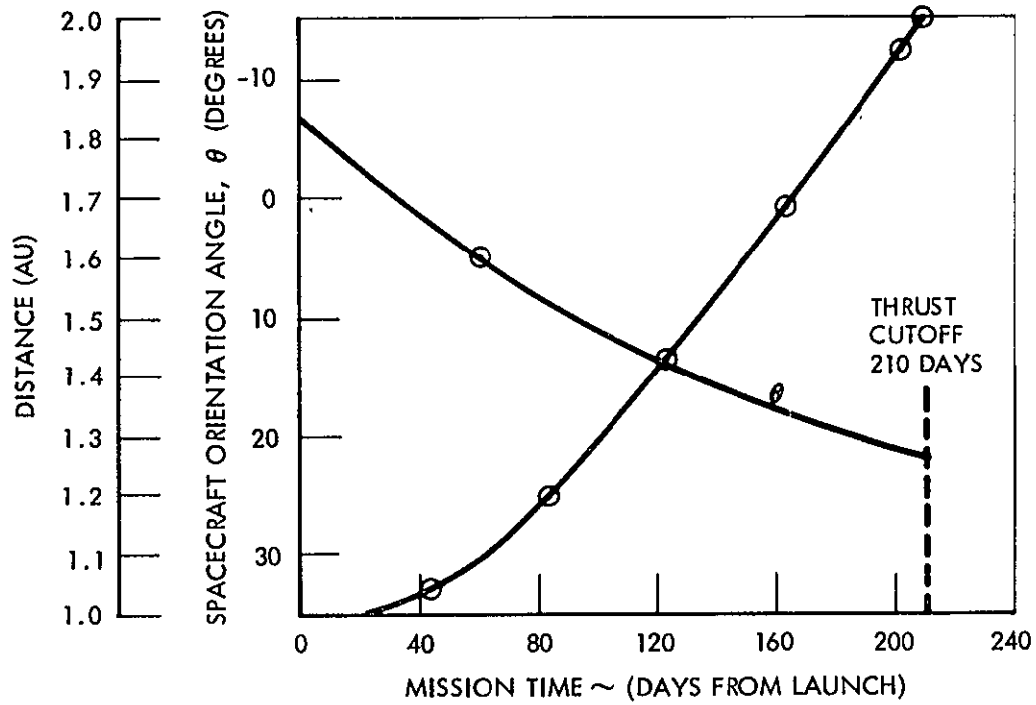
Figure 7-6. Spacecraft Orientation During Thrust Phase

Space Division
North American Rockwell
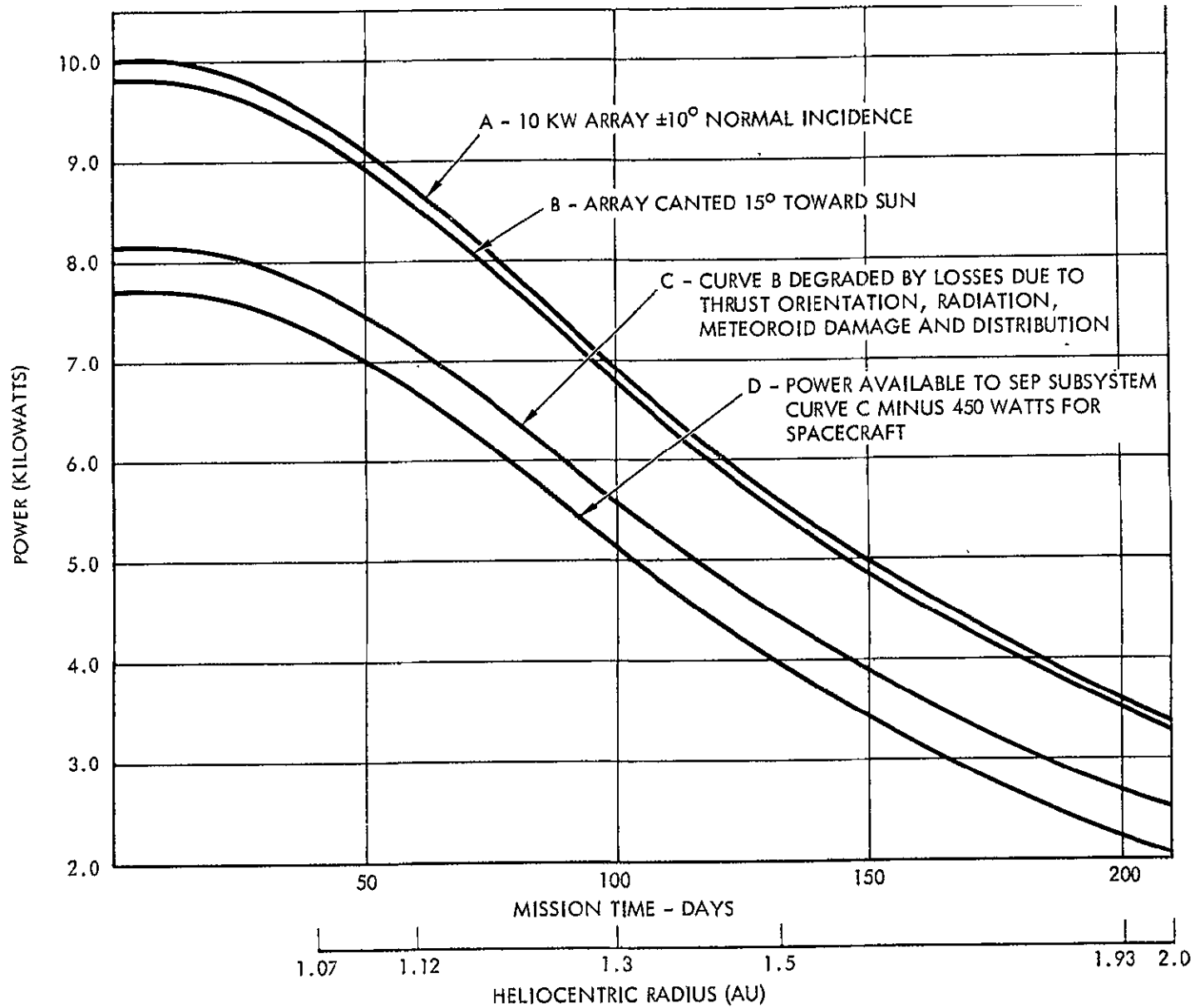
Figure 7-7.   Spacecraft Power Availability Profile for SEP Subsystem
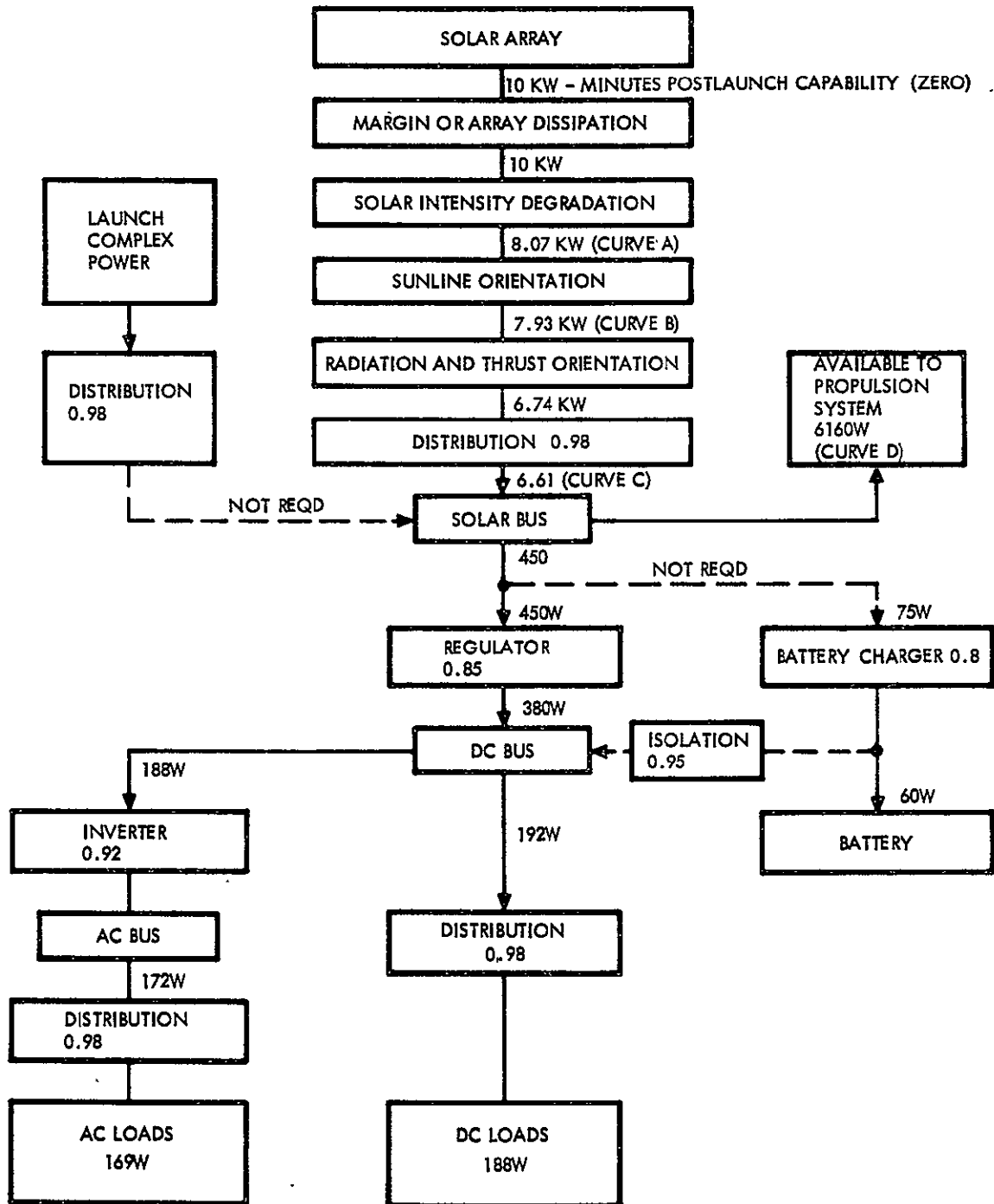
Figure 7-8. Base Point Design Diagram (L + 75 Days)

SD 70-21-2

EPS Weight Summary

A summary of the electrical power subsystem weight requirements is presented in Table 7-3. As specified in the work statement, a specific mass-power ratio of 15 kg/kw was used as the basic weight of the roll-up solar array. An additional weight penalty of 5 kg was incurred as a result of integrating the capacitor sheet meteoroid penetration detector with the solar array. This weight increase was caused by the necessity to beef-up the boom, increase blanket tension, and change in size of the storage drum. To this was added the 31 kg for the $70M^2$ of capacitor sheets, giving a total of 186 kg.

A single PC&C set incorporating the solar bus, peak power monitors, and all components of the auxiliary power subsystem including power management and control logic, but excluding the battery, was selected with a total weight of 10.5 kg. Weight estimates for individual conditioning components separately packaged are shown in Figures 7-9 through 7-14. These weight data were used as a basis for determining the PC&C weight. The limit control regulator is estimated to weigh .03 pounds/watt. Specific design weights achieved for Mariner 1969 components were .025 pounds/watt for the main regulator and .015 pounds/watt for the 2.4 Hz inverter. For the purposes of this study, the PC&C weight was estimated on the basis of .023 kg/watt (.05 pound/watt). The concentration of spacecraft electronics in the equipment section reduces the amount of wire harness weight required. OGO, Pioneer and Vela satellites had harness specific weight factors of 0.22, 0.18 and 0.16 lbs/watt respectively. Using a value of 0.18 lbs/watt, then 36.8 kg (81 lbs) is required for spacecraft electrical distribution. To this must be added the weight of the primary power harness providing power to the electrical propulsion system, which is estimated for the selected spacecraft configuration to weigh (17.7 kg) 39 lbs.

Housekeeping Data

A multitude of measurements are required to monitor the performance of the power subsystem. In general, the telemetry system of a spacecraft is power-limited, requiring the careful selection of housekeeping measurements. As a minimum, the following criteria govern the selection of power system parameters which should be monitored:

1. Measurements necessary for preflight and flight operations,

2. Measurements for evaluation of system and subsystem performance and the necessity for alternate modes of operation.

Table 7-3. Electrical Power Subsystem - Hardware Summary

Item	Quantity per Spacecraft	Development Status	Type	Character	Size (each)	Weight (kg)
1. Solar cell/ capacitor arrays	4	Redesign for voltage and power - add capacitor	GE roll-up	Capacitor sensor on array	2. 5 kw (4)	155 (excludes 31 kg for capacitors)
2. Power conditioning and control set (PCCS)	1	New	Solid State	Mariner	1 ft^3	10.5
3. Batteries	1	SOTA	AgZn	MM 1969	50 AH	18
4. Power harness	1	New	Standard			54.5
					Total (kg)	238
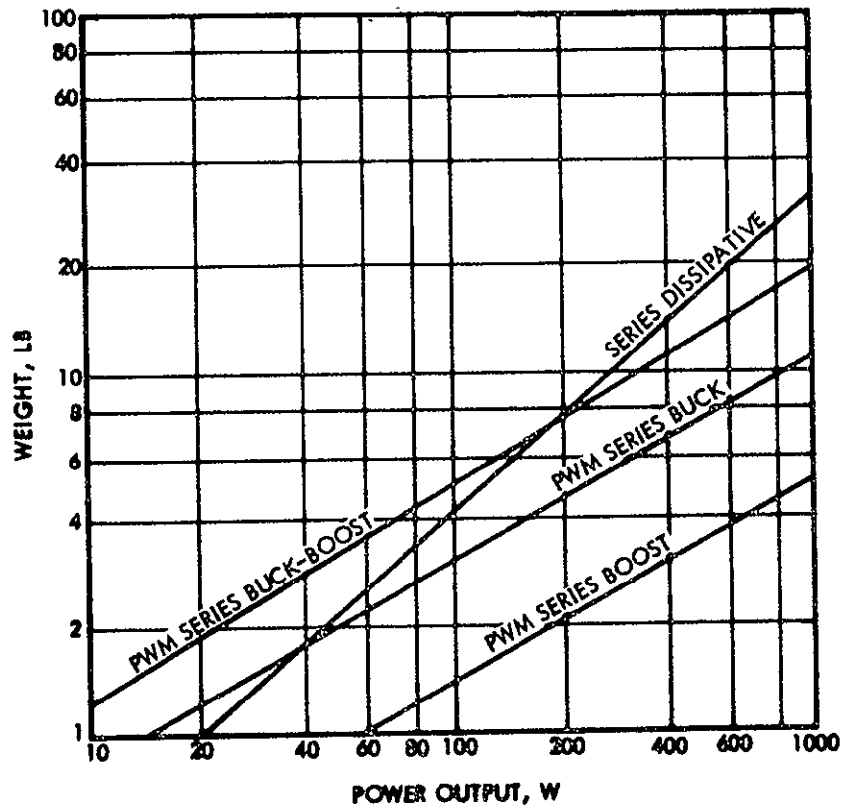
Figure 7-9. Line Regulator, Baseline,
Weight versus Power Output
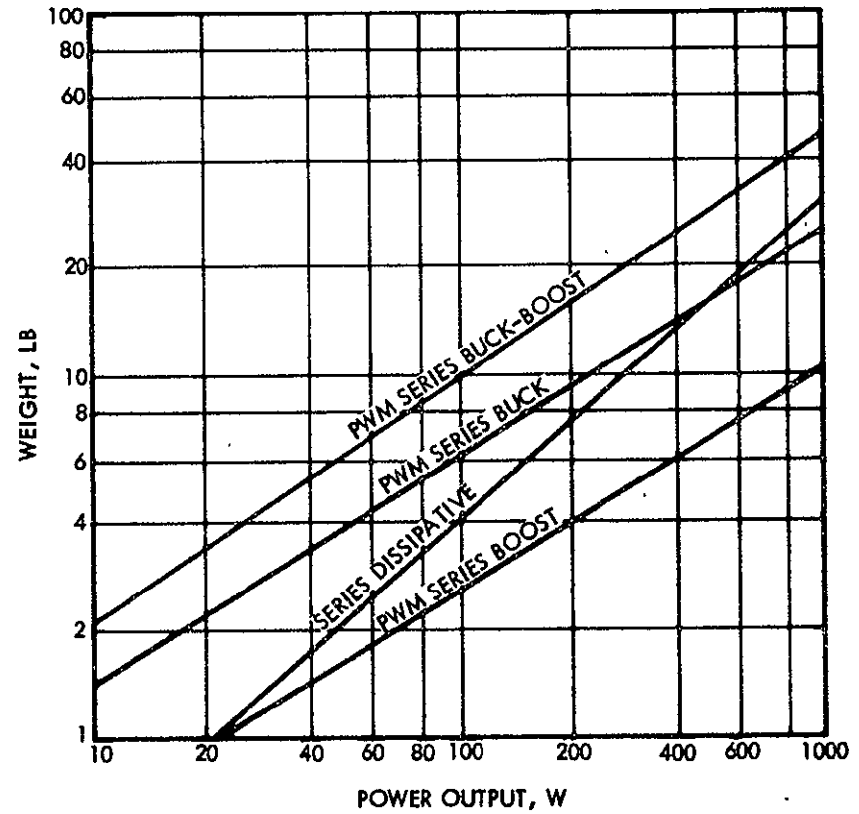
Figure 7-10. Line Regulator, Redundant,
Weight versus Power Output

Space Division
North American Rock\
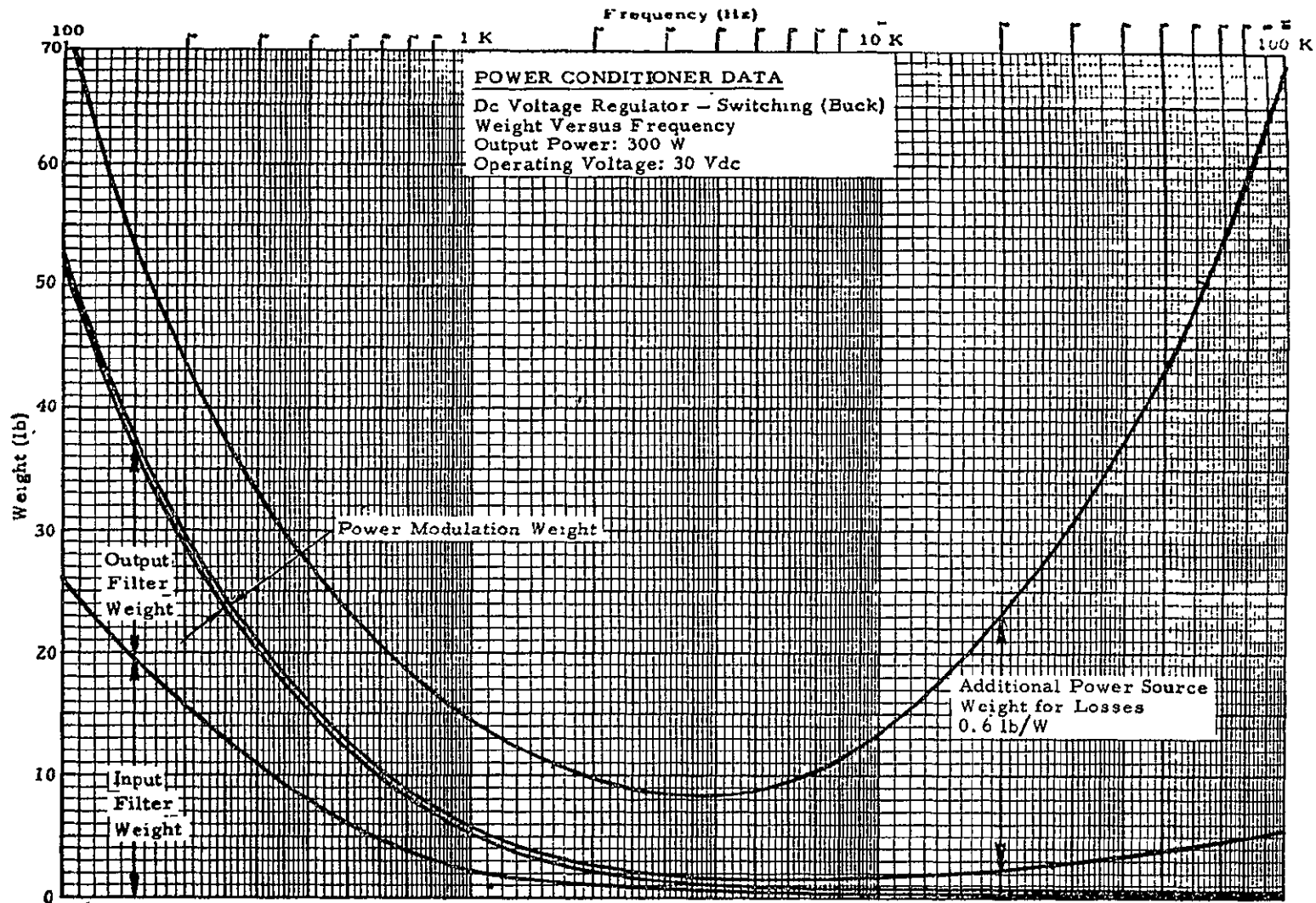
Figure 7-11. Power Conditioner Data, DC Voltage Regulator, I

Space Division
North American Rockwell
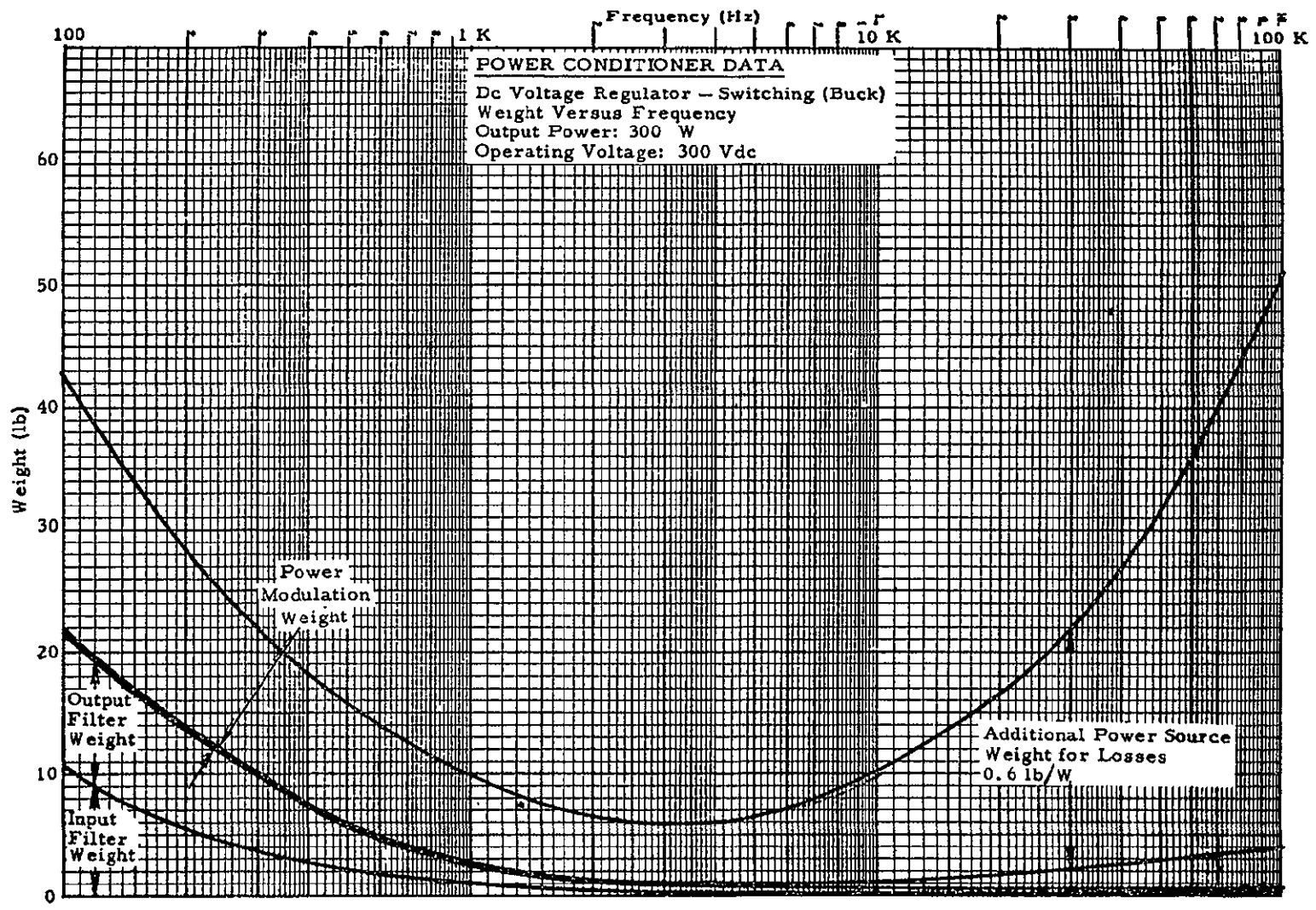
Figure 7-12. Power Conditioner Data, DC Voltage Regulator, II
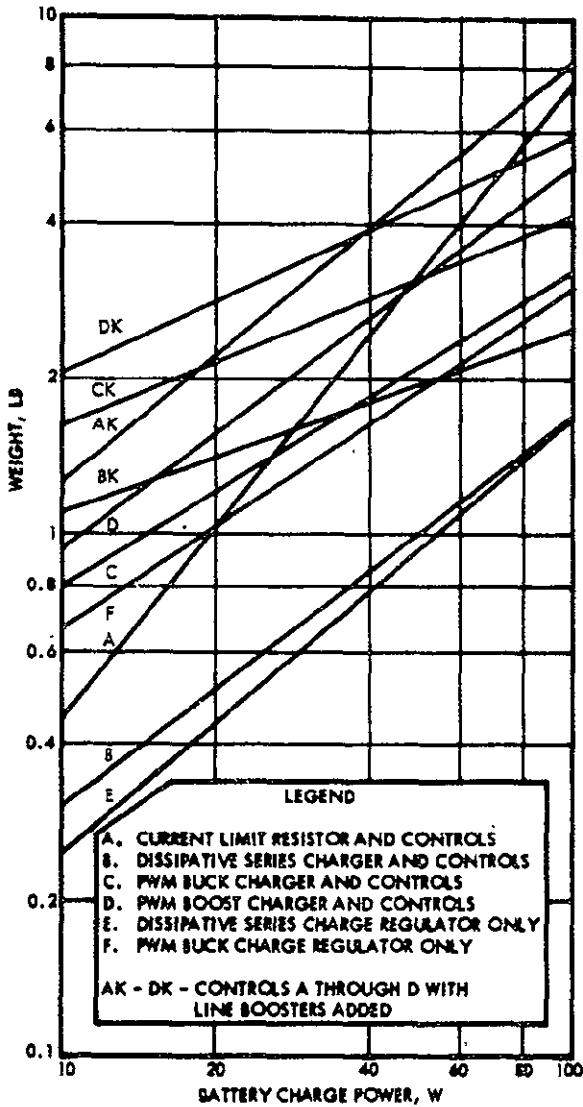
Figure 7-13. Battery Controls,
Baseline, Weight versus
Power Output
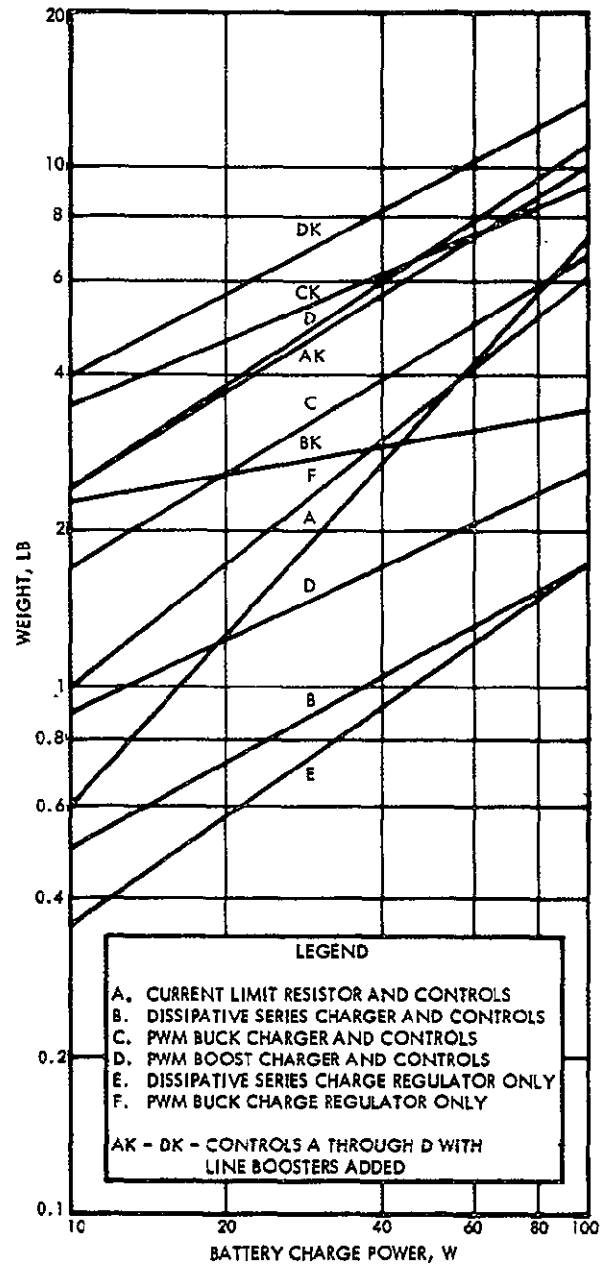
Figure 7-14. Battery Controls,
Redundant, Weight versus
Power Output

7-24

3. Measurement of significant environmental parameters affecting performance, and

4. Verification of significant events.

Table 7-4 contains a list of measurements required as a minimum to meet the governing criteria established above. Subsequently, more detailed studies will result in the requirement to add to this measurements list; however, the measurements in Table 7-4 serve as a valid input for sizing telemetry system channel and multiplexing requirements.

SOLAR ARRAY SUBSYSTEM

Solar Array Description

The primary power source recommended is a modified version of the General Electric 15 kg/kw roll-up solar array currently under development at the GE Valley Forge Space Center. Selection of a roll-up solar array was based primarily on the significant advantage of higher power-to-weight ratio (1 kw/15 kg) over conventional folding arrays (1 kw/21 kg). An additional consideration was the feasibility to incorporate large area capacitor sheeting into the roll-up solar array design for micrometeoroid penetration detection thus providing a reduction in stowed volume. Appendix D-3 contains details of integrating the meteoroid detector with the roll-up solar array. A modified version of the General Electric roll-up solar array was selected based on the advanced state-of-development of prototype flight hardware. GE is currently under contract to Jet Propulsion Laboratory (NASA Contract NAS7-100) to provide a 2.5 kw array (at 1.0AU) weighing 34.8 kg (76.4 pounds) and having an array area of approximately 23.2 square meters (250 square feet). The basic performance characteristics are given in Table 7-5. Figure 7-15 shows the basic 2.5 kw array configuration.

Conventional silicon solar cells are laid down on a Kapton sheet and rolled up on beryllium storage drums for launch. Outboard end supports provide restraint during launch and are released to deploy the array. A center support contains the bearing system for the drums, a mounting point for the deployable boom, and the necessary slip rings to transfer power to the vehicle. This boom is a BiStem actuator that drives the leading edge member which is attached to the array blanket. When the boom is deployed, there is a single point attachment to the spacecraft. Tension in the array blanket provides the necessary rigidity and alignment. The array is designed to be retracted and redeployed to accommodate such mission events as high thrust maneuvers during midcourse corrections and station changing on other type of missions.

Table 7-4. Power System Measurements

Number of Measurement in Category	Measurement	Range	Resolution
12	Panel deployment status (3 per panel)	Discrete	
4	Panel deployment verification indicator (1 per panel)	Discrete	
8	Solar panel temperature (2 per panel)	200 to +200 C	3 C
2	Sample solar cell short circuit current	0 to 100 mA	0.8 mA
1	Solar cell open circuit voltage	0 to 100 mV	
1	Combined solar panel output current	0 to 200 A	3 A
1	Power source voltage	20 to 100 v	1.0 v to 3 v
1	Battery discharge current	0 to 10 A	80 mA
2	Battery voltage (1 per battery)	18 to 33 v	0.5 v
2	Battery temperature (1 per battery)	0 to 250 F	5 F
1	Battery charge current	0 to 3 A	80 mA
1	PC&C input current	0 to 15 A	0.5 A
2	2.4 KHz inverter output current (2)	0 to 3 A	0.2 A
2	2.4 KHz inverter output voltage (2)	45 to 55 v	0.5 v
1	400 Hz inverter output current	0 to 1 A	50 mA
1	PPM power signal	0 to 10 kW	120 W
1	PPM input enable/disable	Discrete	
1	Engine control voltage set point	0 to 5 v	20 mV
2	PC&C temperature	-50 to +200 F	4 F

Table 7-5. GE 2.5 kw Roll-up Solar Array
Technical Characteristics

Power/weight	32.3 W/lb
Size	250 ft^2/panel (100 in. X 410 in.)
Weight	77 lb/panel
Electrical	
Voltage	100 volts
Power takeoff	Slip rings (Nimbus type)
Solar cells	Conventional silicon
	(3 mil glass, 8 mil cell)
Materials	
Blankets	Kapton
Components	Beryllium
Cushioning	RTV 560
Bond	GE-SMRD 745
Resonant frequency	Above 0.04 Hz
(deployed)	

The array is of modular construction to allow for flexibility in design. For example, the dimensions can be changed to provide a wide range of length-to-width ratios. Thin film solar cells can be utilized if they provide advantages. New components, such as an improved deployment boom, can be incorporated without extensive redesign as they become available.

Operating Characteristics

The solar cell operating characteristics which were used as the basis for predicting array performance during the mission were obtained from General Electric (Reference 7.1) and are presented in Figure 7-16. The current voltage (I-V) characteristics for the 2.5 kw array are given in Figure 2-17. These data are based on the performance of the GE RA250 roll-up array, reflecting the necessary cell arrangement changes to reduce the voltage from 102 to 50 v at 1 AU for compatible operation of the SEP power conditioning equipment.

Current, voltage, and power output capabilities of silicon solar cells depend on the temperature and sunlight intensity to which they are exposed during the mission. Figure 7-18 gives array temperature variations as a function of distance from the sun. Curve A presents the average temperature of the basic array without capacitor sensors, assumes normal solar incidence and does not include spacecraft albedo effects. Curves B and C include estimates of the effect of sensor additons, assuming an equivalent emittance for the radiating surface and negligible temperature difference

STORAGE DRUM

BOOM

CENTER SUPPORT

ARRAY BLANKET

OUTBOARD
END SUPPORT

409.35

578.907
FOR 5 KW

99.164

140.239
FOR 5 KW

iUN

LEADING EDGE MEMBER
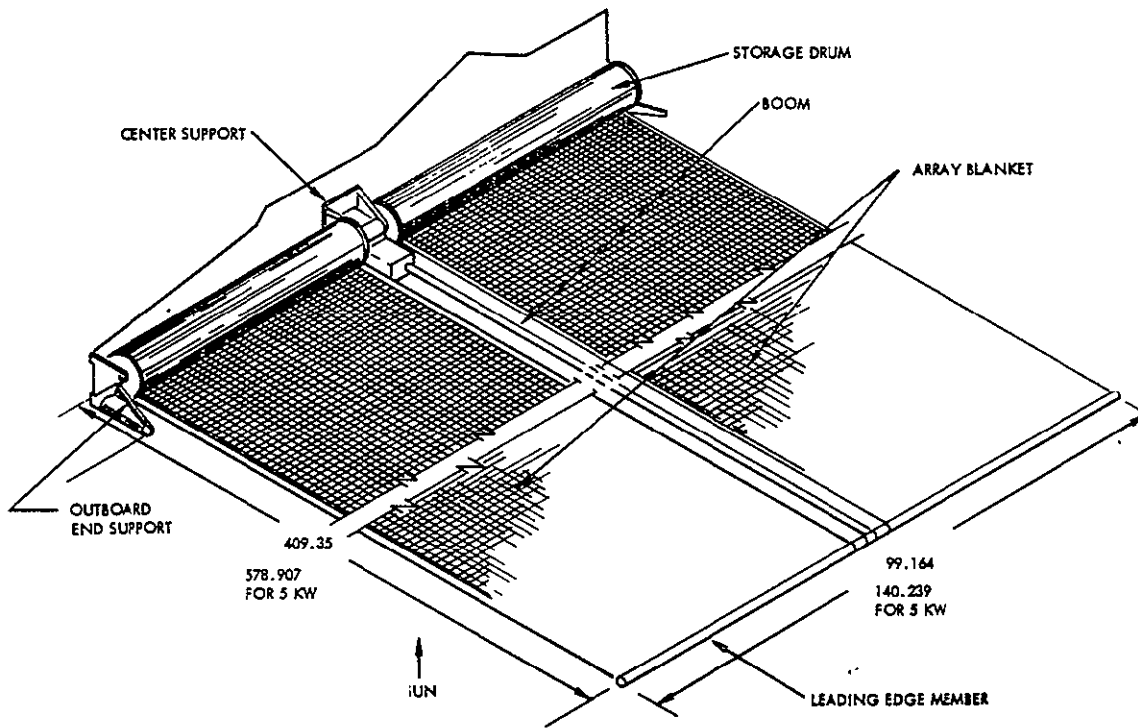
Figure 7-15. General Electric 2.5 KW Roll-up Solar Array Configuration
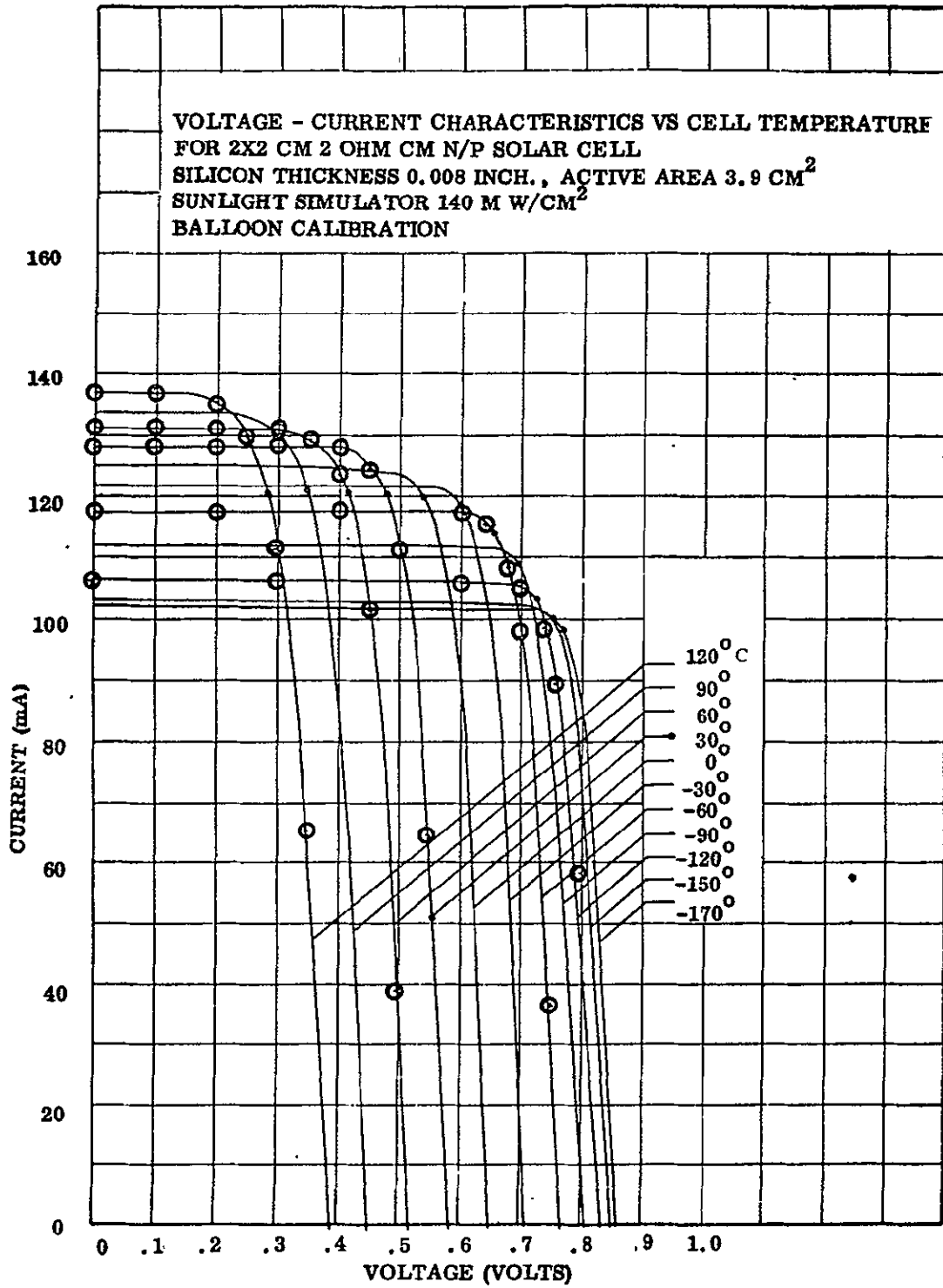
Figure 7-16. Solar Cell Characteristics, 2-Ohm Cm, 8-Mil
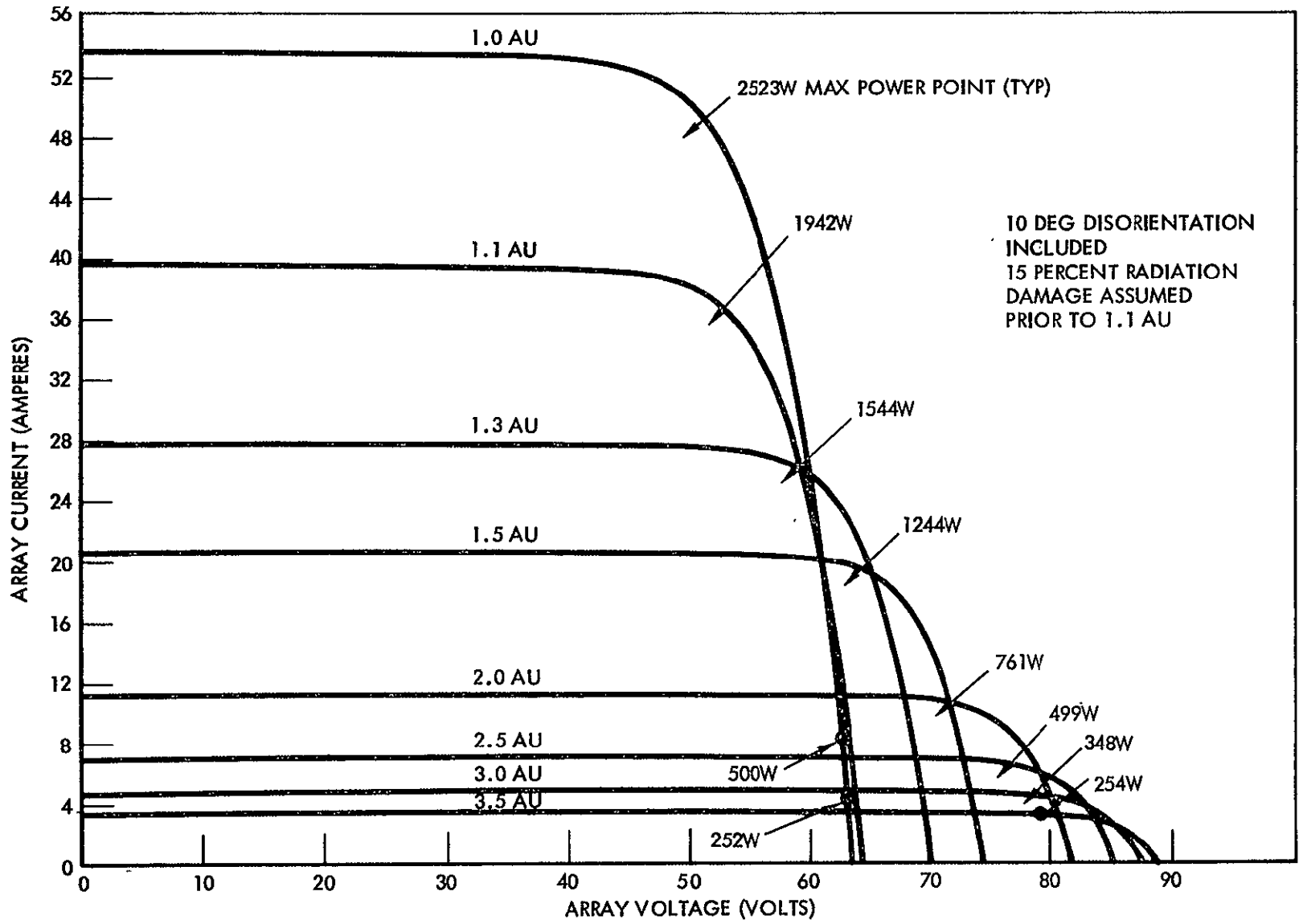
Figure 7-17. Basic Solar Array I-V Curves

A - BASIC ARRAY ONLY
B - ARRAY WITH CAPACITOR SENSOR
C - ARRAY WITH SENSOR (NO LOAD)
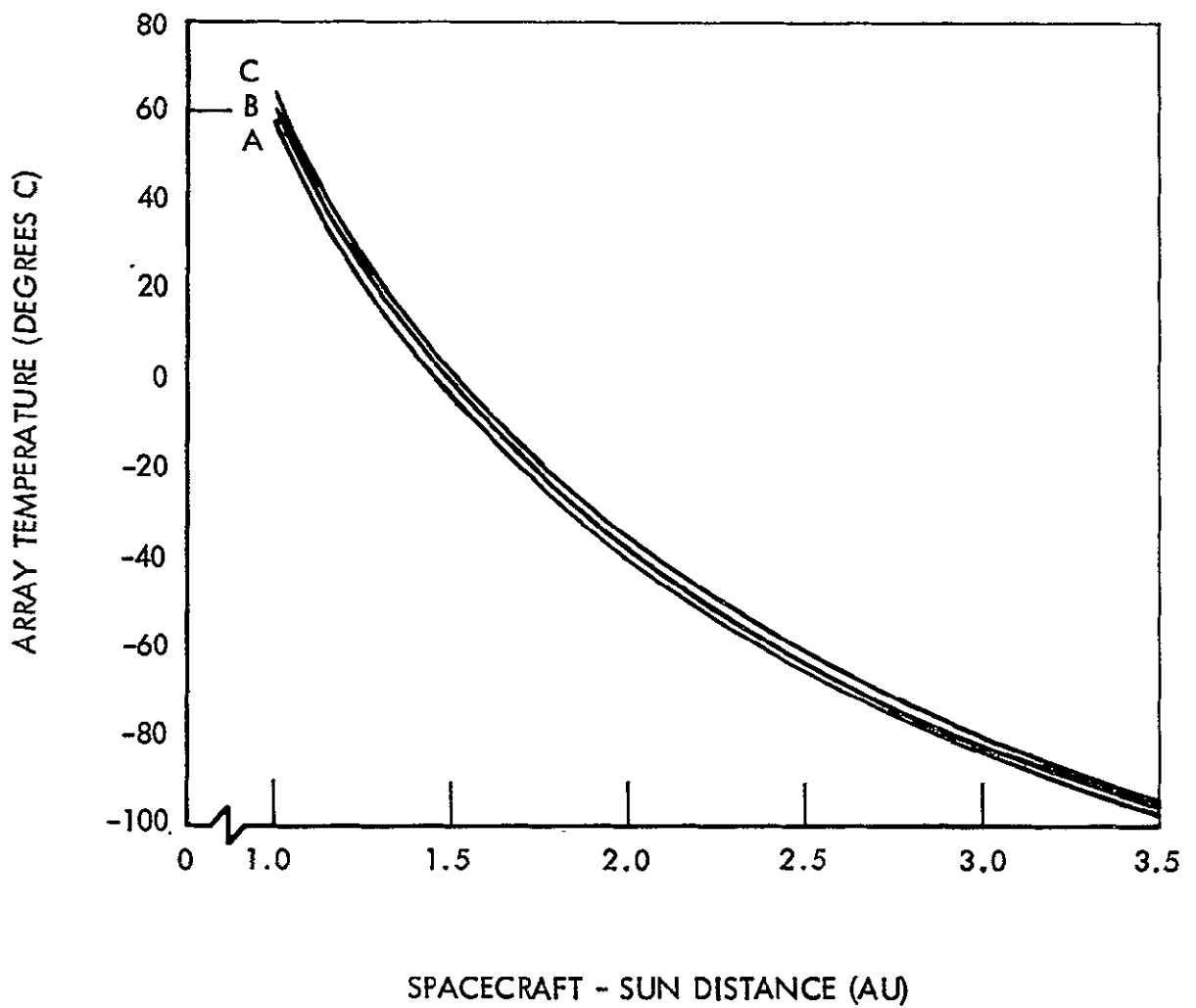
Figure 7-18. Solar Array Temperature Versus Spacecraft-to-Sun Distance

between front and back panel surfaces. Due to the fact that only 10 percent
of the incident radiation can be converted to electrical energy, Curve C
represents only a nominal increase in panel temperature and is a boundary
condition without significant impact on array performance during Phases 3B,
5, and 6 (see Table 7-1) when the spacecraft electrical load is a small
fraction of the array output capability.

Solar Array Performance

Solar model basic solar array power output capabilities as a function
of distance have been specified for this study by JPL. The power-distance
relationship is defined as:

$$P = \frac{P_o \sum a_i R^{-\frac{i}{2}}}{R^2 \sum a_i}$$

where

$$i = 0, 1, 2, 3, 4$$
$$P = \text{power at } R$$
$$P_o = \text{power at Earth } \left[0.10085 \text{ Kw/m}^2\right]$$

and

$$a_0 = 38.6773$$
$$a_1 = 363.8135$$
$$a_2 = -381.5077$$
$$a_3 = 104.7369$$
$$a_4 = 0$$

The actual power output realized from the solar arrays is subject to
degradation from the peak performance, as defined in Figure 7-19. The
power ratio data in Figure 7-19 does not take into consideration additional
mission degradation factors such as influence of solar array orientation
with respect to the sun, radiation induced damage to the solar cells, and
micrometeoroid damage (both asteroidal and cometary).

Solar Array Orientation

Figure 7-17 showed that the solar array rated performance is based
on ±10 degree deviation from the normal plane to the sun. The solar panels
are mounted to the spacecraft in a deployed position, which is canted
15 degrees toward the sun. Power output at 15 degrees = (cos 15°/cos 10°)
x P_{10} (rated power at 10 degrees). No tolerance was considered for attitude
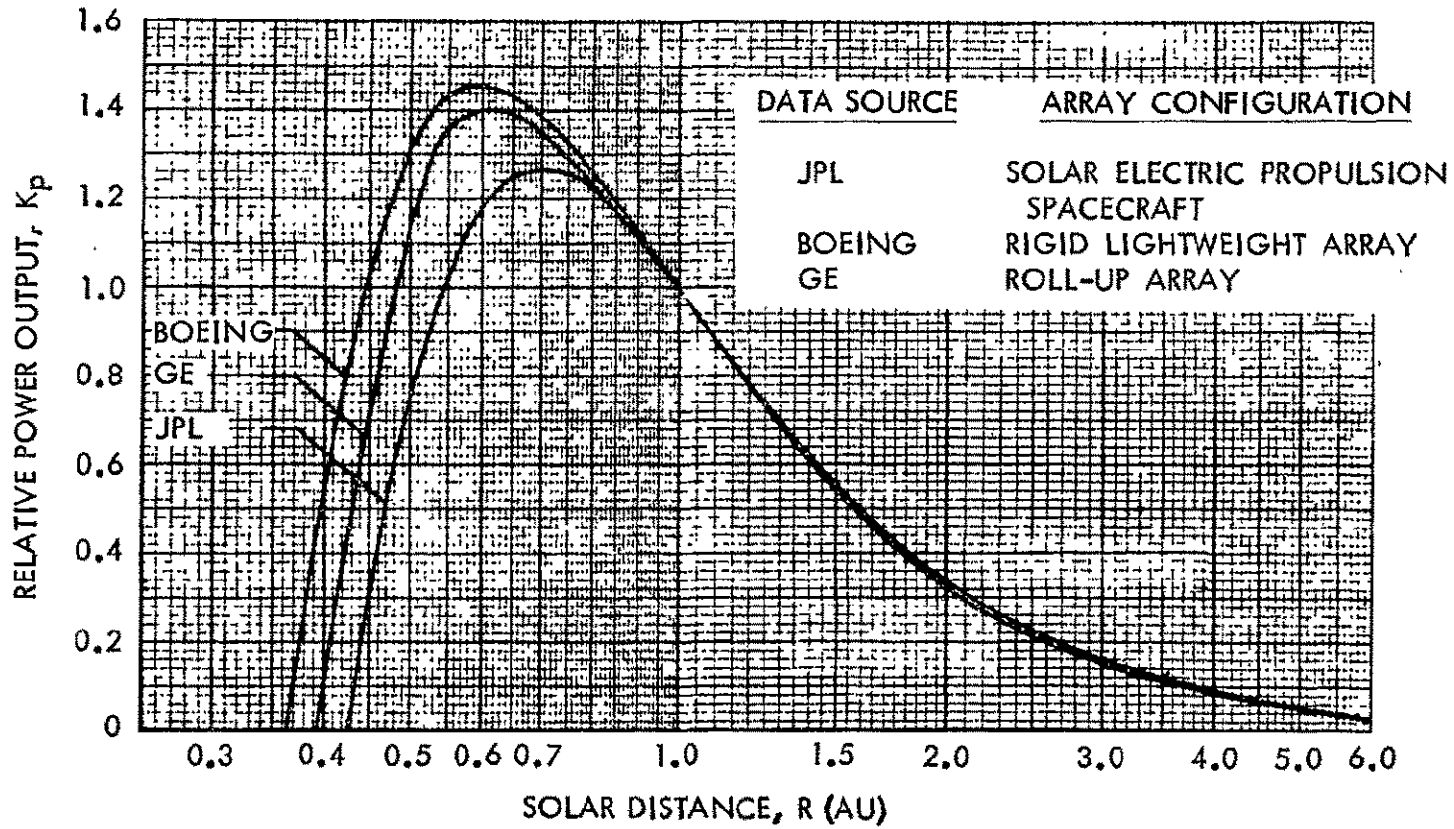
Figure 7-19. Comparison of Basic Solar Array Performance
(Excluding Degradation)

control deadband about the pitch axis as the loss of power in one panel is
offset by the gain in the other for small angle changes. During SEP thrust,
it is anticipated that the thrust vector control can be maintained to within
one degree in the pitch and yaw axis. Motion about the roll axis does not
influence solar array power output. From Figure 7-6, it is seen that an
additional degradation is experienced during the SEP thrust period due to
optimum thrust vector requirements as defined in the trajectory analysis in
Section 2.0. At SEP thrust termination at 2.0 AU, a maximum thrust
angle of 22 degrees from the normal to the spacecraft/sun line is experi-
enced. Upon termination of thrust, the science subsystem dictates the
spacecraft orientation requirements. Figure 7-20 shows the required
spacecraft orientation as a function of mission time and radial distance
from the sun.

Radiation Environment Effects

As stipulated in the contract work statement, 15 percent total degra-
dation in solar array performance due to radiation was used for solar
array performance calculations. However, in actual experience, it has been
determined that this degradation in performance does not occur immediately.
Solar cells are vulnerable to the sporadic emission of high energy particles
emanating from the sun (solar flares) and in particular low energy protons.
The sun spot/solar flare activity of the sun is quite cyclical and exhibits
periods of low and high activity. The activity period varies between 7.5
and 16 years averaging approximately 11.2 years, and varies by as much
as 4 years about a mean. As a result, it is essentially impossible to pre-
dict solar activity with respect to the launch period, and accurate estimates
of proton fluxes would be most difficult at best.

Micrometeoroid Damage Effects

Figure 7-21 shows the total power loss which may be expected for the
Asteroid belt mission. Both front and rear impacts, asteroidal and come-
tary, have been considered. During the first 210 days, SEP thrust phase,
when the power requirements are at a peak, the loss of power due to
micrometeoroid damage is negligible, about 0.02 percent. Over the entire
mission duration, total solar array performance degradation is predicted to
be about 1 percent. A comparatively large degradation occurs if an active
cometary stream is encountered as shown in Figure 7-21. However, the
mission can be planned to avoid these streams, especially during the
thrust phase.
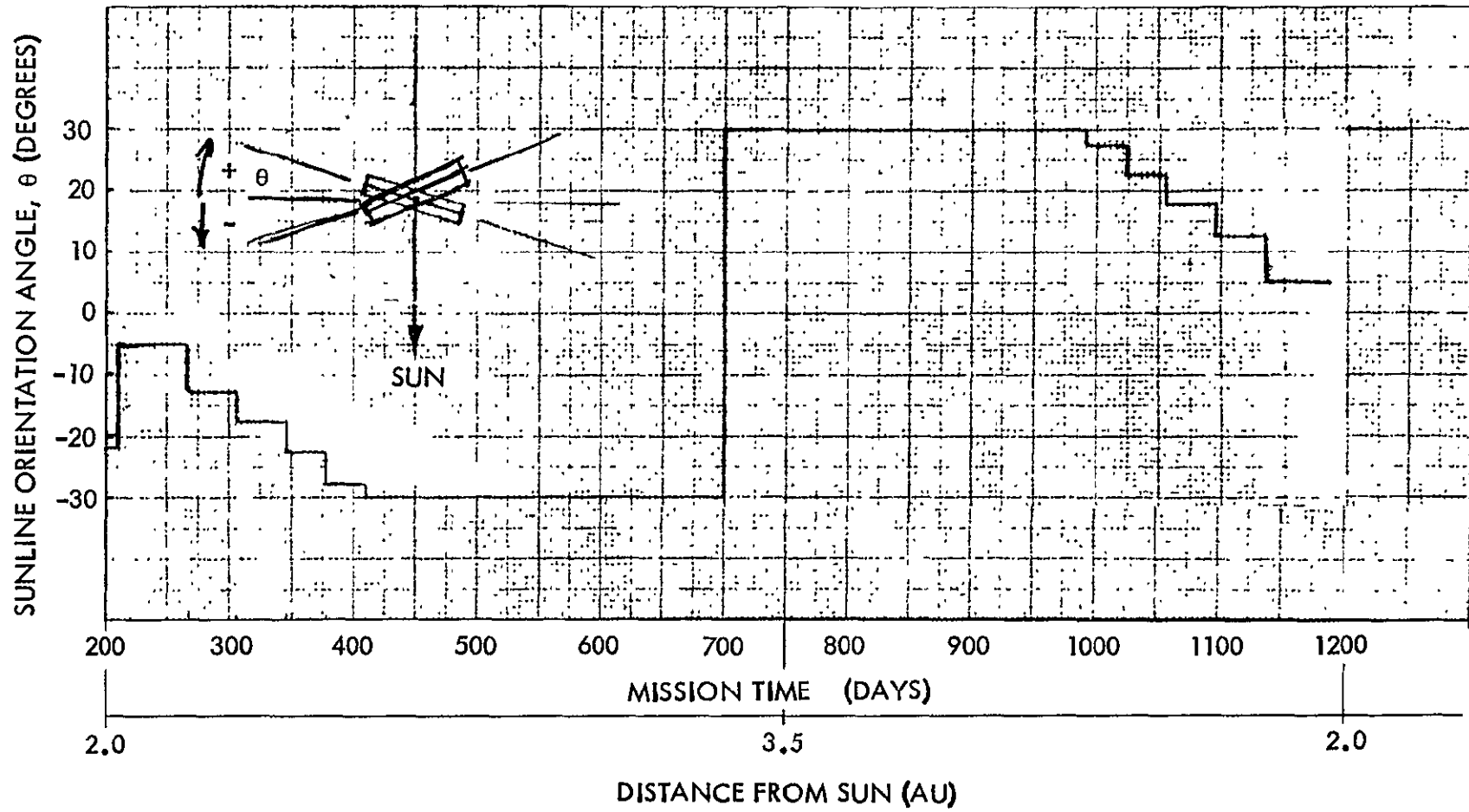
Figure 7-20. Spacecraft Orientation During Coast

Space Division
North American Rockwell
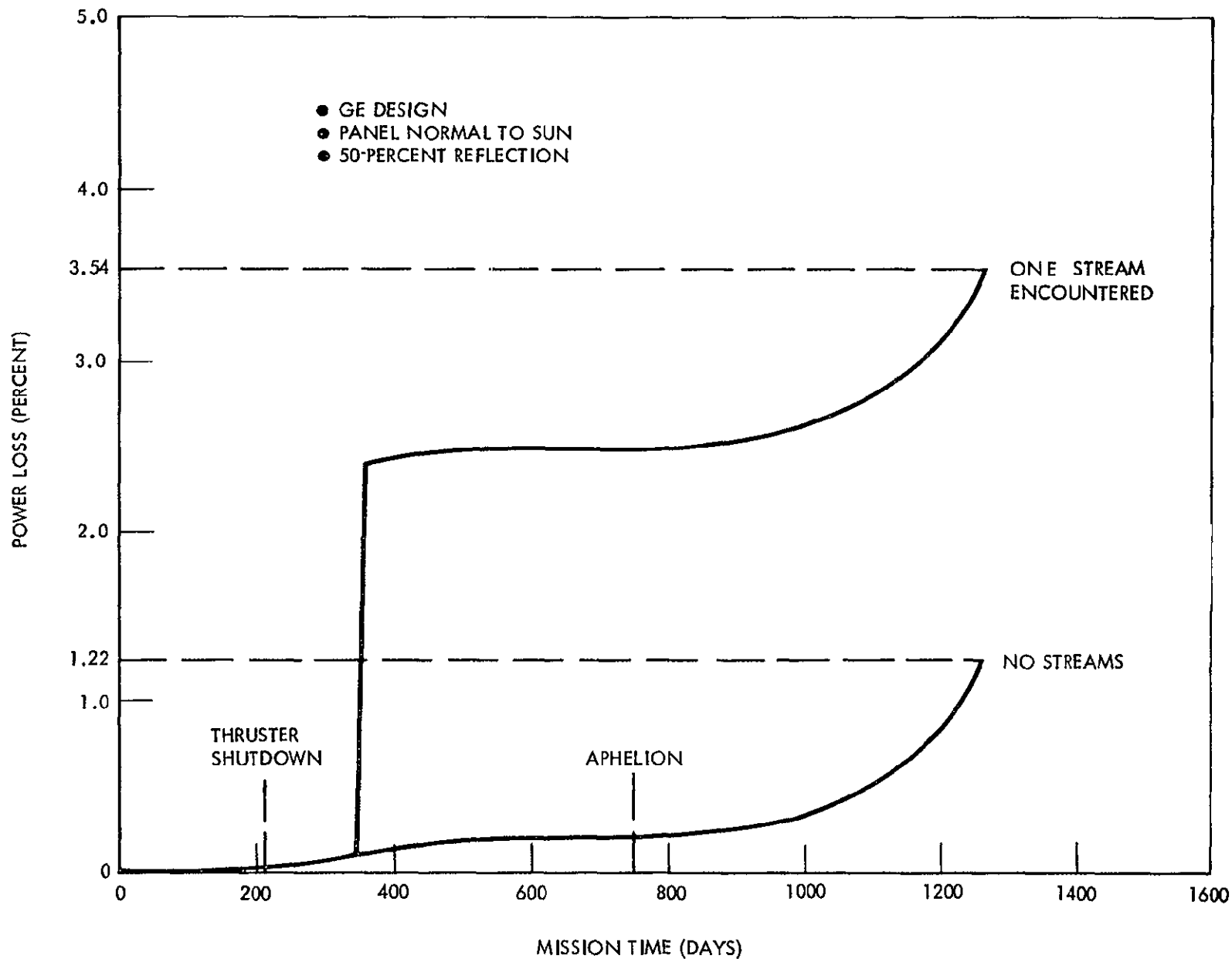
Figure 7-21. Power Loss of Solar Arrays Due to Meteoroid Impacts
(NASA Max Environment) and Cometary Streams (NR-SD Model)

Space Division
ican Rockwell

The multi-layered substrate and the meteoroid capacitor sheet detector offers sufficient protection to keep the overall damage extremely low. For a more detailed analysis on solar array performance degradation, the reader is referred to Section 12 of this report.

Power Output Prediction

No consideration was given to the increase in power output due to thermal bending of the solar arrays. The design specification allowed for a 5-degree bending due to thermal stresses, this bending moment being in a direction away from the sun thus giving an effective solar array maximum area equivalent to an array canted up to 10 degrees from the sun. Within the scope of this study it was assumed that the output of the array would be defined as the cosine of the canted angle times the rated power at normal incidence. In the region of 1 AU, the power output could conceivably be 10 kw when deployed at 15 degrees cant angle due to the maximum 5 degree bending. Since it is extremely difficult, if not impossible, to predict the solar array bending accurately, this additional power output of approximately 190 watts cannot be utilized except to provide design margin. It is reasonably sure that the bending moment of the solar arrays will exceed the expected one degree attitude tolerance about the yaw axis of the spacecraft; as such, the power gain due to solar array bending more than compensates for the loss due to attitude error about the yaw axis. For the power output performance prediction the power loss due to yaw attitude error was neglected.

Assuming a minimum initial power output, P_o, of 10 kw at 1 AU for the roll-up arrays canted 10 degrees to the sun, then the ratio of power (P) at any distance from the sun to initial power (P_o) is given in Figure 7-19. The power level is given by multiplying this ratio P/P_o times $\dfrac{\cos 15°}{\cos 10°}$ 10 kw.

The minimum solar array output occurs at maximum heliocentric distance (3.5 AU). A normally oriented array produces 1016 watts at aphelion. Degraded for 15-degree canted deployment, the power level becomes 982 watts.

BATTERY

Batteries are required to provide power to the spacecraft during the period of operation from termination of ground power to operational deployment of the solar arrays, a maximum of approximately 4.5 hours. Using the subsystem power requirements from Table 7-1 and allowing for distributing

inversion and isolation losses, the maximum energy requirements on the
battery during the period from launch/injection to solar array deployment
are as follows:

$$147 \text{ watts for } 1.3 \text{ hr} = 191 \text{ watt-hours}$$
$$125 \text{ watts for } 2.7 \text{ hr} = 337 \text{ watt-hours}$$
$$245 \text{ watts for } 0.5 \text{ hr} = \underline{123 \text{ watt-hours}}$$

$$\text{Total} \qquad 651 \text{ watt-hours}$$

The Mariner 1969-type AgZn 50 A-H battery was selected for the space-
craft design. It is recognized that NiCd batteries exhibit greater reliability
for long-life operation, greater than 2-3 years; however, NiCd batteries have
a higher specific weight factor than AgZn types. Weight is a prime factor for
consideration in selection of existing hardware in order to maximize science
payload. Although AgZn batteries have usually been restricted to mission
times of 2 years or so, it appears that the operational lifetimes can be
extended. Capacity loss measurements indicate that a 5 to 10 percent loss
occurs over a 4-year period when the ambient temperature is maintained
at 50 F.

The battery operation is required for the first 4.5 hours of the mission.
After this time the battery would be used only for emergency procedures when
the solar arrays fail to produce enough power to meet the spacecraft needs
(excluding the SEP requirements). In the event that such an emergency occurs,
there is a high probability that a catastrophic subsystem failure has occurred
and, with or without a fully charged battery for emergency operation, the
mission would be aborted. The maximum incidence of the solar panels for the
normal to the sun for the Asteroid Belt Mission is 30 degrees. Section 9.0
indicates that the pitch, yaw and roll rates are low, so that adequate time
exists for the attitude control system to correct for sudden valve failure or
any other disturbing influence before solar array output power falls below the
506 watts required by the spacecraft during the coast phase.

Absence of the requirement for cyclical discharge further enhances the
reliability of the AgZn battery. A very important consideration in the selec-
tion of the AgZn battery (with associated weight savings) was the unique con-
dition of not using the battery to augment the primary solar array output to
provide programmed power to the electric propulsion system. Since the
Asteroid Belt Mission does not have a specific trajectory requirement other

than to reach 3.5 AU with a long staytime in the 2.0 to 3.5 AU region, the power profile available from the solar arrays will dictate the programmed thrust magnitude. As the power profile varies from that predicted previously, the thrust program can be updated.

Accepting a reduction in battery reliability, a 50 A-H AgZn (Mariner 1969 design) is available at a weight of 18 kg. This is a weight savings of some 10 kg over the 28.2 kg for two 70 A-H NiCd batteries. The depth of discharge of the AgZn battery is $651/1375 \approx 47.5$ percent.

The battery will be brought up to full charge at least once each six months. Third electrode and temperature sensors are incorporated for battery charge control purposes. The batteries will receive at least 80-85 percent of full charge using the third electrode signal for termination unless temperature limits are exceeded for any reason.

After launch, no overcharging of batteries is planned as a measure to maximize battery life, although a trickle charge capability will be included for pre-launch topping to assure 100 percent capacity during Phase 2, and as a backup capability for subsequent phases.

AgZn battery charging will be accomplished serially at a current limited maximum C/20 ampere rate, or $50/20 = 2.5$ amperes. The battery will be fully charged during the period of the mission after solar array deployment but prior to solar electric propulsion thrust initiation.

DISTRIBUTION, CONDITIONING, AND CONTROL

The auxiliary power subsystem is designed to supply 405 watts of conditioned power to the spacecraft functional systems including payloads, in addition to battery charging requirements (70 watts). The overall regulation and conversion efficiency will be approximately 77 percent. Efficiency factors attributable to subsystem components were extrapolated from data contained in Figures 7-22 through 7-30.

The steady state solar array voltage increases slowly with increase in heliocentric distance during transit from 1 to 3.5 AU, then decreases slowly as the spacecraft returns from 3.5 to 2.0 AU (end of mission). With reference to Figure 7-17, the overall array operating range will be 0 to 89 vdc, but the open circuit bus range will be 63 to 89 vdc, while the range of maximum power points will be 51 to 80 vdc.

The main auxiliary power subsystem regulators accept raw solar power at voltages in the range 45 to 90 vdc and deliver rated power at an output voltage of 28.5 vdc ±1 percent with an efficiency not less than 85 percent.

PERCENT OF 500-W OUTPUT
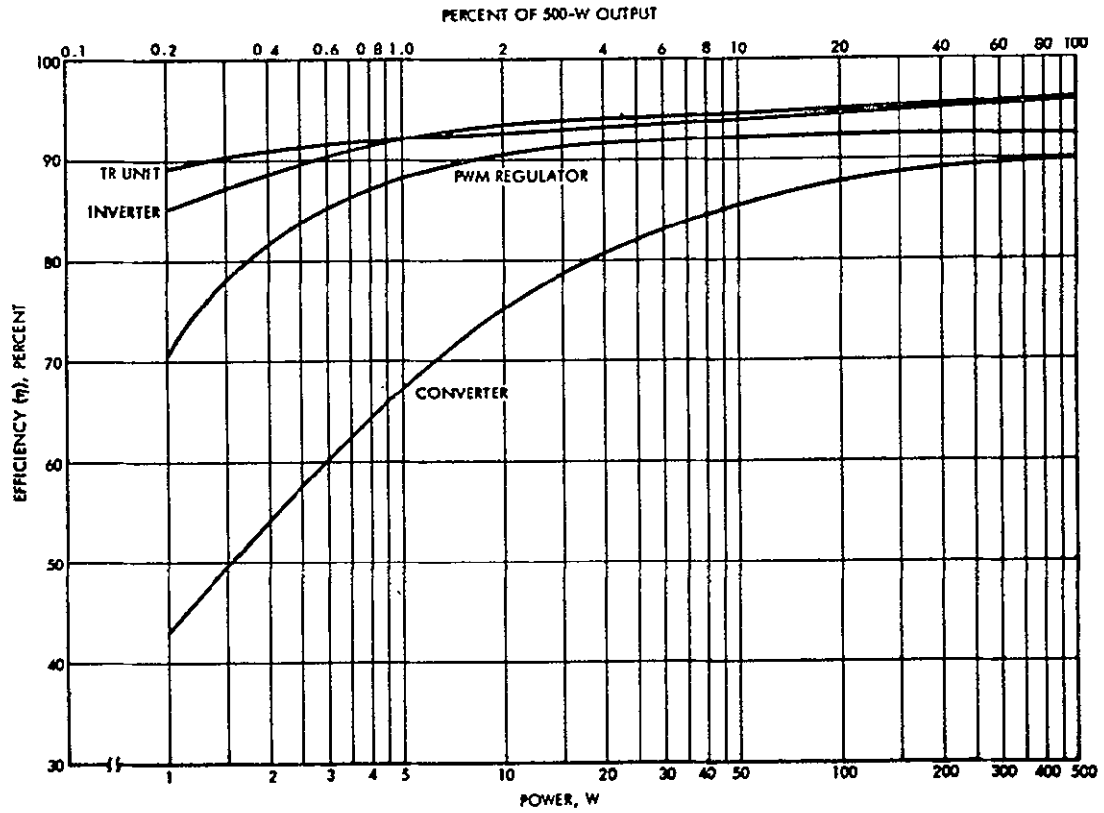
Figure 7-22. Maximum Efficiency as a Function of Power Output
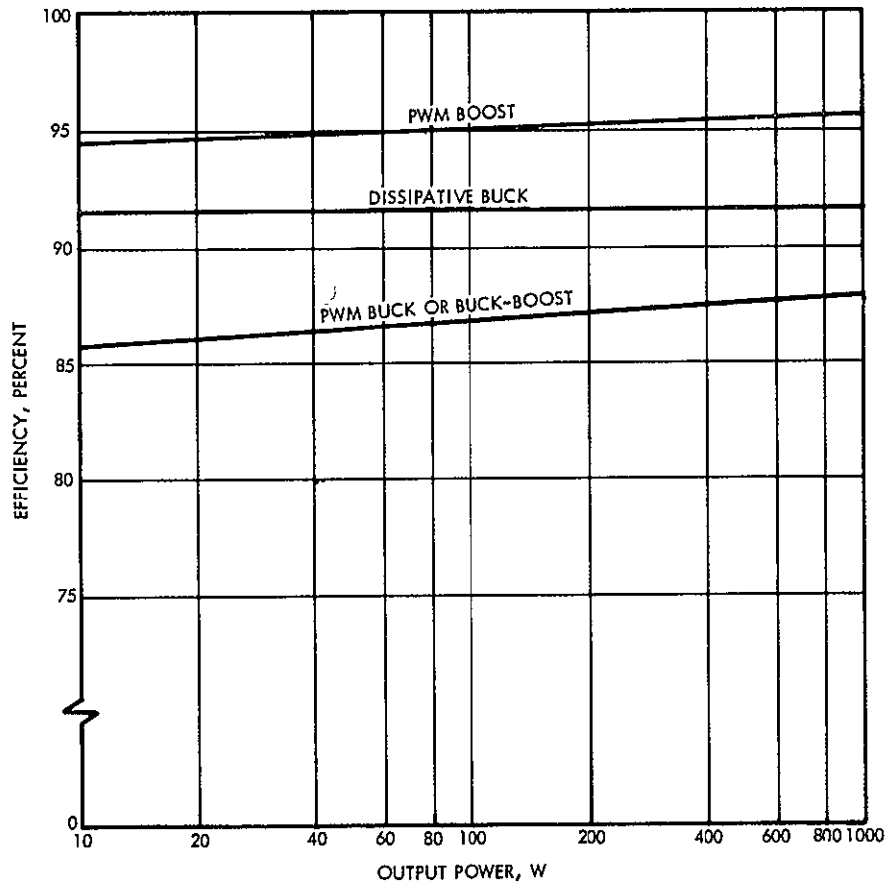
Figure 7-23. Line Regulator, Baseline,
Efficiency versus Power Output
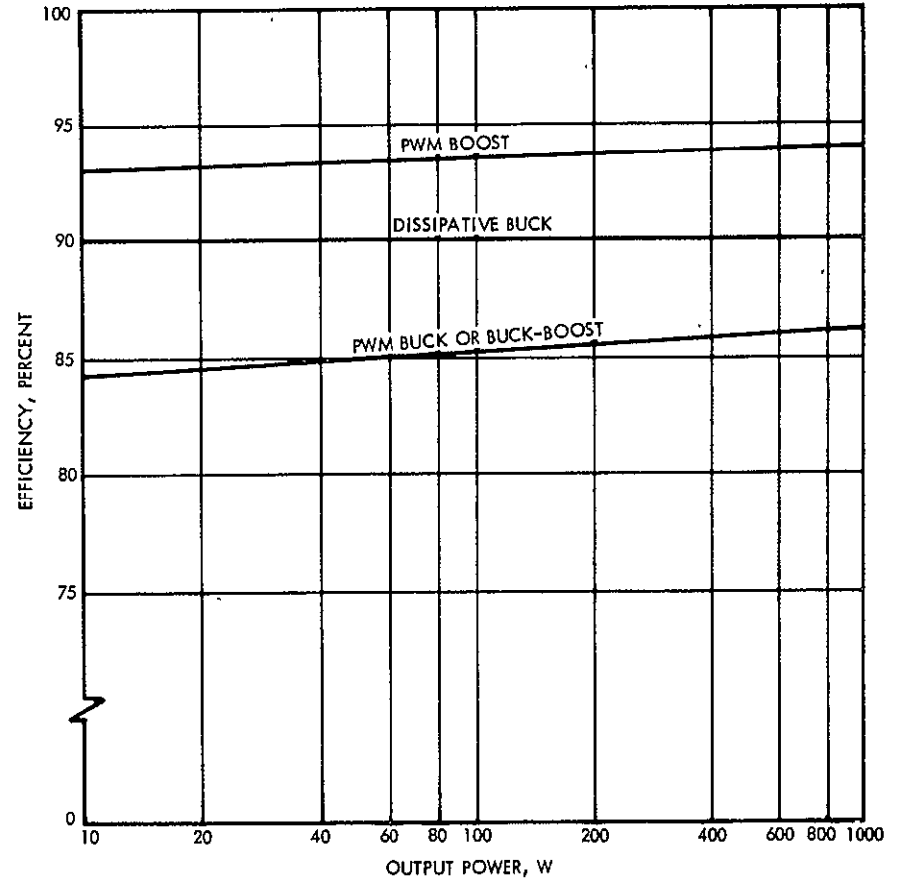
Figure 7-24. Line Regulator, Redundant,
Efficiency versus Power Output
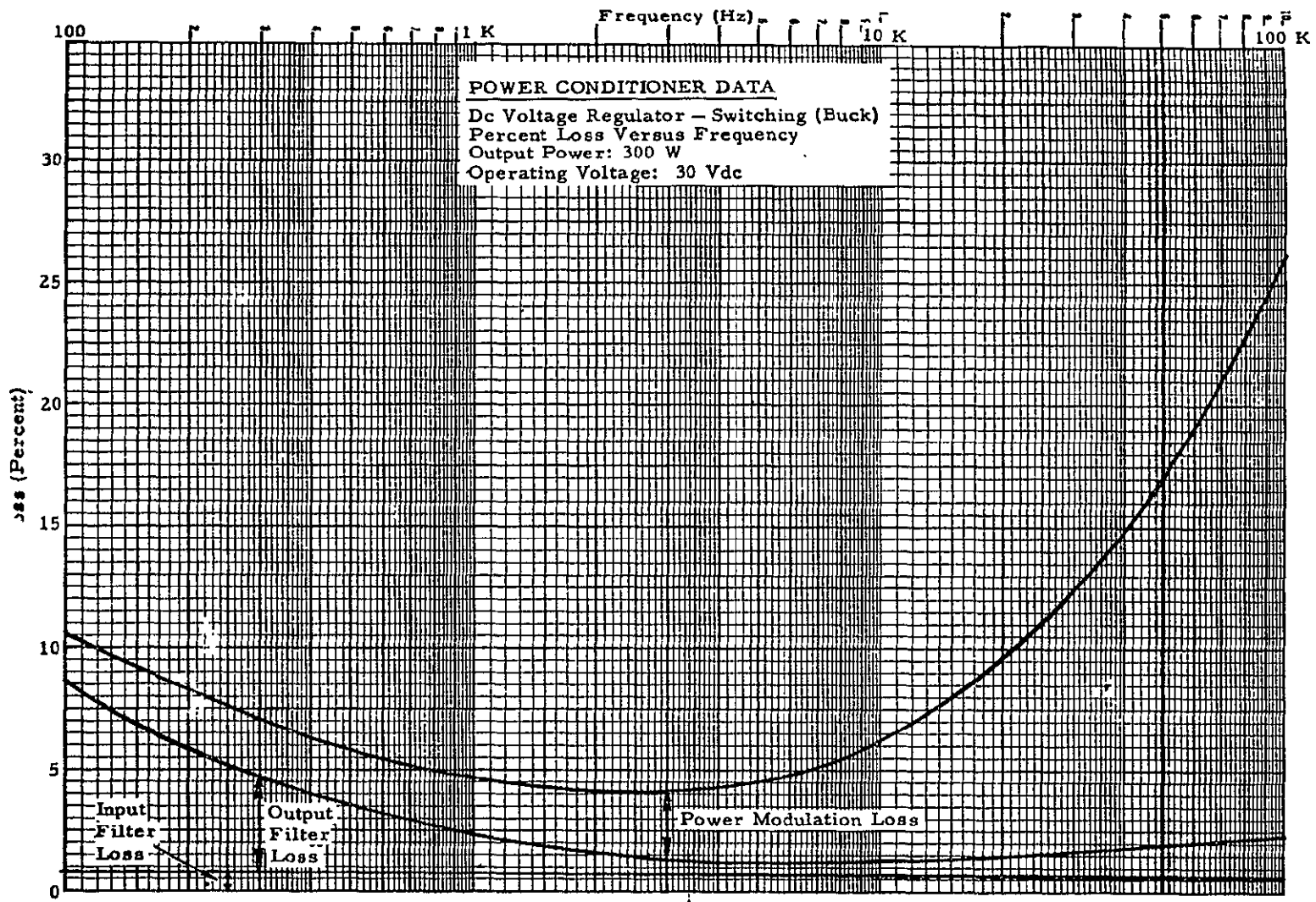
Figure 7-25. Power Conditioner Data, DC Voltage Regulator, I

POWER CONDITIONER DATA

Dc Voltage Regulator — Switching (Buck)
Percent Loss Versus Frequency
Output Power: 300 W
Operating Voltage: 30 Vdc
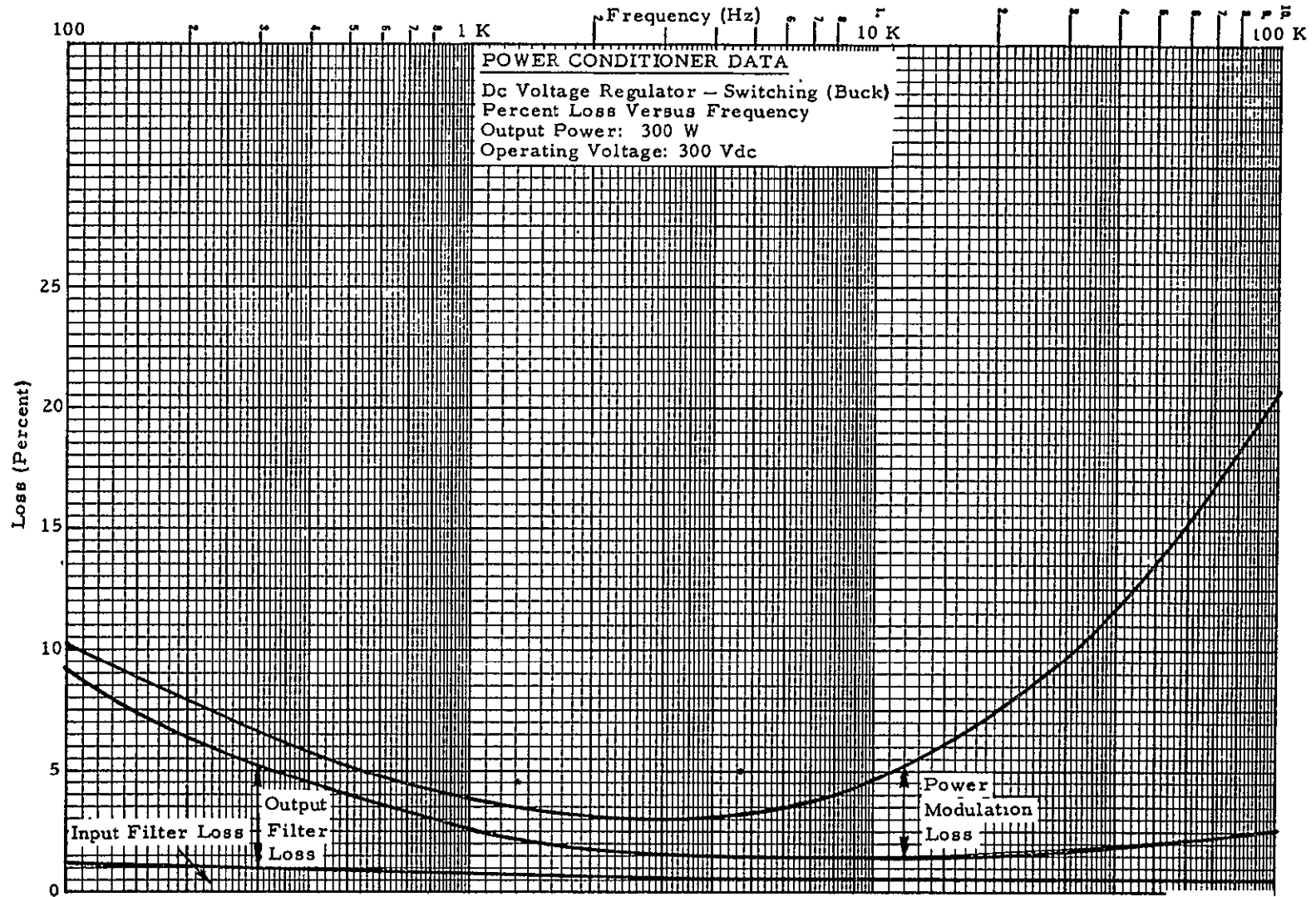
Figure 7-26.   Power Conditioner Data, DC Voltage Regulator, II
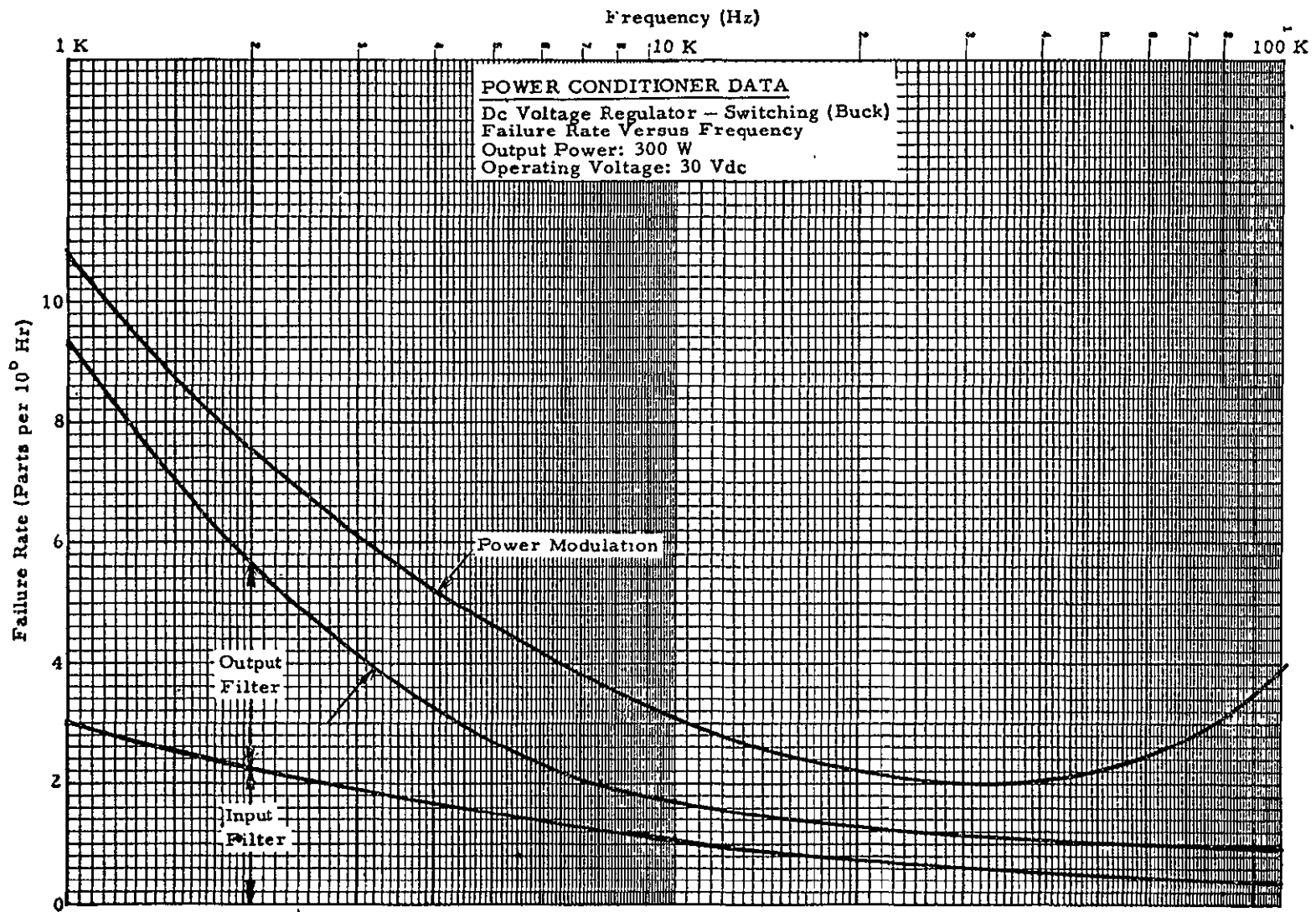
Figure 7-27   Power Conditioner Data, DC Voltage Regulator, III

Space Division
North American Rockwell
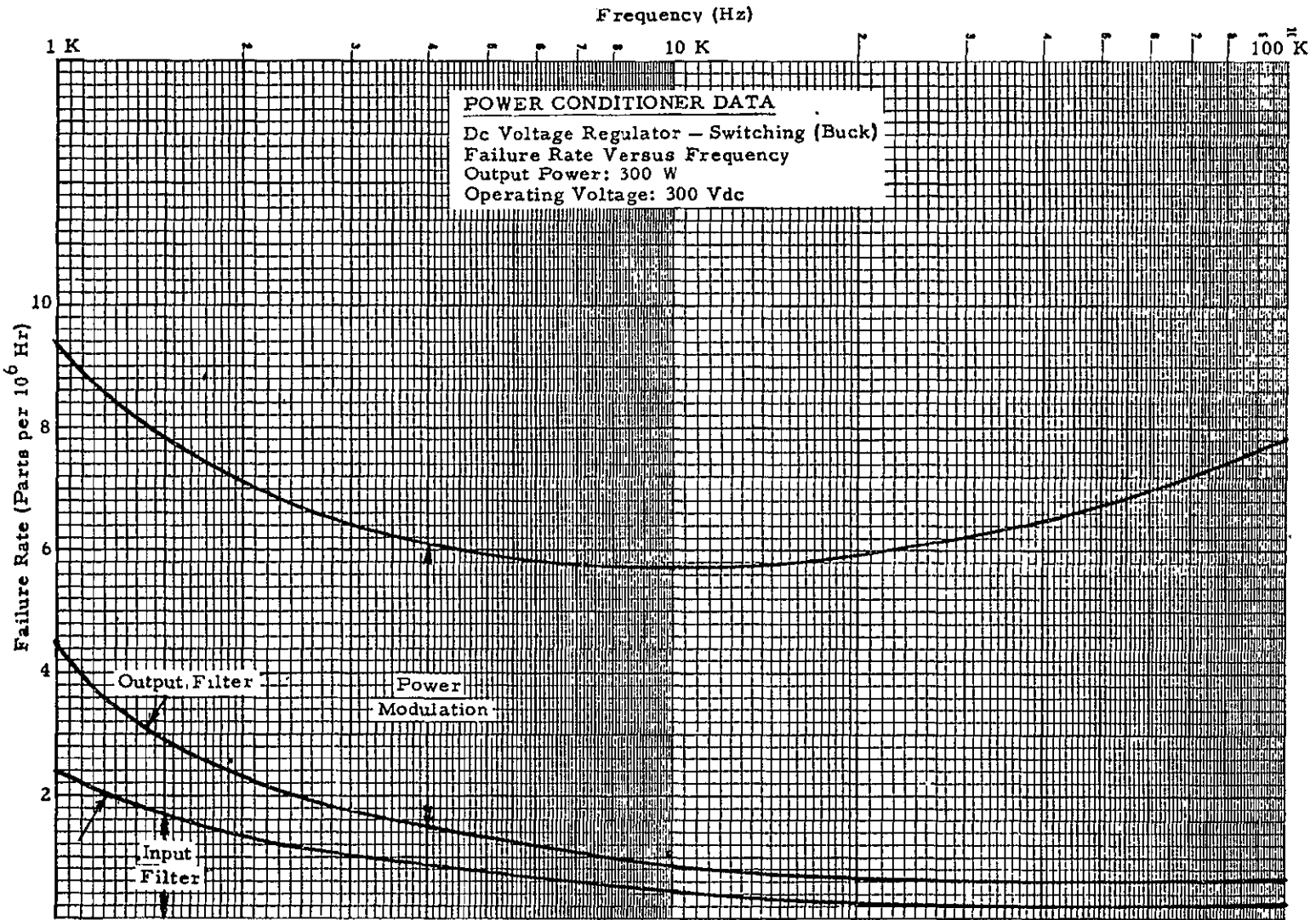
Figure 7-28. Power Conditioner Data, DC Voltage Regulator, IV

Space Division
North American Rockwell
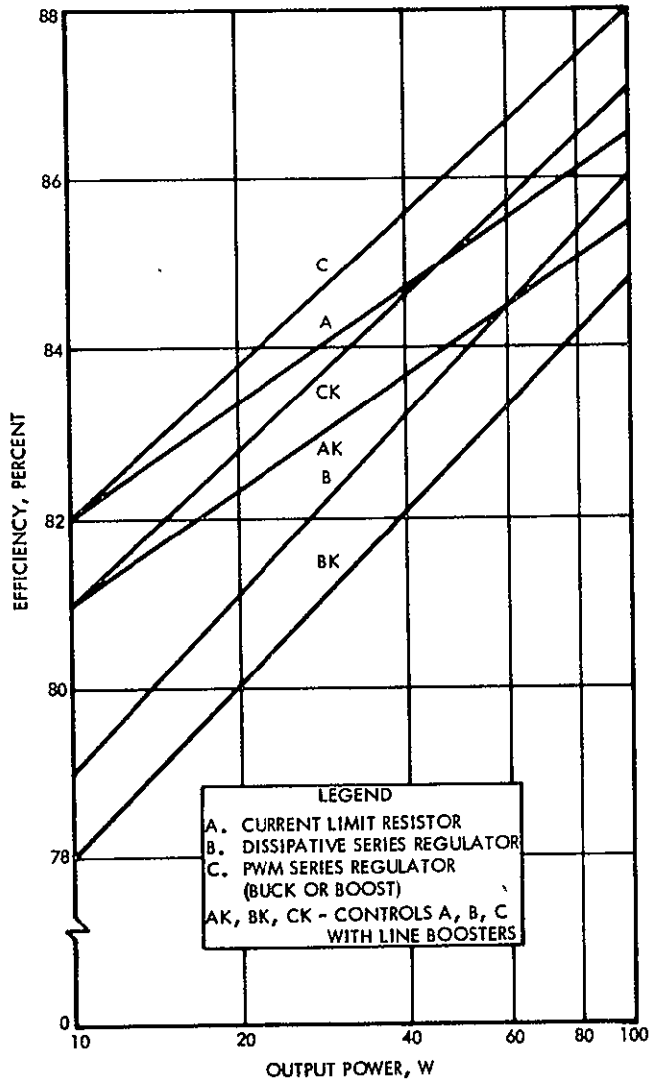
Figure 7-29. Battery Controls,
Baseline, Efficiency versus
Power Output
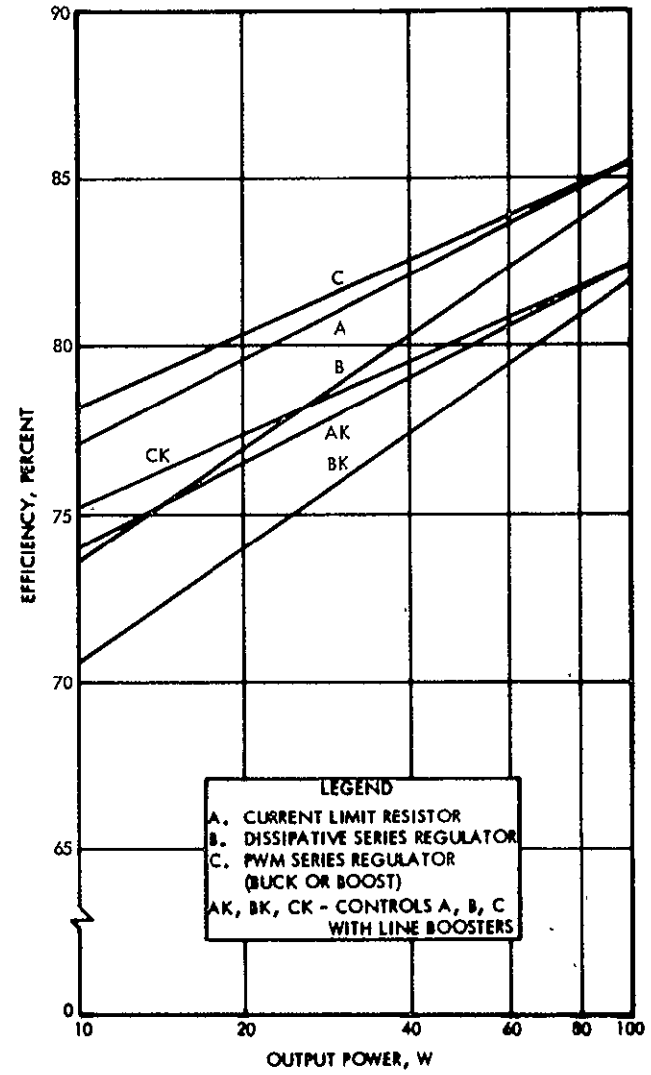
Figure 7-30. Battery Controls,
Redundant, Efficiency versus
Power Output

Space Division
North American Rockwell

These conditions, therefore, characterize a requirement for voltage regulators of the non-dissipative type: bucking limit control or switching regulators. Buck-boost regulators used in the Mariner spacecraft are not required, nor are momentary boosters for the solar bus to discourage load sharing since the batteries are applied to the regulated dc bus.

Mariner 1969 type inverters can be used to provide 2400 Hertz 50 volt rms square wave ac power. Rated output of these inverters is 200 watts with an efficiency of 92 percent, which provides a 16-percent margin over the peak ac requirement of 171 watts.

A three-phase 400 Hertz inverter also of Mariner 1969 design was used to provide the intermittent power requirements of the control system gyro package and array orientation motors. The wave form is square wave; however, the third harmonic should be suppressed to reduce motor heating. Redundancy is not expected to be warranted since the motors and nonredundant gyro packages that it supplies are usually less reliable. Minor redesign of both inverters is necessary in order to operate from the SEP-regulated 28.5 volt bus, which is essentially one-half of the Mariner design bus voltage.

The CC&S provides mission sequence controls. In addition, power control logic will be provided, although not identified in Figure 7-4, to monitor appropriate parameters and control power distribution modes. Solid state switching and/or relays will be utilized as the application dictates. Auxiliary subsystem components are utilized in active redundancy throughout, except for the 400 Hertz inverter. Power to spacecraft components is provided from independent ac and dc buses to provide a maximum capability for fault isolation and load redistribution. Redundant power distribution controls or bus ties afford an additional measure of flexibility, particularly in the event of main regulator and/or inverter failure.

ENGINE POWER AND CONTROL

Engine power is distributed directly to the engine power conditioning equipment in the range 50 to 70 vdc during the thrusting phase. This range is within the operating limits of the engine which is specified at 40 to 80 vdc. It is anticipated for the purposes of this study that power transmission will be accomplished by the distribution system at 98 percent efficiency. Controls incorporated within the engine power conditioner set cutoff input power below 35 vdc.

Both analog and digital peak power monitor mechanization have been investigated in previous studies. For the Asteroid Belt Mission it is reasonably simple to monitor the available power and program the thrust so that the total spacecraft power requirements never exceed the available power.

Utilizing this approach, then the engine power control is maintained by comparing main beam power input available to the engine (using a wattmeter and conditioning to suitable analog range) with the power command from the CC&S. The compared signal (signal error) is then sent to control circuitry which provides an analog signal to the PCC for thrust regulation. Compared signal polarity could be used to determine if commanded power level exceeds available power; the control circuitry would then limit engine control accordingly.

8. COMMUNICATIONS AND DATA HANDLING

The communications and data handling subsystems for the asteroid belt mission spacecraft must provide the spacecraft with capability for automatic processing and transmission of science, engineering, and house-keeping data to receivers of the deep space network (DSN) earth stations. Doppler tracking and ranging must also be provided by mea s of transponder functions in the spacecraft. A further function of the communication subsystem is to receive and process commands transmitted by the DSN. The data handling subsystem must provide for on-board storage, sequencing, and processing of data.

GENERAL REQUIREMENTS

For this study the following constraints and requirements were applied:

The maximum communication distance line of sight from spacecraft to the participating DSN station is 6.75×10^8 kilometers (4.5 AU).

A DSN subnet of at least three 85-foot stations spaced 120 degrees around the earth are available during critical injection and thrust phases of the mission.

A DSN 85-foot station with 40 kilowatts of RF power at S-band will be available when needed for command transmission during the coast phase of the mission duration.

The hardware requirements of the spacecraft communications and data handling functions will be compatible with the performance capabilities of Mariner and Pioneer equipment which is already developed for the time period.

The spacecraft must be continuously capable of receiving commands from the DSN.

In order to relieve S-band traffic and DSN schedule congestion,
24 hours of acquired data shall be returnable during line of sight to one
DSN 85-foot station.

Acquisition of science data shall be continuous throughout the asteroid
belt survey mission.

Self-check and self-maintenance will be designed into the system as
required to sustain critical mission capabilities for the useful life of
the spacecraft.

SPACECRAFT-TO-DSIF TELEMETRY LINK

The study indicates that the required mix of science data plus engi-
neering and housekeeping data under normal conditions covering a 24-hour
period can be returned to a single deep space instrumentation facility
(DSIF) 85-foot antenna at a rate of less than 40 bits per second within the
line-of-sight interval of the single DSN station. An emergency mode giving
priority to all required subsystem monitoring functions is also possible
within the 40 bits per second rate. The spacecraft may operate in either
the normal or emergency modes at any time after separation and out to the
maximum communication distance of 4.5 AU (maximum line of sight
distance of spacecraft to DSIF). The RF power required for maximum
transmission capability is 20 watts at 4.5 AU (6.75×10^8 kilometers).
Details of the spacecraft-to-DSIF downlink analysis are given in the Baseline
Subsystems section.

A time-line analysis showing transmitter bit rate capability versus
communication distance for the asteroid belt mission duration is shown in
Figure 8-1. After separation and before solar array deployment, a bit rate
of 40 bits per second is feasible using the low gain antenna driven by the
transmitter exciter stage to minimize electric power subsystem battery
requirements. (See Radio Frequency Subsystem section). Upon deployment
of the solar array and during warm-up standby of the TWT RF power
amplifier, 40 bits per second rate capability is possible to at least
75×10^3 kilometers, with the exciter-driven low gain antenna.

After switchover to the traveling-wave tube (TWT) RF power, the
40 bits per second is maintained with the low gain antenna and with the RF
system operating in the 10-watt power mode. At 100 days, the 10-watt
RF power is switched to the high-gain antenna enabling a rate of 200 bits
per second, which is maintained until termination of the thrust phase. The
reduction in power demand due to shutdown of the ion engines permits use
of the 20-watt RF power mode after 210 days. This power mode is main-
tained for the duration of the mission. Alternative rates of 80 and 40 bits
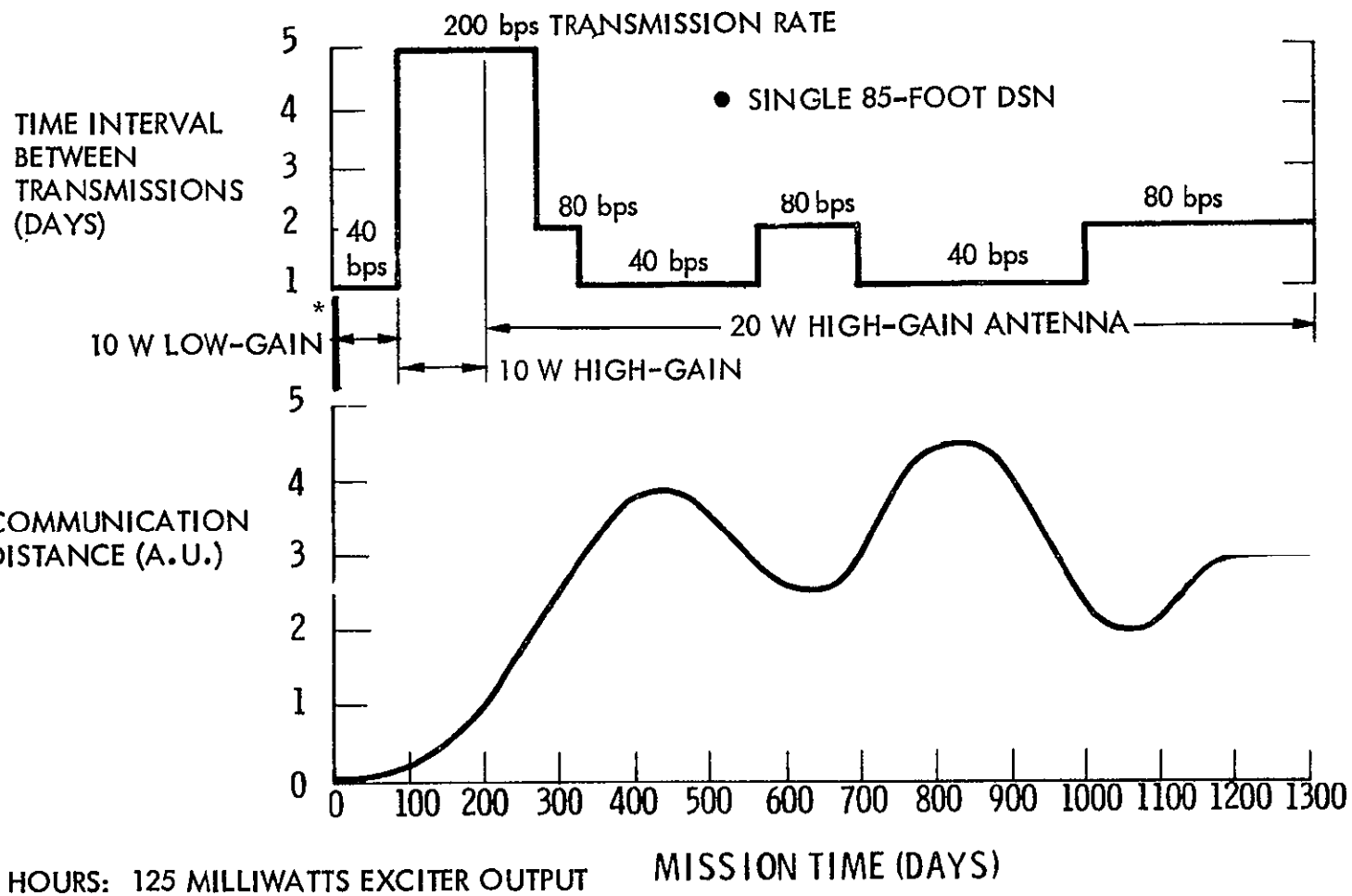
Figure 8-1. Communication History

Space Division
North American Rockwell

per second are permitted sequentially after 270 days, depending on when the spacecraft crosses the 3-AU (4.5 x 10^8) kilometers) communication distance line.

DSIF-TO-SPACECRAFT COMMAND LINK

The spacecraft will be provided with two low-gain antennas each with a hemispherical pattern to provide omnidirectional reception of command signals transmitted by 85-foot antennas of the DSN. Margin calculations are based on the premise that a 40-kilowatt RF power capability will be available at the DSIF set up for command. Table 8-1 shows the uplink margin expected under nominal conditions for the command link at a distance of 6.75 x 10^8 kilometers (4.5 AU). The anticipated transmission rate is 1 bit per second is considered adequate for the mission in view of the experience gained on the Mariner and Pioneer missions.

At 1 bit per second, the margin for the maximum communication distance depends upon favorable minimization of negative tolerances in the system, and upon the 40-kilowatt 85-foot DSIF availability. An alternate design to increase the margin by at least 6 decibels can be implemented. The low gain antenna facing the ground station in the maximum range phase of the mission can be replaced with the medium-gain horn antenna used on Mariner 1971. This would afford use of a 20-kilowatt ground station power capability while providing an additional 3 decibels to accommodate negative tolerances which may accumulate to an order of 5 or 6 decibels during the mission.

DSIF-TO-SPACECRAFT RANGING LINK

The radio frequency subsystem will be designed to accommodate one-way or two-way coherent (Doppler) tracking on command from the ground stations. Table 8-1 shows that the margin available for a two-way coherent loop at maximum range (6.75 x 10^8 kilometers) precludes the possibility of ranging accuracies of the order of tens of meters or better at that distance. For ranging accuracies of the order of 1000 meters, which may be acceptable (at 6.75 x 10^8 kilometers), the use of a completely regenerative signal at the spacecraft for a one-way coherent mode is recommended. The spacecraft is provided with local precision crystal oscillator control for the one-way signal source and complete regeneration of the range signal, including coding.

This combination of tracking circuit design was selected on the basis of availability of hardware from Viking 1973 and demonstration of feasibility from Mariner 1969.

Table 8-1. SEP Asteroid Belt Mission Command Uplink - 85 Feet
DSIF Power Margins

Power Component	Increment	
UPLINK MODE AS A WHOLE		
1. DSIF transmitter power (40 kilowatt)	+ 76	dbmW
2. Transmitting circuit loss	0	db
3. Carrier power versus transmitted total power	- 2.5	db
4. Transmitter antenna gain	+ 52.0	db
5. Space loss at 6.75×10^8 kilometers	-276.3	db
6. Polarization and pointing loss	- 0.5	db
7. Spacecraft antenna gain	+ 7.3	db
8. Spacecraft receiving circuit loss	- 0.2	db
9. Spacecraft received carrier power	-144.2	dbmW
10. Spacecraft received total power	-141.7	dbmW
UPLINK CARRIER (DOPPLER) LOOP		
11. Spacecraft receiver noise spectral density	-167.3	dbmW/Hz
12. Spacecraft receiver APC noise bandwidth (2 B_{LO} = 18 hertz)	+ 12.6	dbHz
13. Spacecraft receiver total noise power	-154.7	dbmW
14. Received carrier signal to noise normalized to 2 B_{LO}	+ 11.5	db
15. Required minimum signal to noise in 2 B_{LO}	+ 6.0	db
16. Spacecraft carrier tracking loop margin	+ 5.5	db
UPLINK COMMAND DATA LOOP		
17. Data noise bandwidth (2 hertz -1 bit per second)	+ 3.0	dbHz
18. Data noise power	-164.3	dbmW
19. Data power/transmitted total power	- 3.3	db
20. Spacecraft received data power	-145.0	dbmW
21. Spacecraft command data signal to noise	+ 19.3	db
22. Required command signal to noise (bit error: 10^{-5})	+ 13.5	db
23. Command margin	+ 5.8	db

BASELINE SUBSYSTEMS

The telecommunications and data handling subsystem for the asteroid belt mission embodies use of major elements of Mariner 1971 and Viking 1973 spacecraft. The features characterized by the asteroid belt mission configuration are summarized as follows:

The transmitter consists of the basic Mariner 1971 module operating in the S-band with dual TWT redundant power amplifiers capable of either 10-watt or 20-watt output. During the critical postseparation phase until solar array deployment, redundant exciters of the transmitter alone are energized to provide ample RF power for data return from a communication distance of 37 x 10^3 kilometers.

Science and engineering data are PCM coded, time-division multiplexed into a serial train, and convolutionally encoded. The composite serial symbol train is then used to biphase modulate one subcarrier. The single subcarrier phase modulates the RF output carrier.

Science data are acquired continuously for each 24-hour period on one of two recorders which alternately play back the stored data at convenient intervals. Playback and transmission of the data can be accomplished in six hours or less to accommodate DSN line of sight and probable scheduling restrictions. The data-return functions are sized to require use of a single 85-foot DSIF.

The weight and power physical parameters for the system are based upon anticipated availability of existing system hardware. The weight and power summary is shown in Table 8-2.

Radio Frequency Subsystem

Functions and performance characteristics of the radio frequency subsystem are described in the following paragraphs. The telecommunications subsystem functional schematic (Figure 8-2) shows the main elements and interfaces of the RF subsystem.

Radio Receiver-Transponder

The functions required of the radio receiver are (1) receive the S-band RF signal transmitted from the DSIF to the spacecraft, (2) demodulate the received radio signal and provide the resulting composite command signal to the flight command subsystem of the spacecraft, and (3) demodulate the radio ranging signal transmitted from the DSIF and provide phase lock and modulation through the transponder for return transmission to the DSIF.

Selection of a receiver to perform these functions is weighted by the overall design objectives necessary to satisfy the requirements stated previously. Choice is narrowed to state of the art hardware capable of or modified to meet range and life expectancy demands of the mission. Restated, the range or distance requirement is 6.75×10^8 kilometers, and the life requirement is continuous operation for 3-1/2 years.

The distance problem is resolved by a system design that assures an adequate signal at the output of the receiver for command and ranging purposes. To achieve an adequate output, the receiver must contribute a minimum level of noise to the system. Present state of art designs for deep space communication are represented in current Mariner and Pioneer receivers with signal threshold at -152 decibels per milliwatt noise power in a double-sided noise bandwidth of 18 hertz. These receivers are double-conversion superheterodynes employing a phase-locked loop (PLL).

Table 8-2. Communications and Data Handling Subsystems —
Weight and Power Requirements

Subsystem	Power Watts	Weight Kilograms (Pounds)
Radio frequency (less antenna)	78 to 114	17.8 (39)
High-gain antenna	--	4.5 (10)
Low-gain antennas (2)	--	3.2 (7)
Flight command	3	2.7 (6)
Flight telemetry	15	11.8 (26)
Data storage	21.5 to 41	15.5 (34)
Data automation and processor	25	5.9 (13)
Total	162 to 198	61.4 (135)

Figure 8-2. SEP Telecommunications Subsystem Functional Schematic

Space Division
North American Rockwell

The Mariner receiver is matched to a diplexer used for isolating it from spacecraft transmitter power levels while coupling it to the low gain antenna. A local oscillator multiplier stage, first mixer and preamplifier, and receiver filter are portions of the receiver contained within the diplexer package. To achieve extended life for the asteroid belt mission, redundant receivers are selected. Additional study is required to determine the advisability of using redundant diplexers containing matched sections of the receiver. The approach taken in the present study is to provide switching of the redundant receivers at the interface with the section contained in the diplexer for matching purposes. The receiver designed for Mariner 1969 and continued in use for Mariner 1971 and Viking 1973 is the type recommended because of its adaptability to this concept.

The composite command signal detected by the receiver is fed to the flight command subsystem for subsequent decoding. The ranging signal when received is supplied to the exciter to modulate the downlink transmitted signal. The ranging channel will be controlled similarly as in the Mariner configurations by being turned on or off by ground command. The ranging channel will be shut off periodically by a cyclic command from the central computer and sequencer as a safeguard to protect against the feedback observed in the Mariner Mars 1964 radio frequency subsystem.

In the ranging channel off mode, the exciter self-contained carrier oscillator must maintain adequate frequency stability for one-way coherent transmissions by the radio frequency subsystem. The Mariner exciter subassembly used in Mariner 1971 and Viking 1973 can provide the required performance, based upon the history of the Mariner VI and Mariner VII (1969) missions. The Mariner exciter is capable of developing an output power of 250 milliwatts. This level of power is adequate, after coupling losses, for driving the TWT power amplifier output stage of the transmitter. The exciter output level is also adequate for direct coupling to the spacecraft low-gain antennas for data signal transmission and Doppler tracking during the first four hours after separation in the asteroid belt mission (Table 8-3). Use of the exciter as an output signal source up to the time of solar array deployment minimizes the load requirements for the battery used in the electric power subsystem during that period. An alternate considered was use of a small solid-state transmitter. The exciter was selected for the signal source to avoid additional switching at the data channel, receiver, and electric power interfaces of the radio frequency subsystem.

Radio Transmitter

Redundant exciters provide the drive for the spacecraft radio transmitter power output stage through a filter/hybrid subassembly as used

on Mariner 1971 and Viking 1973. Switching between the redundant excitation sources may be controlled by ground command. An overcurrent sensor in the radio frequency subsystem also can cause switching of exciters in case of current overload. The filter/hybrid circuit embodies a microwave diode sensor to sense the level of drive to the output amplifier of the transmitter. If the input level falls below a preset value, the drive is automatically switched to the alternate redundant exciter upon verification command by the central computer and sequencer subsystem.

The filter/hybrid assembly filters the exciter drive signal and splits the S-band power between two ports in a matched hybrid. The two output ports supply drive for redundant transmitter output stages so that either of two redundant exciters can drive either of two redundant output amplifiers.

The Mariner TWT power amplifier is recommended for the radio transmitter power output stage based upon (1) indicated availability of hardware (used for Viking 1973), and (2) power output capability to meet SEP requirements for a minimum data return of 40 bits per second from a distance of 6.75×10^8 kilometers, (see High-Gain Antennas), and (3) life expectancy based upon the present history of performance of the TWT amplifier, Watkins-Johnson Type WJ-1084. An additional consideration in the selection is the dual mode capability of the WJ-1084 which permits output power operation at 10 and 20 watts.

Output power of the power amplifier must be capable of being switched from either of the redundant TWT's that are operating to the high-gain antenna or to the diplexer coupling to either low-gain antenna. An RF switch assembly is used to provide the required connections. The switching function is accomplished by ferrite circulator switches operable by means of ground or central computer and sequencer (CC&S) commands. Switching is accomplished by application of a bias voltage to the ferrite circulator, which determines the directional properties of the ferrite.

The switching subassembly will incorporate microwave power monitors to provide RF power output level sensing for in-flight monitoring, control, and telemetering to the ground station. The in-flight monitoring function will serve as a sense for in-flight corrective maintenance.

Low-Gain Antennas

The low-gain antenna must enable the spacecraft to receive ground commands at any time after separation and to transmit emergency engineering and housekeeping data. This results in the requirement for

essentially omnidirectional communication capability. The spacecraft
physical geometry and orientation requirements preclude the possibility of
use of a single omnidirectional stub antenna.

With a requirement for two antennas established, the next considera-
tions are antenna mounting and location. The SEP spacecraft does not
accommodate two antennas closely mounted to the body of the vehicle
because of shadowing by solar arrays, science equipment, and electric
propulsion plume. By devising a boom to mount each antenna to minimize
shadow effects, a feed problem is introduced. The low-gain antenna
problem becomes very similar to that for the Mariner spacecraft.

The Mariner low-gain antenna serves ideally for the SEP spacecraft.
The antenna solves the problem of antenna boom mounting and antenna
feed, providing approximately 7.2 decibels gain above isotropic within a
40-degree cone angle. Two antennas of this type boresighted at the
0-degree and 180-degree cone angles of the spacecraft can provide
essentially dual hemispherical coverage with a -10-decibel minimum
gain at 90- and 270-degree cone angles. At the base of the antenna
assembly, an input probe excites linearly polarized waves that are
propagated internally along the thin aluminum boom to the wave exit
aperture where the RF energy is converted to a circularly polarized mode.
At the aperture of the waveguide, a radome matching disc and a conical
ground plane complete the antenna assembly. This antenna, as refined in
design to its present form on Mariner 1969, will be available as hardware
in use on Viking 1973. Selection of the Mariner low-gain antenna is based
upon the fact that it (1) is compatible with SEP spacecraft mounting
requirements, (2) is space qualified, (3) is projected for use on Viking
1973 as existing hardware, and (4) satisfies uplink and downlink
transmission-reception requirements (see Tables 8-1 and 8-3).

High-Gain Antenna

The rationale for selection of size and configuration of the high-gain
antenna for the SEP asteroid belt mission is based upon (1) availability of
space-qualified hardware, (2) economic advantages of deriving system
technology from previous successful planetary missions, namely Mariner
and Pioneer, and (3) adequate transmission capability.

For a three-axis-stabilized spacecraft, a circular parabolic
reflector antenna is best suited to obtain maximum gain. Two sizes
of parabolic reflector can be considered as available hardware: the

Table 8-3. Spacecraft and DSN Downlink Power Margin Calculations

	Increment
Noise power per unit bandwidth	-185. 6 dbmW
Required signal margin	+ 3. 2 db
Signal power per unit threshold	- 182. 4
System losses 7. 90 db	
Path loss 191. 1 db	
Negative tolerance 4. 1 db	
-203. 1 db	-203. 1 db
85-foot antenna gain	+ 52. 8 db
Net loss	-150. 3 db
Spacecraft omniantenna gain (worst case)	- 10. 0 db
Loss	-160. 3 db
T at 40 bits per second: 16. 00 db	
Signal power per unit threshold -182. 4 dbmW	
Signal power per 40 bits per second -166. 4 dbmW	-166. 4 dbmW
Required carrier power	- 6. 1 dbmW
(Available carrier power 125 megawatts)	+ 20. 9 dbmW
Downlink data margin at 37 x 10³ kilometers	+ 27. 0 db
Downlink data margin at 75 x 10³ kilometers	+ 20. 2 db

Parameters used: 85-foot DSIF, SC omniantenna, temperature 20 K, 2. 3-gigahertz downlink, 37. 04 x 10³-kilometers distance.

Table 8-4. Performance Margin Calculation - 85-Foot, 2.3 GHz

$(4.5 \text{ AU} = 6.75 \times 10^8 \text{ km, } T_e = 20 \text{ K})$	
Noise power/BW at 20 K	-185.60 dbmW
Required signal margin net unit threshold (Mariner)*	+ 3.20
Net unit threshold	-182.40 dbmW
System losses	- 8.10 db
Path loss at 6.75×10^8 km	-276.31 db
Negative adverse tolerances	- 4.10 db
Cumulative losses	-288.51 db
Receiving antenna gain	52.40 db
Net effective loss	-236.11 db
Science channel power at 15.7 w	41.96 dbmW
Transmitter antenna gain at 1.5 m	28.02 db
Power gain product	69.98 dbmW
Required received power after losses	-166.13 db
Max. T for zero margin	16.27 db
Equivalent coded rate	42.4 bps
Minimum return time at 10 bps acquisition rate	5.45 hrs
Available station time at T_e = 20 K and 90-deg to 40-deg elevation	6.6 hrs

*Threshold is for biorthogonal block coding and does not take into account further improvement of approximately 1 db realizable with convolutional coding.

Parameters used: 85-foot DSIF, 2.3 GHz, temperature 20 K, 6.75×10^8 km (4.5 AU) distance.

Mariner 1969 (approximately 1-meter-diameter antenna) and Mariner 1971 and Viking 1973 (1.5-meter-diameter antenna). The ATS F&G 9.14-meter-diameter erectable folding reflector is also available as a choice, but it requires sophisticated pointing equipment aboard the spacecraft due to the narrow beamwidth at S-band. Also, it presents a weight problem and a design constraint relative to solar array deployment.

To take advantage of Mariner technology already proven in space the Mariner 1969-1971 transmitter was used as a model to evaluate various antenna sizes (Figure 8-3). At maximum asteroid belt mission communication distance, 6.75×10^8 km, the Mariner 20-watt transmitter can return 24 hours of data acquired at the rate of 10 bps to a DSN 85-foot-diameter antenna in less than 6 hours using the Viking 1.5-meter-diameter spacecraft antenna. The Mariner 1969 antenna requires more than 12 hours under the same conditions. Since the mean line-of-sight visibility period for stations equipped with DSN 85-foot-diameter antennas is approximately 6.6 hours, the 1.5-meter-diameter antenna is adequate. The physical mounting of the antenna introduces no significant problems.

To illustrate the maximum theoretical capabilities of the model used, a margin calculation taken at minimum data return interval is shown in Table 8-4. Maximum bit rates for distances up to 6.75×10^8 km are given in Table 8-5.

Table 8-5. Maximum Bit Rates Achievable, Mariner/Viking System Model

Communication Distance		Maximum Bit Rate
AU	kilometer x 10^8	(bits per second)
1	1.5	865
2	3.0	217
2.5	3.75	137
3	4.5	94.8
3.5	5.25	70.3
4	6.00	53.2
4.5	6.75	42.4
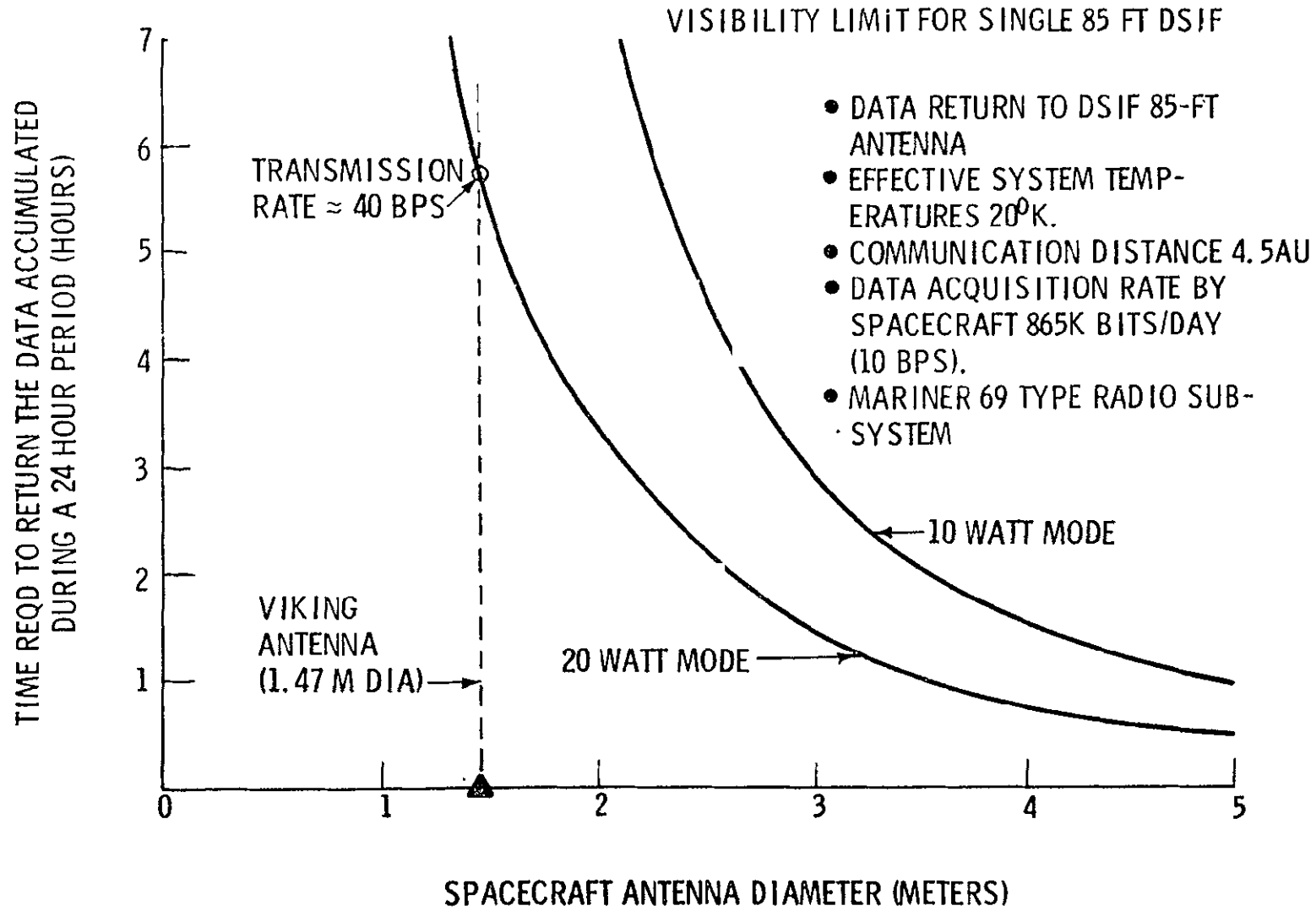
Figure 8-3. Antenna Versus Transmitter Sizing Rationale

Flight Command Subsystem

The flight command subsystem (FCS) must accept the composite command signal received through the RF subsystem, acquire phase lockup, demodulate command-word information, and detect and reconstruct the command-word data bits as sent by the DSIF ground command station. Three types of commands are typically transmitted to the spacecraft: (1) direct command words that momentarily control spacecraft subsystem switch closures, (2) coded command words in serial bit trains that feed the CC&S with maneuver and program modification information, and (3) quantitative command words momentarily actuating various combinations of switches particularly for controlling science subsystem scan.

The command detector must perform the functions of lockup and demodulation. It selects the command word information by filtering the composite command signal and reconstructs the information into binary bits by means of decision and storage circuits. The resulting command words are fed to the command decoder. The decoder processes the command words, reads the addresses, and provides either an appropriate subsystem switch closure, a serial bit word to the CC&S, or a serial pulse train of variable length for quantitative commands as required.

A typical mix of flight commands is shown in Table 8-6. The SEP asteroid belt mission command list is typified by the Mariner 1971 command list plus additional commands associated with control of SEP subsystem and unique mission requirements. A command bit transmission rate of 1 bit per second is postulated as adequate based upon Mariner, Pioneer, and Viking analyses available in the literature.

Output switch requirements for the SEP spacecraft are comparable to Mariner 1971 plus the additional switches for propulsion thrust control. The use of JPL-developed photon-coupled switches affords a reduction of weight below the 11.7 pounds of the Mariner 1969 FCS. With a minimum of 50 photon coupled output switches, each of which is 1/20 the size of the Mariner/Mars 1969 switch, a weight of 4.0 pounds is possible. To extend the reliability of the system by using parallel redundant decoders (and switches) for the asteroid belt mission, a flight command subsystem total weight of 5.8 pounds is achievable. The required modification consists of paralleling existing packaged integrated circuits rather than developing a new assembly.

The compatibility of the Mariner/Viking flight command subsystem plus hardware availability is the basis for selection and recommendation for the asteroid belt mission configuration.

Table 8-6. Typical Command List

Name	Destination	Comment
Engineering Mode	FTS DSS PYRO PWR	Switches FTS to Engineering data mode Spare Spare Spare
CC&S readout select	FTS	Toggles engineering channel from engineering telemetry to CC&S memory data and vice versa
Playback mode	FTS DSS PWR	Switches FTS to playback data mode Initiates playback of data stored on tape To be defined.
DSS ready mode	DSS	Stops the tape if it is in motion by switching the DSS to its standby mode.
Data rate switch	FTS	Toggles engineering channel data rates
Power amplifier switch	RFS	Selects redundant TWT and power supply; is a toggle command
Exciter switch	RFS	Selects redundant exciter unit; is a toggle command
Ranging on and off	RFS	Toggles ranging command on/off
Transmit-receive low-gain antenna	RFS	Selects low-gain antenna for both reception and transmission

Table 8-6. Typical Command List (Cont)

Name	Destination	Comment
Transmit high/receive low-gain antenna	RFS	Selects transmission via high-gain antenna and reception via low-gain antenna
Adaptive gate step	AC	Steps Canopus and/or Vega brightness gate to lower values; next command following minimum gate setting resets logic to maximum value
Maneuver inhibit	AC	Inhibits CC&S commands to AC and initiates Sun and Canopus or Vega acquisition
	CC&S	Resets fixed sequencer and switches maneuver logic to the nontandum standby mode
	PWR	Turns off power to gimbal regulator
	PYRO	Safe capacitor banks C and D
Maneuver enable	AC	Enables CC&S maneuver commands to AC. Turns AC off if previously turned on by maneuver inhibit command
	PYRO	Spare
Inertial roll control step	AC	Turns roll gyros on and places roll axis under inertial control; subsequent commands will generate positive (+) roll increments
Canopus roll control	AC	Resets inertial roll control/step, roll control inhibit, gyros off, roll gyro on; initiates roll search if object not acquired when command received
Roll control inhibit	AC	Removes roll control completely

Table 8-6. Typical Command List (Cont)

Name	Destination	Comment
Roll search/step	AC	Turns roll gyro on and initiates a roll search; if inertial roll control/step is in effect, then all subsequent roll search/steps will generate negative (-) roll increments
Cw rotation/advance track	DSS	Record or playback: reverses tape direction and advanced DSS to next tape pass if tape direction is ccw; no effect if tape direction is cw; switches DSS to ready mode if slewing
Ccw rotation/advance track	DSS	Record or playback: reverses tape direction and advanced DSS to next tape pass if tape direction is cw; no effect if tape direction is ccw; switches DSS to ready mode if slewing
Unlatch low gain antenna	PYRO	Deploys second low gain antenna
RT science	FTS PWR DSS	Switches FTS to real time science Turn on cruise science Spare
Battery charger on/off	PWR	Toggles battery charger on and off
Tape slew mode	DSS	Initiates tape slew mode if DSS logic is initially in ready mode
Gyros off	AC	Unconditional command for turning gyro power off; reset by DC-19

Table 8-6. Typical Command List (Cont)

Name	Destination	Comment
TWT high power	RFS	Switch TWT to its high power output mode
TWT low power	RFS	Switch TWT to its low power output mode
DSS power on and off	PWR	Toggles 2.4 kHz power to tape on/off
High gain antenna update	ANT DRV	Actuates antenna driver mechanism causing high gain to move to its desired position
Battery No. 1 test load	PWR	Toggles battery No. 1 test load on-line/off-line
Transmit-receive LG No. 2	RFS	Selects low gain No. 2 antenna for both transmission and reception
Transmit-receive high gain	RFS	Selects high gain antenna for both transmission and reception
Downlink off	RFS	Turns off power to TWT power amplifier
Downlink on	RFS	Turns on power to TWT power amplifier
FTS maneuver mode	FTS	Toggles engineering channel between standard data format and maneuver format
Playback rate No. 1	DSS	Selects 40-bits per second playback rate
Playback rate No. 2	DSS	Selects 80-bits per second playback rate
Playback rate No. 3	DSS	Selects 200-bits per second playback rate

Table 8-6. Typical Command List (Cont)

Name	Destination	Comment
Simulate Sun gate	AC	Causes attitude control logic to issue Sun gate signal
Roll gyro on	AC	Turns on roll gyro only
AC maneuver telemetry	AC	Toggle function for selecting gimbal or sun sensor telemetry
Battery No. 2 test load	PWR	Toggles battery No. 2 test load on line and off line
Select battery configuration	PWR	Toggle command for placing battery No. 2 on line/off line
Charge battery No. 1 /and No. 2	PWR	Toggle command for selecting which battery can be charged
Propellant feed	SEP PROP	Open isolator switch on Hg tank for propellant feed to heaters
PCC 1 and 2 activate	PCC 1 and 2	Turn on SEP power conditioners
AC deadband	AC	Ingrease GN_2 attitude control deadband to ±3 degrees and activate FCS, translator and gimbal closed loop control
SEP thruster preheat	THR 1 and 2	Turn on power for preheat cycle

Table 8-6. Typical Command List (Cont)

Name	Destination	Comment
SEP thruster operate	THR 1 and 2	Turn on full power for thruster operation
SEP thruster switching	THR 1 and 2	Turn off all power
PCC 1 or 2 operation	PCC 1 or 2	Switch all power to either PCC 1 or 2
SEP thruster preheat	THR 3	Turn on power for preheat cycle
SEP thruster operate	THR 3	Turn on full power for thruster operation
SEP thruster termination	THR (all) PCC (both) SEP PROP TRANS & GIM	Turn off all power Turn off all power Close Hg feed control switch Inactivate closed loop attitude control and turn off all power
Thrust attitude	AC	Provide stepped attitude control reference for thrust orientation as required
Computer load	CC&S	Program computer; antenna pointing and star reference programs successive update as required
Word interrogation	CC&S	Fetches one word from memory
Sequencer load	CC&S	Enters fixed sequencer maneuver parameters

Flight Telemetry Subsystem

The flight telemetry subsystem (FTS) must perform the functions of transducer output conditioning, analog-to-digital conversion, encoding and combining of engineering, housekeeping, and science data into suitable format for modulation and signal transmission by the RF subsystem.

For the SEP asteroid belt mission, the selection of the candidate FTS is based upon the variety and quantity of data parameters to be processed, the existence of hardware available to perform the required processing, and the costs related to weight, power, and reliability in terms of the program budget.

Aside from routine tradeoffs in detail design to accomplish signal conditioning, analog-to-digital conversion, and encoding, the major consideration centers upon the function of processing the data into the best format for return to the ground station. The excellence and commonality of PCM capabilities of the DSN predominantly establishes the use of PCM for primary data encoding. The problem of configuring the FTS resolves into determining the method of combining the various sources of data into a telemetry modulation base band. The choices available are: time-division multiplexing of all data into a serial data train, frequency multiplexing of separate data trains, or a combination of both.

The approach in this study is first, to develop a representative measurements list for engineering and housekeeping data, second, compile a schedule of science readouts, third, determine the peak data loading and traffic congestion, and select the most appropriate multiplexing method(s).

Data Acquisition Rate Requirements

A typical measurements list for the SEP mission is shown in Table 8-7. The sampling rate for each measurement is given in either seconds, minutes, or hours for the modes established in the SEP mission events and time line, Table (X-X). A typical channel distribution for these engineering measurement sample rates is shown in Figure 8-4. Table 8-8 shows the engineering measurements acquisition rates with composite total for the various mission phases. Using a maximum data word length of 7 bits for every measurement, the engineering measurements composite acquisition rates are: for launch, engine startup, and emergency, 25.6 bits per second, for the thrust phase, 3.88 bits per second, and for the final coast phase, 1.47 bits per second. A breakdown of the science data acquisition rates is given in Table 8-9. Composite totals for the thrust phase, and 8.5 bits per second during the coast phase are required.

Table 8-7. SEP Measurements Acquisition List

Measurement	Number Required	Range (F)	Sample Rate* By Mode		
			3	4	5, 6
THERMAL MEASUREMENTS					
Cosmic ray spectrometer temperature 2 on detector, 1 on electronics	3	-300 to +200	2 min	16 min	16 min
Helium magnetometer temperature 1 on detector, 1 on electronics	2	-300 to +200	2 min	16 min	16 min
Triaxial spectrometer temperature 2 on each of 3 orthogonal detectors and 1 on electronics	7	-300 to +200	2 min	16 min	16 min
Faraday cup temperature	1	-300 to +200	2 min	16 min	16 min
Geiger Counter temperature	1	-300. to +200	2 min	16 min	16 min
Capacitors (2 per solar panel) temperature					
Electroballistic pendulum temperature	1	-300 to +200	2 min	16 min	16 min
Sisyphus	1	-300 to +200	2 min	16 min	16 min
Attitude control tank temperature (1 per tank)	2	0 to +250	1 min	8 min	8 min
Engine gimbal motor temperature (1 per motor)	4	-100 to +500	1 min	1 hr	--
Sun sensor temperature (1 coarse, 4 fine)	5	-300 to +200	1 min	1 hr	1 hr

*Mode 3 - SC separation to SEP thrust initiation
Mode 4 - SEP Thrust phase
Mode 5, 6 - Coast phase - science data gathering in asteroid belt

Space Division
North American Rockwell

Table 8-7. SEP Measurements Acquisition List (Cont)

Measurement	Number Required	Range (F)	Sample Rate* By Mode		
			3	4	5, 6
Canopus sensor temperature	1	-50 to +200	1 min	1 hr	1 hr
Gyro temperature	1	-50 to +200	1 min	1 hr	1 hr
Battery temperature (1 per battery)	2	-25 to 250	2 min	32 min	32 min
Panel temperature (2 per panel)	8	-400 to +400	2 min	1 hr	1 hr
Equipment bay temperature	4	-50 to +200	2 min	1 hr	1 hr
Power conditioning and control set temperature	1	-50 to +200	2 min	32 min	32 min
Power amplifier temperature	1	0 to +200	2 min	8 min	8 min
Voltage-control oscillator (VCO) temperature	1	25 to +150	1 min	4 min	8 min
High-gain antenna Motor temperature	1	-300 to +250	2 min	1 hr	1 hr
Low-gain antenna boom temperature	2	-300 to +250	2 min	1 hr	1 hr
Transmitter crystal temperature (1 per crystal)	2	0 to 150	2 min	8 min	8 min
Receiver crystal temperature	2	0 to 150	1 min	4 min	8 min

*Mode 3 - SC separation to SEP thrust initiation
 Mode 4 - SEP Thrust phase
 Mode 5, 6 - Coast phase - science data gathering in asteroid belt

Table 8-7. SEP Measurements Acquisition List (Cont)

Measurement	Number Required	Range (F)	Sample Rate* By Mode		
			3	4	5, 6
Analog-to-digital converter temperature	2	0 to 150	2 min	1 hr	1 hr
Ion engine power conditioner temperature	8	-300 to +300	4 min	32 min	--
Engine Manifold temperature	5	-300 to +300	4 min	32 min	2 hr
Mercury tank temperature	2	25 to 400	4 min	32 min	2 hr
Total thermal = 58					
DATA HANDLING AND TELECOMMUNICATIONS					
Telemetry frame sync	1	Digital	32 sec	1 hr	1 hr
Frame number	1	Digital	32 sec	1 hr	1 hr
Mode identifier	1	Digital	32 sec	1 hr	1 hr
Data handling power supply voltage	1		2 min	1 hr	1 hr
Tape recorder motor voltage	1		.4 min	2 hr	2 hr
Tape recorder motor current	2		4 min	2 hr	2 hr
Tape transport pressure	1		4 min	2 hr	2 hr
Tape motion indicator	1	Binary Discrete	4 min	2 hr	2 hr

*Mode 3 - SC separation to SEP thrust initiation
Mode 4 - SEP Thrust phase
Mode 5, 6 - Coast phase - science data gathering in asteroid belt

Space Division
North American Rockwell

Table 8-7. SEP Measurements Acquisition List (Cont)

Measurement	Number Required	Range (F)	Sample Rate* By Mode		
			3	4	5, 6
Transmitter exciter power supply voltage	2	20 to 30 v	2 min	8 min	8 min
Transmitter exciter RF power ouput	1	1 to 50 mw	2 min	8 min	8 min
TWT amplifier cathode voltage	2	1500 to 3000 v	2 min	8 min	8 min
TWT amplifier cathode current	2	25 to	2 min	8 min	8 min
TWT amplifier anode voltage	2		2 min	8 min	8 min
TWT amplifier filament current	2	0.5 to	2 min	8 min	8 min
Power amplifier RF output	1		2 min	8 min	8 min
High-gain antenna pointing angle (single axis)	1	Digital	2 min	1 hr	1 hr
Low-gain antenna port RF power monitor	1	5 to 25 w	2 min	1 hr	1 hr
TWT helix current	1		2 min	8 min	8 min
Local oscillator drive	1	0 to 1.5 mw	1 min	4 min	8 min
Static phase error	1	±30 near -Δ Odbm	1 min	4 min	8 min

*Mode 3 - SC separation to SEP thrust initiation
Mode 4 - SEP Thrust phase
Mode 5, 6 - Coast phase - science data gathering in asteroid belt

Table 8-7. SEP Measurements Acquisition List (Cont)

Measurement	Number Required	Range (F)	Sample Rate* By Mode		
			3	4	5, 6
Receiver AGC (1 per recovery)					
Coarse	2	-155 to -100 dbm	1 min	4 min	8 min
Fine	2		1 min	4 min	8 min
Command system VCO frequency	1		1 min	4 min	8 min
Command recovery power supply voltage	1	0 to 5v	1 min	16 min	16 min
Command detector lockup		Discrete binary	1 min	4 min	4 min
Last received command	1	Digital	1 min	16 min	16 min
CC&S clock time	1	Digital	4 min	32 min	32 min
Initiator event counter	2	Digital	32 sec	32 min	32 min
Pyro capacitor voltage (1 per capacitor)	4	0 to 50 V	32 sec	32 min	32 min
Pyro initiator voltage (1 per initiator)	2	0 to 50 V	32 sec	32 min	32 min
Current event counter (prime and alternate)	2	Digital	32 sec	32 min	32 min
Sun sensor outputs					
Coarse (2 required)	2	±5 deg	8 sec	2 min	8 min
Fine (4 required)	4		8 sec	2 min	8 min
Canopus sensor error	1	±5 deg	8 sec	2 min	8 min

*Mode 3 - SC separation to SEP thrust initiation
 Mode 4 - SEP Thrust phase
 Mode 5, 6 - Coast phase - science data gathering in asteroid belt

Table 8-7. SEP Measurements Acquisition List (Cont)

Measurement	Number Required	Range (F)	Sample Rate* By Mode		
			3	4	5, 6
Canopus intensity	1	0.01 to 10	8 sec	2 min	8 min
Gyro outputs	3	±1 deg/sec	8 sec	2 min	
Translator positioning command	2		1 min	16 min	16 min
Translator displacement	2	±14 inches	1 min	4 min	8 min
Translator rates	2		1 min	4 min	8 min
Gimbal positioning command	2		1 min	4 min	8 min
Gimbal displacements	2		1 min	4 min	8 min
Gas tank pressure	2	0 to 3000 psi	1 min	8 min	8 min
Attitude error signals	3		8 sec	8 min	--
Solar panel deployment squib status indicator (3 per panel)	2 words	6-bit binary discrete	1 min	--	--
Panel deployment verification	1 word	Binary discrete	1 min	--	--
Sample solar cell short circuit current	2	0 to 100 ma	1 min	1 hr	1 hr
Solar cell open circuit voltage	1	0 to 100 mv	1 min	1 hr	1 hr
Combined solar panel output current	1	0 to 200 a	1 min	1 hr	1 hr

*Mode 3 - SC separation to SEP thrust initiation
 Mode 4 - SEP Thrust phase
 Mode 5, 6 - Coast phase - science data gathering in asteroid belt

Space Division
North American Rockwell

Table 8-7. SEP Measurements Acquisition List (Cont)

Measurement	Number Required	Range (F)	Sample Rate* By Mode		
			3	4	5, 6
Power source voltage	1	20 to 100 v	8 sec	2 min	8 min
Battery discharge current	1	0 to 10 a	1 min	4 min	8 min
Battery voltage (1 per battery)	2	18 to 33 v	1 min	4 min	8 min
Battery charge current	1	0 to 5 a	2 min	32 min	32 min
Power conditioner input current	1	0 to 15 a	1 min	4 min	8 min
2.4-kilohertz inverter output current	2	0 to 3 a	1 min	4 min	8 min
2.4-kilohertz inverter output voltage	2	45 to 55 v	1 min	4 min	8 min
400-hertz inverter output current	1	0 to 1 a	1 min	4 min	8 min
PPM power signal	1	0 to 10 kw	1 min	4 min	8 min
PPM input enable/disable		Binary discrete	1 min	4 min	8 min
Ion engine power conditioner total input power	1	0 to 10 kw	1 min	4 min	--
Engine control voltage (set point)	1	0 to 5 v	1 min	4 min	--
Main vaporizer current	2	0 to 3 a	1 min	8 min	--
Main vaporizer voltage	2	0 to 5 v	1 min	8 min	--

*Mode 3 - SC separation to SEP thrust initiation
 Mode 4 - SEP Thrust phase
 Mode 5, 6 - Coast phase - science data gathering in asteroid belt

Table 8-7. SEP Measurements Acquisition List (Cont)

Measurement	Number Required	Range (F)	Sample Rate* By Mode		
			3	4	5, 6
Cathode vaporizer current	2	0 to 3 a	1 min	8 min	--
Cathode vaporizer voltage	2	0 to 5 v	1 min	8 min	--
Neutralizer vaporizer current	2	0 to 3 a	1 min	8 min	--
Neutralizer vaporizer voltage	2	0 to 5 v	1 min	8 min	--
Main cathode heater current	2	0 to 5 a	1 min	8 min	--
Main cathode heater voltage	2	0 to 10 v	1 min	8 min	--
Cathode keeper current	2	0 to 1 a	1 min	8 min	--
Cathode keeper voltage	2	0 to 400 v 0 to 20 v	1 min	8 min	--
Neutralizer keeper current	2	0 to 1 a	1 min	8 min	--
Neutralizer keeper voltage	2	0 to 400 v 0 to 20 v	1 min	8 min	--
Discharge current	2	0 to 10 a	1 min	8 min	--
Discharge voltage	2	30 to 40 v		8 min	--
Beam current	2	0 to 1 a		8 min	--
Beam voltage	2	1500 to 2000 v		8 min	--

*Mode 3 - SC separation to SEP thrust initiation
 Mode 4 - SEP Thrust phase
 Mode 5, 6 - Coast phase - science data gathering in asteroid belt

ckwell

Table 8-7. SEP Measurements Acquisition List (Cont)

Measurement	Number Required	Range (F)	Sample Rate* By Mode		
			3	4	5, 6
Accelerator current	2	0 to 20 ma		8 min	--
Accelerator voltage	2	1500 to 2000 v		8 min	--
Neutralizer emission current	2	0 to 1 a		8 min	--
Bus voltage	2			8 min	--
Bus current	2			8 min	
Main isolator current	2	0 to 2 a		8 min	
Main isolator voltage	2	0 to 5 v		8 min	
Cathode Isolator current	2	0 to 2 a		8 min	
Cathode isolator voltage	2	0 to 5 v		8 min	
+ High-voltage arcs	2	0 to 10 arcs/min		2 hr	
- High-voltage arcs	2	0 to 10 arcs/min		2 hr	
+ High-voltage and - High-voltage arc coincidence	2	0 to 10 arcs/min		2 hr	
PC shutdown	2		32	32 min	
Inverter on	28			32 min	

*Mode 3 - SC separation to SEP thrust initiation
Mode 4 - SEP Thrust phase
Mode 5, 6 - Coast phase - science data gathering in asteroid belt

Table 8-7. SEP Measurements Acquisition List (Cont)

Measurement	Number Required	Range (F)	Sample Rate* By Mode		
			3	4	5, 6
PC&C heaters on				32 min	32 min
PC&C temperature	20	-50 to +200		8 min	8 min
Main vaporizer flow rate	3	0 to 1cc/hr		8 min	
Cathode vaporizer flow rate	3	0 to 0.1 cc/hr		8 min	
Neutralizer vaporizer flow rate	3	0 to 0.1cc/hr		8 min	
Main isolator temperature	3	-50 to +650		32 min	
Cathode isolator temperature	3	-50 to +650		32 min	
Main isolator leakage current	3	100 a to 10 ma		32 min	
Cathode isolation leakage current	3	100 a to 10 ma		8 min	
Coupling potential	3	0 to 100 v		8 min	
Floating potential	1	0 to 100 v		8 min	
Thruster temperature	6	-50 to 750		32 min	
Flow valve open and close	1			1 min	
Array position	2		2 min	2 hr	
Thruster orientation	3		2 min	2 hr	

*Mode 3 - SC separation to SEP thrust initiation
 Mode 4 - SEP Thrust phase
 Mode 5, 6 - Coast phase - science data gathering in asteroid belt
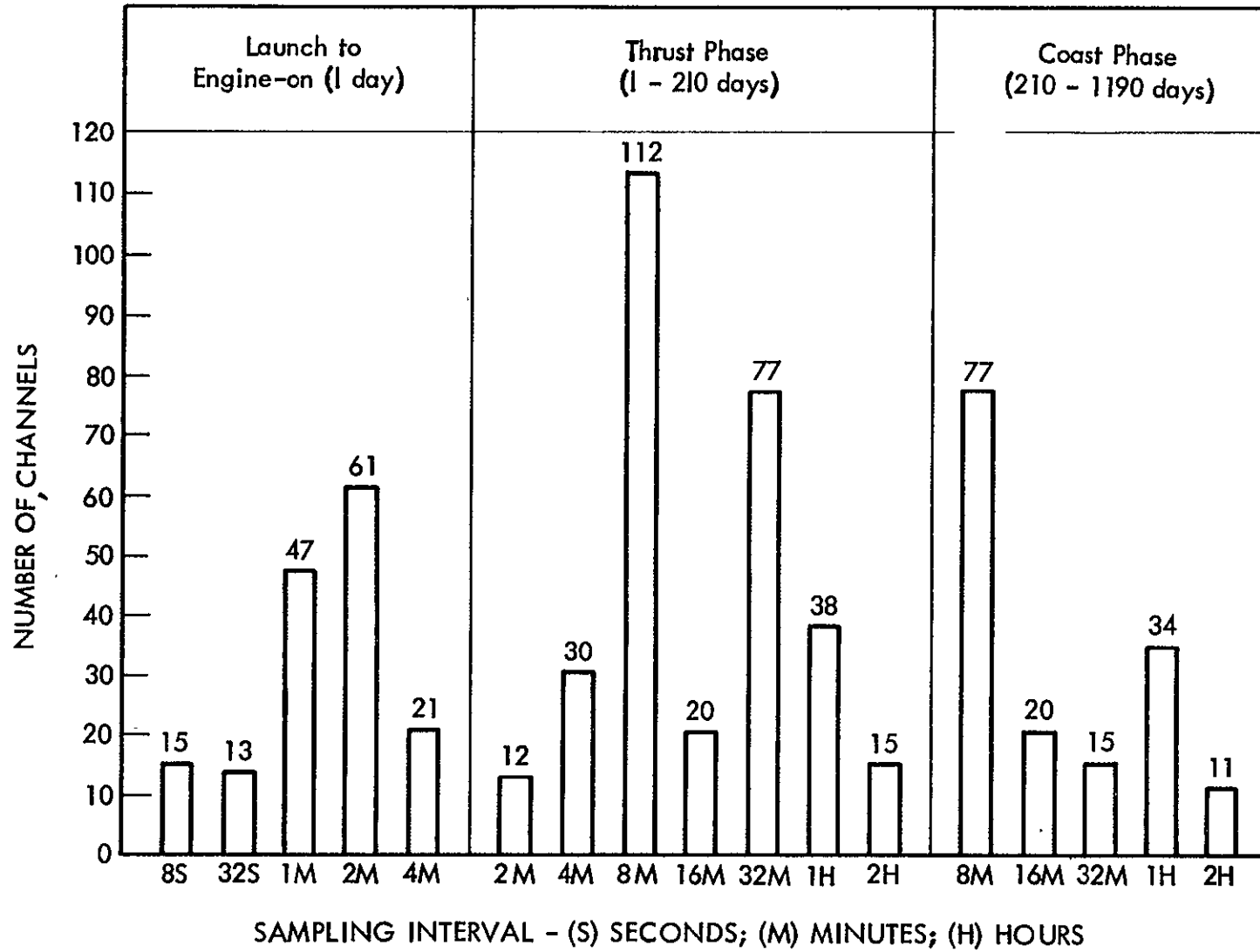
Figure 8-4. Channel Distribution by Sampling Interval

Table 8-8. Engineering Measurement Bit Rates (7-Bit Words)

Channel Quantity	Bit Total/Sampling Interval (sec)	Rate (bps)
LAUNCH, IGNITION PHASES AND EMERGENCY MODE		
15	105/8	13.0
13	91/32	3.0
47	329/69	5.5
61	427/120	3.5
21	147/240	0.6
Composite total		25.6
THRUST PHASE		
12	84/120	0.7
30	210/240	1.0
112	784/480	1.7
20	140/960	0.15
77	539/1920	0.25
38	266/3840	0.07
15	105/7680	0.01
Composite total		3.88
COAST PHASE		
77	539/480	1.2
20	140/960	0.15
15	105/1920	0.05
34	238/3840	0.06
11	77/7680	0.01
Composite total		1.47

Summing both science and engineering requirements, the peak load of the composite data is considerably below the design capability of 40 bits per second. During the early, critical hours of the flight, the engineering data acquisition is predominant. During the thrust phase, the engineering data is approximately one-third of the combined acquisition load. In the final coast phase, the science data is predominant but the composite rate is approximately 10 bits per second. Due to the low percentage of engineering return required for the important science acquisition phases of the mission, the advantages of using a separate engineering subcarrier are obscure. A return capability of four times the acquisition rate at the maximum communication distance for the asteroid belt mission is practical for the selected RFS. This assures that all data can be returned within the line-of-sight visibility period to a single 85-foot DSIF.

The simplicity of increasing the telemetry capacity required for the maximum engineering load by a factory of approximately 30 percent to include the science data return appears to outweigh: (1) cost of duplicating

Table 8-9. Science Data Gathering Rates

Sensor	Thrust Phase	Coast Phase
Sisyphus	<0.1 bps	<0.1 bps
Electroballistic pendulum	2	2
Capacitors	Off	<0.1
Geiger counter	0.1	0.1
Cosmic ray spectrometer	1	1
Faraday cup	Off	1
Helium magnetometer	Off	1
Triaxial spectrometer	3	3
Allowance for growth	0.3	0.2
Total	6.5 bps	8.5 bps

the subcarrier oscillator and biphase modulator, (2) increase in RF band-
width occupancy required for two subcarriers separated by a guard channel
in the base band, (3) penalty of duplicate circuit and modulation efficiency
losses for each subcarrier, and (4) cost of a frequency multiplexer. Use
of a common subcarrier with selected-multiple-frame-format telemetry
channel is recommended on the foregoing basis. Hardware to perform the
telemetry functions required is available in Pioneer F and G and will be
available on Viking 1973 with some modification required for each of the
reference subsystems. The essential modification will consist of deletion
of the high rate elements associated with television inputs not required
for the SEP spacecraft. Rapid refinement progress on space-qualified
integrated circuit hardware implies that a final choice of hardware can be
made best downstream in the schedule. The availability of a compact
off-the-shelf type module in the near future for specific functions is also
certainly possible; as an example, the SPACETAC PCM encoder system
developed for MSC, Houston. The physical parameters of the Mariner 1971/
Viking 1973 telemetry subsystem are used for sizing estimates for the
SEP spacecraft, as listed in Table 8-2.

PCM Encoder

The PCM Encoder is required to process transducer outputs of the
engineering and housekeeping measurement circuits in each spacecraft
subsystem. The processing includes sampling of each analog measurement
in the time domain for conversion of variable amplitude pulses,
analog-to-digital conversion, and parallel-bit-to-serial-bit conversion by
means of output-shift registers. Separate PCM encoder functions will be
performed in the data automation system for science data, to permit
flexibility in frame format required for choice of return options by the
ground station.

Time-Division Multiplexer

The mixing of science and engineering data will be performed by the
time-division multiplexer to satisfy the requirement for one data subcarrier.
The relatively low rates of both data sources as discussed above eases the
problems of multiplexer design for the spacecraft. The engineering
multiplexer used on Viking 1973 affords availability of hardware for the
time period of the SEP asteroid belt mission.

Convolutional Encoder

The recommendation to use convolutional coding is based upon
(1) need for moderate accuracies of data return, (2) requirement for
maximum efficiency and minimum size and weight of data system,
(3) avoidance of complexity in ground station equipment.

Mariner 1969 has demonstrated the feasibility of using the error-reduction coding of PCM data to achieve higher efficiencies in the ratio of the required signal energy per bit to the noise per unit bandwidth. Biorthogonal block coding as used by Mariner 1969 permitted an increase in the rate of transmission over uncoded PCM with no increase in spacecraft transmitter power. Pioneer E demonstrated feasibility of achieving virtually error-free transmission of data at moderate bit rates with no increase in transmitter power, using a high constraint length (K = 25) convolutional coding.

The asteroid belt mission does not require high bit rates or extremely high accuracy, but needs the advantages of efficient data return to span the 6.75×10^8 kilometer communication distance with economical transmitter sizing. This performance level falls somewhere between Mariner and Pioneer capabilities.

Hardware recommended for implementation on the SEP spacecraft must support the requirements for (1) moderate accuracy with bit-error probability of 1×10^{-4}, (2) transmission over distance of 6.75×10^8 kilometer without added size and weight to data-return system, (3) minimum complexity of ground station data processing equipment, and (4) hardware availability.

The moderate accuracy requirement of 1×10^{-4} bit error probability alleviates the requirement for high constraint length (K = 25) coding as used on Pioneer E. Short constraint length convolutional encoding (K = 8) can satisfy the error requirement. SEP spacecraft bit rates are not postulated above the order of 10^2 bps so that the performance of Mariner 196' (at 16.2 kilobits per second is desirable only from an efficiency standpoint. A tradeoff must further satisfy the requirement for minimum complexity of ground station equipment. To satisfy all of these points, the use of convolutional coding with short constraint length (K = 8, r = 1/2) is recommended. This will permit some growth in bit rate, and increase in bit accuracy if required later.

Hardware implementation is less sophisticated than either Mariner or Pioneer. The SEP basic encoder will comprise a shift register of eight stages and two Modulo-2 adders. In present microelectronic packaging, the size and weight are more a function of the number of connectors required. The result is that overall reduction in total telemetry subsystem weight can be realized below Mariner 1971 or Viking 1973, which are extensions of the Mariner 1969 technology, because of the more compact encoding logic.

Efficiency will be higher than the Mariner high-rate telemetry mode by likelihood) or sequential decoding. This assures realization of 10^{-4} bit-error probability with possibility for higher accuracies if sequential decoding is used. Present capabilities of the DSN cover convolutional coding at 16.2 kilobits per second or less so that ground station complexity is not increased by use of the encoder.

Data Automation Subsystem

The functional requirement of the data automation subsystem is to sequence and process all scientific data. It must control and sequence the science instruments, sample and convert the analog data into digital form, provide temporary holding of data by means of buffer storage, and format the processed digital PCM data for routing to the data storage subsystem.

An optional mode must also be available for routing scientific outputs to the flight telemetry subsystem for real-time transmission, under control or command of the ground station.

The requirements for science data have been summarized in Table 8-10. The rates and resolution required are more comparable to Pioneer F and G than to Mariner or Viking because of the absence of visual imaging (television). Selection of hardware to perform the functions required is guided primarily by the availability of hardware for the mission time period. In preference to a complete custom design for the mission, the approach preferred is to delete cards and modules from existing equipment, which provides matched capabilities for the on-board science. This is considered feasible based upon available characteristics of Mariner, Pioneer, and Viking designs.

Mariner 1969 data automation equipment, in providing the baseline for Mariner 1971 and Viking 1973 configurations, could afford use for the SEP spacecraft. By deletion of real-time TV data processing, reduction in size, weight, and power could be anticipated. The mix of particles and fields sensors used on Mariner 1969 parallels that postulated for the asteroid belt mission. For Viking 1973, the science data subsystem, as designated for this function, will have increased flexibility over previous designs for sequencing the instruments and for constructing formats. This favors application for the asteroid belt mission because of similar requirement to make best use of information obtained continuously in prior sequences of collection. The flexibility for modification of the science data return in Pioneer F and G design is reflected in the emphasis on design for variable bit-rate capability with rates ranging from 8 to 512 bits per second. Choice between Pioneer and Viking hardware is largely a selection of the system that affords flexibility in word sequences to provide multiple frame formats. The

Table 8-10. Data Storage Matrix

| Acquisition Duration (hours at 10 bps) | Total Data (kilobits) | Playback | | Rate (bps) |
		Interval (days)	Duration (hours)	
24	864	1	5.5	40
24	864	1	2.75	80
24	864	1	1.1	200
48	1728	2	5.5	80
48	1728	2	1.1	200
120	8640	5	5.5	200

asteroid belt mission requirement gives preference to frame versatility rather than data return rate versatility. Therefore, the Viking configuration is recommended, with deletion of television handling capabilities.

In the Viking design, the science data must be buffered during the time that television video data are being recorded. This requirement is not necessary for the asteroid belt mission, but the core memory used for this purpose would be retained. The core memory will be used for storage of bit patterns used in controlling formats and sequencing in a similar manner to that for Viking 1973 and Mariner 1971. The core memory will be used also in the implementation of a nonvolatile frame count. In Viking 1973, the latter purpose guarantees continuity of science data throughout 60 or more days of the Viking orbital mission. Similar use appears applicable for selected periods of time during the long asteroid belt mission (1190 days).

Data Storage Subsystem

The function of the data storage system is to accept serial pulse-code modulation (PCM) data, to hold those data in its sequential order, and to play the data back for return at a suitable bit rate to the Earth station via the RFS. The storage parameters are constrained by the durations of data acquisition intervals and by the data return rates possible throughout the asteroid belt mission. The combinations of acquisition interval, storage capacity required, and playback rates are shown in Table 8-10.

SD 70-21-2

Maximum capacity requirements for the asteroid belt mission occur during the five-day interval recording mode when 8.64 x 10^6 bits of data are accumulated. In comparison, the Mariner 1969 and the Mariner 1971/Viking recorders have storage capacities of 1.3 x 10^8 bits and 1.8 x 10^8 bits, respectively. Therefore, more than adequate storage capacities are available.

In the Mariner 1971/Viking 1973 recorder, eight data tracks are used. The recorded data is normally split into two channels which are recorded simultaneously on two adjacent tracks at a maximum rate of 132.3 kilobits per second. With the drastically lower bit rate requirements of the asteroid belt mission, modifications in the transport to reduce tape speed are required. A tradeoff of speed reducer train weight to pay for longer life expectancy by virtue of the lower tape speeds appears feasible. Therefore, the Mariner 1971/Viking data storage recorder is recommended for the asteroid belt mission.

9. STABILIZATION AND CONTROL SUBSYSTEM

This section discusses the solar electric propulsion (SEP) stabilization and control subsystem (SCS), covering the following major areas:

SCS functional and performance requirements are discussed. The former, presented chronologically delineate specific functions of the SCS required to satisfy overall mission objectives. The latter transmit performance requirements commensurate, where possible, with the Mariner SCS.

The baseline SCS description is given. Modes of operation required to satisfy functional requirements are discussed indicating periods of SCS component application. In this section the reference sensors and their impact on the baseline configuration are analyzed. The baseline reaction control system is presented, concluding with estimated weight and power requirements.

Results of conceptual design trade studies are presented. Included are attitude control concepts that dictated control methodology of the SEP spacecraft. A section is devoted to the sensor trades where alternatives to the baseline referencing technique are discussed.

The analyses conducted on two areas of major importance are discussed in this section. The first, unique to SEP, is stability of the movable translator concept. It is shown that the control methodology is destabilizing, requiring compensation. The second area discussed is that of solar-panel flexibility effects. It is shown that flexibility is not of major concern for the SEP spacecraft.

SYSTEM FUNCTIONAL REQUIREMENTS

The basic functional requirements for the S&C subsystem are to:

Arrest initial attitude rates resulting from booster separation

Acquire celestial references (sun and Canopus for the baseline configuration)

Provide thrust vector translational (in two axes) and gimbal control during the thrusting interval. The requirement to use a two-axis translator rather than a single-axis device on other control mechanisms was based on the two-axis translational control concepts having the greatest potential application to a wide range of missions, especially for an SEP spacecraft employing more than a single row of electric thrusters. In event of an engine failure, only one engine is lost. As such it appears to be highly desirable to use this concept for the baseline design configuration.

Provide spacecraft attitude hold during cruise intervals

Orient the spacecraft for prescribed maneuvers (magnetometer calibration, solar-panel orientation for asteroid detection during cruise, and possibly thrust interval orientations for trajectory modification)

Provide for celestial reference reacquisition

The above requirements constitute the basic functions of the S&C. Fundamentally the S&C controls the vehicle through achievement of all mission objectives. The dominant control periods are the thrust and cruise intervals. Control during the former is achieved in roll and yaw (Figure 9-1) by commanding movement of the ion engine bank from attitude errors generated from star and sun sensors. In pitch it is achieved by gimbaling the outward engines. (Only one ion engine is operative during portions of the thrust interval requiring reaction-jet pitch control.) Control during the latter is achieved by a three-axes reaction control jet subsystem (RCS). For the baseline configuration the on-board S&C subsystem functions to maintain a sun-star reference and provide maneuver orientations. On-board rate-integrating gyros provide attitude damping during acquisition and maneuvers.

e₁ RADIAL OUTWARD FROM SUN

e₃ NORMAL TO ECLIPTIC

e₂ COMPLETES RIGHT-HAND ORTHOGONAL SET
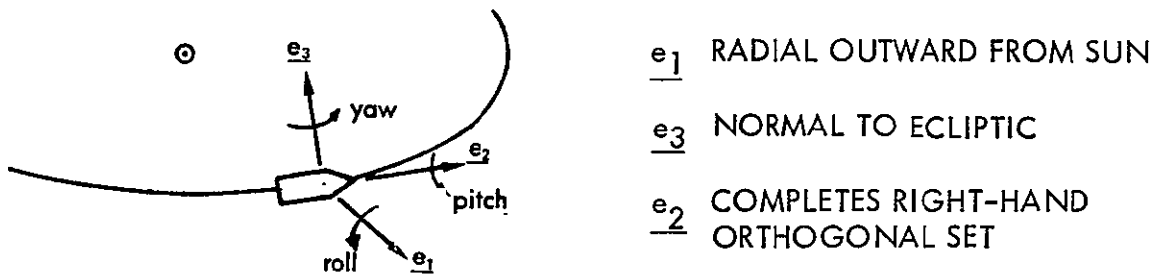
Figure 9-1.   Spacecraft Roll, Pitch, and Yaw Axes Definition

S&C functions are initiated after separation of the spacecraft from the final boost stage.   Separation rates are arrested through use of the rate gyros, with drive provided by the reaction control jets.   Sun acquisition is then accomplished by signals from coarse and fine sun sensors. They sense sun presence and provide control-system error signals to point the vehicle toward the sun.   After sun acquisition is confirmed, a 360-degree roll maneuver is executed to map the star intensities by means of a Canopus sensor.   This is a prelude to acquisition of the star Canopus in roll, thus completing the celestial references.   Vega may also be used.

During the thrusting interval of approximately 210 days after liftoff, correction maneuvers may be required.   The delta velocity for a correction maneuver is accomplished by spacecraft orientation providing an inertial velocity change by the engine array bank, whose thrust vector is fixed with respect to the solar panels.   (Velocity corrections may also be provided by the on-board cold-gas subsystem if the velocity additions are small.)   The spacecraft orientation for inertial attitude delta velocities is commanded by using on-board gyros.

In addition to the velocity corrections, the spacecraft will be oriented at discrete intervals during the mission for trajectory achievement during the thrust interval and for particle detection subsequent to thrust termination. Other than for roll maneuvers for magnetometer calibration, no other special orientations of the spacecraft are required.

PERFORMANCE REQUIREMENTS

Primary performance parameters that will influence the selection of control system parameters are reaction jet minimum on-time, control

acceleration, actuation loop nonlinearities, and transient response char-
acteristics of the spacecraft control system. The control system configura-
tion for various operational modes differs. Thus, each mode must be
analyzed separately to determine required values for the system parameters.
The thrusting-interval attitude-hold mode is performed during phases of
flight that lie between maneuver mode operations. Here performance
operation depends upon translator characteristics. It is shown subsequently
that the dynamical behavior yields a non-minimum phase system. A result
is that a little more care must be exercised in designing compensation and
predicting system behavior. Cruise attitude hold-mode performance
operation depends upon the attitude dead band, hysteresis, pseudo rate
parameters, fine sun sensor, and star-sensor characteristics. Here,
however, behavior is more predictable, with Mariner performance results
dictating system requirements.

For the asteroid belt mission, the attitude control requirements are
moderate. A thrust alignment of 3 to 5 percent should suffice, providing
an attitude control accuracy in the neighborhood of 1.5 to 3.0 degrees.
The moderate accuracy requirements provide little demand on sensing
equipment. However, care must still be exercised in choosing uninten-
tional (and intentional) nonlinearity magnitudes, such as resolution of the
movable ion engine bank.

Other than for a relatively loose accuracy requirement of approx-
imately ±3 degrees dictated by antenna pointing, SEP spacecraft attitude
control requirements are unspecified. The approach taken, as indicated,
is to use where possible the proven Mariner spacecraft equipment.

Accordingly, the chosen acceleration levels, control jet minimum on
times, and acquisition rates are commensurable with Mariner:

Acceleration capability	0.23 m rad/sec^2
Jet minimum on-time	20 ms
Acquisition rates	3 m rad/sec

The first two requirements dictate a cruise interval limit cycle
rate of approximately 0.0023 m rad/sec. In roll, where disturbance torques
are essentially zero, the resulting jet pulses and time between firings (for
a ±3 degree dead band) are expected to be in the neighborhood of 3000 and
10 hours, respectively. Conversely, for pitch and yaw, where significant
disturbance torques are possible, the number of jet firings are expected to
approach 55,000. Table 9-1 summarizes these performance parameters.

9-4

Table 9-1. Performance Parameters

Characteristic	Requirement
Jet minimum on-time	20 ms
Acquisition rate	3 m rad/sec
Acceleration capability	0.23 m rad/sec^2
Limit-cycle rate	0.0023 m rad/sec
Dead band	±3 degrees
Inertial properties	
Roll	5000 slug-ft^2
Pitch-yaw	3000 slug-ft^2
Control torque	
Roll	1.15 ft-lb
Pitch-yaw	0.69 ft-lb
Thrust levels	
Roll	0.33 lb
Pitch-yaw	0.17 lb
Number of pulses	
Roll	3000
Pitch-yaw	55,000

SYSTEM DESCRIPTION AND MODES OF OPERATION

The baseline definition of the S&C subsystem is given in terms of important interfaces, as in Figure 9-2. The S&C subsystem requires both stored commands from the central computer and sequencer and ground-generated commands through telemetry. The S&C subsystem provides the on-board sensors, the gyro package, and the necessary logic and mode switching electronics. In addition to switching, the S&C has electronics to generate control signals for translator actuation. The former are supplied to the propulsion subsystem. The latter are supplied to the actuation subsystem. The servo devices for translator actuation are illustrated in Figure 9-2 as an actuation subsystem interface. They may be considered, however, as part of the S&C subsystem.

The S&C subsystem (Figure 9-2) comprises reaction jets, gyros, a translator actuation subsystem, an engine gimbaling subsystem, Canopus and sun sensors, and control logic. The reaction jets are located to provide control torques about all three space vehicle axes during cruise. Engine-bank translational motion provides the control torques in roll and yaw during the thrusting interval. Pitch control is provided by engine gimbaling. The gyros nominally provide rate information for the damping

OPERATIONS
CONTROL
SUBSYSTEM

CENTRAL
COMPUTER &
SEQUENCE

TELEMETRY

PROPULSION
SUBSYSTEM

RATE-
INTEGRATING
GYROS

FINE
SUN
SENSOR

COARSE
SUN
SENSOR

CANOPUS
SENSOR

LOGIC AND
MODE-SWITCHING
ELECTRONICS

REACTION JET
ENGINE
ON-OFF
CONTROL

COLD-GAS
VALVES

STEPPER MOTOR
POSITIONING
CONTROL

STEPPER
MOTOR, GEAR
TRAIN, AND
ENGINE BANK

ACTUATION
SUBSYSTEM

Space Division
North American Rockwell

Figure 9-2.   Stabilization and Control Base-Line Functional Schematic

of attitude maneuvers and acquisition. Discrete signals to activate equipment, perform mode switching, adjust gain and dead-band values, and terminate the desired mode operation are provided by the logic and mode-switching electronics.

The various operational modes of the spacecraft attitude control subsystem have been listed above. Figures 9-3 and 9-4 are analytical block diagrams of the control system mechanization. The switching logic legend for the various operational modes is given in Figure 9-5.

REFERENCE SENSORS

Two non-colinear vectors whose directions are known are required to define a celestial attitude reference. The sun, being the brightest visible light source in the solar system permitting simple mechanization and ease of identification, is an obvious choice as an attitude reference. A sun orientation is also desirable during the thrusting phase for the collection of solar power. For these reasons, the solar reference is chosen for control of the pitch and yaw axes. The choice of the second attitude reference (roll) is more demanding. The star Canopus is chosen for the baseline configuration because of its relative brightness and its location, which is within 14 degrees of being perpendicular to the ecliptic. However, as will be described, the nominal 14-degree offset has comprised system design.

Location of sun sensor cells is dictated by the field of view requirements, the spacecraft physical layout, and the minimum number of assemblies required to achieve the desired angular coverage.. Both coarse and fine sun sensors must be mounted to. the body rather than to the solar panels. The sensor cells must be body-mounted rather than solar-panel mounted to preclude angular errors attributed to solar-panel deployment and bending. (The continuous thrusting and thermal radiation will produce a steady-state panel deflection.) The coarse sun sensor must have a 4π steradian field of view. Its accuracy requirements are normally not stringent (within 3 to 5 degrees) unless the coarse sun sensor is used as a backup in case of fine sun sensor failure. A fine sun sensor accuracy of the order of ± 0.05 degrees is desirable and achievable with existing hardware. Because of the thrust vector variation with respect to the sun line (approximately 60 degrees) over the course of the mission, the total fine sun sensor field of view is excessive. To overcome this, a number of fine sensors are strategically located on the spacecraft, with minimum overlapping, to encompass collectively the extended field of view. Four to five fine sensors, each having a field of view of approximately 20 degrees, will do the job. Reorientations are achieved by selective switching between fine sun sensors.

9-7
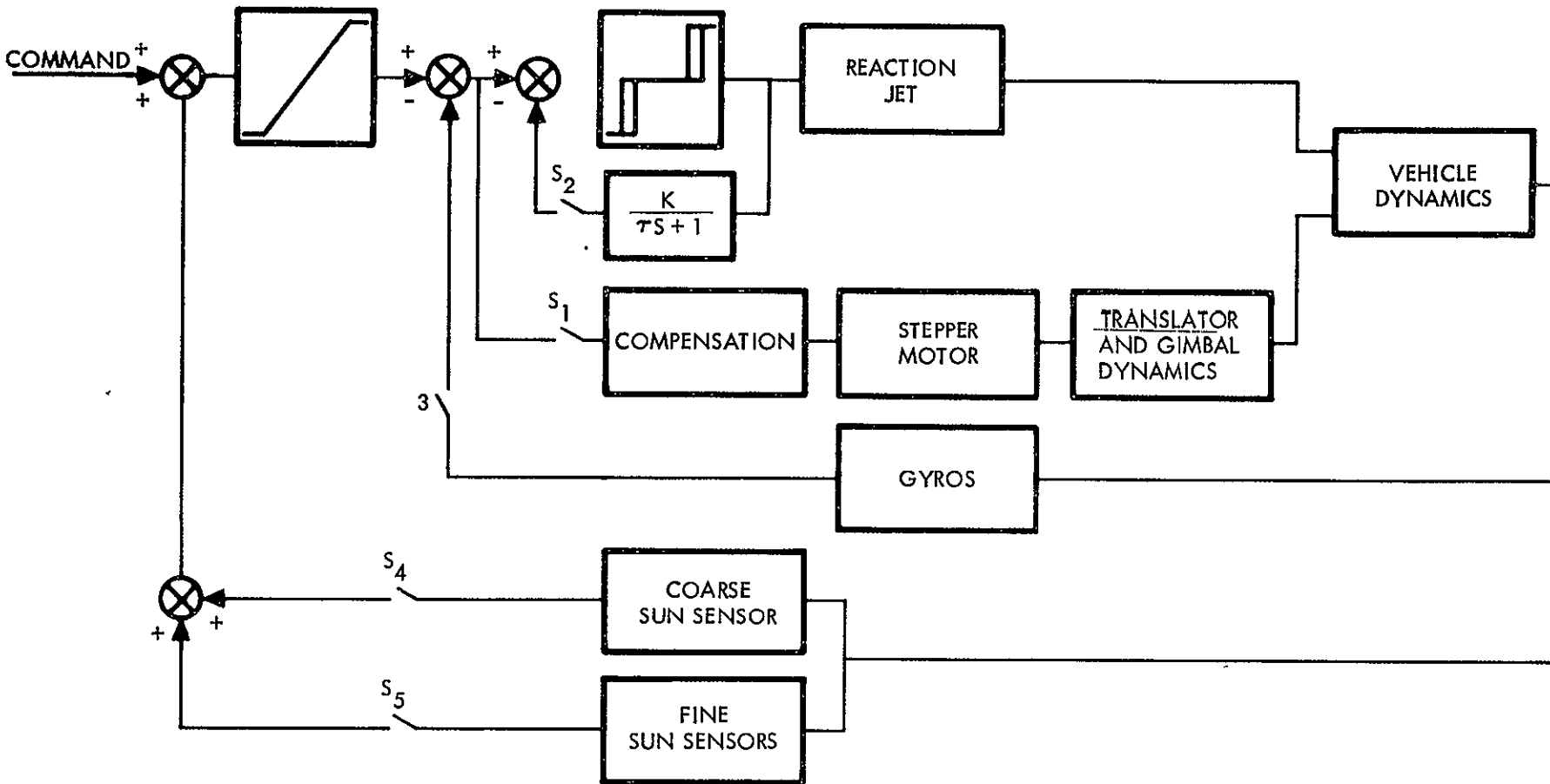
Figure 9-3. Roll-Yaw Block Diagram
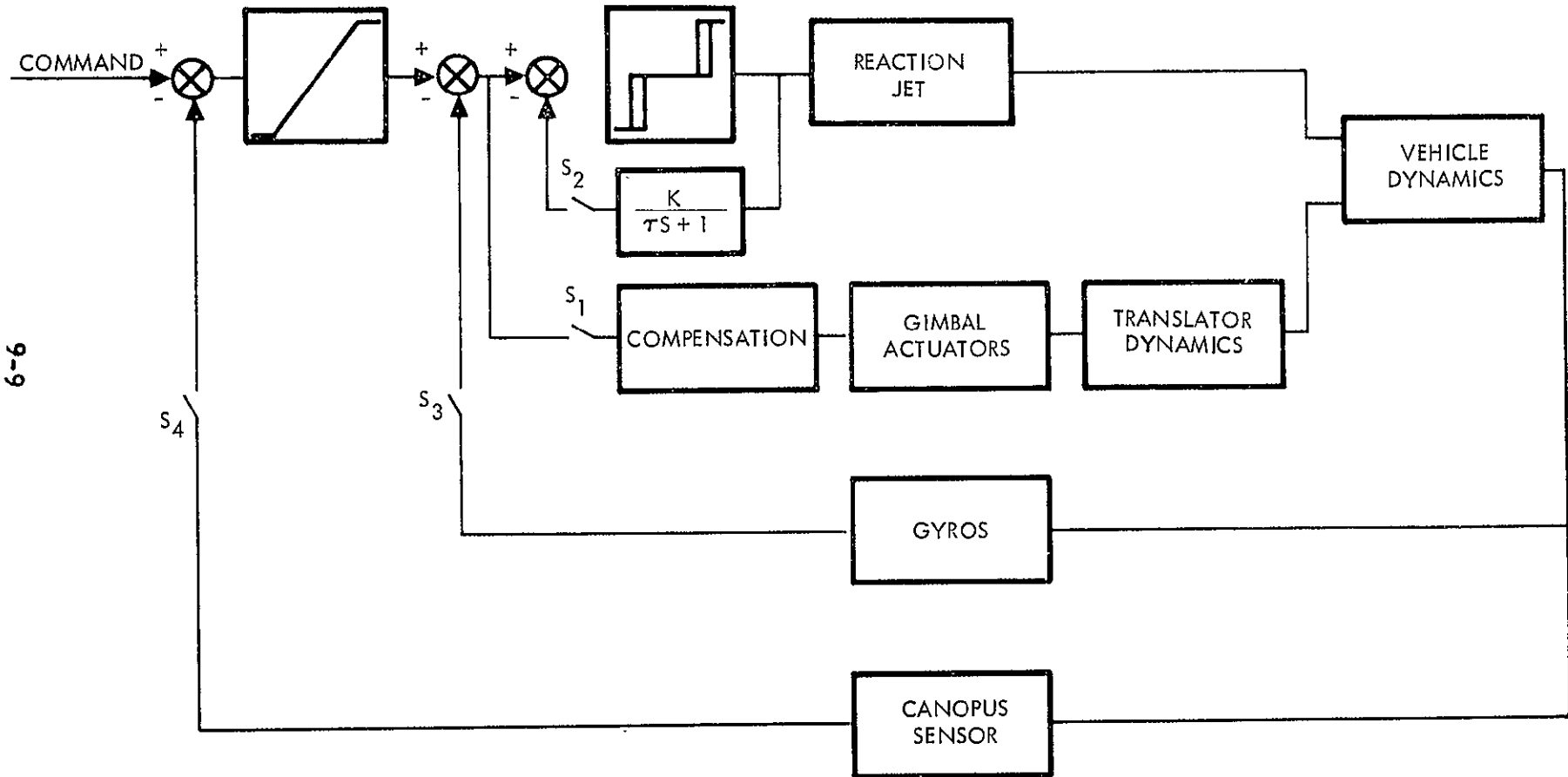
Figure 9-4. Pitch Block Diagram

	S_1	S_2	S_3	S_4	S_5
INITIAL RATE ARREST	0	0	X	0	0
SUN ACQUISITION	0	0	X	X	X
THRUSTING INTERVAL	X	0	0	0	X
CRUISE INTERVAL	0	X	0	0	X
MANEUVERS	0	0	X	0	X

PITCH-YAW SWITCHING MODE

	S_1	S_2	S_3	S_4
INITIAL RATE ARREST	0	0	X	0
CANOPUS ACQUISITION	0	0	X	X
THRUSTING INTERVAL	X	0	0	X
CRUISE INTERVAL	0	X	0	X

ROLL SWITCHING MODE

Figure 9-5. Pitch-Yaw Switching Mode

Sun sensors (both fine and coarse) are generally highly reliable instruments. Nevertheless, it is advisable to provide a sun sensor system that can accommodate at least a single failure without compromising the mission. This may be accomplished by adding redundant sensors or by procedurally accomplishing the same functions with other on-board sensors. The former permits normal operation in the presence of single failures in both the fine and coarse sun sensor systems, but at the expense of additional switching logic, which partially compromises the reliability gain of redundancy. The latter simply accommodates redundancy by using coarse sensor cells in the event of fine sensor failure and using the fine sensors for acquisition in the event of coarse sun sensor failure. The procedural approach, although simpler, is more involved and, for fine sun sensor failure, is less accurate. Selection is biased toward the procedural approach because sun sensors with high reliability have been demonstrated, and the additional complexity of redundant sensors appears unwarranted. Nevertheless, in the final analysis redundant sensors may be employed since the added penalty in weight, power, and configuration design is not demanding.

The selected Canopus sensor is functionally similar to the Mariner 1969 sensor, which has evolved from Mariner 1964 and Mariner 1967 designs. The major exception is the extended field of view required by SEP. With this exception, the Mariner 1969 Canopus sensor satisfies all the S&C requirements of the asteroid belt probe (and procedurally more difficult probes such as a Jupiter flyby) as they are now envisioned.

The Canopus star sensor is body-mounted to the spacecraft and provides a roll attitude error signal to the control electronics when the light intensity level (corresponding to Canopus) falls between the two gate levels. Canopus position may be described by its cone angle from the sun and its clock angle about the sun line (Figure 9-6). The field of view of ±19 degrees is required in both clock and cone. This value reflects the offset of Canopus from the ecliptic normal and such other tolerances at attitude errors, shade requirements, etc. The Mariner Canopus sensor has a large field of view in cone (40 degrees) and a narrow field of view in clock (4 degrees). Clock angle changes that occur during the mission are accommodated by rolling the spacecraft, a luxury that may be ill afforded by SEP because of the resulting out-of-plane thrusting. Hence, the SEP Canopus sensor differs from Mariner 1969 by the requirement of a large field of view in both clock and cone.

In Mariner the Canopus cone angle changes are accommodated through electronic gimbaling of the sensor possessing an instantaneous field of view of 11 degrees in cone. Such gimbaling is required in both clock and cone for SEP. The gimbaling is provided by switching between discrete levels
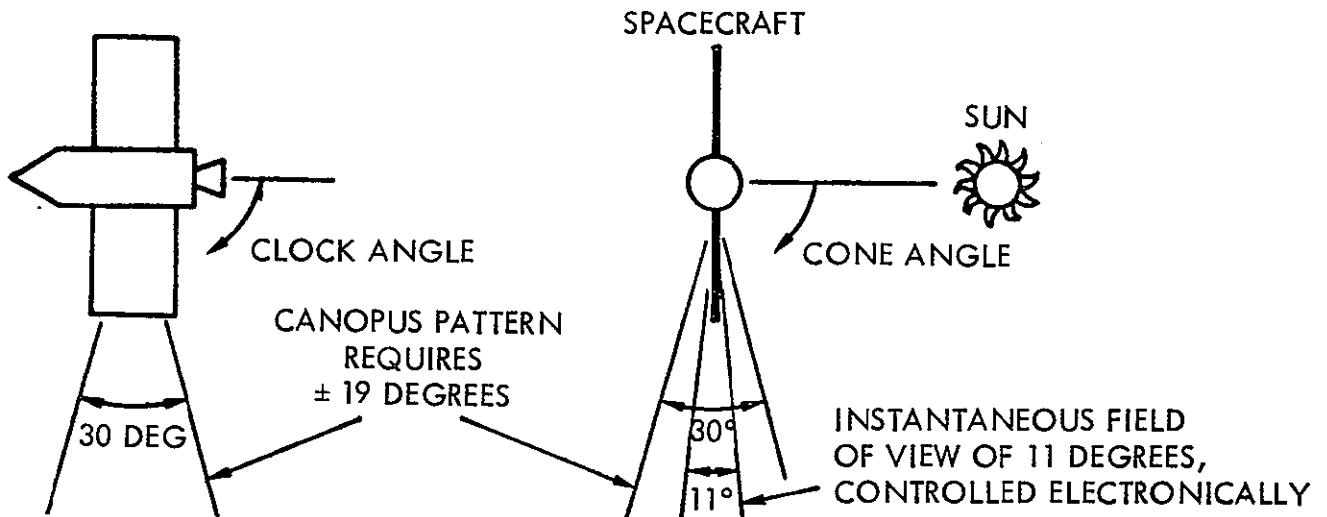
Figure 9-6. Canopus Cone and Clock Angles

that overlap. This allows some latitude in system tolerances and switching times. A baffling system consisting of non-reflective, concentric, sharp-edged rings should be employed to minimize stray light that may enter the sensor, such as sunlight reflected from spacecraft appendages. The output signals from the sensor are roll attitude error, light intensity level, state of the acquisition gates, and an indication of the gimbal step in which the sensor is operating. The sensor should include an automatic light-cell-operated shutter to prevent intense light sources from damaging the sensor. Reliability considerations dictate inclusion of a redundant Canopus sensor. With the exception cited above, the Mariner 1969 sensor, modified to correct problems discovered in the Mariner 1969 flights and changes warranted by improvements in the state of the art, is the recommended star sensor for the baseline design. Sensor performance and physical characteristics are summarized below:

Field of view   At least ±19 degrees in both cone
                                 and clock

Instantaneous field of   May be considerably smaller than
view   the ±15 degree maximum; however,
                                excessive switching (electronic
                                gimbaling) precludes an immoderate
                                value

9-12

Roll error null accuracy	±0. 05 degrees
Power	5 watts
Light sensitivity	Track a star of 0. 02 Canopus intensity
Dimensions (excluding light baffle)	11. 5 by 4. 5 by 5. 0 inches
Weight (excluding baffle)	9. 5 pounds

The above considerations, which resulted in a Mariner '69-type
Canopus sensor, do not include physical location. It turns out, however,
that its impact on the space vehicle design is demanding. To observe this,
consider Figure 9-7, which indicates boundaries of permissible panel loca-
tion. For the sketch on the right, the sun is directed outward from the paper.
The cross-hatched area indicates the required Canopus sensor field of view
(the solar panels must lie outside this boundary). Also shown in the sketch
is a region labeled unacceptable for solar panels because of possible mercury
coating resulting from ion engine exhaust. This also precludes the possibility
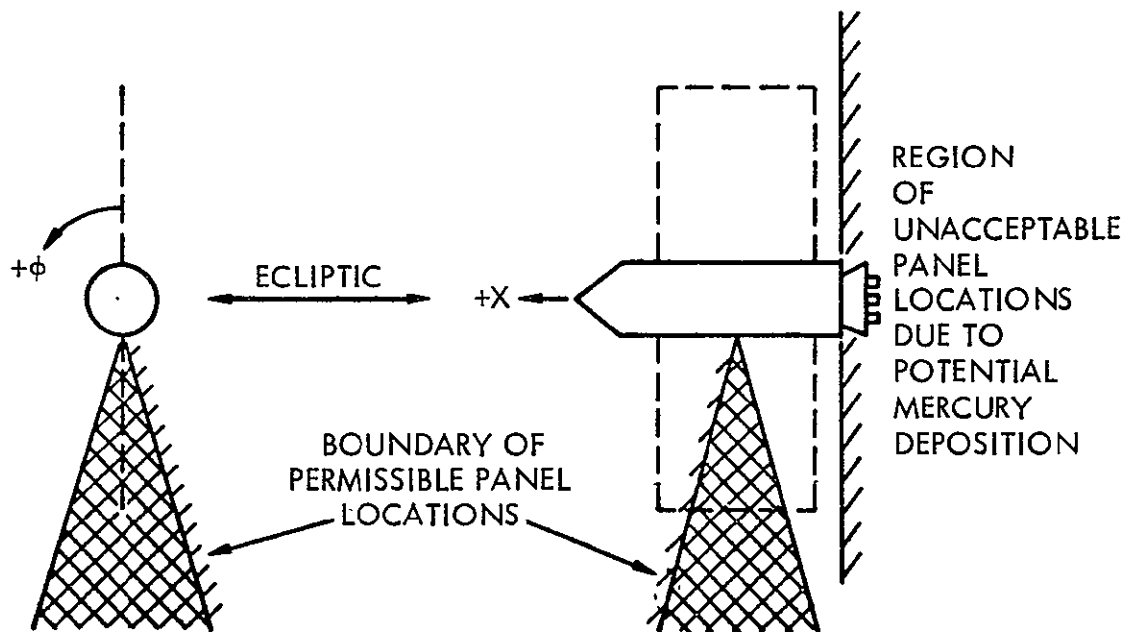
Figure 9-7.   Impact of Canopus Sensor Location on Spacecraft Solar Panels

of leaning the solar panels toward the positive x direction since the resulting asymmetry dictates large solar pressure disturbance torques demanding excessive fuel requirements during the coast interval. If the solar panels when deployed are extended normal to the ecliptic, as shown by the dashed lines in the figure, the Canopus field of view is restricted. This configuration is optimum in terms of power, but precludes Canopus detection during a major portion of the mission. To overcome this deficiency one may either deflect one of the panels (the lower one shown in the figure) to obviate panel impingement, or simply maneuver the vehicle in the positive ϕ direction during intervals of Canopus occultation by the solar panels. In either case some power degradation must be accepted. The former alternative results in a single panel power degradation throughout the mission. The latter degrades both panel power inputs for only a portion of the mission. Maneuvering the vehicle in periods of Canopus occultation by the solar panels does not increase system requirements. It should also be pointed out that the occultation maneuver is purely a pitch orientation, which does not introduce out-of-ecliptic thrusting. Hence, it does not degrade the trajectory. The baseline configuration, however, is to deflect the impinging panel, that is the broken wing concept. Nevertheless, from an S&C perspective, either approach is acceptable.

The magnitude of panel static deflection required to obviate Canopus occultation is a function of a number of factors: sensor field of view, lens diameter, shade geometry, acceptable accuracy, and expected panel dynamic deflection because of thermal distortion.

Figure 9-8 illustrates the required panel deflection as a function of shade length for a 19-degree field of view, a 3-degree accuracy requirement, a 1-degree tolerance, a 1-inch lens diameter, and a 5-degree thermal deflection. It is observed that a 29-degree panel deflection will suffice for a shade length greater than or equal to 10 inches.

REACTION CONTROL SYSTEM

The reaction control system consists of control jets, tankage, plumbing and electronics required for jet logic selection, etc. (Figure 9-2). The RCS is used to control the spacecraft during the following operative modes:

Acquisition

Pitch control during single ion engine operation in the later stages of the thrust interval

Override of thrust vector control during the thrust interval
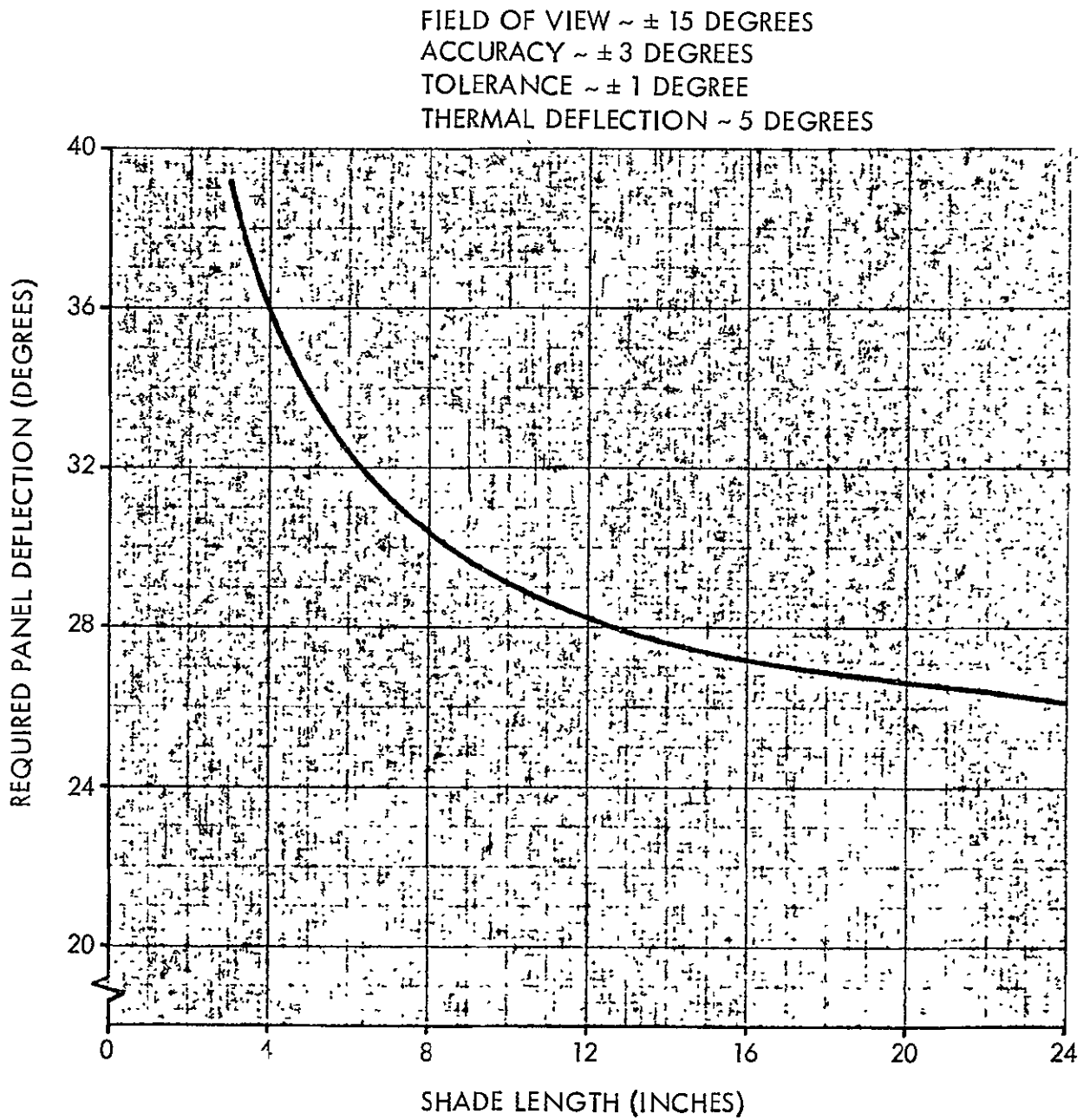
Figure 9-8. Panel Deflection as a Function of Shade Length

Orientations

Three-axes control during the cruise interval

The baseline configuration consists of 12 reaction control jets (0.1 lb-thrust) located along the control axes, providing pure couples in each of the three axes. Three-axes control is still achievable in the event of jet failure by operating with single jet control as opposed to couples. Thus the system can still function with as many as six jet failures.

The total impulse required for attitude control ($\approx$1000 lb-sec) suggests the use of monopropellant propulsion systems for minimum system weight. Although the total impulse requirements are above the impulse regime at which cold-gas systems are competitive on a weight basis with other concepts, cold-gas attitude control systems should also be considered, because of their simplicity, demonstrated reliability, and low cost.

Monopropellant attitude control systems have received considerable attention, particularly in light of successful development of the spontaneous catalyst, Shell 405. Propulsion systems for attitude control functions have been developed and qualified by rocket research for thrust levels varying from 0.5 to 0.25 pounds. Small thrust monopropellant engines have been demonstrated for thrusts as low as 0.02 pounds by various engine manufacturers. However, small thruster technology is comparatively new with little (if any) flight experience behind it. The high freezing temperature of the liquid hydrazine may require elaborate thermal protection measures to assure operational survival within the mission environment constraints. The remote, widely separated thruster quad installation adds to the complexity of the thermal protection system to avoid freezing the propellants. Further studies should be conducted for fuller evaluation of the monopropellant attitude control system and determine if the thermal constraints are as severe as they appear. Such other monopropellant concepts as the gas generator systems may be used to solve the problem of liquid propellant distribution.

A cold gas was selected to provide the spacecraft attitude control and stabilization impulse requirement. Gas nitrogen provides specific impulses ranging from 50 seconds to as high as 73 seconds. The major factors that influenced the selection of a cold gas system were its substantially developed state-of-the-art technology, demonstrated reliability, system simplicity and low cost. Because of these features, cold gas propulsion systems have been extensively used for spacecraft attitude control applications.

One of the major contributors to cold gas system weight is the necessity of loading excess propellant to account for propellant losses from thruster valve leakage. Depending on mission duration, number of thruster valves, and leakage rate, the weight of propellant allocated.to leakage may be a factor of two times that necessary for impulse operation. For study purposes, leakage rates of 3 scc/hr were used for each series of valves.

Figure 9-9 is a schematic of the attitude control system. The system uses readily available components, and consists of two independent but interconnected propellent storage systems. Each has a high pressure gageous nitrogen storage reservoir, propellant fill valve, a normally closed squib-activated pressurant isolation valve, filter assembly, series-parallel redundant pressure regulators, welded or brazed propellant distribution system, and eight nozzles with series propellant valves. A normally closed squib-actuated valve provides for interconnecting both systems upon command. Each subsystem contains one-half of the required propellant.

Series-redundant propellant control valves were provided to reduce the probability of propellant loss from a fail-open thruster. The concept was selected as opposed to a dual redundant gas supply that results in an increase of the gas supply by a factor of three with a corresponding increase in propellant reservoir weight. Examples of system typical weight differences are listed below:

Subassemblies	Weight			
	Dual-Gas Redundancy		Valve Redundancy	
	kg	lb	kg	lb
Tanks	57.2	126	19.55	43
Gaseous nitrogen	41.0	90	13.55	30
Valves, regulators, lines, etc.	9.9	21.8	12.1	26.6
Total	108.1	237.8	45.2	99.6

SYSTEM WEIGHT AND POWER REQUIREMENTS

Estimated power requirements for the SEP stabilization and control subsystem are listed in Table 9-2. The table lists power requirements in terms of both component and mission phase. During the interval from separation to thrust initiation, a power demand of 50 watts is required,
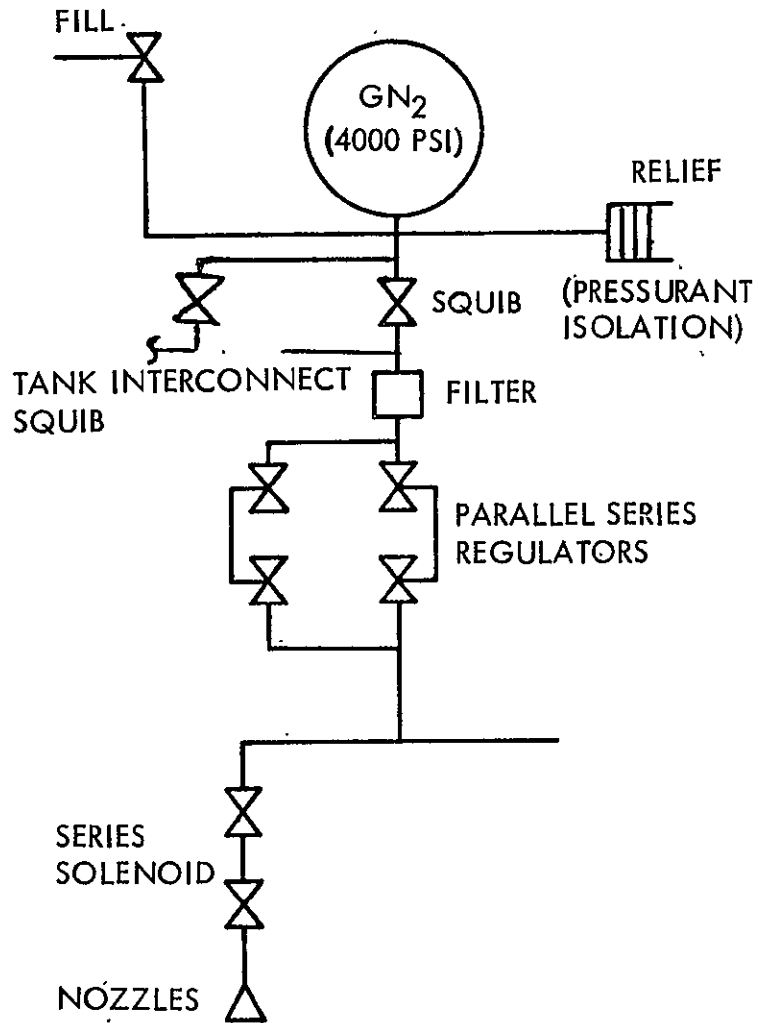
ITEM	QUANTITY	WEIGHT (POUNDS)
TANKS	(2)	43.0
FILL VALVES	(2)	0.2
RELIEF VALVES	(3)	0.6
SQUIB VALVES	(2)	1.2
FILTER	(2)	0.2
REGULATORS	(8)	9.6
SOLENOID VALVES	(24)	9.6
NOZZLES	(12)	1.2
LINES		4.0
TOTAL		69.6

Figure 9-9. GN$_2$ Weight Breakdown and Valve Design

Table 9-2. SEP Estimated Power Requirements (Watts)

Component	Prelaunch	Liftoff To Separation	Separation To Thrust On	Thrusting Interval	Coast Interval
Star tracker	-	Off	7	7	7
Fine sun sensors	-	Negligible	Negligible	Negligible	Negligible
Coarse sun sensors	-	Negligible	Negligible	Off	Off
Sun shutter	-	Off	6	Off	Off
Gyro package	-	21	21	Off	Off
SCS electronics	-	16	16	16	16
Translator and gimbal servos require transient power of approximately 7 watts for each axis.		37	50	23	23

During this interval, which includes sun and Canopus acquisition, operation of the gyros and sun shutter is required. Similar power demands are required for subsequent Canopus reacquisition or vehicle reorientations.

An estimate of weight requirements for the SCS is shown in Table 9-3. The bulk of the weight arises from the cold-gas (N_2) fuel requirements and its plumbing and tankage. They account for approximately 96 pounds. The weight summary includes two Canopus sensors, four fine sun sensors, and two coarse sun sensors. The expected fuel expenditure breakdown includes initial recovery, acquisition, single-engine swirl, leakage (3 scc/hr for each valve), and three-axes control during the coast interval. The weight breakdown for the baseline GN_2 subsystem, along with a series valve design is given in Figure 9-9. Here series-parallel regulators are recommended, along with series solenoid valves, to reduce the probability of fuel depletion due to valve open failure.

Table 9-3. Baseline SEP Estimated
Weight Requirements

Component	Weight (lb)
Star tracker (4)	9. 5 each
Fine sun sensor (4)	0. 5 each
Coarse sun sensor (2)	0. 2 each
Gyro package	11. 0
Electronics	20. 0
Fuel	30. 0
Plumbing, tankage, jets, etc.	69. 6
Total system weight (including four fine sun sensors, two Canopus sensors, and two coarse sun sensors) is approximately 170 pounds.	

CONCEPTUAL ATTITUDE CONTROL DESIGN TRADE STUDIES

A number of attitude control concepts to fulfill the powered and unpowered phase requirements of the solar electric propulsion spacecraft have been evaluated. Results are presented herein. It may be concluded from the study that for weight reasons alone thrust vector control is required during the powered phases of the mission. A 2-degree of freedom linear translator is recommended. It has a superior capability for correcting the large thrust misalignments associated with an engine failure.

Control concepts considered for the SEP mission must satisfy the basic requirements for attitude control during the powered and unpowered portions of the mission. Because of the extended duration of the SEP powered phase and the lack of an active guidance and navigation system (asteroid belt mission), the number of feasible concepts is limited. When thrust vector control (engine translator or gimbal) is used, no additional control is required during the powered phase (except possibly pitch). When the engines are rigidly mounted to the spacecraft, an auxiliary torque-producing system (with its accompanying propellant) must be used during the powered phase to offset the torques produced by engine alignment tolerance, center of gravity (cg) tolerance, and cg shift. The effect of an engine failure is similar to a large cg shift.

If thrust vector control is used during the powered phase, an auxiliary torque-producing system is required to maintain attitude control during the unpowered phase. Both phases of the mission were considered in this study. However, it will be seen that the powered and unpowered phase control systems and requirements are relatively independent of each other.

Table 9-4 summarizes control concepts considered in this study along with the advantages and disadvantages of each. It should be noted that, in general, the thrust vector control systems provide good attitude. control, particularly for engine failures, but are more complicated. RCS attitude control systems are simple but have potentially high propellant requirements when engine failures are considered.

For evaluation of these control concepts in greater detail, the RCS requirements were estimated. The attitude control functions that must be considered are the damping of separation transients from the booster, sun and star search and acquisition maneuvers, attitude control during the powered phase, and attitude control during the nonpowered phase. The propellant requirements are functions of the spacecraft physical characteristics

9-21

Table 9-4. Potential Attitude Control Concepts

Concept	Advantages	Disadvantages
2-DOF translator (roll and yaw), gimbal and RCS (pitch)	• Accuracy control • No side thrust • Good engine-out capability • Does not restrict engine location • Does not restrict engine number	• Complicated • Moderate power requirements
2-DOF translator plus rotator (roll and yaw), gimbal and RCS (pitch)	• Accurate control • No side thrust • Good engine-out capability • Does not restrict engine number • Does not restrict engine location	• Coupled dynamics and control • More complicated control logic • Moderate power requirements
3-DOF gimbaled (pitch, yaw, roll), RCS pitch single engine	• Accurate control	• Side thrust with engine out • Requires specific engine shutdown after engine failure • Restricts engine number and location • Poor engine-out capability • Moderate power requirements
All RCS	• Simple • Lower power requiremen	• Large propellant requirements • For engine-out requires specific engine shutdown • May influence engine location and number
0-DOF gimbal in ecliptic plane, RCS pitch and out-of-plane control	• Accurate in-plane control	• Limits engine location (in line) • Side thrust with engine out
Mixed canted engines in ecliptic plane RCS pitch and adjustable spacecraft— solar panel angle	• Simple • No side thrust with engine out • Good engine-out capability • Propellant requirements independent of engine failures	• Limits engine location (in line) • Moderate RCS propellant • Controlled mass and inertia is maximum
Engines mounted on in-plane translator RCS pitch and out-of-plane control	• Good engine capability • No side thrust with engine out	• Limits engine location (in line) • Moderate RCS propellant
All RCS with translator for trim	• Small RCS requirements? • No side thrust with engine out	• Periodic stability transients • Slow response to and recovery from engine failures • Need engine failure detector (critical)

and the environment. The environment has been defined by the trajectory and thrust history, discussed earlier in Section 2.

As has been mentioned, the attitude control requirements for the thrusting and nonthrusting phases are relatively independent. The non-thrusting requirements can be conveniently grouped in two categories. The phase of flight, including damping of separation transients, sun and star search and acquisition maneuvers (all prepowered phase), have been considered in one group. For the considered vehicle, approximately four pounds of fuel (N_2) are required to accomplish these events.

Because the nonpowered phase requirements are so small, the powered phase of the mission presents the major area for control-system tradeoff. The possible concepts are thrust vector control, RCS control, or combinations of these two. The feasibility of using only a RCS for the powered phase was investigated since the whole mission (powered and unpowered) could then be controlled by the same torque source. The propellant requirements are based on the assumption that the control system must balance the angular momentum of the thrust vector misalignment with the center of gravity (equivalent to assuming a one-sided limit cycle). The thrust vector misalignments are due to engine alignment tolerance, center-of-gravity tolerance, and cg travel during the mission. For this study, an 0.25-inch moment arm was assumed in the pitch and yaw axes and 0.25 degrees in the pitch axis. These values are representative and should not be considered conservative. The resulting propellant consumption is summarized in Table 9-5 for a cold-gas (N_2) system. Approximately 964 pounds of propellant is required for 210 days of powered flight. This amount of propellant would be considered prohibitive for this spacecraft. When engine failures are considered, the propellant weight becomes astronomical unless engines are shut down to preserve thrust symmetry (and appropriate trajectory changes made to complete the mission). To reduce this excessive amount of propellant and to avoid some of the complexity of a thrust-vector control system, a combination system was considered. An engine translator (or gimbal) was considered to control the in-line engines in the ecliptic plane. The ecliptic plane was chosen for the engine degree of freedom so that the programmed solar-panel-to-spacecraft-body angle could be changed to accommodate the thrust-vector variation associated with gimbaled engine failures. The system essentially eliminates the RCS propellant require-

Table 9-5. Propellant Requirements

Time Period Ending (Days)	All RCS					On-Axis Translator Or Gimbal Plus 2-Axis RCS					2-Axis Translator with Hinge			
	Leak-age	Unpowered Solar Pressure Roll and Yaw	Engine Torques Roll, Yaw	Engine Torques Pitch	Total	Leak-age	Unpowered Solar Pressure Roll and Yaw	Engine Torques Roll, Yaw	Pitch	Total	Leak-age	Unpowered Solar Pressure Roll and Yaw	Engine Torque Pitch	Total
0	0	0	0	0	* 4.1	0	0	0	0	* 4.1	0	0	0	*4.1
50	0.5	0	214	43	257.5	0.5	0	107	57	168.6	0.5	0	0	4.6
100	0.9	0	410	82	492.9	0.9	0	205	109	319.0	0.9	0	0	5.0
150	1.4	0	668	120	789.4	1.4	0	276	159	440.5	1.4	0	0	5.5
210	1.8	0	810	142	963.8	1.8	0	334	175	514.9	1.8	0	**0.6	6.5
400	3.7	3.1	810	142	958.8	3.7	3.1	334	175	519.9	3.7	3.1	0.6	11.5
600	5.4	5.5	810	142	962.9	5.4	5.5	334	175	524.0	5.4	5.5	0.6	15.6
800	7.4	7.6	810	142	967.0	7.4	7.6	334	175	528.1	7.4	7.6	0.6	19.7
1000	9.2	10.0	810	142	971.2	9.2	10.0	334	175	532.3	9.2	10.0	0.6	23.9
1200	12.0	13.0	810	142	977.0	12.0	13.0	334	175	538.1	12.0	13.0	0.6	29.7
													0.6	
													0.6	
													0.6	

* Prepowered phase propellant 4.05 lb (rate damping, roll searches acquisitions)
** Total propellant for engine torque control is determined on a single valv · at end of 210 days (thrust termination)

ments in one axis and increases the pitch requirements somewhat because of the change in engine placement. The propellant requirement for this system, as summarized in Table 9-5, is approximately 515 pounds for 200 days. Although this value could be reduced by changing the RCS propellant, a minimum value is in the region of 150 pounds (powered phase only), which is probably still excessive for this spacecraft. When thrust-vector control is considered for attitude control, the only RCS propellant expended is during single-engine operation for pitch to correct the torque produced by the ion stream swirl. The propellant for pitch is estimated to be 0.3 pounds during the 200-day powered phase.

A conclusion that can be reached from this comparison of attitude control concepts for SEP is that some sort of thrust-vector control system is necessary from at least a weight standpoint. A two-degree-of-freedom linear engine translator has the additional advantage of superior capability of correcting the large thrust misalignments associated with an engine failure.

REFERENCE SENSOR TRADES

The star tracking method chosen for the SEP asteroid belt mission baseline configuration is the simplest approach to the problem of roll determination. Canopus, which is inclined 14.17 degrees from the normal to the ecliptic and is the second brightest star in the sky, was chosen as a reference. The tracker is pointed normal to the ecliptic, and, after acquisition, Canopus inscribes a circle around the field of view as the mission progresses. These data are converted to error signals by the CCS, which provides a bias based on projected orbital position. Provisions are included to update this bias via the command system. The field of view of the tracker was chosen as 38 degrees to provide for a 3-degree control dead band and a tolerance of 1.83 degrees. This approach, however, has resulted in limitations to the spacecraft design. Primarily, it has prevented a symmetrical spacecraft configuration. The restriction is imposed by the field of view required, the thermal bending of the solar panels, and the requirement to shade the star tracker from reflections of all spacecraft objects illuminated by the sun (in this case the edge of the solar panel). As a result, the lower solar panel was deflected by 29 degrees. In addition, the use of the single-tracker approach constrains the mission. That is, the chosen star should be within 15 degrees of a unit vector normal to the orbit plane.

Alternative Configuration Field of View Requirements

A configuration that involves a more complex system for roll determination has been developed to circumvent the limitations just discussed. This system will involve two star trackers of the image-dissector type. One will be boresighted to the north ecliptic pole and the other toward the south. Each tracker will be employed for opposing sides of the total possible orbit and provide for four degrees of overlap on each side of the orbit.

The tracker that points toward the south ecliptic pole will use Canopus, as was the case in the basic configuration. The field of view requirements are also the same. However, the portion of the field that would view in the direction of the solar panels is masked by the sun shade 2 degrees from the normal. This portion will not be scanned by the image dissector. This provides an effective field of view of 25 degrees in the direction normal to the solar panel. The tracker that points toward the north ecliptic pole will use Vega as a tracking star. Vega is inclined 28.26 degrees from the pole and is the fourth brightest star in the sky. The differential azimuth between Canopus and Vega in the ecliptic is 180.37 degrees. A 66-degree field of view will be required to track Vega in this manner. This again provides for a 3-degree control dead band and, in this case, a tolerance of 1.74 degrees. As in the case of the Canopus tracker, the direction of the solar panels is masked by the sun shade 2 degrees from the normal for an effective field of view of 39 degrees in the direction normal to the panel. The fact that Vega and Canopus do not lie exactly 180 degrees apart in azimuth is provided for by the four-degree overlap of the respective fields of view. This ensures a minimum of 3.63 degrees with both stars acquired during the transition phase from one tracker to the other.

Utilization of this two-tracker approach enables a symmetrical spacecraft to be designed with both solar panels offset by 15 degrees. Since the addition of the second tracker enables a wider field of view to be utilized for full orbital coverage, a greater choice of missions (out of the ecliptic) is available even though two stars are required for tracking. The utilization of more than two stars increases the orbits available to this concept. There are 13 stars of magnitude one or brighter, 10 of which are more than 15 degrees from each of the others and hence provide relatively simple acquisition for such missions.

Tracker Design Considerations

For this study, an image dissector was chosen. The following excerpt, from the ITT Description of the ITT/Aerospace Electro-Optical Tracker, is a brief description of a typical tracker of this type:

"The basic tracker consists of an optical lens, photosensor, and electronics. The lens system gathers, and brings to focus, radiant energy at the photocathode of an image dissector. The image dissector has a photo-cathode surface which forms an electron image of the focused image. It is constructed such that, when an accelerating voltage is applied between the photocathode and an internal mechanical limiting aperture, only electrons from a particular area of the photocathode will pass through the limiting aperture (see Figure 9-10). This particular area is called the instantaneous photocathode area and, when projected through the tracker lens, represents a region in space defined as the instantaneous field of view. Following the aperture is a secondary emission dynode structure providing a signal amplification.

"To utilize the tube in an optical tracking system, a deflection coil is positioned around the image dissector image section to provide deflection of the electron image. By applying the proper deflection currents, the electron image can be swept across the limiting aperture. Mode control logic locks the tracker operation into the search mode at turn-on. An acquisition field, similar to a television raster, is generated. Acquisition scan stops when an image of the proper brightness and spectral content enters the instantaneous field of view and the tracking mode of operation is initiated.

"In the tracking mode, a cross scan sweep, causing pulse position and pulse duration modulation of the electron beam, is employed. Demodulator circuits develop an analog error which is used to control the dc deflection coil currents such that the cross scan is centered on the target image. These error signals are used in an internal closed-loop control system to follow the target image across the photocathode by electronically offsetting the electro-optical axis of the tracker. The current flowing through the deflection coil will consist of a dc component which is proportional to the angle between the optical axis of the sensor and the target line-of-sight, and an ac component due to the track sweep waveform. The coil current is monitored through a low-pass filter to recover only the dc component. A block diagram of the electro-optical tracker is shown in Figure 9-11.

"Figure 9-12 illustrates the operation of the cross scan that is used to generate error signals. The cross scan pattern is generated by deflecting the square instantaneous field of view from position "1" to form the pattern shown. (Positions 7 and 8 are not shown for simplicity.) The x-y deflec-tion voltages required to generate this pattern are also shown on Figure 9-12. A point source target at various positions and the resulting video signals· are shown as a, b, and c. When the target is in position a, the integral of the output signal between 1 and 3 is equal to that between 3 and 6. The error signal which is the difference between these two areas, after processing, is zero. An output signal occurs at any other position with a maximum at c.
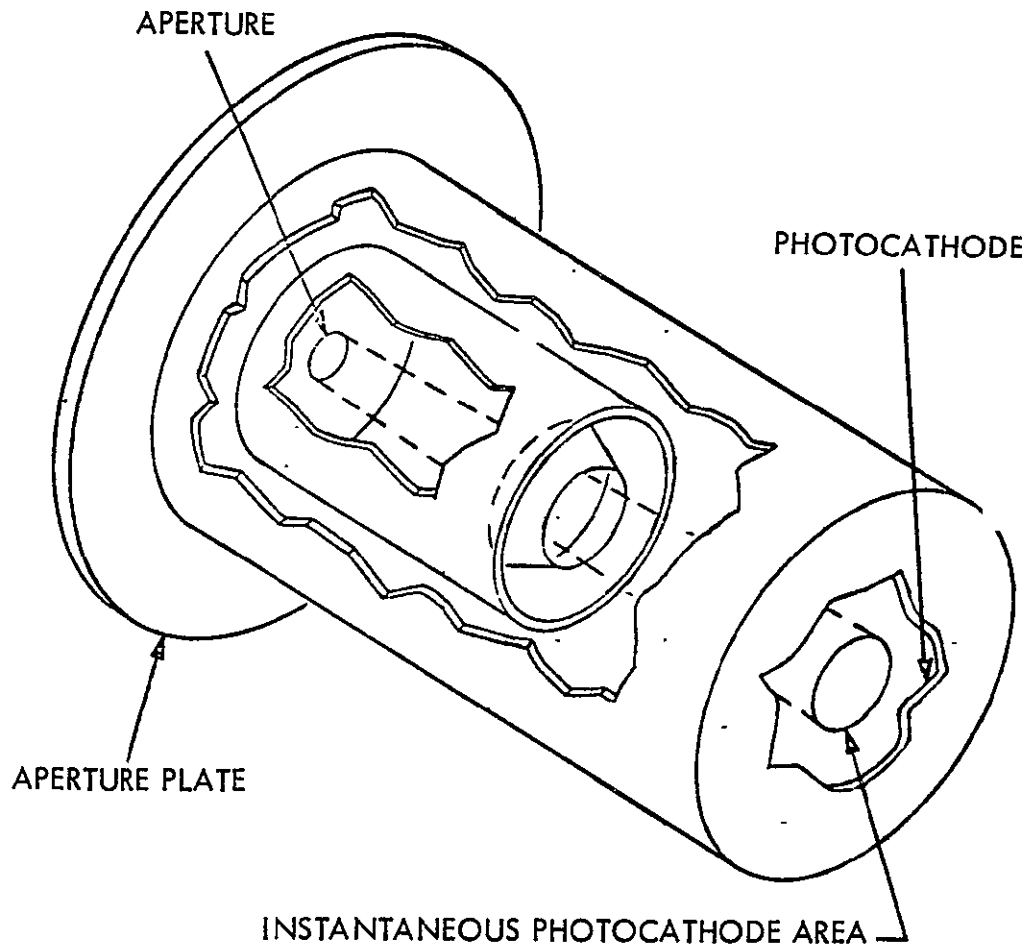
Figure 9-10. Image Dissector
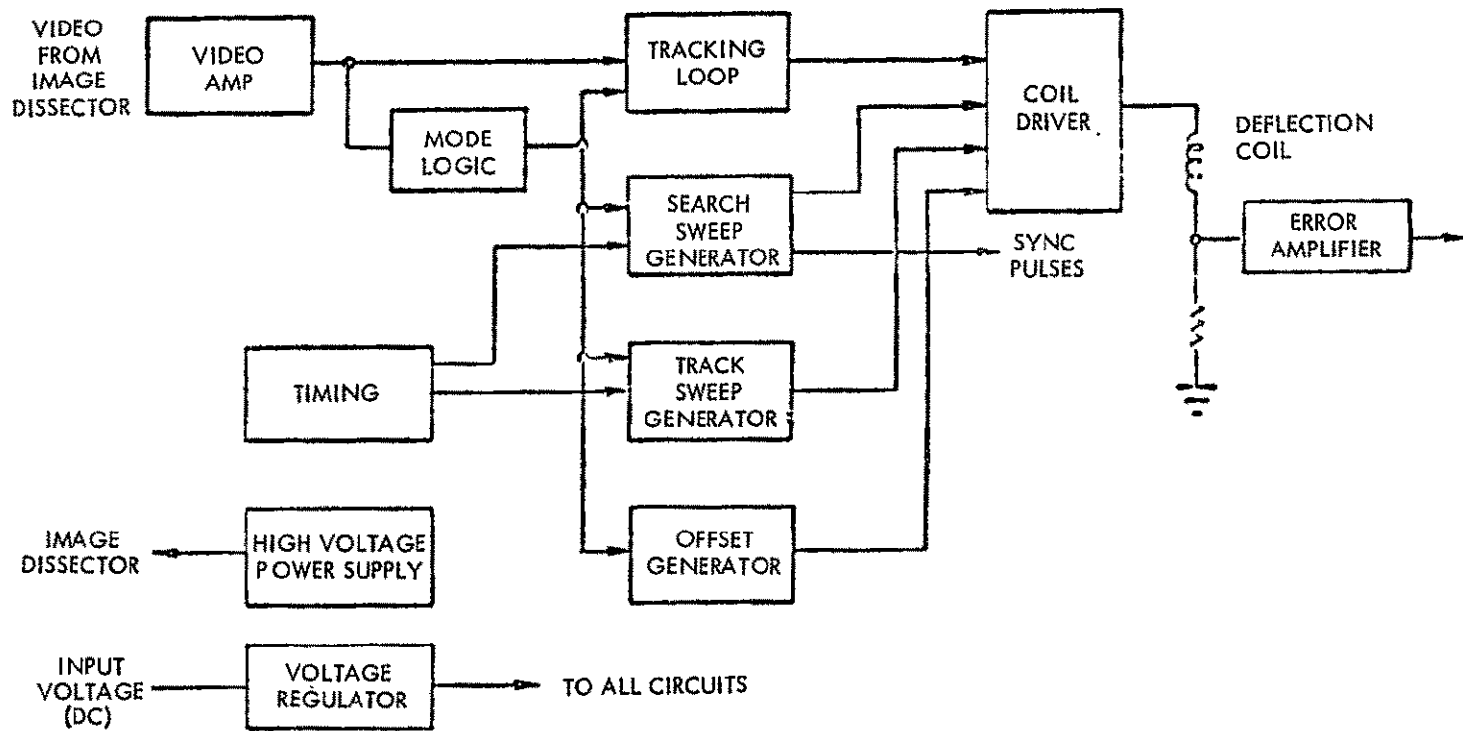
Figure 9-11. Tracker Block Diagram
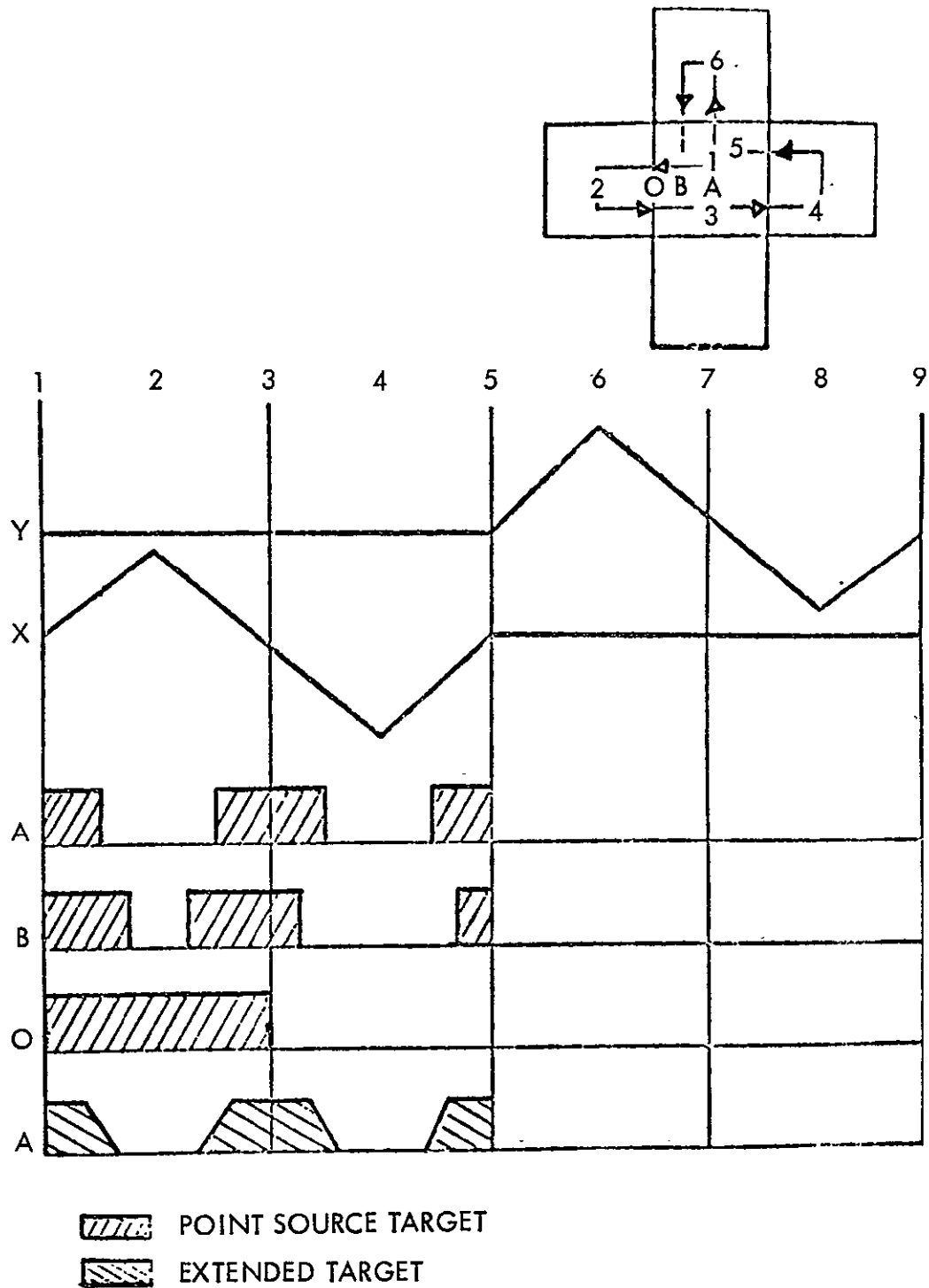
Figure 9-12. Target Signal Characteristics (Track Mode)

POINT SOURCE TARGET

EXTENDED TARGET

One example of an extended target is shown to illustrate that the operation and accuracy of the tracker is not limited to point source targets.

"The use of a small instantaneous aperture resulted in a high signal-to-noise ratio as compared to other systems which utilize the entire surface or a photomultiplier tube or solid-state detector. When the system is in the track mode, stray light (reflection and glint) falling on the photocathode surface will not affect the output signal unless it falls directly on the instantaneous field of view. Although possible, the probability of this occurring is negligible. Background light outside of the instantaneous field of view is completely eliminated from the signal. This is accomplished without sacrificing total field of view due to the ability to position the instantaneous aperture any place on the entire usable photocathode surface. This capability allows tracking of an image any place on the photocathode surface which, in effect, provides electronic gimbaling. "

As stated above, this type of system has a smaller tendency to track random particles or lose acquisition due to stray light than a system which continually scans the entire field (higher signal-to-noise ratio). The stray light problem (a perpetual one for star trackers) has been greatly reduced in this spacecraft design by mounting the trackers on the side of the spacecraft which is shielded from the sun by the solar panels. Reflection from the edges of the panels are prevented from seeing the lens of the tracker by the shade described below.

The wide field of view required by this spacecraft design has not been flown in an image dissector tracker to date. It should be noted that the optical consideration will tend to increase the image size for stars at the field edge with attendant loss of intensity for that star. Fields of view up to 30 degrees have been demonstrated, however, and no special problems are foreseen in extending this to the 66 degrees required.

Acquisition

If the image dissector type of tracker is capable of discriminating against star brightness within ±0.5 visual magnitude, the acquisition problem is greatly simplified with the choice of Vega or Canopus as tracking stars. No other stars are within that ±0.5 visual magnitude for Canopus, and only six other stars are within this range for Vega. Arcturus (α Bootis), at an angular distance of 59.1019 degrees is the only star of this magnitude within 66 degrees of Vega. Spectral filtering, as mentioned in the tracker discussion, may be utilized to enhance discrimination. Since Vega is an Ao spectral type and Arcturus is a Ko type, filtering can provide sufficient magnitude discrimination even if both Vega and Arcturus are both in the field of view during the final portion of the acquisition phase. Table 9-6 shows the angular distances from Canopus, Vega, the North ecliptic pole, and the South ecliptic pole to other stars within the appropriate fields of view.

Table 9-6. Angular Distance Comparison

Field of View (Degrees)	Star Name	Visual Magnitude	Angular Distance From Reference Star (Deg)	Right Ascension (Deg)	Declination (Deg)
33	North Ecliptic Pole			270.0000	66.5502
	A UMI	2.1	23.9086	30.6291	89.1213
	B UMI	2.2	17.0195	222.6941	74.2821
	N DRA	2.9	11.5564	245.8916	61.5838
	B DRA	3.0	14.7124	262.4324	52.3235
	G DRA	2.4	15.0671	268.9712	51.4919
	A LYR	.1	28.2593	278.9720	38.7538
	D CYG	3.0	25.5791	296.0008	45.0541
	G CYG	2.3	32.8696	305.2783	40.1566
	A CYG	1.3	30.8096	310.0933	45.1688
	A CEP	2.6	21.0879	319.4599	62.4538
19	South Ecliptic Pole			90.0000	-66.5502
	Canopus	-.9	14.1657	95.8158	-52.6782
	T PUP	2.8	17.1379	102.2916	-50.5771
	E CAR	1.7	17.3192	125.4699	-59.4094
	B CAR	1.8	17.7710	138.2170	-69.5894
38	Canopus	-.9		95.8158	-52.6782
	A HYI	3.0	35.3656	29.4483	-61.7202
	B LEP	3.0	33.6984	81.7291	-20.7829
	A LEP	2.7	36.2868	82.8404	-17.8432
	A COL	2.7	20.2327	84.6312	-34.0897
	B CMA	2.0	34.7409	95.3333	-17.9393
	A CMA	-1.6	36.2322	100.9458	-16.6721
	T PUP	2.8	4.5336	102.2916	-50.5771
	E CMA	1.6	24.5722	104.3516	-28.9288
	D CMA	2.0	27.5891	106.7824	-26.3430
	P PUP	2.7	18.1567	109.0120	-37.0408
	N CMA	2.4	25.8800	110.7170	-29.2416
	Z PUP	2.3	21.1911	120.6233	-39.9149
	R PUP	2.9	34.4878	121.5558	-24.2138
	G VEL	1.9	17.6719	122.1441	-47.2444
	E CAR	1.7	17.6933	125.4699	-59.4094

Table 9-6. Angular Distance Comparison (Cont)

Field of View (Degrees)	Star Name	Visual Magnitude	Angular Distance From Reference Star (Deg)	Right Ascension (Deg)	Declination (Deg)
38	D VEL	2.0	20.7097	130.9620	-54.5774
	L VEL	2.2	28.4841	136.7137	-43.3069
	B CAR	1.8	25.6503	138.2170	-69.5894
	I CAR	2.2	24.6081	139.0654	-59.1449
	K VEL	2.6	25.9261	140.2883	-54.8777
	T CAR	3.0	34.0007	160.4616	-64.2316
	N VEL	3.0	26.7432	142.5695·	-56.8971
66	VEGA	.1		278.9720.	38.7538
	B CAS	2.4	54.1206	1.8778	58.9788
	A CAS	2.3	58.9471	9.6837	56.3677
	D CAS	2.8	62.4949	20.9428	60.0746
	A UMI	2.1	51.5750	30.6291	89.1213
	G UMA	2.5	65.2629	178.0516	53.8669
	E UMA	1.7	56.5276	193.1674	56.1277
	A CVN	2.9	63.9418	193.6449	38.4852
	Z UMA	2.4	52.8569	200.6699	55.0866
	N UMA	1.9	51.0181	206.5799	49.4674
	N BOO	2.8	63.6477	208.3020	18.5524
	A BOO	.2	59.1010	213.5616	19.3430
	G BOO	3.0	46.9340	217.7074	38.4430
	E BOO	2.7	49.2278	220.9078	27.2038
	B UMI	2.2	43.9576	222.6941	74.2821
	A CRB	2.3	39.7262	233.3433	26.8180
	A SER	2.7	50.5732	235.6845	6.5219
	P OPH	3.0	53.7133	243.1795	-3.6157
	N DRA	2.9	30.5139	245.8916	61.5838
	B HER	2.8	32.1408	247.2212	21.5557
	Z OPH	2.7	56.6900	248.8620	-10.5057
	Z HER	3.0	24.5728	250.0291	31.6577
	N OPH	2.6	58.1481	257.1491	-15.6880
	B DRA	3.0	17.7561	262.4324	52.3235
	A OPH	2.1	29.6069	263.3733	12.5810
	B OPH	2.9	36.3038	265.4849	4.5788
	G DRA	2.4	15.5313	268.9712	51.4919

Table 9-6. Angular Distance Comparison (Cont)

Field of View (Degrees)	Star Name	Visual Magnitude	Angular Distance From Reference Star (Deg)	Right Ascension (Deg)	Declination (Deg)
66	L SGR	2.9	64.2355	276.5141	-25.4405
	S SGR	2.1	65.2186	283.3358	-26.3369
	Z AQL	3.0	25.6992	285.9957	13.8160
	P SGR	3.0	60.2974	286.9799	-21.0744
	D CYG	3.0	14.1152	296.0008	45.0541
	G AQL	2.8	32.1370	296.1962	10.5366
	A AQL	.9	34.1949	297.3174	8.7852
	G CYG	2.3	20.2857	305.2783	40.1566
	A CYG	1.3	23.8498	310.0933	45.1688
	E CYG	2.6	26.3199	311.2387	33.8532
	A CEP	2.6	33.9728	319.4599	62.4538
	E PEG	2.5	50.7270	325.6653	9.7321
	B PEG	2.6	55.4739	345.5670	27.9140
	A PEG	2.6	62.6948	345.8033	15.0380

Acquisition with this configuration will be accomplished by rolling about the sun line and mapping the stars until the target star is in the field of view, then commanding the tracker to terminate the search mode. With additional onboard complexity this phase could be accomplished without ground mapping since the target stars are relatively bright.

Shade Design

Since the reflection of the sun on the structures is expected to be several orders of magnitude greater than the light received from the tracking star, a shade (Figures 9-13 and 9-14) shall be incorporated so that reflection from the edge of the solar panel cannot reach the tracker lens. Baffling shall be geometrically arranged to redirect incoming stray light away from the tracker lens.

This is shown by taking various paths of stray light into the baffling arrangement of Figure 9-14 and tracing through their multiple reflections. All interior walls and baffles are coated with a velvet black finish. Present finishes are available having a reflection coefficient of 0.4 percent of the irradiance. The only path of reflected sunlight from the structure or stray light to the tracker lens is a secondary reflection from the razor edge of the baffle.

The overall shade dimensions in the spacecraft X, Y, Z axes are expected to be approximately 11-by-14-by-8 and 18-by-14-by11 inches, respectively, for the Canopus and Vega trackers. Although a rectangular shade is shown, the final design may be conical in shape to reduce the size and light. Due to effects (thermal deflection and attitude control deadband) other than field of view requirements, the solar panels will still have to be deflected. The amount of deflection is significantly less than the baseline configuration. Figure 9-15 shows the required deflection as a function of sun shade length.

Alternate Concepts

Additional advantages could be incorporated in the design by allowing the mounting plane of the trackers to be set at a predetermined inclination which would involve a function of the sidereal angle at launch and/or mounting the trackers at the forward end of the spacecraft so that one of the trackers could track for more than 180 degrees of azimuth. This approach could result in a reduction of the field of view requirement, but additional investigation would be required to ensure that the shading problem (from the front of the solar panels) could be handled satisfactorily. This approach would involve optimizing the amount of look angle around the solar panel, versus the shading problem, the boresighting elevation, and the field of view.

9-35
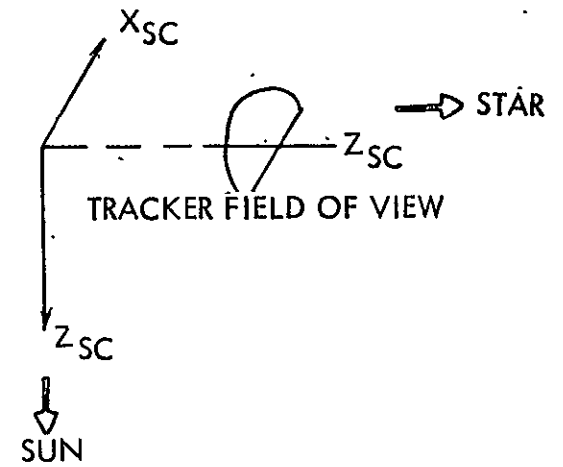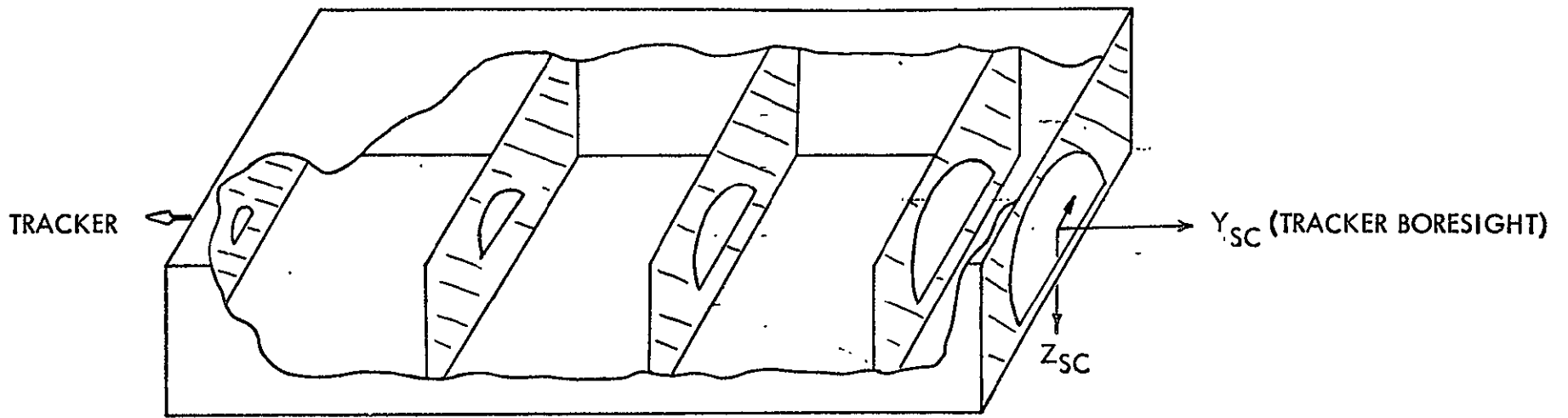
Figure 9-13. Tracker Shade Design
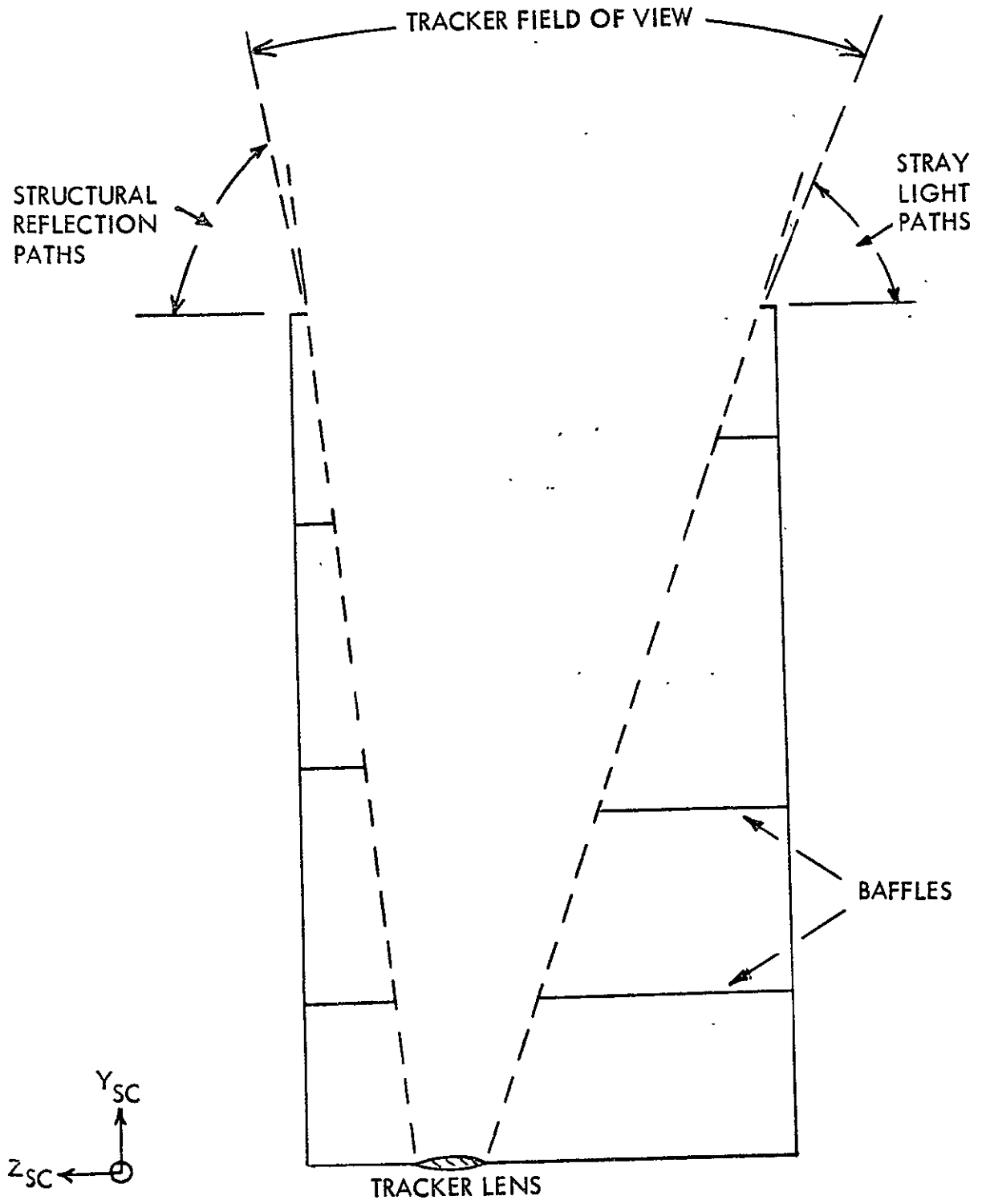
Figure 9-14. Tracker Shade Design (Field of View)
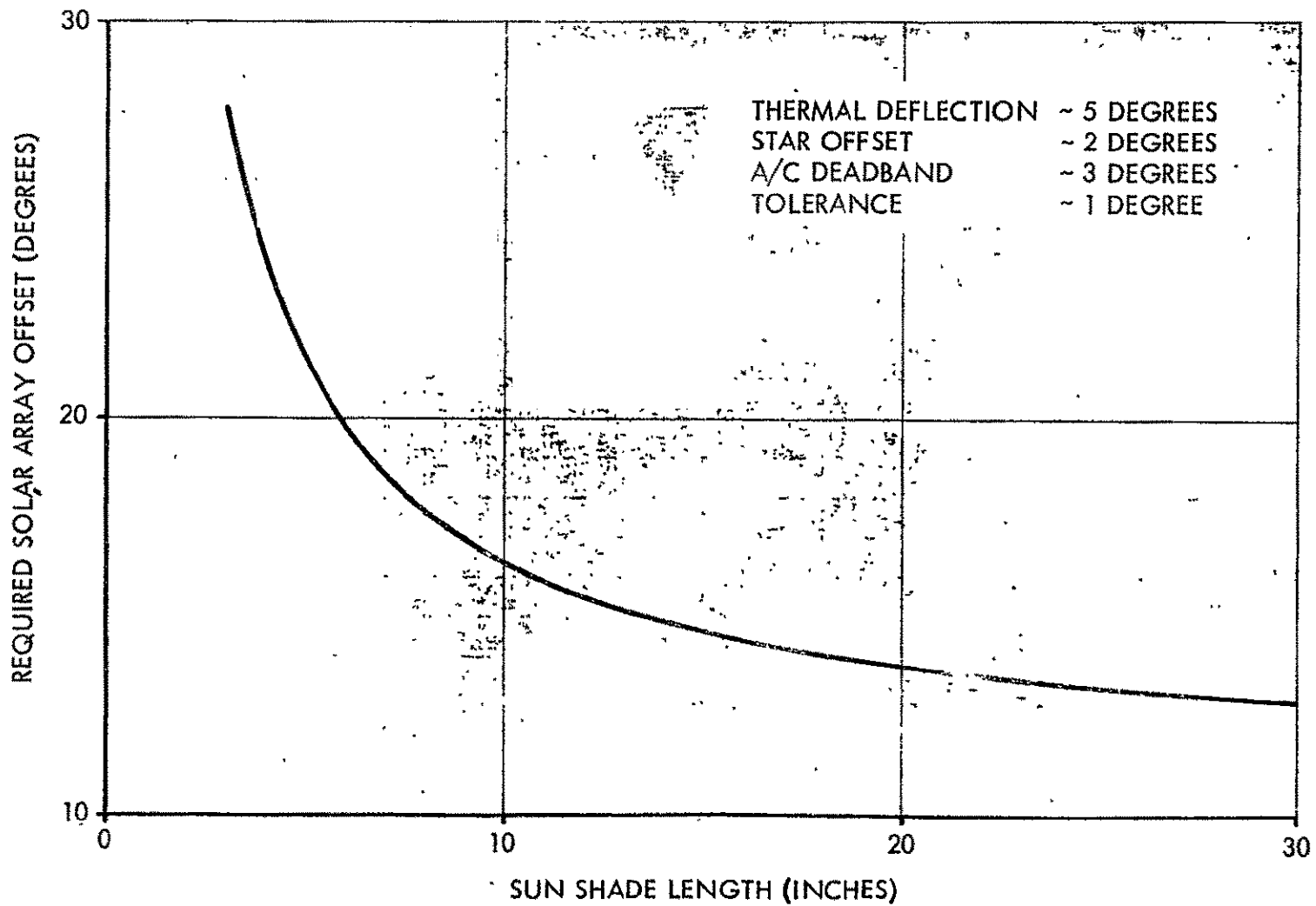
Figure 9-15. Solar Array Offset Versus Star Tracker Shade Length

Legend within figure:

THERMAL DEFLECTION	~ 5 DEGREES
STAR OFFSET	~ 2 DEGREES
A/C DEADBAND	~ 3 DEGREES
TOLERANCE	~ 1 DEGREE

Axis labels: REQUIRED SOLAR ARRAY OFFSET (DEGREES) vs SUN SHADE LENGTH (INCHES)

STABILITY ANALYSIS OF THE SOLAR ELECTRIC PROPULSION SPACECRAFT

The baseline control concept of the SEP spacecraft incorporates a two-degree-of-freedom translator to which an ion engine array is mounted. Control torques are effected by the product of translator displacement and the collective thrust. A stepper motor, driven by attitude errors, translates the mechanism in independent orthogonal directions much in the manner as selecting a point in a cartesian coordinate system. Stability of this concept excluding motor dynamics is the subject of this subsection.

Initially stability is analyzed of a rigid body uncoupled configuration. It is shown that some action must be taken to stabilize even this simple model of the spacecraft. A technique for stabilization is offered by impeding the translator motion with stiffness and damping. Performance is enhanced by a simple lead-lag compensator. It is shown that when flexible solar panels are considered, the same stabilization approach is adequate.

Considering only planar motion, the linearized rigid SEP dynamic equations are found to be:

$$I\ddot{\theta} + cm\,\ddot{\xi} = F\xi \qquad (1A)$$

$$mc\,\ddot{\theta} + m\left(1 - \frac{m}{M}\right)\ddot{\xi} = B \qquad (1B)$$

where θ signifies angular position, m the translator mass, I the nominal total system inertia, M the total system mass, c the distance from the nominal center of mass (cm) to the translator cm, F the total ion engine thrust, ξ the relative displacement of the translator, and B the translator forcing function which is in general some function of vehicle state.

Equation 1A is Euler's equation for the rigid spacecraft; Equation 1B is the translator equation (assumed to be a particle mass). It is observed that the vehicle is accelerated by both position and acceleration of the moving translator similar to the tail-wags-dog effect experienced by vehicles employing gimbaled engines. Here, however, the effects are in opposition; the change in momentum attributed to mass translation is of opposite sign to the torque applied by the engine. As will be demonstrated analytically, this effect is destabilizing.

Denoting the term m(1 - m/M) by m' and the differential operator by s, then by elimination ξ, Equation 1 reduces to

$$S^4 (m'I - c^2m^2)\theta + S^2cmF\theta = B(F - cmS^2) \qquad (2A)$$

Equation 2A could also be written in the form

$$\frac{\theta}{B} = \frac{F - cmS^2}{S^2\left[S^2(m'I - c^2m^2) + cmF\right]} \qquad (2B)$$

For a conventional uncompensated controller, B will in general be a linear function of attitude and its derivative, $B = -K_\theta\theta - K_{\dot\theta}\dot\theta$. Substitution modifies the above equation to:

$$S^4(m'I - c^2m^2) - S^3K_{\dot\theta}cm + S^2(mcF - K_\theta cm) + SK_{\dot\theta}F + K_\theta F = 0 \qquad (3A)$$

or in root locus form

$$-1 = \frac{(F - cm^2)(K_\theta + SK_{\dot\theta})}{S^2\left[S^2(m'I - c^2m^2) + cmF\right]} \qquad (3B)$$

By Routh's necessary condition for asymptotic stability, all coefficients in the characteristic equation must be nonzero and of the same sign. It is observed that Equation 3A is unstable in its given form because terms appear with opposite signs.

The same results can be observed by using root-locus techniques. In a brief summary root locus graphically presents the roots of the characteristic equation of the closed-loop system as a function of the gain. Stability and performance can be determined from the closed-loop roots since they represent terms of the time solution of the differential equations of motion. Any roots on the right-hand side of the vertical imaginary axis indicate system instability, on the imaginary axis is pure oscillatory motion (undamped), and to the left-hand side is asymptotically stable motion. A root locus of Equation 3B with $K_{\dot\theta} = 0$ is shown in Figure 9-16 and can be seen to be purely oscillatory for gains less than the inequality above and unstable for larger gains. Practical applications, of course, require asymptotic stability which cannot be achieved for the system described by Equation 3A. Here we have assumed ideal proportional plus derivative
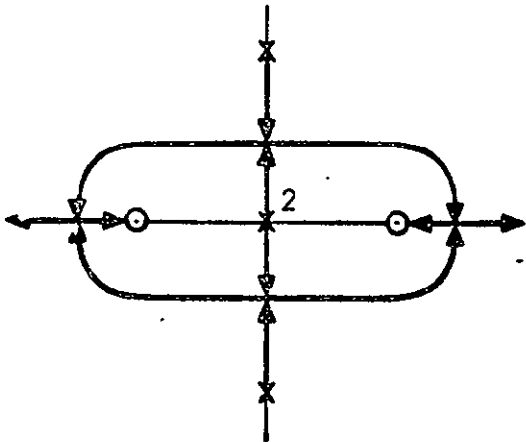
FIGURE A
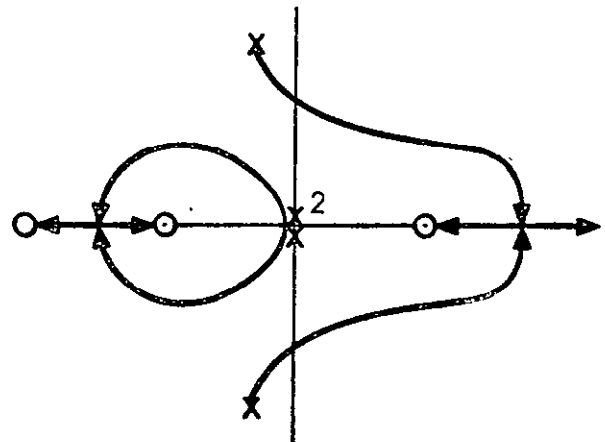
FIGURE B
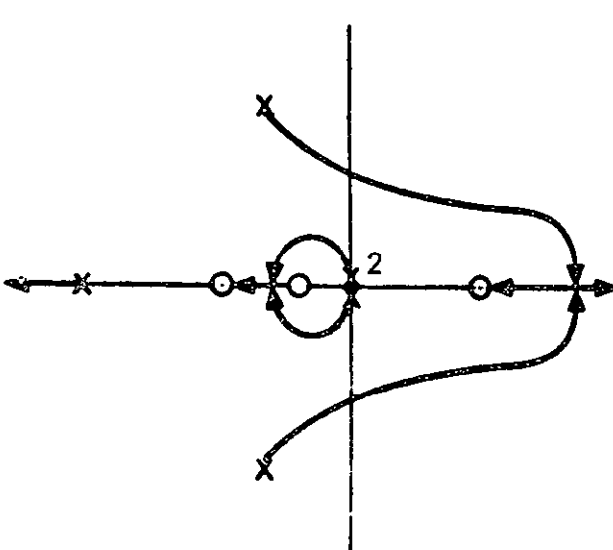
FIGURE C
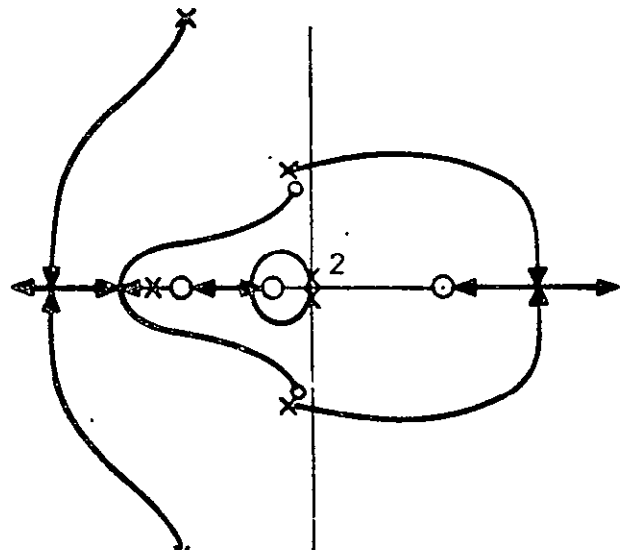
FIGURE D

Figure 9-16. Root Locus Plot Without Motor Dynamics

compensation indicating the use of a rate sensor. However, use of a rate instrument is not acceptable due to the mission duration.

A means of stabilizing this system is to impede the translator motion with stiffness and damping terms. This may be effected either mechanically (spring and dashpot) or electrically (feeding back both position and rate to the motor drive). The introduction of stiffness, k, and damping, d, permits Equation 1B to be written as

$$mc\ddot{\theta} + m'\ddot{\xi} + d\dot{\xi} + k\xi = B \tag{4}$$

which, when combined with the Equation 1A, provides the expression

$$S^4(m'I - c^2m^2) + S^3 Id + S^2(mcF + kI) = -(K_\theta + K_{\dot{\theta}}S)(F - cmS^2) \tag{5}$$

where B is assumed to be a linear function of attitude position. Expansion provides the characteristic equation

$$\tag{6A}$$

$$S^4(m'I - c^2m^2) + S^3(Id - K_{\dot{\theta}}cm) + S^2(mcF + kI - K_\theta cm) + SK_{\dot{\theta}}F + K_\theta F = 0$$

In root locus form this equation becomes

$$\tag{6B}$$

$$-1 = \frac{(F - cmS^2)(SK_{\dot{\theta}} + K_\theta)}{S^2\left[S^2(m'I - c^2m^2) + SId + (mcF + kI)\right]}$$

It can be seen from the plot of the root locus shown in Figure 9-16 B that limited asymptotic stability can be achieved. The position of the open-loop (zero gain) roots for the translator move from the imaginary axis into the left-half plane. Asymptotic stability can then be achieved for a range of gains from zero until the locus crosses into the right-half plane. Subsequent root-locus analysis has shown that when an adequate amount of damping (for system performance) was put into the translator, the pair of roots at the origin would go into the right-half plane instead of the translator roots, thus making the system always unstable for gains larger than zero. Observing Equation 6A suggests that Routh's necessary condition for stability is satisfied if

$$Id > K_{\dot{\theta}}cm \qquad\qquad K_{\dot{\theta}} > 0$$

$$cmF + kI > K_\theta cm \qquad\qquad K_\theta > 0$$

Necessary conditions for SEP stability are easily satisfied. Indeed
by the addition of a simple lag in attitude position (B = -Kθ(s+a)/(s+b)) the
system described by Equation 2 could be modified to possess such qualities
and yet remain unstable. For the system described by Equation 6A,
however, it will be shown that conditions both necessary and sufficient for
stability do exist. To do this we employ Routh's sufficiency condition for
stability. In essence, the "Routhian array" is constructed from the coef-
ficient of the nth derivative as shown below:

$$a_n \quad a_{n-2} \quad a_{n-4} \quad a_{n-6} \quad \ldots$$
$$a_{n-1} \quad a_{n-3} \quad a_{n-5} \quad \ldots$$
$$b_1 \quad b_2 \quad \ldots$$
$$c_1 \quad b_3 \quad \ldots$$

where the constants b_1, b_2, b_3 are given by

$$b_1 = \frac{a_{n-1} a_{n-2} - a_n a_{n-3}}{a_{n-1}}$$
$$b_2 = \frac{a_{n-1} a_{n-4} - a_n a_{n-5}}{a_{n-1}}$$

etc., continuing until all remaining terms b_2 equal zero, and subsequent
rows of constants are obtained similarly from the two rows immediately
preceding:

$$c_1 = \frac{b_1 a_{n-3} - b_2 a_{n-1}}{b_1}$$

Repeated application of this algorithm provides n+1 rows in the array, with
the last two rows each consisting of a single nonzero term.

The entries in the first column of the Routhian array are known as
Routh's parameters. A condition both necessary and sufficient for stability
of a linear system is that the Routh parameters be of the same sign.

Some assumptions facilitating algebraic manipulations are imposed prior to the application of Routh's procedure to Equation 6A:

$$m'I \gg c^2 m^2 \tag{7A}$$

$$I_d \gg K_{\dot{\theta}} cm \tag{7B}$$

$$kI \gg \left| mcF - K_{\theta} cm \right| \tag{7C}$$

Assumption 7A is automatically satisfied by the SEP spacecraft physical characteristics. Assumptions 7B and 7C are a function of system gains and have to be verified. These assumptions modify Equation 6A to the following

$$S^4 m'I + S^3 Id + S^2 kI + SK_{\dot{\theta}}F + K_{\theta}F = 0 \tag{8}$$

Construction of Routh's parameters provide

$$m'I \qquad kI \qquad K_{\theta}F$$

$$I_d \qquad K_{\dot{\theta}}F$$

$$\frac{kd\dot{I} - m' K_{\dot{\theta}}F}{d} \qquad\qquad K_{\theta}F$$

$$\frac{\left(\dfrac{kdI - m'K_{\dot{\theta}}F}{d}\right) K_{\dot{\theta}}F - IdK_{\theta}F}{\left(\dfrac{kdI - m'K_{\dot{\theta}}F}{d}\right)}$$

If we restrict

$$kdI \gg m'K_{\dot{\theta}}F \tag{9}$$

it is observed that Routh's stability criteria are satisfied if

$$kK_{\dot{\theta}} > dK_{\theta} \tag{10}$$

For example, choosing parameters

$m = 2.5$ slugs

$I = 5,000$ slug-ft^2

$c = 2.0$ ft

$d = 1.0$ lb-sec/ft

$k = 2.5$ lb/ft

$K_{\dot{\theta}} = 50$

satisfies automatically the inequalities in Equations 7A, 7B, 7C, and 9.
If, in addition, the position gain is restricted to $K_\theta < 125$, stability is
assured.

In employing Routh's criteria here it is demonstrated that the basic
control concept is unstable, and shown that stability may be achieved by
impeding translator motion with damping and stiffness. The usefulness of
Routh's criteria is, however, limited to simple systems due to the increas-
ing complexity of the Routhian parameters. In addition it gives no measure
of performance. Having established stability criteria by Routh's procedure
it is possible to evaluate both stability and performance using root-locus
techniques. To do this, Equation 6A modified to accept a translator forcing
function $B = [-K(S + a)\theta] / (S + b)$ is rewritten as

$$-1 = \frac{K(S+a)(-cmS^2 + F)}{S^2(S+B)\left[S^2(m'I - c^2m^2) + SId + (mcF + kI)\right]} \tag{11}$$

The resulting root-locus plot shown in Figure 9-16 C indicates that the
lead-lag network has allowed more latitude in placing the translator roots
while maintaining stability. It is possible with the combination of added
translator stiffness and damping and a lead-lag network to achieve reason-
able system damping with the rigid spacecraft dynamics (no body flexibility).
It should be noted that there may be other methods of compensation to
achieve satisfactory system performance.

The addition of flexible appendages to the spacecraft adds another
degree of complexity to the equations of motion. The determination of
stability criteria by an analytical method becomes more difficult. The

equations of motion for one flexible appendage and one bending mode are similar to Equations 1A and 1B with additional terms plus a bending equation.

$$I\ddot{\theta} + cm\ddot{\xi} - S_1\ddot{\eta} = F\xi$$

$$mc\ddot{\theta} + m'\ddot{\xi} + d\dot{\xi} + k\xi = B$$

$$-S_1\ddot{\theta} + \ddot{\eta} + 2\delta_1\sigma_1\dot{\eta} + \sigma_1^2\eta = 0 \qquad (12)$$

The subscripts refer to the first bending mode with η representing the appendage modal coordinate, S_1 the appendage generalized inertia, δ the damping ratio and σ the bending mode frequency. As before B, the control law will be assumed to be of the form:

$$B = -K\left(\frac{S + a}{S + b}\right)\theta$$

The resulting differential equation in root-locus form is

$$-1 = \frac{K(F - cmS^2)(S^2 + 2\delta\sigma S + \sigma^2)(S + a)}{S^2\left| \qquad\qquad \middle| (S + b) \right.}$$

$$\left| \quad \right| = S^4\left[(I-S_1^2)\,m'-c^2m^2\right] + S^3\left[2(Im')\delta\sigma + d(I-S_1^2) - 2(c^2m^2)\delta\sigma\right]$$

$$+S^2\left[m'I\sigma^2 + 2Id\delta\sigma + k\,(I-S_1^2) -cm\,(cm\sigma^2-F)\right]$$

$$+S\left[Id\sigma^2 + 2kI\delta\sigma +2\,F\delta\sigma\,cm\right] + \left[Ik\sigma^2 + Fcm\,\theta^2\right] \qquad (13)$$

The physical characteristics of a large spacecraft make certain assumptions valid. These are

$$c^2m^2 << (I-S_1^2)$$

$$2c^2m^2\delta\sigma << 2Im'\delta\sigma +d\,(I-S_1^2)$$

$$-cm(cm\sigma^2 -F) << m'I\sigma^2 + 2Id\delta\sigma + k(I-S_1^2)$$

$$2F\delta\sigma\,cm << Id\sigma^2 + 2kI\delta\sigma$$

$$Fcm\sigma^2 << Ik\sigma^2 \qquad (14)$$

Verification of these assumptions has been accomplished using SEP space-craft characteristics. In each case the neglected parameter was at least four orders of magnitude smaller than the remaining parameters. The resulting denominator of the differential equation in root-locus form can also be factored:

$$-1 = \frac{K(F-cmS^2)(S+a)(S^2 + 2\delta\sigma S + \sigma^2)}{S^2(m'S^2 + ds + k)(S+b)S^2 + \dfrac{2\delta\sigma S}{\left(1-\dfrac{S_1^2}{I}\right)} + \dfrac{\sigma^2}{\left(1-\dfrac{S_1^2}{I}\right)}} \tag{15}$$

The first group of terms may be recognized as the rigid-body terms of Equation 11 with the assumptions of Equation 14. The second group of terms is the lead-lag network and the third group of terms is the bending equations. The root locus for the system represented by Equation 15 is shown in Figure 9-16D. There is little similarity between the root locus with bending and the rigid-body root locus because the bending poles rather than the translator poles go unstable. It is felt that variations in parameters (moving of pole locations) could cause the translator poles to go unstable rather than the bending poles but there is no obvious performance advantage to doing this. Again it should be noted that there may be other methods of compensation to achieve satisfactory performance. With the lead-lag compensation studied a great deal of latitude exists in selecting parameter values. Regardless of the type of compensation used, the two poles at the origin make the system operating point near the origin which would indicate low frequencies associated with control. This, however, should be expected from a system with extremely low control torques. These low frequency oscillations may determine the absolute attitude accuracy which is possible.

It has been shown that it is possible to stabilize the SEP spacecraft with a translator control system and achieve satisfactory performance. System dynamic operation characteristics are primarily determined by the roots coming from poles at the origin which means the operating frequency will always be low.

The above analysis represents initial thinking concerning translator control. Although it provided a fairly extensive analysis of the translation "tail-wags-dog" effect, it failed in other respects. At that time the complete system dynamics had not been specifically identified. What is alluded to above as actuator dynamics results as a natural consequence of the system exhibiting a large natural frequency; motor dynamics were not included. The following paragraphs relate the analysis above with what has been identified since that investigation. A block diagram is recorded

first that is a representation of a planar translator control loop: a representation in terms of elements which may be mechanized in a digital simulation program. For example, the stepper motor is represented by a limiter, a gain, an integrator, and a quantizer. The former represents a restraint on the maximum achievable rate of the translator, while the latter emulates the discrete motion of the stepper matrix.

K_θ – VOLTS/RADIAN

K   – STEPS/VOLT-SEC

K_m – IN./STEP

E_L – MAXIMUM STEP/SEC
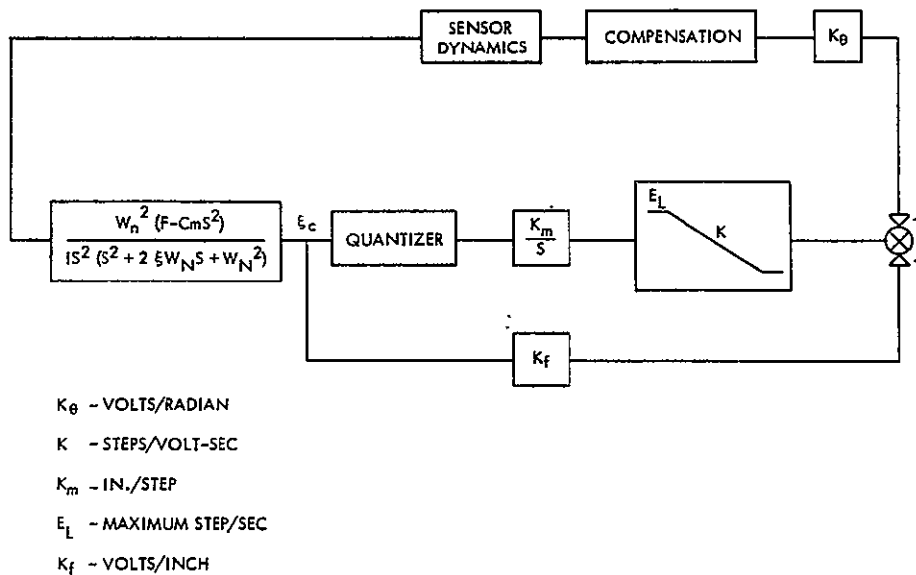
K_f – VOLTS/INCH

Figure 9-17.   Translator Control Block Diagram

$K_\theta \sim$ volts/radian

$K \sim$ steps/volt-sec

$K_m \sim$ in./step

$E_L \sim$ maximum step/sec

$K_f \sim$ volts/inch

The dynamics block, (the transformation between ξ_c and θ) results from combining the translator equation

$$mc\ddot{\theta} + m'\ddot{\xi} + d\dot{\xi} + k\xi = k\xi c \tag{16}$$

with the linearized vehicle equation

$$I\ddot{\theta} + cm\ddot{\xi} = F\xi \tag{17}$$

where the term ξ_c has been introduced for convenience (previously the variable B equal to $k\xi_c$ was employed). It is also assumed that

$$I >> c^2 m$$

$$I\omega_n^2 >> Fc \tag{18}$$

which are both easily satisfied for the SEP spacecraft.

For the first approximation we now neglect the actuator dynamics, which represents a departure from the earlier point of view. (Justification for this assumption is not provided and indeed without actuator damping for a non-minimum phase system it might be difficult to accept, but we shall proceed on this basis recognizing its shortcomings.) Accepting this and neglecting nonlinearities the system under consideration becomes:
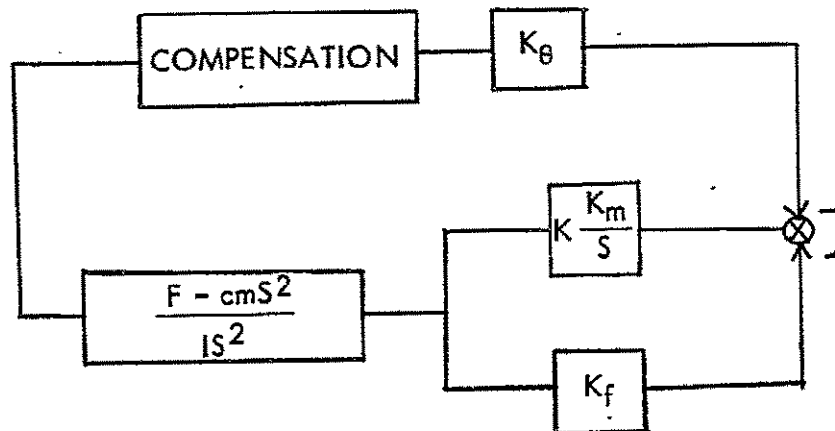
Figure 9-18. Simplified Translator Control Block Diagram

with the system uncompensated the characteristics equation takes the form

$$\tau_m S^3 + (1-K_0) S^2 + \frac{K_0 F}{cm} = 0, \quad K_0 = \frac{cm K_\theta}{IK_f}, \quad \tau_m = \frac{1}{K K_m K_f} \tag{19}$$

which is unstable by inspection independent of the value of K_0.

If a simple lead compensation of the form $(\tau_1 s + 1)/(\tau_2 s + 1)$ is provided, the characteristic equation is altered accordingly

$$\tau_m \tau_2 S^4 + \left[(\tau_m + \tau_2) - K_o \tau_1\right] S^3 + (1 - K_o) S^2 + \frac{K_o F \tau_1}{cm} S + \frac{K_o F}{cm} = 0 \qquad (20)$$

If $\tau_m + \tau_2 > K_o \tau_1$ and $K_o < 1$, then asymptotic stability appears plausible.

Modification of the above equation to a root-locus formulation provides

$$1 = \frac{K_o (S^2 - F/cm)}{S^2 (\tau_m S + 1)} \left(\frac{\tau_1 S + 1}{\tau_2 S + 1}\right) \qquad (21)$$

suggesting one or the other of the two loci exhibited below (not to scale)
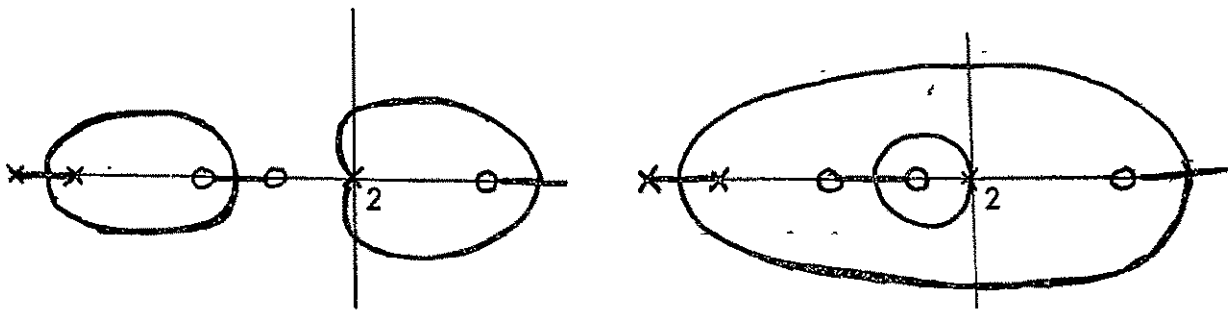
Figure 9-19.   Root Locus Plot With Motor Dynamics

The locus on the right has been verified analytically using the values below:

$$\left.\begin{array}{l} \tau_1 = 50.0 \\[2mm] \tau_2 = 5.0 \\[2mm] \tau_m = .2 \end{array}\right\} \qquad \text{arbitrarily set}$$

$$\left.\begin{array}{l} c = 2.0 \\[2mm] m = 2.5 \\[2mm] F = .025 \end{array}\right\} \qquad \text{fairly realistic}$$

9-50

The locus on the left, although not analytically verified, can be easily visualized as a possibility. In either case a region of asymptotic behavior is observed. For the case described above, instability occurs for $K_o > .104$ which violates the first of the inequalities cited earlier. Adjusting the gain to accommodate a 6 db (factor of 2) gain margin, i.e., $K_o \sim .05$, the characteristic roots were observed to be approximately

$$\lambda_1 = -0.4$$

$$\lambda_2 = -2.29$$

$$\lambda_3, \lambda_4 = -0.00643 \pm 0.0152$$

The complex pair clearly dominating and indicating a damped natural frequency of 0.015 rad/sec and a damping factor of approximately 0.4—not impressive but nevertheless acceptable.

To reiterate, it has been demonstrated that the translator concept is in itself unstable requiring some form of compensation. A simple lead compensator appears satisfactory providing adequate performance.

EFFECTS OF SOLAR PANEL FLEXIBILITY

A natural question which arises when discussing space vehicle dynamics is that of flexibility effects. A reasonable assumption for the SEP spacecraft is to assure total rigidity except for the solar panels. The classical approach, and a valid one, is to identify the natural frequencies of the flexible appendages and compare them with the rigid body natural frequencies. If a wide separation, an order of magnitude, exists, then it may be concluded that the effects of the flexible appendages are minor and may be disregarded in preliminary analysis. Such a condition is sufficient (though not necessary) to assert that dynamic coupling is not of concern. A luxury of this nature is afforded by the SEP spacecraft in that operating frequencies on the order of 0.02 rad/sec (.003 H_z) are expected, whereas the lowest natural frequency of the GE roll-out type solar panel approximately 0.25 rad/sec (.04 H_z). Due to the rather unconventional control concept offered by the movable translator, a fairly extensive study of solar panel flexibility was conducted. These effects were discussed above where the control concept is analyzed with and without flexibility utilizing classical root-locus techniques. It is shown above that rigid-body analysis is of primary concern and that the introduction of flexibility does not seriously degrade stability or performance.

The root-locus approach permits rapid determination of operating gains and a fair estimate of performance but fails to provide response characteristics to expected excitations. To satisfy this need a flexible body digital computer program was developed under North American Rockwell internal research and development programs. Some preliminary results utilizing this program have been achieved and are shown below. Here, however, these results must be accepted in the vein of a demonstrated capability. An extensive analysis was not possible. For example, the results shown are for two solar panels normally extended from the spacecraft (no canting of the solar panel). The panels are also assumed to bend only in the direction normal to their surfaces.

The equations of motion of the flexible body digital computer program referred to above were written utilizing the growing hybrid coordinate approach.* The program accommodates a rigid despun body with attached flexible appendages, a rigid symmetrical rotor, a two-degree-of-freedom movable translator for attitude control, and stepper motor nonlinearities. The inclusion of the rotor is to provide capability of this computer program for the support of other efforts. In its present state of development the program will accept as many as four flexible appendages but the total number of modal coordinates (acceptable appendage discrete frequencies) is limited to twelve.

An example set of results is shown in the set of Figures 9-20 through 9-29 which exhibit the response to a small initial displacement in each of the movable translators. Figure 9-20 shows angular acceleration, angular rate, and angular position about one of the axis controlled by the movable translator. Similar time histories for the other axis are shown in Figure 9-23. The resulting phase planes (angular rate verses angular position) are shown in Figures 9-21 and 9-22. Figures 9-27 and 9-25 exhibit relative translator acceleration, rate, and position. The first three modal coordinates for each of the solar panels are shown in Figures 9-26 and 9-27. Figures 9-28 and 9-29 show the deflection at the tip of each solar panel in response to the initial translator displacements. That the first two traces of Figures 9-28 and 9-29 are zero for all time results from the assumption of flexibility only in the direction normal to the surface of the solar panels.

---

*Described in detail in a completely general fashion in "Dynamics and Control of Flexible Space Vehicles," P. Likins, JPL TR 32-1329.
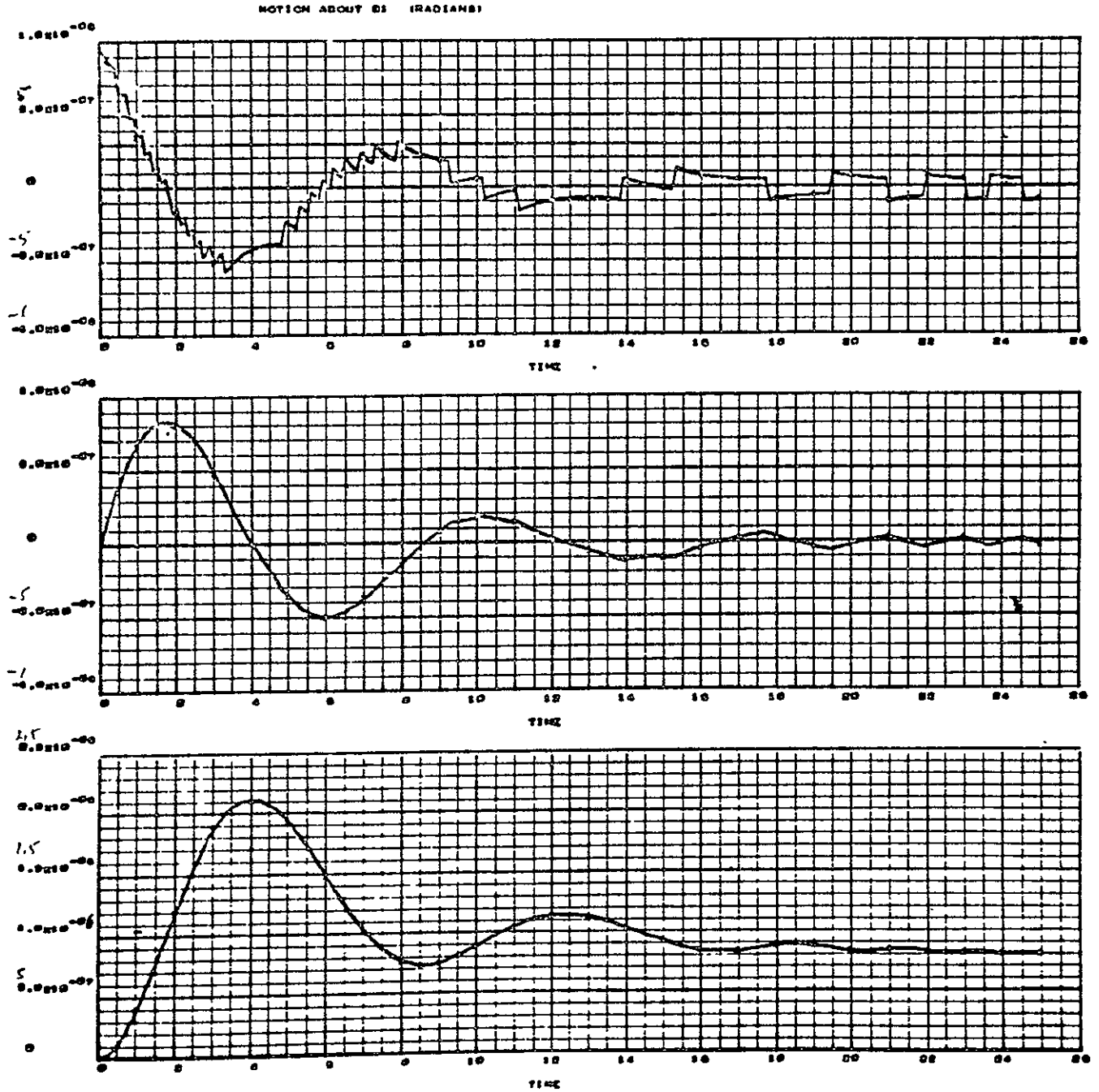
Figure 9-20. Sample Computer Run A
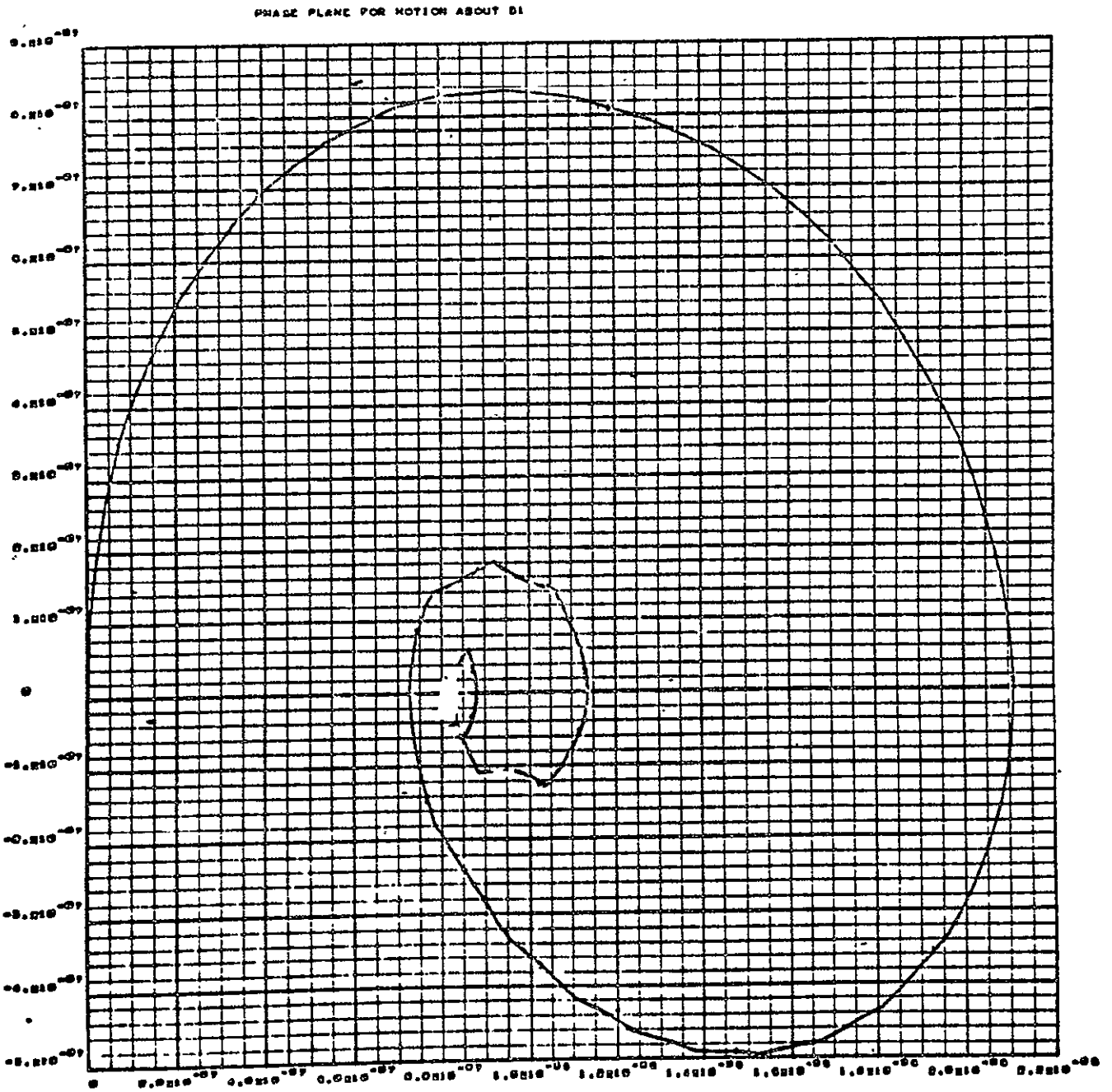
Figure 9-21. Sample Computer Run B

TRANSLATOR MOTION IN 82 DIRECTION (feet)
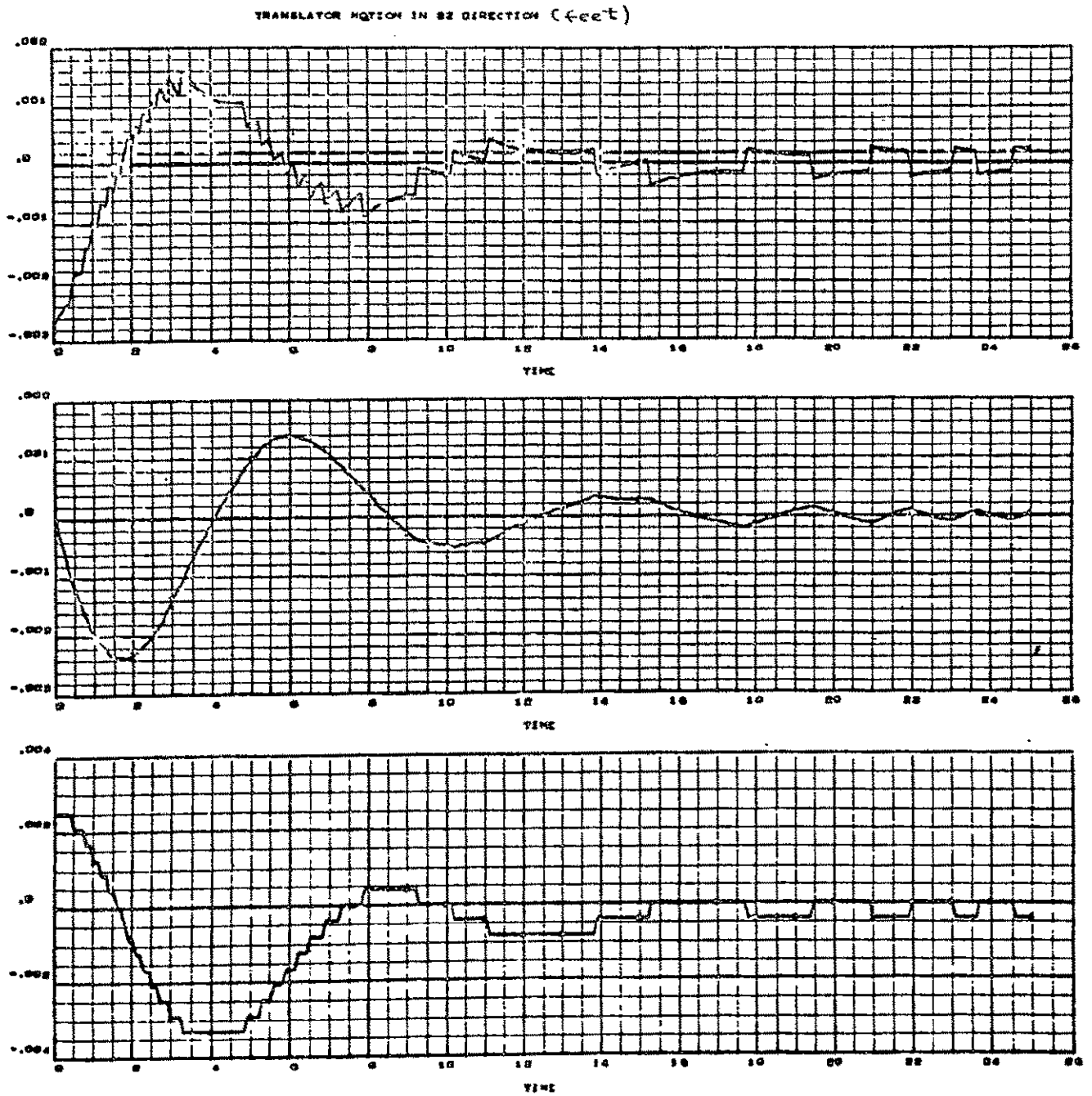
Figure 9-22. Sample Computer Run C

MOTION ABOUT 8Z (RADIANS)
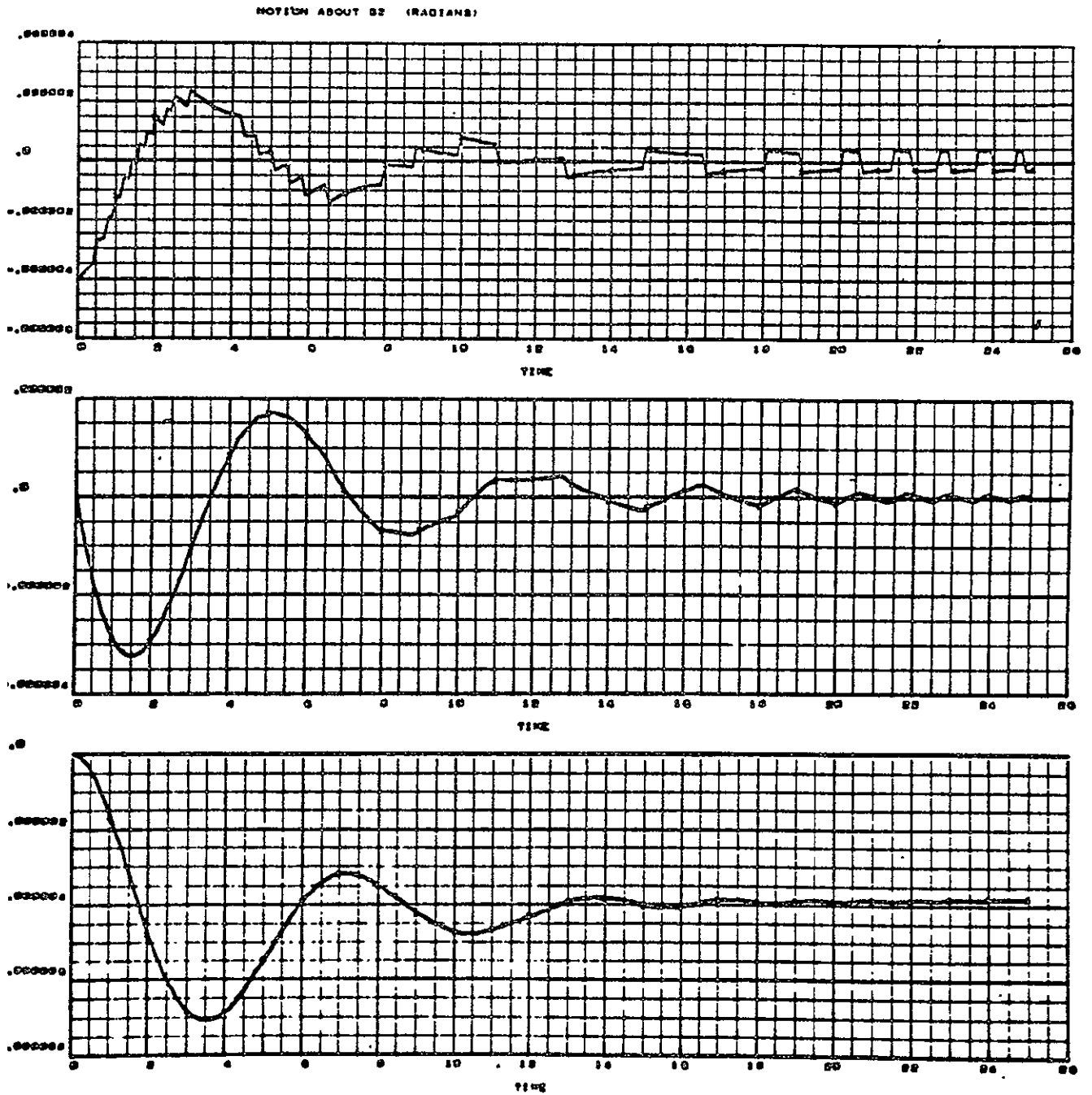
Figure 9-23.   Sample Computer Run D
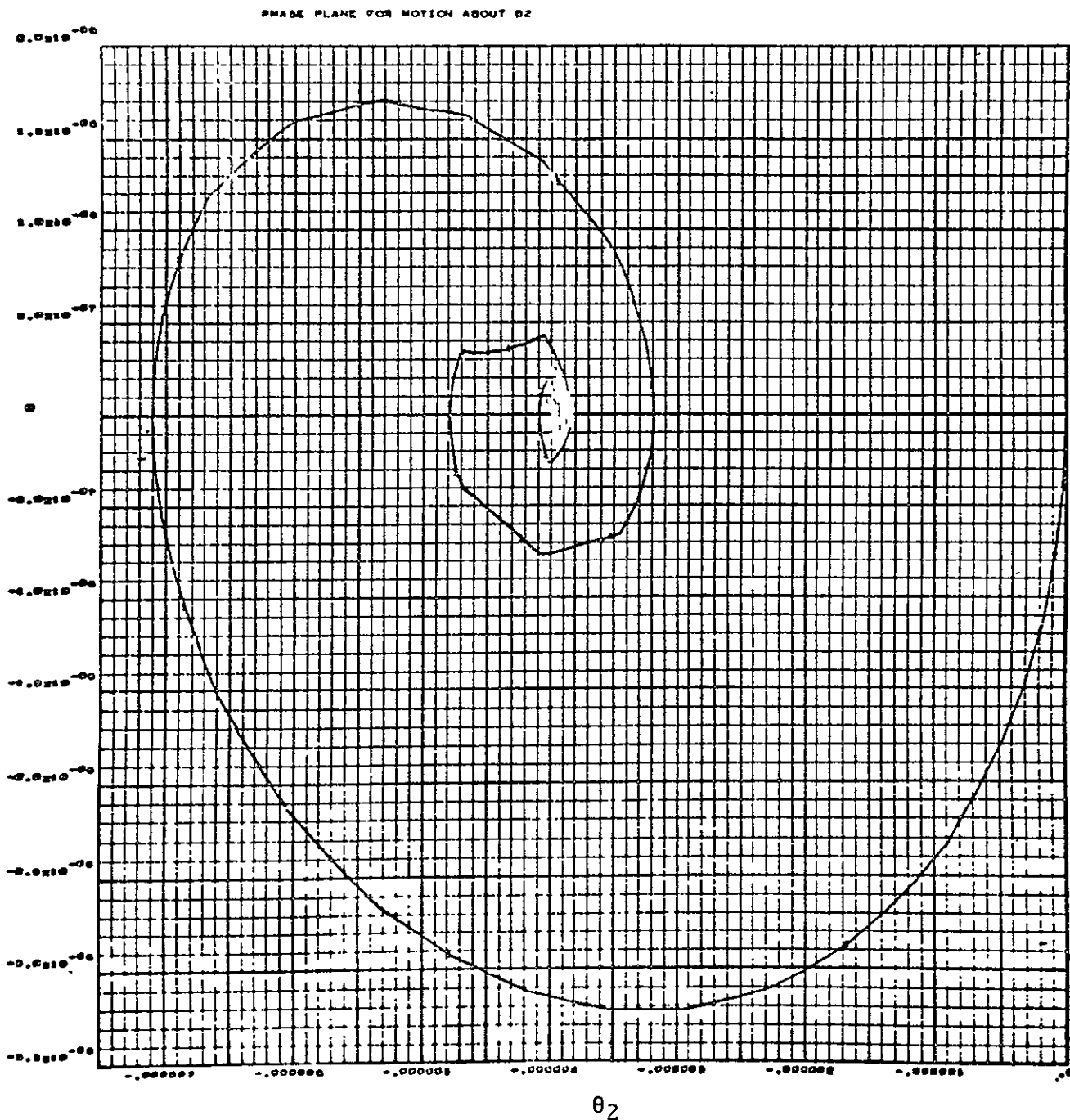
Figure 9-24.   Sample Computer Run E

TRANSLATOR MOTION IN 81 DIRECTION (feet)
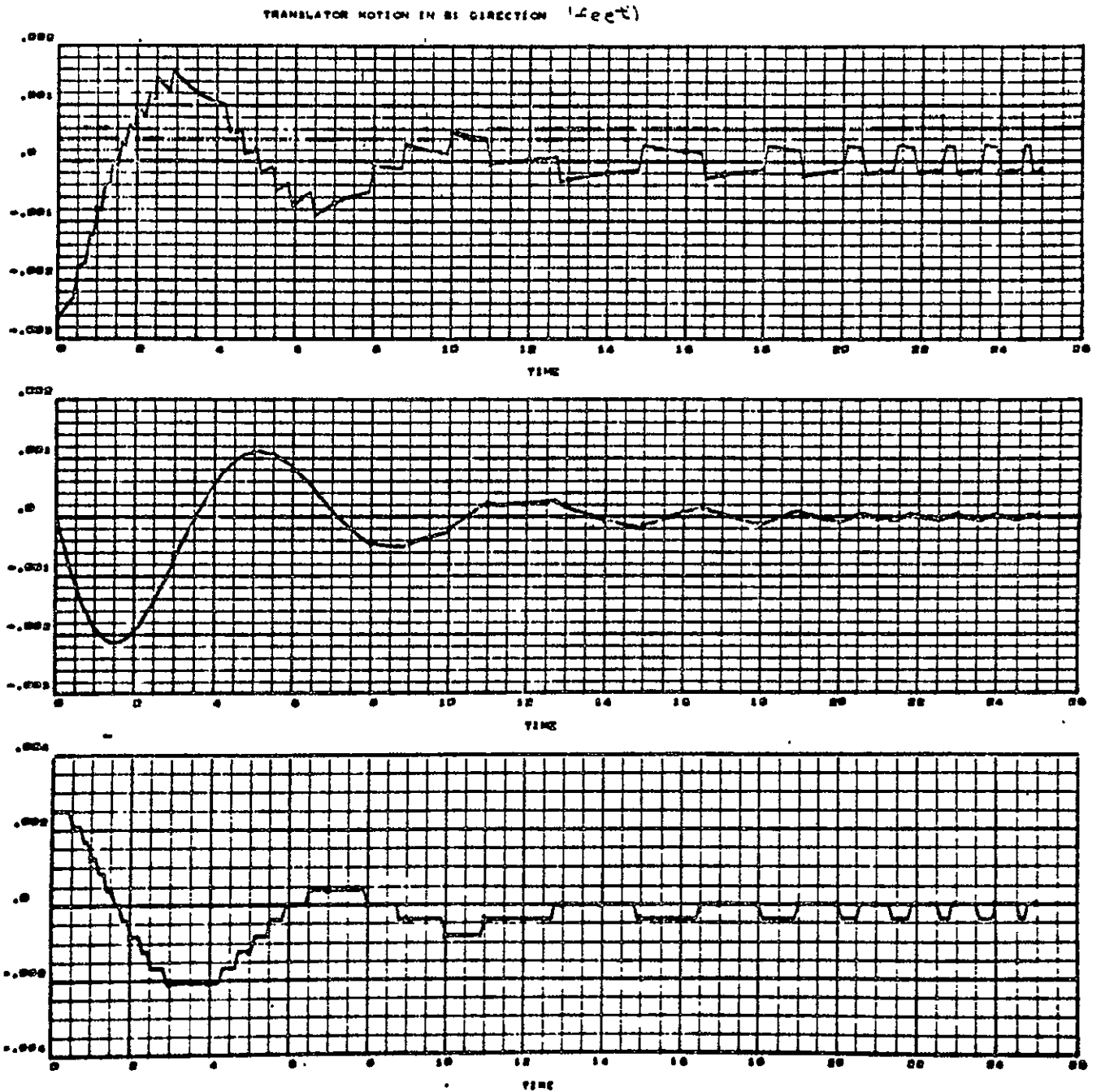
Figure 9-25. Sample Computer Run F

MODAL COORDINATES OF   "A" (FEET)
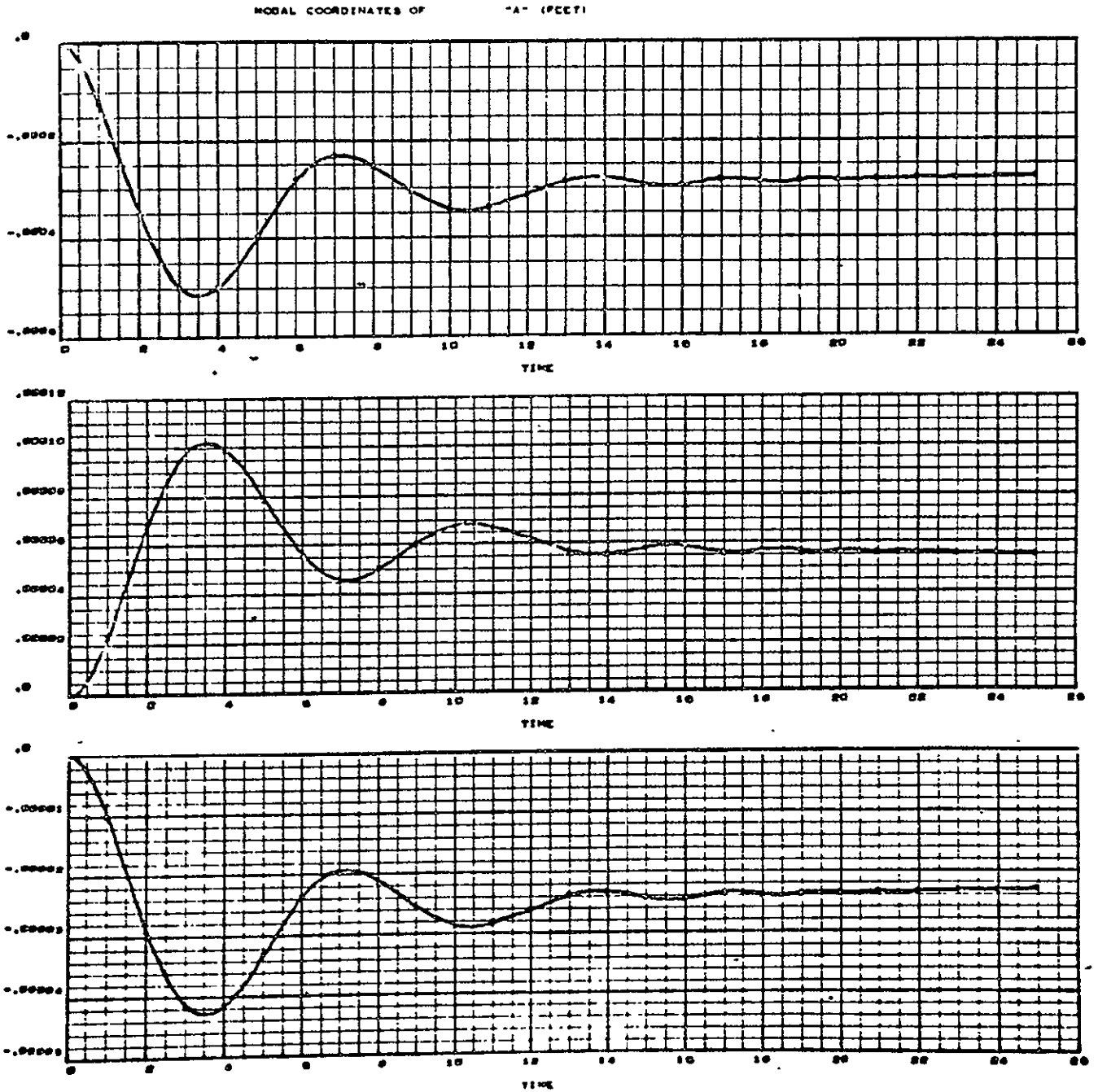
Figure 9-26.   Sample Computer Run G

SD 70-21-2
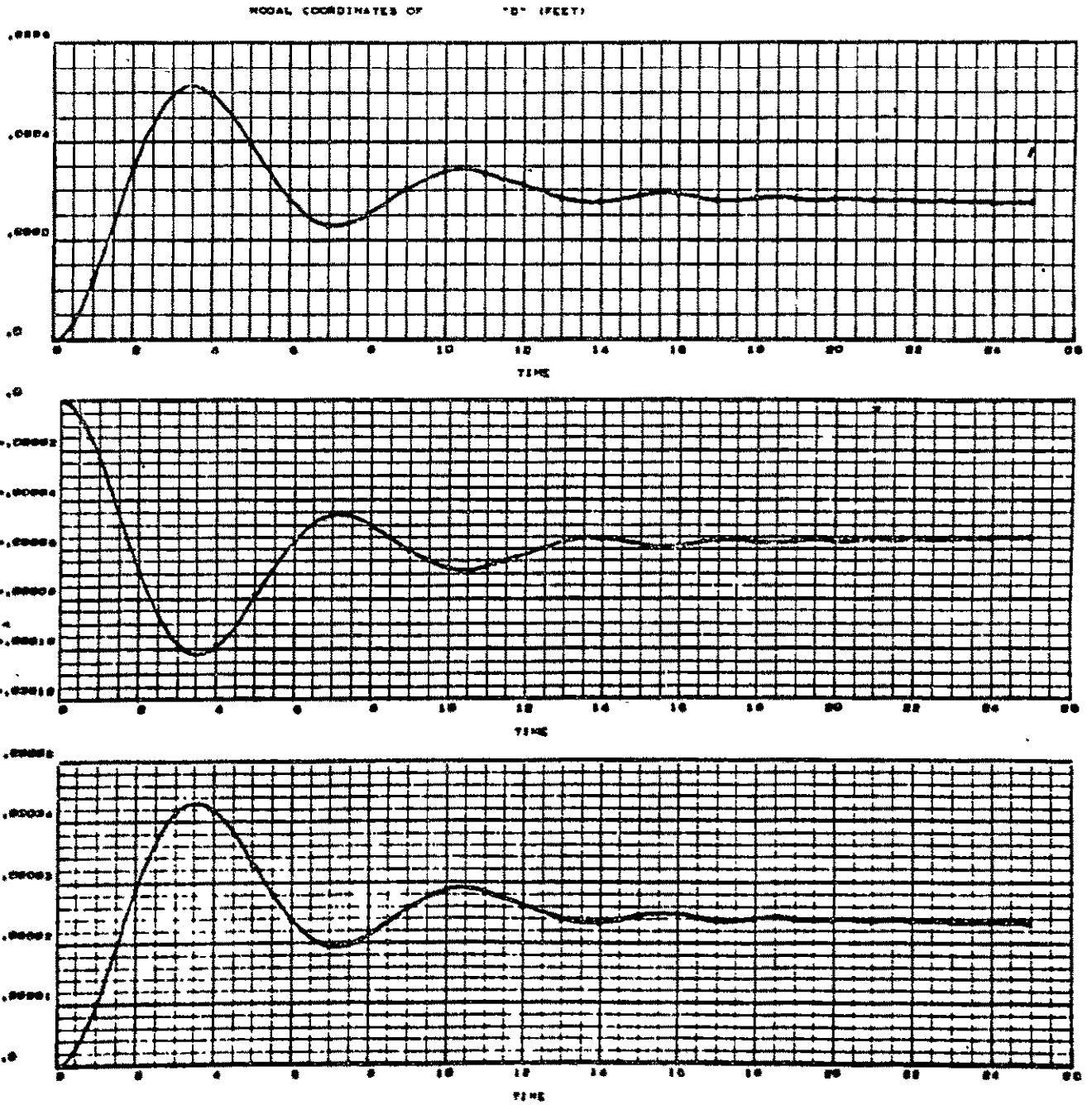
Figure 9-27.   Sample Computer Run H

DISPLACEMENTS AT TIP OF PANEL "A" (INCHES)
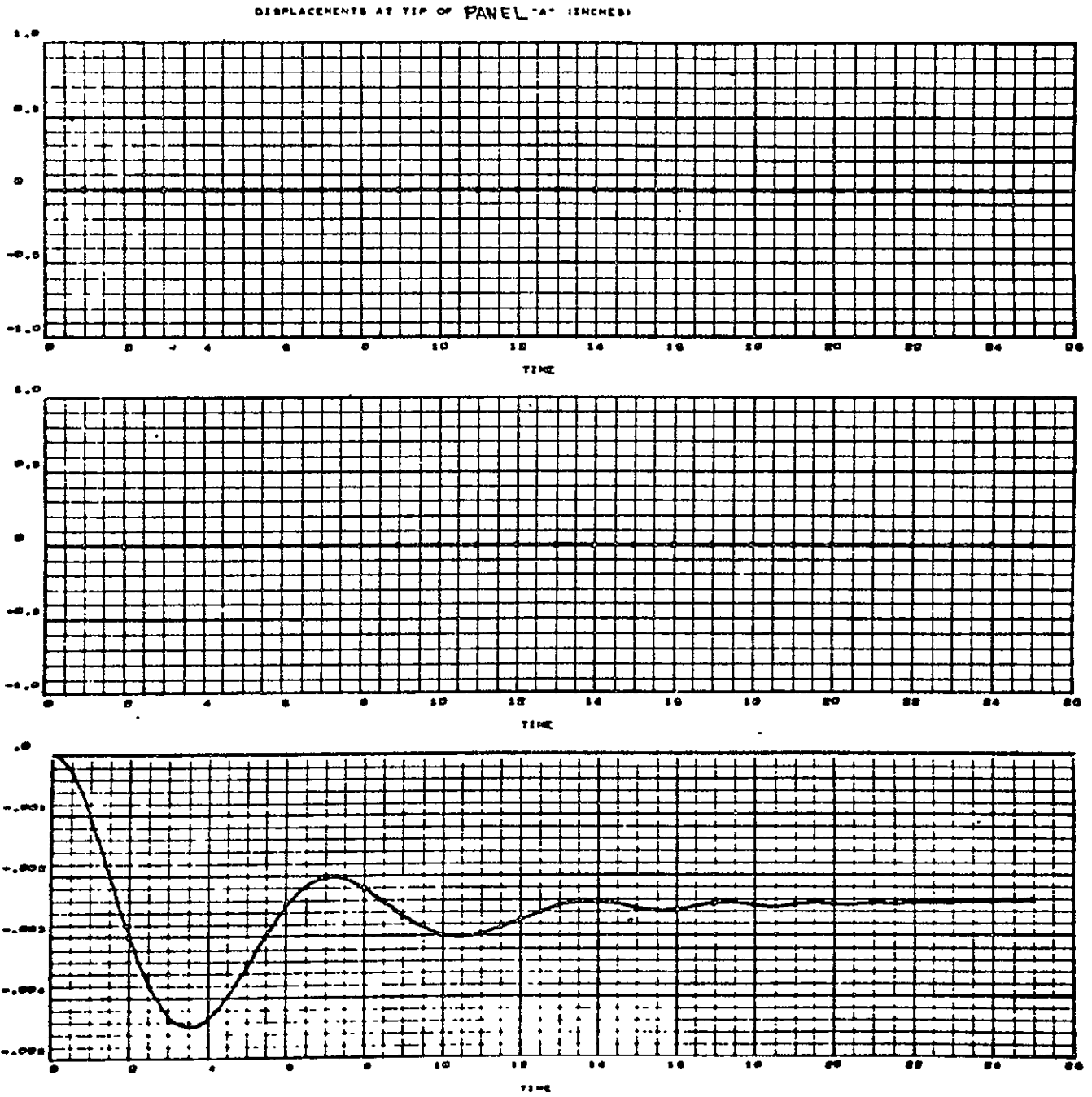
Figure 9-28.   Sample Computer Run I

DISPLACEMENTS AT TIP OF PANEL "D" (INCHES)
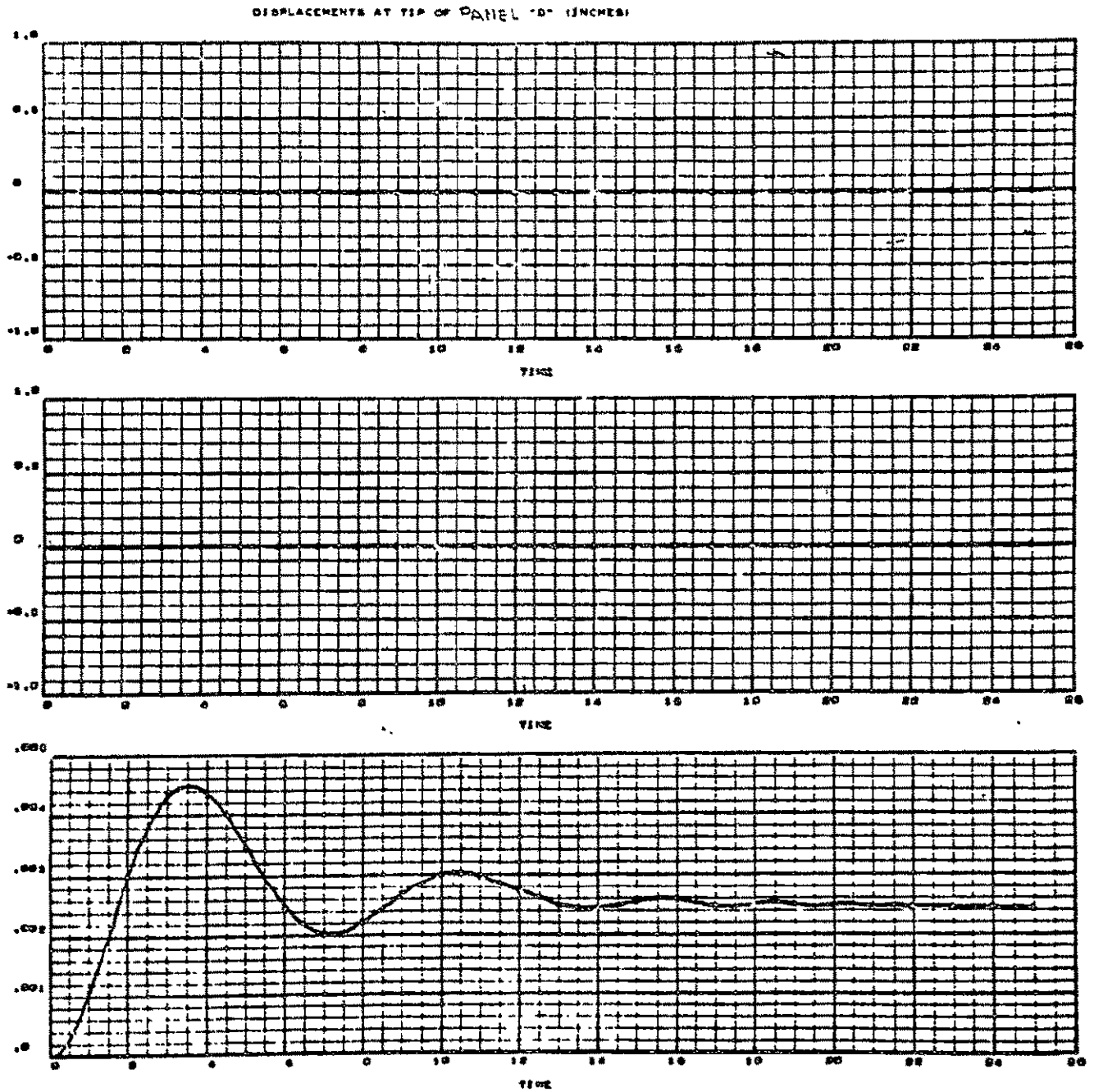
Figure 9-29.   Sample Computer Run J

10 THERMAL CONTROL SUBSYSTEM

THERMAL CONTROL DESIGN REQUIREMENTS

The object of the SEP thermal control design is to ensure long-life operation of all components by maintaining their temperature within design limits. The design approach employed uses standard or state-of-the-art techniques to achieve a low cost, optimum combination of passive control (insulation blankets, structural isolators and optical coatings) and active control (bimetallic louvers and thermostatically controlled heaters).

The principal factors influencing the design are as follows:

1. Large variations in solar intensity as the spacecraft traverses from 1 to 3.5 AU

2. Large amounts of energy dissipated by the electric propulsion subsystem during thrust

3. Transient thermal conditions experienced during sun acquisition and solar panel deployment before equipment operation

4. Spacecraft orientation requirements (±30 with respect to sun normal)

Under these operating conditions, it becomes apparent that it is desirable to isolate temperature-sensitive components from the changing solar environment, that effective use of solar energy irradiation is restricted to near earth operations when the spacecraft is operating on battery power, and that electrical power dissipated in the form of thermal energy by the spacecraft subsystems be used during the thrust and coast phases of the mission.

A primary consideration influencing the thermal subsystem design is the operational concept of rotating the spacecraft such that the power conditioner and control (PCC) and equipment compartment radiators face the sun during the mission flight time from launch vehicle separation to sun acquisition maneuver initiation. This eliminates the requirement for something in excess of 100 watts of heater power for each PCC during this portion of the mission.

Evaluation of the thermal control analysis resulted in the use of a combination of shields and blankets, surface coatings, louvers and heaters to provide adequate thermal control of the spacecraft during all phases of the mission. A total system weight of 14.55 kilograms (32 pounds) was required as given in Table 10-1.

Table 10-1. Weight Estimates of the
Thermal Control System

Component	Weight	
	Kg	(lb)
Shields and blankets	6.36	(14)
Surface coatings	1.82	(4)
Louvers	4.10	(9)
Heaters	2.27	(5)
Total	14.55	(32)

THERMAL REQUIREMENTS

The thermal requirements of the spacecraft electronics and science payload are given in Table 10-2 and were chosen to ensure long-life operation of all components.

SELECTED CONFIGURATION

The essential feature of the selected design concept is that the subsystems requiring temperature control are thermally independent and are isolated from both the spacecraft structure and the external environment by superinsulation blankets, structural isolators, and solar reflectors. Active techniques such as bimetallic louvers (equipment compartment) and thermostatically controlled heaters (science payload) are used where necessary. The subsystems requiring thermal control are shown in Figure 10-1.

10-2

SCIENCE
$0 \leq Q \leq 78W$
$-40 \leq T \leq 105$
NON-OPER
$0 \leq T \leq 32$ OPER

SPACECRAFT
ELECTRONIC EQUIP.
$130 \leq Q \leq 300W$
$40 \leq T \leq 120$ F

POWER CONDITIONER
$136 \leq Q \leq 273$
$-50 \leq T \leq 140$ F

THRUSTER

OPERATING
$32° \leq T \leq 500$ F

MERCURY TANK
$86 \leq T \leq 212$ F OPER
$-22 \leq T \leq 212$ NON-OPER

SOLAR ARRAY
$-200 \leq T \leq 200$
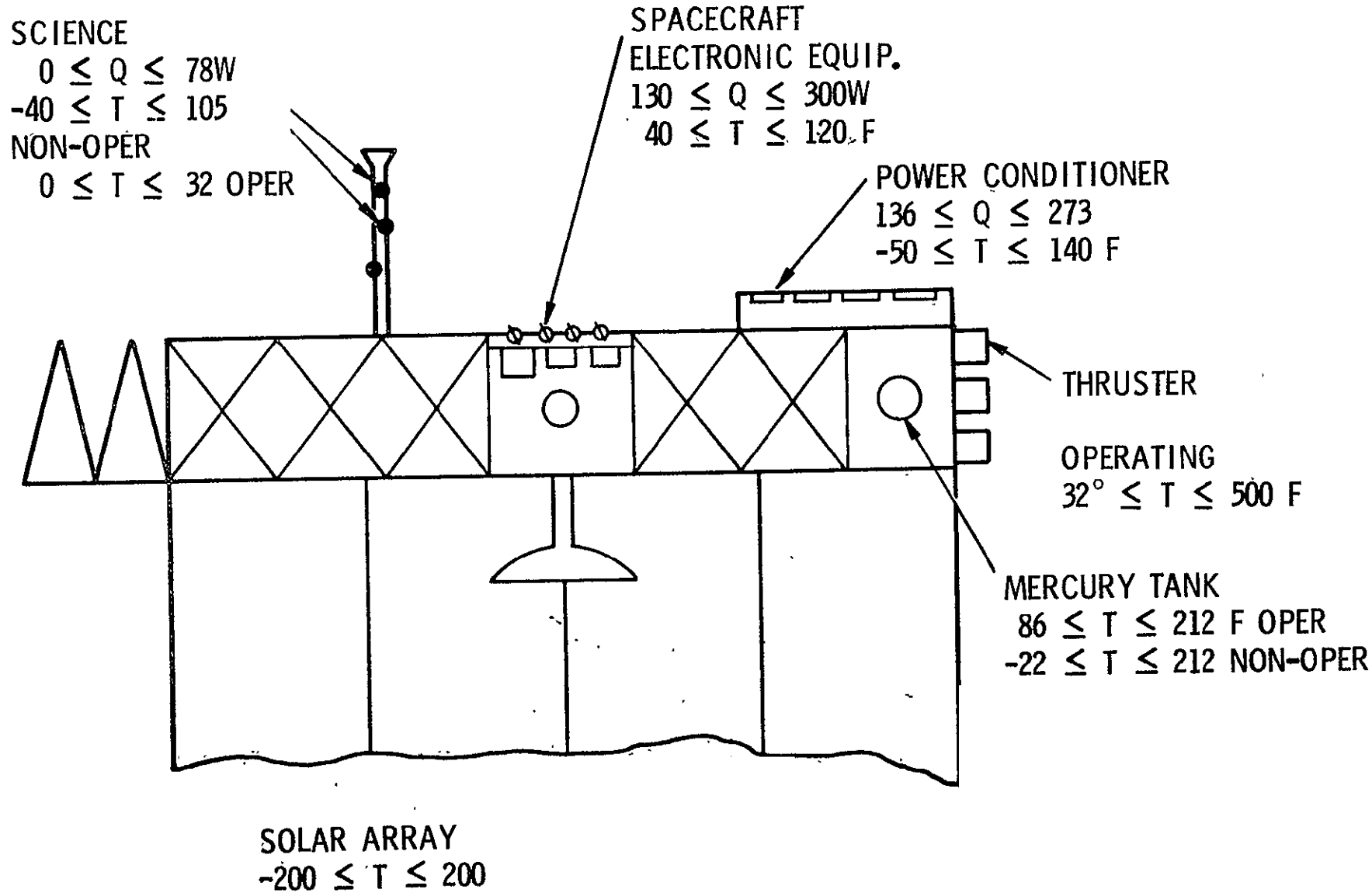
Figure 10-1. Major Subsystems Requiring Thermal Control

Space Division
North American Rockwell

Table 10-2. Equipment Temperature Limits

Subsystem	Temperature Limits (°F)	
	Non-Operating	Operating
Spacecraft electronics	40 to 120	40 to 120
Power conditioner	-50 to 140	32 to 140
Science electronics	-40 to 120	0 to 32
Sun sensor	-60 to 145	-60 to 120
Star tracker	-20 to 145	-20 to 120
Attitude control jets	-40 to 160	0 to 160
Mercury tank	-22 to 212	86 to 212
Thrusters		0 to 500

ELECTRONIC COMPARTMENT

The electronic equipment is mounted on an aluminum mounting platform, thermally isolated from the spacecraft structure by gold-coated fiberglass mounts (Figure 10-2). To minimize thermal gradients, the equipment is arranged to provide uniform heat dissipation within the compartment. All components are also painted black to maximize internal radiation coupling. Good thermal contact between the black boxes and the mounting platform is provided by use of a silicon rubber compound or equivalent. Five of the internal surfaces of the compartment are covered with 15 layers of aluminized mylar. Separation of the layers is provided by nylon netting. The outside surface of the compartment walls has a low α/ϵ to reflect the sunlight impinging on the surface early in life. This is necessary because the effectiveness of the blanket is less when higher external temperatures are experienced. Additional thermal isolation of the compartment is provided by insulating all feedlines and wire bundles where exposed to the outer environment. The outer surface of this insulation may be exposed to direct sunlight, and has a low α/ϵ to avoid overheating and damaging the insulating material as well as increasing the net heat flow into the compartment. The wire bundles and feed lines are attached to the structure by thermal isolators. Vent holes 0.25-inch in diameter are punched on 6-inch minimum centers in all layers except the outer teflon surface to allow trapped air to escape during launch.

Proper balance between thermal input and energy loss by radiation and conduction over the lifetime of the spacecraft cannot be maintained by passive means only. Some type of active control technique is required to

10-4
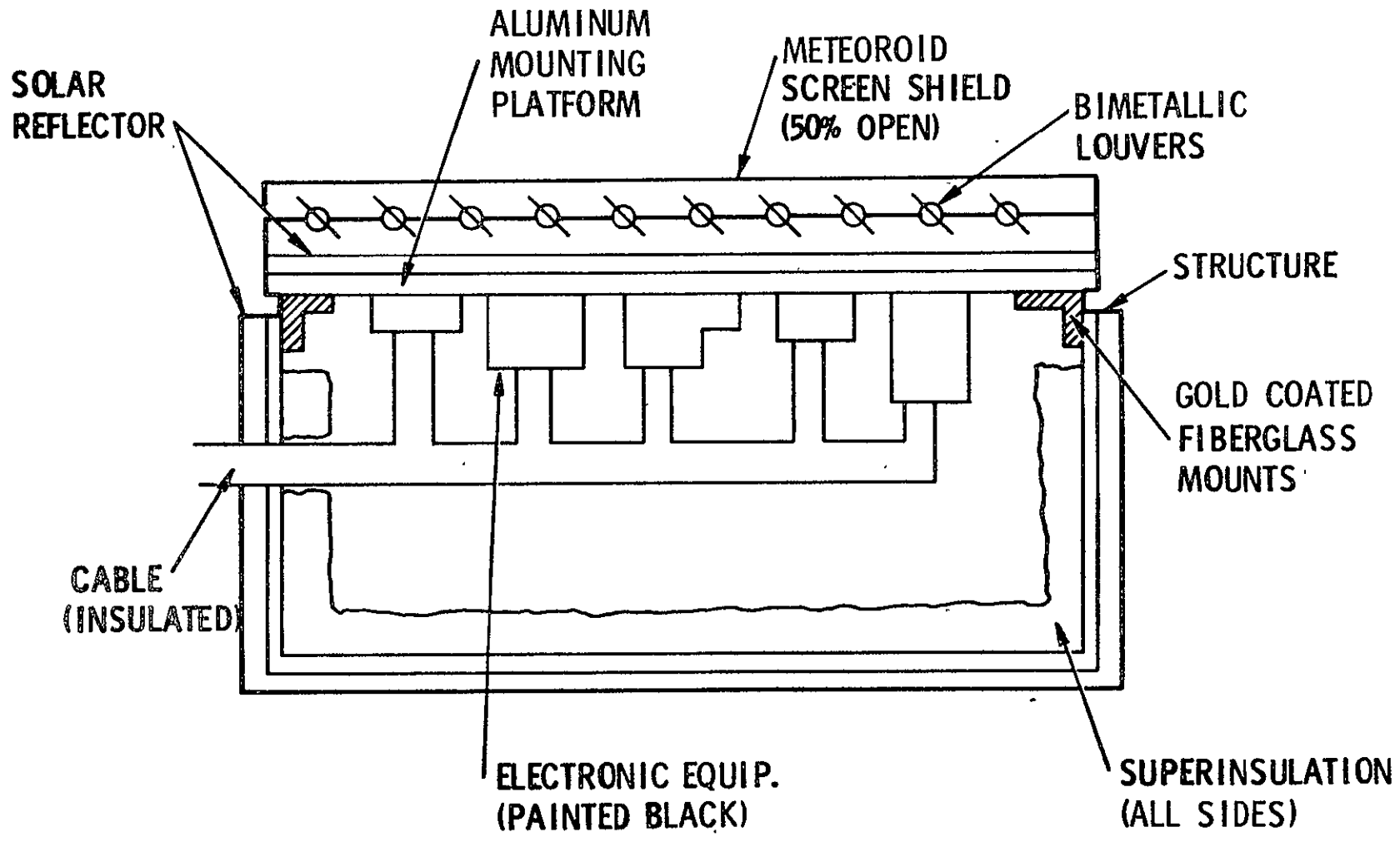
Figure 10-2. Equipment Compartment Thermal Control

regulate this balance. A system of bimetallic louvers has been selected because of its demonstrated reliability. The louver assembly is actuated by bimetallic coils, which are thermally coupled to the equipment mounting platform. The louvers are actuated individually in response to temperature changes in the mounting platform and are designed to provide 90 degrees rotation for a 30 F temperature change. When the compartment is 90 F, the louvers are full open. The louvers are closed when the compartment temperature drops to 60 F.

A meteoroid shield with 50-percent open area is used to protect the equipment compartment side containing the louvers against damaging penetrations. The adoption of this shield reduces the efficiency of the louvers by approximately 33 percent. The external surface of the shield is painted white to reduce solar input, while at the same time providing a high emittance surface. The outside surface of the mounting platform is also painted white to reflect solar energy passing through the shield during that phase of the mission prior to sun acquisition when the PCC is thermally controlled by solar irradiation.

POWER CONDITIONER AND CONTROL

The power conditioners are controlled passively (Figure 10-3). As with the equipment compartment, they are isolated from the structure by fiberglass mounts and superinsulation.

During injection when the spacecraft is powered by batteries, the power conditioners use solar energy for temperature control (Figure 10-4). During normal orientation of the spacecraft the panels view black space. Therefore, the outside surface has an α/ϵ equal to 0.6. As before, all wire bundles leaving the compartment are wrapped with superinsulation to reduce heat leakage. Each power conditioner is supplied with a 100-watt heater to maintain an adequate thermal environment when the unit is on standby.

SCIENCE PAYLOAD

The science payload consists of approximately 10 instruments mounted externally to the electronic compartment (Figure 10-1). The thermal environment of each is controlled independently by a combination of passive and active techniques. Passive control consists of structural isolators (fiberglass washers and bolts) and thermal blankets which enclose all surfaces of the box except the temperature control surface. In most cases the temperature control surface is selected to face black space during the thrust and cruise phases of the mission. All the thermal blankets consist of aluminized mylar separated by nylon net. The outside layers of the blanket are FEP teflon with the inside surface aluminized. Active control consists
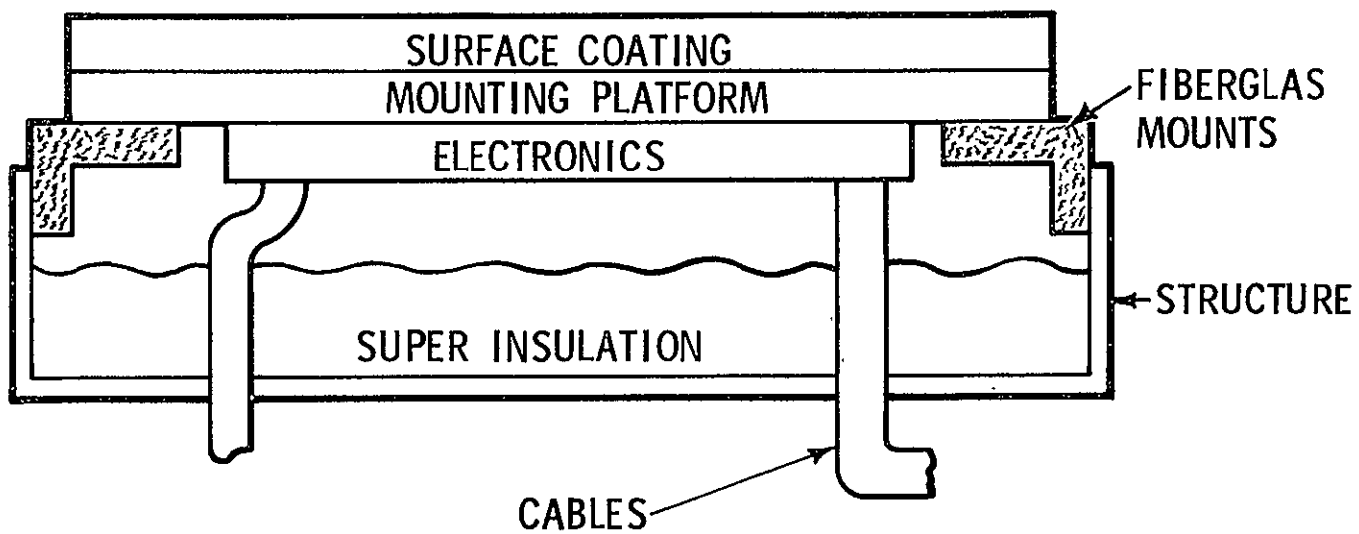
Figure 10-3. Thermal Control of Power Conditioner
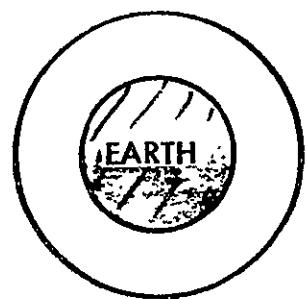
Figure 10-4. PCC Thermal Control Using Solar Energy

Table 10-3. Thermal Surface Coatings

Type	Location	α	ϵ
Inorganic black paint	Equipment boxes and mounting plate inside spacecraft electronic compartment; inner surface of meteoroid shield; baffles.	0.97	0.93
Z-93 white paint	Exterior surfaces of equipment compartment; outer surface of spacecraft electronics mounting platform.	0.17 to 0.35	0.92
Second surface mirror	Exterior compartment surfaces facing sun during thrust and cruise.	0.12	0.85
Cold coated tape	Fiberglass mounts	0.30	0.05
Polished aluminum	Inner surface of propulsion module.	0.10	0..05
Polished aluminum with chemical conversion coating	Basic spacecraft structure	0.10	0.10
Anodized aluminum	Power conditioner	0.26	0.43
Aluminized teflon FEP type A	Outside surface of all exposed thermal blankets	0.15	0.58
Pyrochrome paint	High gain antenna	0.73	0.79
Not selected	Science mounting plate		
Polished aluminum	Low gain antenna	0.10	0.05
Anodized aluminum	Faraday cup (TCS)*	0.25	0.47
Not selected	Cosmic ray spectrometer (TCS)	0.34	0.65
Not selected	Helium magnetometer (TCS)	0.34	0.65
Inorganic black paint	Particle spectrometer (TCS)	0.97	0.93
Gold plate	Attitude control jets**	0.4	0.07
Anodized aluminum	Star tracker (TCS)	0.28	0.55
Aluminum filled paints	Sun sensor (TCS)	0.23	0.20

*TCS - temperature control surface.
**The jet on the same side of the spacecraft as the power conditioner is coated with vacuum-deposited aluminum.

Table 10-4. Thermal Blankets

Description	Location
15 layers of aluminized mylar separated by nylon net	Inner wall of equipment compartment and power conditioners
8 layers of aluminized mylar separated by nylon net. The outer layer is aluminized teflon	Outside surfaces of science packages and star tracker Sisyphus baffle and electronics
12 layers of aluminized mylar separated by crinkling each layer of mylar outer layer is aluminized teflon	Sun sensors
3 layers of aluminized mylar separated by crinkling each layer and an outer layer of aluminized teflon	Exposed wire bundles and feed lines and antenna supports and specified areas of structure

STRUCTURE AND ANTENNA

The solid high gain antenna is covered with a high solar absorptance and high emittance paint. The purpose of the high absorption is to prevent the antenna from overheating the feed by reflected sunlight when the sun becomes incident along the parabolic axis. The high emittance is provided to avoid overheating the antenna. The antenna supports are covered with superinsulation (Tables 10-3 and 10-4).

All structure in the vicinity of the equipment compartment, power conditioners, and independently mounted components is insulated with super-insulation to minimize heat losses from these units. The remainder of the exposed structure consists of polished aluminum with a chemical conversion coating. Early in life when the spacecraft is subjected to incident solar energy this coating acts as a solar reflector to maintain the average structural temperature near room temperature. Near the end of life the low emittance of the surface minimizes the heat loss to space by radiation.

PROPULSION SUBSYSTEM

The mercury tank is located in the propulsion module for protection against meteoroid damage. The tank is isolated from the spacecraft structure by thermal isolators and from the propulsion module by shields (polished aluminum).

The thrusters are isolated from the spacecraft structure by structural mounts and by an aluminized kapton blanket.

The thrusters on standby will be maintained above the freezing temperature of mercury by the thermal energy from the operating thruster.

PERFORMANCE OF THERMAL CONTROL SUBSYSTEM

The thermal analysis of the equipment compartment and power conditioner is based on the parameters listed in Table 10-5.

Table 10-5. Equipment Compartment and Power Conditioners Data

Parameter	Equipment Compartment	Power Conditioner
Surface area (ft) (including edge area)	60	26
Number of cables	6	4
Effective emittance of superinsulation	0.01	0.01
Total conducting area of mounts (in.^{2})	12	6
Radiator area (sq ft)	10.6	11.25

An effective emittance of 0.01 was used in the analysis because actual losses from multilayer insulation always exceed theoretical values by a significant amount when the blanket is geometrically complex and contains outputs for structure, cabling, and feedlines.

The total calculated heat losses from the equipment compartment and the power conditioner at three points in the mission are given in Table 10-6, while the breakdown of the equipment compartment losses at 3.5 AU are given in Table 10-7.

Table 10-6. Total Losses

Subsystem	Total Losses (watts)		
	Thrust		Cruise
	1 AU	2 AU	3.5 AU
Spacecraft electronics	0	32.5	54.
Power conditioner	0	13.9	23.9

Table 10-7. Spacecraft Electronics
Maximum Heat Losses

Type	Heat Loss (watts)
Insulation	24.6
Wire bundles	9.0
Feedlines	6.0
Mounts	14.7
Total	54.3

The requirements for an active thermal control for the spacecraft electronics were established early in the analysis, when a passive system failed to maintain the equipment compartment within the proper bounds. The temperature of the spacecraft electronics exceeded the temperature limit of the equipment by 45 F during injection with normal orientation of the spacecraft (electronic compartment shaded) and by 60 F during cruise.

The most severe demands made on the thermal control system occur during injection, when the spacecraft is powered by batteries; thrust at 1 AU; and cruise at 3.5 AU.

BATTERY OPERATION

During battery operation, the equipment compartment is maintained between 75 and 85 F by the system of louvers which compensate for the loss of solar energy during injection when the equipment compartment becomes shaded. The power conditioners, which are passively controlled, however, experience a severe temperature drop (to -108 F). Approximately 100 watts of battery power are needed for heaters to maintain these units at 0 F.

By changing the orientation of the spacecraft so that the power conditioners view the sun during the early stages of flight when on battery power, the temperature of these units is maintained at 130 F. The equipment compartment now also views the sun but its temperature is increased only 15 F. An additional advantage of this orientation is a reduction in the temperature excursions of the power conditioners when the spacecraft is in the parking orbit (Figure 10-5). During sun acquisition and solar array deployment (2.75 hour duration planned), the thermal inertia of the equipment is sufficient to prevent excessive temperature drops (Figure 10-6). When power is available from the solar panels, it is supplied to heaters in the power conditioners, mercury tank, and thruster for preignition warmup. The power requirements of these heaters has not been established.

THRUST AND CRUISE

The hottest environment in the mission is encountered during thrust at 1 AU, where the maximum power is being dissipated by the spacecraft electronic and the propulsion subsystem, and the solar intensity is highest.

The coldest environment in the mission is encountered during cruise at maximum 3.5 AU, when the spacecraft is not transmitting. At this time the propulsion system is off, solar energy is negligible, and the leakage from the equipment compartment is maximum. The power dissipated in each of the subsystems for these conditions is given in Table 10-8.

The temperature extremes experienced by various subsystems vary from a hottest condition at 1 AU to a coldest condition at 3.5 AU (maximum distance from the sun). Table 10-9 gives the range of subsystem predicted temperatures. Also given is the heater requirements for worst conditions just prior to termination of powered flight at 2 AU and again at 3.5 AU. The results demonstrate that the selected design meets all of the thermal requirements of the spacecraft equipment and science payload.
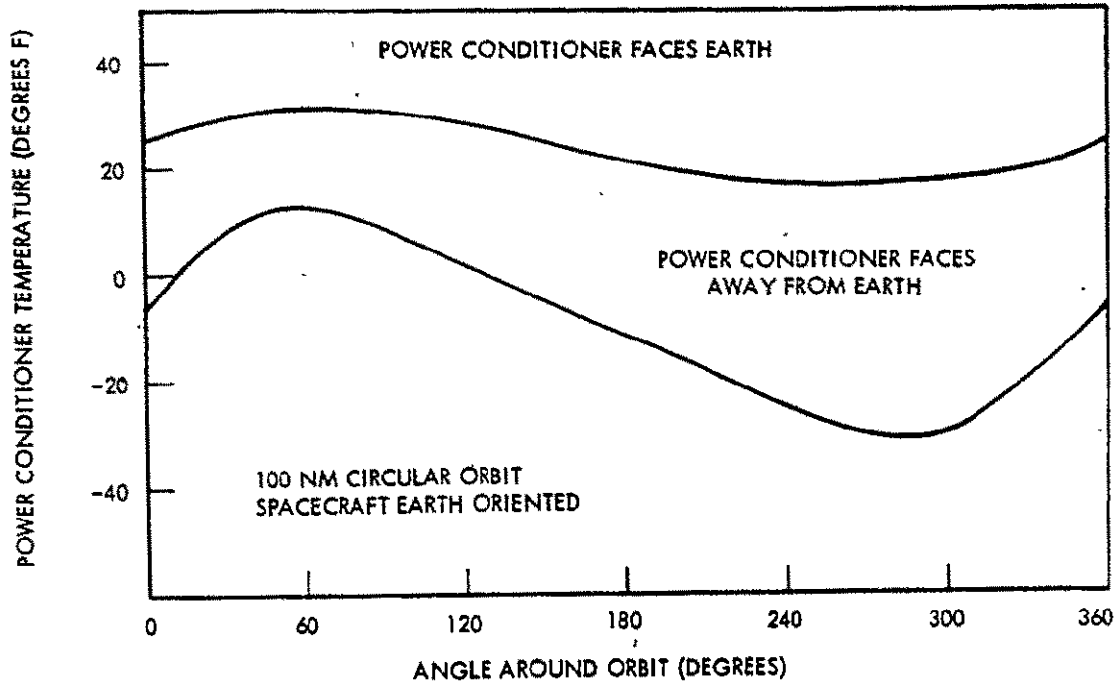
Figure 10-5. Temperature History of Power Conditioner
During Parking Orbit
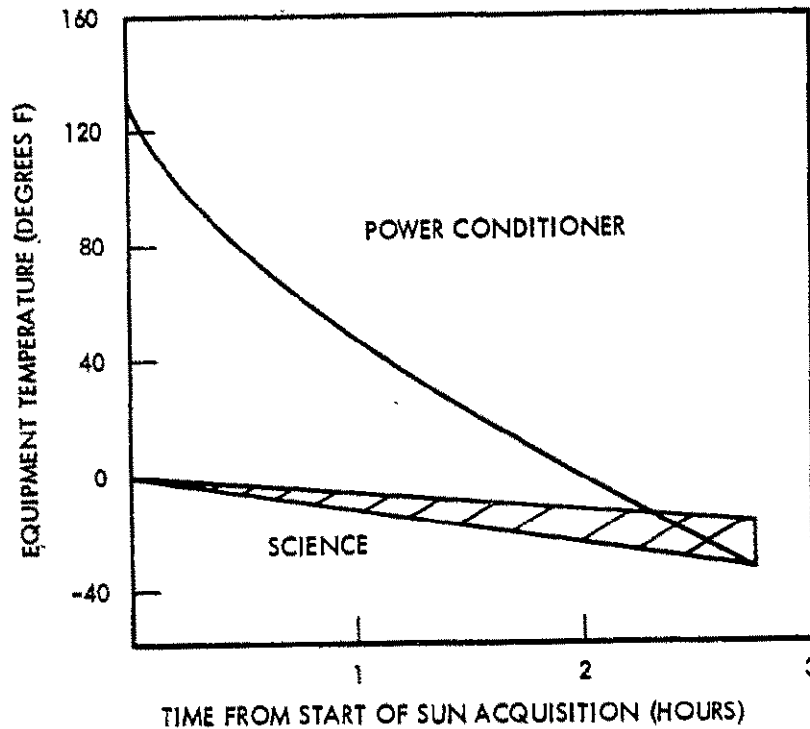
Figure 10-6. Temperature History of Power Conditioners and
Science During Sun Acquisition and Solar Array Deployment

10-14

Table 10-8. Subsystem Power Dissipation

Subsystem	Power Dissipation (watts)	
	Thrust	Cruise
Spacecraft electronics	305	160
Power conditioner (Each)	273	0
Science	69	78
Thrusters	7050	0

Table 10-9. Predicted Temperature

Subsystem	Predicted Temperatures (°F)	Required Heating (watts)	
		Thrust	Cruise
Spacecraft electronics	70 to 100	0	0
Power conditioner*	5 to 115	0	0
Standby power conditioner	-25	100	
Science payload	0 to 25	18	42
Star tracker	-10 to 100	5	12
Sun sensors	-40 to 100	2	6
Attitude control jets	0 to 110	2	5
Mercury tank*	90 to 120	6	0
Thruster*	32 to 482	0	0
Total		133	65

*Equipment is operating.

11. CENTRAL COMPUTER AND SEQUENCER

INTRODUCTION

In general, the primary application of the central computer and sequencer (CC&S) is to provide event timing and sequencing of all spacecraft functions generated on a time-dependent basis. The sequencing operation is performed by either a fixed sequencer, general purpose sequencer, or a special purpose programmable magnetic core storage computer. In some cases when using a programmable magnetic core storage computer, it is desirable to have a fixed program hardwire sequencer operating as a parallel redundant backup due to the vulnerability of core during addressing and rewrite.

The timing and sequence instructions are programmable into the CC&S before launch. The general and special purpose computer programs are capable of modification and selective readout via coded commands from the spacecraft telemetry system after launch.

A new application for the CC&S is the requirement for controlling the ion engine thrust vector (orientation and magnitude) for the 210-day thrust phase of the mission. This control involves either curve-fitting for continuously changing thrust vector requirements or sequenced steps at specified time intervals; the final choice is dependent upon the overall mission requirements.

CC&S FUNCTIONS

The CC&S provides a variety of spacecraft timing signals and computing functions; essentially, the CC&S serves as the "brain" of the spacecraft. The basic functions of the CC&S include providing discrete electrical signals for launch, cruise and encounter events; providing serial binary coded signals for various components requiring pointing control (antenna pointing, thrust attitude, etc.). The CC&S must be reprogrammable and interrogatable before or after launch at any time during the mission. Specifically, the following functions are at least a minimum for the Asteroid Belt Mission:

1. The CC&S shall provide, at the prescribed intervals, relay contact closures initiating subsystem responses including (but not limited to) backup post-separation events, appendage deployment, stellar reference search initiation and update, gyro control science

deployment, ion engine thrust vector control, spacecraft roll, attitude, telemetry data rate control, and antenna switchover control.

2.   Program storage and modification capability shall exist before launch by direct contact while the spacecraft is on the ground and during flight via coded commands from the spacecraft telemetry subsystems.   The computer memory shall also be addressable to check the contents of any address of the computer core memory.

3.   The baseline CC&S shall have maximum protection against abnormal input voltages, to protect the core contents from accidental modification.   During the long interval when core is vulnerable, such as during a maneuver program, certain redundancies are desirable to enhance mission reliability.

Since the Asteroid Belt Mission may be the first flight using solar power for primary propulsion, the on-off switching control, thruster selection and thrust termination will be performed by direct ground command. CC&S functions associated with control of the ion propulsion system are limited to programmed thrust vector control.   Ion propulsion system monitoring will be performed by recording housekeeping data and relaying to the ground readout station.   The SEP power conditioning and control unit has build-in restart operations, eliminating the need for CC&S emergency control.   Backup emergency operation procedures programmed into the CC&S could be achieved at no increase in cost or complexity to protect the spacecraft in the event of SEP propulsion control procedure failure.

CC&S commands for control of the SEP propulsion thrust program include output signals for attitude control and ion engine beam current.

Dual stellar references are anticipated in the SEP mission, to allow two-axis reference (Sun, and at least one star) even when one of the two selected stars is obscured by the large solar cell arrays.   The two selected stars are Canopus and Vega, essentially separated by 180 degrees.   The CC&S shall be preprogrammed to provide acquisition while in parking orbit, updated as required during the thrust phase, and given final update after the magnetometer calibration roll maneuver following initiation of the coast phase at 210 days into the mission.

The data words for both the Vega and Canopus electronic scanner-type star tracker will be "bias" signals.   The stars will not be tracked in "the center" of the scanner, but rather around the perimeter of constant azimuthal angle resulting in a signal proportional to the image location.   The star tracker output signals will be compared to the programmed star reference (data) and attitude error signals are generated for driving the attitude control system.

11-2

DESIGN GUIDELINES AND CONSTRAINTS

The following design considerations influenced the selection of the CC&S design concept and hardware:

1. Reliability. Of paramount importance is overall CC&S reliability. Failure of a component in the CC&S during the 3.5 year lifetime may jeopardize mission performance. Redundancy within the CC&S in some areas is desirable. Provision for CC&S override via telemetry commands from earth for essential functions is required to reduce the possibility of mission failure due to specific CC&S failures.

2. Availability. To maintain low cost and minimize procurement leadtime, the SEP CC&S shall preferrably be a special purpose computer, flight proven, available, and requiring a minimum modification for the SEP mission.

3. Physical Characteristics. Minimum size and weight, consistent with the task, is fundamental due to the low thrust and small size of the overall spacecraft.

4. Electrical Characteristics. The CC&S shall derive its input power from the spacecraft power bus which is 50 volts ac square wave, with a frequency of 2.4 KHz, derived from a precision oscillator. The 2.4 KHz shall be used also for computer cycle clocking and event timing via divider chains.

COMMAND LIST, CC&S

The following command list is typical for the asteroid belt mission. This list illustrates CC&S requirements only and does not include sequence of commands. (See Table 2-6 for mission events timeline). As more detailed analyses are performed it is anticipated that this list will increase rather than decrease in number. The CC&S ultimate capabilities therefore should not be limited to the presently formatted requirements.

No.	CC&S Command
1	Remove relay hold and enable CC&S Command
2	Arm pyrotechnics
3	Deploy low gain antenna (2)

No.	CC&S Command
4	Initiate transmission via low gain antenna (use 125 milliwatt exciter output)
5	Activate SCS (except translator and gimbal closed loop system)
6	Reduce rotation rates
7	Spacecraft orientation command
8	Release solar panel boost tiedowns
9	Solar array deployment
10	Initiate Sun acquisition (first 180-degree roll)
11	Antenna switching low gain
12	Magnetometer power on
13	360-degree roll maneuver (magnetometer calibration) and sun reacquisition
14	Antenna switching (low-gain)
15	Switch from exciter to 10-watt transmitter mode
16	Initiate roll reference star acquisition (Canopus or Vega)
17	Release and deploy high-gain antenna (Orient as required)
18	Gyros to standby mode
19	Group B experiments off (magnetometer and Faraday cups)
20	Release translator and thruster boost tiedowns
21	Energize translator and gimbal circuitry (open-loop)
22	Position translator and orient thrusters to initial position

No.	CC &S Command
23	Increase GN$_2$ SCS deadband to ±3 degrees to allow translator and gimbal control to take over
24	Activate flight control system, translator and gimbal (closed loop)
25	Gyro power off
26	Sun sensor switching (4)
27	Star sensor switching
28	Switch transmitter (10-watt) to high-gain antenna
29	Gyros in standby mode
30	Gyros on (for backup during SEP thruster switching)
31	Gyros off
32-38	Spacecraft orientation (thrust attitude GN$_2$ system)
39-54	High-gain antenna pointing
55-69	Thrust vector magnitude
70	Group B and C experiments on
71	Gyros on
72	Spacecraft roll (magnetometer calibration)
73	Reference star reacquisition (Canopus or Vega)
74-110	Spacecraft orientation maneuvers during coast phase (12 spacecraft orientations)
111	Rotate solar array (2) 180 degrees at aphelion passage
112-	Command associated with possible restart of SEP thrusters (after return through asteroid belt below 2 AU)

(Commands 31 through 69 bracketed: as required)

COMPUTER SURVEY FOR SEP APPLICATION

General Purpose Computers

The use of a small aerospace "state-of-the-art" general purpose computer was considered for SEP application. One consideration was clear, however, in considering a general purpose computer. The general purpose computer would merely serve as the "heart" of the CC&S subsystem, with development still then required for such "peripheral" circuitry, as the command decoder, output command word decoder and relays, parallel-to-serial buffering registers, clock shaping circuitry, power supplies, etc. Therefore, the CC&S function really requires a special purpose device, tailored to the mission specifics.

A comparison of existing "general purpose" computers possibly adaptable to spaceborne applications (Table 11-1) indicates one or more shortcomings. In general, they are much too fast for the application resulting in unnecessary power and size penalty. In addition these computers do not exhibit the long-term reliability required for the SEP mission.

Special Purpose Computers

It is clear from the above that a computer per se is insufficient. The baseline control system must be primarily a highly reliable event sequencer, secondarily a reprogrammable sequencer, and thirdly, capable to a limited extent of closed loop arithmetic control, for instance, comparing ion engine differential thrust and providing new thrust level commands based on the thrust differential. A special purpose computer would contain the necessary "non-computer" circuitry to interface itself with the rest of the spacecraft. Clearly, a special purpose device seems the best choice for the SEP CC&S.

Computer Comparison Summary

Hardwire sequencer, special purpose and general purpose computers resulted in the following conclusions:

1. "Hardwired" or Fixed Sequencer. Used on all Ranger and Mariner flights to 1967. Use is characterized by fixed events time sequence well known in advance. As events control requirements increase, the hardware also increases: i.e., double the number of controlled events results in doubling the size and weight of the sequencer hardware.

2. Special Purpose Digital Computer. Currently under intense development and refinement for support of Mariner Mars

Table 11-1. Comparison of Existing General Purpose and Special
Purpose Computers for SEP

	Operation Speed	Word Size	Memory Size	Interrupt	Input	'Weight	'Volume	*Power	'Reliability
JPL MM/71	C	C	C	C	C	C	C	B	C
Autonetics D26C	A	B	B	C	D	D	D	E	D
CDC 449	B	C	C	D	D	B	A	A	D
Honeywell Alert	A	C	C	B	C	C-D	D-E	D	E
Hughes HCM-206	A	B	E	B	D	B	B	D	E
IBM 4PI/TC	A	D	B	C	C	C	C	C-D	D-E
General Precision GPK-20	B	C	C	D	B	C	C	C-D	E
Litton L-3050	A	B	C	B	D	D	C	D	E
MIT AGC Block II	A	C	B	C	C	D	E	D	NA
TRW Marco 4418	A	C	C	D	E	C-D	C	C-D	C-D
Univac 1.13	A	C	C	C	C	C-D	D	E	E

A. Very excessive *Excellent

B. Excessive/'Very good

C. Acceptable

D. Insufficient/ Unacceptable

E. Very Insufficient Very unacceptable

1971 flight. Used on Mariner Mars 1969, highly flexible in capability for controlling time variable sequencing of events. Hardware growth is less closely related to events increase compared to the "hardwired" sequencer.

3. General Purpose Digital Computer. Any general purpose computer can be adapted to handle easily the types of functions required of the CC&S. The computer capability greatly exceeds that required for normal CC&S sequencing functions, being able to solve on-board guidance problems, optimizing data management and control, and in general continuously managing the spacecraft in an optional manner. The computer size is virtually unrelated to the number and type of events in the sequencing process as they represent a small fraction of the computer capability. This performance is obtained at the expense of weight.

CC&S SELECTION

The CC&S used for the Mariner 1969 Mars mission marginally meets the requirements for the SEP program (assuming all SEP associated commands are direct) except for memory size. However, the Mariner Mars 1971 computer (already in production) more than adequately meets SEP requirements since its memory has been increased from 128 words (Mars mission 1969) to 512 words, with insignificant increase in cost, size, weight, or power requirements. Assuming 2 to 2.5 words per event, 200- to 300-word capacity is required for the Asteroid Belt mission, depending on the extent the CC&S is used for closed loop arithmetic control. The choice for the SEP mission is thus established as the Mariner Mars 1971 CC&S.

The basic design of the Mariner 1971 CC&S is really universally oriented, the idea being that the CC&S would be a "shelf" item for a multitude of forthcoming space probes. In fact, the Mars mission 1971 CC&S is programmed for use in the forthcoming "Viking" Lander mission. GSE and software are also available from the subcontractor, Motorola, Inc., Military Products Division, Phoenix, Arizona.

The Mars mission 1971 CC&S is the only existing (or in production) unit found acceptable for selection as the SEP CC&S. The conservative design affords very high reliabilities. The MTBF is almost equal to the mission duration, but a simple MTBF figure is virtually meaningless here, since it refers to MTBF of any component in the CC&S, not MTBF of the CC&S as a whole.

During the Mariner 1969 flight, the only failure (non-catastrophic) was determined to be a micro-circuitry failure apparently due to problems with metallic growths on the chip interconnect wires. This has been verified by

observing some failure in recent ground testing. Some bonding problems have also been observed. It is anticipated these problems will be resolved shortly. Although a MTBF of 30,000 hours results in a reliability of 0.36 for a 3.5 year mission, $R = e^{-\frac{Time}{MTBF}}$. The CC&S has performed the major bulk of its tasks at 210 days into the mission, when the flight thrust phase is completed. After this time, the CC&S primary function is to maintain spacecraft orientation and attitude control for optimum science sensor positioning, and command 180-degree rotation of two solar arrays at 3.5 AU aphelion passage. The foregoing functions could be accomplished by direct command, if necessary. The reliability factor for 210 days becomes $e^{-\frac{5.03}{30}}$; again, this does not take into account redundant circuitry and bypass techniques.

DESCRIPTION OF MARS MISSION 1971 CC&S

Figure 11-1 is a block diagram of the CC&S selected for the SEP spacecraft. Approximately 80 percent of the total CC&S subsystem is related to the computer classified as a stored program, serial operating special purpose digital device. The essential items related to this portion of the CC&S are the following:

1. Input decoder

2. Clock

3. Processor

4. Memory

5. Event decoder

6. Volatility protection

7. Power conversion

The remaining portion of the CC&S is related to the "hardwired"(fixed program) sequencer, used for redundancy during maneuver phases only. Roll, yaw and thrust ΔV data must be introduced via telemetry into the magnetic core storage registers prior to the maneuver. The essential elements in the sequencer are as follows:

1. Input decoder

2. Counter
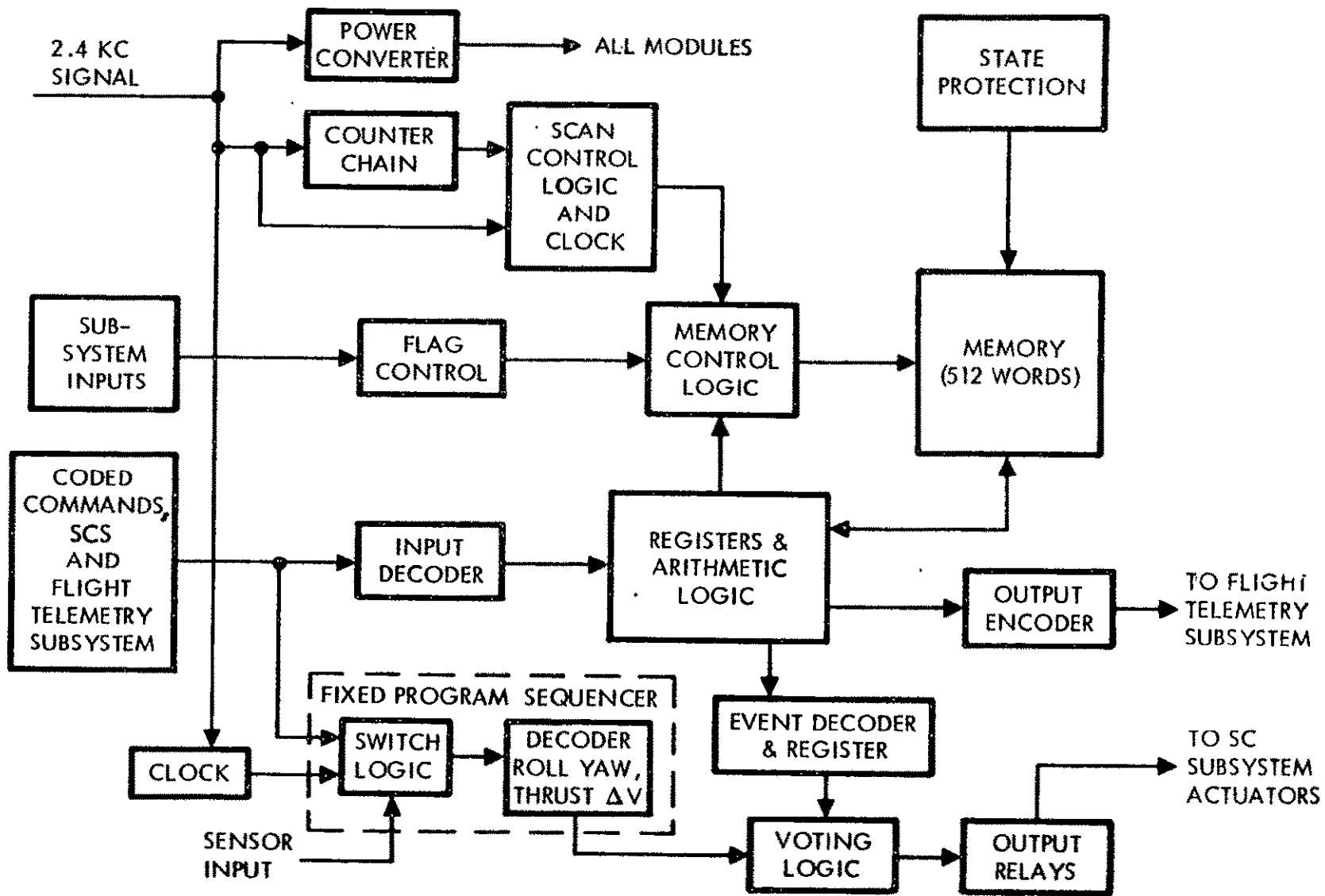
Figure 11-1. Central Computer and Sequencer Block Diagram

3. Duration control logic

4. Storage registers

5. Relay drivers

6. Power conversion

Description of Computer Section Operation

Inflight coded commands from the flight control system, inflight memory readout control, attitude control pre-aim data transfer and prelaunch memory loading and readout are controlled via the input decoder. Such command loading is restricted to cruise or prelaunch modes only, to avoid operational complexity.

Functions of the computer clock/counter include input (2.4 KHz) signal shaping and division for scan control, memory read/write rate control, event duration countdown, and external subsystem time updates, if required. The processor provides the following functions: addressing, fetching and storing memory, sequencing memory, arithmetic and time-dependent processing, and relay actuation control. The scan control logic controls the processor on a second, minute, or hour basis, depending upon the "flag" set for the function in question. External interrupts initiate the "seconds" flag for immediate computer response. Three word formats are used, each 22 bits long.

The instruction format is a multiple-address word with the first four bits being the operation code, followed by two nine-bit address locations. The time/event address format utilizes the first fourteen bits for time magnitude and eight bits for event address. The third format (for internal CC&S words), is a pure data format using all 22 bits for data value.

Memory capacity is 512 words, 22 bits per word. Being a core memory, readout is destructive and requires rewrite after reading.

The event decoder translates via matrices the commanded event words into 112 discrete outputs from a nine-bit address. From one to three of these discrete outputs can be simultaneously activated by one event word providing single word multiple-events control. Much emphasis has been placed on protecting core from accidental modification. The program memory is vulnerable only during memory storage scanning (addressing, reprogramming) which occurs during approximately 0.001 to 0.005 percent of the mission time. Transient signals occurring during memory addressing could

destroy or modify existing stored programs. To prevent wholesale destruc-
tion of the core program, transient protection and voltage level tolerance
detection is employed to disconnect the processor from core during such
occurrences.

A power converter is included integral with the computer for operating
the sections of the computer. For reliability, electronic regulators are not
included in the design, but transient protection is included.

Description of Sequencer Operation

The redundant fixed program sequencer (used for maneuvers only) is
electrically independent of the computer proper, with the output interfaces
voted upon with quad redundancy. Thus, maneuver operations are protected
from single component failures. Data for roll, yaw, and thrust are fed into
magnetic core storage registers from ground commands. At the receipt of
the proper command, the maneuver sequence begins. The input decoder
provides this information. Check logic is included here, for double entry
into the decoder of commands and bit-by-bit word verification. A sequence
counter utilizing the 2.4 KHz input reference divides down to provide proper
maneuver interval timing: initial delay for gyro warm-up and fixed delays
between maneuver sequences.

The sequencer relay drivers are also independent of the computer to
guarantee that a single component failure in the relay drivers will not
jeopardize the mission. Power conversion is provided independently by
components similar in design to that used in the computer proper.

Closed Loop Control

The Mars mission 1971 CC&S instruction repertoire (Table 11-2) is
basically the same as the Mars mission 1969 CC&S, with the exception of
the addition of the "compare" function. The "compare" function is very
useful for the SEP spacecraft allowing differential engine monitoring and/or
responsive thrust modification, solar power supply monitoring, load-sharing
and other closed-cycle control functions normally achieved by analog elements
fixed in operation. The main advantage of using the CC&S for these functions
is the extreme control versatility, since access via telemetry provides capa-
bility of modification of programmed operation.

The compare function capability incorporated into the Mars mission
1971 CC&S provides the capability to control the SEP thrust vector. Inputs
to the CC&S from the peak power monitor (PPM), the SEP engine status,
spacecraft attitude sensor are operated on (analog to digital, if required) and

Table 11-2. Computer Instruction List - CC&S

Number	Instruction	Mnemonic Code	Binary Code MSB, LSB	Execution Time (Memory cycles)
1	No Operation	NOP	0000	4
2	Conditional Jump	CLJ	0001	22
3	Count and Jump	CTJ	0010	5 to 22
4	Word Output and Halt	WOH	0011	44
5	Add	ADD	0100	66
6	Transfer A to B	TAB	0101	66
7	Subtract	SUB	0110	66
8	Word Input and Halt	WIH	0111	66
9	Halt	HLT	1000	4
10	Decrement Address and Jump	DAJ	1001	44
11	Unconditional Jump	UNJ	1010	22
12	Reset Operation Code and Jump	ROJ	1011	44
13	Decrement Hours and Jump (Wrong Resolution) (Correct Resolution)	DHF	1100	4 / 23 to 44
14	Decrement Variable and Jump	DVJ	1101	—
15	Decrement Minutes and Jump (Wrong Resolution) (Correct Resolution)	DMJ	1110	4 / 23 to 44
16	Decrement Seconds and Jump (Wrong Resolution) (Correct Resolution)	DSJ	1111	4 / 23 to 44
17	Compare	CMP		

are appropriately compared in the arithmetic unit with the stored star position programs and the thrust vector program. Error signals are generated for ion thruster control and SCS attitude control, conditioned (digital to analog) and distributed to the assigned terminal points: PC&C, cold gas thruster, ion thruster gimbal, translator driver, etc.

A more detailed analysis is required to determine whether or not it is more desirable to perform the ion thruster control signal comparison operations external to the CC&S. In either case, the complexity of the control circuitry presents no significant design problem and does not result in a significant weight difference for the system.

The minimum word requirement for the SEP CC&S is estimated at about 200 words based on a nominal rule of 2 to 2-1/2 words per event, thus allowing about 300 words for closed loop control. This word capacity greatly exceeds the demand for thrust vector program control, antenna pointing, and spacecraft attitude control. Utilization of the CC&S for these functions at this time is highly recommended.

JPL Mariner Mars 1971 CC&S Characteristics

The following physical and performance characteristics are typical of the Mars mission 1971 CC&S:

1.	Size	- $0.011M^3$ (650 in.^{3})
2.	Weight	- 10.5 Kg (23 lb)
3.	Power	- 22.5 watts during flight 42 watts during launch (bi-polar magnetic-latch relays all held "off" during launch)
4.	Input power	- 50 volts, 2.4 KHz, square wave
5.	Storage capacity	- 512 words, 22 bits each, serial entry/exit from core
6.	Power Monitor	- Decreases core content vulnerability
7.	Reliability	- Magnetic cores used for memory and certain registers for increased reliability
8.	Discrete outputs	- 112 discrete contact closures with some restricted combinations available
9.	Construction	- Modular elements composed, single mounting rack

11-14

CONCLUSIONS

The CC&S designed by the Jet Propulsion Laboratory and built by Motorola Military Products Division for the Mariner 1971 and Viking missions in general best meets or exceeds the requirements of the SEP spacecraft. Modification may be required in the redundant fixed sequencer, taking into account the long-term thrust phase of the ion engines as opposed to the shorter-term burns of chemical propulsion spacecraft. This CC&S has more than adequate discrete outputs for subsystem control, and considerably more memory than required. This is a good feature, allowing expansion of the computer application, and readdressing of data in memory in the event part of the memory on the drive circuitry fails.

The CC&S performs its major functions during the first 210 days of the mission. After the thrust phase is complete, the CC&S provides only sun-sensor switching and fixed program cold-gas system controlled attitude updates, as well as one 180-degree solar panel rotation command at the 3.5 AU aphelion. To lessen the strain or reliability requirements for the CC&S during the full 3-1/2 years of the mission, it is recommended that provisions on the spacecraft be made for supplying the small number of coast phase events via telemetry on parallel control circuits with the CC&S output.

12. METEOROID HAZARD ANALYSIS

The meteoroid hazard to the solar electric propulsion (SEP) spacecraft may be considered to consist of two damage modes: degradation of subsystem performance due to cumulative effect of numerous meteoroid impacts which could ultimately lead to failure, and critical failure as a result of a single large meteoroid encounter.

The large area required for solar power (10-kilowatt system) immediately poses the hazard of loss of significant power due to meteoroid impacts. This power loss is caused by pitting of cell surface and resultant loss of solar energy transmission through the cell protective coat; loss of whole cells as result of impact of sufficiently large meteoroid, and loss of power due to numerous severings of the solar cell interconnecting wire harness.

The primary hazard due to a chance impact of a single large particle is the loss of a critical spacecraft subsystem function due to a vital subsystem component failure. The major area of concern here is the equipment compartment being penetrated, causing mission failure.

The following analysis investigates the problem of solar panel performance degradation due to meteoroid impacts; defining anticipated performance losses which may be compenstated for in the subsystem design. Also included is an analysis of the shielding requirements necessary to protect the equipment compartment from penetration of a particle of sufficient size to cause a critical failure and perhaps loss of mission. Hazards included in this analysis are the asteroid belt and the cometary and stream cometary environments.

NOMENCLATURE

$f(R)$ Meteoroid flux function as defined in Table 12-1.

T_a Actual mission duration time (sec)

P Total penetration depth (cm)

P_s Penetration depth into solar cell from rear surface impact, (cm)

ρ Meteoroid particle density (gm/cm^3)

V_i	Impact velocity (km/sec)
d	Meteoroid particle diameter (cm)
D_{fz}	Fracture zone diameter (cm)
m	Meteoroid particle, mass (gm)
N	Meteoroid flux per unit area per sec
A_{sp}	Effective solar cell area for the entire solar panel array
T_R	Effective exposure time (sec)
α	Ratio of fracture zone diameter to penetration depth for glass
t_s	Substrate thickness (cm)
t_3	Thickness of glass substrate equivalent to the actual substrate (cm)
K, K_t	Coefficient of penetration equation
ρ_t	Substrate density (gm/cm^3)
H_t	Substrate hardness, Brinell

CRITERIA

The reference mission considered for the solar electrical spacecraft was an asteroid belt flythrough to 3.5 AU (Figure 12-1). All of the solar cells will be facing the sun until aphelion, after which two panels are rotated to face away from the sun.

Table 12-1 and Figure 12-2 define the NASA-MSC environment model used in this analysis (Reference 12-1). Also shown are the charts for determining the impact velocities for cometary and asteroidal particles (Figures 12-3 through 12-6). Meteoroid stream environments are based on recent Space Division investigations (Reference 12-2).

The basic spacecraft configuration is shown in Figure 12-7. The panel arrays consist of many individual solar cells mounted as shown to a substrate and electrically interconnected. The cells are composed of a
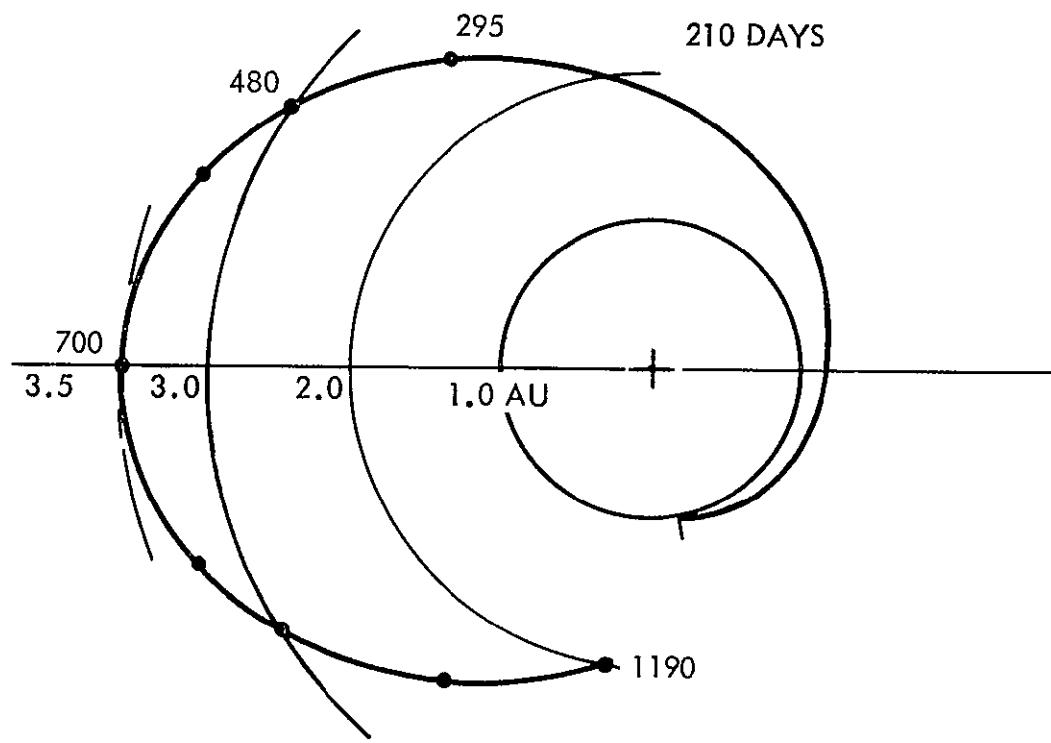
Figure 12-1. Reference Mission
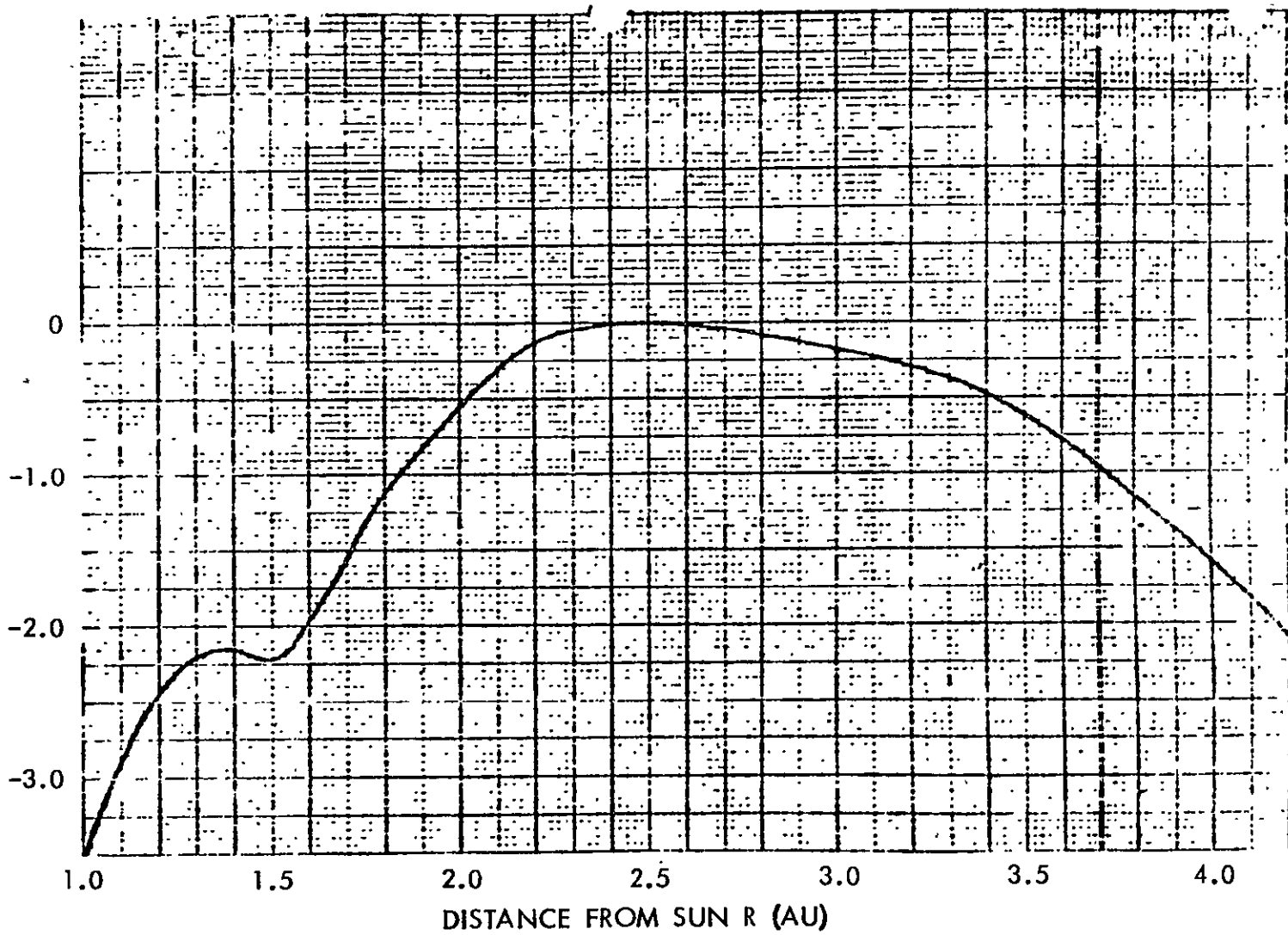
Figure 12-2. Asteroid Particle Radial Distribution

Space Division
North American Rockwell

σ IS THE RATIO OF THE HELIOCENTRIC SPACECRAFT SPEED TO THE SPEED OF A CIRCULAR ORBIT THE SAME DISTANCE FROM THE SUN.
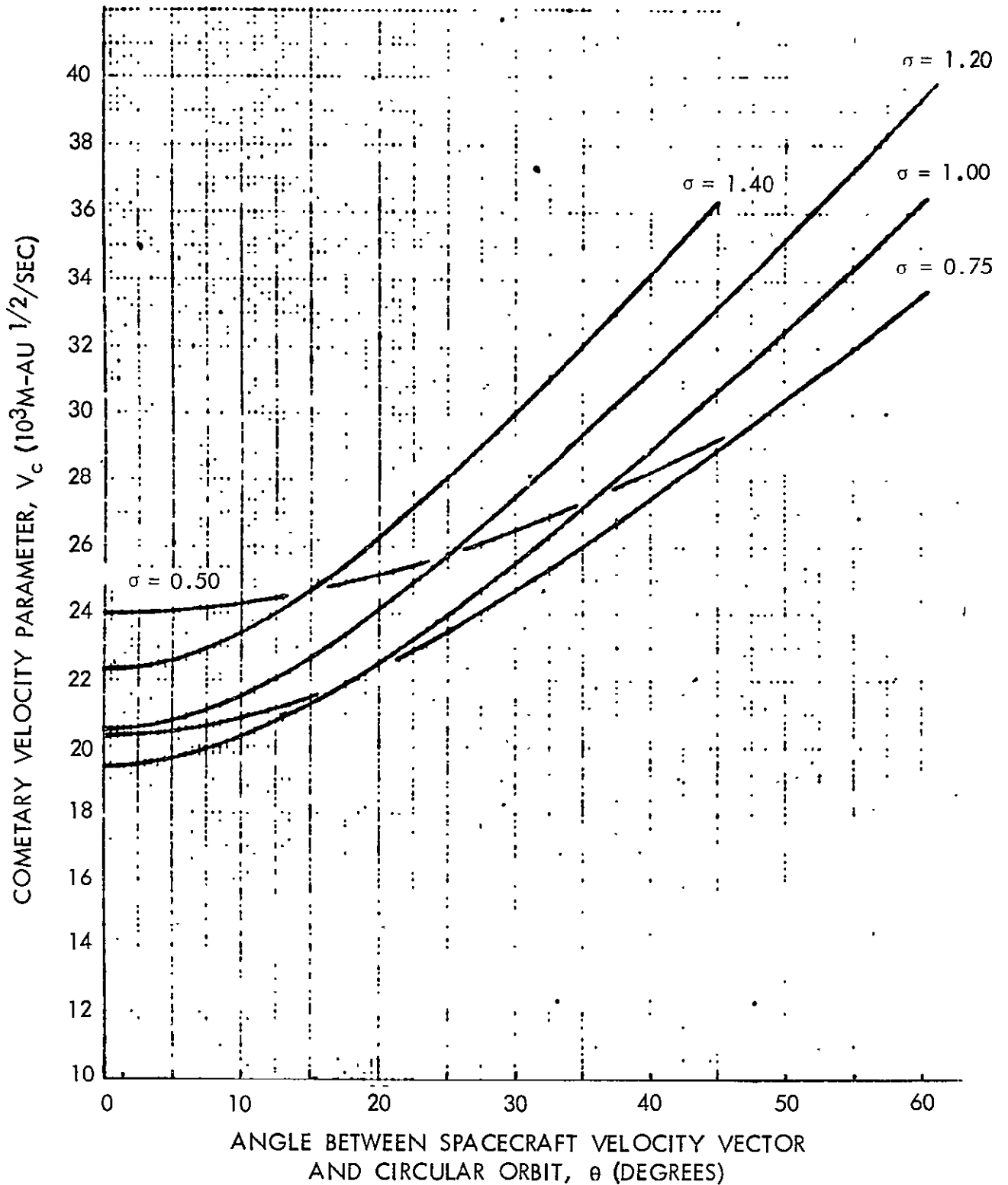
Figure 12-3. Average Relative Velocity - Cometary Particles
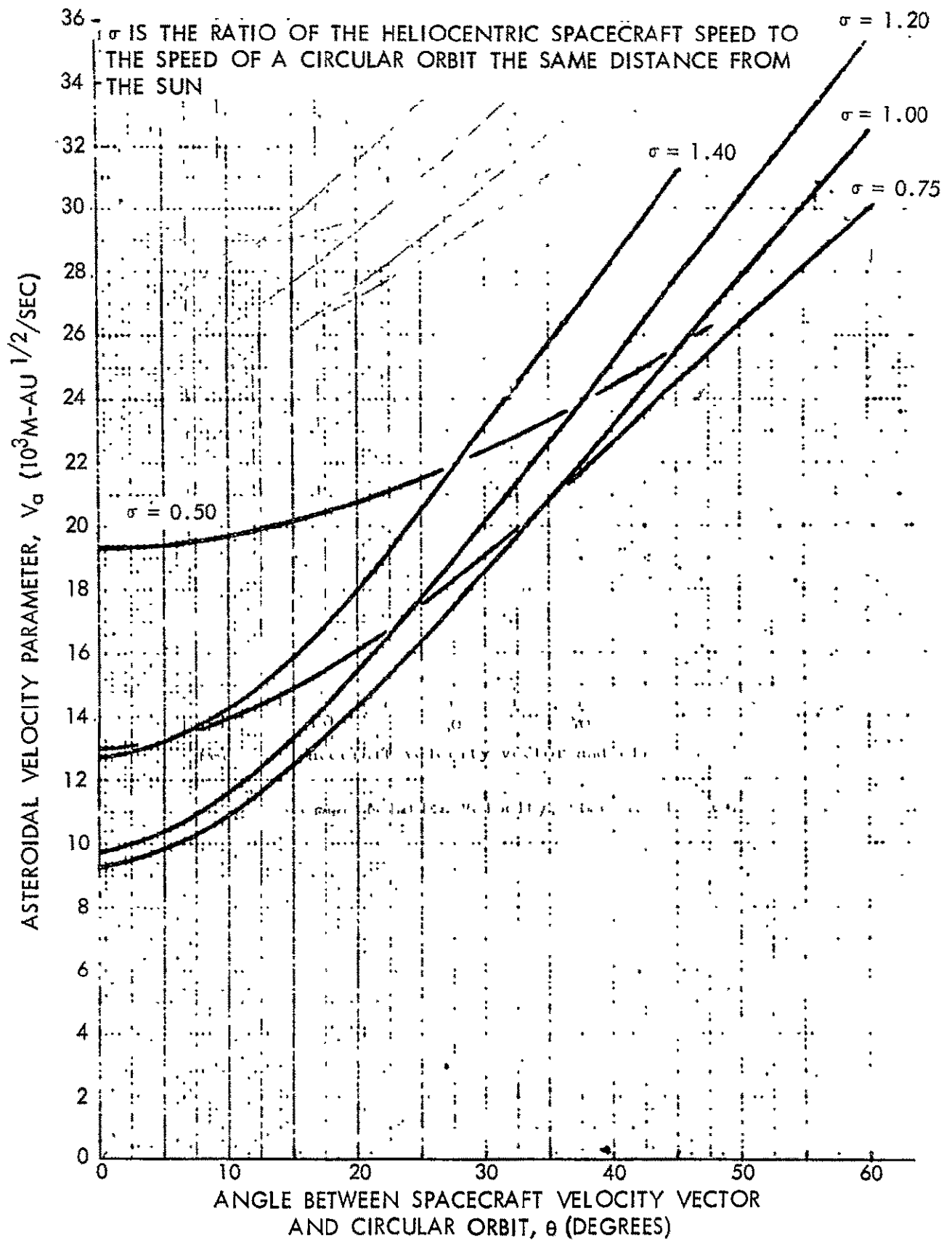
Figure 12-4. Average Relative Velocity - Asteroidal
Particles at R = 1.7 AU

12-6
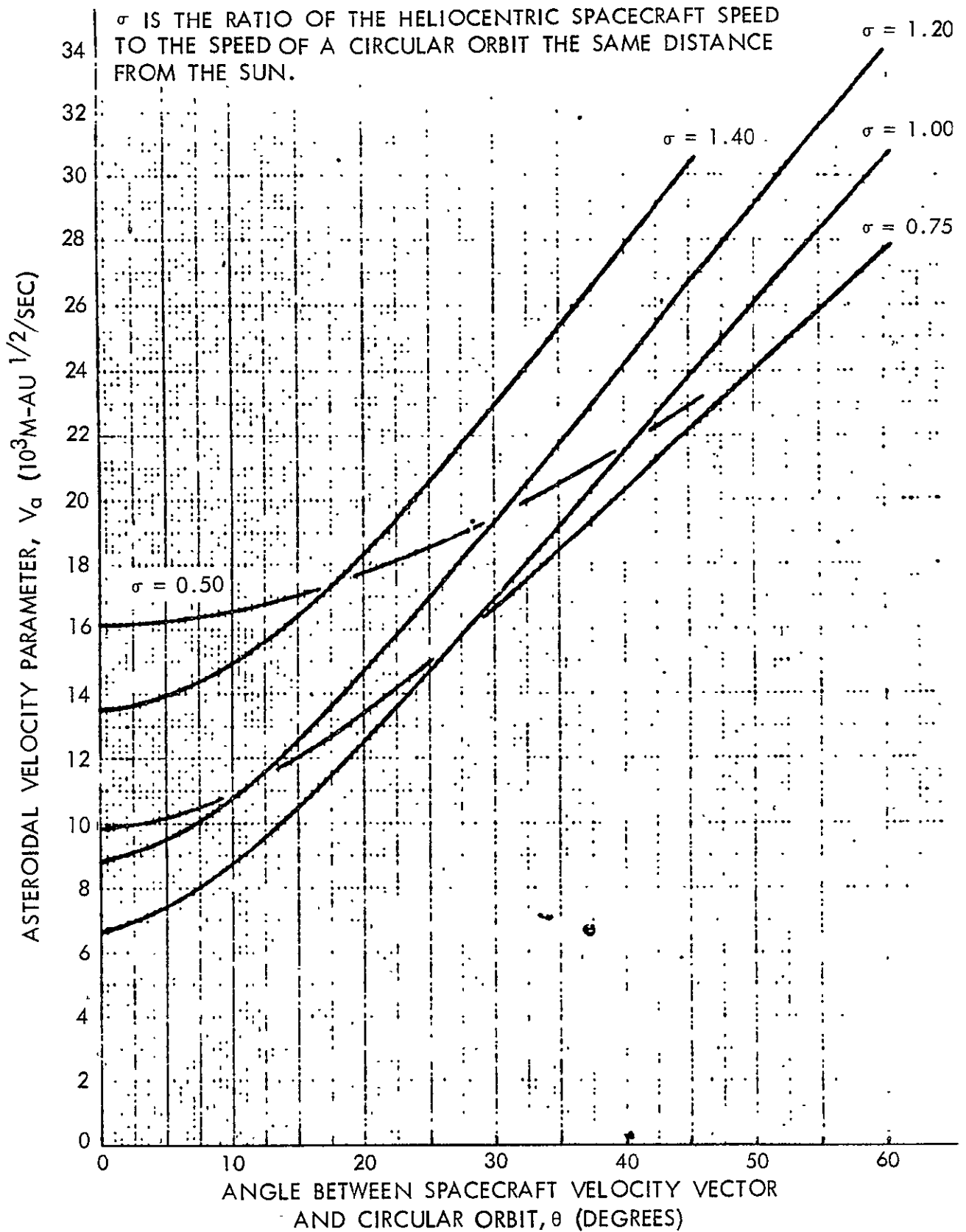
Figure 12-5.   Average Relative Velocity - Asteroidal
Particles at R = 2.5 AU
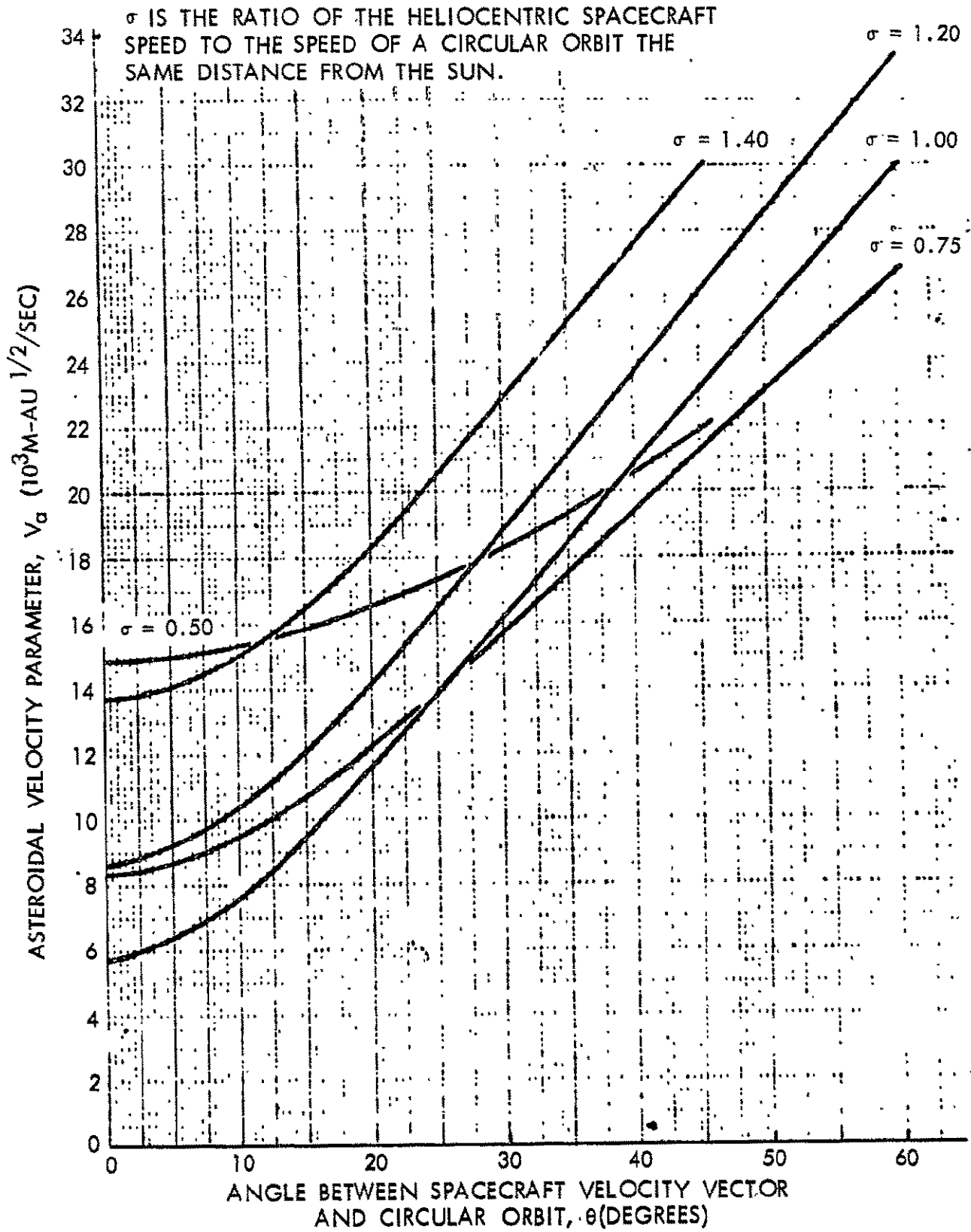
Figure 12-6. Average Relative Velocity - Asteroidal
Particles at R = 4.0 AU

INTEGRATED
SOLAR ARRAY
AND METEOROID
SENSOR PANEL

1.1M

EQUIPMENT
COMPARTMENT

0.9M

10.4M

5.0M
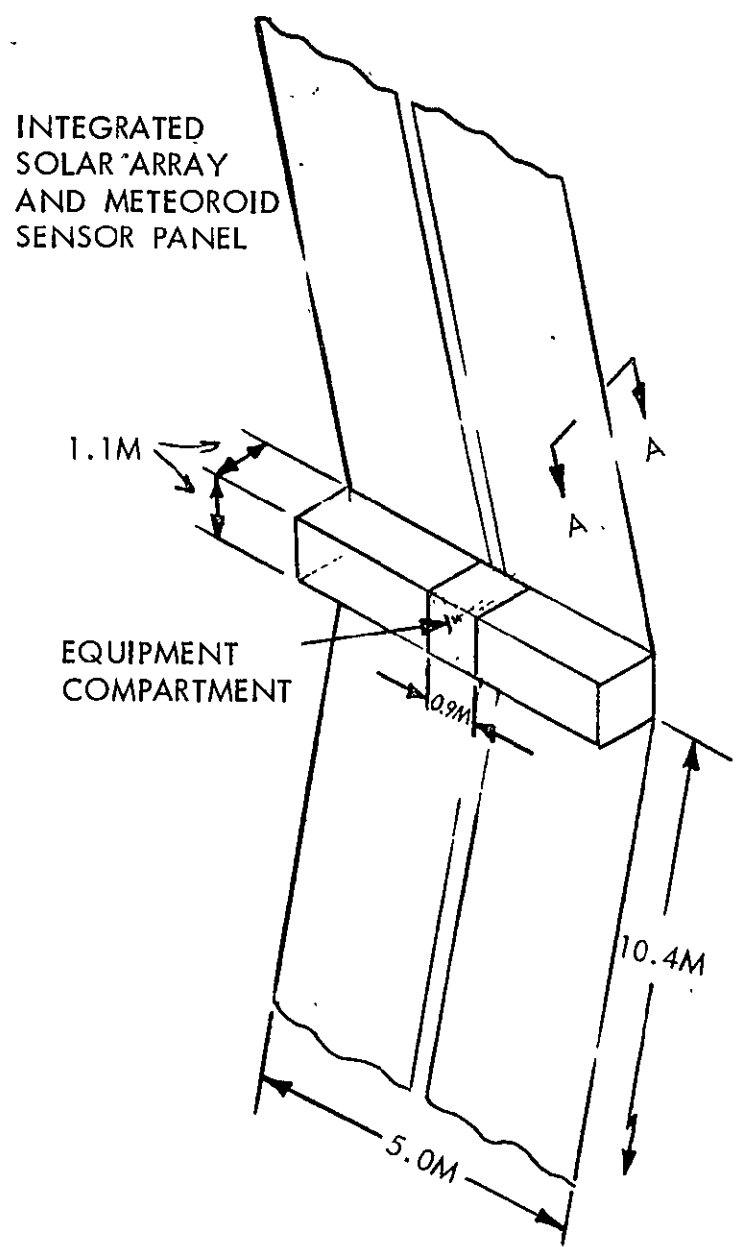
		THICKNESS (CM)	EQUIVALENT GLASS THICKNESS (CM)
COVER GLASS		—	—
SOLAR CELL		—	—
745 ADHESIVE		2.03×10^{-2}	.000768
KAPTON		5.08×10^{-3}	.002250
GT 304 ADHESIVE (3 SHEETS)		1.7×10^{-4}	.000615
ALUMINUM		15×10^{-3}	.017400

A-A

$\epsilon = .021033$ CM

Figure 12-7. Solar Electric Propulsion Spacecraft Model

glass cover and a glass energy converter. To this is attached a capacitor-type meteoroid sensor. The center section of the spacecraft frame is enclosed, forming the equipment compartment.

Table 12-1. NASA-MSC Nominal Sporadic Planetary Meteoroid Environments

Asteroidal	$N = \frac{1}{4} V_{AST} \frac{10^{-15.79}}{m^{0.84}} f(R), (m^{-2} - sec^{-1})$
Cometary	$N = \frac{1}{4} V_{COM} \frac{10^{-18.27}}{m^{1.207}} R^{-1.5}, m^{-2} - sec^{-1}$ $(10^{-6} \leq m \leq 10^{2})$ $N = \frac{1}{4} V_{COM} \frac{10^{-18.27}}{m^{1.584}} R^{-1.5} 10^{-0.063 (\log_{10} m)^2}$ $m^{-2} - sec^{-1} (10^{-12} \leq m \leq 10^{-6})$

where:

   N - Number of impacting particles of mass m or greater

V_{AST}, V_{COM} - Impact velocities (meters per second)

   m - Particle mass (grams)

   R - Radial distance from sun (AU)

   f(R) - Radial dependence of asteroidal flux

SOLAR PANEL DEGRADATION

Damage Mechanisms

Meteoroid impact damage to solar arrays may occur in such ways as cratering and fracturing of the surface, resulting in a change in transmission of incident solar radiation and subsequent reduction in solar cell performance; severing of the cell/wire junction and severing of the wire harness connecting

the total array. An assumption is made that single catastrophic collisions are not of interest in this analysis as they would destroy a section of cells instantaneously rather than result in gradual performance degradation. Such an occurrence is not expected during the asteroid belt mission, but if it occurs, it is highly probable that it will happen sometime after the electric propulsion system has been turned off and therefore does not represent a major threat to mission success.

.Previous studies performed at the Space Division have shown that meteoroid impacts on glass produce a crater of depth P surrounded by a fracture zone of diameter D_{fz} (Figure 12-8). The glass in the fracture zone is thoroughly cracked, opaque to light and without tensile strength. Due to the opacity of the fracture zone, that portion of the solar cell or cover glass area damaged in this manner was considered as operating at reduced power. Damage due to impacts from the rear side of the panel would not occur except for meteoroid penetration depths greater than the substrate thickness. Thus, different methods of analysis were developed for front and rear surface impacts.

The fracture zone was reviewed from the viewpoint of optical mechanics. It was concluded that the craters and fracture zones which would be produced by the extremely small meteoroid particles would indeed produce a certain amount of back-scattered light. Due to the complex nature of the fissures formed in the fracture zone, theoretical methods appear to be inadequate to analyze this problem at present. It appears that experimentation is the only method available to determine accurately the amount of light transmitted through a damaged surface. Present indications are that at least 50 percent of the light striking such a damaged surface would be transmitted through the crater and fracture zone areas, possibly more. The analysis performed is based on this estimate.

An attempt was made to correlate the power loss from solar cells as predicted by the method described in the following section with the test data of Reference 12-3. These data were generated by subjecting solar cells to repeated impacts by microparticles traveling at 3 to 4 kilometers per second and then measuring the change in power output. Reliable quantitative results could not be obtained from the correlation because of the absence of data on the size of fracture zones obtained per impact. Also, the cells were impacted by many times the number of impacts that is predicted for the worst-case mission studied. The correlation did indicate that the 50-percent factor noted above seems to be a reasonable choice until more detailed and more applicable test data are generated.

The solar cells are connected electrically, both in series and in parallel. The connection is a silver mesh which covers the full width of the edges of two adjacent cells (cells are 2.0 cm square). The main current

12-11

A) FRONT SIDE IMPACT

FRACTURE ZONE

CRATER

A'

SUPPORT PANEL

SOLAR CELL

COVER GLASS

D_{fz1}

P_{t1}

t_s

VIEW A'

D_{fz1} = DIAMETER OF FRACTURE ZONE
P_{t1} = PENETRATION DEPTH FOR FRONT SIDE IMPACT
t_s = SUPPORT PANEL THICKNESS

B) REAR SIDE IMPACT

CRATER

B'

FRACTURE ZONE

P_{t2}

t_s

P_s

D_{fz2}

VIEW B'

D_{fz2} = DIAMETER OF FRACTURE ZONE
P_{t2} = PENETRATION DEPTH FOR REAR SIDE IMPACT
P_s = PENETRATION DEPTH INTO THE SOLAR CELL
t_s = SUPPORT PANEL THICKNESS
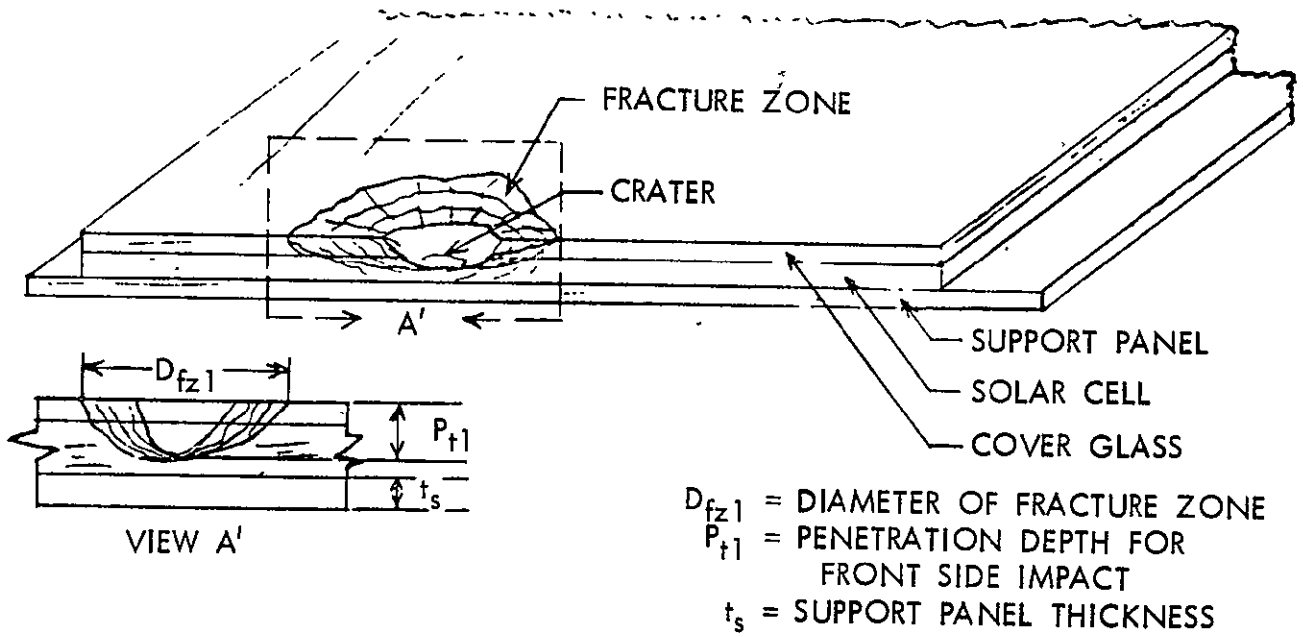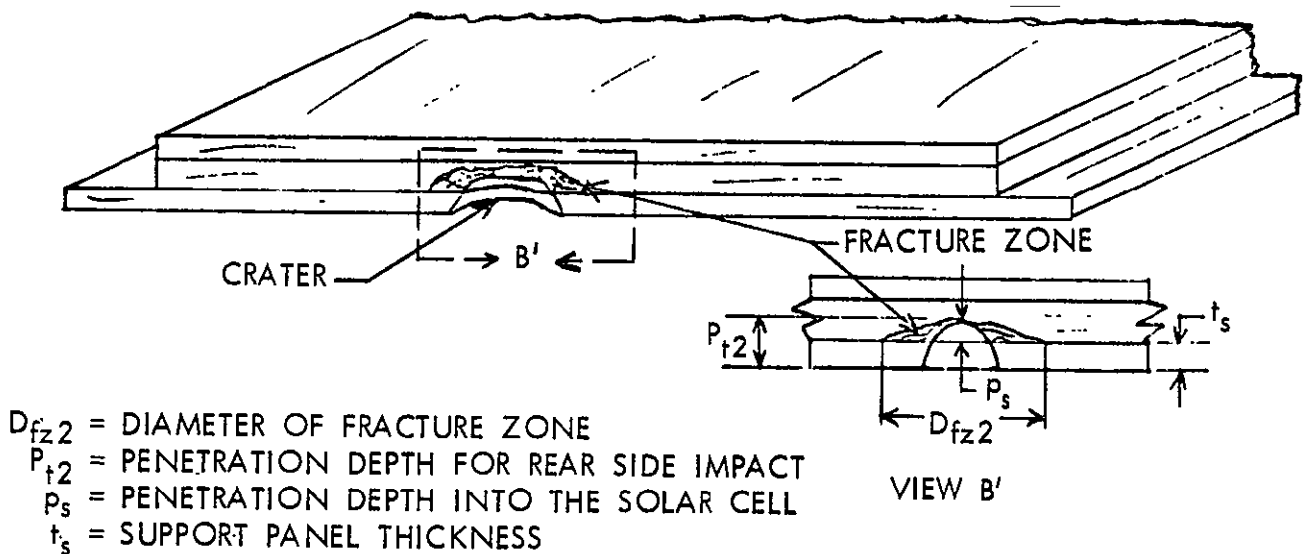
Figure 12-8. Solar Cell Damage Modes Due to Micrometeoroid Impacts

SD 70-21-2

flow is through the series connection and even if the entire width of a series conductor were removed between two cells, only these two cells would be lost. Power from the other cells in that series would pass through the parallel connectors.

Meteoroid impacts would be distributed over the entire panel, and due to the width of the connectors it is very unlikely that even one cell would be lost from meteoroid impact.

Solar Panel Area Loss Due to Meteoroid Impacts on the Front Surface

The penetration depth (P) for glass is given by the NR/SD equation

$$P = K \, \rho^{1/2} \, V^{2/3} \, d^{1.2} \, \text{(cm)} \tag{12-1}$$

where ρ, V, and d are, respectively, the particle density, velocity, and diameter, and k is an empirical constant. The penetration depth is related linearly to the diameter of the fracture zone resulting from the impact.

$$D_{fz} = \alpha \rho \quad \text{(cm)} \tag{12-2}$$

The area lost by the impact of one particle of diameter (d) will be

$$A_{L_1}' = \frac{\pi}{4} \, D_{fz}^2 = \frac{\pi}{4} \, \alpha^2 \, (K \rho^{1/2} \, V^{2/3} \, d^{1.2})^2 \, \text{(cm}^2) \tag{12-3}$$

The total area of the panels which will be fractured by particle impacts is found by combining the area lost per impact with the meteoroid flux equations of Table 12-1. For each type of particle, the flux equation can be rearranged to yield a relation for the number of particles with mass between m and m + dm which will impact the spacecraft during the mission. Assuming that all particle impacts are nonoverlapping, the total area lost by impacts of particles of mass m to m + dm is

$$dA_{L_1} = C \, V \, A_{L_1}' \, A_{sp} \, T_R \, dm \tag{12-4}$$

where T_R is an effective exposure time as explained below, A_{sp} is an effective solar panel area, A_{L_1} is the area lost per impact as given by equation (12-3), and C is a constant which must be computed for each type of particle. The details of this derivation for each type of particle are shown in Appendix A. Equation (12-4) is integrated over the range of masses encountered during the mission to give the total area lost by particle impacts. Typical of the results is the expression for the percentage of area lost due to impacts into the front surface of the solar panels by asteroidal particles.

$$\frac{A_{L_1}}{A_{sp}} = (69.3)10^{-15.79} \, T_R \, \alpha^2 \, K^2 \, \rho^{0.2} \, V_{AST}^{7/3} \left(\frac{1}{m_1^{0.04}} - \frac{1}{m_2^{0.04}} \right) \text{(percent)} \quad (12\text{-}5)$$

where m_1 and m_2 are the lower and upper limits of the range of masses encountered during the mission. The procedure for defining these limits and the equations for the area lost due to impacts of the two ranges of cometary particles are given in Appendix A.

Solar-Panel Area Loss Due to Meteoroid Impacts on the Rear Surface

      Meteoroids impacting the rear surface of the solar panels will not result in solar cell damage unless the penetration exceeds the thickness of the substrate material. In this case, solar cell penetration (P_s) will be

$$P_s = P - t_3 = K\rho^{1/2} \, V^{2/3} \, d^{1.2} - t_3 \text{ (cm)} \quad (12\text{-}6)$$

where t_3 is a thickness of glass with penetration properties equivalent to those of the substrate material. The diameter of the fracture zone is

$$D_{fz} = \alpha P_s = \alpha(P - t_3) \text{ (cm)} \quad (12\text{-}7)$$

and the resulting area loss per impact is

$$A'_{L_2} = \frac{\pi}{4} \, \alpha^2 \, (K^2 \, \rho V^{4/3} \, d^{2.4} - 2K \, \rho^{1/2} \, V^{2/3} \, d^{1.2} \, t_3 + t_3^2 \text{ (cm}^2) \quad (12\text{-}8)$$

By the same reasoning as in the front surface analysis, the total area lost is found by calculating the area lost from impacts of an incremental range of masses and then integrating over the applicable range of mass. The resulting relations for the percentage of area lost are Equations (A-28) and (A-31) of Appendix A.

Effect of Substrate Material and Thickness

In the degradation method, the effect of substrate material on solar panel protection is accounted for by reduction in crater depth by the amount t_3. Here t_3 is the thickness of glass substrate which would give a reduction in solar cell penetration equal to that given by the actual substrate material. It is of interest to express t_s in terms of substrate material properties.

Glass penetration is given by

$$P_g = K \rho^{1/2} V^{2/3} d^{1.2} \quad \text{(cm)} \tag{12-9}$$

The penetration into metal-like materials is given by (Reference 12-4)

$$P_m = K_t \rho^{1/2} V^{2/3} d^{1.1}/H_t^{1/4} \rho_t^{1/6} \quad \text{(cm)} \tag{12-10}$$

Ratioing penetration yields

$$t_3 = t_s \frac{K}{K_t} d^{0.1} H_t^{1/4} \rho_t^{1/6} \tag{12-11}$$

For a variety of materials, the K_t value has been established as 1.38. Let d be the diameter associated with a 10^{-6}-gram particle, since this is in the range of greatest interest, then

$$d = \left[\frac{(6)(10^{-6})}{\pi(3.5)}\right]^{1/3} = 0.818 \times 10^{-2} \quad \text{(cm)} \tag{12-12}$$

When values are inserted

$$t_3 = \frac{(0.64)(0.818 \times 10^{-2})^{0.1}}{1.38} t_s H_t^{1/4} \rho_t^{1/6} \tag{12-13}$$

$$= 0.287 t_s H_t^{1/4} \rho_t^{1/6} \quad \text{(cm)}$$

12-15

The above equation can be used to determine the effective thickness of various substrate materials for use in the area loss equations. Thickness values obtained for the study spacecraft are presented in Figure 12-7.

Degradation Analysis and Results

Once the meteoroid environment has been defined and the analytical equations developed to predict damage to exposed components, it is necessary to define the mission path through the meteoroid environment, both temporal (time in a region of space) and spatial (orientation of spacecraft component in question giving projected area) as the meteoroid flux density is dependent upon the region in space.

Using velocity data associated with the recommended mission profile (Figure 12-1) and measuring the angle between the spacecraft trajectory and a circular orbit, Figures 12-3 through 12-6 can be used to find the impact velocity for various times along the mission.

The meteoroid flux densities are strongly dependent on the distance of the spacecraft from the sun. To find the actual flux encountered, this radial dependence, $f(R)$, must be integrated over the spacecraft trajectory. This was accomplished by defining an effective exposure time T_R.

$$T_R = \int_{T_1}^{T_2} f(R) \, d \, T_a \qquad (12\text{-}14)$$

For cometary particles, $f(R) = R^{-1.5}$

For asteroidal particles, $f(R)$ is defined by Figure 12-2.

The cometary particles are assumed to be omnidirectional so that the effective area of impact will be the actual panel areas. The asteroidal particles are assumed to be in a circular orbit near the ecliptic plane. Therefore the effective area for asteroidal impacts is defined as

$$A_{sp} = A' \, \sin \phi \qquad (12\text{-}15)$$

where

A' = exposed area projected perpendicular to ecliptic plane

ϕ = angle between incident particles and solar panels (See Figure 12-9).

12-16
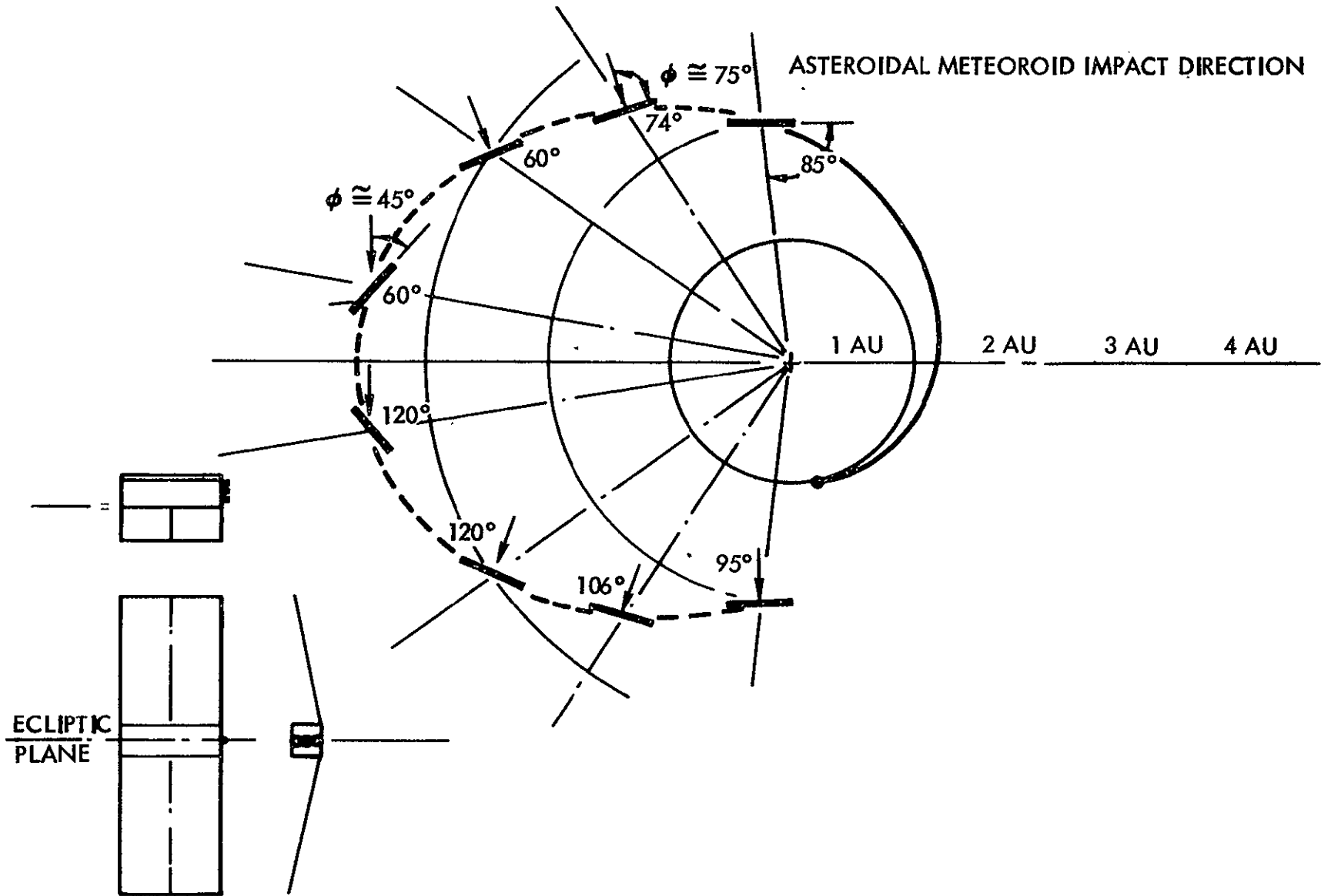
Figure 12-9. Spacecraft Orientation

Since there are large variations in impact velocities and flux throughout the mission, the area losses were calculated for five segments of the mission and then summed for the total area loss. In this way, the calculations were able to account for the changes in orientation at aphelion and for the strong influence of the asteroid belt in the region from 2 AU to 3 AU   The five regions into which the mission was partitioned are listed below.

Region	Position (AU)	Assumed Mission Time (Days)
I	1 - 2	0 - 240
II	2 - 3	240 - 460
III	3 - 3.5 (aphelion)	460 - 750
IV	3.5 - 3	750 - 1040
V	3 - 2	1040 - 1260

Table 12-2 is a summary of the parameters found for the various time regions.

The preceding equations were used to calculate front and rear surface areas losses for the asteroidal and cometary particles. The input data used are summarized below and in Table 12-2.

Power loss = (0.5) (area loss)

$$\alpha = 20$$

$$K = 0.64$$

$$K_1 = 1.38$$

$$\rho = 0.5 \text{ gm/cm}^3 \text{ cometary, } 3.5 \text{ gm/cm}^3 \text{ asteroidal}$$

$$m_1 = 10^{-12} \text{ gram}$$

$$N_{AST_{max}} = 10^2 \ N_{AST_{nominal}}$$

$$N_{COM_{max}} = 5 \ N_{COM_{nominal}}$$

Figure 12-10 shows the total power loss which may be expected for the asteroidal belt mission exclusive of cometary stream losses. Both front and

SOLAR ARRAY (GE MODIFIED)
55.7 m² (600 FT²) TOTAL AREA

ECLIPTIC PLANE

2.5 (100)

66° (REF)

12.5 (492)

3.2 (125)

CANOPUS

29°

CANOPUS SENSOR F.O.V. ±24°

HIGH GAIN ANTENNA

POWER CONDITIONING PANEL

1.3 (50)

1.0 (40)

LOW GAIN ANTENNA

DIMENSIONS IN METERS
INCHES IN PARENTHESIS

FOLDOUT FRAME #1

FOLDOUT FRAME #2
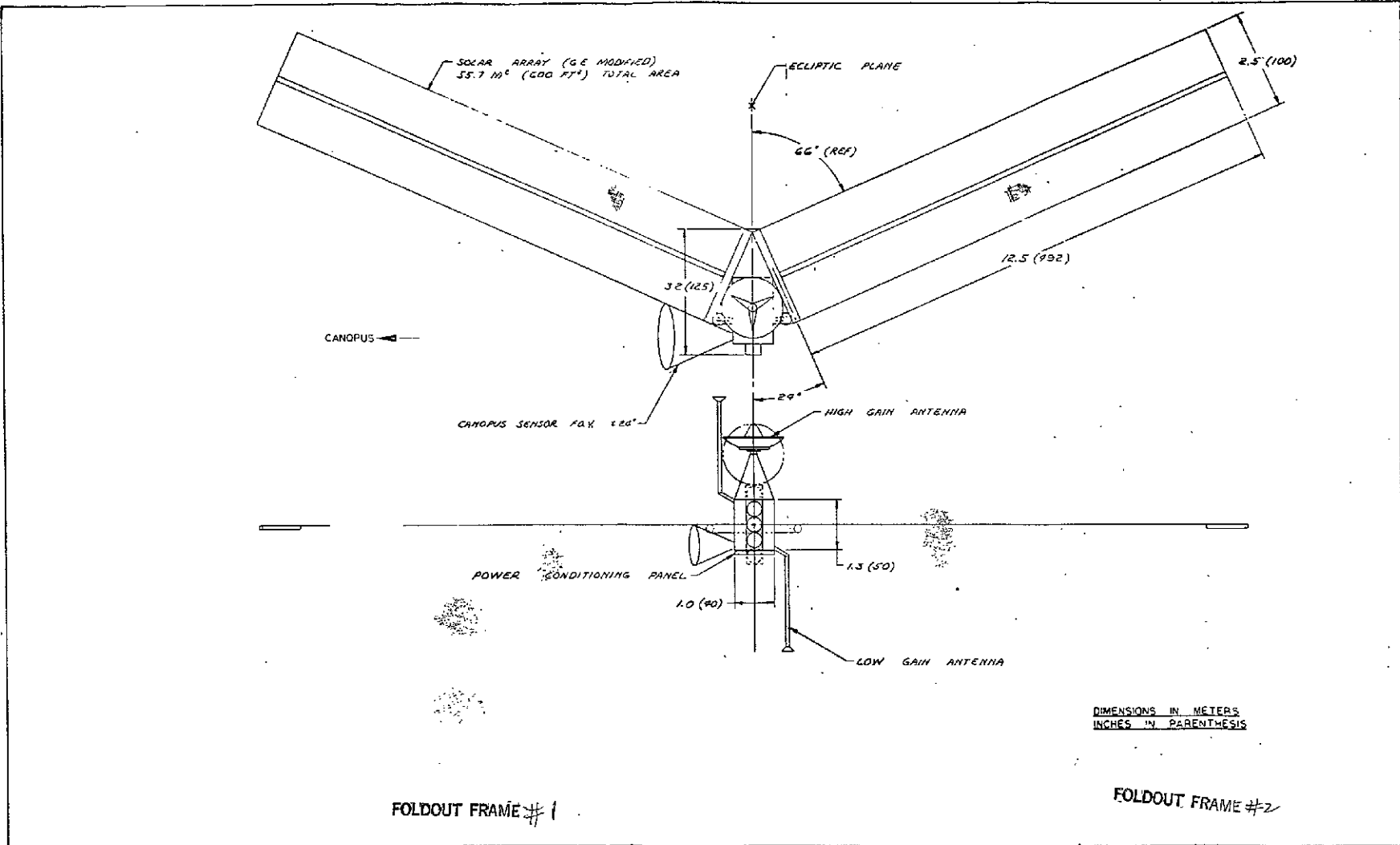
Figure D-3. Six-Kilowatt Spacecraft, Atlas/Centaur Launch Configuration
(Drawing 5349-21)

D-9, D-10
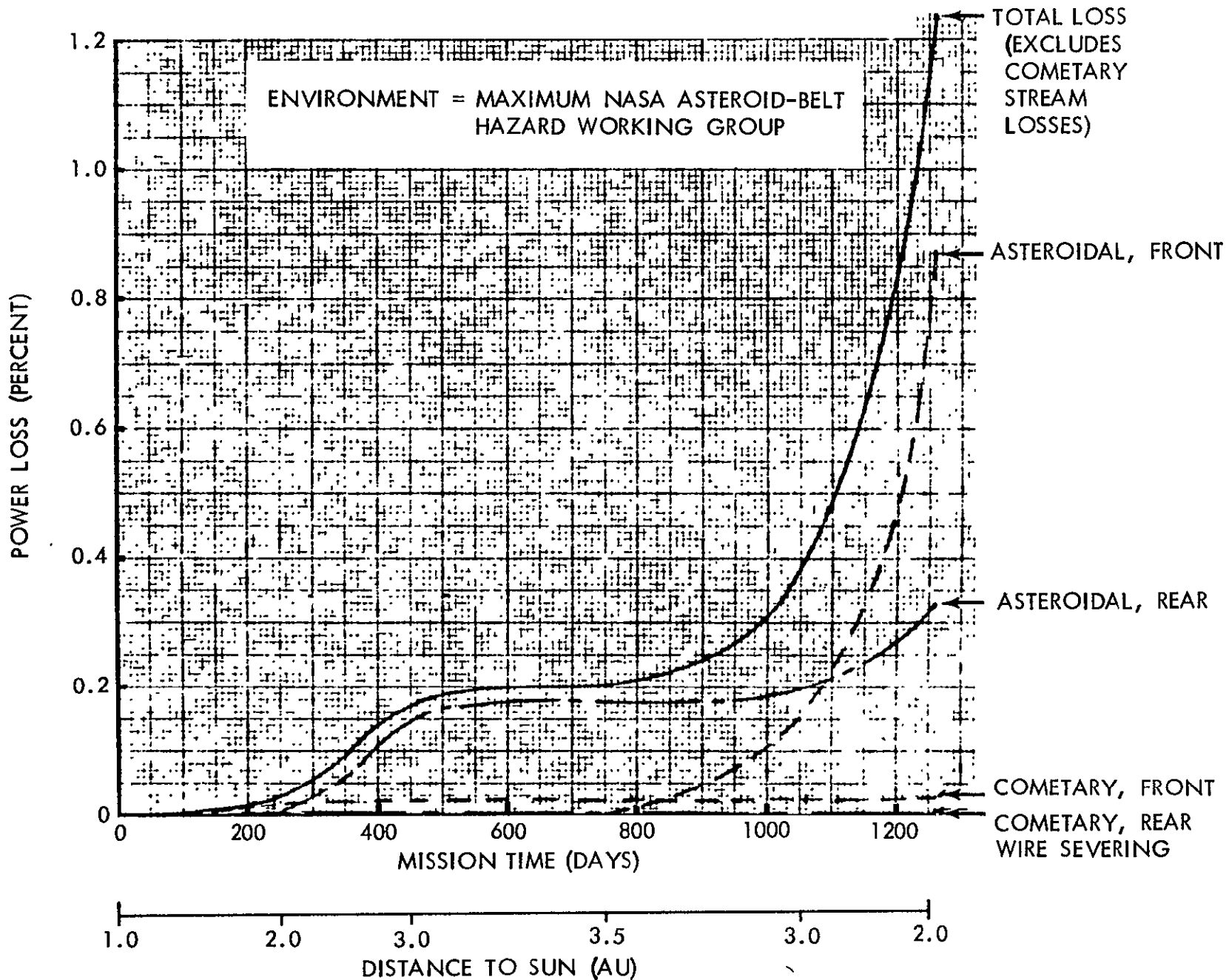
Figure 12-10. Power Loss of Solar Cells Due to Meteoroid Impacts -
1260-Day Mission, MSC Maximum Environment

Space Division
North American Rockwell

rear impacts, asteroidal and cometary, have been considered. From Figure 12-10 it may be seen that cometary damage is minimal in comparison with asteroidal damage. This can be attributed to the fact that the NASA-MSC environment specifies a smaller population of cometary particles. The fact that most of the cometary damage occurs at the start of the mission reflects the strong radial dependence of the cometary flux in the NASA-MSC model. The major part of the power loss occurs from asteroidal impacts on the front surface of the panels occurring after aphelion. The rear surface is subjected to far more impacts during the mission, but the multilayered substrate and the meteoroid capacitor sheet detector offer sufficient protection to keep the overall damage extremely low.

METEOROID STREAM ANALYSIS

For a long-duration mission such as the asteroid belt tour, consideration must be given to the possibility of encountering an active meteoroid stream. The NAR model for this hazard is based on the observed relation between the orbits of meteoroid streams and the orbits of comets. Figure 12-11 shows the asteroid belt tour trajectory superimposed on a plot of the points where observed cometary orbits intersect the ecliptic plane. Different launch dates would correspond to rotating the trajectory curve with respect to the comet locations. By plotting the trajectory for several launch dates, it was found that a typical trajectory will intersect approximately four comet orbits, but not all of these intersections will coincide with the appearance of the comet and its associated meteoroid stream (active encounters).

Figure 12-11 shows an October 1, 1975 launch for which one active stream would be encountered and a November 1, 1975 launch for which no active streams would be encountered. The significance of one active encounter on solar panel performance was investigated using the October 1, 1975 launch trajectory. This trajectory would pass close to the orbit of the comet Schaumasse in the Fall of 1977. Figure 12-12 shows that the power loss expected during the 10 days of active encounter is greater than the total for the entire remainder of the mission. However, even with this increased panel degradation, the total power loss is of a level which would be acceptable, provided the encounter occurs after the termination of powered flight.

A trajectory with a starting date of October 22, 1975 was also investigated and was found to intersect four active shower zones. This indicates the strong sensitivity of meteoroid shower damage to spacecraft launch date. This finding corresponds to planetary spacecraft experience where Mariner VI suffered no apparent meteoroid damage, and Mariner VII following a short time later suffered an apparent shower encounter near Mars.
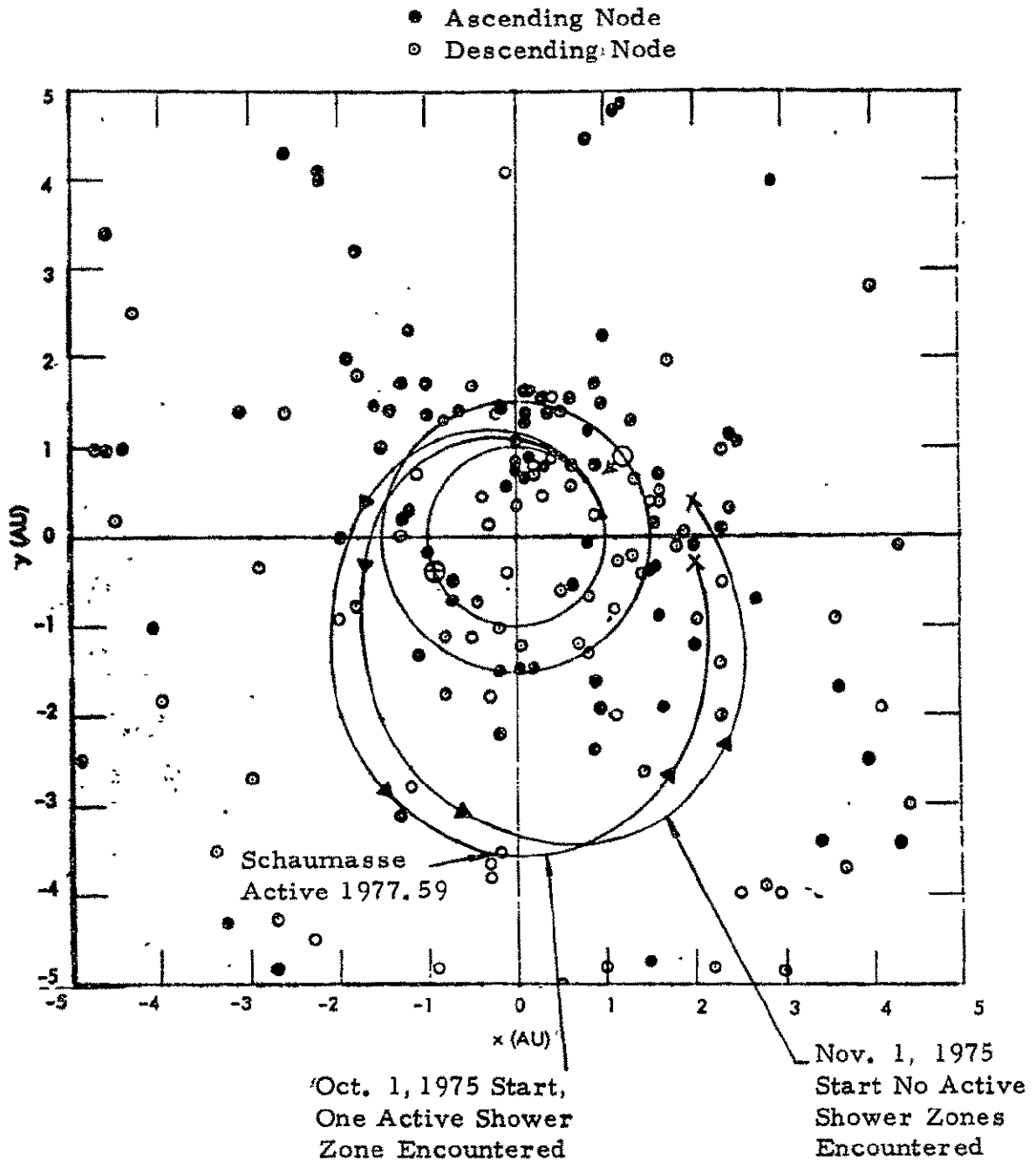
Figure 12-11. Major Cometary Streams Encountered During 1260-Day
Asteroid Belt Tour - NR/SD Stream Environment

12-23
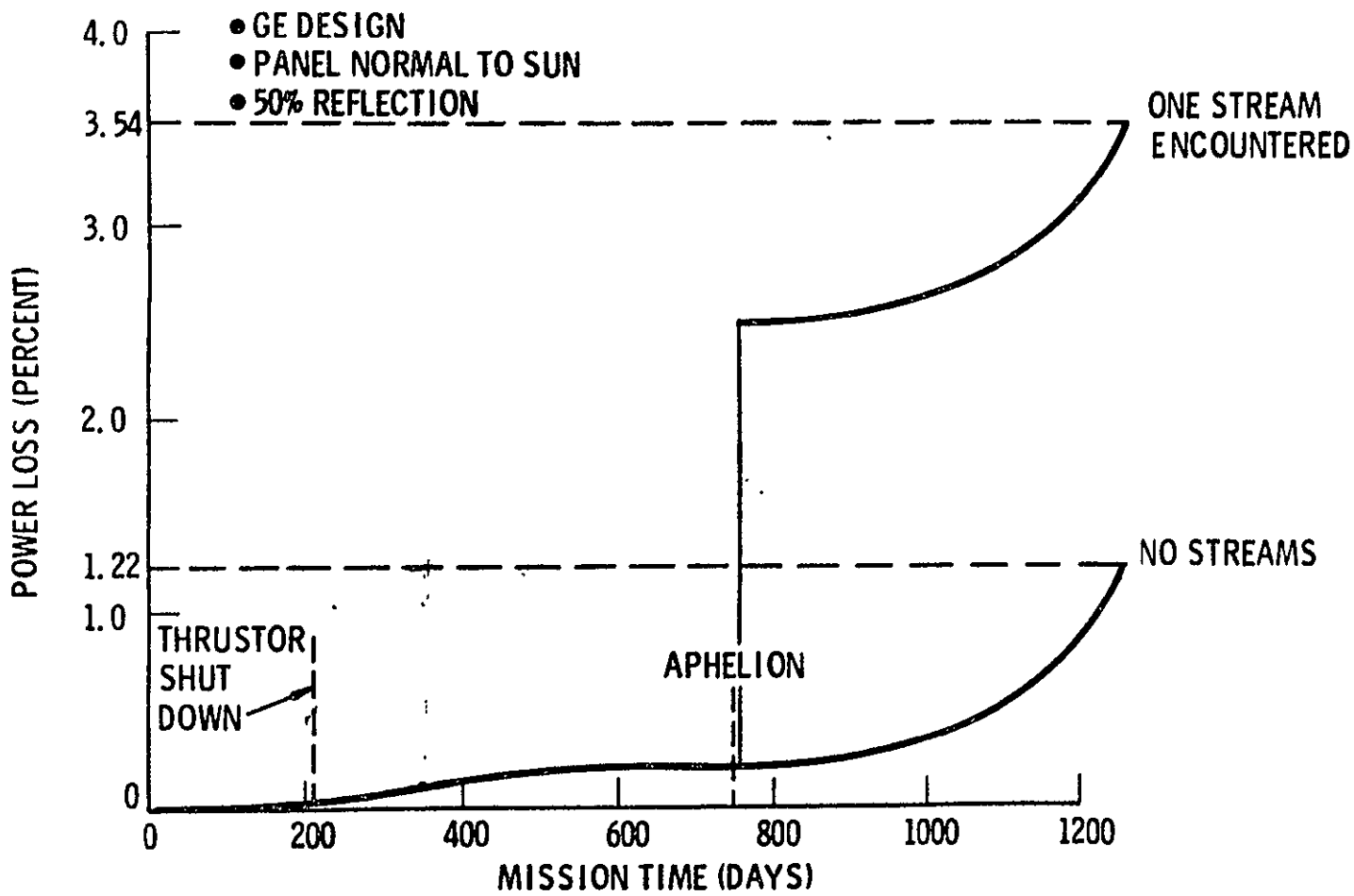
Figure 12-12. Power Loss of Solar Arrays Due to Meteoroid Impacts (NASA Maximum Environment) and Cometary Streams (NR-SD Model)

EQUIPMENT COMPARTMENT SHIELDING ANALYSIS

A study was made of the shielding requirements to prevent perforation of the equipment compartment. The size of particle which will be stopped by an aluminum wall is given by the NR/SD penetration equation for single sheet metal of thickness t, (Reference 12-4).

$$d = \left(\frac{t \, H_t^{1/4} \, \rho_t^{1/6}}{1.38 \, f_f \, \rho^{1/2} \, V^{2/3}} \right)^{0.91} \tag{12-16}$$

For a given wall thickness, the largest cometary and asteroidal particles which would be stopped are calculated for each region of the trajectory. Then the probability of no compartment perforation is found by calculating the probability that no particle larger than that which can be stopped will impact the compartment.

$$P_o = e^{-N \, A_{sp} \, T_R} \tag{12-17}$$

Here N is a function of m and m is set equal to the largest mass stopped by a given wall. P_o was calculated separately for each type of particle and each time region of the trajectory.

The probability of no perforation for each kind of particle and time region are multiplied together to form the overall probability of no failure due to meteoroid impacts.

$$P_{o_{TOTAL}} = P_{o_{AST_I}} \times P_{o_{COM_I}} \times P_{o_{AST_{II}}} \times \cdots \times P_{o_{COM_V}} \tag{12-18}$$

This procedure was used to obtain the single sheet, nominal environment curve shown in Figure 12-13.

Penetration mechanics relations developed at the Space Division have shown that a double sheet bumper system is a more efficient way of stopping a given particle. Using these analysis methods, a first wall is sized to give optimum fragmentation of the meteoroid particle. After a minimum spacing, the fragmented and scattered particle can be stopped by a thin second sheet. The combined thickness of the two sheets for this case is approximately one fifth of the thickness of the equivalent single sheet bumper. Results for
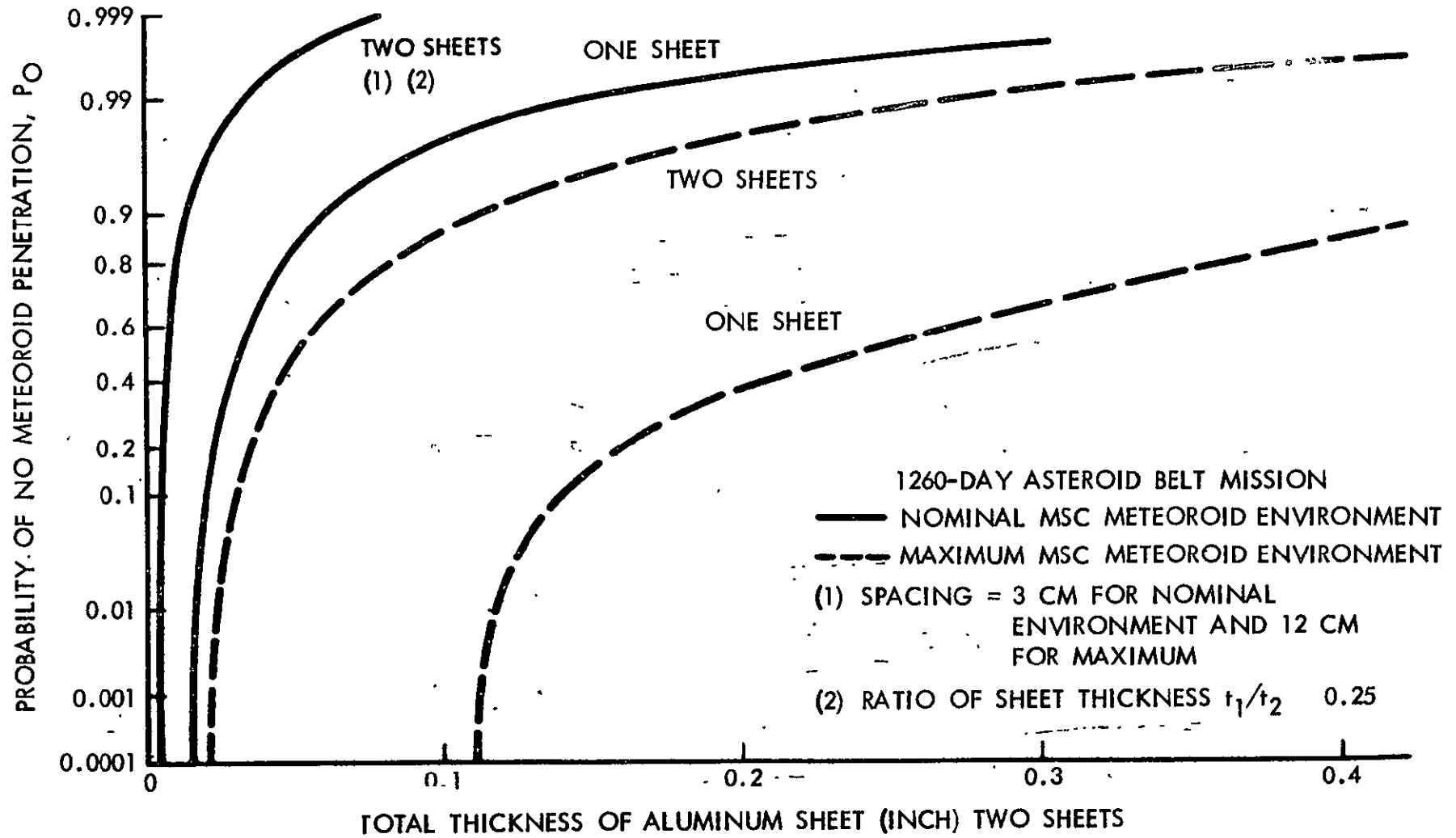
Figure 12-13. Resistance of Solar Electric Spacecraft Equipment
Compartment to Perforation by Meteoroids

two-sheet sizing are also shown in Figure 12-13. From this plot it can be concluded that a considerable weight savings should result from a two-wall structure. The thermal insulation in the compartment would also contribute to the shield thickness.

One side of the equipment compartment has a system of louvers for controlling the thermal environment. Immediately inside of the louvers is a panel on which the various instruments are mounted. This panel could be sized to stop any small particle passing through the open louvers. For larger particles the outer bumper employed around the rest of the compartment would impair the thermal performance of the louver system. Figure 12-14 illustrates the mesh concept which would satisfy both the meteoroid protection and thermal control requirements. The mesh size and spacing would be sized to fragment meteoroid particles so that they could be stopped by the instrument mounting panel.

Figure 12-14. Screen - Meteoroid Bumper Concept

SCREEN FEATURES

- WILL PROTECT AGAINST
  LARGE METEOROIDS

- ALLOWS EFFICIENT HEAT
  TRANSFER FROM EQUIP-
  MENT COMPARTMENT

SMALL PARTICLE RESISTED
BY MTG PLATE

LARGE PARTICLE
FRAGMENTED BY
BUMPER

SCREEN
BUMPER

LOUVER

MOUNTING
PLATE

Space Division
North American Rockwell

13. REFERENCES

2-1   The Outer Solar System, National Academy of Sciences, Washington (1969).

2-2   Robey, D. H. , A New Theory on the Nature and Origin of Comets, General Dynamics/Convair, PN 2-1-65 (28 June 1965).

2-3   Weddell, J. B. , Solar Proton Event Production by Hydromagnetic Shocks, Planet, Space Science 13, 789 (1965).

2-4   Haffner, J. W. , Solar Flare Proton Propagation, NR-SD, 69-585 (September 1969).

2-5   Haffner, J. W. , and E. R. Beever, A Theoretical Study of the Thermal Control Coating Degradation in the Space Environment, NR-SD 69-45 (1 March 1969).

2-6   Report of Asteroid Belt Hazard Working Group, NASA unpublished report (1969).

5-1   Sisyphus Optical Meteoroid Detector System.   Unpublished report, General Electric Co. (1968).

5-2   Burbank, P. B. , and B. G. Cour-Palais, Measurement of the Dynamic Properties of Interplanetary Matter, NASA-MSC (27 November 1968).

6-1   "Electric Propulsion Design Optimization Computer Program Development, " Final Report on Contract No. NAS7-559 conducted by the Hughes Research Laboratories for the Jet Propulsion Laboratory, to be published.

6-2   "A Study of Liquid Mercury Isolator Development, " Final Report Contract No. NAS7-539, Sept. 1967.

6-3   "Data Collection for Nonelectric Reliability Handbook (NEDCO II)" Technical Report No. RADC-TR-68-114, Yurkovisky, W., Hughes Aircraft Company, June 1968.

6-4   MIL-HDBK-217A, "Reliability Stress and Failure Rate Data for Electronic Equipment, " 1 December 1965.

6-5 "Reliability Data Book" Martin Company, June 1962, Baltimore, Maryland.

6-6 Reliability Application and Analysis Guide - Martin Company, July 1961, Denver, Colorado.

6-7 Masek, T.D., and J.R. Womack, "Experimental Studies With a Clustered Ion Engine System," AIAA Electric Propulsion and Plasmadynamics Conference, Colorado Springs, Colorado, Report No. 67-698, September 11-13, 1967.

7-1 A Proposal for Phase II 30 Watt Per Pound Rollup Solar Array, Volume 1. MSD Proposal No. F-20430, General Electric MSD, Valley Forge, Penn., 31 May 1968.

7-2 Analysis of Aerospace Power Conditioning Component Limitations, Final Report. TRW Systems Group, Redondo..Beach, Calif., Contract NAS7-546, NASA CR-97000, April 1969.

7-3 Study and Analysis of Satellite Power Systems Configurations for Maximum Utilization of Power. TRW Systems, Redondo Beach, Calif., NASA Contract NAS 5-9178, NASA CR-898, October 1967.

7-4 Power System Configuration Study and Reliability Analysis, Final Report. NASA Contract 951574, TRW Report No. 07171-6001-R000, 18 September 1967.

12-1 The Interplanetary Meteoroid Environment - 1969, NASA Asteroid Belt Hazard Working Group, 1969.

12-2 Dycus, R.D. and A.J. Richardson "A Meteoroid Stream Model for Evaluation of the Stream Hazard to Interplanetary Flight," Journal of Spacecraft and Rockets. (September 1969).

12-3 Bowman, Robert L., Michael J. Mirtich, and John R. Jack, Performance of N/P Silicon and Cadmium Sulfide Solar Cells as Affected by Hypervelocity Particle Impacts, NASA TN D-5133, Lewis Research Center, March 1969.

12-4 Richardson, A.J. and A.H. McHugh. Hypervelocity Impact Penetration Equation for Metal by Multiple Regression Analysis. NAA/S&ID Report STR 153. (March 1966).

APPENDIX A. ANALYSIS OF SOLAR CELL AREA LOSS
DUE TO METEOROID IMPACTS

The possibility of a catastrophic failure of the solar panels as a result of collisions with very large particles is quite unlikely. The major portion of the meteoroid damage to a solar panel will be in the form of a gradual degradation of solar cell performance. This will be a result of the fracture zone produced by a hypervelocity impact into glass. This fractured area will have a reduced efficiency. In order to assess the cumulative damage, it is necessary to determine relations for the percentage of panel area which has been fractured at any time during the mission. The procedure for calculating this area loss is explained in the following pages. The nomenclature for this analysis is listed at the front of Section 12.

EQUATIONS FOR SOLAR PANEL AREA LOSS DUE TO METEOROID IMPACTS ON THE FRONT SURFACE

The penetration depth for glass is given by the NR/SD equation

$$P = K \, \rho^{1/2} \, V^{2/3} \, d^{1.2} \text{ (cm)} \tag{A-1}$$

and the relation between penetration depth and fracture zone diameter is

$$D_{fz} = \alpha P \text{ (cm)} \tag{A-2}$$

The area lost per impact is

$$A'_{L_1} = \frac{\pi}{4} D_{fz}^2 = \frac{\pi}{4} \alpha^2 \, (K \rho^{1/2} V^{2/3} d^{1.2})^2 \text{ (cm}^2) \tag{A-3}$$

Equation A-3 may be expressed in terms of the mass of the impacting particle by·

$$d = \left(\frac{6m}{\pi \rho}\right)^{1/3} \text{ (cm)}$$

$$d^{2.4} = \left(\frac{6m}{\pi \rho}\right)^{\frac{2.4}{3}} = 1.68 \frac{m^{0.8}}{\rho^{0.8}} \text{ (cm}^{2.4}) \tag{A-4}$$

Equation A-3 becomes

$$A'_{L_1} = 1.32 \, \alpha^2 K^2 \, \rho^{0.2} \, V^{\frac{4}{3}} m^{0.8} \text{ (cm}^2) \tag{A-5}$$

The flux of asteroidal meteoroid particles per unit area per second is given by

$$N_{AST} = \frac{1}{4} V_{AST} \frac{10^{-15.79}}{m^{0.84}} \text{ (m}^{-2} - \text{sec}^{-1}) \tag{A-6}$$

The flux of particles of mass m to m + dm is

$$dN = \frac{1}{4} V_{AST} \, 10^{-15.79} \left[\frac{1}{m^{0.84}} - \frac{1}{(m+dm)^{0.84}} \right] \tag{A-7}$$

using a Taylor Expansion

$$(m + dm)^{0.84} = m^{0.84} + 0.84 \, m^{-0.16} \, dm + \dots \tag{A-8}$$

A-2

SD 70-21-2

Excluding second-order terms

$$dN = \frac{1}{4} V_{AST} \frac{(0.84) \, 10^{-15.79}}{m^{1.84}} dm \quad (m^{-2} - sec^{-1}) \qquad (A-9)$$

and the total impacts of particles of mass m to m + dm is

$$dn = \frac{0.84}{4} V_{AST} \frac{10^{-15.79} A_{sp} T_R \, dm}{m^{1.84}} \qquad (A-10)$$

The area lost by impacts of particles of mass m to m + dm is

$$dA_{L_1} = A'_{L_1} \, dn = \frac{0.84}{4} V_{AST} \frac{10^{-15.79} A'_{L_1} A_{sp} T_R \, dm}{1.84} \qquad (A-11)$$

Assuming that all particle impacts are non overlapping, then the total area lost by all impacts becomes

$$A_{L_1} = \int_{m_1}^{m_2} A'_{L_1} \, dn$$

$$A_{L_1} = 1.32 \left(\frac{0.84}{4}\right) 10^{-15.79} A_{sp} T_R \, \alpha^2 \, K^2 \, \rho^{0.2} \, V_{AST}^{7/3} \int_{m_1}^{m_2} \frac{dm}{m^{1.04}}$$

$$(cm^2) \qquad (A-12)$$

Note that some of the terms from different equations have different dimensions. Putting all velocities in km/sec and all areas in cm² gives the area loss for asteroidal particles as

$$\frac{A_{L_1}}{A_{sp}} = 0.132 \left(\frac{0.84}{4}\right) 10^{-15.79} T_R \, \alpha^2 \, K^2 \, \rho^{0.2} \, V_{AST}^{7/3} \left(\frac{1}{-0.04}\right)\left(\frac{1}{m_2^{0.04}} - \frac{1}{m_1^{0.04}}\right)$$

$$\frac{A_{L_1}}{A_{sp}} = (69.3) \, 10^{-15.79} T_R \, \alpha^2 K^2 \rho^{0.2} V_{AST}^{7/3} \left(\frac{1}{m_1^{0.04}} - \frac{1}{m_2^{0.04}}\right) (percent)$$

$$(A-13)$$

For the lower limit, m_1 is assumed to be the mass of the smallest particle that can be held in orbit around the sun,

$$m_1 = 1 \times 10^{-12} \, (gm) \qquad (A-14)$$

The upper limit of mass is established so that there is a probability of only 0.001 that a particle of mass m_2 or greater will impact on the area A_{sp} during the time T_R. From Equation A-6,

$$0.001 = \frac{1}{4} V_{AST} \frac{10^{-15.79} A_{sp} T_R}{m_2^{0.84}}$$

$$m_2 = \left[\frac{1}{4} V_{AST} \frac{10^{-15.79} A_{sp} T_R}{0.001}\right]^{\frac{1}{0.84}} \text{(gm)} \qquad \text{(A-15)}$$

The NASA-MSC cometary environment is defined for two separate ranges of particle mass. For the case $10^{-6} \leq m \leq 10^2$:

$$N_{COM} = \frac{1}{4} V_{COM} \frac{10^{-18.27}}{m^{1.207}} \quad (m^{-2} - sec^{-1}) \qquad \text{(A-16)}$$

As before

$$dn = \frac{1.207 V_{COM}}{4} \frac{10^{-18.27} A_{sp} T_R \, dm}{m^{2.207}} \qquad \text{(A-17)}$$

By following the same procedure used above, a percentage area loss for large cometary particles is

$$\frac{A_{L1}}{A_{sp}} = 9.78 \, \alpha^2 \, K^2 \, \rho^{0.2} \, V_{COM}^{7/3} \, 10^{-18.27} T_R \left(\frac{1}{m_1^{0.407}} - \frac{1}{m_2^{0.407}}\right) \text{(percent)}$$

$$\text{(A-18)}$$

where

$$m_1 = 10^{-6} \text{ gm}$$

$$m_2 = \left[\frac{1}{4} V_{COM} \frac{10^{-18.27}}{0.001} A_{sp} T_R\right]^{\frac{1}{1.207}} \text{gm}$$

The NASA-MSC cometary environment for small particles $(10^{-12} \leq m \leq 10^{-6})$ is of a mathematical form which does not readily adapt to the analysis procedure used above. Therefore it was necessary to make an approximation for the flux of this range of particles. A plot of the actual environment and the approximation is given in Figure A-1.
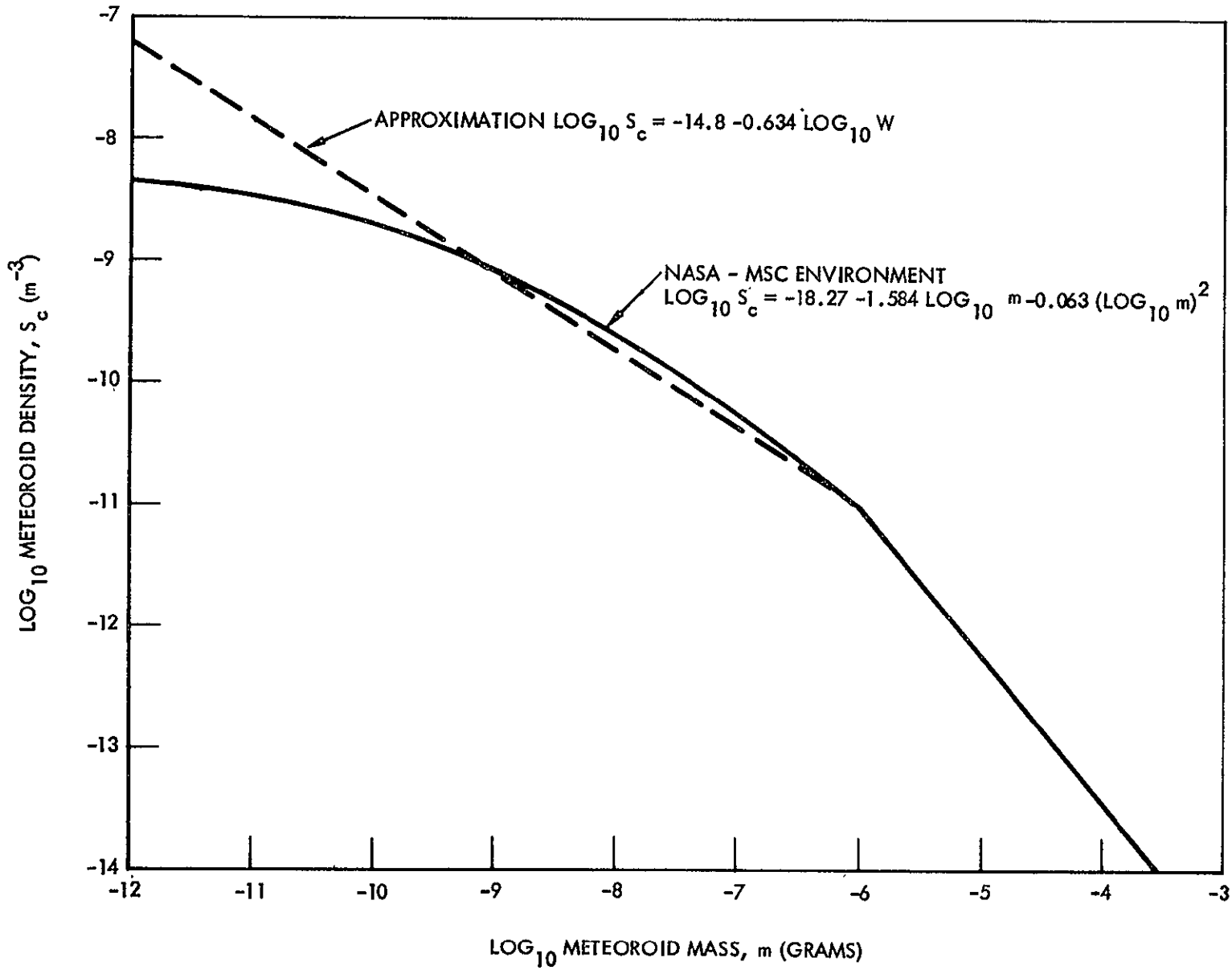
Figure A-1. NASA-MSC Cometary Particle Density and Approximation

Space Division
North American Rockwell

$$N_{COM} = \frac{1}{4} V_{COM} \frac{10^{-14.8}}{m^{0.634}} (m^{-2} - sec^{-1}) \qquad (A-19)$$

By following the analysis procedure used above, the area loss for small cometary articles is:

$$\frac{A_{L1}}{A_{sp}} = 12.62 \; \alpha^2 K^2 \rho^{0.2} \; V_{COM}^{7/3} \; 10^{-14.8}$$

$$T_R \left(m_2^{0.166} - m_1^{0.166} \right) \text{ (percent)} \qquad (A-20)$$

where

$$m_1 = 10^{-12} \text{ gm}$$

$$m_2 = 10^{-6} \text{ gm}$$

EQUATIONS FOR SOLAR PANEL AREA LOSS DUE TO METEOROID IMPACTS ON THE REAR SURFACE

The penetration depth into the solar cell for a rear surface impact is

$$P_S = P - t_3 = K \; \rho^{1/2} \; V^{2/3} \; d^{1.2} - t_3 \text{ (cm)} \qquad (A-21)$$

The fracture zone diameter is

$$D_{fz} = \alpha P_s = \alpha (P - t_3) \text{ (cm)} \qquad (A-22)$$

and the area lost per impact is given by

$$A'_{L2} = \frac{\pi}{4} \alpha^2 (K \; \rho^{1/2} \; V^{2/3} \; d^{1.2} - t_3)^2 \text{ (cm}^2)$$

$$A'_{L2} = \frac{\pi}{4} \alpha^2 \left(K^2 \; \rho V^{4/3} \; d^{2.4} - 2K \; \rho^{1/2} \; V^{2/3} \; d^{1.2} t_3 + t_3^2 \right) \text{(cm}^2) \qquad (A-23)$$

A-6

Using Equation A-4,

$$d^{2.4} = 1.68 \frac{m^{0.8}}{\rho^{0.8}} \tag{A-24}$$

$$d^{1.2} = 1.296 \frac{m^{0.4}}{\rho^{0.4}}$$

and Equation A-23 becomes

$$A'_{L_2} = \frac{\pi}{4} \alpha^2 \, (1.68 \, K^2 \, m^{0.8} \, V^{4/3} \rho^{0.2}$$

$$-2.592 \, K \, m^{0.4} \, V^{2/3} \rho^{0.1} \, t_3 + t_3^2) \ (cm^2) \tag{A-25}$$

By the same reasoning as in the front-surface analysis, the total area lost is found by calculating the area lost from impacts of an incremental range of masses and then integrating over the applicable range of mass.

For the asteroidal particles

$$dn = \frac{0.84}{4} V_{AST} \frac{10^{-15.79}}{m^{1.84}} A_{sp} \, T_R \, dm \tag{A-26}$$

Assuming all particle impacts are separate, total area loss is

$$A_{L_2} = \int_{m_1}^{m_2} A'_{L_2} \, dn = \frac{\pi}{4} \alpha^2 \left(\frac{0.84}{4} \right) V_{AST} \, 10^{-15.79} \, A_{sp} \, T_R$$

$$\left(1.68 \, K^2 \, \rho^{0.2} \, V_{AST}^{4/3} \int_{m_1}^{m_2} \frac{dm}{m^{1.04}} \right.$$

$$-2.592 \, K \, \rho^{0.1} \, V_{AST}^{2/3} \, t_3 \int_{m_1}^{m_2} \frac{dm}{m^{1.44}}$$

$$\left. + t_3^2 \int_{m_1}^{m_2} \frac{dm}{m^{1.84}} \right) \tag{A-27}$$

A-7

When units on A_{sp} and V_{AST} are corrected as above, the area loss due to asteroidal particles is

$$\frac{A_{L_2}}{A_{sp}} = 2.5 \pi \alpha^2 \left(\frac{0.84}{4}\right) V_{AST} \ 10^{-15.79} \ T_R \left[1.68 \ K^2 \ \rho^{0.2} \ V_{AST}^{4/3} \right.$$

$$\left(\frac{1}{-0.04}\right) \left(\frac{1}{m_2^{0.04}} - \frac{1}{m_1^{0.04}}\right) - 2.592 \ K \ \rho^{0.1} \ V_{AST}^{2/3} \ t_3$$

$$\left(\frac{1}{-0.44}\right) \left(\frac{1}{m_2^{0.44}} - \frac{1}{m_1^{0.44}}\right) + t_3^2 \left(\frac{1}{-0.84}\right) \left(\frac{1}{m_2^{0.84}} - \frac{1}{m_1^{0.84}}\right) \Bigg]$$

(percent) $\hspace{6cm}$ (A-28)

For the large cometary particles $(10^{-6} \leq m \leq 10^2)$

$$dn = \frac{1.207}{4} \ V_{COM} \ 10 \frac{-18.27}{m^{2.207}} A_{sp} \ T_R \ dm \hspace{2cm} \text{(A-29)}$$

If all particle impacts are separate, total area loss is

$$A_{L_2} = \int_{m_1}^{m_2} A'_{L_2} \ dn = \frac{\pi \alpha^2}{4} \left(\frac{1.207}{4}\right) V_{COM} \ 10^{-18.27} \ A_{sp} \ T_R$$

$$\left(1.68 \ K^2 \ \rho^{0.2} \ V_{COM}^{4/3} \int_{m_1}^{m_2} \frac{dm}{m^{1.407}} - 2.592 \ K \ \rho^{0.1} \right.$$

$$V_{COM}^{2/3} \ t_3 \int_{m_1}^{m_2} \frac{dm}{m^{1.807}} + t_3^2 \int_{m_1}^{m_2} \frac{dm}{m^{2.207}} \right) \hspace{1.5cm} \text{(A-30)}$$

When units on A_{sp} and V_{COM} are corrected as above, the area loss due to large cometary particles is

$$\frac{A_{L_2}}{A_{sp}} = 2.5 \ \pi \ \alpha^2 \left(\frac{1.207}{4}\right) V_{COM} \ 10^{-18.79} \ T_R \left[1.68 \ K^2 \ \rho^{0.2} \ V_{COM}^{4/3}\right.$$

$$\left(\frac{1}{-0.407}\right) \left(\frac{1}{m_2^{0.407}} - \frac{1}{m_1^{0.407}}\right) -2.592K \ \rho^{0.1} \ V_{COM}^{2/3} \ t_3$$

$$\left(\frac{1}{-0.807}\right) \left(\frac{1}{m_2^{0.807}} - \frac{1}{m_1^{0.807}}\right) + t_3^2 \left(\frac{1}{-1.207}\right)$$

$$\left(\frac{1}{m_2^{1.207}} - \frac{1}{m_1^{1.207}}\right) \right] \quad \text{(percent)} \tag{A-31}$$

When $t_3 = 0$, the equations are the same as for the front surface analysis. For both particles, the upper limit of mass is defined as in the front-surface analysis. The lower limit is defined as the mass of the smallest particle that will just penetrate t_3.

$$K \ \rho^{1/2} \ V^{2/3} \ d^{1.2} = t_3 \quad \text{(cm)} \tag{A-32}$$

From Equations A-24

$$d^{1.2} = 1.296 \ \frac{m^{0.4}}{\rho^{0.4}} \tag{A-33}$$

then

$$m_1 = \left(\frac{t_3}{1.296 \ K \ \rho^{0.1} \ V^{2/3}}\right)^{2.5} \quad \text{(gm)} \tag{A-34}$$

As shown in Table 12-2, the value m_1 for cometary particles is greater than 10^{-6} grams. Thus it is not necessary to write a rear surface area loss equation for the smaller range of cometary particles.

APPENDIX B-1. SOLAR ELECTRIC PROPULSION TRAJECTORY
DISPERSION ERROR MODEL

The primary purpose of the SEP trajectory dispersion error model is
to determine the deviations from the nominal SEP powered flight trajectory
as caused by all significant causative factors: to determine the trajectory
dispersions (position and velocity errors) as a function of the primary error
sources. The primary error sources can be categorized into the following
two types:

1. Static errors, or errors that do not change during flight. These
    include heliocentric injection errors, astrodynamic constants
    uncertainties, control body mass uncertainty, and planetary
    ephemeris errors.

2. Dynamic errors, or random acceleration errors that vary during
    flight. These include: low-thrust magnitude and direction errors,
    external forces, (solar winds, light pressure variations, and
    meteoritic impacts), and internal forces, (attitude control jet
    leakages and misfirings).

Of particular interest are the effects of heliocentric injection errors
and in-flight random accelerations (primarily thrusting errors. Accordingly,
the present error model is primarily concerned with the determination of the
nominal powered-flight trajectory dispersions as a function of heliocentric
injection errors and random in-flight thrusting errors, which are the domi-
nant error sources considered. Both of these error sources can be described
statistically as unbiased Gaussian random phenomena with known covariance
or correlation matrices. The explicit desired result is the covariance
matrix of the trajectory dispersions, where it is tacitly assumed that the
position and velocity deviations lie within the range of linearized equations of
motion about the nominal powered trajectory; that is, the actual in-flight
position and velocity state vector are written in terms of the nominal powered
trajectory state vector and a dispersion vector as follows:

$$X(t) = X_N(t) + \delta(t) \tag{B-1}$$

where $X_n(t)$ denotes the nominal state vector, $\delta(t)$ denotes the position and
velocity deviations, and $X(t)$ denotes the actual state vector. The nominal

state vector is determined by a set of nonlinear first-order differential equations as a function of nominal initial conditions and nominal control, $U_n(t)$:

$$\dot{X}_N(t) = F\left[X_N(t), U_N(t)\right] \tag{B-2}$$

with initial conditions $X_N(t_o)$.

For sufficiently small deviations, Equation B-2 can be expanded in a first-order Taylor series to determine a linear, time-varying first-order differential equation for $\delta(t)$:

$$\dot{\delta}(t) = A(t)\,\delta(t) + B(t)\,u(t) \tag{B-3}$$

where $A(t)$ and $B(t)$ are the first-order partials of $\dot{X}_N(t)$ with respect to $X_N(t)$ and $U_N(t)$, respectively, and $u(t)$ denotes the control errors. The initial conditions for $\delta(t)$ are the errors in nominal initial conditions or injection errors. In this manner, the trajectory dispersions can be written as follows:

$$\delta(t) = \phi(t, t_o)\,\delta(t_o) + \int_{t_o}^{t} \phi(t, \tau)\,B(\tau)\,u(\tau)\,d\tau \tag{B-4}$$

where $\phi(t, t_o)$ is the state transition matrix for Equation B-3 which satisfies the following differential equation.

$$\dot{\phi}(t, t_o) = A(t)\,\phi(t, t_o) \tag{B-5}$$

with $\phi(t_o, t_o) = I = 6 \times 6$ identity matrix. In Equation B-4, $\delta(t_o)$ denotes the initial injection errors.

Using Equation B-4, the time-varying covariance matrix for the trajectory dispersions can be written as follows:

$$P(t) = E\left[\delta(t)\, \delta^T(t)\right]$$

$$= \phi(t,\, t_o)\, P_o\, \phi^T(t,\, t_o) \tag{B-6}$$

$$+ \int_{t_o}^{t} \int_{t_o}^{t} \phi(t,\tau)\, B(\tau)\, R(\tau,\rho)\, B^T(\rho)\, \phi^T(t,\rho)\, d\rho\, d\tau$$

where P(t) is the covariance matrix of the trajectory dispersions, P_o is the covariance matrix of the injection errors, and $R(\tau,\rho)$ is the correlation matrix of the control errors:

$$P_o = E\left[\delta(t_o)\, \delta^T(t_o)\right] \tag{B-7}$$

$$R(\tau,\rho) = E\left[u(\tau)\, u^T(\rho)\right] \tag{B-8}$$

where $E[\ ]$ denotes expectation of the argument and T denotes transpose. It should be noted that Equation B-6 assumes that the injection errors $\delta(t_o)$ and control errors u(t) are uncorrelated:

$$E\left[\delta(t_o)\, u^T(t)\right] = 0 \qquad (6 \times 3 \text{ null matrix})$$

The foregoing equations provide a succinct mathematical description of the present problem under consideration: the solution of Equation B-6 yields the trajectory dispersion covariance matrix as a function of injection conditions (the first term) and the random accelerations (the second term). Unfortunately, an explicit analytical solution for P(t) is not possible. The primary difficulty is determining an analytical expression for the state transition matrix $\phi(t, \tau)$, which can be considered as the matrix of first partial derivatives of X(t) with respect to $X(\tau)$. It is noted that for pure conic motion the state transition matrix can be determined in analytical form, but even in this case, the double integral in the second term is difficult to determine analytically. Therefore, equation B-6 must be evaluated numerically, which would require the numerical evaluation of $\phi(t, \tau)$ and then numerical

integration of the second term of Equation B-6. However, this approach is rather inefficient in terms of numerical computations. It is preferrable to define a trajectory dispersion error model which would be highly efficient and sufficiently accurate.

Accordingly, an error model for the present problem is postulated on the basis of an osculating ellipse (Reference B-2): for small intervals of the nominal powered trajectory, the state transition matrix is computed on the basis of local conic motion with the conic motion parameters varying throughout the entire flight trajectory. This assumes that the state transition matrix for the powered trajectory can be defined with sufficient accuracy as the same as that for conic motion which is matched to the powered trajectory over a small interval. The state transition matrix can thus be computed over a sufficiently small interval by using existing computer subroutines for conic motion (Reference B-3). The time-varying state transition matrix can be computed without lengthy numerical computations. It is also postulated that the small time-varying random accelerations can be propagated over each small interval on the basis of rectilinear motion. In this manner, the trajectory dispersions can be written as follows:

$$\delta(t_{i+1}) = \phi(t_{i+1}, t_i) \, \delta(t_i) + \int_{t_i}^{t_{i+1}} \phi(t_{i+1}, \tau) \, B(\tau) \, u(\tau) \, d\tau$$

(B-9)

$$= \phi(t_{i+1}, t_i) \, \delta(t_i) + \int_{t_i}^{t_{i+1}} \Gamma(t_{i+1}, \tau) \, u(\tau) \, d\tau$$

where

$$\delta(t) = \begin{bmatrix} 3 \times 1 \text{ POSITION DEVIATION VECTOR} \\ 3 \times 1 \text{ VELOCITY DEVIATION VECTOR} \end{bmatrix}$$

$$\Gamma(t, \tau) = \begin{bmatrix} I(t-\tau) \\ I \end{bmatrix}$$

(B-10)

$$I = 3 \times 3 \text{ identity matrix}$$

B-4

Now, the trajectory dispersion covariance matrix can be propagated on a discrete basis over sufficiently small time intervals, $t_{i+1} - t_i$, of the powered flight trajectory:

$$P(t_{i+1}) = \phi(t_{i+1}, t_i) P(t_i) \phi^T(t_{i+1}, t_i)$$

$$+ \int_{t_i}^{t_{i+1}} \int_{t_i}^{t_{i+1}} \Gamma(t, \tau) R(\tau, \rho) \Gamma^T(t, \rho) \, d\tau d\rho \qquad (B-11)$$

where

$$P(t_k) = E\left[\delta(t_j) \delta^T(t_j)\right]$$

It is important to note that in Equation B-11 it is assumed that the in-flight random accelerations or control errors are statistically equivalent to a white-noise process or can be simulated by a linear system excited by white noise; that is, either

$$u(t) = w(t) \qquad (B-12)$$

or

$$\dot{u}(t) = K u(t) + w(t) \qquad (B-13)$$

where

$$E\left[w(\tau) w^T(\rho)\right] = I \cdot \delta(\tau - \rho) \cdot \sigma_w^2$$

$$\delta(\tau - \rho) = 1, \text{ for } \tau = \rho \qquad (B-14)$$

$$\delta(\tau - \rho) = 0, \text{ for } \tau \neq \rho$$

$(\sigma_w^2 = \text{white noise variance})$

For present purposes, to separate the effects of the heliocentric injection errors and the control errors upon the trajectory dispersions, it is desirable to express $P(t_{i+1})$ explicitly in terms of the contribution of injection errors and the contribution of control errors to the trajectory dispersions, so the effect of each error source can be assessed separately. It is seen that

$$P(t_i) = J(t_i) + C(t_i)$$

where

$$J(t_i) = \phi(t_i, t_o) P_o \phi^T (t_i, t_o)$$

$$C(t_i) = \int_{t_o}^{t_i} \int_{t_o}^{t_i} \Gamma(t, \tau) R(\tau, \rho) \Gamma^T(t, \rho) \, d\tau d\rho$$

In this manner, $J(t_i)$ is the effect of injection errors and $C(t_i)$ is the effect of control errors upon the trajectory dispersions at the end of the first interval. In general, if

$$P(t_i) = J(t_i) + C(t_i)$$

then

$$P(t_{i+1}) = J(t_{i+1}) + C(t_{i+1}) \tag{B-15}$$

where

$$J(t_{i+1}) = \phi(t_{i+1}, t_i) J(t_i) \phi^T (t_{i+1}, t_i) \tag{B-16}$$

$$C(t_{i+1}) = \phi(t_{i+1}, t_i) C(t_i) \phi^T(t_{i+1}, t_i) + \Delta(t_{i+1}) \tag{B-17}$$

B-6

$$\Delta(t_{i+1}) = \int_{t_i}^{t_{i+1}} \int_{t_i}^{t_{i+1}} \Gamma(t, \tau) \, R(\tau, \rho) \, \Gamma^T(t, \rho) \, d\tau d\rho \qquad (B\text{-}18)$$

Using the principle of mathematical induction, it is seen that a recursive relationship can be used to determine the trajectory dispersion covariance matrix at time t_i, $P(t_i)$, in terms of the contribution of injection errors, $J(t_i)$, and the contribution of thrusting errors, $C(t_i)$. It should be noted that the term $\Delta(t_{i+1})$ is the contribution to trajectory dispersion of the in-flight control errors over the interval $t_{i+1} - t_i$. It is necessary to determine $\Delta(t_{i+1})$ for the type of control errors to be considered, which is a function of $R(\tau, \rho)$. Two types of control errors are considered which are statistically equivalent to: (1) white noise and (2) exponentially correlated noise. The derivation of $\Delta(t_{i+1})$ for each case is given below.

White Noise Case

In this case the three components of control errors are uncorrelated in ensemble and time;

$$E\left[u(\tau) u^T(\rho)\right] = R(\tau, \rho) = I \cdot \delta(\tau - \rho) \cdot \sigma_u^2 \qquad (B\text{-}19)$$

where

$$I = 3 \times 3 \text{ identity matrix}$$

$$\delta(\tau - \rho) = 1 \text{ for } \tau = \rho$$

$$= 0 \text{ for } \tau \neq \rho$$

$$\sigma_u^2 = \text{control error variance}$$

B-7

By substituting Equation B-10 and B-19 into Equation B-18, it is found that

$$\Delta(t_{i+1}) = \sigma_u^2 \int_{t_i}^{t_{i+1}} \int_{t_i}^{t_{i+1}} \left[\frac{I(t_{i+1} - \tau)}{I}\right] \left[I(t_{i+1} - \rho) \mid I\right] \delta(\tau - \rho) \, d\tau d\rho$$

$$= \sigma_u^2 \int_{t_i}^{t_{i+1}} \left[\frac{I(t - \rho)^2}{I(t - \rho)} \middle| \frac{I(t - \rho)}{I}\right] d\rho \qquad (B-20)$$

$$\Delta(t_{i+1}) = \begin{bmatrix} I \cdot \sigma_x^2 & I \cdot \mu_{xv} \\ I \cdot \mu_{vx} & I \cdot \sigma_v^2 \end{bmatrix}$$

where

$$\sigma_x^2 = \sigma_u^2 \cdot 1/3 \cdot (t_{i+1} - t_i)^3 \qquad (B-21)$$

$$\sigma_v^2 = \sigma_u^2 \cdot (t_{i+1} - t_i) \qquad (B-22)$$

$$\mu_{xv} = \mu_{vx} = \sigma_u^2 \cdot 1/2 \cdot (t_{i+1} - t_i)^2 \qquad (B-23)$$

$$I = (3 \times 3) \text{ identity matrix}$$

It is noted that Equations B-21 and B-22 are the position and velocity deviation variances, respectively, and Equation B-23 is the covariance between position and velocity deviations.

Exponentially Correlated Case

In this case the three components of control errors are generated by white-noise excitation of a first-order system:

$$\dot{u}(t) \ = \ - k\,I\,u(t) + w(t) \tag{B-24}$$

where $k > 0$ and

$$E\left[w(\rho)\,w^T\,(\tau)\right] \ = \ I \cdot \delta(\tau - \rho) \cdot \sigma_w^{\ 2} \tag{B-25}$$

It is noted that the solution to Equation B-24 can be written as follows:

$$u(t) \ = \ \int\limits_{-\infty}^{t} e^{-kI(t\,-\,\tau)}\,w(\tau)d\tau \tag{B-26}$$

Thus, the correlation function $R_u(\tau, \rho)$ of $u(t)$ becomes

$$R_u\,(\tau, \rho) \ = \ E\left[u(\tau)\,u^T(\rho)\right]$$

$$= \ \int\limits_{-\infty}^{\tau} \int\limits_{-\infty}^{\rho} e^{-kI(\tau\,-\,t_1)}\,E\left[w(t_1)\,w^T(t_2)\right]e^{-kI(\rho\,-\,t_2)}\,dt_1\,dt_2$$

$$R_u\,(\tau, \rho) \ = \ \sigma_w^{\ 2}\,e^{-kI(\tau + \rho)} \int\limits_{-\infty}^{\tau} \int\limits_{-\infty}^{\rho} e^{+kIt_1}\left[I \cdot \delta(t_1 - t_2)\right]e^{+kIt_2}\,dt_1\,dt_2$$

Now, for $\rho > \tau$

$$R_u(\tau, \rho) = \sigma_w^2 \, e^{-kI(\tau + \rho)} \int_{-\infty}^{T} e^{+2KIt_2} \, I \, dt_2$$

$$= \frac{\sigma_w^2}{2k} \, e^{-kI(\tau + \rho)} \cdot e^{2kIt_2} \, \Big|_{-\infty}^{T}$$

$$R_u(\tau, \rho) = \frac{\sigma_w^2}{2k} \, e^{-kI(\rho - \tau)} \; ; \; \rho > \tau$$

Similarly, for $\tau > \rho$

$$R_u(\tau, \rho) = \frac{\sigma_w^2}{2k} \, e^{-kI(\tau - \rho)} \; ; \; \tau > \rho$$

Thus,

$$R_u(\tau, \rho) = \frac{\sigma_w^2}{2k} \, e^{-kI|\tau - \rho|}$$

$$\text{(B-27)}$$

$$R_u(\tau, \rho) = I \cdot \sigma_u^8 \, e^{-k|\tau - \rho|}$$

where $\sigma_u^2 = \sigma_w^2 / 2k$.

The foregoing shows that the above definition of control errors yields a set of three components of control errors which are uncorrelated in ensemble but each component is exponentially correlated in time with a correlation time constant of $1/k$.

Substituting Equation B-24 into Equation B-18 it is found that

$$\Delta(t_{i+1}) = \left[\begin{array}{c|c} I \cdot \sigma_x^2 & I \cdot \mu_{xv} \\ \hline I \cdot \mu_{vx} & I \cdot \sigma_v^2 \end{array} \right] \tag{B-28}$$

where

$$\sigma_x^2 = \sigma_u^2 \int_{t_i}^{t_{i+1}} \int_{t_i}^{t_{i+1}} (t_{i+1} - \tau)(t_{i+1} - \rho) \, e^{-k|\tau - \rho|} \, d\tau d\rho \tag{B-29}$$

$$\sigma_v^2 = \sigma_u^2 \int_{t_i}^{t_{i+1}} \int_{t_i}^{t_{i+1}} e^{-k|\tau - \rho|} \, d\tau d\rho \tag{B-30}$$

$$\mu_{xv} = \mu_{vx} = \sigma_u^2 \int_{t_i}^{t_{i+1}} \int_{t_i}^{t_{i+1}} (t_{i+1} - \tau) \, e^{-k|\tau - \rho|} \, d\tau d\rho \tag{B-31}$$

Performing the double integrations of Equation B-26 through B-28, the following results are obtained:

$$\sigma_x^2 = \frac{\sigma_u^2}{k^4} \left[\frac{2}{3} T_{i+1}^3 + T_{i+1}^2 + 2 + (T_{i+1} - 1) e^{-T_{i+1}} \right] \tag{B-32}$$

$$\sigma_v^2 = \frac{\sigma_u^2}{k^2} \left[2T_{i+1} + 2(e^{-T_{i+1}} - 1) \right] \tag{B-33}$$

B-11

$$\mu_{xv} = \mu_{vx} = \frac{\sigma_u^2}{k^3} \left[T_{i+1}^2 + T_{i+1} (e^{-T_{i+1}} - 1) \right] \qquad (B\text{-}34)$$

where $T_{i+1} = k(t_{i+1} - t_i)$. As before, Equations B-29 and B-30 are the position and velocity deviation variances, respectively, and Equation B-31 is the covariance between position and velocity deviations. Equations B-32 through B-34 are expressed in terms of a normalized time interval: T_{i+1} is the time interval $t_{i+1} - t_i$ divided by the control error correlation time of $1/k$. For present purposes, the normalized time will be significantly greater than unity, a time interval of several days versus a correlation time of several thousand seconds for which $T_{i+1} = 85.$; thus, the foregoing can be approximated by

$$\sigma_x^2 \simeq \frac{\sigma_u^2}{k^4} \left[\frac{2}{3} T_{i+1}^3 - T_{i+1}^2 + 2 \right] \qquad (B\text{-}35)$$

$$\sigma_v^2 \simeq \frac{\sigma_u^2}{k^2} \left[2 T_{i+1} - 1 \right] \qquad (B\text{-}36)$$

$$\mu_{xv} = \frac{\sigma_u^2}{k^3} \left[T_{i+1}^2 - T_{i+1} \right] \qquad (B\text{-}37)$$

for $T_{i+1} \gg 1.0$

It is of interest to compare the trajectory deviation contributions of control errors over an interval for the white-noise case versus the exponentially correlated case. In general terms, it is seen that for $T_{i+1} > 10.0$, the variances of T_{i+1} position and velocity deviations for the correlated case will increase by a factor of twice the correlation time as compared to those for the white-noise case. Moreover, for a correlation time of one-half second the results are very nearly equal for the two cases considered.

Equations B-15, B-16, B-17, and B-18, represent the error model used in the present analysis. A digital computer program has been written which computes $J(t_i)$, $C(t_i)$, and $P(t_i)$ for a set of discrete times t_i. The program requires a nominal powered trajectory with position and velocity given at small intervals along the entire trajectory. The state transition matrix for

each interval is computed on the basis of conic motion using the average position and velocity for each interval along the powered trajectory. Also, the control error variance σ_u^2 is taken to be proportional to the average thrusting acceleration over each interval.

APPENDIX B-2.   SOLAR ELECTRIC PROPULSION GUIDANCE ANALYSIS MATHEMATICAL MODELS

In Appendix B-1, an error model was defined which determines the terminal trajectory dispersions as a function of heliocentric injection errors and in-flight random accelerations, such as those due to thrusting control errors. The guidance requirements for reducing the terminal trajectory dispersions or errors are of interest. Specifically, an assessment of the delta-velocity and thrusting acceleration requirements to reduce the terminal positional errors is of particular interest. In the following sections the mathematical models which are used as a basis of this assessment are presented. In Section A, the equations for delta-velocity midcourse guidance analysis are given. In Section B, the equations for a basic mode of adaptive guidance, a constant acceleration, are given.

It should be noted that the mathematical models as defined do not represent optimal guidance policies in either case, nor are they intended to. Rather, the purposes of the models are to assess requirements on a parametric basis and to establish feasibility.

A.   DELTA-VELOCITY GUIDANCE MATHEMATICAL MODEL

In this section the set of equations (mathematical model) is derived which determines:

1.   The ΔV guidance requirements for a midcourse correction (applied after heliocentric injection and before the end of powered flight) as a function of heliocentric injection errors, in-flight thrusting control errors, state estimation errors, and ΔV control errors.

2.   The resulting trajectory dispersions after midcourse correction as a function of state estimation errors, in-flight thrusting control errors, and ΔV control error.

The fundamental assumption in the present analysis is the same as that made in the SEP trajectory dispersion analysis (Appendix B-1); i. e. , the trajectory dispersion position and velocity deviations defined with respect to the nominal powered-flight trajectory lie within the region of

B-15

linearized equations of motion. In this manner, the state variables necessary for the present analysis can be defined by a set of linear time-varying differential equations as follows:

$$\dot{X}(t) = A(t)\,x\,(t) + B(t)\,u(t) \tag{B-38}$$

where $X(t)$ is a state deviation vector of three components of position and velocity defined with respect to the nominal powered-flight trajectory and $u(t)$ is a set of in-flight random accelerations, e.g., thrusting control errors (see Appendix B-1). The solution to Equation B-39 can be expressed as follows:

$$X(t) = \Phi(t, t_o)\,X(t_o) + \int_{t_o}^{t} \Phi(t, \tau)\,B(\tau)\,u(\tau)\,d\tau \tag{B-39}$$

where $X(t_o)$ is a set of initial conditions (heliocentric injection errors) and $\phi(t, t_o)$ is the state transition matrix for Equation B-39 which satisfies the following set of differential equations:

$$\dot{\Phi}(t, t_o) = A(t)\,\Phi(t, t_o) \tag{B-40}$$

with initial conditions $\Phi(t_o, t_o) = I = $ (6 x 6 identity matrix). The state transition matrix for two arbitrary times, t_1 and t_2, $\Phi(t_1, t_2)$, is the essential requirement for the present analysis. A method for determining $\Phi(t_1, t_2)$ for a particular powered flight trajectory is discussed in Appendix B-1; thus, for the present analysis it is assumed that $\Phi(t_1, t_2)$ is known.

For present purposes, the following notation will be used:

1. $R(t)$ and $V(t)$ denote position and velocity vectors, respectively, defined with respect to the nominal trajectory (the state vector) $X(t)$ is partitioned such that:

$$X(t) = \begin{bmatrix} R(t) \\ \hline V(t) \end{bmatrix} \tag{B-41}$$

2. $\Phi(t_1, t_2)$ will be written as a partitioned matrix consisting of four
    3 x 3 submatrices:

$$\Phi(t_1, t_2) = \begin{bmatrix} \Phi_{11}(t_1, t_2) & \Phi_{12}(t_1, t_2) \\ \hline \Phi_{21}(t_1, t_2) & \Phi_{22}(t_1, t_2) \end{bmatrix} \tag{B-42}$$

It is noted that the submatrices of $\Phi(t_1, t_2)$ represent the various transitions of the position and velocity vectors $R(t)$ and $V(t)$.

3. The times t_o, t_N, and t_F denote the initial time (heliocentric injection), the time of impulsive delta-velocity correction, and the terminal time of interest (end of powered flight), respectively. Usually $t_o < t_N < t_F$.

4. The state vector $X(t)$ at times t_o, t_N, and t_F will be denoted by X_o, X_N, and X_F, respectively. Similarly, $R(t_o) = R_o$, $V(t_o) = V_o$, etc. Also, $\Phi(t_N, t_o) = \Phi(N, o)$ and $\Phi(t_F, t_N) = \Phi(F, N)$ and a similar notation will be used for the submatrices of $\Phi(N, o)$ and $\Phi(F, N)$.

5. The state vector $X(t)$ before and after a ΔV correction will be denoted by a superscript "-" or "+," respectively; e.g., R_F^- and R_F^+ denote the terminal position vector before and after a ΔV correction at t_N, respectively.

6. ΔX_N and ΔX_F will denote the effects of in-flight random accelerations upon the state vector between the times $t_o \le t \le t_N$ and $t_N \le t \le t_F$, respectively; i.e.,

$$\Delta X_N = \int_{t_o}^{t_N} \Phi(t_N, \tau) \, B(\tau) \, u(\tau) \, d\tau$$

$$\tag{B-43}$$

$$\Delta X_F = \int_{t_N}^{t_F} \Phi(t_F, \tau) \, B(\tau) \, u(\tau) \, d\tau$$

7. Finally, I and $\Box$ will denote the 3 x 3 identity and null matrices, respectively.

Using the foregoing notation, the final state vector, at t_F, before and after a delta-velocity correction at time t_N can be written as follows.

$$X_F^- = \Phi(F, N) X_N^- + \Delta X_F \qquad (B-44)$$

$$X_F^+ = \Phi(F, N) X_N^+ + \Delta X_F \qquad (B-45)$$

$$X_N^+ = \begin{bmatrix} R_N^+ \\ \overline{V_N^+} \end{bmatrix} = \begin{bmatrix} R_N^- \\ \overline{V_N^- + \Delta V_N^-} \end{bmatrix} \qquad (B-46)$$

where ΔV_N denotes a delta-velocity correction applied at t_N. It should be noted that at the correction time t_N the velocity vector is changed discretely by a delta-velocity correction ΔV_N.

$$R_N^+ = R_N^- = R_N$$

$$V_N^+ = V_N^- + \Delta V_N \qquad (B-47)$$

Now, the terminal position vector before the velocity correction is

$$R_F^- = \begin{bmatrix} I & \Box \end{bmatrix} X_F^- = \begin{bmatrix} I & \Box \end{bmatrix} \begin{bmatrix} \Phi(F, N) X_N^- + \Delta X_F \end{bmatrix}$$

$$(B-48)$$

$$R_F^- = \Phi_{11}(F, N) R_N + \dot{\Phi}_{12}(F, N) V_N^- + \Delta R_F$$

where

$$\Delta R_F = \begin{bmatrix} I & \Box \end{bmatrix} \Delta X_F \qquad (B-49)$$

Similarly, the terminal position vector after the velocity correction is as follows:

$$R_F^+ = \Phi(F, N) R_N + \Phi_{12}(F, N) V_N^+ + \Delta R_F \qquad (B-50)$$

$$R_F^+ = R_F^- + \Phi_{12}(F, N) \Delta V_N \qquad (B-51)$$

From Equation B-51 it is easily seen that if R_F^- were known, then a delta-velocity correction could be made in such a way that the terminal position after correction would be zero, or nulled; i.e., if

$$\Delta V_N = -\Phi_{12}^{-1}(F, N) R_F^- \qquad (B-52)$$

ther

$$R_F^+ = 0 \qquad (3 \times 3 \text{ null vector}) \qquad (B-53)$$

The ΔV_N in Equation B-52 could be considered as the ideal, or desired, delta-velocity correction to reduce the terminal position trajectory deviations to zero. However, R_F^- is generally not known because (1) the term ΔR_F arises from random accelerations after the delta-velocity correction is applied and (2) only an estimation of the present state vector is available from which an estimation of the terminal state vector can be made. Still, it is possible to define a useful delta-velocity correction at time t_N based upon the knowledge of the terminal state position vector at the time the velocity correction is made. In this manner, the delta-velocity correction is defined by

$$\tilde{\Delta V}_N = -\Phi_{12}^{-1}(F, N) \tilde{\dot{R}}_F^- \qquad (B-54)$$

where

$$\tilde{R}_F^- = \left[I \mid \square \right] \Phi(F, N) \hat{X}_N^- \qquad (B-55)$$

$$\tilde{R}_F^- = \Phi_{11}(F, N) \hat{R}_N + \Phi_{12}(F, N) \hat{V}_N^- \qquad (B-56)$$

In Equation B-55, $\hat{X}_N^-$ denotes the available estimation of the state vector at time t_N, and in Equation B-56, $\hat{R}_N$ and $\hat{V}_N^-$ denote the estimation of position and velocity vectors at time t_N. Generally,

$$\hat{X}_N^- = X_N^- + \epsilon_s \tag{B-57}$$

where ϵ_s denotes the state estimation errors at time t_N. Now, it is possible to determine the effects of the delta-velocity correction by substituting Equations B-54 and B-55 into Equation B-51; however, it should be noted that an error will usually exist in the execution of the delta-velocity correction; therefore, the actual applied delta-velocity correction will be given by

$$\Delta V_N = \Delta \tilde{V}_N + \epsilon_c$$

$$= - \Phi_{12}^{-1} (F, N) \tilde{R}_F^- + \epsilon_c \tag{B-58}$$

$$\Delta V_N = - \Phi_{12}^{-1} (F, N) \left[I \mid \square \right] (F, N) \hat{X}_N^- + \epsilon_c$$

where ϵ_c denotes a set of errors in executing the delta-velocity correction.

From Equation B-58 it is seen that the ΔV_N correction is dependent upon the state vector at t_N, $\hat{X}_N^-$, since $\hat{X}_N^- = \hat{X}_N^- + \epsilon_s$. Now, X_N^- can be expressed in terms of the initial conditions, which represent the heliocentric injection errors and the in-flight random accelerations $u(t_i)$; i.e.,

$$X_N^- = \Phi(N, O) X_o + \Delta X_N$$

Thus,

$$\Delta V_N = -\Phi_{12}^{-1} (F, N) \left[I \mid \square \right] \Phi(F, N) \left[X_N^- + \epsilon_s \right] + \epsilon_c$$

$$= -\Phi_{12}^{-1} (F, N) \left[I \mid \square \right] \Phi(F, N) \left[\Phi(N, O) X_o + \Delta X_N + \epsilon_s \right] + \epsilon_c \tag{B-60}$$

$$\Delta V_N = -\left[\Phi_{12}^{-1} (F, N) \Phi_{11} (F, N) \mid I \right] \left[\Phi(N, O) X_o + \Delta X_N + \epsilon_s \right] + \epsilon_c$$

B-20

Equation B-60 defines the delta-velocity correction in terms of the initial conditions, X_0 (heliocentric injection errors); the effort of in-flight random accelerations, ΔX_N; the state estimation errors at t_N, and the delta-velocity control errors, ϵ_c.

Now, by substitution of the foregoing equations, the terminal position after delta-velocity correction can be determined:

$$R_F^+ = R_F^- + \Phi_{12}(F, N) \Delta V_N$$

$$= R_F^- + \Phi_{12}(F, N) \left[\Delta \tilde{V}_N + \epsilon_c \right]$$

$$= R_F^- - R_F^{\tilde{-}} + \Phi_{12}(F, N) \epsilon_c \tag{B-61}$$

$$= \left[I \mid \square \right] \Phi(F, N) \left[X_N^- - \hat{X}_N^- \right] + \Phi_{12}(F, N) \epsilon_c + \Delta R_F$$

$$R_F^+ = -\left[\Phi_{11}(F, N) \mid \Phi_{12}(F, N) \right] \epsilon_s + \Phi_{12}(F, N) \epsilon_c + \Delta R_F$$

It is easily seen that the residual terminal position after correction (final position errors) are dependent upon only the state estimation and delta-velocity control errors at time t_N and the effects of in-flight random accelerations from the time of the delta-velocity correction to the terminal time t_F.

The delta-velocity correction defined by Equation B-60 essentially nulls the effects of initial conditions (heliocentric injection errors) and the effects of in-flight random accelerations from the initial time, t_0, to the time of delta-velocity correction, t_N. However, it should be noted that

B-21

only the effects upon terminal position are nulled; i. e., the terminal velocity is not nulled or controlled. Thus, the terminal velocity after correction should be considered, which can be determined from the foregoing as

$$V_F^+ = \begin{bmatrix} 0 & \vdots & I \end{bmatrix} X_F^+$$

$$= \begin{bmatrix} 0 & \vdots & I \end{bmatrix} \left[\Phi(F, N) X_N^+ + \Delta X_F \right]$$

$$= \Phi_{21}(F, N) R_N^+ + \Phi_{22}(F, N) V_N^+ + \Delta V_F$$

$$V_F^+ = \Phi_{21}(F, N) R_N + \Phi_{22}(F, N) \left[V_N^- + \Delta V_N \right] + \Delta V_F$$

(B-62)

$$V_F^+ = \Phi_{21}(F, N) R_N + \Phi_{22}(F, N) V_N^- + \Delta V_F + \Phi_{22}(F, N) \Delta V_N$$

$$V_F^+ = \left[\Phi_{21}(F, N) - \Phi_{22}(F, N) \Phi_{12}^{-1}(F, N) \Phi_{11}(F, N) \right] R_N^-$$

$$+ \left[\Phi_{22}(F, N) \Phi_{12}^{-1}(F, N) \Phi_{11}(F, N) \vdots \Phi_{22}(F, N) \right] \epsilon_s$$

$$+ \left[\Phi_{22}(F, N) \right] \epsilon_c + \Delta V_F$$

where

$$\Delta V_F = \begin{bmatrix} 0 & \vdots & I \end{bmatrix} \Delta X_F$$

It is seen that the effect of the delta-velocity correction upon the terminal velocity is the same as the velocity at the correction time and, generally, the delta-velocity correction does not null the terminal velocity.

The terminal state vector, including position and velocity, after the delta-velocity correction, can be determined in the following manner.

$$X_F^+ = \Phi(F, N) X_N^+ + \Delta X_F$$

$$= \Phi(F, N) X_N^- + \Phi(F, N) \begin{bmatrix} \square \\ \hline \Delta V_N \end{bmatrix} + \Delta X_F \qquad (B-63)$$

$$X_F^+ = \Phi(F, N) X_N^- + \begin{bmatrix} \Phi_{12}(F, N) \\ \hline \Phi_{22}(F, N) \end{bmatrix} \Delta V_N + \Delta X_F$$

By substituting Equation B-60 into Equation B-63 it is found that

$$X_F^+ = A(F, N) X_N^- - B(F, N) \epsilon_s + C(F, N) \epsilon_c + \Delta X_F \qquad (B-64)$$

where

$$A(F, N) = \begin{bmatrix} \square & \vdots & \square \\ \hline \Phi_{21}(F, N) - \Phi_{22}(F, N) \Phi_{12}^{-1}(F, N) \Phi_{11}(F, N) & \vdots & \square \end{bmatrix} \qquad (B-65)$$

$$B(F, N) = \begin{bmatrix} \Phi_{11}(F, N) & \vdots & \Phi_{12}(F, N) \\ \hline \Phi_{22}(F, N) \Phi_{12}^{-1}(F, N) \Phi_{11}(F, N) & \vdots & \Phi_{22}(F, N) \end{bmatrix} \qquad (B-66)$$

$$C(F, N) = \begin{bmatrix} \Phi_{12}(F, N) \\ \hline \Phi_{22}(F, N) \end{bmatrix} \qquad (B-67)$$

and

$$\Delta X_F = \int_{t_N}^{t_F} \Phi(t_F, \tau) B(\tau) u(\tau) d\tau \qquad (B-68)$$

B-23

The foregoing equations define the delta-velocity correction, Equation B-60, and the resulting terminal state, Equation B-64, in terms of the following:

1. X_o Heliocentric injection errors

2. $u(t)$ In-flight thrusting control errors

3. ϵ_s State estimation errors at t_N

4. ϵ_c Delta-velocity control errors

Thus, the delta-velocity correction and the resulting terminal state are dependent upon a set of errors which, in turn, are random phenomena; therefore, the delta-velocity correction and resulting terminal state will be random phenomena and must be described accordingly. The general assumption made at this point is that the four error sources are each unbiased Gaussian random phenomena which are statistically independent with known covariance matrices. Under this assumption, both ΔV_N and $X_F^{\pm}$ are unbiased Gaussian random phenomena with covariance matrices given by the following equations:

$$\Gamma_{\Delta VN} = E\left[\Delta V_N \Delta V_N^T\right]$$

(B-69)

$$\Gamma_{\Delta VN} = \Gamma_{\Delta VIE} + \Gamma_{\Delta VTE} + \Gamma_{\Delta VSE} + \Gamma_{\Delta VCE}$$

$$\Gamma_{XF+} = E\left[X_F^+ X_F^{+T}\right]$$

(B-70)

$$\Gamma_{XF+} = \Gamma_{XFIE} + \Gamma_{XFTE} + \Gamma_{XFSE} + \Gamma_{XFCE}$$

where

$$\Gamma_{\Delta VIE} = \left[\Phi_{12}^{-1}(F, N) \Phi_{11}(F, N) \; \vdots \; I \right] \Phi(N, O) \Gamma_{XO} \Phi^T(N, O)$$

(B-71)

$$\left[\Phi_{12}^{-1}(F, N) \Phi_{11}(FN \; \vdots \; I \right]^T$$

$$\Gamma_{\Delta VTE} = \left[\Phi_{12}^{-1}(F, N) \Phi_{11}(F, N) \; \vdots \; I \right] \Gamma_{\Delta XN} \left[\Phi_{12}^{-1}(F, N) \Phi_{11}(F, N) \; \vdots \; I \right]^T$$

(B-72)

$$\Gamma_{\Delta VSE} = \left[\Phi_{12}^{-1}(F, N) \Phi_{11}(F, N) \; \vdots \; I \right] \Gamma_{SEN} \left[\Phi_{12}^{-1}(F, N) \Phi_{11}(F, N) \; \vdots \; I \right]^T$$

(B-73)

$$\Gamma_{\Delta VCE} = E \left[\epsilon_c \, \epsilon_c^T \right] = \Gamma_{\Delta VE}$$

(B-74)

$$\Gamma_{XFIE} = A(F, N) \Phi(F, O) \Gamma_{XO} \Phi^T(F, O) A^T(F, N)$$

(B-75)

$$\Gamma_{XFTE} = A(F, N) \Gamma_{\Delta XN} A^T(F, N) + \Gamma_{\Delta XF}$$

(B-76)

$$\Gamma_{XFSE} = B(F, N) \Gamma_{SEN} B^T(F, N)$$

(B-77)

$$\Gamma_{XFCE} = C(F, N) \Gamma_{\Delta VE} C^T(F, N)$$

(B-78)

$$\Gamma_{XO} = E(X_o X_o^T)$$

(B-79)

$$\Gamma_{SEN} = E(\epsilon_s \epsilon_s^T)$$

(B-80)

$$\Gamma_{\Delta XN} = E\left[\Delta X_N \, \Delta X_N^T\right]$$

$$= E\left[\int_{t_o}^{t_N} \int_{t_o}^{t_N} \Phi(t_N, \rho) \, B(\rho) \, u(\rho) \, u^T(\tau) \, B^T(\tau)\right.$$

$$\left. \Phi(t_N, \tau) \, d\rho d\tau \right] \qquad (B-81)$$

$$\Gamma_{\Delta XN} = \int_{t_o}^{t_N} \int_{t_o}^{t_N} \Phi(t_N, \rho) \, B(\rho) \, R(\rho, \tau) \, B^T(\tau) \, \Phi(t_N, \tau) \, d\rho d\tau$$

$$\Gamma_{\Delta XF} = E\left[\Delta X_F \, \Delta X_F^T\right]$$

$$= E\left[\int_{t_N}^{t_F} \int_{t_N}^{t_F} \Phi(t_F, \rho) \, B(\rho) \, u(\rho) \, u^t(\tau) \, B^T(\tau)\right.$$

$$\qquad (B-82)$$

$$\left. \Phi^T(t_F, \tau) \, d\rho d\tau \right]$$

$$\Gamma_{\Delta XF} = \int_{t_N}^{t_F} \int_{t_N}^{t_F} \Phi(t_F, \rho) \, B(\rho) R(\rho, \tau) B^T(\tau) \Phi^T(t_F, \tau) \, d\rho d\tau$$

$$R(\rho, \tau) = E\left[u(\rho)\, u^T(\tau)\right] \tag{B-83}$$

The terminal position covariance matrix is as follows:

$$\Gamma_{RFt} = E\left[R_F^+ \; R_F^{+T}\right]$$

$$\Gamma_{RFt} = \Gamma_{RFSE} + \Gamma_{RFCE} + \Gamma_{RFTE} \tag{B-84}$$

where

$$\Gamma_{RFSE} = \left[\Phi_{11}\,(F,N) \;\vdots\; \Phi_{12}\,(F,N)\right]\Gamma_{SEN}\left[\Phi_{11}(F,N) \;\; \Phi_{12}(F,N)\right]^T \tag{B-85}$$

$$\Gamma_{RFCE} = \Phi_{12}\,(F,N)\; \Gamma_{\Delta VE}\,\Phi_{12}^{\;T}\,(F,N) \tag{B-86}$$

$$\Gamma_{RFTE} = E\left[\Delta R_F\, \Delta R_F^{\;T}\right]$$

$$= E\left\{\left[I \;\vdots\; \square\right]\Delta X_F\, \Delta X_F^{\;T}\left[I \;\vdots\; \square\right]^T\right\}$$

$$= \left[I \;\vdots\; \square\right] E\left[\Delta X_F\, \Delta X_F^{\;T}\right]\left[I \;\vdots\; \square\right]^T \tag{B-87}$$

$$= \left[I \;\vdots\; \square\right]\, \Gamma_{\Delta XF}\left[I \;\vdots\; \square\right]^T$$

B. ADAPTIVE GUIDANCE MATHEMATICAL MODEL

In the following discussion, the mathematical model for the adaptive guidance analysis is presented. As noted earlier, the present adaptive guidance consists of applying a constant acceleration to the spacecraft to null the position deviations at thrust cutoff as considered previously in the delta velocity guidance analysis. This mode of adaptive guidance does not represent an elaborate optimal guidance policy, nor is it so intended. Rather, the primary purpose of the present analysis is to assess the feasibility of adaptive guidance methods which require an additional acceleration to be imparted to the spacecraft. The feasibility of this mode of guidance is assessed in terms of the required acceleration increment as compared to the thrusting acceleration available.

In this analysis, the constant acceleration is considered to be applied at some time after heliocentric injection and to remain constant to the end of the powered flight phase. In this manner, the required acceleration can be determined as follows. Consider the terminal state due to a constant acceleration over the interval t_N to t_F; i.e.,

$$X_c(t_F) = \int_{t_N}^{t_F} \Phi(t_F, \tau)\, B(\tau)\, C\, d\tau$$

$$X_c(t_F) = \left[\int_{t_N}^{t_F} \Phi(t_F, \tau)\, B(\tau)\, d\tau \right] C \qquad (B\text{-}88)$$

where C is a constant acceleration over the interval $t = t_F - t_N$ and $X_c(t_F)$ is the resulting state vector at t_F due to the acceleration C.

The primary requirement in the present analysis is the evaluation of the integral

$$\int_{t_N}^{t_F} \Phi(t_F, \tau) \, B(\tau) \, d\tau \tag{B-89}$$

This integral can be evaluated numerically using the same approach employed in the SEP trajectory dispersion analysis (see Appendix B-1); that is, for a sufficiently small interval over the nominal powered trajectory, the acceleration C can be propagated on the basis of rectilinear motion. In this manner,

$$\int_{t_{i-1}}^{t_i} \Phi(t_i, \tau) \, B(\tau) \, d(\tau) = \begin{bmatrix} I \cdot T_i & \Box \\ \\ \Box & I \cdot \frac{1}{2} \cdot T_i^2 \end{bmatrix} \tag{B-90}$$

where I = 3 x 3 identity matrix, $\Box$ = 3 x 3 null matrix, and $T_i = t_i - t_{i-1}$. Using this approach, the acceleration is propagated over two adjacent time intervals by

$$\Phi(t_{i+1}, t_i) \, D_i C + D_i + IC \tag{B-91}$$

where

$$D_j = \begin{bmatrix} I \cdot T_j & \Box \\ \\ \Box & I \cdot \frac{1}{2} \cdot T_j^2 \end{bmatrix}$$

In general, the state vector due the acceleration C at the end of time t_{i+1} is given by

$$X_c(t_{i+1}) = \Phi(t_{i+1}, t_i) \, X_c(t_i) + D_{i+1} \, C \tag{B-92}$$

Thus, it is seen that

$$X_c(t_1) = D_1 C$$

$$X_c(t_2) = \left[\Phi(t_2, t_1) D_1 + D_2\right] C \qquad (B-93)$$

$$X_c(t_3) = \left[\Phi(t_3, t_1) D_1 + \Phi(t_3, t_2) D_2 + D_3\right] C$$

Generally,

$$X_c(t_n) = \left[\sum_{j=1}^{n} \Phi(t_n, t_j) D_j\right] C \qquad (B-94)$$

where n is the number of intervals from t_1 to t_n. Now, the terminal position due to the acceleration C is given by

$$R_c(t_F) = [I \mid \square] \; X_c(t_F)$$

$$= \left\{ [I \mid \square] \left[\sum_{j=1}^{n} \Phi(t_n, t_j) D_j\right] \right\} C$$

$$= \left\{ \sum_{j=1}^{n} [I \mid \square] \; \Phi(t_n, t_j) D_j \right\} C \qquad (B-95)$$

$$= \left\{ \sum_{j=1}^{n} \left[\Phi_{11}(t_n, t_j) \mid \Phi_{12}(t_n, t_j)\right] D_j \right\} C$$

$$R_c(t_F) = \left\{ \sum_{j=1}^{n} \left[\Phi_{11}(t_n, t_j) T_j \mid \frac{1}{2} \Phi_{12}(t_n, t_j) T_j^2\right] \right\} C$$

where $t_n = t_F$.

The **terminal position vector** can be written as

$$R_F = R(t_F) = R_F^- + R_c(t_F)$$

where

$$R_F^- = [I \mid \Box] \; X_F^- \tag{B-96}$$

and

$$X_F^- = \Phi(t_F, t_o) X_o + \int_{t_o}^{t_F} \Phi(t_F, \tau) B(\tau) u(\tau) d\tau$$

It is noted that R_F^- is the terminal position vector due to the injection conditions (errors) and the in-flight thrust control errors, $u(t)$. Now, it is possible to apply a constant acceleration at some time t_N, where $t_o \, t_N \, t_F$, such that the terminal position deviation due to injection conditions (errors) and in-flight thrusting control errors for the time interval from t_o to t_N, i.e., X_F^- can be written as follows:

$$X_F^- = \Phi(t_F, t_N) X(t_N) + \int_{t_N}^{t_F} \Phi(t_F, \tau) B(\tau) U(\tau) d\tau \tag{B-97}$$

where

$$X(t_N) = \Phi(t_N, t_o) X_o + \int_{t_o}^{t_n} \Phi(t_N, \tau) B(\tau) U(\tau) d\tau \tag{B-98}$$

Thus,

$$X_F^- = \Phi(t_F, t_o) X_o + \Phi(t_F, t_N) \Delta X_N + \Delta X_F \qquad \text{(B-99)}$$

where

$$\Delta X_N = \int_{t_o}^{t_N} \Phi(t_N, \tau) B(\tau) U(\tau) d\tau \qquad \text{(B-100)}$$

and

$$\Delta X_F = \int_{t_N}^{t_F} \Phi(t_F, \tau) B(\tau) U(\tau) d\tau \qquad \text{(B-101)}$$

Assuming that the state $X(t_N)$ is known at time t_N, a constant acceleration can be applied to null the effects of injection conditions, X_o, and in-flight thrusting control errors, ΔX_N, on the terminal position deviation; that is, if

$$R_c(t_F) = - \begin{bmatrix} I & | & \square \end{bmatrix} \begin{bmatrix} \Phi(t_F, t_o) X_o + \Phi(t_F, t_N) \Delta X_N \end{bmatrix} \qquad \text{(B-102)}$$

then

$$R_F = \begin{bmatrix} I & | & \square \end{bmatrix} X_F$$

The required constant acceleration is given by

$$C = - \begin{bmatrix} D^{-1}(F, N) \end{bmatrix} \begin{bmatrix} I & | & \square \end{bmatrix} \begin{bmatrix} \Phi(t_F, t_o) X_o + \Phi(t_F, t_N) \Delta X_N \end{bmatrix}$$

$$\text{(B-103)}$$

where

$$D(F, N) = \left\{ \sum_{j=1}^{n} \left[\Phi_{11}(t_n, t_j) T_j \;\middle|\; \frac{1}{2} \Phi_{12}(t_n, t_j) T_j^2 \right] \right\} \qquad (B\text{-}104)$$

As noted before, both the injection errors and in-flight thrust control errors are random phenomena; therefore, the applied acceleration will be a random over an ensemble of flights. The covariance matrix for the acceleration vector is given by

$$\Gamma_C = E\left[CC^T \right]$$

$$\Gamma_C = \Gamma_{CIE} + \Gamma_{CTE} \qquad (B\text{-}105)$$

where

$$\Gamma_{CIE} = \left\{ D^{-1}(F, N) \left[\Phi_{11}(F, O) \;\middle|\; \Phi_{12}(F, O) \right] \right\} \Gamma_{XO} \left\{ D^{-1}(F, N) \left[\Phi_{11}(F, O) \right.\right.$$

$$\left.\left. \Phi_{12}(F, O) \right] \right\}^T \qquad (B\text{-}106)$$

$$\Gamma_{CTE} = \left\{ D^{-1}(F, N) \left[\Phi_{11}(F, N) \;\middle|\; \Phi_{12}(F, N) \right] \right\} \Gamma_{XN} \left\{ D^{-1}(F, N) \left[\Phi_{11}(F, N) \right.\right.$$

$$\left.\left. \Phi_{12}(F, N) \right] \right\}^T \qquad (B\text{-}107)$$

and where Γ_{XO} and $\Gamma \Delta_{XN}$ are defined in Appendix B-1 and $\Phi_{11}(F, O) = \Phi_{11}(t_F, t_o)$, etc.

APPENDIX C. PARTICLE AND FIELD SENSOR SURVEY

INTRODUCTION

This appendix presents the results of an investigative effort to identify the various types of sensor applicable in making particle and field measurements on solar winds and intergalactic media out to 3.5 AU. Categories investigated include magentic field, solar plasma radiation, and solar and cosmic corpuscular radiation sensors.

For each sensor identified, the measurement objective, the principle of operation, use on earlier flights, operational results, operational difficulties, and limitations are presented.

MAGNETIC FIELD SENSORS

Available sensors and vehicle support requirements are described in this section. Aspects of the environment to be measured, possible as yet undetected phenomena to be sought, and performance requirements are discussed.

Measurement Objectives

The basic aspects of the magnetic environment to be measured are listed in Table C-1. To perform all of the measurements in Table C-1, both direction and magnitude should be determined each second, and time averaged values determined from data analysis on the ground. For the range from 0.1 to 100 gammas, with a precision of ±0.1 gammas, only 40 bits per second are required. This data rate can be reduced by sampling the environment less frequently.

Available sensors

Magnetometers which have been flown include the helium and rubidium vapor optically-pumped types, the flux gate and spin coil magnetometers. Potentially, Hall effect units may also be developed for later missions. Magnetic sensors which have been used successfully are described in Table C-2.

Table C-1. Basic Magnetic Field Parameters and Phenomena to be Measured

Parameter	Measurement	Phasing	Range	Units	Sampling Rates
Field vector	Magnitude	Continuous	0.1 to 100	gamma	1 hr to 1 sec
Solar radial component	X component	Continuous	0.1 to 100	gamma	1 hr to 1 sec
Orthogonal ecliptic plane component ratio	Y/X component	Continuous	0.1 to 100	- - -	1 hr to 1 sec
Out-of-ecliptic component ratio	Z/X component	Continuous	0.1 to 100	- - -	1 hr to 1 sec
Perturbation of field of asteroids	Magnitude				
Dependence on solar activity	Magnitude direction change	After Solar Flares			
Radial dependence of magnitude	Magnitude direction	Daily- Average	0.1 to 60	gamma	~hr

C-2

SD 70-21-2

Space Division
North American Rockwell

Table C-2. Magnetometers Available for Solar Electric Missions

Sensor Type	Special Feature	Flights	Best Choice for SEP	Mass (Kg)	Power (watts)
Spin-coil or search coil	Fixed coil on rotating spacecraft (x-y components)	Pioneer V		0.5-2	1-3
Motor driven spin-coil	(z-component)	-		2-3	3-5
Proton precession	Magnitude only for strong fields slow response time	Vanguard 3			
Flux-gate	Orthogonal set of three sensors (x, y, z components)	Mariner II Pioneer II IMP	X	1.5-2.1	1.8-6
Rubidium vapor	Optically pumped sensor for field magnitude only	-		-	-
Helmholts coil array plus rubidium vapor	Optically pumped sensor with orthogonal array of three coils to give components (magnitude, and x, y, z components)	Explorer 10	X	1.4	3.5
Helium vapor	Optically pumped sensor for field magnitude only	-		-	-

Table C-2. Magnetometers Available for Solar Electric Missions (Cont)

Sensor Type	Special Feature	Flights	Best Choice for SEP	Mass (Kg)	Power (watts)
Helmholtz coil array plus Null-Field helium vapor	Determines field components by varying currents in 3-axis Helmholtz coils to give zero internal field detected by Helium vapor magnetometer	Mariner IV	X	3.1-3.4	7.3
Helmholtz coil array plus Total Field helium magnetometer	As above but measures total field, then components in each operating cycle		X	-	-

Spin Coil Magnetometer

The simplest form of magnetometer is a coil of wire which is flipped 180 degrees or spun with a motor (spin coil magnetometer). On a spin-stabilized spacecraft, the magnitude of the field and direction can be determined only in the plane of spin. To obtain the component of the field normal to the plane of spin (parallel to the spin vector), a motor driven spin coil magnetometer would be required. On a three-axis stabilized spacecraft, three motor-driven spin-coil magnetometers would be required. The power requirements for the motors and reliability problems would make such an instrument a poor choice in comparison with the flux gate or optically pumped units.

Proton Precession Magnetometer

Proton precession sensors which have been flown do not have an acceptable frequency response for the low field strengths encountered in the solar environment, and are therefore inapplicable to the SEP mission.

Flux-Gate Magnetometer

The low-field flux gate magnetometer may be a good choice for outer planet missions due to its simplicity, ruggedness, high frequency response for weak fields, and long term stability. A difficulty in this sensor is that it uses ferromagnetic core which may become permanently magnetized at some low but undetermined level. With correct design, however, the field retention in the core can be made small and stable in time so that it will not interfere with operation.

Three separate orthogonal coils are required to determine all three components of the field. The instrument can be used on either a spin stabilized or a three-axis stabilized spacecraft. The spin which induces an oscillatory output from one to all three axes depending on alignment must be rectified or the maximum determined. On a spin stabilized spacecraft, short term variations in the field may be lost. Either very slow or very fast spins may be used, but not spins near 1 rps, if variations on the order of one second are to be detected.

Principle of Operation. Each axis sensor consists of two identical parallel strips of Permalloy or other highly permeable ferromagnetic material, wound with a primary and a secondary coil of wire (Figure C-1). The primary and secondary windings are identical except that the directions of the two primary windings are reversed. A 2-KHz oscillatory current is

C-5

DRIVING
OSCILLATOR
~ 2 to 10 kHz

PERMALLOY
CORES

SERIES-OPPOSING
WINDING

CALIBRATE
CIRCUIT

FEEDBACK
CIRCUIT

SERIES-AIDING
WINDING

20kHz FILTER AND
AMPLIFIERS
SECOND HARMONIC
PROPORTIONAL TO
AMBIENT FIELD

→ OUTPUT
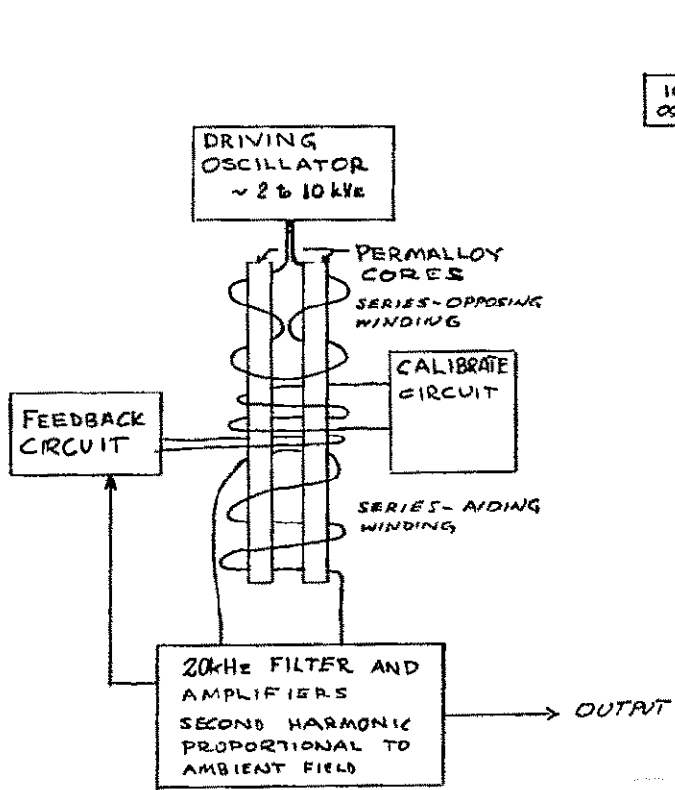
SCHEMATIC OF ONE AXIS
OF TYPICAL FLUX-GATE
MAGNETOMETER

10 kHz
OSCILLATOR

CALIBRATE
SIGNAL
GENERATOR

Z

SENSOR N°1
ELECTRONICS
FILTERS (20kHz)
AND
AMPLIFIERS

TO FEEDBACK
LOOP

SENSOR N°2
ELECTRONICS

Y

TO FEEDBACK
LOOP

SENSOR N°3
ELECTRONICS

TO FEEDBACK
LOOP

RESPONSE
AVERAGING
AND
CORRELATION
OVER
SAMPLING
INTERVAL
AND
A/D
CONVERSION

DATA
COMMUTATOR
OUTPUT
TO
TELEMETRY

TELEMETRY
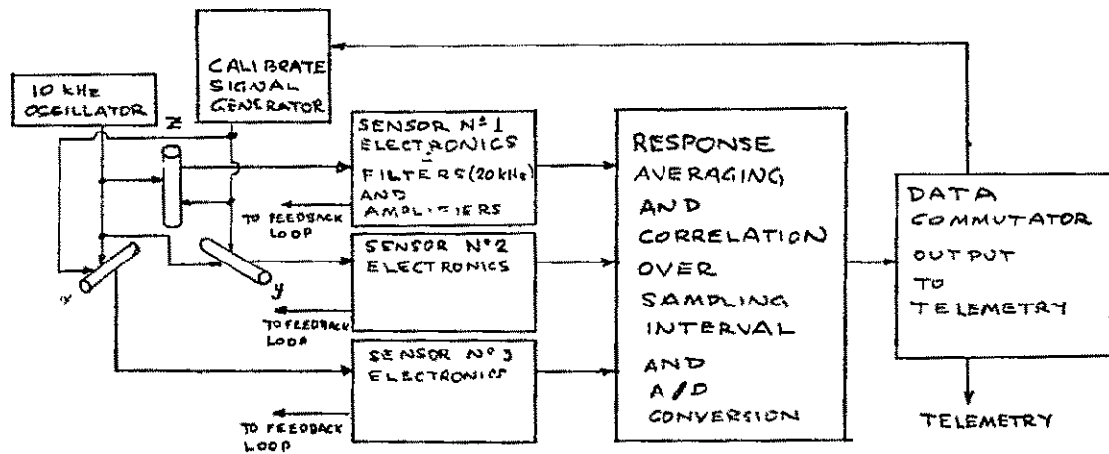
SIMPLIFIED BLOCK DIAGRAM FOR A TRI-AXIAL
FLUX GATE MAGNETOMETER

AXIS-1 MAGNETOMETER ELECTRONICS

PHASE-SHIFT
NETWORK

REF AMPL

2 FREQ
OSC

÷2

FREQ
AMPL

PROBE

PRI   SEC

AUX

2 FREQ
FILTER

GATED
ATTEN

2 FREQ
AMPL

2 FREQ
AMPL

PHASE
DET

P-P DET

LP FILTER
τ=1 SEC

LP FILTER
τ=1 SEC

E/F

TRIGGER

TO AXIS 1
TO AXIS 3

NULL
FIELD

RELAY LOGIC

RELAY DRIVER

ONE SHOT   ONE SHOT

NOTE FUNCTIONS IN
PHANTOM ARE
TRIPLICATED

IN-FLIGHT
CALIBRATE

IN-FLIGHT
CALIBRATE
RESET

A₁ RANGE
(AXIS 1)

DATA
(AXIS 1)
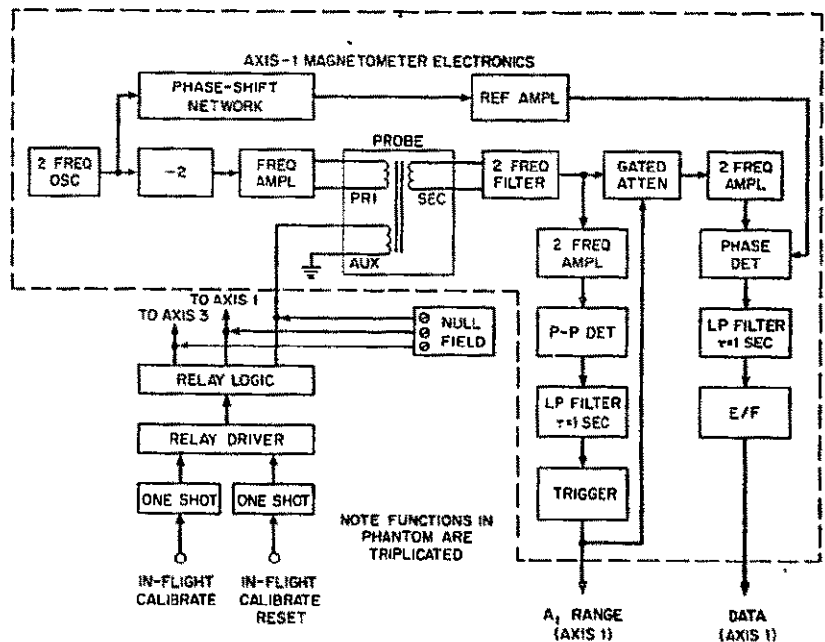
Figure C-1.   Schematic and Block Diagrams of a Flux-Gate Magnetometer
(sheet 1 of 2)
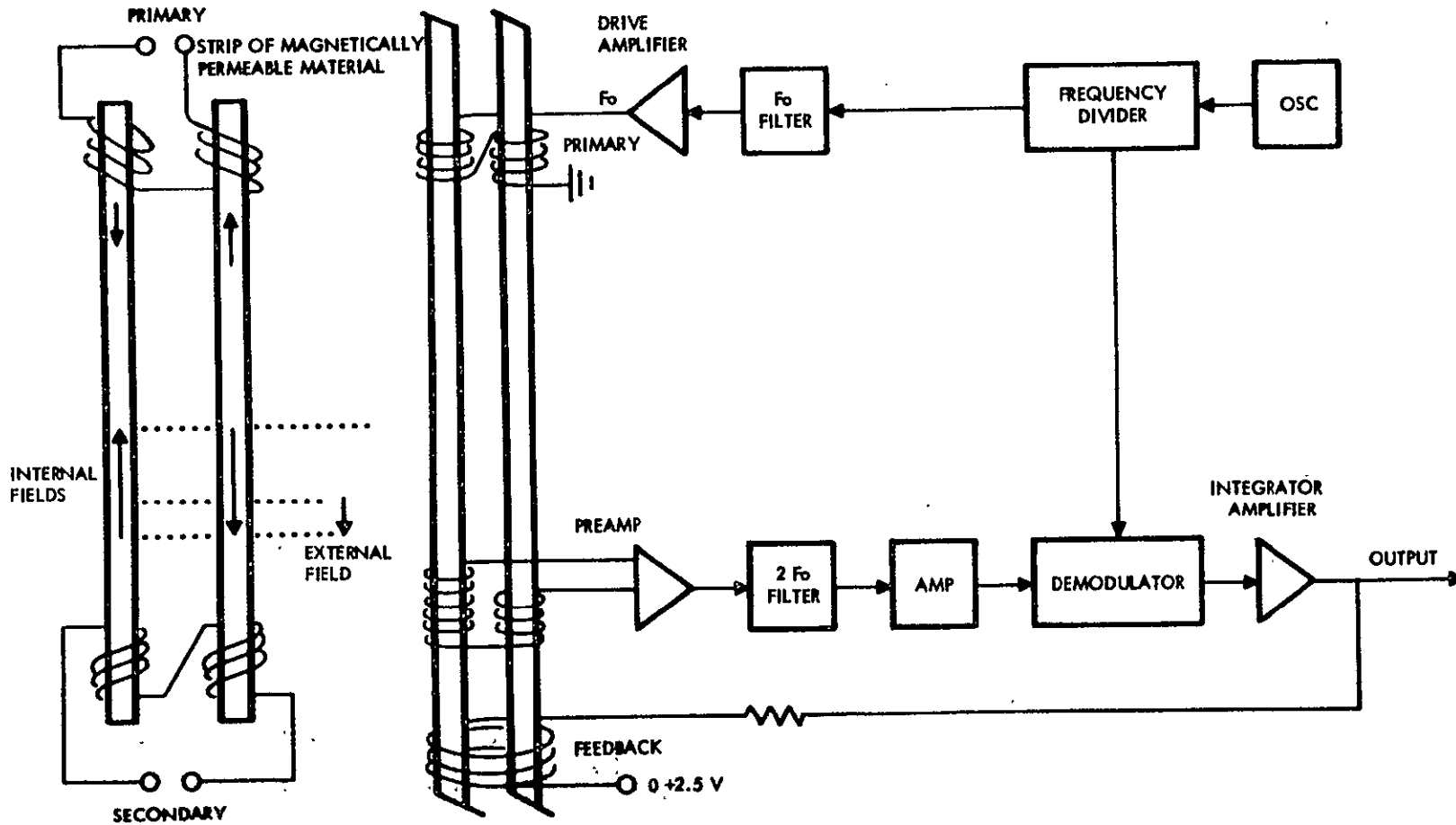
Figure C-1. Schematic and Block Diagram of a Flux-Gate Magnetometer (Sheet 2 of 2)

connected to the primary windings in series so that an oscillatory field is induced in the cores. One of the two parallel strips is magnetized in one direction, the other in the opposite direction.

The secondary coils are wound in the same direction so that if the field variations in the two cores are identical over the hysteresis loop, no output current in the secondary is produced. But if an external field exists, the fields in the cores vary differently giving rise to even harmonics in the output current wave form. The second harmonic is proportional to the external magnetic field component in the direction of the core.

To prevent stray magnetic field retention, the magnetometer output is amplified reversed in phase and used to drive a third feedback coil to null out the external field. Then the nulling current is measured to determine the external field on each component. The second harmonic component is extracted by filtering the secondary output with a 4-KHz band pass filter.

Typical Usage and Response (Table C-3). Explorer 6 carried a single-axis flux-gate instrument with ranges of 0 to 25, 25 to 500, and 500 to 10,000 gamma. Atlas-Able 5A and Atlas 5B carried similar instruments. Explorer 10 carried two flux-gate magnetometers that had a sensitivity of 10 gamma and a range of 1000 gamma. Explorer 12 and Explorer 14 carried flux-gate magnetometers that required only 0.405 watt. Explorer 15 carried a biaxial flux-gate with a range of 4000 gamma and a sensitivity of 10 gamma. It weighed 1.5 kg, including a 0.5-kg sensor package, and required 0.320 watt.

The Ames magnetometer built by Honeywell is described in Table C-4 (from Reference C-1) as used in ALSEP on Apollo 12.

A much improved flux-gate was flown on Mariner II. The instrument was triaxial with a sensitivity of 1 gamma, a range of from ±5 - 300 gamma, weight 2.2 kg, power 6 watts, and packaged in a cylinder 7.5 cm in diameter and 15 cm in length.

The OGO-E flux-gate magnetometer is described in Table C-5 (Reference C-2).

Difficulties and Problems. The six cores must be rigidly held in place and fixed rigidly on a stiff boom so that no change in position occurs relative to spacecraft sources of stray field. Vibration and shock not only produces errors in position but induces strains in the core which can change the. ferromagnetic characteristics. Thermal stresses may be more serious

Table C-3. Typical Instrument Specifications

Specification	Characteristic
Configuration:	Three-axis, orthogonal
Electronics:	Second harmonic, saturable-core closed loop
Outputs: (0 to 5 v)	Analog ±16γ Medium Offset -512γ to +496γ at 16γ per bit (64 levels) Coarse Offset -65,536γ to +64,512γ at 1024γ per bit (128 levels)
Resolution	1/16γ
Response:	Basic magnetometer, flat to 100 cps, analog output to telemetry low pass filtered to .3, 2.5 or 20 cps depending on telemetry bit rate
Power:	3.2 w
Absolute Stability:	±1/16 for field < 1000γ ±1 part in 2^{14}, >1000γ
Weight:	Sensor 1.05 lb Preamp 0.75 lb Electronics 4.71 lb*
Size:	Sensor 3.0 x 3.3 x 3.6 in. Preamp 1.4 x 3.6 x 5.6 in. Electronics 7.5 x 7.6 x 5.6 in.

*Exclusive of power supply
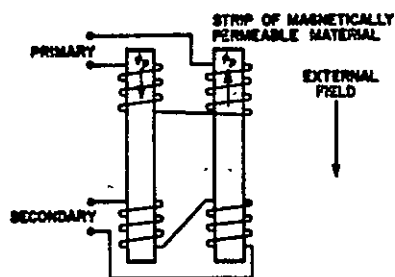
Schematic Representation of a
Single Axis Magnetometer Probe.
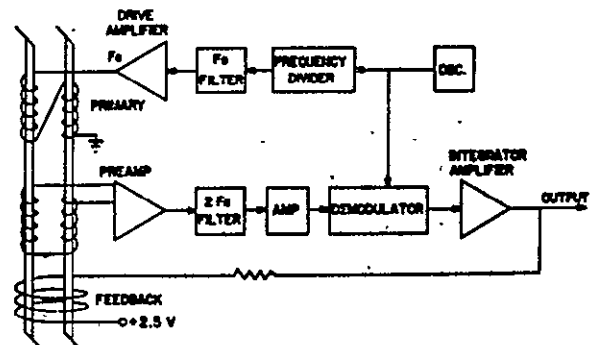
Basic Magnetometer.

Table C-4. Ames Magnetometer Performance

Specification	Characteristic
Configuration	3-axis, orthogonal
Electronics	2nd harmonic, saturable core, closed loop
Outputs	Analog
Dynamic Range	0 to 200 gamma
Noise	0.4 gamma peak to peak in 0.01 to 10 Hz for 1 minute
Zero Field Offset	Less than ±0.5 gamma
Offset due to induced permanent field	Less than ±0.15 gamma after exposure to 1 Oersted field
Long term Drift	Less than ±0.3 gamma in 24 hours after initial warmup
Temperature Drift	Less than 0.03 gamma per degree centigrade in the operating range below
Temperature Range (Operating)	-40C to +71C

than shock induced strain, if the sensor is subjected to extremes beyond ±150 F. At such extreme temperatures the magnetic characteristics are also subject to change.

Magnetic and electrostatic fields generated by the operating ion thruster will produce a varying field at the magnetometer, hence measurements of neither the solar interplanetary field nor the spacecraft magnetic signature may be made meaningful during thrusting.

C-10

Table C-5. . Instrument Performance of the
OGO-E Magnetometer

Specification	Characteristic
Configuration	Three-axis, orthogonal
Electronics	Second harmonic, saturable-core closed-loop
Outputs (0 to 5v)	Analog ±16Y
	Medium Offset -512Y to +496Y at 16Y per bit (64 levels)
	Coarse Offset -54, 536Y to +64, 512Y at 1024Y per bit (128 levels)
Resolution	1/16 Y
Response	Basic magnetometer, flat to 100 cps, analog output to telemetry low pass filtered to 0.3, 2.5 or 20 cps depending on telemetry bit rate
Power	3.2 watts
Absolute Stability	±1/16Y for field ≤ 1000Y ±1 part in 214, ≥ 1000 Y
Weight	Sensor 0.48 kg Preamp 0.34 kg Electronics 2.14 kg*
Size	Sensor 7.6 x 8.4 x 9.1 cm Preamp 3.5 x 8.4 x 14.2 cm Electronics 19.1 x 19.3 x 14.2 cm
*Exclusive of power supply	

Helium Magnetometer

The helium magnetometer measures the total magnitude of the external field. By surrounding the sensing element by a set of three orthogonal Helmholtz coils, field components can be determined. This sensor was used satisfactorily on Mariner IV.

Principle of Operation. The helium magnetometer consists of a helium vapor cell illuminated by a 1.8-micron infrared beam of light from a helium lamp. The light is circularly polarized by a linear polarizer and a quarter-wave plate. The absorption of light in the cell is observed by a lead sulfide detector.

The circularly polarized light excites the helium vapor into a metastable (long-lived) state. The excited atoms can be deexcited from this metastable state by an RF signal at exactly the precessional frequency (Larmor frequency) of the electrons in the helium atoms in the ambient magnetic field. The absorption in the cell varies periodically with this Larmor frequency as the number density of atoms in the excited state varies in the excitation and deexcitation cycle.

The external magnetic field determines the Larmor frequency as well as the energy width of Zeeman splitting of the optical lines of the helium gas in the exciter lamp. Since the density of excited helium atoms varies with a frequency directly proportional to the ambient field (23 Hz per gamma), and since the cell opacity varies with this density of excited atoms, the output intensity detected by the lead sulfide detector oscillates at the Larmor frequency. Therefore, the output frequency indicates the ambient field strength (0.0435 gamma per cycle per second). The Mariner IV magnetometer is shown in Figure C-2, C-3 and C-4.

Advantages. The helium magnetometer may be preferred to the rubidium vapor types because of the small temperature sensitivity, greater precision (23 Hz per gamma as compared to 7 Hz per gamma), and a somewhat lower zero drift than a flux-gate magnetometer.

Flight Experience

The helium magnetometer has been flown only on Mariner IV at this time. Mariner IV encountered a problem in that the spacecraft had a 140-gamma stray field which was determined to be stable on the ground to less than 2 gamma (Reference C-3).

To distinguish between the spacecraft field and to determine the direction of the external field, the magnetometer absorption cell was surrounded by a set of three orthogonal Helmholtz coils carrying currents varied to null precisely the net detected field. The output from the
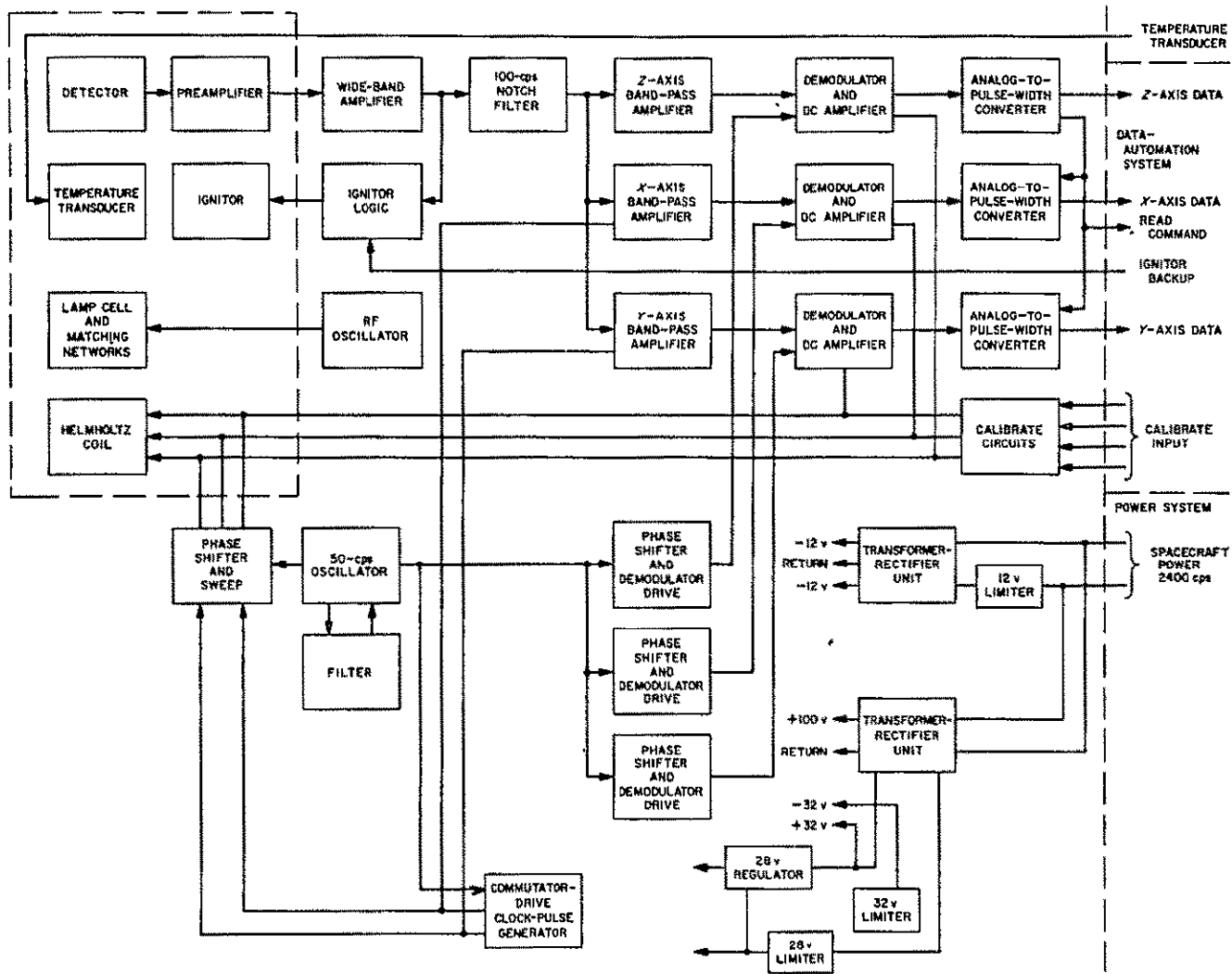
Figure C-2. Mariner IV Magnetometer Functional Block Diagram

Space Division
North American Rockwell
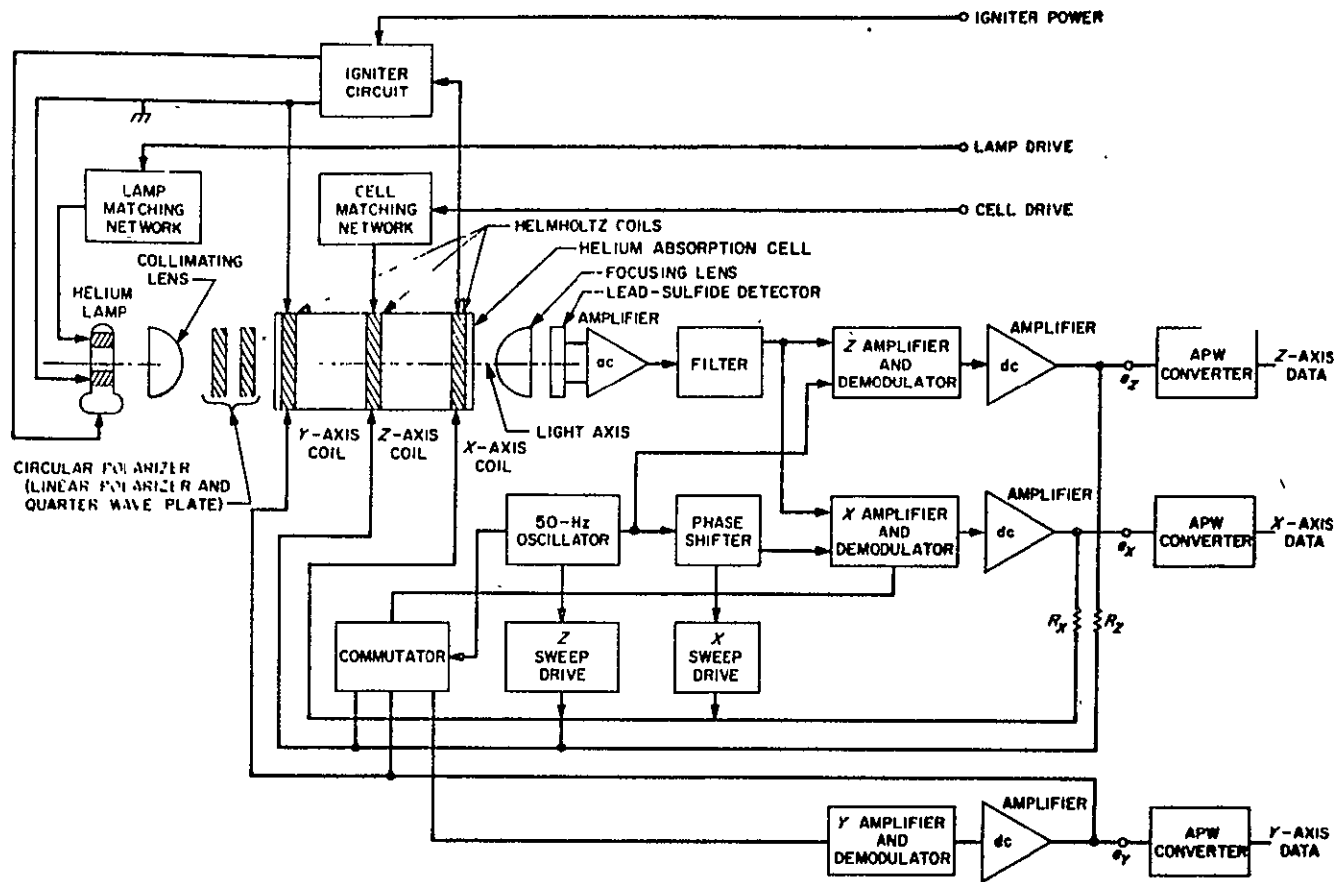
Figure C-3.   Mariner IV Magnetometer Simplified Schematic

Space Division
North American Rockwell
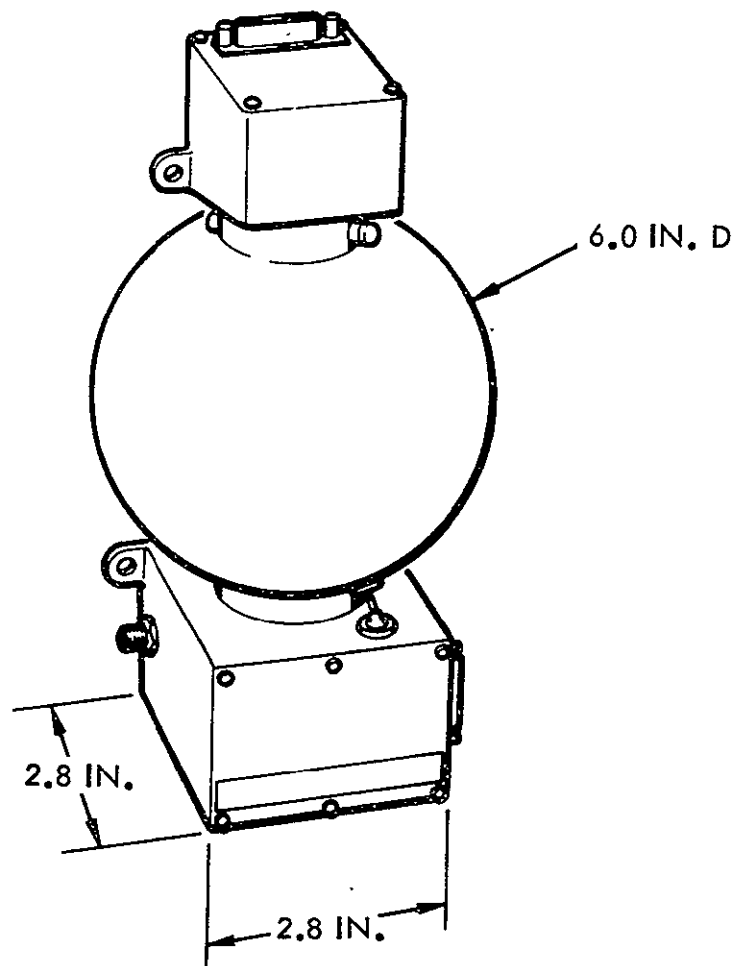
Figure C-4.   Mariner IV Helium Magnetometer

instrument was the currents in these three sets of coils at the time the net field was zero.

Performance Characteristics

The performance of the instrument is summarized in Table C-6 from References 1, 3, and 4.

Problem Areas

The helium magnetometer has a limited lifetime dependent on life of the exciter lamp, filters, and helium absorption cell. The lead sulfide detector signal-to-noise ratio is the limiting component in system operation. This sensor has an impedance which increases as the temperature drops and an output signal noise that increases with the temperature. Since the lamp is hot compared to proper operating temperature of the detector, large temperature gradients across the sensor head are unavoidable. This temperature gradient (~15 C per inch) raises questions concerning long-term missions. Heaters will have to be added for ranges beyond 1.5 AU from the sun. Radiation cooling fins may be incorporated in the lamp housing. Means for replacement of the helium lamp in the event of failure may be considered, as may ways of controlling the pressure in the helium vapor cell. Higher lamp output results in better operation and lower noise, but requires a power increase and lowered lamp life. The helium discharge lamp has a life limited by penetration of helium through the glass. The Mariner IV instrument used in initial excess of pressure, and had been preconditioned by operation for a period of time, with calibration immediately before launch after the glass cell had been saturated with the helium.

Rubidium Vapor Magnetometer

This instrument is very similar to the helium magnetometer. It has been extensively used in Earth orbit for measurement of higher field strengths than common in space. The fundamental frequency output is also proportional to field strength, but is only about 7 Hz per gamma instead of 23. Hence, for weaker fields the rubidium vapor instrument should be one-third as precise as the helium magnetometer.

The rubidium magnetometer uses R_u - 87 gas. A spectral lamp is also used, but in the visible spectrum. A silicon photocell is used to detect the light. An ac magnetic field is used to deexcite the gas.

Major Problems. The rubidium vapor lamp is highly temperature sensitive (110 ± 10 C for the lamp and 42.5 ± 5 C for the absorption cell). Present lamp life is less than 1000 hours (Reference C-1).

Table C-6. Performance of the Mariner IV Helium Magnetometer

Characteristic	Performance
Dynamic Range	±360 gamma on each axis
Noise	0.5 gamma peak to peak
Instrument zero offset	±2 gamma
Spacecraft zero offset	140 gamma
Null stability	0.5 gamma
Accuracy	$\pm(0.005\left\|B\right\| + 0.5)$ gamma
Temperature range	-45 to +65 C (sensor head)
	-20 to +65 C (electronics)
Power	7.30 watt
Mass	0.57 kg sensor head
	2.72 kg electronics
	3.29 kg total

Hall Effect Magnetometer

This magnetometer does not appear to be directly applicable to this program due to difficulties with large drifts in the zero field indication which increase with time due to changes in the semiconductor material caused by radiation and long-term thermal effects. If, however, radiation damage can be prevented or countered, then the device would be applicable for measurement of extremely low fields (~0.001 gamma), 100 times smaller than can be measured by the helium or flux gate devices. Temperature stability of ±1 C would be required during operation.

The magnetometer measures one component only, hence three elements must be used to obtain the total field. Each unit consists of two end-to-end Permalloy rods with a semiconductor such as indium antimonide placed in a gap between the rods.

C-17

The Hall effect is the development of an external magnetic field dependent voltage difference between two edges of a strip of metal or semi-conductor within which an electric current is flowing longitudinally.

There is a possibility that a Hall effect magnetometer can be modified into a form useful for 10^{-3} to 10-gamma fields in deep space. Problems with temperature instability, drift, radiation damage, and stray field retention by the Permalloy rods will have to be overcome. Perhaps parallel units mounted in the same envelope can be used with an oscillatory signal (similar to the flux gate magnetometer operation) instead of using the sensor in its dc form. But for the present study, no spacecraft integration type of design features can be described at this time.

Magnetic Cleanliness

To perform acceptable measurements of magnitude and direction in a low field environment (0.1 to 10 gamma), the spacecraft must have a low background field level at the magnetometer boom. In addition, the background field must be shown to be stable in time by adequate testing before launch. During test of the spacecraft, repeated magnetization is used to "cure" the vehicle magnetically. At the end of the test, the spacecraft is permanently magnetized to a low level so that the remaining field is stable in time to better than 0.1 gamma as measured at the end of the boom at the sensor head. Recent spacecraft have been built with fields as low as 0.1 to 1 gamma (Reference C-5).

The SEP electric engine may pose several new problems into the magnetic cleanliness picture. The electric engine produces small fields for a long period of time which could change the degree of magnetization of the spacecraft. These fields are produced partly from remnant charged particles in the engine exhaust, and partly from fields generated by engine parts and unbalanced currents in power lines. These parts may have to be shielded magnetically and designed so they can not vary the spacecraft fields; or at least so they do not vary in an unpredictable manner.

Operation of the science package during thrusting is not planned in the baseline mission. However, it is suggested that if the magnetometer were turned on on the launch pad and operated throughout the mission, sudden changes in the spacecraft field due to launch or thrusting operations could be detected by direct measurement and indirectly by comparison of data from other magnetometers on other spacecraft in the near vicinity.

Data Rates

There appears to be fine structure of importance in 1-second intervals of time. Thirty or forty bits per second are needed during these times. If the continuous rates are less than 10 to 40 bits per second, a high rate non-real-time "flare" mode is required. To achieve a low average data rate without storage, the environment can be sampled at 1-second time resolution during intervals of 30 to 60 seconds, spaced 16 minutes apart to fit the data commutation cycle.

SOLAR PLASMA MEASUREMENT SENSORS

Plasma measurements are to be correlated with magnetic field measurements to extend knowledge of the radial dependence of the solar plasma and field densities, flow direction, spectra, propagation of disturbances, and interactions of the plasma with planetary bodies and with the galactic environment. Table C-7 presents the basic plasma parameters and phenomena to be measured.

Available Plasma Spectrometers

About a half a dozen different plasma spectrometers have been flown, but all are versions of four basic types: the curved plate electrostatic analyzer, the Faraday cup, the Langmuir probe, the ion trap, possibly the foil ion trap (Apollo 11), magnetic analyzers (which have not been flown in deep space). Available sensors are used in Table C-8.

Langmuir Probe

This sensor consists of a long conducting probe extended through an insulated ring in the wall of a spacecraft. An ac signal is applied between the probe and metal spacecraft wall to accelerate and repel ions alternately in the field between the probe and spacecraft. The potential-current characteristics of the probe and spacecraft in the plasma environment are dependent on the low energy electron density and temperature in the environment. The Langmuir probe is sensitive to such thermal plasmas as found in a planetary ionosphere, and has not been used to measure the higher energies in the solar plasma.

Electrostatic Plasma Spectrometers

Curved plate analyzers are used for measurements of weak fluxes of high energy solar plasmas (protons and electrons), while the Faraday cup types are used for higher fluxes at low energies. Combined electrostatic and electromagnetic analyzers capable of increased species and energy discrimination have not been flown as yet.

C-19

Table C-7. Basic Solar Plasma Parameters and Phenomena to be Measured

Parameter	Measurement	Phasing	Range	Sampling Rate
Positive ion flux versus energy	number-density-spectrum	Continuously alternating with negative flux measurements	10^{-9} to 10^{-13} amp 10^5 to 10^{10} particles-cm^{-2}-sec^{-1} 10^1 to 10^4 eV	1 output channel per 100 seconds to 32 channels per second
Negative ion flux versus energy	number-density-spectrum	Continuously alternating with positive flux measurements	10^{-9} to 10^{-13} amp 10^5 to 10^{10} particles-cm^{-2}-sec^{-1} 10^1 to 10^4 eV	1 output channel per 100 seconds to 32 channels per second
Direction of flux	Azimuth and elevation relative to ecliptic plane and spacecraft-sun line	Continuous	±90 degrees	1 per minute to 1 per hour
Dependence of flux and spectrum on solar activity	-	After large solar flares and M region passage	-	-
Radial dependence of quiescent particle densities	-	Continuous	-	-
Deep space plasma shock wave densities and thickness	-	After large solar flare	-	-

Table C-8. Available Solar Plasma Sensors

Sensor Type	Special Feature	Flights	Best for SEP	Mass (kg)	Average Power (watt)
Langmuir probe	For low energy ions	Low altitude Earth orbiters	-	-	-
Electrostatic plasma spectrometer (Curved cylindrical plate)	For low fluxes at higher energies	Mariner II Pioneer 6	+	3-4	3-9
(Curved spherical plate)	Increased aperture and angular selection		*		
Curved channel multiplier	minimizes electro- meter demands	OGO-III	*		
Faraday cup plasma spectrometers	Large circular aperture for higher flux low energy region of environment	Mariner IV IMP Pioneer 6 Explorer 10	*	2.9	2.65
Spherical ion traps	Hemispherical inlet aperture. Used primarily by USSR	Lunik 2 Sputnik 3 Venus 1961			
Planar probe	Insulated plate on space craft	Explorer 8			
Aluminum foil particle traps	Lightweight Simplicity for manned deployment	Apollo 11, 12			

Curved Plate Analyzers

A charged particle with energy (E) entering the space between two parallel plates will be deflected at right angles to both the velocity vector and to the plane of the plates. If the plates are curved, there may exist incident particles in a small range of energies per unit charge and initial directions that are bent into a path curved with the same radius of curvature as the plates. For a cylindrically shaped pair of plates, the energy per unit charge of particles which will pass through the plates, for a potential V, is

$$\frac{E}{q} = \frac{V}{\ell n \left(\frac{r_2}{r_1} \right)} = \frac{m}{q} v^2$$

where r_1 and r_2 are the radii of the cylindrical plates, m is the particle mass, v the velocity, and q the charge.

For a spherical pair of plates,

$$\frac{E}{q} = V \frac{r_1 r_2}{r_2 - r_1} \left(\frac{r_1 + r_2}{2} \right) = \frac{m}{q} v^2$$

For positive voltages, one set of particles is obtained (protons, alphas, and other positively charged species); for negative voltages, electrons and possibly other negative particles are detected. On Mariner II, no electrons were detected. To obtain the spectrum of particles within the range of the instrument, the potential V is stepped through a cycle of small increases from about 50' to 2500 volts, plus a zero-current reading and calibration at about -2 volts.

Particles of different species but with the same charge-to-mass ratio cannot be distinguished by this type of instrument unless a magnetic selection subsystem is added, except when the energies of different species are widely separated.

Block diagrams and sketches of Mariner-type plasma spectrometers and Faraday cups are presented in Figures C-5 through C-8 from References C-6 and C-7. Pioneer 6 also carried a Faraday cup instrument (Reference C-8).
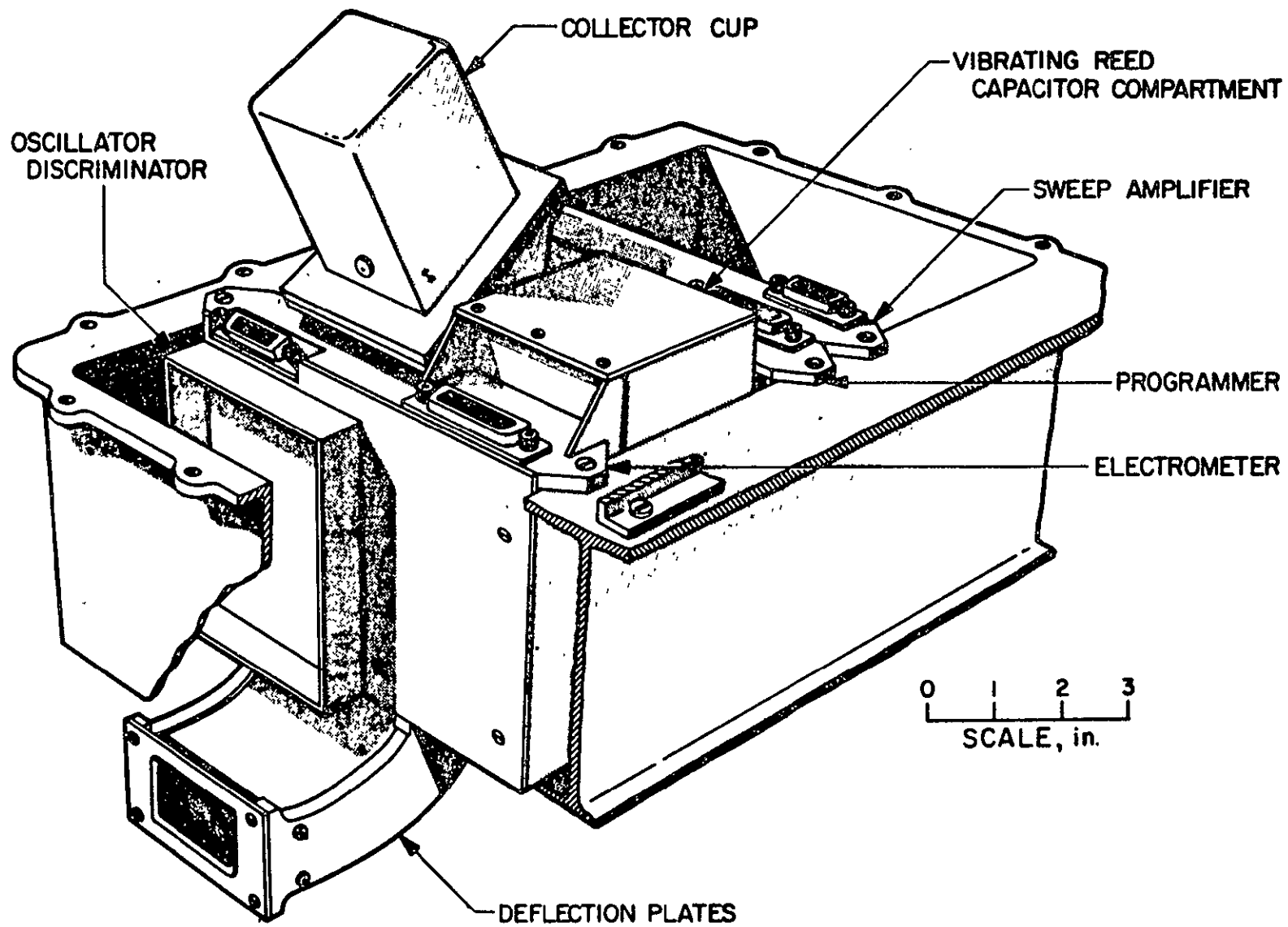
Figure C-5. Mariner II Solar Plasma Spectrometer Experiment Assembly
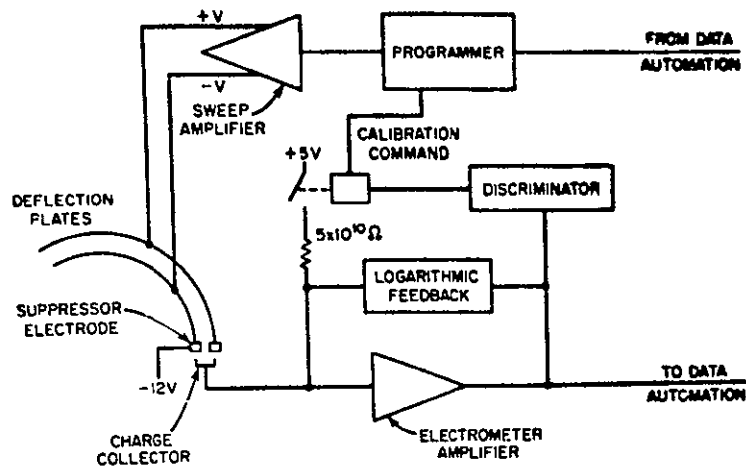
Figure C-6. Mariner II Plasma
Spectrometer Block Diagram
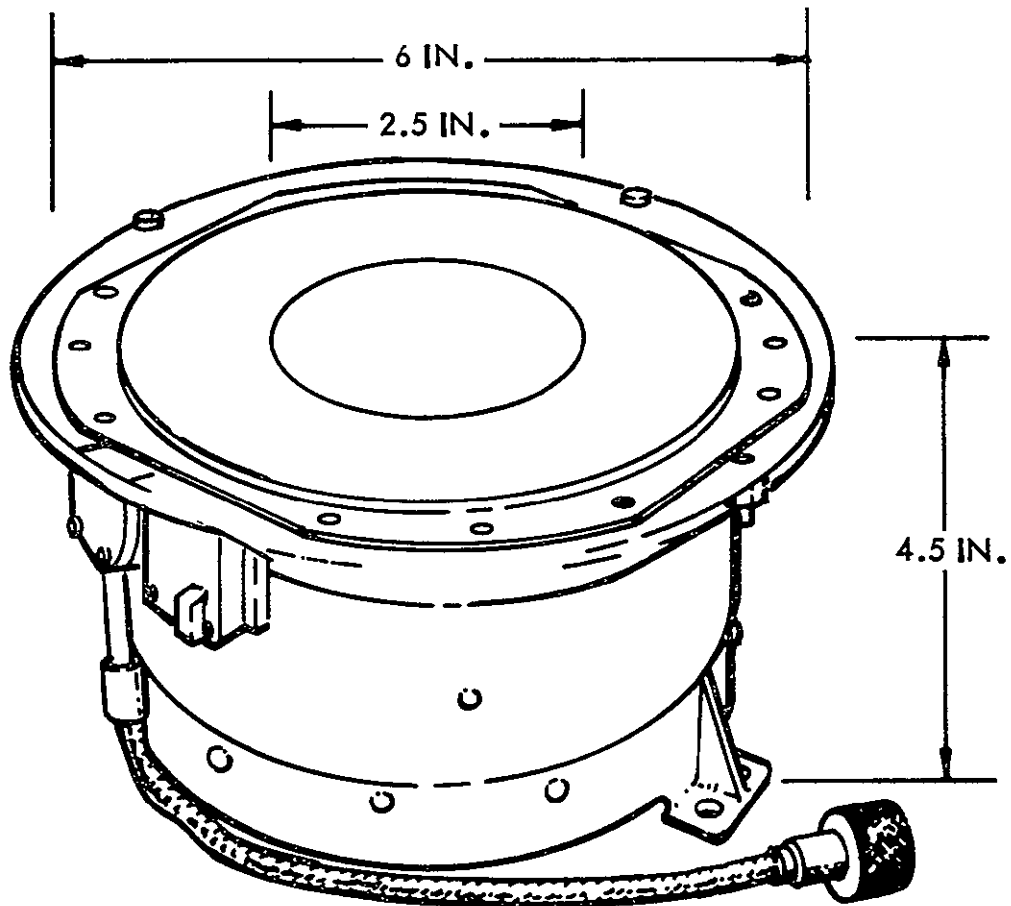
Figure C-7. Mariner IV MIT Solar Plasma Faraday Cup Sensor Head
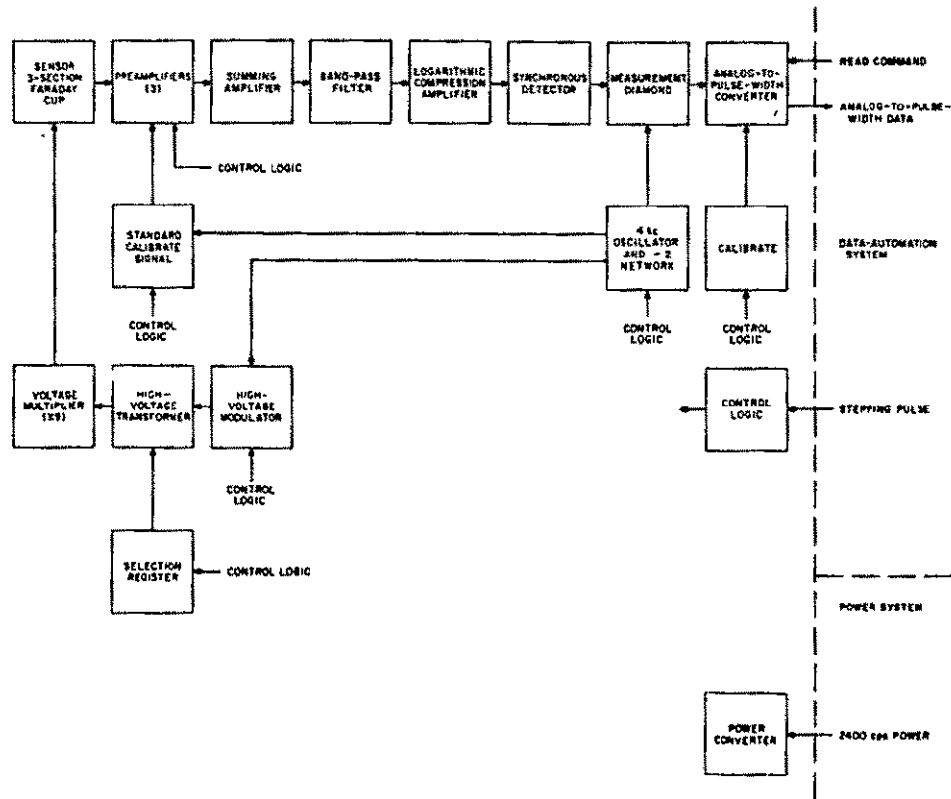
Figure C-8.   Mariner IV MIT Faraday Cup
Plasma Spectrometer Block Diagram

Typical instrument performance is described in Table C-9 for the
Faraday plasma cup and in Table C-10 for the curved plate.

Channel Multiplier Type

An improvement of the curved plate analyzer has been flown by the
University of Iowa using a Bendix channel multiplier for the curved plates
to measure electrons and protons from 100 eV to 50 Kev as shown in
Figure C-9 (from Reference 9).   This instrument was flown on OGO III
where it discovered a large flux of low energy protons at 3 Earth radii,
intense enough to account for the field changes during magnetic storms,
which effect had been attributed previously to the never-discovered ring
current.

Difficulties and Problems

During the Mariner IV sensor, power and weight reductions had to be
imposed.   Smaller high voltage pulse transformers than feasible for a long
duration mission were used.   Bleeder resistances in the high voltage power
supply filter units were made as high as possible to minimize power loss.
The Mariner 4 bleeder on the plasma probe high voltage supply was
increased from 100 to 300 megohms to conserve 0.7 watt.   This bleeder
failed after only eight days of operation after launch.   The resistor failed

due to a radial ac electrostatic field (that existed between the resistor and the surroundings) strong enough to cause the thin-film resistive element to strip off of the ceramic base. Loss of the bleeder caused the high voltage to hold on during the following voltage reduction cycle when low energies were to be measured.

On long duration missions, sputtering from engine operation may short out some of the grids in the Faraday cups, unless design features can be added to prevent this effect. It may be wise to operate the plasma spectrometer or Faraday cup with the internal grids at a high positive potentials relative to the spacecraft to repel engine mercury ions and other metals which may have been vaporized. If these ions are not repelled, they may deposit on the insulators in the plasma sensors shorting out the electrodes. As an alternative to operating the plasma sensor during thrusting, a cover plate could be kept across the entrance aperture. After engine shutdown, this cover plate could be released by a spring with an electrical latch.

USE OF THE CONTINUOUS CHANNEL MULTIPLIER IN THE LOW ENERGY PROTON ELECTRON
DIFFERENTIAL ENERGY ANALYZER (LEPEDEA)
UNIVERSITY OF IOWA

MULTIPLICATION PROCESS IN THE
CHANNEL MULTIPLIER
(A)

SALIENT FEATURES OF THE LEPEDEA
(B)

NASA SD68-S37
1-5-68
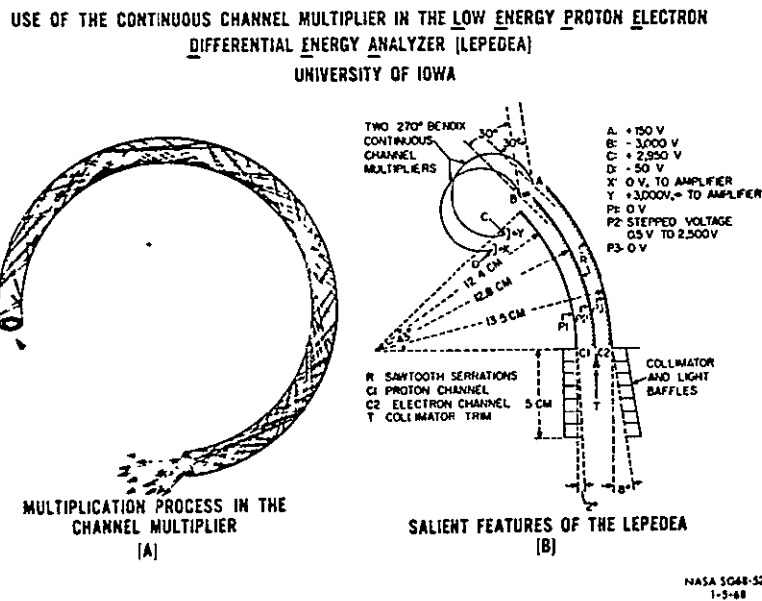
Figure C-9. Channel Multiplier

Table C-9. Instrument Performance, Mariner IV-Type Plasma Cup

Characteristic	Description
Configuration	Two cylindrical units about 6 inches in diameter and 4 inches deep, with a 2-inch circular aperture on the face to be mounted on a boom, or wall of spacecraft if boom mount is not possible.
Acceptance Cone	15-degree half angle cone, 10 degrees off Sun-probe line.
Electronics	Ac or dc to high voltage (10 kv) dc converter Pulse generator, voltage stepper. Electrometer current detector
Outputs	32 channels covering range of positive energies plus two calibration channels, all subcommutated over high voltage cycle. Extra power supply for negative particle detection. Two outputs (one for each cup). Outputs digital or analog
Inputs	28 V dc or ac 2400 cps 2.65 watt per cup for positive particles only. For both positive and negative particles, about 3 watts would be required. Per cup 2.9 watt peak required.
Weight	2.9 kg per cup 2400 cps ac Positive Particle Detection For negative particle detection add 0.2 kg.
Dimensions	6-inch diameter, 4 inches deep
Sensitivity	5×10^5 to 5×10^9 particles/(cm^2 sec) 30 eV to 10 Kev

Table C-10. Instrument Performance, Electrostatic Analyzer Type

Characteristic	Description
Configuration	Cylindrical or hemispherical plates Rectangular aperture or half-annular ring aperture (4 cm^2) Mounted on boom or wall if boom mount is not possible
Electronics	Channel multipler or Vibrating Reed Electrometer current detector Pulse generator, voltage stepper
Outputs	24 to 32 channels covering range of negative and positive energies plus two calibration channels, all subcommutated over high voltage cycle. Extra power supply for negative particle detection. Three outputs from unit for three directions of incidence in accpetance cone.
Acceptance Cone	10-degree half angle acceptance cones in each of three directions in ecliplic plane, centered with respect to line 10 degrees from sun-probe line
Inputs	2.4 KHz or 28 V dc 3 to 9 watts
Weight	3-6 Kg
Dimensions	6 x 6 x 10 inches
Sensitivity	4×10^6 to 10^{12} particles/(cm^2 sec) 100 eV to 10 Kev

SOLAR AND COSMIC CORPUSCULAR RADIATION SENSORS

More corpuscular radiation sensors have been flown than most other types of sensors and a great deal of experience has been accumulated upon which reliability can be based for such instruments. The earliest flights (with balloons) of a radiation spectrometer were in 1929 by Bothe and Kohlhoerster with Geiger-Meuller counters and in the same year by Skobeltzyn with a cloud chamber. In the United States, Neher and Millikan flew their ion chamber and Geiger-Meuller counters on balloons as early as 1936. Similar ion chambers and Geiger-Mueller counters were flown on Mariner II and IV by Neher and Anderson to give results comparable with the standardized instruments developed by Neher back in the mid-1930's. These instruments are still used on balloons to monitor the long-term cosmic ray flux variations.

There is very little that the most recent sensors can do that cannot be done also by ion chambers and Geiger-Mueller (GM) counters, although these older sensors provide less data per pound per second, and require greater extensive data reduction work than the more modern sensors. In deep space missions, both the older and newer sensors still may be needed.

The basic aspects of the corpuscular radiation environment to be measured are presented in Table C-11. These measurements are to be made in the asteroid belt in such a fashion that the results can be corre-lated with results from Pioneer F and G Jupiter flights and as well as with near-Earth measurements.

Of particular interest is the intensity, spectrum and time dependence of both the galactic and solar corpuscular flux throughout the mission. These measurements are of critical importance to finding out what factors govern the behavior of the solar corpuscular radiation transport and the changes in the galactic flux. Preparatory to later flights to Jupiter and the outer planets, the long-term radiation environment must be known. Radiation damage in electronics systems and sensors is possible. But present information on the deep space flux is not adequate to set design requirement for those later flights.

Many different types of nuclear sensors are available. The ion chamber measures the total ionization rate produced by all ionizing com-ponents of the radiation. The GM countermeasures the flux of all ionizing particles which pass through into the sensitive volume of the counter plus a fraction of the bremsstrahlung flux produced by absorption of electrons in the spacecraft. The semiconductor spectrometers measure the flux and

C-29

Table C-11. Basic Corpuscular Radiation Parameters and
Phenomena to be Measured

Parameter	Sensor Types Used	Range	Sampling Rates
Solar protons	Semiconductor charged particle	0.5 to 100 Mev	1 sec to 1 hr
Solar alphas	Spectrometers	10 to 400 Mev	
Solar electrons	Magnetic type spectrometers	0.01 to 5 Mev	
Galactic protons	Semiconductor charged particle spectrometers	0.1 to 10 Gev	
Galactic alphas	Spectrometers plus scintillation	0.4 to 40 Gev	
Galactic electrons	Counters and Cerenkov spectrometers	0.005 to 0.5 Gev	
Galactic/solar ion rate	GM and ion chamber	10 to 10^3 ions/$(cm^3$-sec-atm)	
Galactic secondary rate	GM and ion chamber	10 to 10^3 ions/$(cm^3$-sec-atm)	
Directionality versus energy	Triaxial particle spectrometer	± degrees over 4	
Flux and spectra Correlated with solar activity	All above sensors	As above	
Radial Dependence of solar proton	All above sensors	As above	
Radial Dependence of galactic flux	All above sensors	As above	

quantity of ions produced in a junction by ionizing particles. Scintillation counters are used for high energy particles and neutrons. Cerenkov counters are essentially scintillation counters and are also used for high energy particles.

There are some radiation sensor types that could perform the measurements in the previous table, but are not applicable to a long duration, unmanned, low data rate mission. Such sensors as nuclear emulsions, and bubble chambers will not be discussed.

Basic nuclear radiation sensor types which would be applicable to the mission are presented in Table C-12. Each of these potential sensors has been flown on at least several, if not many, different spacecraft. The proposed mission is not a short one, and lifetime and reliability for each type must be considered carefully. Potential lifetime and reliability problem areas are indicated in the table and discussed separately for each sensor type listed.

Geiger-Mueller Counter Plus Shield

This instrument consists of a small cylinder with closed ends filled with an insulating gas. A thin tungsten wire is stretched along the central axis of the cylinder. This wire is insulated from the end walls by ceramic to metal seals. Various gases or mixtures of gases can be used. For long life, about 10^{-5} gram/cm^3 (about 100 torr) of argon plus a trace of chlorine is frequently used. The wire is made about 900 volts positive with respect to the cylinder for most gases.

When an ionizing particle or gamma ray passes through the counter, the secondary electrons are accelerated to the central wire and the positive ions to the cathode. The Geiger-Mueller (GM) counter, the proportional counter, and ion chamber all work similarly, according to the voltage applied between the wire tap and cathode. As this voltage is increased to 100 to 300 volts, the instrument acts as an ion chamber. In the ion chamber voltage region no electron multiplication occurs as the electron accelerates to the anode wire. For voltages between about 300 and 600 volts, the electrons gain sufficient energy to produce one additional or more secondary electrons in the acceleration process. Thus, the number of electrons collected on the anode is greater than the original number of ions produced by the radiation quanta counted. This voltage region is called the proportional region, because the counter pulse is proportional to the number of ions produced (whereas in the ion chamber region not enough ions are collected per quantum to give an output pulse. The ion chamber is therefore a current device only, using very large coupling impedances).

Table C-12. Basic Types of Nuclear Radiation Sensors
Applicable to Solar Electric Missions

Sensor Type	Special Features	Typical Flights	Best Choices for SEP	Approximately Mass (kg)	Approximately Power (watt)
Geiger-Mueller counter plus shield	Counts charged particles with enough energy to pene-penetrate shield	Mariner II, IV Pioneer 5, IMP-1	X	0.5	0.2
GM counters with mag-netic spectrometer	Magnetic field used to sepa-rate counts of different particle energies	Explorer Discoverer		-	-
Ion chamber plus shield	Measures average rate of ionization in a gas due to penetrating particles	Mariner II, IV	X	0.7	0.2
Plastic phoswich scintillator	Uses pulse-shape and pulse height analysis to dis-tinguish protons, elec-trons and gammas			1-3	2-4
Proportional	High energy proton & elec-tron flux and directional dependence (can be used for neutrons with ^{3}He or BF_3 gas & plastic moderator	Pioneer 5			
Counter telescope plus shield				1-3	0.5
Silicon surface barrier or diffused junction semiconductor with anticoincidence counter and shield	Counts integral flux of high energy charged particles & measures spectrum of low energy particles that penetrate shield.	Mariner IV Telstar IMP Pioneer	X	0.5	0.4
Lithium drifted silicon detector with anticoincidence coun-ter and shield	As above, but measures spectrum of somewhat higher energies due to thicker sensor element	-	X	0.7	0.4

Space Division
North American Rockwell

Table C-12. Basic Types of Nuclear Radiation Sensors
Applicable to Solar Electric Missions (Cont)

Sensor Type	Special Features	Typical Flights	Best Choices for SEP	Approximately Mass (kg)	Approximately Power (watt)
Totally depleted plus lithium drifted silicon de/dx -E spectrometer	Determines particle type & energy by measuring loss rates (de/dx) and total remaining energy (E) in coincidence over 45 degrees cone	Mariner IV ATS	X	1.2-4	0.4-3
Telescope, version of above	As above, but limited to 10 degree half-angle cone	-	X	1.2-3	0.4-3
Lithium iodide - plastic scintillator and plastic shield neutron counter	Moderates and detects neutrons from ^{6}LiI in anticoincidence with plastic crystal. Similar to several other neutron sensitive inorganic crystals in this type of counter.	-		3	2-4
Cerenkov spectrometer	Detects high energy cosmic rays using lucite crystal and photomultiplier in coincidence with CSI crystal for $E \geq 0.25$ GeV/nucleon	Explorer	X may be too heavy	3-10	2-5

For voltages greater than about 600 volts, enough electrons are generated per incident quanta that an avalanche of secondary electrons is produced in a sheath about the central wire. The output pulse of the GM counter is very large compared to the propulsional counter. All pulses from the GM counter are of the same size, characteristic of the voltage, counter dimensions, filling gas, temperature, and coupling impedances.

Theory of Operation

Textbooks discussing GM and proportional counters and ion chambers generally present in an output pulse height versus applied voltage curve as shown in Figure C-10. Such curves can be produced with special counters, but the above curve is a diagram only. One has great difficulty producing such a curve with a real GM or proportional counter, or ion chamber, primarily due to the large variation in pulse height requiring different coupling impedances and time constants. Since the time constants of the pulses are varying, it is hard to make a good comparison of pulse heights so that one obtains a smooth curve. Further, most ion chambers use high gas pressures (several atmospheres), which would result in no effective proportional or GM regions. Most GM counters use gases at low pressures and with a quenching mixture (a halogen or alcohol) to shorten the time required for the avalanche electrons to be absorbed. These quenching mixtures generally result in a counter with an extremely limited region of proportionality. Any good proportional counter gases and gas pressures are such that operation is permited at several thousand volts, but such operation provides an extremely limited GM plateau region. Therefore a counter cannot be bought or built that is even approaching optimization for all three if not even two regions in the above curve. Otherwise, it would be possible to use a single counter, and just change the amplifier type and applied voltage to obtain data in all three regions. Clearly, separate counters are required.

Each GM counter output pulse height is of the same voltage regardless of particle energy in the region of the GM plateau, though the pulse height can be varied by adjusting the applied voltages, circuit parameters, and counter dimensions (especially the central wire diameter). The physical size of a GM counter may be adjusted to meet requirements of needed sensitive area, weight and volume limits, and optimum length to diameter ratio for the particular experiment. Either side-wall or end-wall windows can be provided, but a counter with a thin end-wall will have to use a short, thick, stiff central wire at higher voltage than would be used for a thin wire (1-mil) which must be held taut at both ends.
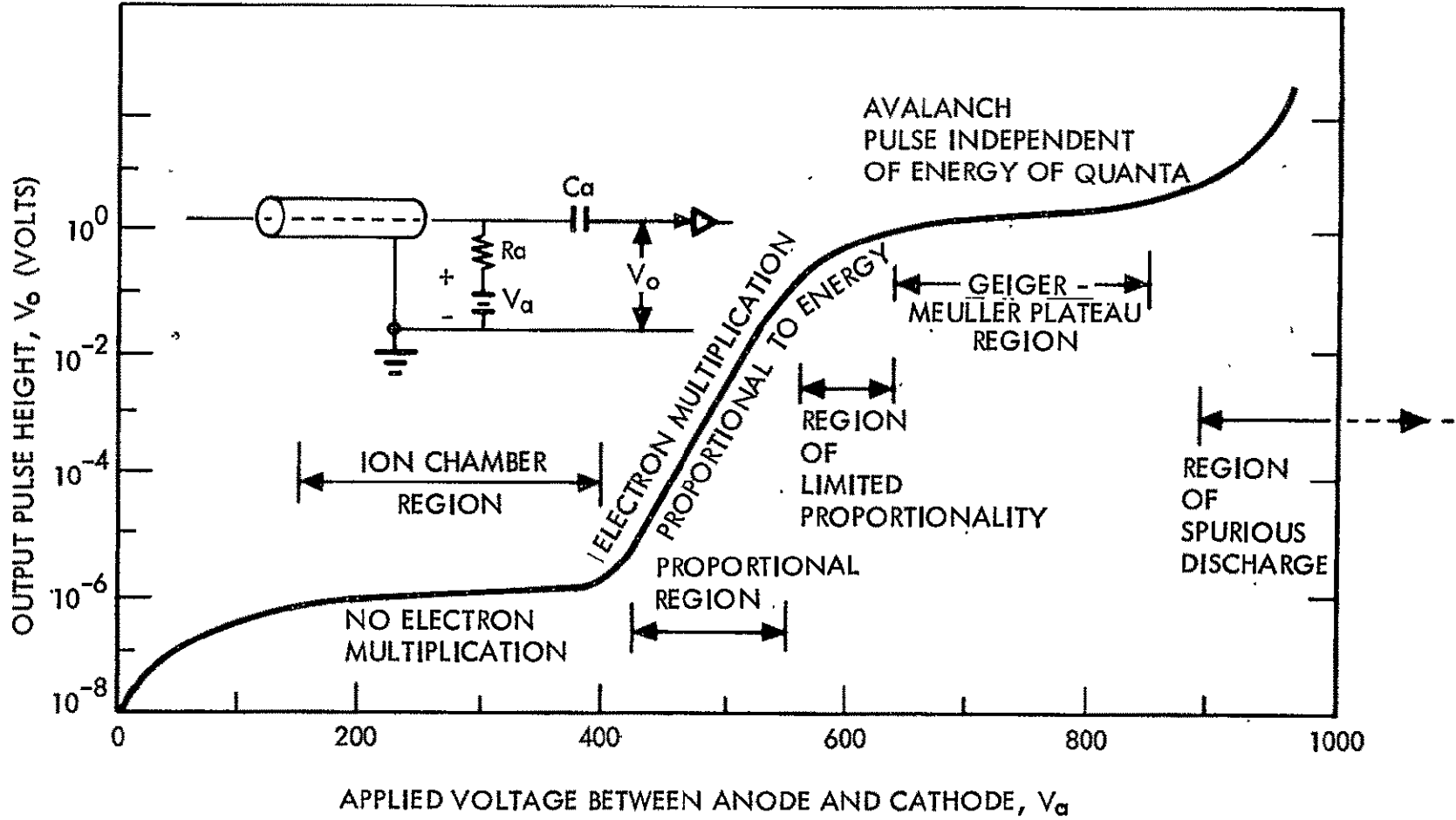
Figure C-10. Pulse Height Versus Applied Voltage

The electric field in the counter increases toward the central wire, hence most of the electron-ion collisions, responsible for creating an avalanche discharge, occur in the last collision length from the central wire. For a given applied voltage, higher maximum fields exist for smaller wire diameters, regardless of counter diameter. Therefore, the wire diameter sets the required operating voltage for a particular gas and pressure.

Temperature is also a factor even in a counter designed to minimize this dependence. It may be necessary to heat the sensor to keep temperatures above -40C. Temperatures above 125C will cause trouble due to high probability of causing spurious continuous discharge. To prevent the possibility of damage from continuous discharge, a semiconductor may be useful in the high voltage lead to the counter, so that a short or continuous discharge would be prevented from damaging the high voltage power unit feeding several counter units. A high voltage temperature cutoff might also be useful to prevent operation in a region known to be useless and damaging to the counter.

One of the Mariner IV GM counters failed because of a related problem. A large solar event occurred and the counter registered a saturated condition for a short period of time. During this period, pitting of the central wire was indicated to the extent that spurious continuous discharges were noticed afterwards. Eventually the counter shorted out the power supply, indicating that the wire has broken and had fallen against and welded to the cathode.

To prevent such wire damage, several things could be done. A thicker wire could be used with higher voltage. A continuous discharge indicator could be placed into the circuitry with a controlled means for reducing the applied voltage to stop continuous discharges. And several counters connected to a common supply should be isolated by semiconductors to prevent loss of one affecting others.

Output Pulse Characteristics

The GM counter produces a pulse with a rise time characteristic of the mean acceleration time for electrons to the anode pulse subsequent spreading of the avalanche sheath along the anode. The mean acceleration time is proportional to the voltage and counter diameter. The mean time for the sheath to spread is proportional to counter wire length. Typical rise times are 2 to 10 microseconds. The pulse decay time is governed by the quenching speed. The avalance discharge in a pure gas such as argon

would last at least several milliseconds. Older counters used quenching circuits which in effect reduced the applied voltage until the discharge stopped. Later counters use a trace of alcohol which broke down under avalanche to stop (quench) the discharge more quickly. The alcohol quench limits counter life to $\sim 10^6$ counts. A trace halogen gas has a similar quenching effect but is not used up and does not limit counter life. Most modern tubes are chlorine- or bromine-quenched giving about a 40 to 200-microsecond decay time.

This 100-microsecond response time is a serious limitation on uses in space. For a small counter having only 1 cm^2 cross-sectional area in a near 4π-steradian shield, saturation would occur at a penetrating flux of only 10^4 protons cm^{-2}-sec^1. The statistical accuracy of 10^4 counts is 1 percent and would be the maximum accuracy of the GM counter with that area for protons for sampling intervals equal to 1 second. A larger counter would reach 10^4 counts saturation for a smaller flux, hence larger counters give the same 1 percent accuracy of 10^4 counts, or better than a 1 percent accuracy, for a lower flux in proportion to cross sectional area. For longer sampling intervals, greater precision than 1 percent would be achieved. Hence, the minimum time required to obtain a given accuracy is a function of the counter area and response time.

For use in the asteroid belt, the counter is built large enough to obtain good accuracy in measuring the flux of cosmic rays in the time interval as small as important fluctuations in the magnetic field. The counter is then shielded so that the maximum expected penetrating solar proton flux is equal to the saturation level. Ideally, several different shield thickness with separate counters will be used to determine spectral information. Shield thicknesses from 0.044 g/cm^2 of polyethylene plus a 0.03 g/cm^2 stainless steel wall (10-Mev proton cut off), to 7.2 g/cm^2 of polyethlene or 11.8 g/cm^2 of copper (100-Mev proton cut off) are typical.

Typical GM counter specifications are presented in Table C-13. Mariner IV was one of the last planetary probes to use the GM counters, due to emphasis on atmospheric and surface studies and the lack of trapped radiation at Mars. The Mariner IV GM counter units are described in References C-10 and C-11.

Typical GM counter units are shown in Figures C-11, C-12, and C-13. System block diagrams are included showing types of components used in the electronic systems. Due to the thinnest wall units available (~ 1.4 to 30 mg/cm^2) and to the rather large weights for cut offs beyond 100 Mev, the GM counter is restricted essentially to the 3 to 100-Mev region with one integral spectrum point per unit. The low energies do not require mica type windows, as thin walled stainless tubular types are available with

Table C-13. Typical GM Counter Specifications for
Solar Electric Propulsion Mission

Characteristic	Specification
Applied voltage, v_a	425 to 450 volts
Plateau at 100 counts/sec	75 volts
Plateau slope at 100 counts/sec, $\Delta v/v_a$	0.15 percent
Counter dead time	40 microseconds
Maximum count rate	25,000/sec
Background count rate	5/minute
Operating temperature limits	-55 C to +75 C
Cathode material	stainless steel (28% Cr, 72% Fe)
Cathode thickness	30 mg/cm^2
Output pulse amplitude across 10 Meg resistor	1.5 to 7.5 volts
Sensor Capacitance	2.0 to 3.5 μ μf

Sensor plus shield mass			
	7.2 cm shield	1.6 Kg	100 Mev p^+ cut off
	4.8	0.47	80
	2.8	0.10	60
	1.4 cm shield	0.03	40 Mev

C-38

Figure C-11. Mariner II Ionization Chamber and Geiger-Mueller
Counters Block Diagram
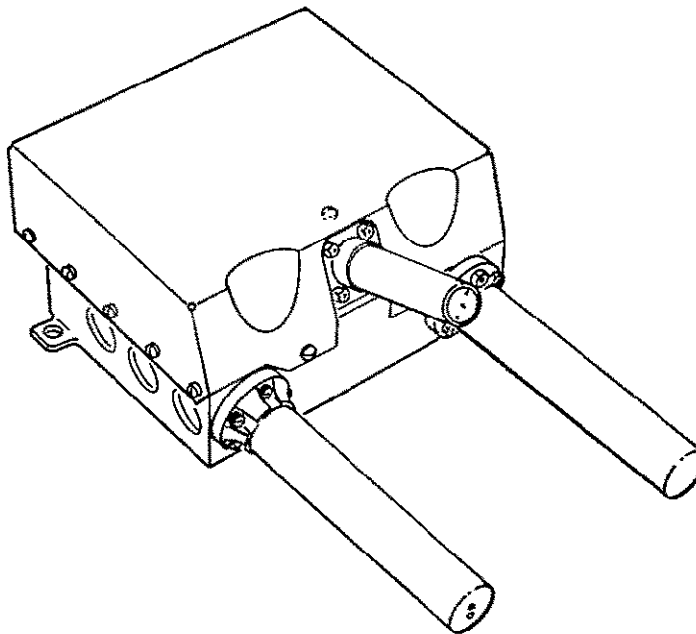
Figure C-12. Mariner II Geiger-Mueller
Tube Package
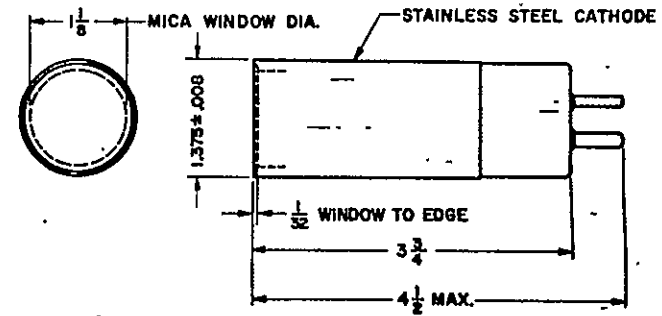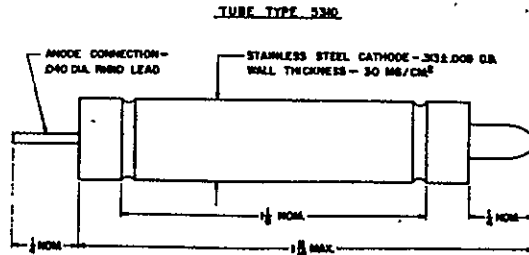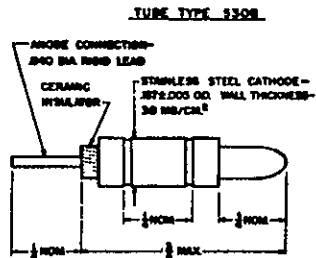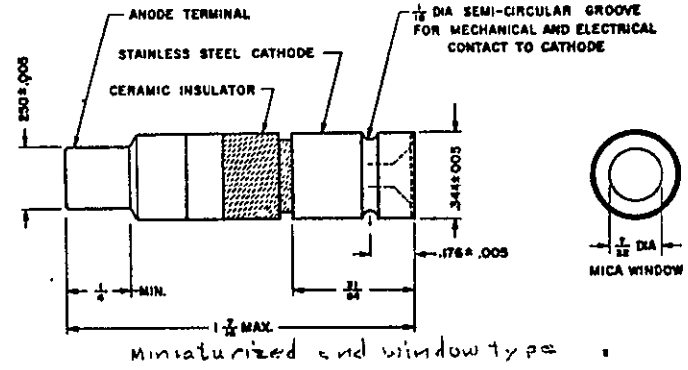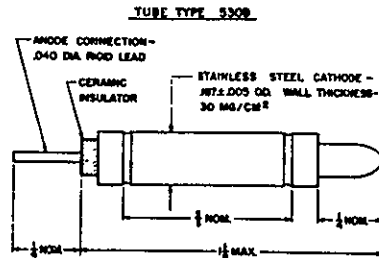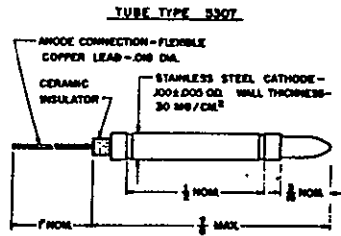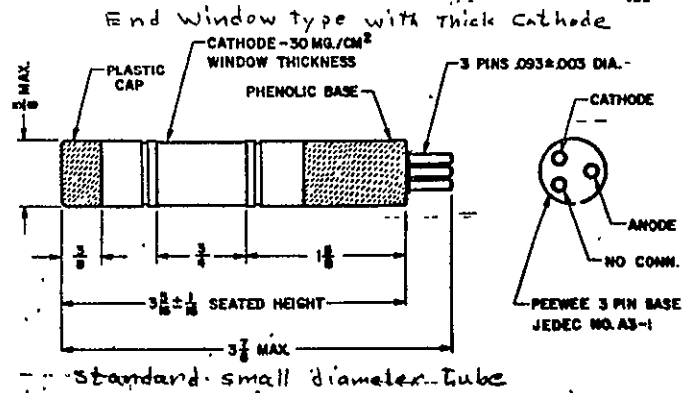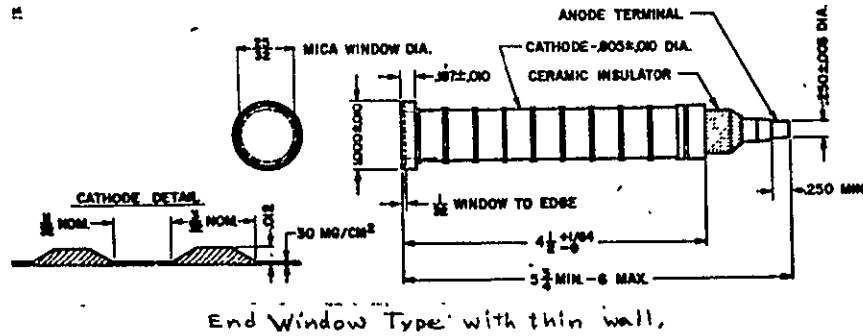
Figure C-13. Several Typical Halogen-Quenched Geiger-Mueller Counter Tubes

nearly as low cut offs (3 Mev). Such thin walled units are stronger in the vacuum environment than the thin mica end window units.

Problem Areas

The GM counter is relatively free of spacecraft integration problems as long as the units are mounted on a boom. If wall mounting is required, end-window types would be indicated as used by Van Allen on Mariner IV. A more serious problem stems from spurious response from bremsstrahlung produced by absorption of an unknown flux of electrons incident on the spacecraft. In the asteroid belt, protons are expected to predominate over electrons and alphas. If the flux of alphas or electrons, however, becomes large, then an ambiguous result is expected from the GM counter which must be resolved using data from other sensors.

Engine operation should have no effect on the behavior of the GM counters, hence it is suggested that they could be operated periodically as a check on behavior during thrusting.

Ion Chambers

Ion chambers have inherent slow responses compared to GM counters, and thus are generally operated in the current mode. The typical flight units are about 7 to 13 cm-diameter spheres with a thick aquadag or metallic coated quartz anode collector rod fixed at the center. A thin quartz fiber conductor mounted at one end is placed near the anode. This quartz fiber acts as a single pole, double throw switch which can charge the control rod and at the same time send a strong pulse to the electronics. The charging rate of the quartz fiber is proportional to the discharge rate in the ion chamber due to the incident radiation.

The ion chamber is an integrating type instrument, and is used along with GM counters and other nuclear sensors. This sensor has been flown on Pioneer 5, Mariners II and IV, and IMP, as well as on many balloon and aircraft high altitude flights.

Principle of Operation

The ion chamber is rugged and reliable as well as consistent in response over long periods of time. The principles of operation have been mentioned in the previous section on GM counters. The basic differences from GM counters are the high gas pressures and low voltages used. Amplifiers and very high input impedances are required unless a Neher type unit is used, from which large pulses are available due to the switch

action of the thin electrometer type quartz fiber rod. The natural frequency of this fiber determines the limiting response rate of the ion chamber of the Neher type.

Typical Characteristics

Drawings of the sensor and block diagrams for the Mariner units are given in Figure C-14 through C-17 from References C-10 and C-12. Typical operation is described in Table C-14.

Problems

The ion chamber is relatively free from spacecraft integration problems. It must be boom-mounted. The pulse rate limits has to be adjusted so that 10^8 counts are expected up to the end of the mission. If more than 10^8 counts are to be expected, then some means for disconnecting the power supply should be provided when the count rate exceeds about 10 counts per second. The unit should be operated periodically during thrusting for calibration purposes.

Proportional Counters

These types of sensors have been flown on Pioneer 5 to measure the directionality of cosmic rays and also on ballistic probes for ultraviolet and X-ray detection. They are somewhat heavier than silicon type semiconductor spectrometers, but have been used to provide greater resolution for X-rays in 0.1 to 1000 keV regions than possible with single semiconductor units.

Low weight proportional counter spectrometers, however, provide poor resolution for charged particles due to the large wall absorption compared to gas absorption, and higher noise levels. Hence, use of proportional counters for charged particles is not expected and soft gamma ray or X-ray measurements are not presently an objective. For fast or slow neutron measurements, the He^3 or BF_3 gas-filled proportional counters are an ideal instrument, and could be used if neutron detection were needed on a SEP mission.

Scintillation and Cerenkov Counters

The scintillation counter consists of a crystal which fluoresces when irradiated by a quantum, and a photomultiplier tube to detect the light produced. Most phototubes operate at 800 to 2000 volts at 1 to 2 ma depending
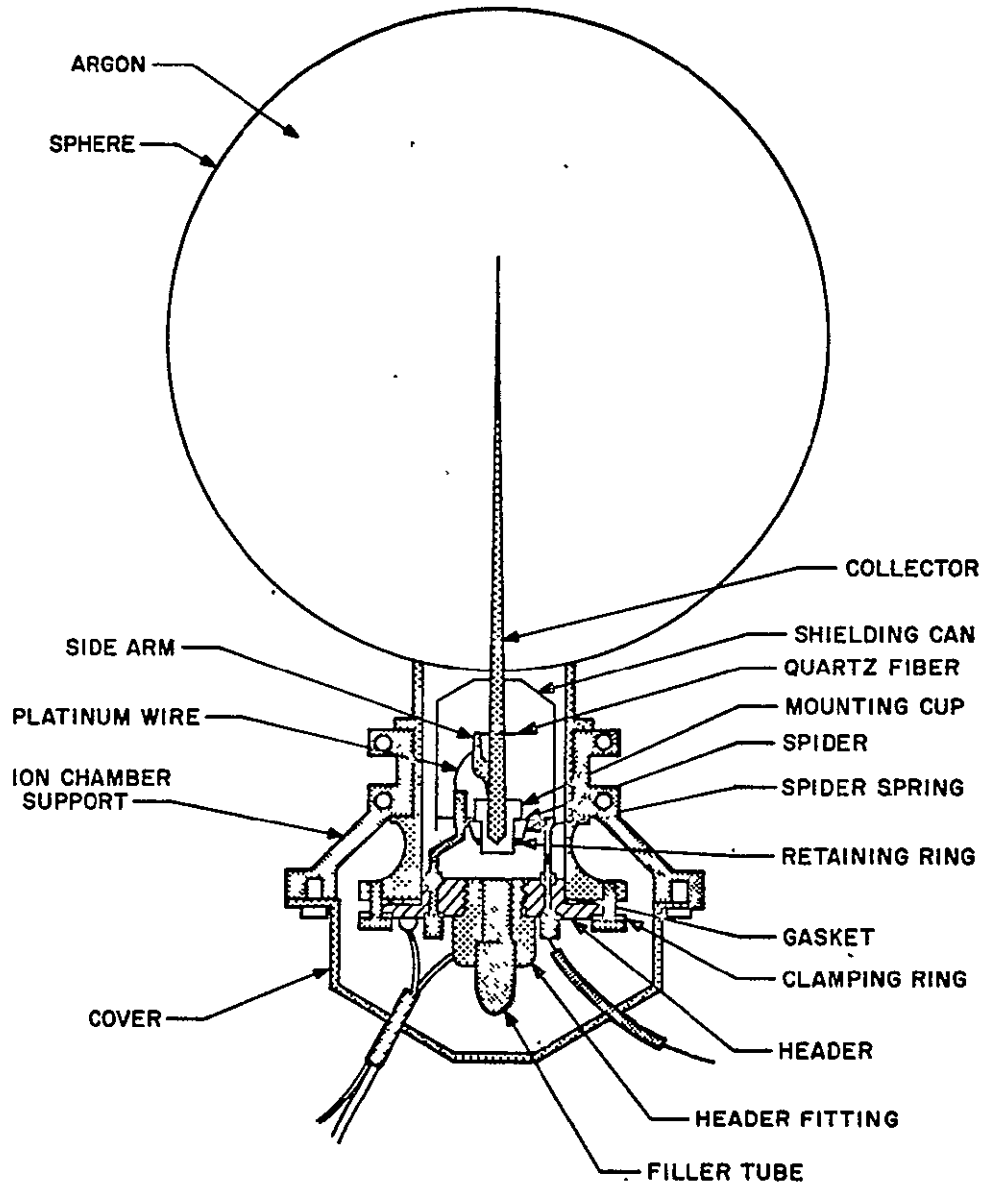
Figure C-14. Cross-Section of Mariner II (and IV) Ion Chamber
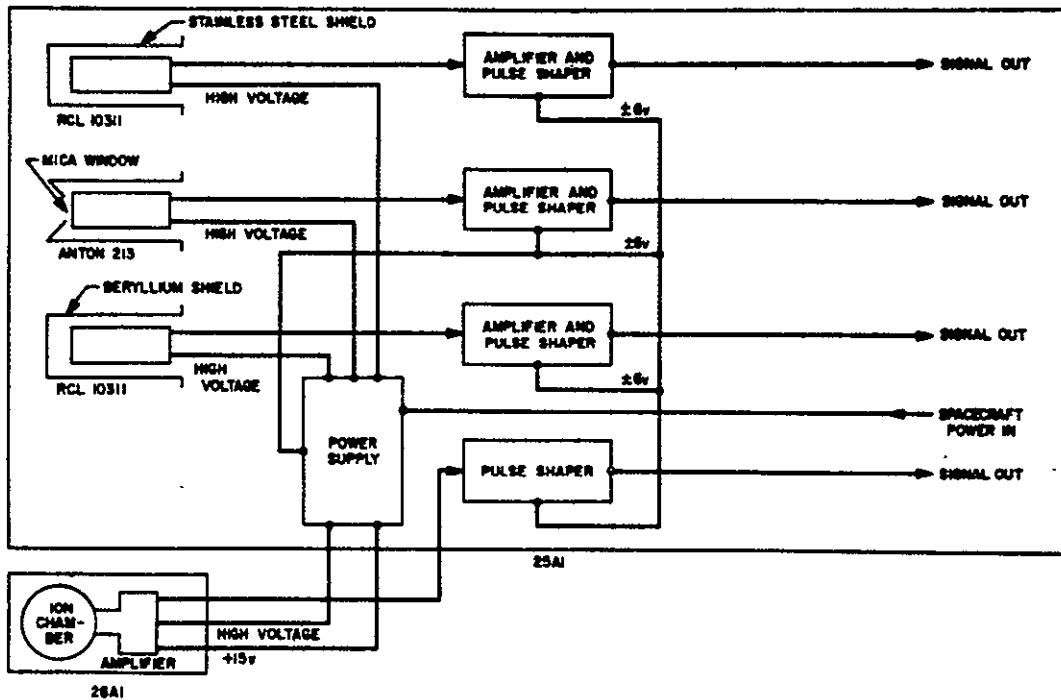
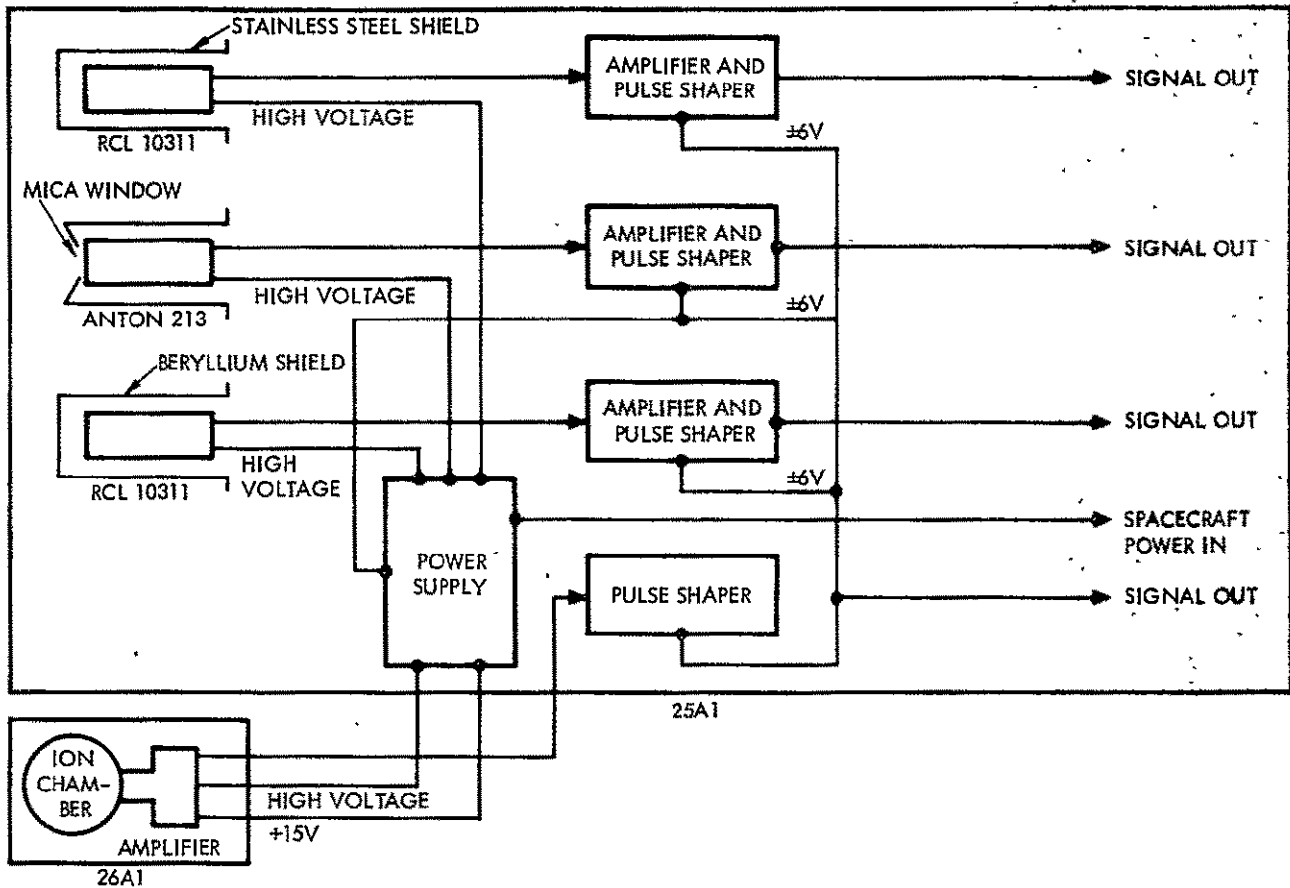Figure C-15. Mariner II Ion Chamber and Geiger-Mueller Counters
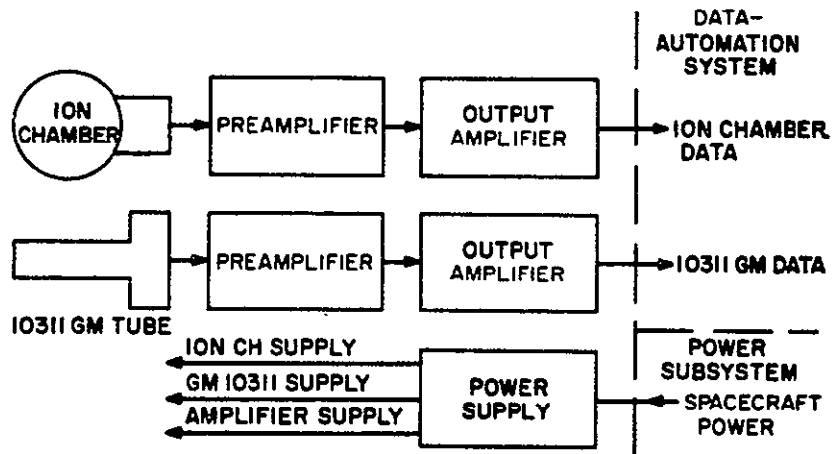
Figure C-16. Mariner II and Mariner IV Ion Chamber
and Geiger-Mueller Counter Block Diagram

13.4

4.8

10°

3.56

1.5 D

2.05 R

5.0D

CHASSIS

GEIGER-MUELLER TUBE

9.8

0.83 D

IONIZATION CHAMBER

NOTE: ALL DIMENSIONS IN INCHES

CONNECTORS

4.0

4.8

5.0

5.0 D

(REF: IONIZATION CHAMBER)

Space Division
North American Rockwell
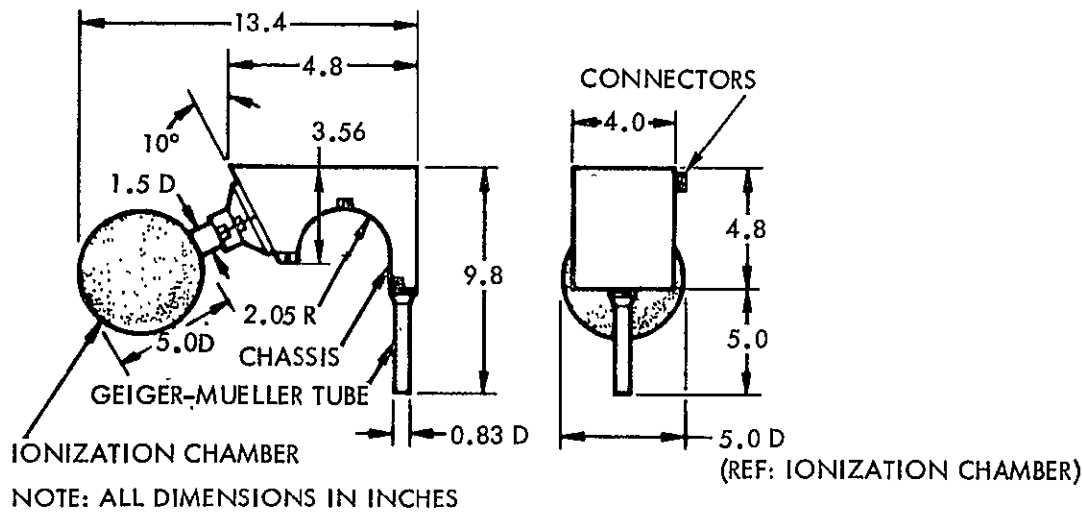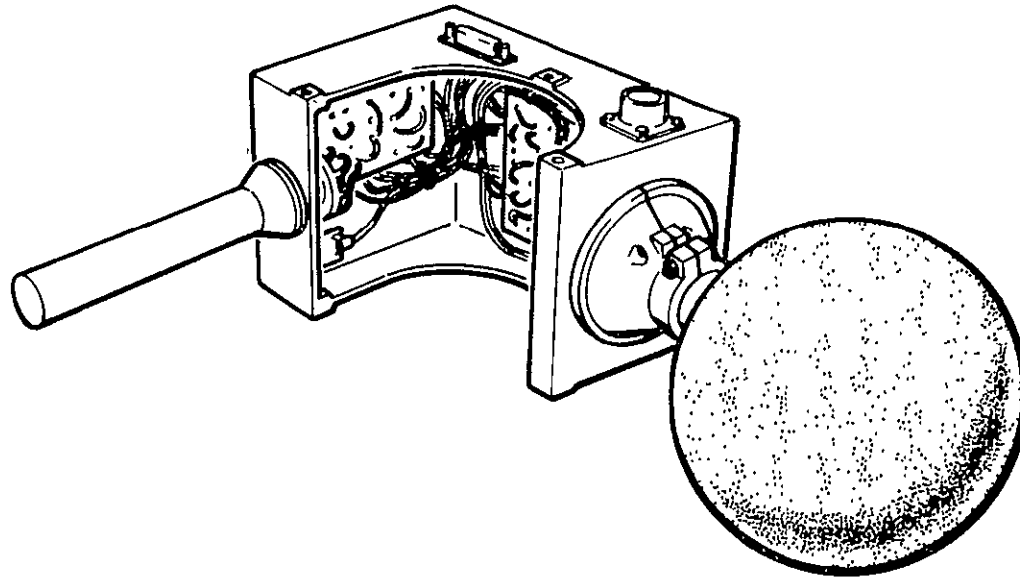
Figure C-17.   Mariner IV Ionization Chamber and Geiger-Mueller Counter

Table C-14. Typical Operation of Mariner-Type Ion Chambers

Characteristic	Specification
Chamber diameter (cathode)	12.7 cm
Wall thickness (stainless steel)	0.025 cm 200 mg/cm^2
Anode-to-cathode impedance	10 megohms
Lifetime of unit in pulses in seconds at 100 pulses/sec	3×10^8 pulses 3×10^6 seconds minimum
Maximum counting rate (limited by natural frequency of charging fiber)	10^2 counts/sec
Applied Voltage	300 to 400 volts
Gas	Argon
Pressure	4-10 atmospheres
Dynamic range	3×10^{-5} to 10^{+2} pulse/sec

Vibration limit	36 sec of 14-g RMS noise
	600 sec of 5-g RMS noise
	   plus 15-2000 Hz
	   sine wave at 2 to 9 g

Temperature limits	-30° to +65°C
Shock	200-g 0.5 to 1.5 ms on each of three axes
Acceleration	±14-g for 5 minutes along each of three axes.

on dynode resistances used, hence an input power of about 1.5 to 8 watts is required. Such counters are used primarily for obtaining high counting efficiencies for gamma, neutrons, and for cosmic rays (Cerenkov counter). The crystals for these applications weigh for 2 kg (3 in.-by-3 in. NaI type) to more than 200 kg. The scintillator cannot complete in resolution, mass, volume, and power with semiconductor spectrometers for protons between 1 and 200 Mev, electrons between 0.01 and 6 MeV, and heavier low energy particles. For cosmic ray energies greater than 100 Mev, the Cerenkov spectrometer may be a good selection for advanced missions.

The Cerenkov detector is basically a scintillation counter with a block of Lucite for a crystal. When a relativistic particle traverses the crystal at a velocity greater than the speed of light in the crystal, a core of light is emitted as the particle slows down in the crystal (Cerenkov radiation). The angle θ of the cone of light is

$$\theta = \cos^{-1}(c/nv)$$

where n is the index of refraction, v the particle velocity, and c the speed of light in a vacuum. The quantity of light ΔE projected into the cone is proportional to the energy of the particle with charge Z according to

$$\Delta E = k \frac{(Z v n)^2}{v^2 n^2 - c^2}$$

whereas from a thin plastic scintillator the pulse of light $\Delta E'$ would be proportional to

$$\Delta E' = k \left(\frac{Z c^2}{v} \right)$$

But for the low flux of very fast particles, large area thin crystals are needed (12 cm diameter).

Semiconductor Spectrometers

For 1 to 200 Mev per nucleon spectral measurements, the semiconductor element is the best available choice for solar and galactic corpuscular radiations. The semiconductor used for charged particle spectroscopy is similar to a circular silicon solar cell, but uses somewhat different doping

material and is biased in the reverse direction by several hundred volts. The output charge is proportional to the energy deposited in the sensitive junction. If the crystal is thin compared to the particle range, then the charge pulse produced is proportional to the characteristic energy loss rate dE/dx which is a function of particle energy and type. If the crystal is thicker than the range of the particle then the charge is proportional to total energy E.

In the simpler form, a thick crystal is used to stop as high an energy as possible. An anticoincidence crystal is placed behind the first crystal to reject counts from particles which penetrate the first crystal. Conversely, if a coincidence occurs the pulse from the first counter may be proportional to the loss rate of the particle. In either the simple total E or dE/dx spectrometers, it is difficult to distinguish different particles types without restricting response to a narrow range. By combining the dE/dx detector followed by a total E sensor, particle mass can be determined also. Generally, a totally depleted transmission type sensor is used for the first element in a dE/dx system. Surface barrier or lithium drifted sensors may be used for total E measurements.

Totally Depleted Silicon Sensors

The totally depleted dE/dx sensor consists of a circular disk of n-type silicon with a thin surface barrier p-n junction on the front and a thin ohmic contact on the rear. A reverse bias is applied across the junction to create a depletion region. The thickness of the depletion region is proportional to the square roots of the bulk resistivity of the junction (which is a function of temperature) and also the bias voltages (Reference C-13). The depletion region set by adjusting the bias voltage is to extend from the front p-n junction to the electrode on the rear for a totally depleted counter.

Electron-hole pairs produces in the depletion region are separated by the bias field producing a voltage pulse proportional to energy lost. An energy of about 3.5 ev per ion pair is required. This energy is smaller than for other sensors such as the scintillator, and essentially all of this charge is detected in the sensor, hence superior resolution is possible compared to a scintillator where only a fraction of the ion pairs produced results in light emission and only a fraction of that light reaches the photomultiplier.

The front p-n junction is only about 3×10^{-5} g cm^{-2} thick and the rear element only about 4×10^{-5} g cm^{-2}, hence low energy protons, alphas, and electrons can be counted. The low energy limit of sensitivity to protons and electrons is set by the preamplifier and crystal noise level and by the absorption by the front p-n junction dead layer. Resolution on the order of

C-48

20 kev is possible for electrons and protons of either high enough energies
to pass completely through the sensitive region or low enough to be totally
absorbed in it.

Totally depleted silicon detectors are available up to several centi-
meters in diameter and with thicknesses from 25 to 1000 microns. The
sensor is mounted in a circular ring so that both the front and rear surfaces
are open and particles can pass through the sensor without interference from
structural support. The totally depleted sensor type is used especially for
measurements of the energy loss rate rather than total energy. As small
a thickness sensor as possible should be used in the dE/dx measurement.
The minimum thickness usable is that in which the highest energy particle
to be detected by dE/dx can deposit an energy about 5 to 10 keV greater than
the preamplifier noise levels (5 to 25 keV equivalent). The energy loss rates
of particles decreases with energy towards about 2 Mev cm^2/gram or
0.36 kev per micron of silicon. Thus, for a relativistic particle depositing
0.36 kev /micron, and a preamp with a 10-keV noise level, about a 50-
micron totally depleted silicon detector would be selected.

Now, with a 50-micron silicon sensor, protons with energy less than
2 Mev, or electrons with energy less than 90 kev, are stopped entirely in
the silicon detector. Therefore, protons with energy between about 20 kev
and 2 Mev are counted producing pulses equal to the total energy of the
particle. Similarly, electrons with energy between 10 and 90 keV are
totally absorbed, giving an output pulse proportional to the total energy.

An anticoincidence-coincidence detector following the totally depleted
counter is required to determine that the particle passed through the detector
or not. For protons totally absorbed (anticoincident pulses in the first
counter or AB) the pulse heights are proportional to total energy ranging
from 10 to 2000 kev. For protons penetrating into the second sensor
(coincidence counts or AB) the pulse outputs are proportional to the energy
loss rates integrated over the thickness of the counter and range from
2000 keV for the 2 Mev proton, down to 10 to 20 kev for a 500 Mev proton.

Similarly for electrons, AB counts represent energies from 20 keV to
90 keV and AB counts represent energies from 90 keV to approximately
1 Mev corresponding to pulse heights from 20 kev to 90 kev. But electrons
cannot be distinguished from low energy protons, and electrons with energy
greater that about 300 kev deposit about the same energy and produce pulse
heights about the size as the preamplifier noise level.

C-49

Thus the basic limitation of the two-element dE/dx-E spectrometer is brought out in the above discussion. Protons with energy less than 90 kev or more than 75 Mev cannot be distinguished from electrons (unless either the electron or proton flux were known to strongly dominate over the other flux). To measure high energy electrons, the preamplifier noise level must be less than 10 kev, such as 2 to 5 kev as is presently possible in field effect transistor (FET) type preamplifier at cryogenic temperatures. But the FET preamp may not be very radiation resistant due to the high input resistance and low capacitance. Problems of confusion of alphas and protons must also be considered. One way to resolve those problems is to add several more detectors in the spectrometer with absorbers in between to optimize particle separation.

When flyable preamplifier and silicon sensors were not as noise free as today's units, thick sensors has to be used which increased the problems of distinction of electrons from protons. For use in the Van Allen zones, the electron flux dominates the proton flux by at least several orders of magnitude, therefore the thicker units have been satisfactory. In the solar radiation environment, the proton flux was throught to dominate. But recently (since 1965) solar electrons have been resolved out of the somewhat higher proton flux. Therefore, for a solar electric asteroid belt or deep space mission where the electron and proton flux are both small and about equal, the thick-entrance sensor units discussed in the next section probably would not be used.

Surface Barrier, Diffused Junction, and Lithium-Drifted Silicon Spectrometers

These types of sensors are available in increasingly greater thicknesses. With greater thickness, the detector output is proportional to total charged particle energy up to relatively high near-relativistic energies. But there is no way to distinguish between a 0.5 Mev electron and a 0.5 Mev proton when using a single thick crystal. For this reason, among others, some early difficulty was found in distinguishing the low energy Van Allen protons from the high energy electron component. In the laboratory, the thicker silicon sensing elements have important applications, but use in a mixed-particle radiation environment can lead to difficulties even when backed up by anticoincidence sensors as discussed in the last section.

The surface barrier or partially depleted surface barrier detector consists of a disk of n-type silicon with an ohmic contact on one side and a thin gold plated (or evaporated) layer over an oxidized surface on the other side. The front of the detector is the gold face. The rear of the detector has the ohmic contact at the center of the rear face. This ohmic contact is frequently noisy in the partially depleted surface barrier detection. The surface barrier detectors are limited to thicknesses up to about 1 mm.

C-50

The diffused junction detector consists of a disk of either a p- or n-type silicon (usually p-type phosphorus diffused material is used). The phosphorus diffusion layer is about 1 micron deep on one face. Aluminum is diffused into the other face to provide an ohmic contact (Reference C-14). The diffused junction detector can be used in a transmission type mount along with one or more totally depleted detectors. The largest available diffused junction detectors has about a 1-mm depletion region.

The lithium drifted silicon sensor can be as thick as 0.5 cm (5000 microns), but there are various difficult problems in manufacturing. Usually boron doped silicon is used. The crystal may be painted with lithium in an oil solution or evaporative methods may be used. The crystal is then baked to cause the lithium to diffuse into the crystal. A reverse bias is applied across the crystal to cause the mobile lithium ions to drift through the crystal. The crystal is heated and the lithium ions bond chemically to the boron to join a stable complex ion of low mobility. Non-uniformities of such detectors are difficult to prevent, but much work has been done recently to develop processes giving good results (Reference C-14).

The thicker based sensors have important new applications for long long-term monitoring of high energy radiations such as cosmic rays and also as may be found near Jupiter. For high energies, the Cerenkov spectrometer using large arrays of plastic crystals and photomultipliers, spark chambers, and bubble chambers are generally preferred where large volume type sensors can be used. Such large volume counters cannot be used on small low data rate spacecraft, of course. Further, large volume counters probably can not be used near Jupiter, because the trapped radiation fluxes may be so great that large area sensors would be saturated. Although the solar electric asteroid belt mission spacecraft is not going near Jupiter it might carry similar types of sensors as Jupiter probes so that the data can be compared.

The small diameter lithium-drifted silicon thick-depletion layer Si(Li) type sensors may be considered for cosmic ray measurements. Thin depletion layer sensors may not be as useful for high energies because the dE/dx of fast charged particles is a slowly varying function of energy per nuclear per unit charge. These high energy particles produce small pulses in thin detectors. But in thick detectors, larger pulses are produced. The problem is how to distinguish the particle types and energies in a simple sensor unit.

An example of a small-volume spectrometer for high energies is as follows. If two 0.5-cm diameter by 0.5-cm thick lithium drifted silicon detectors are mounted together in a 6.5-cm thick sphere of aluminum (for example) protons with energy less than 300 Mev will be shielded out,

C-51

and a large fraction of electrons with energy less than 10 Mev will be stopped. If the two sensors are used in coincidence, the remaining energy loss rates in the two detectors can be compared. For very high energies, the pulse heights will be nearly equal in both counters. For incident proton energies between 300 and 400 Mev, the pulse heights will be different in relation to the energy differences.

If an alpha penetrated the aluminum, and were counted, and the pulses were equal, the pulse height would be related to the particle mass and charge. If the pulse heights were unequal, then the energy per nucleon could be determined, though the particle type could be difficult to distinguish for energies near the aluminum shield cutoff.

Such a small-volume counter might have an important application for measuring large fluxes of high energy particles as expected near Jupiter. For high fluxes the dE/dx-E or dE/dx-range spectrometers as discussed in the next section, would be inoperable. The counters for Jupiter should be carried also if possible on the asteroid belt mission to allow comparison of results for the galactic environment along deep space trajectories versus those going near the strong fields of Jupiter.

Charged Particle Telescope Spectrometers

Two or more nuclear detectors using coincidence circuits to establish a narrow solid angle of sensitivity is referred to as a telescope. By placing absorber materials between the detectors, it becomes possible to measure the energy dependence of the directional component of the ambient radiations. The technique of measuring particle loss rates in a thin detector and total energy in a second thick detector has been discussed in the previous section. Problems of particle type distinction were pointed out to be associated with use of only one or two sensors in coincidence. In this section, spectrometer telescopes using three or more sensors with absorbers in between are discussed briefly showing how particle types are distinguished; several minor problems associated with an ion engine and potential solutions are pointed out.

Theory of Operation

Three or more silicon detectors are mounted in a cylindrical collimator and absorbers of increasing thickness are placed in between the detectors as shown in Figure C-18. The detector thicknesses also increase from the aperture of the collimator to the last which could be a stack of several 5-mm lithium drifted detectors.

C-52

COLLIMATOR
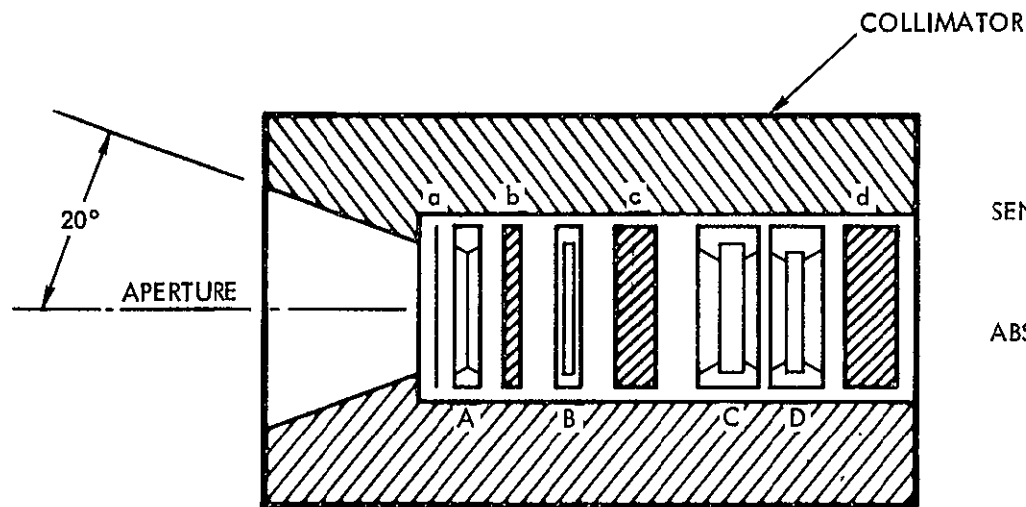
SENSORS
    A = 50 μ TOTALLY DEPLETED SILICON
    B = 500 μ TOTALLY DEPLETED SILICON
    C, D = 5000 μ LITHIUM DRIFTED SILICON
ABSORBERS
    A = 4 MG/CM^2 MYLAR
    B = 200 MG/CM^2 POLYETHYLENE
    C = 1.2 G/CM^2 ALUMINÚM
    D = 40 G/CM^2 TUNGSTEN

20°

APERTURE

Figure C-18.   Representative Charged Particle Spectrometer and Telescope

The pulse height versus energy response for all low energy charged particles in each of the detectors in the telescope is linear up to that energy which can penetrate through the detector. Beyond that energy, the pulse heights are decreasing with energy and are equal to the incident minus the penetrant energy which approaches the energy loss rate dE/dx for very high energies and/or small detector thicknesses.

Figure C-19 presents the range of electrons, protons, and alphas in silicon versus energy plotted from Reference C-15 and C-16. Similarly, Figure C-20 presents the loss rate curves. These data are used to generate response curves for each detector in the telescope as presented in Figure C-21.

Detector A (Figure C-19) takes a higher energy alpha to penetrate than a proton or an electron. The maximum pulse height in detector A from an electron corresponds to the penetration energy (1). For protons, (2) is the maximum pulse height. Pulse heights between (2) and (3) are due only to alphas (neglecting other heavier charged particles for the moment). Below (2), pulses could be due to protons or alphas. Below (1), pulses could be electrons also. A good way to distinguish between the charged particles is to use coincidence analysis on the penetrating particle flux and thus establish the ratios of the fluxes of each particle type. It may be assumed that the ratio established for energies above the penetrating threshold will be a good estimate of the ratios of energies somewhat less than the penetrating energy. This would hold true, pragmatically at least, if one of the particle types were found to dominate strongly, and hence essentially all of the low energy flux could be attributed to that particle.

Above the penetrating energies, the response of detector A is proportional to the difference of the incident and penetrant energies. Two values for this deposited energy are obtained from detectors A and B. If a coincident count occurs in A, B, and C (refered to as ABC), dE/dx type pulses are observed in A and B. If no pulses occurred in c (AB$\bar{C}$), then $\Delta E/\Delta X$ and E-type pulses are observed. With the two indepent functions of energy, particle types can be determined, if not too many different types of particles in the environment have nearly equal fluxes.

Similar procedures are used with pulses in B and C and with C and D to extend the energy spectral measurements and particle discrimination to higher energies. But it is to be noted that the pulse heights for high energy particles in C and D are nearly independent of energy over a wide range. In this region there are relatively large statistical fluctuations in the ionization produced (the Landau effect) which introduces about a 20 to 30-percent limit to the resolution (for protons) in this region for detectors
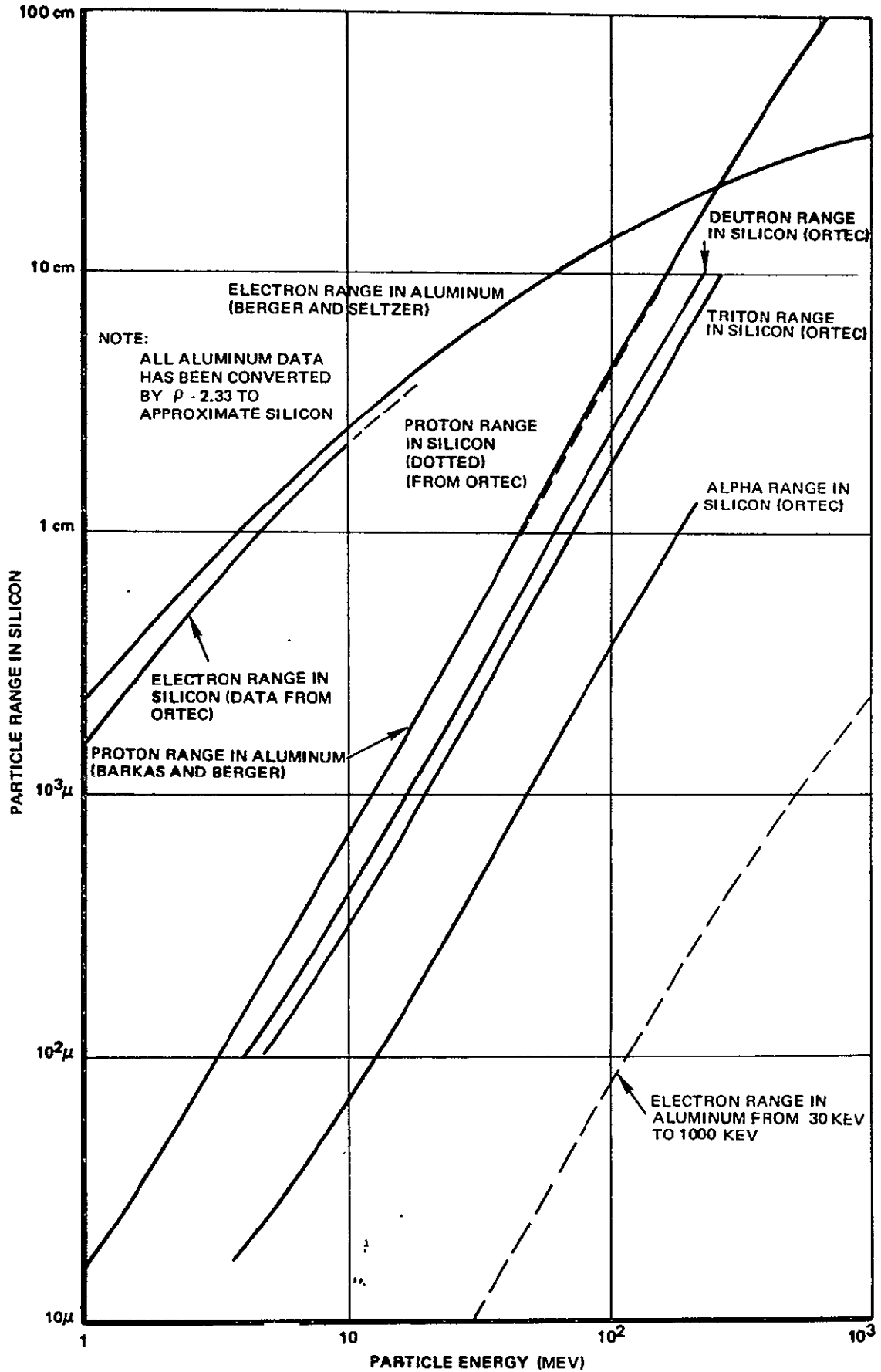
Figure C-19.   Range of Electrons, Protons, and Alphas in Silicon
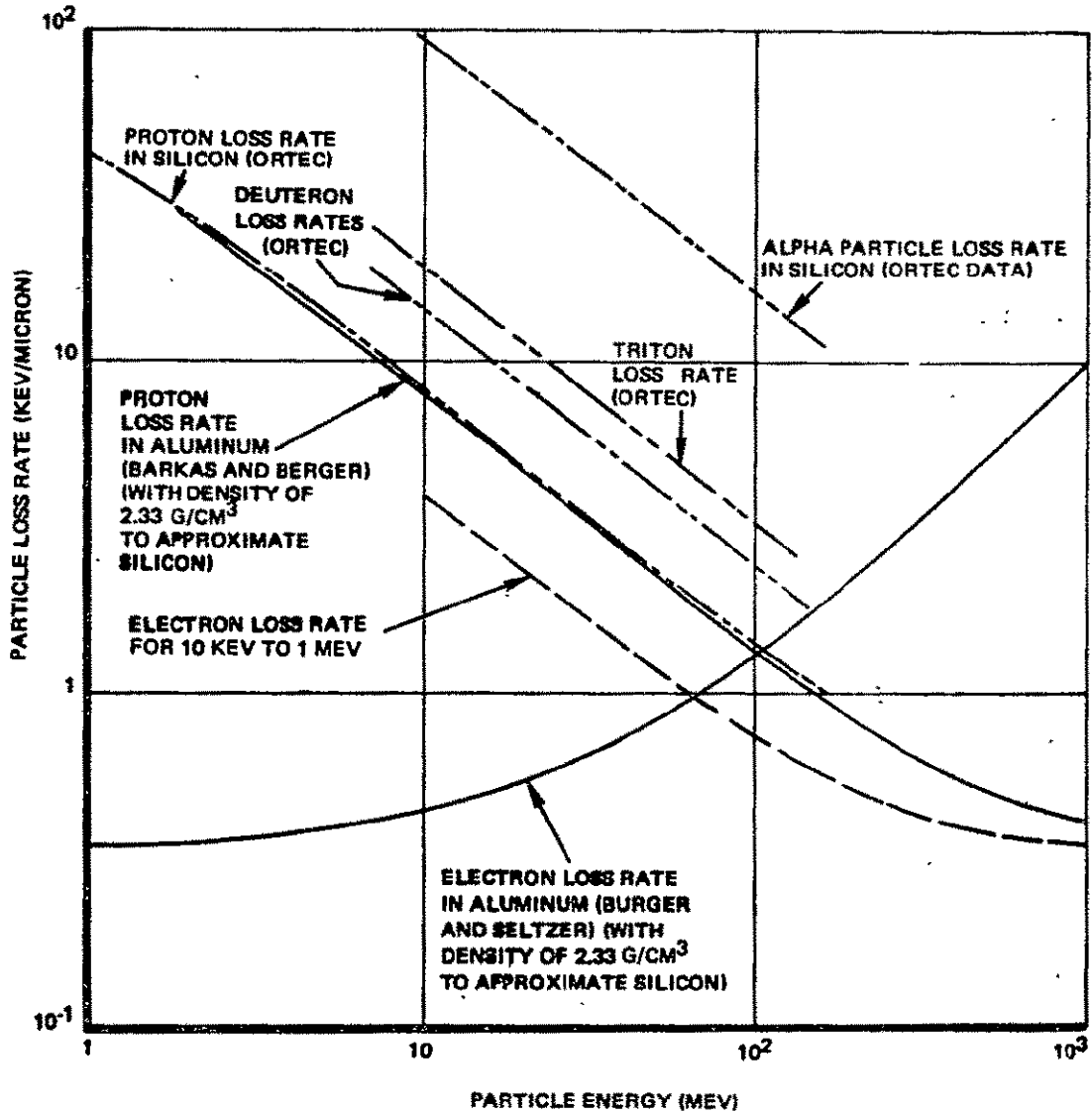
Figure C-20. Charged-Particle Energy Loss Rates in Silicon
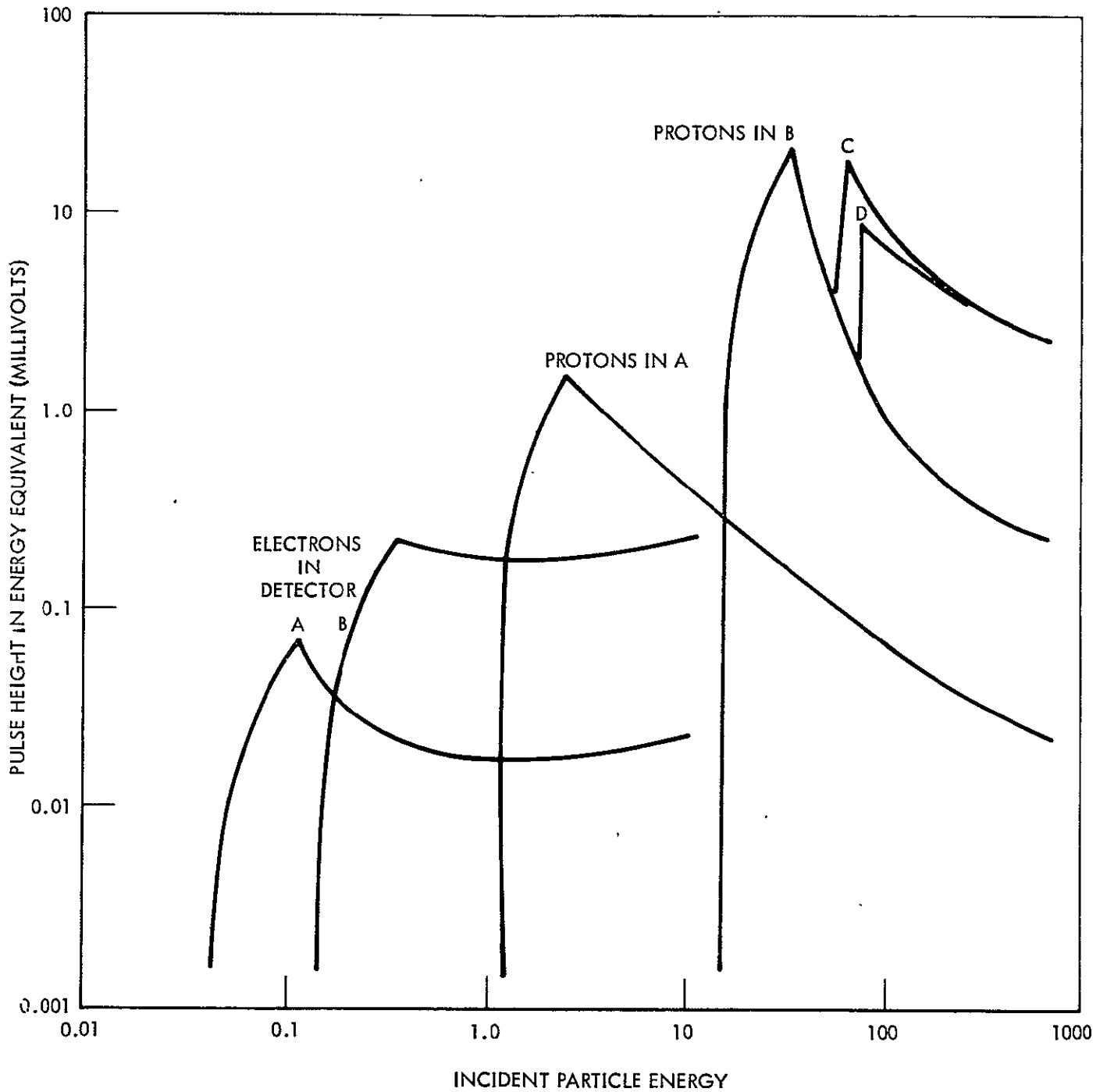
Figure C-21. Output Pulse Height Response Versus Energy Input

only 1-to 5-mm thick. Thus poor energy resolution is obtained for energies well above the energy cut offs for detector C, and similarly for D, except that whether the particle penetrated D or not is not determined (unless still another detector is added).

The rear end of the spectrometer must be shielded by at least as much material as in the forward direction, and in addition an anticoincident detector may be required with a bias set so that if an equal or higher pulse in the last sensor is observed compared to the next to last sensor, then a moderately high particle in the reverse direction is indicated. If an extremely high energy particle enters in the reverse direction, then a DCBA count is obtained which would differ from an ABCD count in that the pulse height from the last sensor traversed is slightly larger per micron of thickness than the first sensor entered.

The side wall thickness must also be thick compared to the range of the highest energy particle to be detected. For protons with energy greater than several hundred Mev, the dimensions of the counter begin to grow exponentially as can be indicated by noting the ranges in Figure C-21 for silicon. At 300 Mev, the proton range is 67 g/cm^2 of aluminum and at 1000 Mev, it is over 400 g/cm^2. Therefore this type of telescope on this mission will probably be limited to 100 to 200 Mev in spectral coverage.

Typical Flight Spectrometer Units

A three-detector telescope of this type was flown by J. A. Simpson and O'Gallegher (References G-17 and G-18) on Mariner 4, and a six-detector telescope was flown on one or two ATS spacecraft (Reference C-19). Figures C-22 and C-23 are a drawing and block diagram of the Mariner IV spectrometer.

This spectrometer used a 128-channel multichannel pulse height analyzer and a count rate meter type outputs for coincidence or anticoincidence pulses: D_3, $D_1D_2D_3$, $D_1D_2\bar{D}_3$, and $D_1\bar{D}_2$. Digital pulse-height outputs were provided for all D_1 pulses for which coincidences occurred as: $D_1D_2\bar{D}_3$, $D_1D_2D_3$, and $D_1D_2D_3\bar{D}_3$ where $\bar{D}_3$ is the condition for a high energy particle entering from the rear as indicated by a higher pulse from D_3 than expected from any likely particle from the front.

The instrument weighed only 2.6 lb and consumed only 0.6 watt. During the lifetime of the sensor no significant degradation of performance was noted.

2-1/2 IN.

2 IN.

6 IN.

0   1   2   3
INCHES
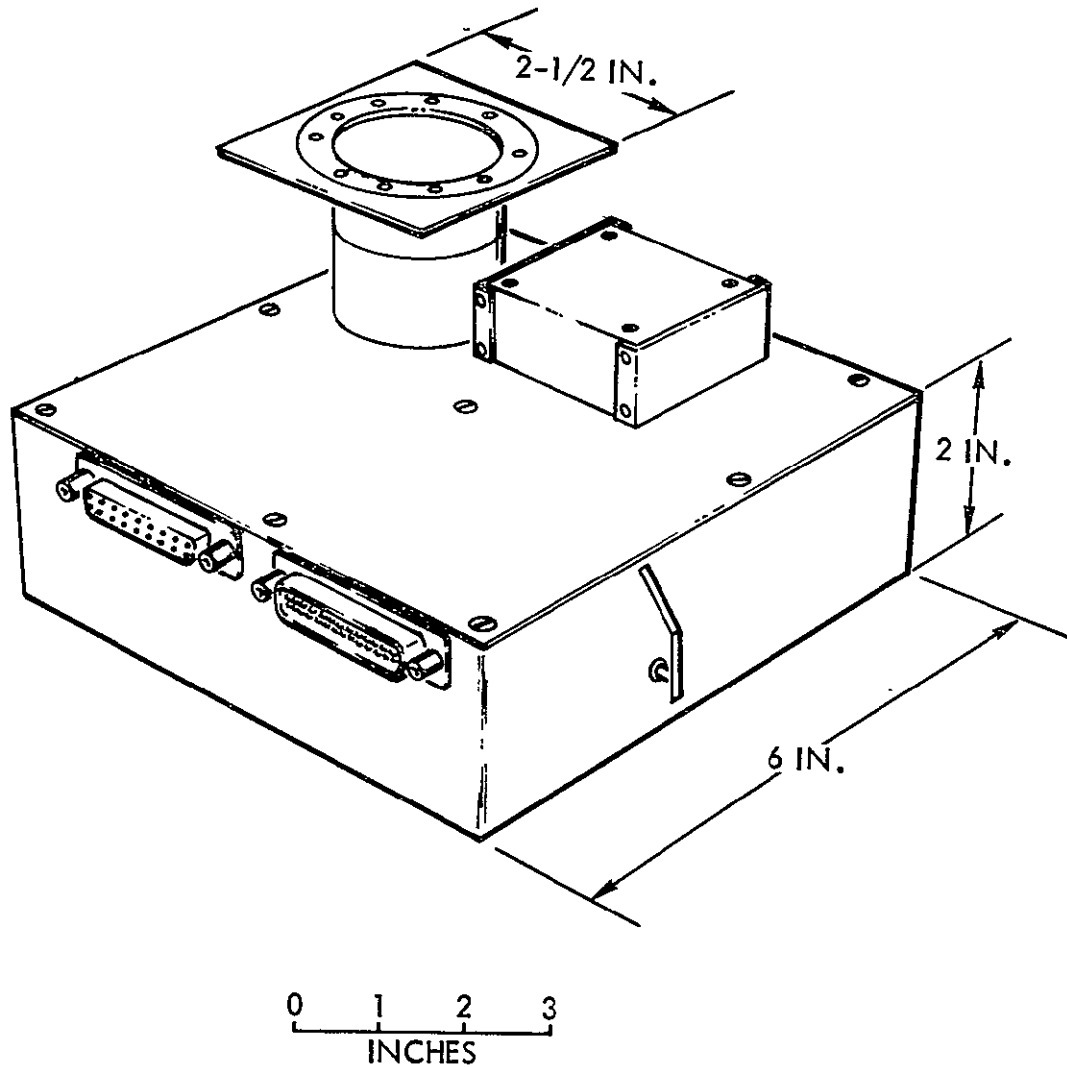
Figure C-22.   Mariner IV University of Chicago Cosmic Ray Telescope and
High-Energy Charged Particle Spectrometer

Figure C-23. Mariner IV Cosmic Ray Spectrometer Block Diagrams

Problems Expected for an Asteroidal Mission

The time integrated extent of the radiation environment is unknown.
Each high energy particle, counted or not, produces some degradation in the
counters. There are several damage mechanisms, but the production of
Frenkel type defects from lattice displacements is the most important. For
a 1000-day mission some degradation may be noticed. Some means of
inflight calibration will be required, possible nothing more than provided in
the Mariner IV instrument. But if such a sensor were used on a mission
going near Jupiter, considerable alteration of the detectors must be
expected and taken into account.

No serious effects from operation of the ion engine are expected, but
the presence of a large mass of mercury (which is classed as high-Z
material) must be considered. High-Z materials in a spacecraft lead to
production of bremsstrahlung and cosmic ray interactions more than
normal.

When bombarded by cosmic rays, a large mass of mercury may
become somewhat radioactive. As the mercury is expelled, some of it
may coat and become amalgamated to the outside and window of the particle
spectrometer. The thickness expected is not known, but only a very slight
background radiation increase would be expected lasting until the radio-
active products had decayed. The decay products expected would be
primarily betas and gammas from radioactive isotopes of thallium or lead,
except for more complicated breakup of the mercury atoms which could
lead to generation of a small number of a large variety of radioisotopes.

If an intense flux of electrons in the 80-keV region were encountered,
the thick silicon sensors would respond to the 79.9-kev photons produced
by electron absorption in the mercury, even if the only mercury present
were that coating the spectrometer head. As mentioned before, this coating
should be thin and should evaporate quickly after engine shutdown.

LIST OF APPENDIX C REFERENCES

C-1. Fuchs, R. A., Experimenters' Design Handbook for the Manned Lunar Surface Program, Hughes Aircraft Co. SSD-60352R (January 1967).

C-2. Snare, R. C., and C. R. Benjamin. "A Magnetic Field Instrument for the OGO-E Spacecraft," IEEE Transaction on Nuclear Science, Vol. NS-13, No. 6, p. 333 (December 1966).

C-3. Bastow, J. G., Proceedings of the Magnetics Workshop in 1965, JPL TM 33-216 (1965).

C-4. Slocum, R. E., and F. N. Reilly. "Low Field Helium Magnetometer for Space Application," IEEE Trans., Vol, NS-10, pp. 165-171 (1963).

C-5. Norris, D. D., J. L. Lawrence, and J. S. Bunn. Magnetometer, Mariner-Mars Science Subsystems, JPL TR-32-813, pp. 45-57 (August 1966).

C-6. Graham, R. A. Plasma Probe, Mariner-Mars Science Subsystem, JPL TR-813, pp. 36-44 (August 1966).

C-7. Josias, C., and J. L. Lawrence. An Instrument for the Measurement of Interplanetary Solar Plasma, NASA CR-56038, JPL TR 32-492 (May 1964).

C-8. Lazarus, A. J., H. S. Bridge, and J. Davis. "Preliminary Results from the Pioneer 6 M. I. T. Plasma Experiment," J. Geo. Res., Vol. 71, p. 3787 (August 1966).

C-9. U. S. House of Representatives, 1969 NASA Authorization Hearings, U. S. Government Printing Office, Washington (1969), Part 3, p. 264.

C-10. Despain, L. G., and H. A. Andersen. Ionization Chamber, Mariner-Mars Science Subsystem. JPL TR-32-813 (August 1966), pp. 29-35.

C-11. Schofield, D. K., and D. Chinburg. Trapped-Radiation Detectors. Mariner-Mars Science Subsystem. JPL TR-814 (August 1966), pp. 26-28.

C-12. Neher, H. V., and H. R. Anderson. "Cosmic-Ray Intensity at Thule, Greenland during 1962 and 1963 and a Comparison with Data from Mariner 2," J. Geo. Res., Vol. 69 (March 1964), p. 807.

C-13. Walters, F. J., W. T. Dabbs, and L. D. Roberts, Large Area Germanium Surface Barrier Counters, Rev. Sci. Inst. 31, 756 (1960).

C-14. Dearnaley, G., and D. C. Northrop, Semiconductor Counters for Nuclear Radiations, John Wiley, Inc., New York (1963).

C-15. Barkas, W. H., and M. J. Berger. Tables of Energy Losses and Ranges of Heavily Charged Particles, NASA SP-3013 (1964).

C-16. Berger, M. J., and S. M. Seltzer. Tables of Energy Losses and Ranges of Electrons and Positrons, NASA SP-3012 (1964).

C-17. Simpson, J. A. and J. J. O'Gallegher. Cosmic Ray Telescope, Mariner-Mars Science Subsystem, JPL TR-813 (August 1966), pp. 19-22.

C-18. O'Gallegher, J. J., and J. A. Simpson. "Search for Trapped Electrons and a Magnetic Moment at Mars by Mariner IV," Science, Vol. 149 (10 September 1965), p. 1233.

C-19. Lanzerotti, L. J. Calibration of a Semiconductor Detector Telescope for Space Experiments, Nucl. Instrum. Methods 61, 99 (1968).

APPENDIX D-1. CONCEPTUAL DESIGN STUDIES OF SOLAR ELECTRIC PROPULSION SPACECRAFT

This Appendix was prepared by the Space Division of the North American Rockwell Corporation under Internal Research and Development Activities associated with Electric Propulsion Technology studies during 1969.

In order to define candidate solar electric spacecraft conceptually, a set of design general guidelines was adopted. This preliminary list consisted of:

1. Compatibility with either Atlas/Centaur or Titan III-C launch vehicles

2. Use of five or four mercury electron bombardment ion thrusters

3. Use of   ieneral Electric Company type roll-up solar arrays

4. Three-axis stabilization (translation of ion engine array and cold gas system)

As a result of the general guidelines several concepts were established. These are shown in Figure D-1 (Drawing 5349-24). All of the configurations are of the 10-kilowatt power level. The first shown is the classical Mariner type of spacecraft; the solar arrays are the standard 2.5-kilowatt arrays mounted on opposing sides of the spacecraft. A 90-degree clearance field of view is provided for the Canopus star tracker. The tracker, however, is on the sun side of one of the arrays which will produce a great amount of stray or glint light into the tracker baffle system. Two of the arrays also extend aft of the ion thrusters and may be subject to mercury deposition.

The second configuration is similar to the first, except for the angle between the arrays. The 90-degree angle between the two aft extending arrays has been increased to 140 degrees and the clearance between the arrays for the Canopus tracker reduced to 40 degrees. This reduction in the tracker field of view clearance is significant; with one array behind the tracker the stray light problem is increased.

D-1

A third concept was to mount two arrays lengthwise and deploy them forward to an angle of 24 degrees from the longitudinal axis of the spacecraft to provide clearance for the Canopus tracker field of view. The additional weight of the structure for the mechanism would probably not be within the launch vehicle capability and would definitely increase the spacecraft complexity. Also, the extended arrays produce a large center of gravity/center of pressure offset.

The next concept shown is similar to the third except that the array does not have to be articulated before rollout deployment. The array used is considered to be a modified GE roll-up array producing 5 kilowatt each. The spacecraft body has been lengthened to accommodate the star tracker field-of-view clearance. This concept experiences the same difficulty as the preceding, plus the additional requirement for a new array configuration. The advantage with this concept is the 18-degree angle required from the longitudinal axis to provide the field-of-view clearance. This smaller angle reduces the center of gravity and center of pressure offset, but not to acceptable levels.

A similar concept is next shown which tips the array 24 degrees. This allows the spacecraft body to be considerably shorter than the previous two configurations but again increases the center of gravity-center of pressure offset. The last concept utilizes the standard GE 2.5-kilowatt array as in the third concept, but cants them forward and overlaps them slightly, partially shadowing the rear array. The shadowed area is very small and occurs on the array where thermal blankets rather than solar cells are mounted.

Since many concepts could be designed to meet the general guidelines, it was necessary to adopt more stringent standards to arrive at an acceptable configuration concept. Additional guidelines and constraints were imposed on the configuration as the result of subsystem area tradeoffs and better definition of the subsystem requirements. The guidelines and constraints were then modified to include the following:

1. Thrust vector shall lie in a plane parallel to the plane of the solar arrays and be aligned with the longitudinal axis of the spacecraft.

2. Roll-up solar arrays will be used fix mounted to the spacecraft.

3. A dual-axis linear translator with individually gimbaled (single-axis) engines will be used

4. A hemisphere of clearance will be provided aft of the ion thruster exit planes

D-2

5. The high gain antenna will be single axis gimbaled

6. A 24-degree half-angle cone clearance for the Canopus tracker will be provided

7. Dual low gain antennas will be provided: one each in opposing hemispheres

8. Spacecraft orientation with respect to the sun-spacecraft line will be optimized

9. Large areas of meteoroid impact/penetration detectors will be provided mounted to the solar arrays as well as on independently provided mounting structures

10. Maximum use of existing hardware

With the introduction of the additional guidelines and constraints, several additional concepts were configured.

The first such configuration is a 6 Kw T-III-C launched configuration as shown on Figure D-2 (Drawing 5349-22). The spacecraft consists of a rectangular body to which are attached two roll-up solar arrays. The solar arrays are modified versions of the General Electric 2.5 kilowatt design. The array has been lengthened 20 percent while other components have remained as in the present GE configuration. The arrays are mounted in an A-frame type of attachment truss which then allows a clear field of view for the Canopus tracker of ±24 degrees half-cone angle. Two Mariner-type low gain antennas are mounted to the aft portion of the solar array support truss. These antennas are stowed during boost by rotating them to a position parallel to the solar array storage drums. A Viking type high gain antenna is mounted in front of the deployed solar array, but does not shadow the cells. This antenna is folded into the forward solar array support truss during launch. The high gain antenna is single axis pivoted 180 degrees in the ecliptic plane. A three-ion engine cluster is utilized with two engines initially operating and one on standby. The engines are single-axis linearly-translated in the ecliptic plane. An independent meteoroid penetration detector array is deployed after ion engine thrusting. This array consists of Explorer satellite type pressure cells and comprises 215 square feet of area on a single side. The array is capable of rotating through 180 degrees to offer the maximum area perpendicular to the meteoroid impact direction for penetration at all times during the mission. The configuration is shown stowed within the 240-inch-long version of a standard T-III-C boost fairing.

A 6 kilowatt Atlas/Centaur configuration is shown in Figure D-3 (Drawing 5349-21). This is an early concept, and was later revised as shown on Figure D-4 (Drawing 5349-23). The configuration shown is identical to that shown in Figure D-2 for the Titan III-C launch vehicle, with the exception of the size of the independent meteoroid penetration detector array. The Atlas/Centaur configuration utilizes a smaller area array (75 square feet). All other aspects of the configuration are identical to the T-III-C launch concept.

A 10 kilowatt spacecraft was also configured as shown in Figure D-5 (Drawing 5349-26). The configuration is identical to that shown on Figure D-4 with the exception of the number of thrusters, the power level and the area of the independent meteoroid penetration detector array. The detector array is increased to 133 square feet, and four engines are utilized.

An additional 10 kilowatt Atlas/Centaur spacecraft is shown in Figure D-6 (Drawing 3020-1). It utilizes four standard 2.5 kilowatt arrays and cants one pair of arrays 24 degrees away from the sun to provide star tracker clearance. Four ion engines are used with two power conditioning panels. The spacecraft is 1 meter (40 inches) square and 5.6 meters (220 inches) long. A 107-square foot independent meteoroid penetration detector is attached to the body structure and is oriented throughout the mission to optimize particle encounters. This configuration requires the development of a new solar array for the canted array and does not use four identical arrays. A center-of-gravity offset also exists because of the canted array.

Another 10-kilowatt design which eliminates the center of gravity offset is shown in Figure D-7 (Drawing 3020-2). This symmetrical configuration utilizes identical arrays but they are not the standard array. It also uses three ion thrusters instead of four. This configuration appeared to offer an additional penalty in the dual canted arrays. Additional guidelines and constraints were imposed at this time which led to the selection of the baseline configuration. The additional constraints were the selection of a 10-kilowatt total power level, three ion thrusters, and better definition of the payload scientific experiments and their viewing requirements.

Configuring a concept to meet the new constraints evolved the concept shown in Figure D-8 (Drawing 3020-3A). The spacecraft is similar to that shown in Figures D-6 and D-7. The new concept cants the bottom pair of arrays toward the sun to provide the star tracker field of view clearance. The payload has influenced the design by incorporation of the Sisyphus meteoroid detector mounted on the forward end of the structure as well as the dark side mounting of the other payload instruments.

D-6

The last configuration, shown in Figure D-9 (Drawing 3020-7) is similar to the previous configuration. A need was recognized to simplify the configuration shown in Figure D-8 by using the standard 2.5 kilowatt solar arrays. Consequently, the use of two stars in opposing hemispheres was investigated. As a result of this study the configuration shown was adopted as a recommended configuration. This concept cants four standard arrays toward the sun and provides sufficient field-of-view clearance for two star trackers. The penalty for this was less than that for the single pair of canted arrays and this concept allowed use of presently developed hardware.

In selecting the recommended configuration four candidates were traded off against a symmetrical configuration (Figure D-10) which did not meet all of the constraints but offered a "no penalty" concept to compare the candidates.

The candidate configurations are all some modification of the symmetrical concept and are weight-penalized because of increased number of star trackers, canted (longer) solar arrays, out-of-ecliptic thrusting and attitude control gas to compensate for differences in center of gravity and center of pressure. The first candidate concept was one with the solar arrays canted toward the forward end of the spacecraft as shown in Figure D-11, which is similar to that in Figure D-5. The canting provided the necessary clearance for the star tracker field of view and the engine clearance requirement. This configuration, however, required 40 kilograms (87 pounds) of attitude control equipment to compensate for the difference between the spacecraft center of gravity and the center of pressure. The high delta weight penalty associated with this configuration concept as well as possible problems involved with the stowage of the arrays within the launch vehicle existing fairing payload envelopes for a 10-kilowatt concept did not make this concept appealing. The next configuration concept (Figure D-12) utilized the ideal symmetrical configuration and thrusted out of the ecliptic plane to provide sufficient star tracker field of view clearance. This concept was considered because the final orbit inclination (3.5 degrees) did not appear unreasonable. The additional amount of mercury required to perform this mission (delta weight) was significantly high, 41 kilograms (90 pounds), which discouraged any further assessment of the feasibility of the concept. The third configuration concept (Figure D-13) canted the lower solar array 29 degrees toward the sun to provide star tracker field of view clearance. This configuration had a delta weight of 4.7 kilograms (10.3 pounds) due to the increased length of the canted array. This penalty did not appear too severe but the increased array length would require the development of a modified array and the spacecraft would then not employ identical arrays.

△ WEIGHT INCREASE = 0.0

DOES NOT MEET GUIDELINES
AND CONSTRAINTS BUT USE
AS ZERO PENALTY CONCEPT
FOR CANDIDATE CONFIGURATION
COMPARISONS
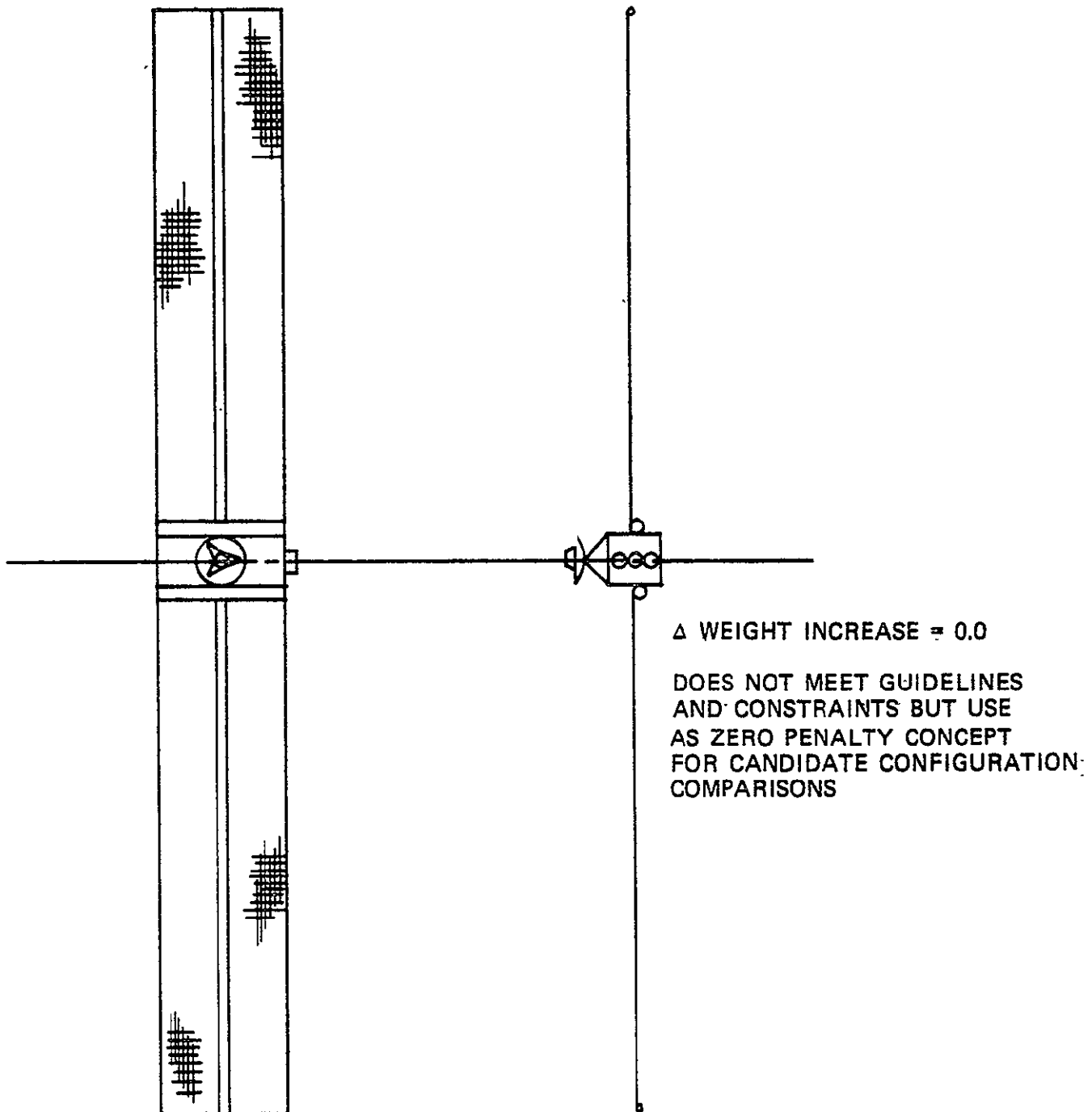
Figure D-10. Ideal Configuration for 5-Kilowatt Spacecraft

△ WEIGHT PENALTY ≈ 40 KILOGRAMS
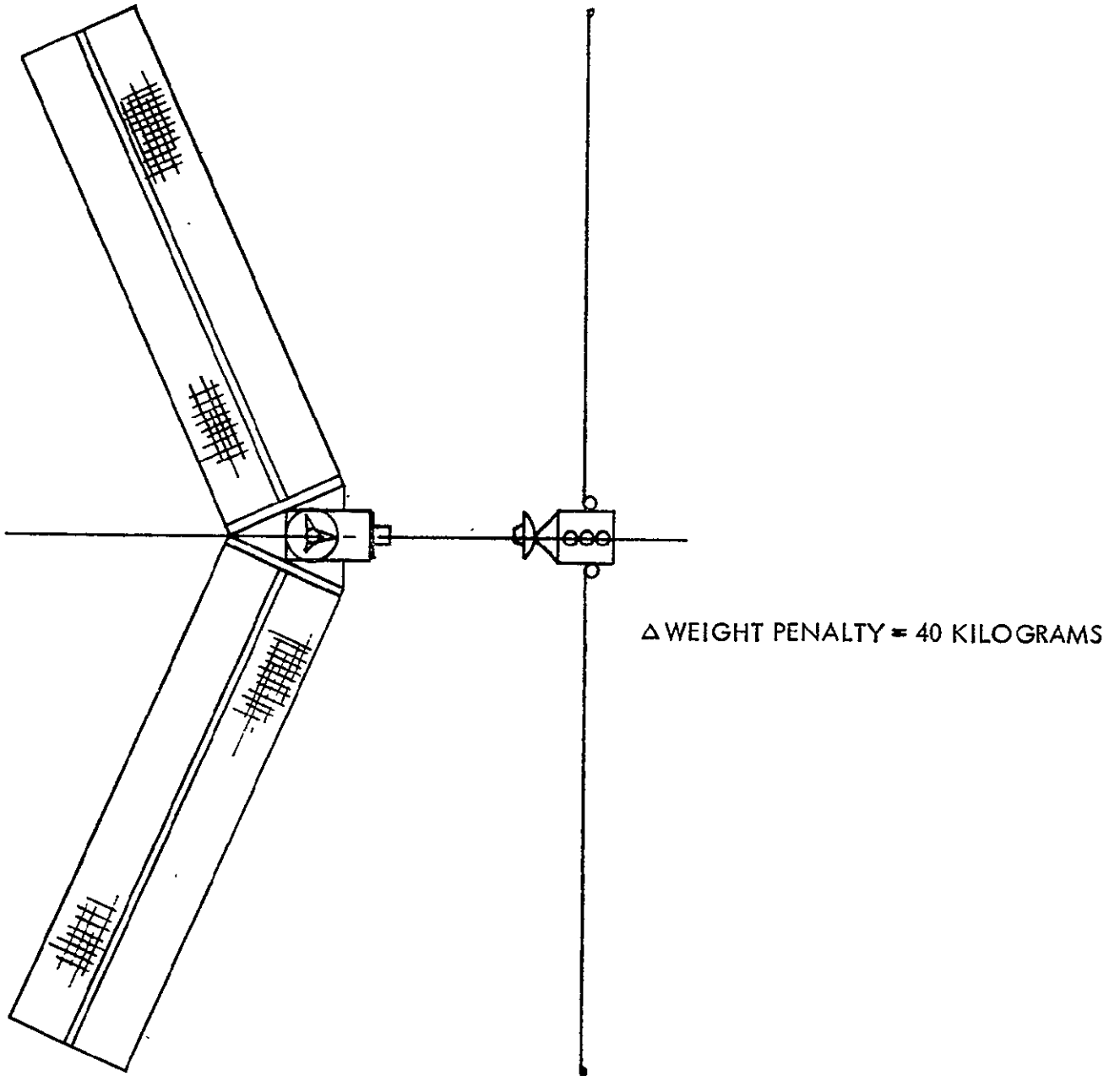
Figure D-11. Forward Canted Solar Array 5-Kilowatt Spacecraft

FINAL ORBIT INCLINATION ≈ 3.5°

Δ WEIGHT PENALTY ≈ 41 KILOGRAMS
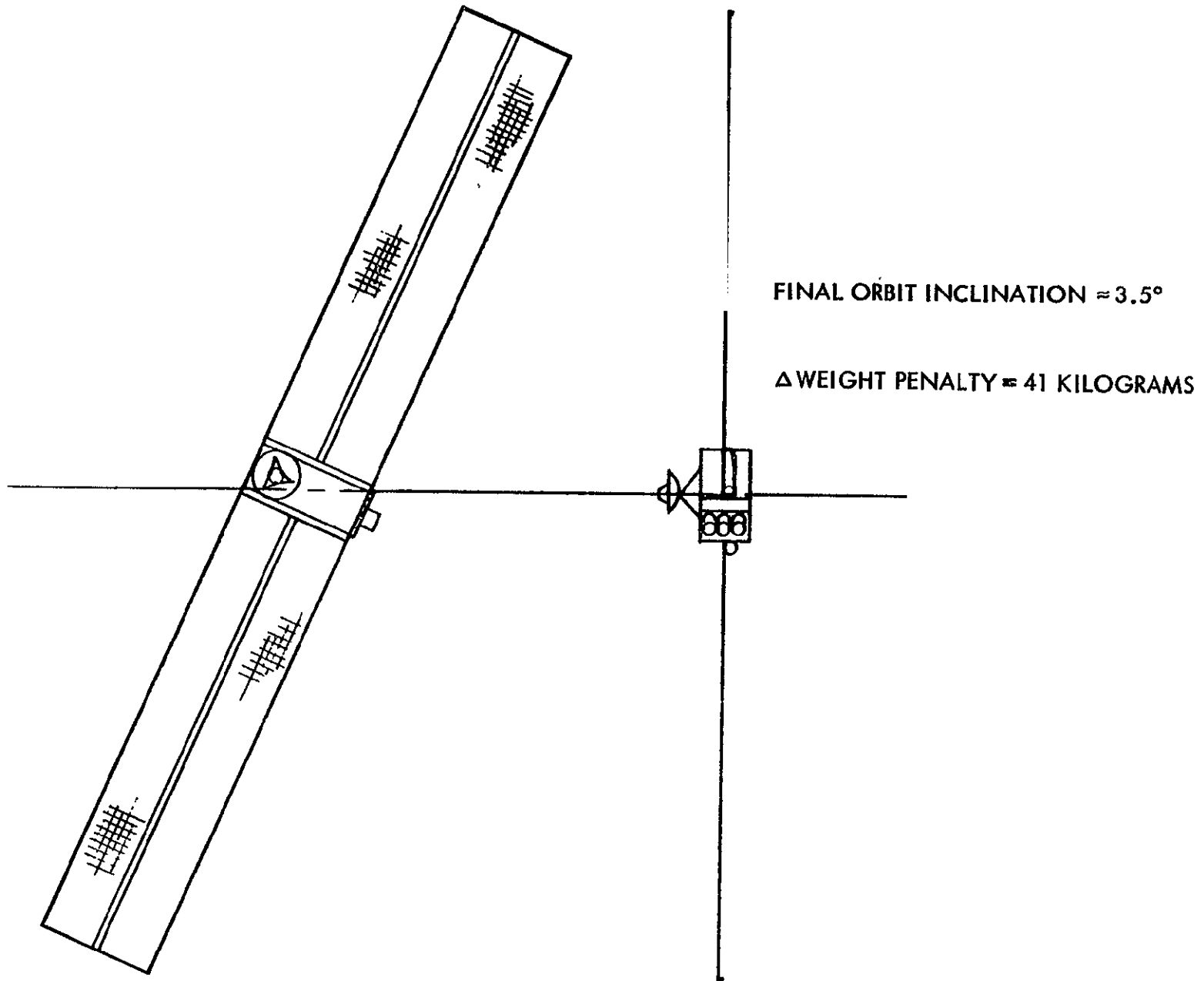
Figure D-12.   Thrusting Out-of-Ecliptic 5-Kilowatt Spacecraft

Space Division
North American Rockwell

△WEIGHT PENALTY = 4.7 KILOGRAMS
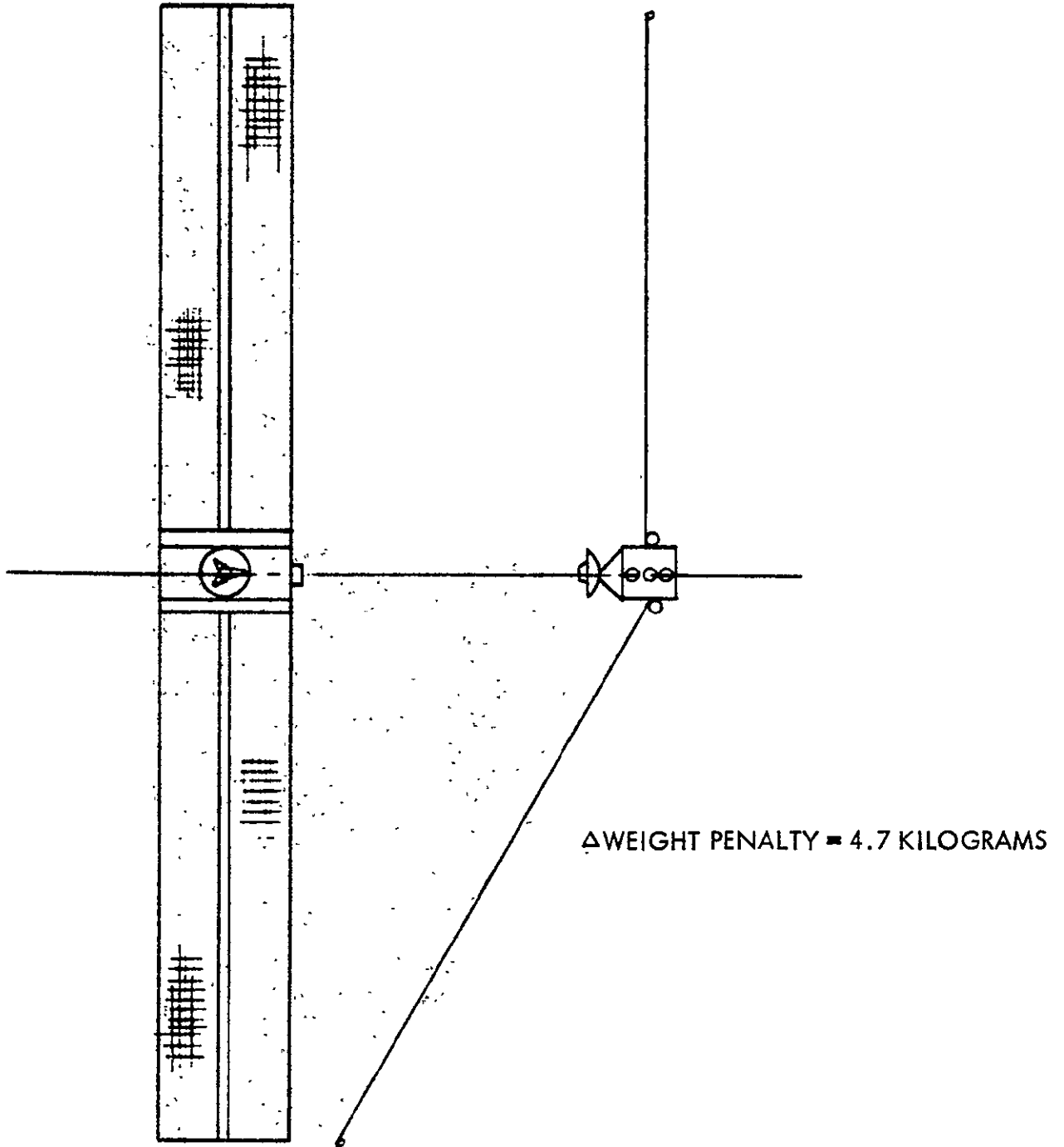
Figure D-13. Unsymmetrical Solar Array 5-Kilowatt Spacecraft

The last configuration concept candidate considered the use of two stars and trackers in opposing hemispheres. This concept (Figure D-14) utilized Canopus and Vega trackers with the solar arrays being canted 15 degrees toward the sun to provide the required star tracker field of view clearances. The concept had a delta weight penalty of only 3 kilograms (7.2 pounds). The solar arrays are identical and are of the same size and power as the originally designed General Electric arrays. The net mass or weight penalty is least with this final concept. For these reasons this candidate was selected as the recommended configuration.
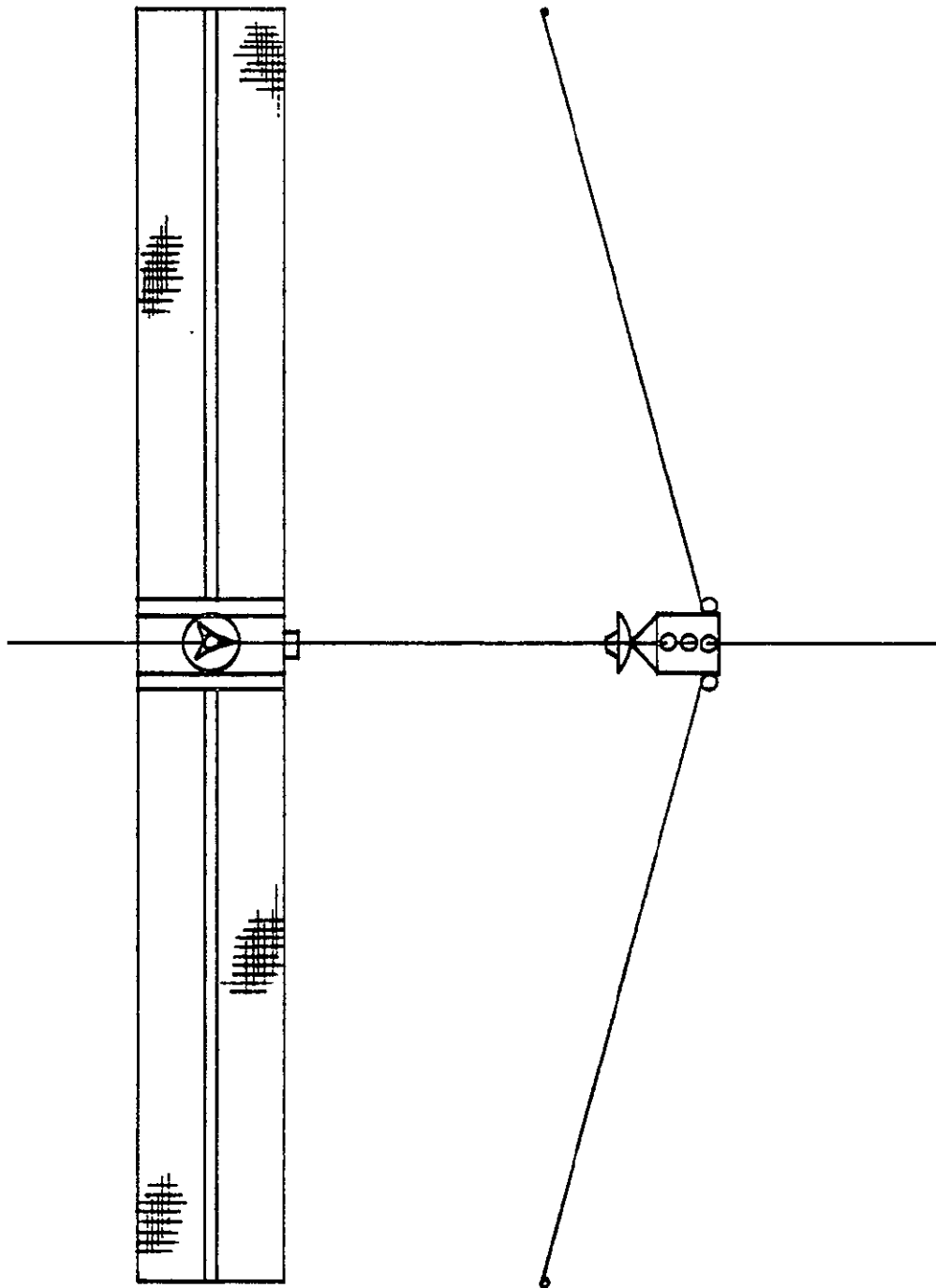
ΔWEIGHT PENALTY = 3 KILOGRAMS

Figure D-14. Recommended Configuration Concept for
5-Kilowatt Spacecraft

D-29

APPENDIX D-2. SOLAR ELECTRIC SPACECRAFT ENGINE ARRAY TRANSLATION STUDY

This Appendix was prepared by the Space Division of the North American Rockwell Corporation under Internal Research and Development activities associated with Electric Propulsion Technology Studies during 1969 prior to award of this JPL study contract.

A solar electric propulsion spacecraft maintains continuous thrusting over extended periods of time. During these long thrust periods it is essential that the electric engine thrust vector be aligned with the vehicle center of mass. To maintain continuous attitude correction by the use of an auxiliary propulsion system would require a prohibitive amount of fuel. Therefore, a means must be implemented to maintain thrust vector alignment without increasing fuel requirements. A five ion-engine cluster was considered for this investigation. Consideration was given to gimbaling the entire five-engine cluster as well as individual gimbaling of each engine. However, this concept experiences difficulty in recovering from an engine failure condition. In most cases, an engine failure requires the shutdown and startup of additional engines resulting in a 25 percent decrease in total thrust at the start of the mission. If additional engines are not shut down, to balance the thruster platform when an engine failure occurs, then the spacecraft must be flown in a new orientation. These large changes in the orientation require changes to the onboard attitude reference equipment which increase the complexity of the entire control system. For the above reasons, gimbaling of the entire engine cluster as well as individual engines was not considered as a simple solution to the thrust vector positioning mechanization during this investigation. The four outboard thrusters in the engine array can be single-axis gimbaled in a plane tangent to their mounting ring, and in opposing pairs, to eliminate any swirl torque which might be generated by individual thruster misalignment, thus also providing spacecraft roll attitude control capability. Engine single-axis gimbal mechanisms have been developed for some time and have been proven reliable in both ground test programs and in space applications. It is considered that a gimbal mechanism of the type required for the electric engines can easily be provided with the individual engine mounts. Translation of the five thruster array in two mutually perpendicular directions to align the resultant thrust vector with the spacecraft center of mass will provide spacecraft pitch and yaw attitude control. Therefore, by gimbaling the outboard engines and translating the entire engine array, three-axis attitude control can be

accomplished during powered flight without additional fuel requirements. Since engine gimbal mechanisms are well within the present state-of-the-art, the design problem is to provide a simple mechanism for translating the engine array in two orthogonal directions. Five conceptual designs of simple mechanisms to provide this dual axis translation were conceived during this investigation and are described below.

The first mechanism is a dual-axis linear translator (Figure D-15, Drawing 5349-5). The mercury electron bombardment ion engine cluster mount is translated ± 12 inches along the Z axis in a carriage. The carriage then is translated ± 12 inches along the Y axis on guide rails, which are rigidly attached to the spacecraft structure. The engine mount is attached to the five ion-engine array. The carriage is considered as a floating or suspended member. Four drive mechanisms are incorporated in the system; two drive the engine mount in the carriage and the other two drive the carriage in the guide rails. The drive mechanisms are identical and interchangeable. Each consists of a 90-degree permanent magnet stepper motor in conjunction with a gear reduction unit. The output shaft of the gear reduction unit is rigidly attached to a roller within either the carriage or the guide rail. The roller is an integral part of the drive process. This drive mechanism is basically a low-friction suspension system which in its simplest form consists of two rollers which are cylindrical and whose surfaces are fairly smooth. A flat metal band is wound in an S-shaped loop around the rollers. An added guideway serves to position the rollers to each other, provides an anchor for the band, and provides surfaces for rolling. When tension is applied to the band and its ends are fastened to the guideway, the rollers assume the configuration shown in section E-E of Figure D-15. In this configuration, the roller cluster can easily move back and forth in the guideway. As the roller attached to the gear reduction unit output shaft is rotated, it will either reel the band in or out while its counterpart roller, rotating in the opposite direction, is either reeling out or reeling in band. This rotation of one roller then produces linear motion of the roller cluster attached to either the engine mount or the carriage. As the roller cluster moves between the parallel guide surfaces of the carriage or the rails, the rollers maintain a constant angle of repose. Closer inspection of the motion involved in this mechanism reveals that all mating surfaces are moving in unison and there is no sliding of surfaces, hence no sliding friction. The only friction is rolling friction which tests have shown to be an order of magnitude better than the coefficient of friction for the best ball or roller bearings. Even this small amount of rolling friction improves because all parts remate precisely in use, including any surface imperfections which may wear down. Because there is no sliding friction, the surfaces of the rollers do not require lubrication; because of surface remating, the rollers improve with use while operating unlubricated. This roller-band concept is an application of the Rolamite concept developed by the Sandia Corporation.

The drive mechanism is designed so that the engine mount and/or carriage is translated 0.005-inch per motor step. The stepper motor is capable of 100 steps per second, which results in a capability of translating the engine mount and/or carriage at a rate of 1/2-inch per second. This rate is selected as a basepoint only and can easily be changed by altering the gear reduction unit without disturbing the motor or rollers.

To ensure straight line translation of the engine mount and/or carriage, each is guided by self-aligning V-groove guide rollers as shown in section A-A and D-D of Figure D-15. The guide roller sets are mounted at four points on the engine mount and carriage. The drive band (shown in section B-B and C-C) is split to allow the guide rollers to seat in the V-grooves in the carriage and rails. Since rollers are used to guide the translation of the engine mount and carriage, there is no sliding friction to overcome. Close tolerancing of the V-grooves and the guide rollers as well as stringent assembly, alignment, and checkout procedures will ensure the straight line translation of 0.005 inch per motor step.

. The overall dimensions of the mechanism are 49.4 inches by 68.8 inches by 4.7 inches. It is estimated that the entire mechanism, exclusive of the engine mounts, weighs 15 pounds. This estimate is based on utilizing aluminum for the structural members and catalog weights for stepper motors and gear reduction units.

An additional dual axis linear mechanism concept, shown in Figure D-16 (Drawing 5349-9), is similar to that shown in Figure D-15. The difference is in the actuators. Where a tension band was used on the previous design, this mechanism uses screw actuators to translate the ion engine mount and carriage linearly in two orthogonal directions. The engine mount is translated ±12 inches along the "Z" axis within the guide rail carriage. The carriage is translated ±12 inches along the "Y" axis on guide rails. The guide rails are rigidly attached to the spacecraft structure. The five mercury electron bombardment ion engines are attached to the engine mount and the carriage is again a free or floating member. Two screw actuators are incorporated into the system. The first drives the carriage relative to the spacecraft, and the second drives the engine mount within or relative to the carriage and 90 degrees to the carriage motion. The engine mount is then capable of being translated to align the resultant thrust vector with the center of gravity of the spacecraft, allowing for large center of gravity shifts. The five ion engines on the engine mount are allowed to gimbal as in the dual-axis linear translator mechanism described above.

The drive mechanisms consist of 90-degree permanent magnet stepper motors in conjunction with gear reduction units. The output shaft of the gear reduction unit in both mechanisms is attached to the screw actuator. As the screw actuators are rotated, they translate a follower block attached

to the engine mount or the carriage. The follower blocks utilize spring-loaded ball bearings to follow the threads and assure that there is no backlash between the follower and the screw. Both mechanisms are essentially identical and could therefore be interchangeable. The screw actuator portion of the mechanisms can be hermetically sealed within bellows. This action would provide proper lubrication of the actuator and insure its performance. The linear translator mechanisms translate the engine mount or carriage 0.005 inch per motor step. This coupled with the 100 step per second capability of the stepper motor produces a translation rate of 1/2-inch per second. This rate is selected as a basepoint only and can easily be changed with minor modifications to the gear reduction unit.

To ensure straight line translation of the engine mount and/or carriage, each is guided by self-aligning V-groove guide rollers as shown in sections A-A and B-B. The roller sets are mounted at four points on the engine mount and carriage. Since rollers are used to guide the translation of the engine mount and carriage there is no sliding friction in the mechanism. Close tolerances of the V-groove and the guide rollers as well as stringent assembly and checkout procedures will ensure the proper functioning of the guide rollers as well as the straight line translation of the engine mount and/or carriage.

The overall mechanism dimensions are 48.0 inches by 58.7 inches by 2.2 inches. The mechanism is estimated to weigh 17.0 pounds based on using aluminum for the structural members, catalog weights for stepper motors and gear reduction units, and hollow tube aluminum screw members.

The mechanism shown in Figure D-17, (Drawing 5349-7), utilizes rotary-on-linear actuators to produce a net translation of the resultant thrust vector. The concept as shown utilizes two guide rails rigidly attached to the spacecraft structure. A carriage is translated linearly ±17 inches along the Z axis within the guide rails. A fitting on the carriage provides the attach point for the engine mount. This fitting is capable of being rotated ±180 degrees. The center of rotation of the engine mount is offset from the geometrical center of the carriage. The combination of rotation and linear translation then enables the resultant thrust vector to be aligned with the spacecraft center of gravity. This concept assumes that the center of gravity could be located anywhere within a 1.5-inch diameter circle about the spacecraft longitudinal axis. The five ion engines on the engine mount are allowed to gimbal as in the dual axis linear mechanism described on Figure D-15.

Figure D-17 shows two carriage concepts. The first is as stated above: rotation ±180 degrees and linear translation ±17 inches. The alternate concept rotates the engine mount ±180 degrees and then tranlates +17.0 and -4.0 inches along the Z axis. This alternate concept allows the

guide rails to be considerably shorter than those required to translate ±17 inches, but the engine mount must be rotated nearly 180 degrees in many instances to obtain a very small net translation of the thrust vector. In both carriage concepts, the drive mechanisms are identical. The basic linear mechanism uses a 90-degree permanent magnet stepper motor in conjunction with a gear reduction unit. The output shaft of the gear reduction unit is attached to a roller which is used to reel in or reel out a drive band whose ends are attached to the carriage and whose center portion is wound over a constant force idler roller. The idler roller ensures constant tension in the band as it passes over the drive roller. A similar stepper motor and gear reduction unit are attached to the carriage. The output shaft of this gear reduction unit is attached to a roller which reels in or reels out a band attached to a drum which rotates the engine mount fitting. This mechanism also employs a constant force idler roller to ensure constant tension in the drive band as it passes over the drive roller. The linear translator is such that the carriage is translated 0.005 inch per motor step. This coupled with the 100 step-per-second rate of the motor produces a carriage translation rate of 1/2-inch per second. The rotational mechanism produces a rotation rate of 1/2-degree per second. Both the linear and rotational translator rates are arbitrary (selected as a basepoint only) and can easily be changed if required with modifications to the gear reduction unit.

Straight line translation of the carriage is assured by self aligning V-groove guide rollers as shown in Section B-B of Figure D-17. The guide roller sets are located at four points on the carriage and are guided by the guide rails attached to the spacecraft structure. All motion in both the linear and rotational mechanisms is rolling and consequently no sliding friction exists. The constant force idler roller assures positive motion of the two mechanisms regardless of changes in the bands or mechanisms due to thermal expansion or contraction.

The mechanism is 38.50 inches by 56.50 inches (40.0 inches with alternate carriage) by 3.0 inches. The entire mechanism weighs 12.0 pounds. The concept employing the alternate carriage configuration is estimated to weigh 11.4 pounds. These weights are based on the use of aluminum for all structural members and catalog weights for the stepper motors, gear reduction units, and miscellaneous hardware.

The mechanism concept shown in Figure D-18, (Drawing 5349-8) is a linear-on-rotary approach. The ion engine cluster mount is translated linearly ±17 inches within a guide rail carriage. The guide rail carriage is rotated ±180 degrees relative to the spacecraft. The center of rotation of the guide rail carriage is offset from the theoretical center of gravity longitudinal axis of the spacecraft. This combination of linear-on-rotary motion then allows the resultant thrust vector to be aligned with the space-craft center of gravity. The concept assumes that the center of gravity lies within the limits of the mechanism's travel; a center of gravity shift well
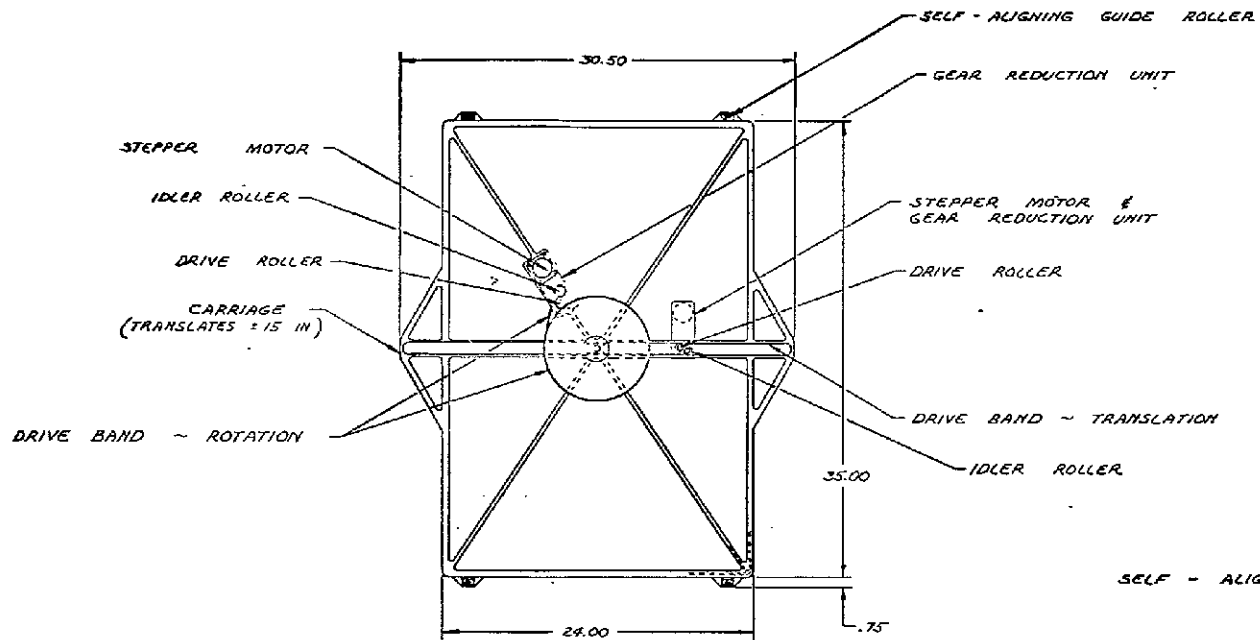
D-41

above the anticipated shift, 1. 5-inch diameter, can easily be accommodated. The five ion engines on the engine mount are allowed to gimbal as in the previously described concepts.

The drive mechanisms for both the linear translation and the rotation are identical units. The linear translation mechanism uses a 90-degree permanent magnet stepper motor in conjunction with a gear reduction unit. This unit is rigidly attached to the guide rail carriage. The output shaft roller of the gear reduction unit is used to reel in or reel out a drive band whose ends are attached to the guideway which is an integral part of the ion engine mount. The center portion of the drive band is wound over a constant force idler roller. The idler roller ensures constant tension in the drive band as it passes over the drive roller. This linear translator mechanism's travel rates are comparable to the previous designs. The concept is estimated to weigh 8. 0 pounds. The translator is 35. 0 inches by 56. 5 inches by 3. 75 inches.

A second rotary-on-linear mechanism, shown in Figure D-19 (Drawing.5349-6), will be described but the concept should not be considered seriously as a solution to the translation problem. The concept utilizes two guide rails rigidly attached to the spacecraft structure. A carriage is translated linearly ±15 inches along the Z axis within the guide rails. A centrally-located fitting on the carriage provides the attach point for the engine cluster mount. This fitting is capable of being rotated ±90 degrees about the center of the carriage. The combination of rotation and linear translation then enables the resultant thrust vector to be aligned with the spacecraft center of gravity. This concept assumes the spacecraft center of gravity to be centrally located on the spacecraft longitudinal axis. In a realistic spacecraft configuration, it is felt that this condition is highly improbable. Most spacecraft experience some center of gravity shifts. This concept assumes zero shift, which is reason for not seriously pursuing a detailed design of the mechanism. The five engines on the engine mount are allowed to gimbal as in the dual-axis linear mechanism depicted in Figure D-15.

Figure D-19 shows two carriage concepts. The first concept is as previously mentioned (rotation ±90 degrees and translation ±15 inches). The alternate concept rotates the engine mount ±180 degrees and then translates a total of 19 inches along the Z axis. This alternate concept allows the guide rails to be considerably shorter in length than those required to translate ±15 inches. In both carriage concepts the drive mechanisms are identical.

The carriage translation rate is 1/2 inch per second. The rotational mechanism produces a rotation rate of 1/2 degree per second. Both the linear and rotational translator rates are selected as a basepoint only and can easily be changed, if required, with modifications to the gear reduction unit.

SELF - ALIGNING GUIDE ROLLER

GEAR REDUCTION UNIT

STEPPER MOTOR

IDLER ROLLER

DRIVE ROLLER

STEPPER MOTOR &
GEAR REDUCTION UNIT

DRIVE ROLLER

CARRIAGE
(TRANSLATES ±15 IN)

DRIVE BAND ~ TRANSLATION

IDLER ROLLER

DRIVE BAND ~ ROTATION

30.50

35.00

24.00

.75

DETAIL A

STEPPER MOTOR

ION ENGINE CLUSTER MOUNT

SELF - ALIGNING GUIDE ROLLER

SPACECRAFT STRUCTURE

CARRIAGE

ENGINE MOUNT ATTACH FITTING
(ROTATES ±90°)

DRIVE BAND ~ ROTATION

3.00

GEAR REDUCTION UNIT

STEPPER MOTOR

SELF - ALIGNING GUIDE ROLLER

CARRIAGE

SPACECRAFT STRUCTURE

GUIDE RAIL

2.50

SECTION B - B

FOLDOUT FRAME #1

FOLDOUT FRAME #2

The translator concept as shown on Figure D-19 is estimated to weigh 12.0 pounds. The estimated weight of the translator utilizing the alternate carriage concept (shown in detail A alternate) is 11.4 pounds. The mechanism is 38.5 inches by 52.5 inches by 3.0 inches. The use of the alternate carriage reduces the overall length to 38.0 inches.

The five mechanism concepts for translating the ion engine cluster resultant thrust vector have several common attractive features. Five of the significant features are:

1. All of the translator concepts are simple mechanisms

2. The concepts employ mechanisms which overcome rolling friction rather than sliding friction.

3. Interchangeability of components within the individual concept mechanisms is at a maximum for minimum spare component requirements

4. Where possible, the area between the spacecraft structure and the engine mount is kept clear for electrical and propellant lines

5. All of the mechanisms utilize off-the-shelf space-proven components and materials

The actuator characteristics of the four feasible mechanism concepts are summarized in Figure D-20. Three configurations are shown which include two configurations each of the dual-axis linear concepts. All of the mechanisms utilize metal band type of actuators with the exception of the second dual-axis linear concept which employs screw actuators. The mechanism parameters are listed in the first column and are grouped as either design criteria, characteristics or considerations. The design criteria parameters are resolution for both linear and rotary motion, motor stepping rates, and spacecraft center-of-gravity shift limitation. The linear resolution for all configurations was assumed to be 0.005 inch per motor step. A rotary resolution of 18 arc seconds per motor step was used for all configurations utilizing rotary motion. In all instances the motor stepping rate was 100 steps per second. A 1.5-inch diameter spacecraft center of gravity shift was allowed in all configurations.

The design characteristics are listed as the mechanism output travel and the actuator slewing rate. The output travel in each instance was sufficient to recover from an engine failure condition, and allowed for travel necessary to compensate for center of gravity shifts. The output travel is given in inches for the linear motion and degrees for the rotary motion.

D-47

Space Division
North American Rockwell

CONFIGURATION / PARAMETERS				
CONCEPT	1	2	3	4
ACTUATOR MECHANISM TYPE	DUAL AXIS LINEAR		ROTARY-ON-LINEAR	LINEAR-ON-ROTARY
ACTUATOR TYPE	METAL BAND	SCREW	METAL BAND	METAL BAND
DESIGN CRITERIA				
RESOLUTION, IN./STEP	0.005 EACH AXIS		0.005	0.005
RESOLUTION, ARC SEC/STEP			18	18
MOTOR STEPPING RATE, STEPS/SEC	100		100	100
CG SHIFT LIMITATIONS, IN.	1.5 DIA		1.5 DIA	1.5 DIA
CHARACTERISTICS				
OUTPUT TRAVEL, IN.	± 12 EACH AXIS		±17	±17
OUTPUT TRAVEL, DEGREES			±180	±180
ACTUATOR SLEWING RATE, IN./SEC	0.5 EACH AXIS		0.5	0.5
ACTUATOR SLEWING RATE, ARC MIN/SEC			30	30
CONSIDERATIONS				
POWER REQUIRED, WATT	15		15	15
WEIGHT, LB	15	17	12	8.5
CONTROL LOGIC	LINEAR TRANSLATION REDUCES COMPLEXITY		CROSS COUPLING INCREASES COMPLEXITY	CROSS COUPLING INCREASES COMPLEXITY
OPERATION (BASED ON WORST CASE TRANSLATION OF THRUST VECTOR (⊕) TO CENTER OF GRAVITY (⊕))				

NOTE: ALL OF THE MECHANISMS EXHIBIT THE FOLLOWING:

1. SIMPLE STATE-OF-ART MECHANISM WHICH OVERCOMES ROLLING FRICTION ONLY.

2. MINIMUM DISTANCE BETWEEN SPACECRAFT AND TRANSLATOR WITH MAXIMUM ACCESSIBILITY FOR WIRES AND PLUMBING LINES.

3. INTERCHANGEABILITY OF COMPONENTS WITHIN EACH MECHANISM CONCEPT.

FOLDOUT FRAME #1

FOLDOUT FRAME #2

Figure D-20. Actuator Mechanisms Study Summary

Actuator slewing rate is a result of the resolution and motor stepping rate. The linear slewing rate was 0.5 inches per second. The rotary rate was 30 arc-minutes per second.

Design considerations are the last group of parameters in the figure. Four considerations are listed: power required, weight, control logic, and operation. The power required for all the mechanisms is less than or equal to 15 watts. The weights varied between configurations by as much as a factor of two. Under control logic considerations, in all configurations employing rotation the control logic is much more complex due to the cross coupling effects. The dual-axis linear concepts do not experience this cross-coupling, and consequently their control logic is less complex. The operation considerations describe how each configuration would move to align the resultant thrust vector with the center of gravity shown. The motion is described as two single motions when in reality both motions would occur simultaneously. The motion described may also be considered a worst case condition.

Figure D-20 shows that even though the dual-axis linear translator mechanisms are not the lightest configurations, they appear to offer more advantages than the configurations employing rotation and linear translation. The dual-axis linear concepts offer more clear area between the spacecraft and the engine mount for electrical and propellant lines. Attitude corrections are less complex with the dual-axis linear concepts than with the other concepts. The distance between the spacecraft structure and the ion engine mount for the dual axis linear concept is less than for the other concepts. It is therefore recommended that a dual axis linear type of translator mechanism be adopted for further study and detail design to provide translation in two orthogonal directions for a solar electric spacecraft ion engine cluster.

APPENDIX D-3. METEOROID PENETRATION DETECTOR/SOLAR
CELL ARRAY INTEGRATION STUDIES AND INDEPENDENT
DETECTOR ARRAY CONCEPT

The solar electric spacecraft mission to the asteoroid belt represents a significant platform for near-term analysis of the asteroids and meteoroid flux which are unobservable from earth. Data obtained by such a mission would permit better resolution of the small particle hazard that will be encountered by outer planet probes during their pass through this region.

The large solar arrays on the solar electric spacecraft represent large surface areas for potential detection of meteoroid impacts. For this reason, it is of primary interest in this study to determine the design feasibility of integrating meteoroid penetration detectors with the substrate on the dark side of the large area solar arrays.

A preliminary investigation of the various types of meteoroid penetration detectors revealed the existence of two candidate detectors. The first is the pressure cell type as flown on the Explorer type of spacecraft. The second type of detector is a capacitor type similar to those used on the Pegasus.

The conceptual designs considered incorporation of the detector panels onto both fold-out and roll-up types of large area solar arrays. The first concept is based on a fold-out array as shown in Figure D-21 (Drawing 5349-10). The Boeing Company type of array was used as representative of a large area fold-out solar array concept. The capacitor type detectors are bonded either directly to the dark side of the substrate or the edge frames of the structure (sections A-A and C-C). Also shown is an exploded view of each concept describing the layered construction of the integrated assembly. Basically, the capacitor type of penetration detector selected consists of a meteoroid penetration sheet (40, 200, and 400 micron aluminum sheets are shown as examples) which is bonded to a 12.6 micron trilaminate mylar dielectric. The last mylar sheet is covered with 0.07 microns of vapor deposited copper. This capacitor then is bonded to the dark side of the solar array.

The detectors on the Pegasus consisted of the capacitors bonded to a combination of flexible and rigid foam. The foam provided structural support for the capacitor as well as protection from damage resulting from meteoroid impact on the rear surface (copper side). However, foam backing was not used on the concepts utilizing the solar array for attachment of the detectors

since the cover glass, cells, and substrate of the solar array panel provide both structural support and rear surface impact damage protection.

Also shown are views of the Langley Research Center pressure cell and the Explorer satellite type of pressure cell detectors attached to the back of the fold-out solar array.

The second concept is based on a roll-up solar array as shown in Figure D-22 (Drawing 5349-13). The roll-up solar array selected as representative of such arrays is the General Electric configuration, presently being developed under contract for JPL/NASA. The capacitor is bonded directly to the dark side surface of the substrate. The only change made to the array structure is the removal of the foamed RTV buttons from the substrate and their addition to the impact surface (aluminum skin) of the capacitor. The buttons serve as cushions between successive layers of solar array in the stowed configuration; no difficulty or degradation in their performance is anticipated in making this change.

To perform a quantitative analysis of the meteoroid penetration detector/solar array integration concepts, it was desirable to configure a third concept. This concept, shown on Figure D-23 (Drawing 5349-14) consisted of a separate meteoroid penetration detector array. The array is an independent deployable structure, shown in the stowed and deployed configurations. The rigid frame structure is adaptable for mounting either capacitor arrays or pressure cell arrays. The detector array is deployed with the panels normal to the ecliptic plane. Rotation of the array during the spacecraft cruise mode enables the detectors to be normal to the anticipated meteoroid impact direction at all times, thus exposing maximum area for meteoroid impacts.

As configured, the array consists of two paddles of three frames each. The detector panels are mounted two to a frame with flexible rubber Lord mounts. The frames are constructed of square tube beryllium and are deployed by torsion springs that are an integral part of the hinges joining adjacent frames. Two such spring hinges are on each frame joint but one is sufficient to successfully deploy the frames. Deployment dampers and locking mechanisms are incorporated into corner fittings on the longitudinal edge members. During boost, the stowed array is held against the spacecraft body by tie-down fittings. The 12-panel array accommodates four 50-by-100 centimeter capacitor panels for each of the three different penetration sheet thicknesses. This size was arbitrarily chosen as a base point and could easily be enlarged without intefering with the payload envelope (as shown in the stowed boost configuration view).

The array structure is also compatible with pressure cell penetration detectors. Either the Langley Research Center pressure cell array (shown in section C-C) or the pressure cells of the type flown by the Explorer series of satellite can be accommodated on the array frames.

Before a recommendation can be made to integrate a particular meteoroid penetration detector with a particular solar array configuration, other aspects affecting performance must be investigated. A cursory investigation of potential problem areas has been performed and will now be discussed. From a materials viewpoint, it appears that no problem exists in bonding the capacitor arrays to both the fold-out and roll-up type of solar array. However, shear stresses within the capacitor structure induced by rolling the capacitor onto the roll-up solar array drum have not been analyzed. A curling problem may also exist in this configuration due to long time storage in the stowed configuration. The most reliable solution to these problem areas would be to perform a ground test on an integrated array. Discussions with General Electric personnel indicate that no major design problems are expected in integrating the capacitor detectors with the roll-up array. It was indicated that the deployment drive mechanism and support boom would require strengthening, the storage drum diameter would probably be enlarged and the retraction tension increased.

At this time no material problems are anticipated with the fold-out solar array configuration with the exception of possible material thickness changes to accommodate the increased weight of the array.

Thermally, the capacitor panels on both the fold-out and roll-up array configurations present no problems to the solar array operating temperature. The array temperature can be maintained well below the limiting temperature (65 C, 150 F) of the array by applying a thermal coating with an emittance value of 0.875 to the aluminum sheet of the capacitor. Obtaining an emittance of 0.875 entails painting the aluminum surface with a black thermal control paint.

The array temperature can thus be maintained at about 40 C (103 F) for the fold-out array with the panels bonded directly to the substrate and 48 C (118 F) with the panels bonded to the frame structure. The fold-out solar array concept with pressure cell detectors operates at 68 C (154 F) with either Langley Research Center or Explorer satellite type cells. If the cells are bonded directly to the substrate the operating temperature drops to 54 C (130 F). The pressure cell/solar array concepts utilize an emittance value of 0.9 which is also obtainable with black thermal control paint. The roll-up solar array/capacitor panel concept is maintained at 43 C (110 F) with the same thermal control paint suggested for the fold-out array.

Of particular interest to the solar array is the electrical problem associated with installing a capacitor on the rear surface of an array. Electrical interactions between the solar array and the capacitors need to be analyzed as well as any problems that may arise from routing the capacitor and solar array wires. At the present time, it appears that sufficient insulation between the solar array and the detector capacitor, in the form of substrate and additional mylar sheets, can be provided. The interaction problem, however, needs to be thoroughly analyzed.

The basic structure of the fold-out and roll-up solar array should be checked to determine compatibility with the additional weight imposed by the detector panels. It has been assumed that the only changes necessary to these structures would be small increases in material thicknesses. The structure of the independent fold-out detector array should also be analyzed. A significant structural problem area can be realized if pressure cell detectors are incorporated into the fold-out solar array, as this structure is very lightweight and near marginal in some areas for supporting only the solar array. Structural problems induced in the roll-up solar array by rolling the capacitors onto the storage drum must also be analyzed.

An additional problem area as yet untouched is that associated with orienting the solar array normal to the meteoroid impact directions. In Figure D-24 it can be seen that all impacts occur on the dark side of the integrated meteoroid penetration detector/solar array before reaching aphelion. After reaching aphelion, however, the impact direction is such that the meteoroids impact the sun side of the array and are consequently not recorded. If the solar arrays are fixed oriented to the spacecraft body the only method by which the detector panels can be maintained normal to the meteoroid impact direction is to reorient the entire spacecraft. This will introduce additional requirements on other spacecraft systems.

The independent meteoroid penetration detector array is always oriented normal to the expected meteoroid impact direction (Figure D-25). Prior to reaching aphelion paddle 1 is partially shielded from impact by the spacecraft ion engine cluster. After reaching aphelion paddle 2 is then partially shielded.

Weights for the concepts discussed have been generated in order to perform a preliminary quantative weight analysis. These weights are presented in Table D-1. The weights given for the capacitor detectors on the roll-up and fold-out arrays are the weights of the detector panels only, exclusive of the weight of the solar array or supporting structure. The

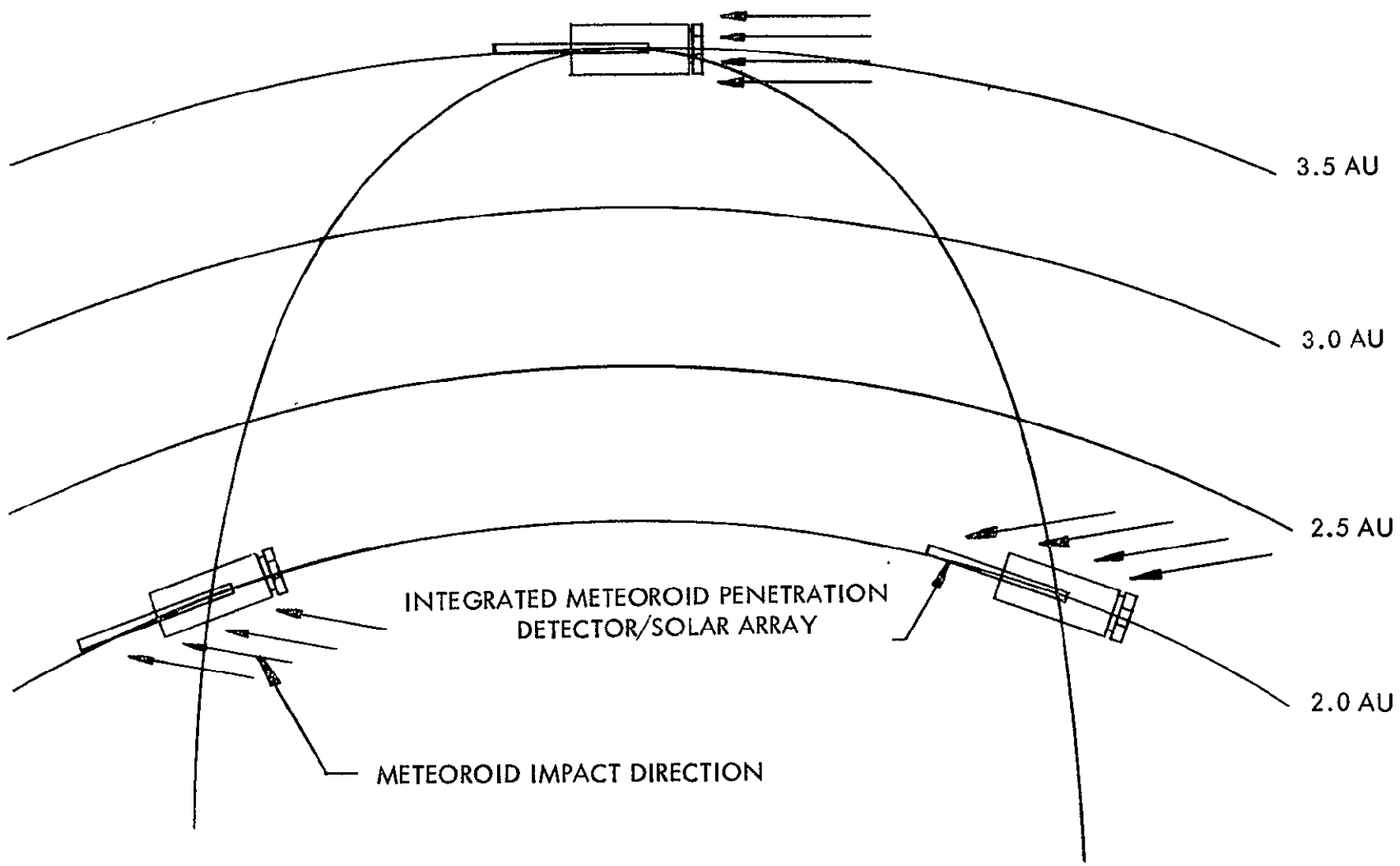Figure D-24. Orientation of Integrated Meteoroid Penetration Detector and Solar Array

3.5 AU

3.0 AU

2.5 AU

2.0 AU

INTEGRATED METEOROID PENETRATION
DETECTOR/SOLAR ARRAY

METEOROID IMPACT DIRECTION

Space Division
North American Rockwell

PADDLE 2

PADDLE 1

3.5 AU

3.0 AU

2.5 AU

SOLAR ARRAY

2.0 AU

METEOROID IMPACT DIRECTION

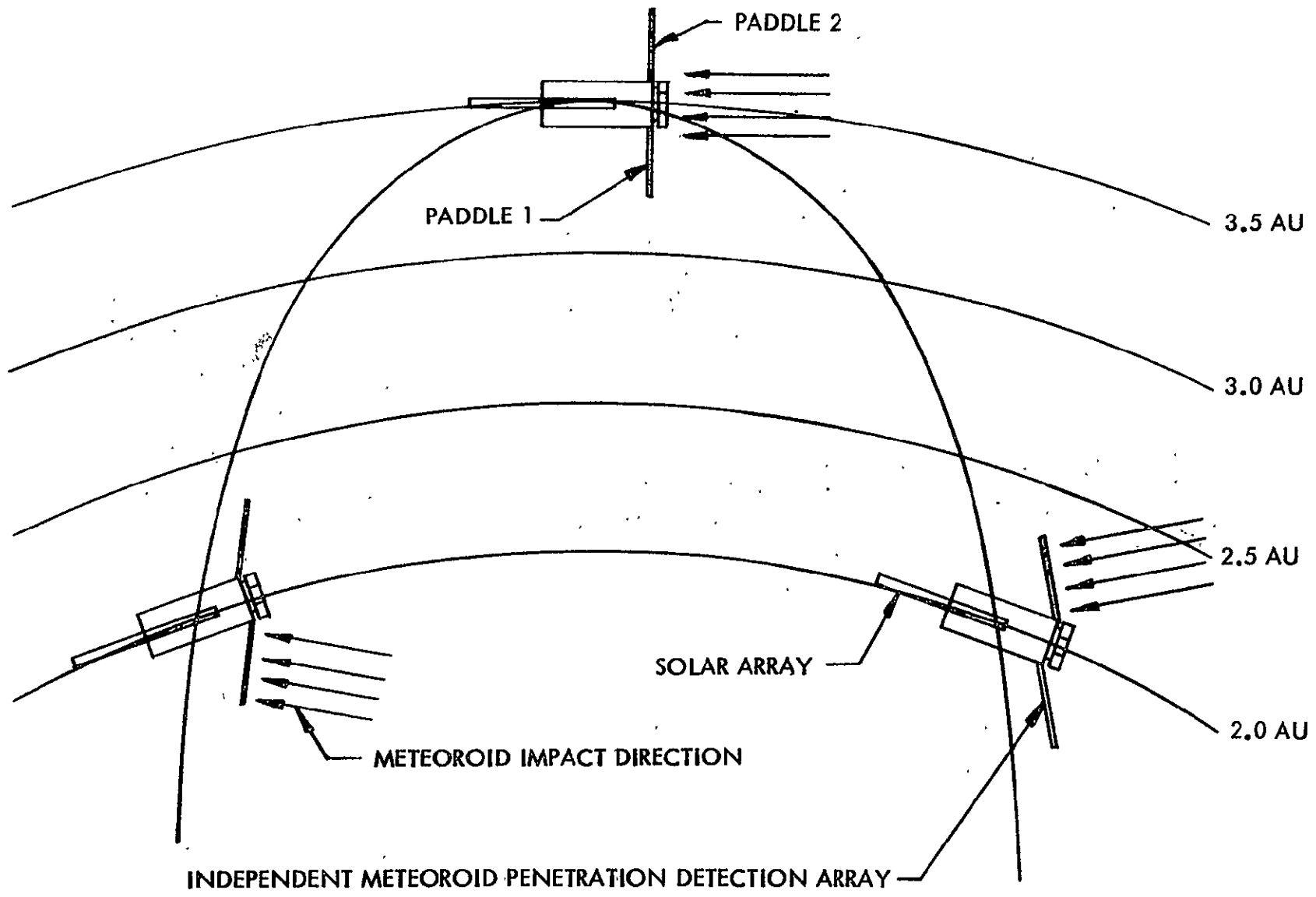INDEPENDENT METEOROID PENETRATION DETECTION ARRAY

Figure D-25. Orientation of Independent Meteoroid Penetration Detector Array

Table D-1. Integrated Meteoroid Penetration Detector/Solar Array Weight Penalty Summary

Configuration Concept[1]	Fold-Out Solar Array		Roll-Up Solar Array
Solar Array/Capacitor Panel	Capacitor panels bonded directly to substrate (Figure D-21)	Capacitor panels bonded to frame structure edges only (Figure D-21)	Capacitor panels bonded directly to substrate (Figure D-22)
40 micron target sheet[2]	0.285 kg/m^2 0.058 lb/ft^2	0.155 kg/m^2 0.032 lb/ft^2	0.285 kg/m^2 0.058 lb/ft^2
200 micron target sheet[3]	0.742 kg/m^2 0.152 lb/ft^2	0.612 kg/m^2 0.125 lb/ft^2	0.742 kg/m^2 0.152 lb/ft^2
400 micron target sheet[4]	1.305 kg/m^2 0.267 lb/ft^2	1.175 kg/m^2 0.241 lb/ft^2	1.305 kg/m^2 0.267 lb/ft^2
Solar Array/pressure Cells	Bonded to substrate	Not bonded to substrate	
Langley Research Center Pressure cell	5.254 kg/m^2 1.076 lb/ft^2	5.254 kg/m^2 1.076 lb/ft^2	N/A
Explorer Satellite Pressure cell	7.239 kg/m^2 1.483 lb/ft^2	7.239 kg/m^2 1.483 lb/ft^2	

Independent Meteoroid Penetration Detector Array[5]
(Figure D-23)

Capacitor Detector Array	2.268 kg/m^2 0.464 lb/ft^2
Detector Only	1.266 kg/m^2 0.259 lb/ft^2
Pressure Cell Array (Langley cell)	6.198 kg/m^2 1.269 lb/ft^2
Detector Only	5.254 kg/m^2 1.076 lb/ft^2
Pressure Cell Array (Explorer cell)	9.766 kg/m^2 2.000 lb/ft^2
Detector Only	7.239 kg/m^2 1.483 lb/ft^2

[1] Weight penalty is exclusive of solar array weight
[2] 40 micron (0.0015 in.) is 2024-T3 aluminum
[3] 200 micron (0.008 in.) is 2024-T3 aluminum
[4] 400 micron (0.016 in.) is 1100-S aluminum
[5] Array weight includes structure, attachment and deployment hardware

independent array weight is broken down into weights for both the structure and the detector panels. The weight of an independent capacitor detector array (2.27 kg/m^2, 0.46 pounds/ft²) compared to that of bonding only the 400 micron (16 mil) capacitor detectors to the solar array substrate (1.31 kg/m^2, 0.27 pound/ft²) differs by a factor of 1.7 to 1.

A meteoroid penetration detector design considerations summary is presented in Table D-2. The potential problem areas previously discussed have been tabularized for convenient comparison.

It is recommended that further investigations in the area of integrating capacitor-type penetration detectors with the roll-up solar arrays be conducted to ensure concept feasibility.

Table D-2. Meteoroid Penetration Detector Design Considerations Summary

Design Factors \ Configuration Concept	Integrated Fold-out Solar Array/Capacitor Panels	Integrated Fold-out Solar Array/Pressure Cells	Integrated Roll-up Solar Array/Capacitor Panels	Independent Array/ Capacitor Panels	Independent Array/ Pressure Cells
Structural	Solar array structure requires strengthening Possible thermal distortion of structure Intermediate support of capacitor panel bonded to edge frame may be required	Solar array structure requires strengthening Increased weight could require structural redesign Possible thermal distortion of structure	Strengthen deployment boom Possible increase in stowage drum diameter Retraction tension increased Possible capacitor edge curling Possible shear stresses in capacitor when stowed	Requires sizing of structural members Possible thermal distortion of structure Array orientation mechanism may be required New appendages required	Requires sizing of structural members Possible thermal distortion of structure Array orientation mechanism may be required New appendages required
Thermal	Solar cell temperature 40 C (103 F) with capacitor bonded to substrate Solar cell temperature 48 C (118 F) with capacitor bonded to edge frames	Solar cell average temperature 54 C (130 F) with detector bonded to substrate, thermal gradients exist which influence solar cell performance Solar cell temperature 68 C (154 F) with detector above substrate	Solar cell temperature 43 C (110 F)		
Material	Potential problem in bonding capacitor to edge frames	Potential problem in bonding of detectors to substrate	Possible capacitor edge curl and bending		
Electrical	Possible interaction between solar cells and capacitors Routing of wires and connection of capacitors Potential solar cell efficiency decrease No access to substrate for repair of solar cells	Routing of wires and connection of detectors Solar cell efficiency decrease No access to substrate for repair of solar cells in bonded concept	Possible interaction between solar cells and capacitors Connection of capacitors and wire routing Use of additional slip rings versus coiled wire bundle No access to substrate for repair of solar cells		
Operational	After aphelion most impacts occur on solar cell side (sun side)	After aphelion most impacts occur on solar cell side (sun side)	After aphelion most impacts occur on solar cell side (sun side)	Potential interference with spacecraft stabilization and control	Potential interference with spacecraft stabilization and control

Solar cell operating temperature without meteoroid detectors is 40 C (103 F) at 1 AU